# Analysis and Measurement of Horn Antennas for CMB Experiments

**Ian Mc Auley (M.Sc. B.Sc.)**

A thesis submitted for the Degree of

**Doctor of Philosophy**

**Maynooth University Department of Experimental Physics,**

**Maynooth University,**

**National University of Ireland Maynooth,**

**Maynooth, Co. Kildare,**

**Ireland.**

**October 2015**

Head of Department

**Professor J.A. Murphy**

Research Supervisor

**Professor J.A. Murphy**

# Abstract

In this thesis the author's work on the computational modelling and the experimental measurement of millimetre and sub-millimetre wave horn antennas for Cosmic Microwave Background (CMB) experiments is presented. This computational work particularly concerns the analysis of the multimode channels of the High Frequency Instrument (HFI) of the European Space Agency (ESA) Planck satellite using mode matching techniques to model their farfield beam patterns. To undertake this analysis the existing in-house software was upgraded to address issues associated with the stability of the simulations and to introduce additional functionality through the application of Single Value Decomposition in order to recover the true hybrid eigenfields for complex corrugated waveguide and horn structures.

The farfield beam patterns of the two highest frequency channels of HFI (857 GHz and 545 GHz) were computed at a large number of spot frequencies across their operational bands in order to extract the broadband beams. The attributes of the multimode nature of these channels are discussed including the number of propagating modes as a function of frequency. A detailed analysis of the possible effects of manufacturing tolerances of the long corrugated triple horn structures on the farfield beam patterns of the 857 GHz horn antennas is described in the context of the higher than expected sidelobe levels detected in some of the 857 GHz channels during flight. Additionally the pre-flight measurements of the flight horns and qualification horn are analysed in detail which verifies the multimode nature of the horns.

This computational work is complemented by a novel approach to the measurement of millimetre-wave antennas using digital holographic techniques particularly with the location of their phase centres in mind. The measurement at 100 GHz of a horn antenna specially designed for future CMB polarisation experiments is presented. Finally some additional applications of millimetre-wave holography are discussed.

# Acknowledgements

# Contents

# Chapter 1 Introduction

The research described in this thesis is concerned with the modelling and laboratory test measurement of novel horn antennas for Cosmic Microwave Background (CMB) experiments. The computational modelling work involved improvements and upgrading of pre-existing in-house software for more realistic simulations of the sub-millimetre multimode horn antennas of the high frequency channels of the European Space Agency (ESA) Planck satellite mission using mode-matching techniques. These were employed in the analysis of pre-launch laboratory test measurements of the flight horns to understand the actual in-flight spillover beams on the sky. An application of millimetre-wave holography was applied in the laboratory verification of specially designed profiled smooth walled horns for future CMB polarisation experiments. An experimental setup was actually developed in the Experimental Physics Laboratories at Maynooth University to test W-band (75-110 GHz) antennas for such applications using digital holographic techniques to recover the amplitude and phase of the beams from the antennas. The work described in this thesis was in general undertaken by the author and where others were involved is made clear in the text.

This chapter serves to outline the scientific motivational background for the ESA Planck mission and future proposed space and ground based CMB experiments. This entails a brief summary of the current standard model of Cosmology with a short history and discussion of the Cosmic Microwave Background (CMB). These provide context for the goals and achievements of the Planck mission in particular. An overview of the Planck satellite includes the main elements of the satellite payload comprising the optics, the Low Frequency Instruments (LFI), and the High Frequency Instruments (HFI). Work relating to the multimode channels of HFI is described in Chapters 3, 4, and 5 while chapter 6 is concerned with the novel experimental holography set-up for verifying a special horn design for future CMB space missions.

# 1.1 Cosmology and the Cosmic Microwave Background

The Cosmic Microwave Background (CMB) is often referred to as a relic of the Big Bang. Just after the Big Bang when the universe was much smaller and denser than it is today its temperature was in excess $10^6$ K. The average photon energy in the thermal distribution would have been more than sufficient to ionise hydrogen (or helium) atoms, as only an energy 13.6 eV ($\approx 5 \times 10^4$ K) is needed to free an electron from the ground state of hydrogen for example, implying that atoms could not exist at this time. Thus, the universe was an ionised plasma consisting of a primordial soup of free nuclei, electrons, and photons. The mean free path of the photons was short as they interacted strongly with free electrons via Thomson scattering. As the universe expanded and cooled, the photons lost energy until they were no longer able to ionise any atoms that formed. This era of stable atom formation is known as "recombination" (Figure 1-1). Since neutral hydrogen atoms had a smaller scattering cross-section than free electrons the mean free path of the photons increased. Then once the energy of the photons dropped sufficiently low the universe began to become transparent as the photons could no longer interact with the hydrogen or helium atoms forming and there were fewer free electrons present [Liddle,2003]. This process is known as decoupling and the photons began to travel less impeded through the universe.

The temperature of the universe at this time can be estimated from a knowledge of the degree of ionisation of a plasma which depends on temperature and the ionisation energy of the atoms from the Saha ionisation equation. It has been deduced that the temperature of the universe was in the region of 3,000~4,000 K at the time of decoupling (when the number of free electrons had dropped to 50%). As the universe has since continued to expand, and thus cooled further, these photons are now observed at much longer wavelengths which are equivalent to a temperature of 2.72548 ± 0.00057 K [Fixsen, 2009]. These photons are what we call the CMB and have travelled unimpeded for over 13.8 billion years with their wavelengths being

stretched by the cosmological expansion of space. By observing the CMB we can thus map the sky at the era of decoupling about $3.8 \times 10^5$ years after the Big Bang. This map is of what is referred to as the "surface of last scattering" which is a sphere with a radius of the order of 13.8 billion light years centred on us (this radius depends on the cosmological model) which is far enough away that the CMB photons which last interacted with matter at decoupling are only reaching us now.
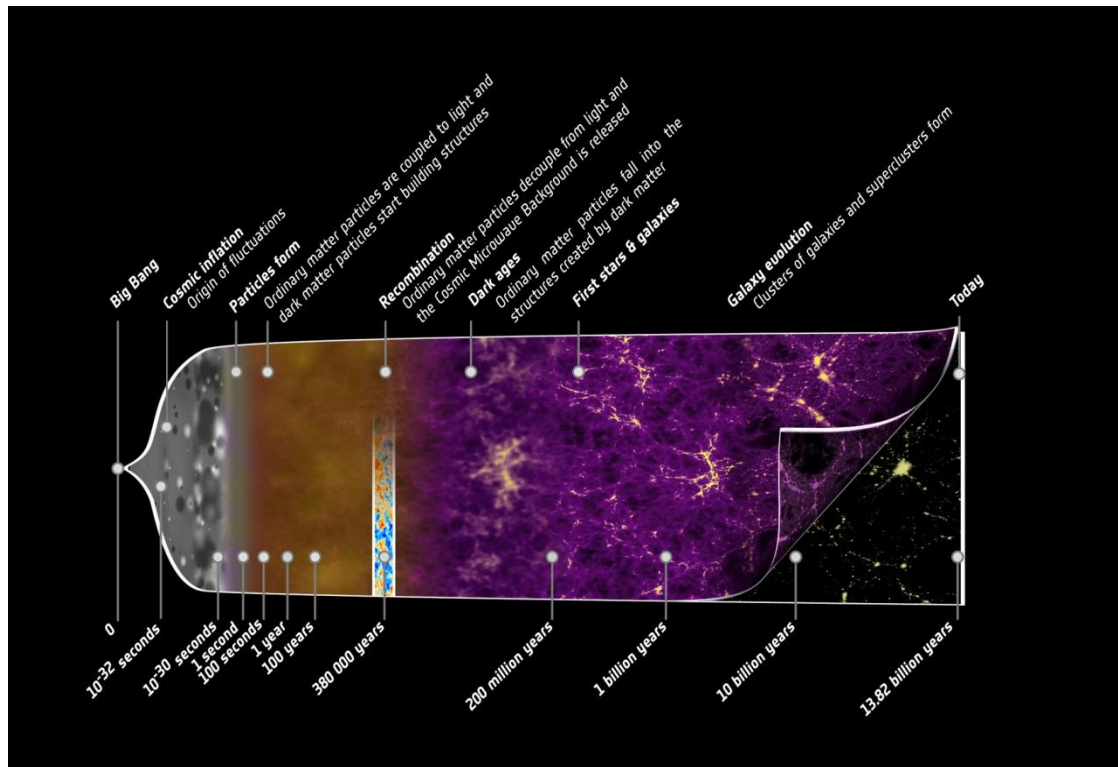


**Figure 1-1: A visual representation of the history of the universe from the Big Bang to the present day [ESA, 2015]**

## 1.2 Early CMB Research

The CMB was discovered by Arno Penzias and Robert Wilson in 1964 when they were unable to filter noise from their microwave antenna signal [Penzias & Wilson, 1965]. They encountered this noise at the low level of around $3.5 \pm 1.0$ K wherever in the sky they pointed their antenna. Having ruled out all possible other sources they concluded that this background noise must be coming from outside our galaxy and possibly be cosmological in nature. They were put in touch with Robert

Dicke who was preparing his own experiment to search for just such a background signal to confirm his own theoretical work on the Big Bang. He was able to confirm Penzias and Wilson's results and conclude that they had indeed detected the Cosmic Microwave Background radiation from the Big Bang [Dicke, 1965].

The current cosmological model of an expanding universe can be traced back to Alexander Friedmann who first proposed a universe which could either expand or contract in 1922 [Friedman, 1999]. His equations fitted with Einstein's theory of General Relativity providing a new perspective as they were inconsistent with a static universe without the addition of an adhoc "cosmological constant". In 1927 the concept of an expanding universe was furthered by Lemaître who proposed that the rate at which galaxies recede from each other is proportional to the distance between them.

$$v = H_0 d \,, \tag{1.1}$$

where $v$ is the velocity at which the galaxy is moving away from the observer, $d$ is the distance from the observer to the galaxy, and $H_0$ is a constant now known as the Hubble's constant. In fact equation 1.1 is known as Hubble's Law after Edwin Hubble who independently proposed the equation after measuring the distances to 22 nearby galaxies and the redshifts of their spectra [Hubble,1929]. This verification by Hubble of the concept of an expanding universe led Lemaître to propose the 'theory of the primeval atom' or the Big Bang Theory as it is now known. In fact the comological constant, abandoned for many years after Hubble's work, has now been reintroduced as it appears that the universe is actually accelerating as it expands rather than slowing down (this is due to what is called "dark energy" but not understood as yet).

This theory was consolidated in 1948 by George Gamow and Ralph Alpher who outlined how the present abundance of fundamental elements in the universe, that is hydrogen and helium, could be explained by reactions triggered by the Big Bang [Alpher, Bethe & Gamow, 1948]. These basic elements were formed when sub-atomic particles fused under high temperatures and pressures during the first few seconds just after the Big Bang. Fred Hoyle showed how the heavier elements were formed at a later stage of the universe's evolution in early stars by detailed theoretical work on reaction rates for nuclear fusion in stellar cores [Hoyle,1946]. Gamow

additionally predicted a unique blackbody distribution for the big bang radiation intensity as a function of wavelength, based on the universe being in thermal equilibrium before decoupling as the mean free path of photons were so short. This was expanded on by Alpher and Herman in 1948, who remarked that as the universe expanded the temperature would drop and the wavelength of the photons would be proportionally redshifted by the expansion of space, and that these photons would now appear to arrive from every direction in space with a constant temperature of approximately 5 K [Alpher & Herman,1948, 1949].

Robert Dicke, who was unaware of the previous theoretical work done in the area, independently derived a prediction for the temperature of the CMB radiation at approximately 20K. Dicke collaborated with David Todd Wilkinson and Peter G. Roll to invent the differential microwave radiometer (Dicke radiometer) to search for the CMB signal. He was beaten to the punch by Penzias and Wilson who, as mentioned above, accidentally stumbled upon an isotropic background signal which pervaded all of space and that could only be produced by a $3.5 \pm 1.0$ K blackbody source [Penzias & Wilson, 1965]. After consultations with Dicke and his subsequent verification of the signal [Dicke, 1965] it was concluded that this isotropic background signal must be the predicted CMB radiation, thus validating the Big Bang theory and paving the way for modern cosmology and its insight into the early universe.

# 1.3 CMB Anisotropies

Although the Big Bang theory provides an explanation for the formation of basic elements and the blackbody spectrum of the CMB, it does leave some questions unanswered. For example, our present day universe has structure with matter clumped together into galaxies, galactic clusters, and super-clusters but the Big Bang model does not provide an explanation of the origin of this structure. The fact that this matter appears redshifted means that the universe is expanding but again the Big Bang model cannot provide an answer as to why. Another important problem is the 'horizon problem', which is that when we look at two points on the sky both regions appear to have the same temperature even when they are too far apart apparently to have been in

contact at any time and thus achieve thermal equilibrium. It is clear that the Big Bang theory alone cannot explain the current state of the universe and additions to the theory are needed.

The Lambda-CDM model came about in the 1990's as cosmologists sought to resolve these issues, and reconcile theory and observations [Frieman, 2008]. This model is the simplest model of the universe that provides a reasonable match to observations. The model assumes the existence of cold dark matter (CDM) and uses a cosmological constant, $\Lambda$, which is equivalent to the energy density of empty space (dark energy) that appears to be causing the current acceleration of the expansion of the universe. The horizon problem was resolved by so called inflationary theory which proposes that shortly after the Big Bang there was a brief period of exponential expansion which lasted about $10^{-32}$ seconds. Regions which were in contact became separated by this rapid expansion and now appear isolated, thus explaining how they have the same temperature [Guth,1981]. However, the universe is not isotropic on all scales and different kinds of anisotropies are visible in the CMB at various levels. A temperature dipole anisotropy of $3.5 \pm 0.6$ mK was discovered in the CMB in 1977, [Smoot, 1977], due to the Doppler effect as a result of our motion relative to the CMB (the "rest frame" of the universe), which red or blue shifts the CMB with respect to us. Even smaller fluctuations at the $10^{-5}$ level in the temperature map of the CMB were discovered in 1992 by the COBE-DMR mission [Smoot, 1992]. These fluctuations were predicted due to primordial quantum fluctuations in the very early universe that were then amplified as the universe expanded (e.g. [Carroll, 2006]).
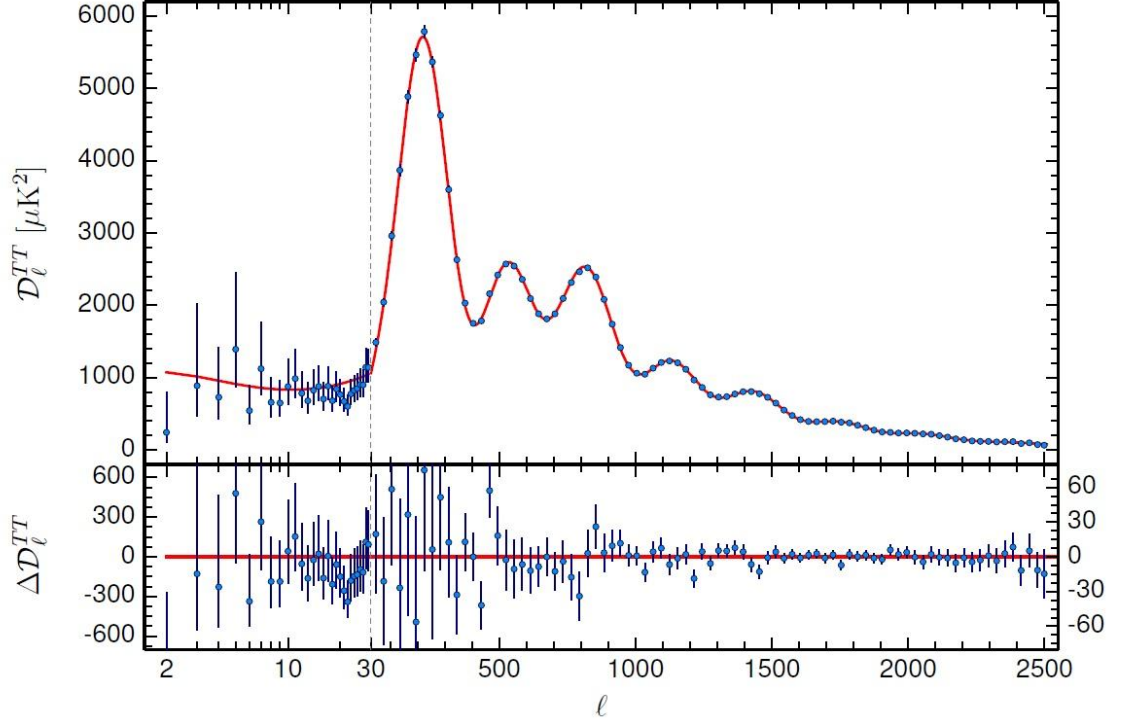
**Figure 1-2: The CMB angular power spectrum as measured by Planck [Planck Collaboration, 2015a].**

The CMB power spectrum shown in Figure 1-2 describes the temperature fluctuations as a function of the scale on which they were measured [Planck Collaboration, 2015a]. As matter (electrons) and photons were coupled before recombination fluctuations in the density of matter were imprinted onto the CMB as temperature fluctuations, with the slightly higher density regions appearing as slightly cooler as photons lose more energy escaping from these regions due to realitvistic effects. A multipole moment of $l = 0$ corresponds to an angular scale of $360^o$, i.e. the whole sky, over which the CMB temperature is isotropic. At $l = 1$, angular scale $180^o$, the dipole fluctuation due to our motion is observed. It is thus at $l = 2$, angular scale $90^o$, that primordially relevant information begins to be revealed (hence the plot in Figure 1-2 includes multipole moments of $l = 2$ or greater only). The largest peak in the power spectrum is observed at an angular scale of $1^o$ and beyond this the fluctuations decease with increasing multipole moments (or with decreasing angular scale). These peaks are due to acoustic waves in the early universe set up by radiation pressure acting as a restoring force against over-density in a region caused by primordial fluctuations. Overall the temperature anisotropies vary by as little as one part in $10^5$ from one point on the sky to another, nonetheless the fact that they exist means that the universe was not completely isotropic prior to inflation, and the

refinement of the measurements of these peaks constrain the parameters of the Lambda-CDM model and so are critical to observe.

## 1.3.1 CMB E-mode and B-mode Polarisation

In addition to the temperature power spectrum, the polarisation of the CMB photons also provides information about the early universe. The CMB photons were polarised by Thompson scattering at the time of recombination. The resultant field can be decomposed into scalar E-modes, which are curl-free or non-rotational, and tensor, rotational or curl-induced, E-modes and B-modes. Energy density fluctuations in the primordial plasma (resulting in slightly hotter and colder regions) cause velocity distributions within the plasma. The fluid velocity from hot to colder regions cause a blueshift of the photons, resulting in quadrupole anisotropy. E-modes were created by Thompson scattering of this quadrupole (see Figure 1-3). As density fluctuations also generated the temperature anisotropies, by measuring E-mode polarisation this non-rotational velocity field as it was at recombination is reproduced. This E-mode polarisation field is much weaker than that of temperature anisotorpies and hence more difficult to measure. However due to the intrinsic relationship between temperature and E-mode polarisation, cross power spectra can be generated to refine the expectations of both [Wayne, 1997]. The scalar E-modes were first detected by the DASI experiment, a ground based experiment, [Carlstrom, 2003] and confirmed by the WMAP satellite mission [Spergel, 2003]. The QUaD experiment, the follow up to DASI, provided the most sensitive measurements of the E-modes before the measurements made by the Planck mission (Figure 1-4) [QUaD collaboration, 2009][ Planck Collaboration, 2015a].
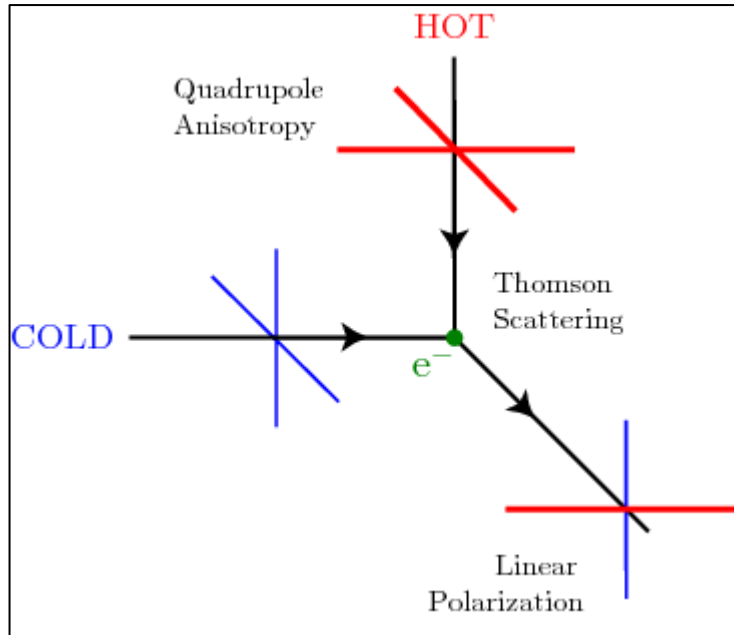
**Figure 1-3: Diagram showing how Thompson scattering of photons from hot and cold regions results in E-mode (linear) polaristion.**

Gravitational waves in the early universe are predicted to have produced both B-mode and E-mode polarisation both with the same power levels although much lower than the scalar E-modes. Of particular interest are the B-modes produced by the gravitational waves caused by the rapid expansion of the universe during the inflation era. The detection of these B-modes in the CMB would cement inflationary theory as a cornerstone of cosmology. To date primordial B-modes have not yet been detected however ground based (QUaD & BICEP) and space experiments have allowed an upper limit to be placed on the tensor-to-scalar ratio, $r$, of polarisation modes [BICEP2/Keck & Planck Collaboration, 2015]. The tensor-to-scalar ratio, $r$, relates the ratio of tensor E-modes and B-modes (produced by gravitational waves) to scalar E-modes (produced by energy density fluctuations). The Far Infrared Space Optics Group at Maynooth University Department of Experimental Physics is involved in the proposed QUBIC experiment, which will search for B-modes [Battistelli, 2011]. In chapter 6 of this thesis the measurement of a specially designed horn for a future B-mode experiment on a space platform is described. In general the detection of B-modes is much more challenging from a technical viewpoint [Wayne, 1997].
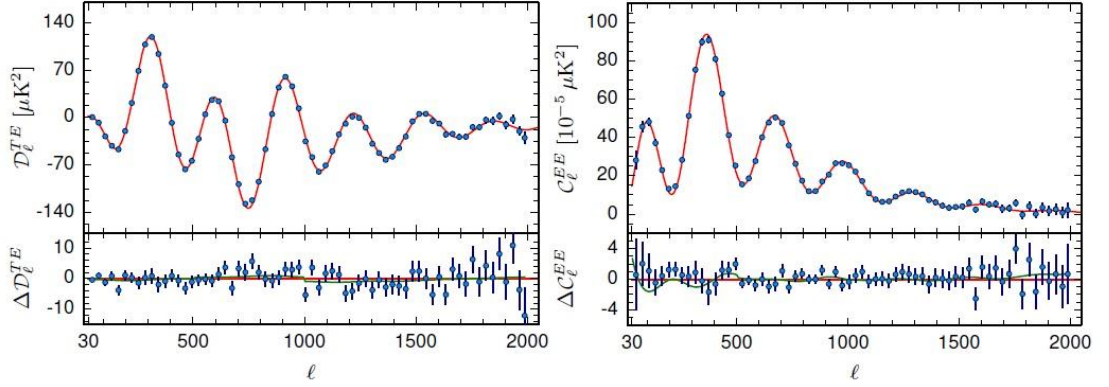
**Figure 1-4: Frequency-averaged TE (left) and EE (right) spectra. The theoretical TE and EE spectra are plotted in the upper panel of each plot. Residuals with respect to this theoretical model are shown in the lower panel in each plot. The green lines in the lower panels show the best-fit temperature-to-polarisation leakage model, fitted separately to the TE and EE spectra. [Planck Collaboration, 2015a]**

# 1.4 CMB Experiments

Since its discovery by Penzias and Wilson in 1964 numerous observations of increasing sensitivity have been made of the CMB by both ground based and space based experiments. Ground based experiments set increasingly stricter limits on the primary CMB anisotropy, the dipole due to our motion through the universe, until the first space based experiment, RELIKT-1, set a definitive upper-bound in 1983. In 1989 NASA launched its first CMB mission COBE, the COsmic Background Explorer, which confirmed the primary anisotropy and measured the blackbody distribution of the CMB [Smoot, 1992]. Low-level, large-scale anisotropies were also discovered in the data recovered at the telescope's angular resolution of only $7^{\circ}$. The Cosmic Anisotropy Telescope (CAT) was the first experiment to measure small-scale structure in the CMB in 1995 [Baker, 1999]. In 1998 the BOOMERang experiment (Balloon Observations of Millimetre Extragalactic Radiation and Geomagnatic) was flown over Antarctica and measured the CMB with a 10′ resolution. It provided the first high fidelity maps of the CMB anisotropies on small scales and the first accurate measurement of the first three peaks of the angular power spectrum predicted beyond $1^{\circ}$ [Netterfield,2008].

The first measurement of the polarisation of the CMB was made by the DASI (Degree Angular Scale Interferometer) a ground based experiment in Antarctica and

was found to be an order of magnitude weaker than the temperature fluctuations [ Kovac, 2002]. Launched in 2002, WMAP (Wilkinson Microwave Anisotropy Probe) mapped the CMB over the whole sky at the same resolution as BOOMERang providing a improved map of the temperature anisotropies and accurate measurements of the CMB polarisation. The QUaD experiment provided the most sensitive measurements of the polarisation of the CMB prior to the measurements made by the Planck mission [QUaD collaboration, 2009]. Figure 1-5 illustrates the improvement in measurements of the CMB from first detection by Penzias and Wilson to COBE and then WMAP showing the all-sky maps of the temperature fluctuations.
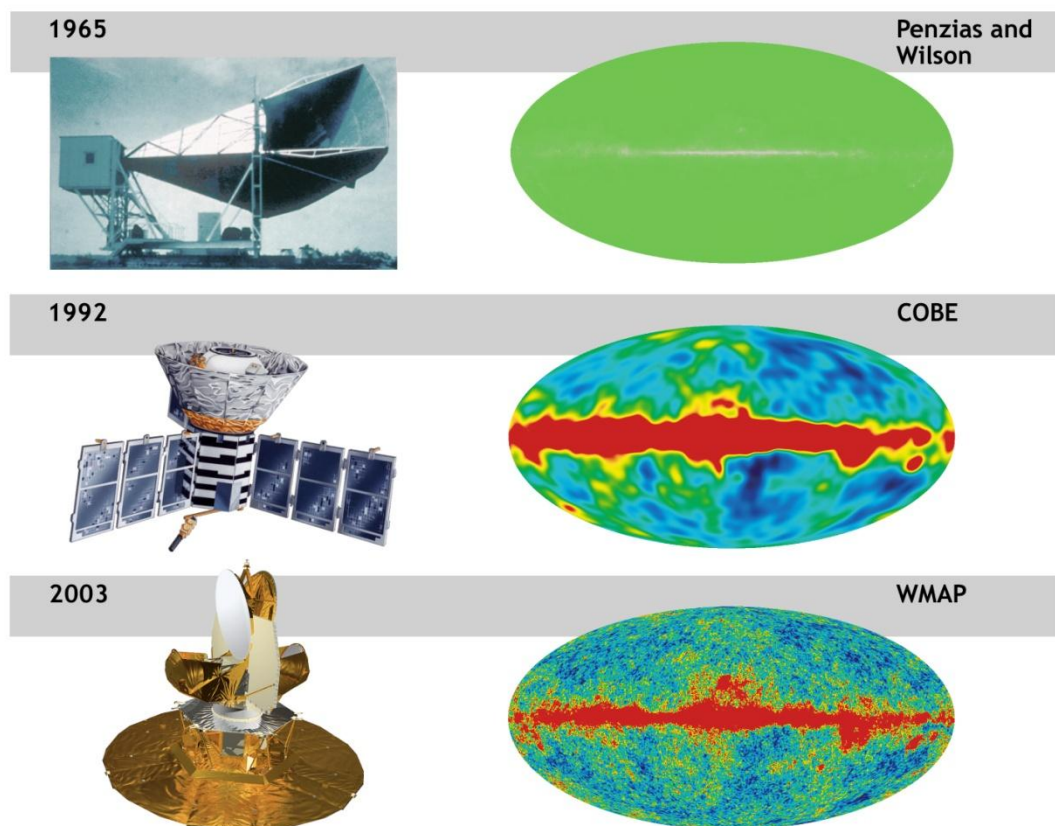


**Figure 1-5 : Top the first measurement of the CMB by Penzias and Wilson measuring an almost perfect blackbody 3K source in all directions; Middle The improved measurement by COBE in which anisotropies are visible; Bottom the measurement made by WMAP which had increased resolution over COBE. Credit: NASA/JPL-Caltech/ESA**

ESA Planck satellite mission was launched in 2009 with the aim of making the highest resolution maps so far of the spatial anisotropies of the temperature of the CMB [Planck Collaboration, 2014a]; an overview description of the Planck satellite is provided in the next section of this chapter. The full sky map of the temperature anisotropies of the CMB made by Planck is shown in Figure 1-6. A comparison of the

resolution of Planck, COBE and WMAP is shown in Figure 1-7 and the evolution of accuracy of the measurement can be clearly seen as each mission provides a more detailed map than the last one with higher spatial resolution. Planck mapped the sky with an angular resolution 2.5 times that of WMAP and with greater sensitivity. In addition to making measurements of the temperature anisotropies both WMAP and Planck also recorded the polarisation characteristics of the CMB photons incident on its detectors. A visualisation of the polarisation is shown in Figure 1-8 where the texture indicates the direction of the polarisation. The patterns seen in the texture are characteristic of 'E-mode' polarisation, which is the dominant type for the CMB. As previously mentioned in the last section, while Planck did not definitively detect B-modes when combined with results from BICEP it did refine the upper limit to be placed on the tensor-to-scalar ratio. A large number of experiments are now focused on the detection of the B-mode polarisation signal and a more extensive list of CMB experiments is provided for reference in Appendix A.
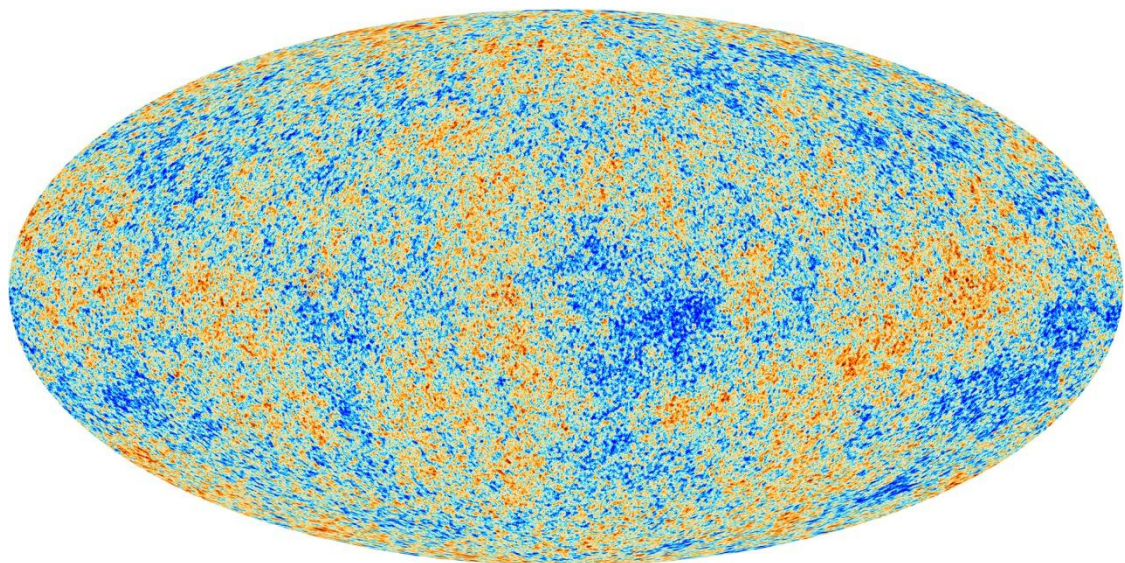


**Figure 1-6 : The anisotropies of the Cosmic microwave background (CMB) as observed by Planck. Credit ESA. [Planck Collaboration, 2014a]**
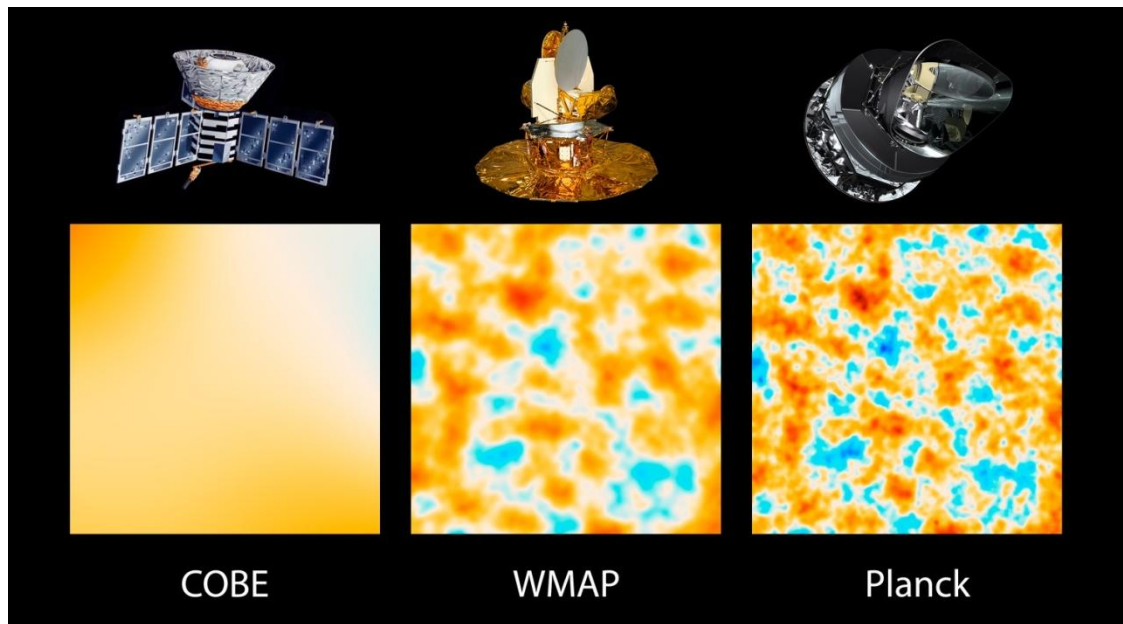
**Figure 1-7 : Close up of the same part of the CMB showing the increse in resolution of the anisotropies with sucessive generations of experiments from NASA's COBE and WMAP to ESA's Planck. Credit: NASA/JPL-Caltech/ESA**
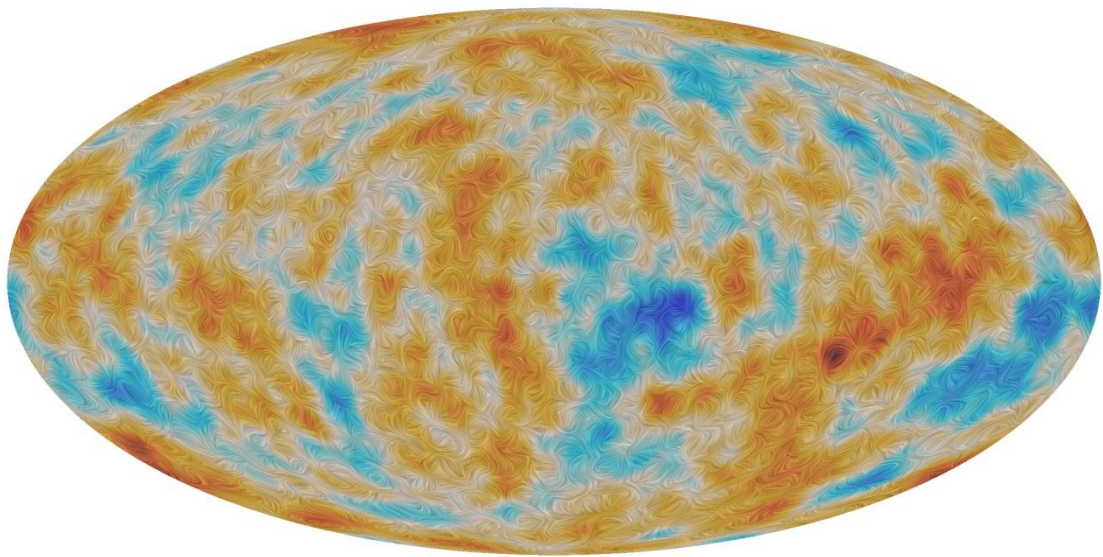


**Figure 1-8: A visualisation of the polarisation of the Cosmic Microwave Background, or CMB, as detected by ESA's Planck satellite over the entire sky. The colour scale represents temperature differences in the CMB, while the texture indicates the direction of the polarised light.  Credit ESA.**

# 1.5 Submillimetre Foreground

In to order obtain the temperature anisotropy and polarisation maps shown in the last section, Figure 1-6 and Figure 1-8 , the CMB must first be disentangled from signals produced by foreground sources between us and the surface of last scattering (see Figure 1-9). The Planck satellite, described in detail in the next section, had a number of frequency channels dedicated to measuring foreground sources for this purpose. While the primary goal was to remove these foreground sources from the CMB signal in the process these channels also provided a wealth of new information about the foreground sky which was highly valuable in its own right, in particular for Galactic science. A plot of the contributions of different kinds of foreground sources as a function of frequency (relative to the CMB signal) is shown in Figure 1-9. At frequencies below approximately 30 GHz synchrotron and free-free radiation are larger than CMB signal while at frequencies above approximately 200 GHz it is swamped by the thermal dust emission. The CMB dominates over the foreground sources in a window between these two frequencies which is therefore the best range in which to observe it [Planck Collaboration, 2014a].

There are four primary sources of diffuse Galactic emissions which contaminate the CMB signal: synchrotron, free-free, spinning dust, and thermal dust. The synchrotron radiation (see Figure 1-9) is produced when relativistic cosmic rays are accelerated in interstellar magnetic fields and the excited emissions are mainly in the Galactic plane [Smoot,1999]. This radiation dominates at lower frequencies less than 30 GHz but falls off at higher frequencies and towards the THz region it adds little to the foreground signal. Free-free emission, or Bremsstrahlung, arises from hot electrons in diffuse interstellar clouds that have been scattered by Galactic ultra-violet radiation. It has a similar spectral profile to synchrotron radiation in that it contributes to the foreground mostly at low frequencies and then also falls off towards the THz region (Figure 1-9).
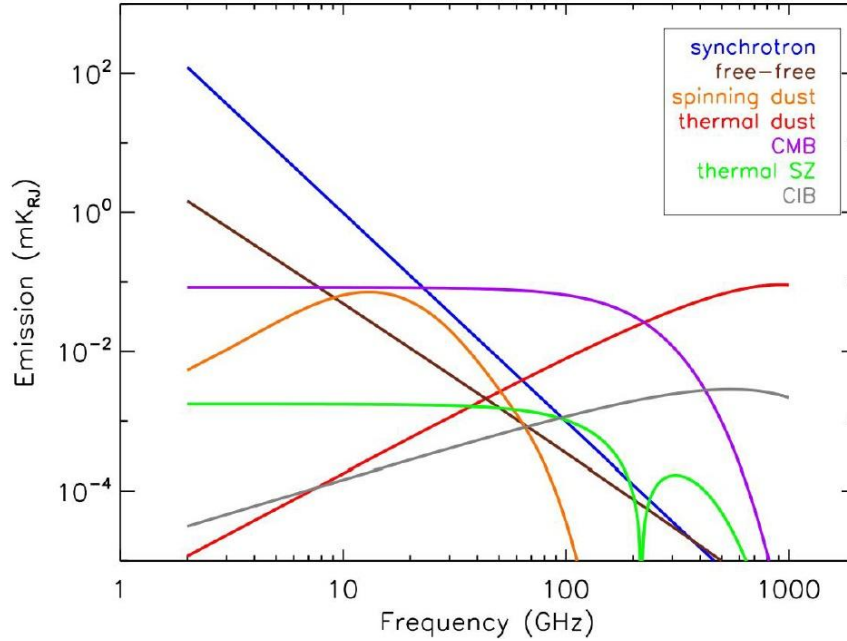
**Figure 1-9 : A plot of the major foreground sources which contaminate the CMB signal as a function of frequency. [Puget,2013]**

Dust emission is the dominant foreground at high frequencies, above 200 GHz, with its contribution rising towards 1 THz [Planck Collaboration, 2014c]. Unlike synchrotron and free-free, which are concentrated along the Galactic plane, thermal dust emission is more diffuse. This can be seen in the all sky maps produced by the individual frequency channels of the Planck satellite which are shown in Figure 1-10. In the low frequency channels the contribution of foreground sources to the maps are confined along the Galactic plane which can be clearly picked out in each of the maps. The three highest frequency channels (353 GHz, 545 GHz, and 857 GHz) all show much more diffuse foreground signals in addition to those along the Galactic plane. In the two multimode channels, 545 GHz and 857 GHz, the CMB signal is absent because of its blackbody spectrum and dust emission dominates. The analysis of the optical performance of these two channels is the focus of the work described in chapters 3, 4 and 5 of this thesis.

The Sunyaev–Zel'dovich effect is another source of foreground contamination [Planck Collaboration, 2014e]. Here CMB photons undergo inverse-Compton scattering in regions of high density such as Galactic clusters. The CMB photons receive an average energy boost during collisions with relativistic electrons leading to a distortion of the measured CMB temperature. An additional contributor to the foreground contamination of the CMB is the Cosmic Infrared Background (CIB)

[Planck Collaboration, 2014f]. This is produced when dust within distant galaxies is warmed by stars forming within the dust. Again it is a signal which is most prevalent at higher frequencies and contributes observable anisotropies to the all sky map of the 857 GHz channel of Planck.

Data from the three highest frequency channels of the Planck HFI (353 GHz, 545 GHz and 857 GHz) were used to produced the first all-sky map of polarised emission from dust at sub-mm wavelengths [Planck Collaboration, 2014c]. This survey was an immense step forward in sensitivity and coverage compared to earlier ground based observations. As the dust is well mixed with gas and reacts to UV photons from stars, it is a good tracer of the interstellar medium (ISM) and of star formation activity [Planck Collaboration, 2015c]. Polarised thermal dust emissions also carry important information on the interstellar magnetic field structure [Planck Collaboration, 2015b]. Additionally Planck HFI produced a catalogue of cold dust clumps, which are mainly associated with dense regions within molecular clouds, observations of which are relevant for the study of the early stages of star formation [Planck Collaboration, 2015d].
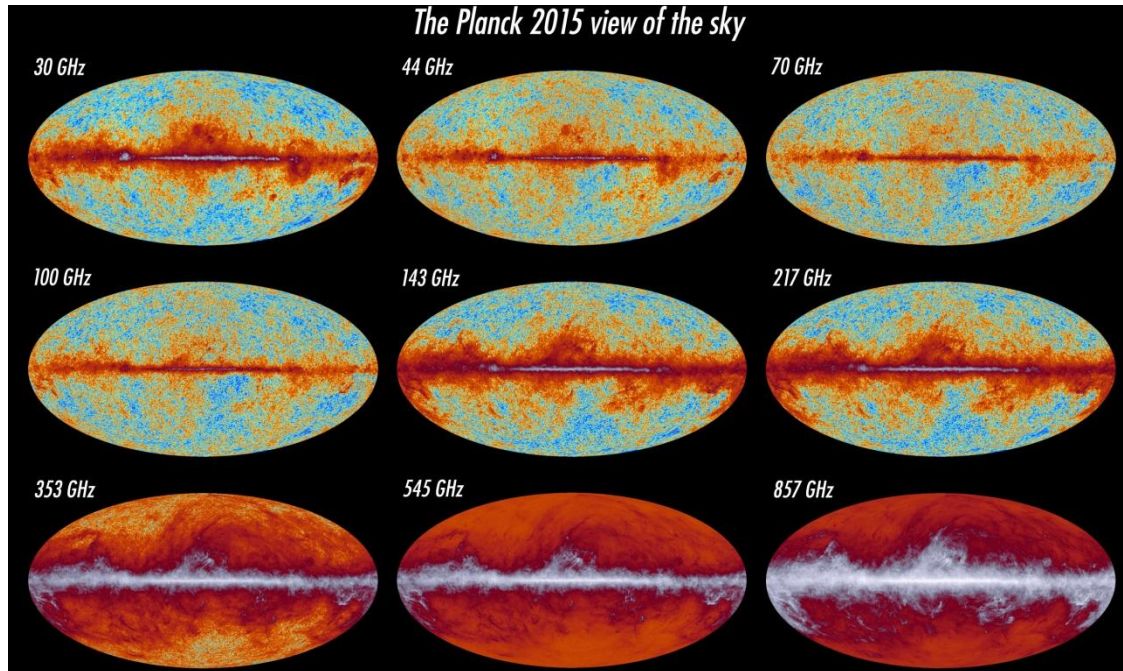


**Figure 1-10 : Full sky maps for each of Planck's frequency channels. Credit ESA.**

# 1.6 An overview of the Planck Satellite

The Planck satellite was launched on May $14^{th}$ 2009 and entered its final orbit at the Earth-Sun $L_2$ point in July of that year [Planck Collaboration, 2014a]. The original main objective of the Planck mission was to measure the spatial anisotropies of the temperature of the cosmic microwave background (CMB). Planck's performance goals were set to enable the extraction of the cosmological information embedded in the CMB temperature anisotropies. Planck was also designed to measure the polarisation of the CMB anisotropies, which in addition to containing cosmological information and breaking some of the model dependent degeneracies associated with the temperature anisotropies, provided insights into the early history of the universe at the time when the first stars and galaxies were forming [Planck Collaboration, 2014a]. Furthermore Planck's sky survey maps yielded information on the dust and gas within our own galaxy and extragalactic sources.

The Planck mission was actually first conceived in 1992 following the release of the results from the COBE satellite. The detection of the spatial anisotropies of the temperature of the CMB by COBE prompted proposals for space experiments to map the anisotropies in both Europe and the USA [Tauber, 2010a]. Two such experiments were presented to the European Space Agency (ESA): the COsmic Background Radiation Anisotropies Satellite (COBRAS) and the SAtallite for Measurement of Background Anisotropies (SAMBA). Both proposals featured an offset Gregorian telescope to focus the light from the sky onto an array of detector corrugated horn assemblies. An ESA-led team used these proposals to design a single satellite using a COBRAS-like telescope to feed two instruments located at the telescope focal plane. These two instruments were a Low Frequency Instrument (LFI) based on the COBRAS instrument and a High Frequency Instrument (HFI) based on the SAMBA instrument. This design was selected by ESA in 1996 and shortly afterwards was renamed after the German scientist Max Planck [Tauber, 2010a].

Following its selection, development of the Planck mission proceeded jointly with that of ESA's Herschel space telescope [Planck Collaboration, 2005]. This was done as both missions shared an number of commonalities. The most important of these was that both missions were planning orbits around the second Lagrangian point

of the Earth-Sun system thus it was possible for both missions to share the same Ariane 5 launch vehicle. After a long development period both missions were launched May 14th 2009 and in August 2009 Planck began scanning the CMB sky.

Figure 1-11 shows the main elements of the Planck satellite. Planck was designed and built around a two module idea. The top section of Planck was the payload module containing the telescope, the main instruments (LFI & HFI), the telescope baffle, and the three "V-groove" baffles. The lower module was the service module featuring the solar panel, the cooling systems, electronics, attitude control systems, and communications systems. The telescope baffle in addition to its primary function of providing stray light shielding for the telescope also played a role in the complex cooling systems on board Planck. In particular together with the "V-groove" shields it formed the Planck's passive cooling system and acted as a high-efficiency radiator, the telescope baffle consisted of approximately 14 $m^2$ of open aluminium honeycomb coated with black cryogenic paint. The "V-grooves" were a set of three conical shields with a relative angle of 5$^o$ between adjacent shields. The surfaces of the shields were aluminium coated except for the top most "V-groove" which had the same coating as the telescope baffle. This geometry provided efficient radiative coupling to cold space and high thermal insulation between the warm service module and the cold payload module. The passive cooling provided by these systems ensured a temperature of approximately 40-45K for the telescope and the baffle. [Tauber, 2010a]

The active cooling systems reduced the detector temperatures significantly. The operational temperature of the LFI detectors was 20 K and 100 mK for the HFI bolometers. This active system was based on a chain of three distinct refrigeration units working in series. The first section of the chain was the hydrogen sorption cooler. The sorption cooler produced liquid hydrogen in two liquid-vapour heat exchangers, one which directly cooled the LFI to its operational temperature and the other providing the pre-cooling for the HFI. The efficiency of the sorption cooling depended on passive cooling by radiation to space, which was achieved using gas piping to exchange heat to the three "V-grooves". The 4K cooler used to cool the HFI focal plane unit was based on the closed circuit Joule-Thomson (JT) expansion of helium and was initially developed under the ESA program to provide 4 K cooling for the Herschel satellite. It also provided pre-cooling for the third and final dilution

cooler unit. The dilution cooler consisted of two cooling stages using helium 4 and helium 3. The first stage was again based on JT expansion while the second stage was based on a dilution cooling principle, which provided the cooling to the 100 mK operating temperature for the HFI bolometers. After the dilution process the gas was vented into space so that the cooler had a limited lifetime and actually defined the operational lifetime of the HFI. [Tauber, 2010a]
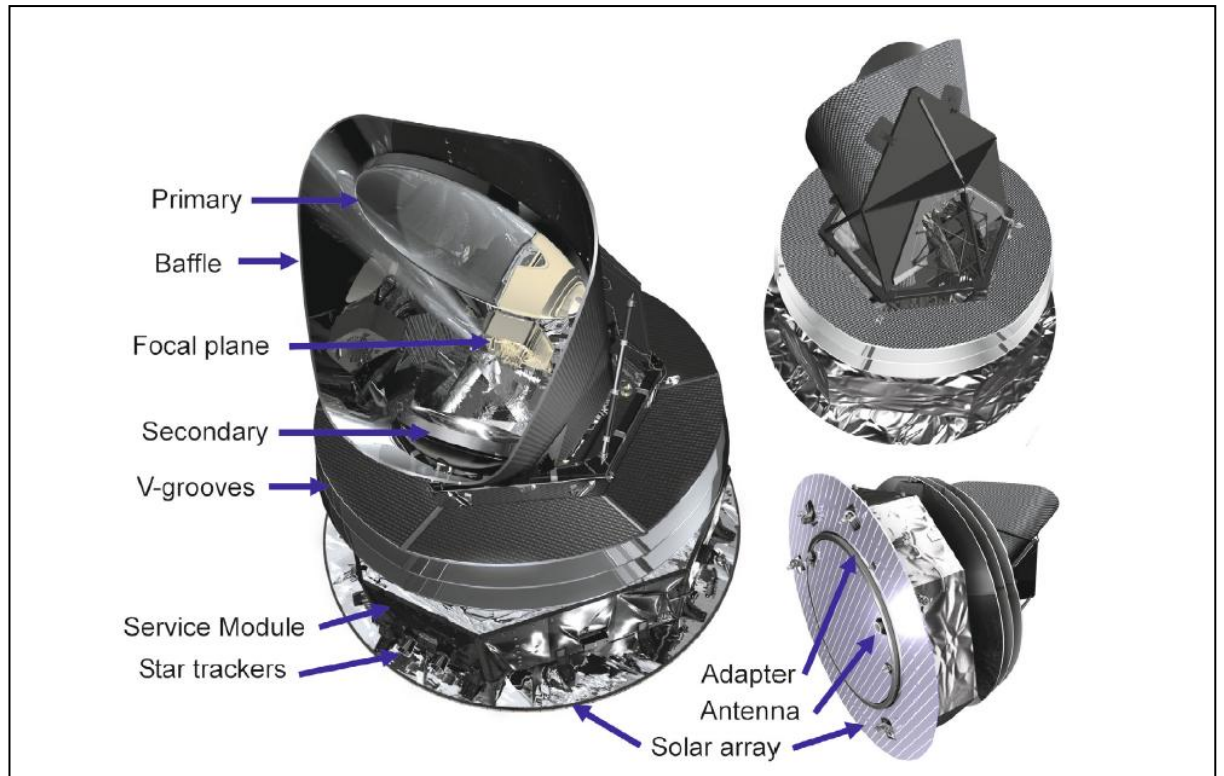


**Figure 1-11 Diagram of the Planck satellite showing the main components. [Tauber, 2010a]**

# 1.7 The Planck Telescope

The telescope built for the Planck mission was based on the original COBRAS design proposal which originally consisted of a Gregorian paraboloid-ellipsoid combination using the Dragone-Mizuguchi condition to preserve polarisation purity on the optical axis. The final design was substantially different from the original COBRAS design; it was an aplanatic design, consisting of two ellipsoidal reflectors, to extend the field of view to include the LFI which was positioned outside the HFI locations. [Tauber, 2010b] The telescope focused the radiation from the sky onto the

two instruments, the LFI and the HFI, located in the telescope focal plane. The primary reflector of the telescope was an off-axis ellipsoid 1.556 m × 1.887 m in size. While the secondary reflector was also an off-axis ellipsoid of size 1.051 m × 1.104 m. The dual ellipsoid combination was designed to provide the extended field of view on its focal plane necessary to fit both the LFI and HFI instruments (horn arrays). An operational temperature of 40 K was required for the reflectors to minimise their thermal noise in the measurements of the CMB temperature variations. This operational temperature had an impact on the design of the reflectors requiring them to have minimum levels of deformations in going from their manufacture at room temperature, 300 K, to their operational temperature at 40 K. A carbon fibre reinforced plastic (CFRP) honeycomb sandwich technology was used to achieve this stability, the mixture of carbon fibres and resins being controlled to yield an near zero thermal expansion coefficient. A facesheet was adhered to the honeycomb structure and coated with 0.5 μm of vacuum-deposited aluminium. Each cell of the honeycomb structure had a tendency to become slightly concave producing slight dimpling on the reflector. Although the effect was small the thickness of the facesheet was increased from its original design thickness to minimise this dimpling.

The other main elements of the Planck optical system were the detector feed horns, and the stray light baffle and the third V groove. The feed horns along with the telescope determined the main beam shapes on the sky of each channel frequency (the LFI 30 GHz, 44 GHz and 70 GHz channels, and the HFI 100 GHz, 143 GHz, 217 GHz, 353 GHz, 545 GHz and 857 GHz channels). The other elements, while they were not in reality optical elements, did play a role influencing the near and far sidelobes of the beams on the sky in terms of edge truncation and sidelobe scattering. The feed horns are detailed in the sections of this chapter describing the LFI and HFI, and the feed horns of the HFI multimode channels centred on 545 GHz and 857 GHz are the focus of much of the research work presented in this thesis. Shown in Figure 1-12 are typical main beam and spillover paths for a Planck channel. While the main beam follows a path from the sky to the focal plane via the telescope optics the "far-out" sidelobes are due to spillover past the baffle and the primary and secondary reflectors along with diffraction also at these edges. The resulting sidelobe spillover pattern is shown in Figure 1-13. The "baffle spillover" shown, for example, is power

from the sky reflected from the inside of the baffle onto secondary reflector and thus onto the feedhorns in the focal plane.
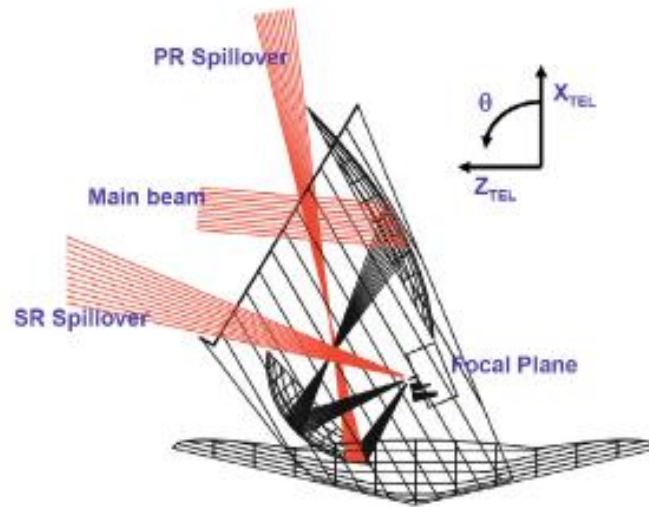


**Figure 1-12: Diagram showing a main beam and sidelobe spillover past the primary reflector (PR) and past the secondary reflector (SR). [Tauber, 2010b]**
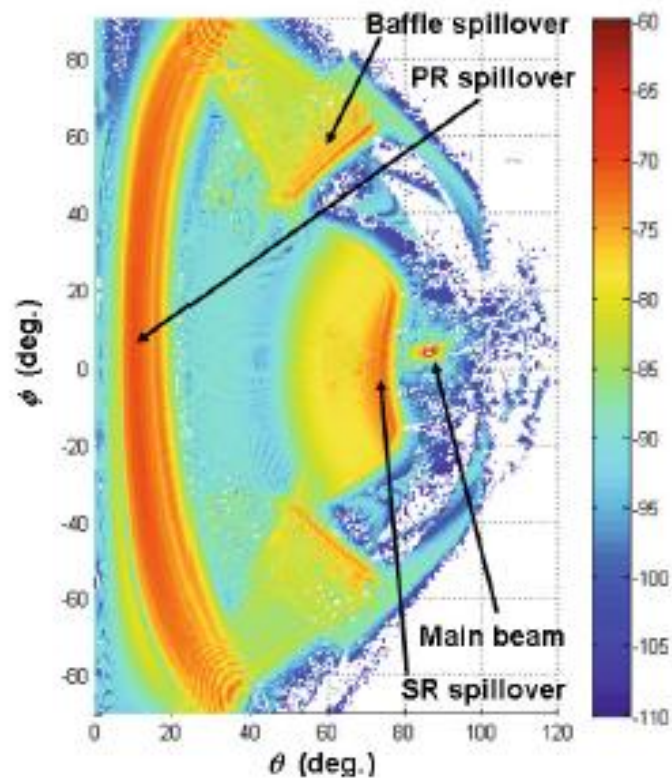


**Figure 1-13 : Plot showing a typical main beam and spillover for Planck. [Tauber, 2010b]**

Located in the focal plane are the two main instruments: the Low Frequency Instrument (LFI) and the High Frequency Instrument (HFI). The HFI horn antennas is

21

located in the middle of the focal plane unit with the LFI antennas positioned surrounding it. The positions of the various frequency channels of each instrument is shown in Figure 1-14(bottom). The crosses in the diagram indicate the relative direction of sensitivity to linear polarisation of the bolometer in each of the polarised channels. The HFI can be seen in the middle of the photograph (Figure 1-14 top), it is the central circular section with the array of horn antenna. The three LFI channels are the larger horn antennas arranged on the focal plane unit outside and around the HFI.
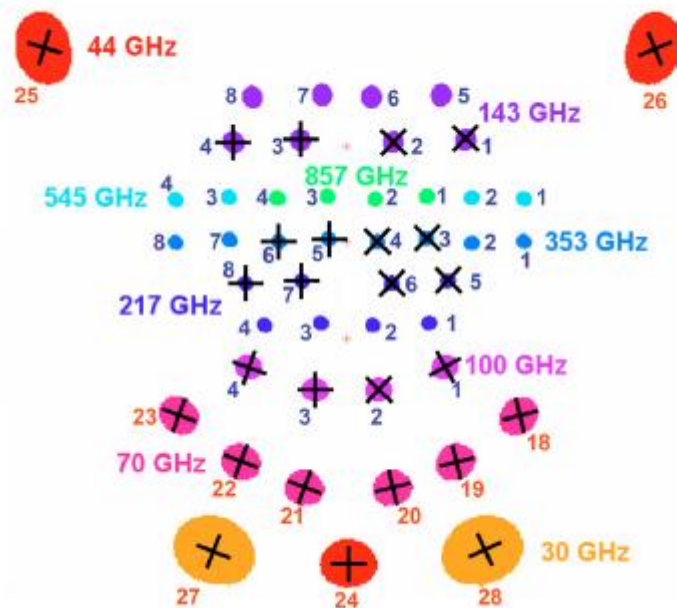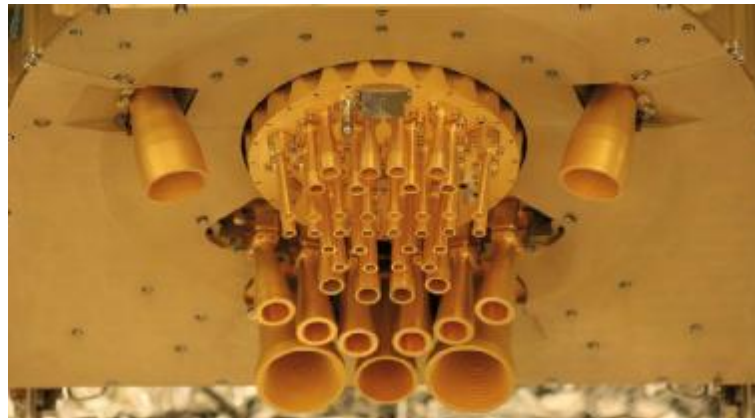


**Figure 1-14 : Top, photograph showing the layout of the focal plane of Planck. Bottom, diagram of the focal plane with the positions of the various frequency channels indicated. [Tauber, 2010b]**

# 1.8 The LFI and HFI Instruments

The Planck scientific objectives set out a sensitivity requirement of $\Delta T/_T \approx 2 \times 10^{-6}$ for each beam width $\Delta \theta \approx 10'$ pixel. Additionally the frequency range of Planck, 30 GHz to 857 GHz, was chosen to ensure that CMB could be dissimilated from foreground emissions with high accuracy. To do this Planck produced an all sky map for each of its nine frequency bands. As no single detector technology could provide the required accuracy over this entire frequency range two instruments, one using radiometers and the second using bolometers, were selected. This instrument pair reflected the fact that the Planck mission began with two separate proposals as explained earlier.
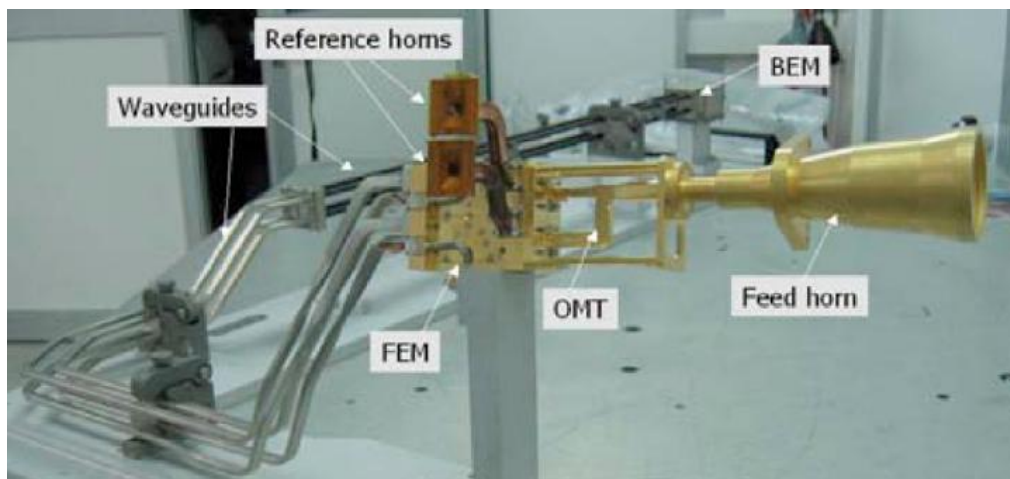


**Figure 1-15 : A photo of the LFI 30 GHz channel under test. [Bersanelli B, 2010]**

The LFI covered 27 to 77 GHz and the HFI covered the range from 90-900 GHz. The frequency range is covered in 9 bands with typically 30% bandwidth whose respective central frequencies were approximately logarithmically spaced as described above (Figure 1-14) [Bersanelli, 2010]. Consisting of 22 radiometers fed by 11 corrugated feedhorns the LFI was divided into 3 bands centred on 30 GHz, 44 GHz, and 70 GHz, with each feedhorn used to couple two radiometers with orthogonal linear polarisations to the telescope. This was achieved by using an orthomode transducer (OMT) behind each horn to separate the signal into two orthogonal polarisations. The radiometers used in the LFI were based on indium phosphide cryogenic high electron mobility transistors (HEMT) amplifiers, with the front end of

the LFI channels cooled to 20 K for optimal sensitivity while 4 K reference loads were used to minimise low frequency noise. Clearly the LFI was designed to cover the frequency range below the peak of the CMB spectrum. In fact the 70 GHz channel offered the clearest view of the CMB as it was the closest frequency channel to the optimal (minimum) combination of foreground emissions relative to the CMB spectrum which occurs at $\lambda \approx 4$ mm. In addition to the CMB, the 30 and 44 GHz channels were sensitive to foreground emissions such as synchrotron, free-free, and anomalous dust diffuse radiation from the galaxy [Bersanelli, 2010]. The 30 GHz channel is shown in Figure 1-15 during prelaunch testing and the feed horn, OMT, and front end module (FEM) are clearly visible in this image. [Bersanelli, 2010].

The High Frequency Instrument (HFI) contained 32 polarised detectors and 20 unpolarised detectors fed by 36 horn antenna chains, consisting of a back-to-back horn arrangement coupling a detector feed horn to the telescope (Figure 1-16) [Bersanelli, 2010]. The horn assembly also contains a set of filters between the back-to-back horn pair and the detector horn. The instrument was divided into six frequency bands centred on 100 GHz, 143 GHz, 217 GHz, 353 GHz, 545 GHz, and 857 GHz respectively with 30% bandwidths. There were four 100 GHz horn antenna assemblies feeding 8 polarised detectors, one orthogonally polarised detector pair per antenna assembly. The two highest frequency bands, 545 GHz and 857 GHz, were each made up of 4 horn antenna assemblies feeding an unpolarised detector. The remaining three frequency bands, 143 GHz, 217 GHz, and 353 GHz, each contained 4 unpolarised detectors and 8 polarised detectors. The polarised detectors were again arranged in orthogonally polarised pairs fed by a horn assembly while the unpolarised detectors each had a single bolometer each (see Figure 1-14 for the layout).

The three lowest frequency HFI bands were polarisation sensitive and dedicated to CMB measurements, while the 353 GHz channel was for the removal of polarised foreground sources and the two highest frequency HFI bands were also designed to measure foregrounds for removal from the CMB signals and for Galactic science [Lamarre J.-M, 2010]. Thus, the frequency range of the LFI and HFI were designed to cover the peak of the CMB spectrum and also to characterise the main Galactic foregrounds. As mentioned earlier these foregrounds include synchrotron and free-free emissions at the low frequencies (30 GHz ,44 GHz) and dust emissions

at the high frequencies (>70 GHz) as described in section 1.5  [Planck Collaboration, 2014a].
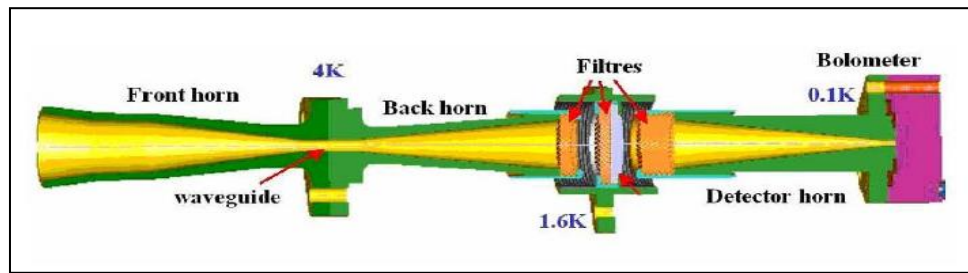


**Figure 1-16 : Diagram of the back-to-back horn and the detector feed horn assembly which was used in each of the HFI channels. [Lamarre J.-M, 2010]**

As mentioned above the HFI back-to-back horn assembly arrangement, as shown in Figure 1-16, was used to couple the detector feed horn to the telescope and provided the thermal isolation of the detector and the bolometer as the bolometer detectors operated at 100 mK.  The back-to-back horns were cooled to 4 K, which can be contrasted with the 40 K temperature of the telescope reflectors.  Also as mentioned above each of the frequency bands had a 30% band width around their central frequency.  For the single-moded channels (100 GHz-353 GHz) the lower end of each band was defined by the cut off frequency of the corrugated waveguide section of the back-to-back horn which allows only the fundamental hybrid mode through.  In order to define the upper limit of the bands a low pass filter was used.  The multi-moded channels (545 GHz and 857 GHz) rely on both a low and high band pass filter to define the frequency bands with the waveguide filter section of the multi-moded horns allowing a finite number of hybrid modes through.  Each mode is degenerate in general with a pair of orthogonal fields per mode except for the lowest order cylindrically symmetric modes (azimuthal order $n = 0$) which only have a single field per mode, i.e. azimuthal $\varphi$ dependence, see chapter 2.

The beam patterns of each horn determined the effective aperture of the telescope, and angular resolution on the sky, for each channel.  The beam pattern also determined the spillover which is the amount of the beam that did not hit both the secondary and primary mirrors and thus could couple to off-axis sources on the sky. Tradeoffs were made during the horn design to optimise angular resolution and minimise spillover for each frequency, with a flared corrugated horn design optimised to produce a near Gaussian horn beam pattern [Maffei, 2010a].  The two high

frequency channels were designed to be multimode to ensure the same angular resolution of 5' as the other high resolution HFI channels (353 GHz and 217 GHz) but without a loss of aperture efficiency and sensitivity [Murphy J.A., 2010] [Lamarre J.-M, 2010]. The predicted beam widths and those measured inflight for the LFI and HFI are summarised in Table 1-1.

| Frequency (GHz) | Number of detectors | Predicted FWHM (arcmin) | Measured FWHM (arcmin) |
|:---:|:---:|:---:|:---:|
| 30 | 4 | 32.71 | 33.16 |
| 44 | 6 | 29.54 | 28.09 |
| 70 | 12 | 13.00 | 13.08 |
| 100 | 8 | 9.58 | 9.59 |
| 143 | 12 | 7.11 | 7.18 |
| 217 | 12 | 4.62 | 4.87 |
| 353 | 12 | 4.59 | 4.7 |
| 545 | 4 | 4.7 | 4.73 |
| 857 | 4 | 4.3 | 4.51 |

**Table 1-1 : The predicted and inflight measured beam full width half maxima (FWHM) for each frequency channel in both the LFI and HFI. [Tauber, 2010b][Planck Collaboration, 2014a]**

Spider-web bolometers (SWBs) were used in the unpolarised channels of HFI. In SWBs metal grids deposited on $Si_3N_4$ in a spider-web shape absorbed the incoming radiation transforming it into heat. The resulting change in temperature of the absorber was measured with a neutron transmuted doped germanium thermistor. Figure 1-17 (left) shows a photograph of an SWB that was used in one of the unpolarised 143 GHz channels [Lamarre J.-M, 2010]. These SWBs absorb all radiation falling onto them independent of the polarisation of the incoming radiation.

So called polarisation-sensitive bolometers (PSBs) were used in the polarisation sensitive channels of HFI. The absorbers of the PSBs were metal grills with metallization in one direction. Electric fields parallel to this direction developed currents which deposited power in the grid. Electric fields perpendicular to this direction pass through the grid without interaction and so can couple to another perpendicularly oriented grid beyond. A pair of PSBs perpendicular to each other were thus placed in the detector cavity of the polarisation sensitive channels so that orthogonal polarisations could be detected using the same horn assembly to minimise systematic errors.

The Stokes parameters are a set of values which are used to describe the polarisation state of electromagnetic radiation. From the measurements made by each pair of PSBs the intensity of the Stokes parameters could be measured. The Q Stokes parameter describes the degree of polarisation that is the differences in intensities between horizontal and vertical linearly polarised components. The U Stokes Parameter describes the plane of polarisation, i.e. the differences in intensities between linearly polarized components oriented at $+45^o$ and $-45^o$. The Q Stokes parameter associated with its local frame could be extracted by a pair of PSBs. A second associated pair of PSBs rotated by $45^o$ relative to the first pair scanning the same line allowed the U Stokes parameter to be measured. Figure 1-17 (right) shows a photograph of a PSB that was used in one of the 217 GHz channels. [Lamarre J.-M, 2010]
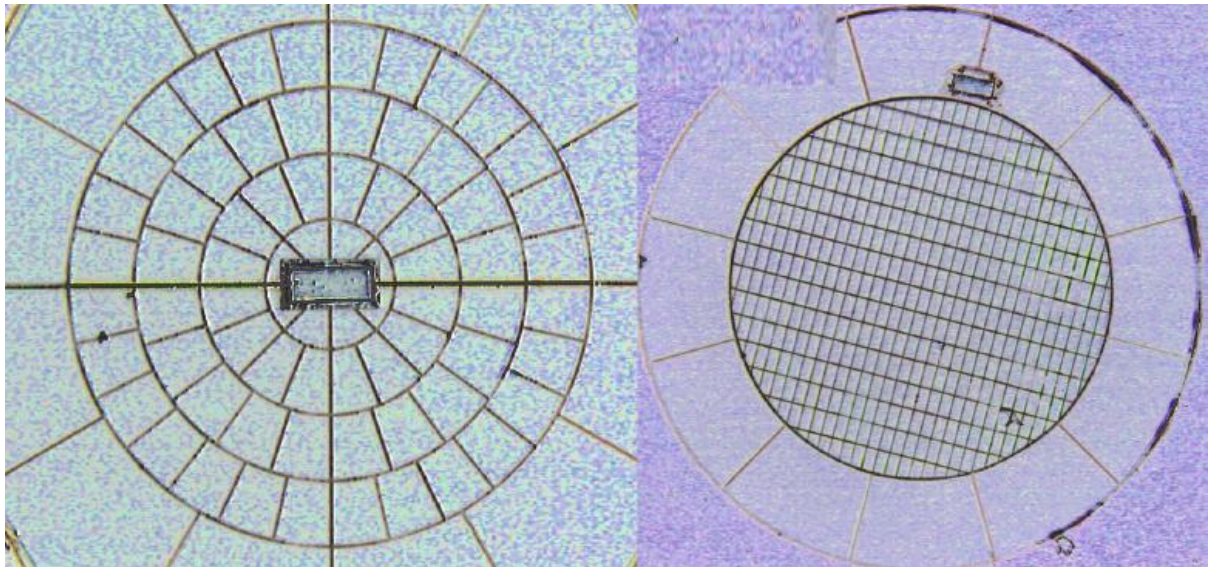


**Figure 1-17 : Photograph of a spider web bolometer (left) and a polarisation-sensitive bolometer (right). One can see the temperature sensor at the centre of the SWB and at the upper edge of the PSB. [Lamarre J.-M, 2010]**

# 1.9 Thesis Outline

The subsequent chapters of this thesis concentrate on improvements to the computational modelling of horn antennas for CMB experiments in order to understand the behaviour of the multimode channels in terms of their broadband responses and actual performance in prelaunch testing and during in flight

observations. The understanding and characterisation of the beam patterns is essential for CMB experiments. After than a novel application of millimetre-wave digital holography to the measurement of a specially designed CMB horn antenna for a future space mission.

Chapter 2 is concerned with the modelling of horn antennas at millimetre wavelengths. The mode-matching technique for modelling horn antennas as a series of wave-guide sections using the natural TE and TM modes of cylindrical guides is detailed. The pre-existing in-house SCATTER software designed to calculate the scattering matrixes used in this technique is described and modifications made by the author to the software along with other software tools for an extension of the analysis, such as the application of single value decomposition, are also related in this chapter.

Chapter 3 concentrates on improving the broadband modelling of the 545 GHz and 857GHz multimode horn antennas. Issues associated with the stability of the pre-existing in house SCATTER software as well as the effects of the source spectrum on the effective broadband are discussed and the software upgrades and improvements to the modelling approach detailed. A full model that included the cavity coupled bolometer in the analysis is also described and compared with the standard approach using reciprocity and assuming black body illumination of the filter waveguide at the back of the front horn. Work on the single mode 353 GHz channel is also included.

Chapter 4 is concerned with the effects of manufacturing tolerances on the far sidelobe structure of the multimode channels during in-flight observations . A detailed analysis of the effects of non-ideal corrugations (such as missing fins and filled grooves) in various sections of the horns is provided. The implications for the far-out sidelobes of the multimode beams is discussed and conclusions with respect to actual in-flight performance drawn.

Chapters 5 relates the author's work analysing the pre-flight tests measurements of the 857 GHz multimode flight horns. The differences between the predictions of the SCATTER simulations of the farfield beam patterns of the horn antennas and the actual measured beam patterns are discussed and carefully analysed. It turned out that the non-ideal test setup and difficult laboratory measurements could have contributed to the discrepancies with the simulations and a plausible scenario for these is presented. A comparison of the predicted beam width with the beam width

28

measured in flight is also provided which ultimately in fact verified the predictions of the simulations.

Chapter 6 complements the work in the previous chapters in that it is concerned with the measurement of horn antennas for future CMB missions using digital holographic techniques developed for the W-band (75-110 GHz). These techniques are introduced including some holographic imaging of some test objects. The use of the experimental setup and associated analysis techniques to examine the properties of horn antennas, such as the location of their phase centres, in particularly the properties of horn antennas specially designed for future CMB polarisation missions using digital holography are reported. Finally some other applications of millimetre-wave holography are discussed for completeness.

Chapter 7 draws conclusions from the work presented in Chapters 2 to 6 and potential future work is discussed.

# Chapter 2  Modelling Single Mode and Multimode Corrugated Horn Antennas

## 2.1 Introduction

Horn antennas, as the name suggest, are flared metal waveguides shaped like a horn that provide a gradual transition structure to match the impedance of a waveguide to the impedance of free space, thus enabling the electromagnetic waves to radiate efficiently into space. They also allow the radiation beam pattern to be shaped, as well as controlling the directionality of the beam. This thesis deals mostly with corrugated horn antennas such as those used in the Planck satellite, and this chapter is concerned with how these electromagnetic structures can be efficiently modelled.

A single-mode corrugated conical horn is designed to allow only one particular hybrid field combination of transverse electric (TE) cylindrical waveguide modes and transverse magnetic (TM) cylindrical waveguide modes to propagate. The term single-mode refers to the fact that only one coherent hybrid mode field is actually propagating and this requires the horn to be fed by some single waveguide mode (smooth walled or corrugated, depending on the application), where a transition from waveguide to horn may be required to minimise reflections. Any cylindrical hybrid mode, usually designated a HE or an EH mode, propagating in a regular corrugated structure can be considered as some combination of TE and TM waveguide modes. The $HE_{11}$ fundamental hybrid mode is normally the only one propagating within a single-mode corrugated waveguide feeding a single mode horn. In a multi-mode horn a number of higher order hybrid modes other than the fundamental mode can also propagate in the waveguide feeding the horn. These hybrid modes, $HE_{nl}$ and $EH_{nl}$, can be derived using the same computational techniques used for single-mode waveguides and horns, except of course that all necessary azimuthal orders, $n$, are also included, not just those with $n = 1$. This chapter summarises the waveguide mode theory that allows the hybrid fields to be extracted using software called SCATTER, which has been developed in-house in the Experimental Physics Department at National University of Ireland Maynooth (Maynooth University), to simulate the radiation

pattern of a corrugated horn antenna using a mode-matching technique that is based on a TE and TM smooth walled cylindrical waveguide mode basis set [Colgan, 2001][Gleeson, 2004]. Further code has now been developed that applies single value decomposition (SVD) to the scattering matrices produced by the mode matching code in order to obtain the true hybrid modes (or eigenfields) of multimode horn antennas.

As stated above, a mode matching modal technique is used in the SCATTER software to simulate the beam patterns of corrugated horn antennas. In this approach a corrugated waveguide or horn structure is regarded as a sequence of circular waveguide segments of varying radii in which the natural modes of propagation for each segment are the $TE_{nl}$ and $TM_{nl}$ modes of a smooth walled circular waveguide. At the interface between two segments, the power carried by the individual incident modes is scattered between the backward propagating reflected modes in the first guide segment and the forward propagating modes in the second guide segment. Similarly, there may be incident power from the second section towards the interface with the first section which was scattered in subsequent later sections. For this reason a "scattering matrix" approach is required that includes all of these possibilities [Murphy, 2001]. In terms of beam patterns, reciprocity can be assumed and the horn treated as a radiator even though it is a receiver in reality. It is also generally assumed that any cavity with an absorbing detector (bolometer) at the back of the horn antenna behaves like a black-body absorber and thus invoking reciprocity radiates like a black body radiator. From this point of view all waveguide modes are equally excited in power at the input to the system and are independent of each other, so there is no phase relationship between them. Therefore these input modal fields then propagate through the horn antennas and contribute independently to the beam on the sky [Murphy, 2001][Gleeson, 2005]. In chapter 3 this point will be revisited to check the veracity of the approximation that the cavity is a perfectly absorbing black body.

## 2.2 Cylindrical waveguides modes

First we consider the natural waveguide modes for a smooth walled cylindrical waveguide. The electric and magnetic fields can be decomposed into axial ($E_z$ & $H_z$) and transverse components ($E_t$ & $H_t$). The *forward* propagating fields are

$$\mathbf{E} = \mathbf{E}_t(u_1, u_2)e^{-\gamma z + iwt} + E_z(u_1, u_2)e^{-\gamma z + iwt}\hat{k}$$
$$\mathbf{H} = \mathbf{H}_t(u_1, u_2)e^{-\gamma z + iwt} + H_z(u_1, u_2)e^{-\gamma z + iwt}\hat{k} \qquad , \qquad (2.1)$$

where $u_1$ and $u_2$ are the transverse coordinates of the system [Olver, 1994]. The axial-field components satisfy the usual scalar electromagnetic-wave equations

$$\nabla_t^2 E_z + K^2 E_z = 0 \qquad \nabla_t^2 H_z + K^2 H_z = 0 \qquad , \qquad (2.2)$$

where $K$ is the wave number given by

$$K^2 = \omega^2 \varepsilon \mu + \gamma^2 . \qquad (2.3)$$

For just dielectric media possibly filling the waveguide we can take $\mu = \mu_0$ and also if the dielectric is air we can take $\varepsilon = \varepsilon_0$. For these cases, therefore, the equation for the wave number becomes $K^2 = k_0^2 + \gamma^2$, where $k_0^2 = \omega^2 \varepsilon_0 \mu_0 = \omega^2 c$, and $c$ is the speed of light in vacuum. In a smooth walled waveguide with perfectly conducting walls for electric currents (Perfect Electrical Conductor) one of the axial components either $E_z$ or $H_z$ can be set to zero at the walls, $E_z = 0$ for TE modes, and $H_z = 0$ for TM modes; while in an inhomogeneous waveguide with effectively non-perfectly conducting walls, both components may have to exist together (a corrugated waveguide with many corrugations per wavelength can be regarded in this way as discussed in section 2.3). The Laplacian operator for cylindrical co-ordinates is

$$\nabla_t^2 = \frac{1}{r}\frac{\partial}{\partial r}\left(\frac{r\partial}{\partial r}\right) + \frac{1}{r^2}\frac{\partial^2}{\partial \phi^2} . \qquad (2.4)$$

The transverse-field components are then obtained from $\mathbf{E}_z$ and $\mathbf{H}_z$ using [Olver, 1994]

$$\mathbf{E}_t = -\frac{\gamma}{\mathbf{K^2}}\nabla_t\mathbf{E}_z + \frac{j\omega\mu}{\mathbf{K^2}}\hat{\mathbf{u}}_z \times \nabla_t\mathbf{H}_z$$
$$\mathbf{H}_t = -\frac{\gamma}{\mathbf{K^2}}\nabla_t\mathbf{H}_z - \frac{j\omega\mu}{\mathbf{K^2}}\hat{\mathbf{u}}_z \times \nabla_t\mathbf{E}_z \qquad , \qquad (2.5)$$

where $\mathbf{E}_z = E_z(u_1, u_2)e^{-\gamma z + iwt}\hat{k}$ and $\mathbf{H}_z = H_z(u_1, u_2)e^{-\gamma z + iwt}\hat{k}$. Furthermore, by applying the appropriate boundary conditions we can obtain the characteristic

equations for the waveguide. The general boundary conditions between two regions, 1 and 2, are

$$\hat{\mathbf{u}}_n \times (\mathbf{E}_1 - \mathbf{E}_2) = 0 \qquad \hat{\mathbf{u}}_n \times (\mathbf{H}_1 - \mathbf{H}_2) = 0 \ , \qquad (2.6)$$

where $\hat{\mathbf{u}}_n$ is a unit vector normal to the boundary. If one of the regions (i.e. the walls of the waveguide) is a perfect conductor then the electric field inside the conductor has to be zero and the **E** field parallel to the walls must also be zero so that

$$\hat{\mathbf{u}}_n \times (\mathbf{E}_1) = 0 \qquad . \qquad (2.7)$$

On the other hand, Ampére's Law implies that in the second equation (2.6) the magnetic field is zero inside the conductor (skin depth shrinks to zero as conductivity, σ, goes to infinity over a very short distance as the conductor is perfect), so that

$$\hat{\mathbf{u}}_n \times (\mathbf{H}_1) = \mathbf{J}_s \ , \qquad (2.8)$$

where $\mathbf{J}_s$ is the surface current density. This implies in a cylindrical waveguide that the wave number for the TE and TM modes are different. The axial electric field and wave number for $TM_{nm}$ modes are given by the possible solutions

$$E_z(r,\phi) = A_n J_n(Kr) \begin{pmatrix} -\sin n\phi \\ \cos n\phi \end{pmatrix} \ , \qquad (2.9)$$

and
$$J_n(Ka) = 0 \ , \qquad (2.10)$$

where $J_n$ is a Bessel function of order $n$ and $a$ is the radius of the waveguide and thus $E_z = 0$ at the walls. For the $TE_{nm}$ modes the possible solutions are:

$$H_z(r,\phi) = B_n J_n(Kr) \begin{pmatrix} -\sin n\phi \\ \cos n\phi \end{pmatrix} \ , \qquad (2.11)$$

and
$$J'_n(Ka) = 0, \qquad (2.12)$$

where

$$J'_n(z) = \frac{d J_n(z)}{dz} . \qquad (2.13)$$

So that $H_z = 0$ at the walls. Therefore the wave number $K_{TM}$ for TM modes depends on the roots, $p_{nl}$, of the Bessel function (i.e. $J_n(p_{nl}) = 0$) of order $n$ giving $K_{TM} = \dfrac{p_{nl}}{a}$. While for the TE modes the wave number depends on the roots, $q_{nl}$, of the derivative of the Bessel function (i.e. $J'_n(q_{nl}) = 0$) giving $K_{TE} = \dfrac{q_{nl}}{a}$.

For convenience we write for pure TE and TM modes

$$\mathbf{E}_t = \mathbf{e}_{nl}(r,\phi)e^{-j\gamma z}e^{j\omega t} \qquad \mathbf{H}_t = \mathbf{h}_{nl}(r,\phi)e^{-j\gamma z}e^{j\varpi t} \; .$$

From the equations (2.5) two sets of transverse components for the degenerate pair of electric and magnetic fields for each TM mode can be derived as given by E. Gleeson, [Gleeson, 2004],

$$\mathbf{e}_{nl}(r,\phi,z,t) = \sqrt{\frac{(2-\delta_{n0})|Z_{TM_{nl}}|}{\pi a^2 J_{n+1}^2(P_{nl})}} \left[ J'_n\left(p_{nl}\frac{r}{a}\right)\binom{\cos n\phi}{\sin n\phi}\hat{\mathbf{r}} + \frac{nJ_n\left(p_{nl}\frac{r}{a}\right)}{p_{nl}\frac{r}{a}}\binom{-\sin n\phi}{\cos n\phi}\hat{\boldsymbol{\varphi}} \right]$$

(2.14)

$$\mathbf{h}_{nl}(r,\phi,z,t) = \frac{1}{Z_{TM_{nl}}}\sqrt{\frac{(2-\delta_{n0})|Z_{TM_{nl}}|}{\pi a^2 J_{n+1}^2(P_{nl})}} \left[ -\frac{nJ_n\left(p_{nl}\frac{r}{a}\right)}{p_{nl}\frac{r}{a}}\binom{-\sin n\phi}{\cos n\phi}\hat{\mathbf{r}} + J'_n\left(p_{nl}\frac{r}{a}\right)\binom{\cos n\phi}{\sin n\phi}\hat{\boldsymbol{\varphi}} \right]$$

(2.15)

where $Z_{TM}$, the characteristic waveguide impedance, is

$$Z_{TM_{nl}} = Z_0\sqrt{1-\left(\frac{p_{nl}}{\omega a\sqrt{\mu\varepsilon a}}\right)^2} \; , \qquad (2.16)$$

where $Z_0 = \sqrt{\dfrac{\mu}{\varepsilon}}$ is the characteristic impedance of the waveguide medium. The pairs of $\cos n\phi$ and $\sin n\phi$ terms in the 2×1 column matrix corresponds to the two degenerate fields of each mode (except for those of azimuthal order $n = 0$). For the TE modes the pair of $\mathbf{e}_{nl}$ and $\mathbf{h}_{nl}$ fields are

34

$$\mathbf{e}_{nl} = \sqrt{\frac{(2-\delta_{n0})\left|Z_{TE_{nl}}\right|}{\pi a^2 (1-(n/q_{nl})^2)J_n^2(q_{nl})}} \left[ \frac{nJ_n\left(q_{nl}\frac{r}{a}\right)}{q_{nl}\frac{r}{a}}\left(\begin{array}{c}\cos n\phi \\ -\sin n\phi\end{array}\right)\hat{\mathbf{r}} - J_n'\left(q_{nl}\frac{r}{a}\right)\left(\begin{array}{c}\sin n\phi \\ \cos n\phi\end{array}\right)\hat{\boldsymbol{\phi}} \right]$$

(2.17)

$$\mathbf{h}_{nl} = \frac{1}{Z_{TE_{nl}}}\sqrt{\frac{(2-\delta_{n0})\left|Z_{TE_{nl}}\right|}{\pi a^2 (1-(n/q_{nl})^2)J_n^2(q_{nl})}} \left[ J_n'\left(q_{nl}\frac{r}{a}\right)\left(\begin{array}{c}\sin n\phi \\ \cos n\phi\end{array}\right)\hat{\mathbf{r}} + \frac{nJ_n\left(q_{nl}\frac{r}{a}\right)}{q_{nl}\frac{r}{a}}\left(\begin{array}{c}\cos n\phi \\ -\sin n\phi\end{array}\right)\hat{\boldsymbol{\phi}} \right]$$

(2.18)

where $Z_{TE}$, the characteristic waveguide impedance for the TE modes, is

$$Z_{TE_{nl}} = \frac{Z_0}{\sqrt{1-\left(\dfrac{q_{nl}}{\omega a\sqrt{\mu\varepsilon}}\right)^2}} \quad .$$

(2.19)

Again, two solutions exist for each $n$ and $l$ for azimuthal orders $n > 0$ which are represented by a $2\times1$ column matrix with the $\cos n\phi$ and $\sin n\phi$ terms. For the $n = 0$ azimuthal order, clearly the sin terms are zero, and there is only one TE and TM mode rather than a pair as for orders $n > 0$. Thus there is a degeneracy of 2 associated with each so called $TE_{nl}$ and $TM_{nl}$ mode. In an unpolarised symmetric system a bolometric detector will detect both modes, each of which can carry power from the source through the waveguide structure.

## 2.3  Mode-matching in Circular Waveguides

As stated above, in the mode-matching technique a corrugated waveguide or horn structure is regarded as a sequence of circular waveguide segments with the radius stepping between the top and bottom of the corrugation slots (Figure 2-1). The natural modes of propagation for each segment are the TE and TM modes of a uniform circular waveguide as derived in the last section (2.2). At the interface between two segments, the power carried by the individual incident modes is scattered between the

backward propagating reflected modes in the first guide segment (left side of the junction by convention), and the forward propagating modes in the second guide segment (right side of the junction). [Murphy,2001] [Gleeson,2005] [Olver,1994]
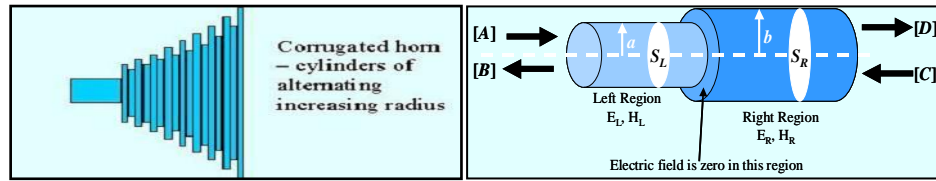


**Figure 2-1 (a) A corrugated horn antenna showing the alternating section radii. (b) A junction between two sections [Gleeson, 2004].**

The number of propagating and evanescent modes required to describe the total power needs to be sufficient to accurately describe any possible field that can propagate through the system. Therefore, for a waveguide, we should include all possible propagating modes plus enough evanescent modes to describe any trapped power close to a junction where modes are scattered. For a horn as it flares out more modes can propagate but do not necessarily need to be included in the analysis if very little power is coupled to them.

The advantage of the mode-matching approach is that the amplitudes of the scattering effects between modes can be expressed in a scattering matrix formulisation. A scattering matrix can be calculated for each junction (step) in a waveguide or horn profile and these matrices are then cascaded together to form an overall scattering matrix. The elements of this overall scattering matrix are the reflection and transmission coefficients from which the aperture fields of the horn can be computed for given input fields for the waveguide feeding the horn.

If column submatrices [A] and [B] contain the forward propagation and reflection coefficients respectively for all modes at the input (source side) of the horn, then the equivalent submatrices [C] and [D] at the output side of the horn can be obtained using the scattering matrix [S], equation 2.20.

$$\begin{bmatrix} [B] \\ [D] \end{bmatrix} = [S] \begin{bmatrix} [A] \\ [C] \end{bmatrix}, \tag{2.20}$$

where the scattering matrix [S] can be expressed as:

$$[S] = \begin{bmatrix} [S_{11}] & [S_{12}] \\ [S_{21}] & [S_{22}] \end{bmatrix} \quad . \tag{2.21}$$

The elements of [S] are submatrices which provide details of how the power is coupled between the incident modes and the transmitted and reflected modes. The matrix of transmission coefficients of the horn as a whole, [D], is thus

$$[D] = [S_{21}][A] \ , \tag{2.22}$$

where there is no incident power from free space (the right of the junction, Figure 2-2), i.e. [C] = 0. [$S_{21}$] is the scattering matrix for the horn as a whole in that case.



**Figure 2-2: Scattering matrix [S] for a modular section of a horn antenna relates the coefficients on the input side (left) to those on the output side (right).**

On the other hand the [D] submatrix associated with a single junction (or step) between two sections within the horn will also contain an $S_{22}$ term representing the scattering for power incident on the right of the junction which can exist because of possible scattering from steps further on in the horn (or waveguide). Thus, in general, matrices for two junctions *a* and *b* will have the form

$$[S^a] = \begin{bmatrix} [S_{11}^a] & [S_{12}^a] \\ [S_{21}^a] & [S_{22}^a] \end{bmatrix} \qquad [S^b] = \begin{bmatrix} [S_{11}^b] & [S_{12}^b] \\ [S_{21}^b] & [S_{22}^b] \end{bmatrix} \quad . \tag{2.23}$$

The cascading of these two matrices, where junction *a* comes before *b*, results in an overall scattering matrix which describes both junctions combined and which also must include any waveguide propagation between them:

$$[S^c] = \begin{bmatrix} [S_{11}^c] & [S_{12}^c] \\ [S_{21}^c] & [S_{22}^c] \end{bmatrix}, \tag{2.24}$$

where

37

$$[S_{11}^c] = [S_{12}^a][[I] - [S_{11}^b][S_{22}^a]]^{-1}[S_{11}^b][S_{21}^a] + [S_{11}^a]$$
$$[S_{12}^c] = [S_{12}^a][[I] - [S_{11}^b][S_{22}^a]]^{-1}[S_{12}^b]$$
$$[S_{21}^c] = [S_{21}^b][[I] - [S_{22}^a][S_{11}^b]]^{-1}[S_{21}^a]$$
$$[S_{22}^c] = [S_{21}^b][[I] - [S_{22}^a][S_{11}^b]]^{-1}[S_{21}^a][S_{12}^b] + [S_{22}^b]$$

$$, \qquad (2.25)$$

where $[I]$ is a unit matrix and $[]^{-1}$ represents the inverse of the matrix. Using this formulism, the scattering matrices for the individual junctions of the horn and the propagation between the junction steps are cascaded together to form the overall scattering matrix for the horn.

The propagation 'scattering' matrix in a uniform guide section can in fact be written as elements

$$[S_{11}] = [S_{22}] = [0]$$
$$[S_{12}] = [S_{21}] = [V]$$

$$, \qquad (2.26)$$

where $[V]$ is a diagonal matrix whose elements are $V_{nn} = \exp(-\gamma_n l)$, where $l$ is the length of the section, and $\gamma_n$ is the propagation constant for the $n^{th}$ mode. This propagation constant is normally purely imaginary for propagating modes ($\gamma_n = j\beta_n$) and purely real ($\gamma_n = \alpha_n$) for evanescent modes. The lengths of the uniform sections are in general short and thus the amplitude of the evanescent modes may still be significant by the time the mode has reached the next junction. For this reason a sufficient number of evanescent modes must be included in the analysis in order to fully describe the overall field propagating in the horn, as alluded to earlier.

At a junction between two uniform sections the total power in all the modes propagating in the forward and reverse directions in both sections must be conserved. Clearly, however, this implies an infinite number of modes is required ideally to precisely satisfy this requirement for all possible fields that could be transmitted across the two sections. For computational efficiency a finite number of modes is chosen with this number being ideally determined by minimising the number of modes required to give an accurate description of any possible transmission scenario. The chosen number of modes propagating in each section in the computation thus does not need to be necessarily the same as long as the description is sufficiently accurate.

However to simplify the analysis the number of modes $N$ on each side of the junction is chosen to be the same for the moment.
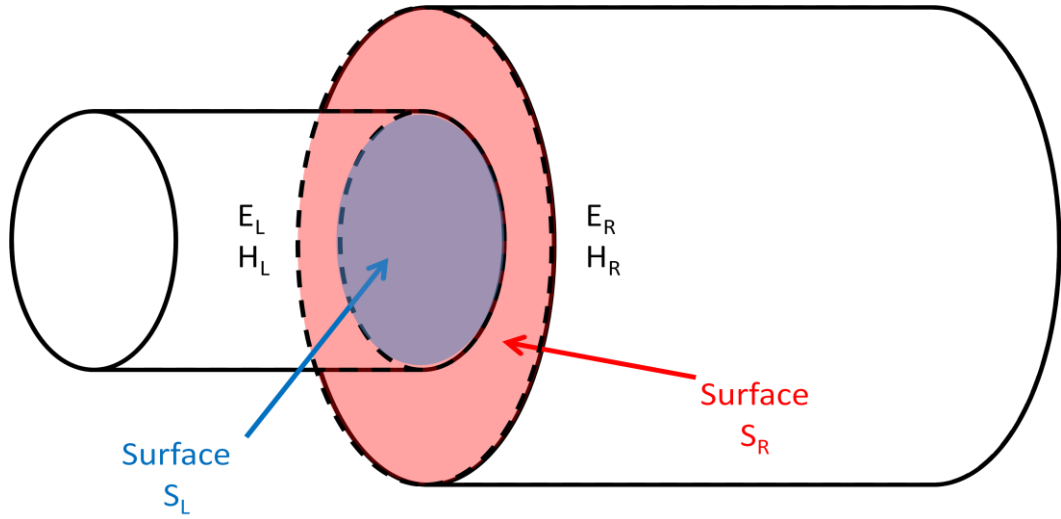


**Figure 2-3 : Fields at a junction of two horn sections.**

Let us now consider the case of a junction between two sections of cylindrical waveguide as shown in Figure 2-3. The transverse electric and magnetic fields on the left-hand side of the junction are denoted with the subscript $L$ (i.e. $E_L$ and $H_L$) while those on the right are denoted with the subscript $R$. The electric and magnetic fields on the left-hand side are, [Olver,1994],

$$\mathbf{E}_L = \sum_{n=1}^{N} \{A_n \exp(-\gamma_n z) + B_n \exp(\gamma_n z)\} \mathbf{e}_{nL}$$
$$\mathbf{H}_L = \sum_{n=1}^{N} \{A_n \exp(-\gamma_n z) - B_n \exp(\gamma_n z)\} \mathbf{h}_{nL} \quad , \quad (2.27)$$

where $A_n$ and $B_n$ are the forward and reflected amplitudes coefficients of the $n^{th}$ mode on the left-hand side of the junction (for example $n = 1$ represents the $TE_{11}$ mode, while $n = 2$ represents the $TE_{12}$ mode, etc.). It should be noted that clearly $n$ does not refer to the azimuthal order of the mode here but rather a number that is assigned to a mode. Similarly on the right-hand side of the junction the electric and magnetic fields are, [Olver,1994],

$$\mathbf{E}_R = \sum_{n=1}^{N} \{C_n \exp(-\gamma_n z) + D_n \exp(\gamma_n z)\} \mathbf{e}_{nR}$$
$$\mathbf{H}_R = \sum_{n=1}^{N} \{-C_n \exp(-\gamma_n z) + D_n \exp(\gamma_n z)\} \mathbf{h}_{nR} \quad , \quad (2.28)$$

where $C_n$ and $D_n$ are the forward and reflected amplitudes coefficients of the $n^{th}$ mode on the right-hand side of the junction. At the junction the total transverse fields must match over the common cross-sectional area. For the moment, choosing the junction to be at $z = 0$ for convenience, this condition yields,

$$\sum_{n=1}^{N}(A_n + B_n)\mathbf{e}_{nL} = \sum_{n=1}^{N}(C_n + D_n)\mathbf{e}_{nR}$$
$$\sum_{n=1}^{N}(A_n - B_n)\mathbf{h}_{nL} = \sum_{n=1}^{N}(-C_n + D_n)\mathbf{h}_{nR} \qquad . \qquad (2.29)$$

If the cross-sectional area of the waveguide on the left-hand side of the junction is $S_L$ and on the right-hand side is $S_R$, see Figure 2-3, the transverse electric field over the area of the conducting wall, $S_L - S_R$, must be zero due to boundary conditions. Therefore, either $\sum(C_n + D_n)\mathbf{e}_{nR} = 0$ if the second guide section is wider than the first guide section, i.e. $a < b$, or $\sum(A_n + B_n)\mathbf{e}_{nL} = 0$ if the first guide is wider than the second, $b < a$. For the moment the second guide will be assumed to be wider thus

$$\sum(C_n + D_n)\mathbf{e}_{nR} = 0 \quad \text{for } a < r < b \quad . \qquad (2.30)$$

Over the area $S_L$ the fields must be continuous. Taking the orthogonality between modes leads to the simultaneous equations

$$\sum(A_n + B_n)\int_0^a \mathbf{e}_{nL} \times \mathbf{h}_{mR}^* dA = \sum(C_n + D_n)\int_0^a \mathbf{e}_{nR} \times \mathbf{h}_{mR}^* dA = \sum(C_n + D_n)\int_0^b \mathbf{e}_{nR} \times \mathbf{h}_{mR}^* dA \qquad (2.31)$$

which can be re-expressed in matrix form as

$$[P][[A]+[B]] = [Q][[D]+[C]] \quad , \qquad (2.32)$$

where $[A]$ and $[B]$ are column matrices (vectors) containing the modal coefficients associated with the fields on the left-hand side of the junction $A_1$ to $A_N$ and $B_1$ to $B_N$ respectively. Similarly $[C]$ and $[D]$ contain the coefficients $C_1$ to $C_N$ and $D_1$ to $D_N$, and $[P]$ is an $N \times N$ matrix whose elements are the integrals representing the power coupled between the $i^{th}$ mode on the left-hand side of the junction and the $j^{th}$ mode on the right.

40

$$P_{ji} = \int_{S_L} \left( \mathbf{e}_{iL} \times \mathbf{h}_{jR}^* \right) \cdot d\mathbf{s}_L \quad . \tag{2.33}$$

The $N \times N$ diagonal matrix $[Q]$ describes the self-coupled power between the modes on the right-hand sides of the junction.

$$Q_{jj} = \int_{S_R} \left( \mathbf{e}_{jR} \times \mathbf{h}_{jR}^* \right) \cdot d\mathbf{s}_R \quad . \tag{2.34}$$

Similarly $[R]$ describes the self-coupling on the left-hand side of the junction.

$$R_{jj} = \int_{S_L} \left( \mathbf{e}_{jL} \times \mathbf{h}_{jL}^* \right) \cdot d\mathbf{s}_L \quad . \tag{2.35}$$

On the other hand for the magnetic field equation (2.29) we get

$$\sum \left( A_n^* - B_n^* \right) \int_0^a \mathbf{e}_{mL} \times \mathbf{h}_{nL}^* dA = \sum \left( C_n^* + D_n^* \right) \int_0^a \mathbf{e}_{mL} \times \mathbf{h}_{nR}^* dA$$

$$\left[ P^* \right]^T \left[ [D] - [C] \right] = [R]^* \left[ [A] - [B] \right] \quad . \tag{2.36}$$

Using that $[B] = S_{11}[A] + S_{22}[C]$ and that $[D] = S_{21}[A] + S_{22}[C]$ it is possible to solve for $S_{11}$, $S_{12}$, $S_{21}$, and $S_{22}$ in terms of $[R]$, $[P]$, and $[Q]$ to obtain

$$
\begin{aligned}
[S_{11}] &= \left[ [R] + [P]^+ [Q]^{-1} [P] \right]^{-1} \left[ [R] - [P]^+ [Q]^{-1} [P] \right] \\
[S_{12}] &= 2 \left[ [R] + [P]^+ [Q]^{-1} [P] \right]^{-1} [P]^+ \\
[S_{21}] &= 2 \left[ [Q] + [P][R]^{-1} [P]^+ \right]^{-1} [P] \\
[S_{22}] &= - \left[ [Q] + [P][R]^{-1} [P]^+ \right]^{-1} \left[ [Q] - [P][R]^{-1} [P]^+ \right]
\end{aligned}
\quad . \tag{2.37}
$$

As stated above in the analysis to derive equations (2.37), it has been assumed that the cross-sectional area on the right-hand side of the junction is greater than the cross-sectional area on the left-hand side, i.e. $S_R > S_L$. If this is not the case ($a > b$) then clearly $\sum \left( A_n + B_n \right) \mathbf{e}_{nL} = 0$ for $a < r < b$ and therefore

$$[R][[A] + [B]] = [P][[C] + [D]] \quad \text{and} \quad [P]^+ [[A] - [B]] = Q^* [[A] + [B]] \,, \tag{2.38}$$

where now $P_{ij} = \int_{S_R} \left( \mathbf{e}_{iL} \times \mathbf{h}_{jR}^* \right) \cdot d\mathbf{s}_R$ and the elements of $[S]$ thus become

$$[S] = \begin{bmatrix} [S'_{11}] & [S'_{12}] \\ [S'_{12}] & [S'_{22}] \end{bmatrix} = \begin{bmatrix} [S_{22}] & [S_{21}] \\ [S_{12}] & [S_{11}] \end{bmatrix}, \tag{2.39}$$

where the dashed terms imply true scattering matrix terms for $b < a$ and the undashed terms are those defined in equation (2.37).

## 2.3.1 Mode-matching for cylindrical waveguides

The mode-matching technique detailed in the previous section can be applied to the junctions of cylindrical waveguides in a straightforward manner by evaluating the power-coupling integrals equations (2.33) to (2.35) over the desired cylindrically symmetric geometry. These can then be used to determine the scattering matrices for a waveguide or conical horn system. The power coupling integrals involve the evaluation of the integrals of the form

$$\int_s \left( \mathbf{e} \times \mathbf{h}^* \right) d\mathbf{s} = \int_0^{2\pi} \int_0^a \left( e_r h_\phi^* - e_\phi h_r^* \right) r dr d\phi \tag{2.40}$$

The transverse fields are evaluated for each mode on each side of the junction from the axial TE and TM fields (equations (2.9) and (2.11)). Correspondingly, the transverse field components are summarised in equations (2.14), (2.15), (2.17), and (2.18) [Olver, 1994]. Inserting these field components into the self-coupling power integrals $Q_{jj}$ and $R_{jj}$ and evaluating these integrals of the products of Bessel functions gives for the TE modes

$$Q_{TM-TM} = \frac{\left| Z_{TM}^b \right|}{Z_{TM}^{b*}} \tag{2.41}$$

$$Q_{TE-TE} = \frac{Z_{TE}^{b*}}{\left| Z_{TE}^b \right|} \tag{2.42}$$

$$R_{TM-TM} = \frac{|Z_{TM}^a|}{Z_{TM}^{a*}} \tag{2.43}$$

$$R_{TE-TE} = \frac{Z_{TE}^{a*}}{|Z_{TE}^a|} \tag{2.44}$$

where $Z_{TE}$ and $Z_{TM}$ are the characteristic waveguide impedance as given by equations (2.16) and (2.19) and the $Q_{jj}$ and $R_{jj}$ terms are either 1 or $\pm i$ depending on whether the mode is real or evanescent respectively. The mutual power coupling integrals $P_{ij,}$ between the left and right hand waveguides over their common cross-section are given in Olver, [Olver, 1994], and E. Gleeson, [Gleeson, 2004]. For TM modes on the left of the junction coupling to TM modes on the right of the junction (for $a<b$)

$$P_{TM_{nl'}-TM_{nl}} = \frac{(1+\delta_{n0})\pi C_{nl}(a) C_{nl'}(b) a}{Z_{TM_{nl'}}^{b*} \left[ \left(\frac{p_{nl'}}{b}\right)^2 - \left(\frac{p_{nl}}{a}\right)^2 \right]} \left(\frac{p_{nl'}}{b}\right) J_n'(p_{nl}) J_n\left(\frac{p_{nl'}a}{b}\right) \tag{2.45}$$

where $C_{nl}(a) = \sqrt{\dfrac{(2-\delta_{n0})|Z_{TM,nl}^a|}{\pi a^2 J_{n+1}^2(p_{nl})}}$ and $D_{nl}(a) = \sqrt{\dfrac{(2-\delta_{n0})|Z_{TE,nl}^a|}{\pi a^2 (1-(n/q_{nl})^2) J_n^2(q_{nl})}}$ .

For TE modes on the left hand side of the junction coupling to TE modes on the right of the junction (for $a<b$)

$$P_{TE_{nl'}-TE_{nl}} = \frac{-(1+\delta_{n0})\pi D_{nl}(a) D_{nl'}(b)}{Z_{TE_{ml'}}^{b*} \left[ \left(\frac{q_{nl'}}{b}\right)^2 - \left(\frac{q_{nl}}{a}\right)^2 \right]} q_{nl} J_n(q_{nl}) J_n'\left(\frac{q_{nl'}a}{b}\right). \tag{2.46}$$

For TE mode on the left coupling to TM modes on the right (for $a<b$)

$$P_{TE_{nl'}-TM_{nl}} = \frac{\pi D_{nl}(a) C_{nl'}(b)}{2 Z_{TM_{nl'}}^{b*}} J_n(p_{nl}) J_n\left(\frac{p_{nl'}a}{b}\right) \tag{2.47}$$

And for TM modes on the left coupling to TE modes on the right (for $a<b$)

$$P_{TM_{nl'}-TE_{nl}} = 0 \tag{2.48}$$

In these cases the dash refers to the mode number in the right hand guide. It should be noted that only modes of the same azimuthal order and degeneracy type can couple to each other because of the cylindrical symmetry.
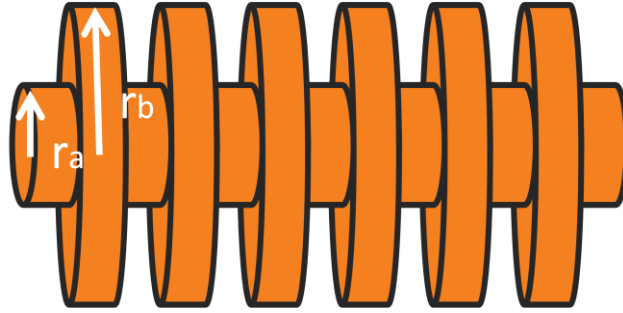
**Figure 2-4 : A diagram showing a corrugated waveguide where each corrugation slot and fin is a sequence of short cylindrical waveguides with the radius stepping between the deeper slots (radius $r_b$) and the narrower waveguide radius for the fins (radius $r_a$).**

A corrugated horn can be modelled by regarding each corrugation slot and fin as a sequence of short cylindrical waveguides with the radius stepping between the deeper slots and the narrower waveguide radius for the fins (see Figure 2-4). The number of modes depends on the relative diameters at each junction. The larger the change in diameter the greater, the number of modes that are excited, and the higher the level of mode conversion. Clearly, the time taken to compute the overall scattering matrix for the horn depends on the number of these modes required for an adequate description of the scattering process, and the number of steps in waveguide radius (or junctions) encountered in the horn. As to be expected, this computational time is proportional to the number of sections and approximately proportional to the square of the number of modes [Olver, 1994]. This is an important consideration for the modelling of the highest frequency channels, 545 GHz and 857 GHz, of the ESA Planck satellite High Frequency Instrument. Each of the four 857 GHz channels consisted of a back-to-back corrugated horn antenna pair coupling a corrugated detector horn antenna to the mirror optics of the satellite telescope with more than 1150 corrugations over the length of the entire back-to-back and detector horn arrangement. This corresponds to a total of 2300 junctions (or waveguide steps) for the purposes of mode-matching modelling.

Additionally of course, these highest frequency channels are multi-moded, or over moded, in that they support the propagation of hybrid modes of higher combinations than that of $TE_{11}$ and $TM_{11}$ for the $n = 1$ azimuthal order and also for azimuthal orders other than $n = 1$. A separate scattering matrix $S$ can be calculated for each azimuthal order since the modes of different azimuthal orders are orthogonal. This means in the case of the 857 GHz channels that a $60 \times 60$ scattering matrix for

each of the five azimuthal orders needed to be calculated by cascading the scattering matrices for each of the 2300 junctions. The approach taken to this modal modelling of these high frequency multi-moded horn antennas is described in detail in the next chapter. What makes the modelling approach, as presented here, very efficient computationally is the fact that the analytical expressions exist for all the coupling terms.

## 2.4 Computing Aperture Beam Patterns

For each waveguide mode at the input waveguide to the horn the hybrid output field at the horn aperture can be computed using the respective scattering coefficients as contained in the $S_{21}$ scattering matrix. This can be expressed by the equation

$$\mathbf{e}_n^{sc,out} = \sum_{n'} [\mathbf{S}_{21}]_{n'n} \mathbf{e}_{n'}^{out} \quad , \tag{2.49}$$

where $\mathbf{e}_n^{out}$ represents a output hybrid field at the output plane, where $\mathbf{e}_{n'}^{out}$ are the TE or TM waveguide modes at the output to the waveguide horn system, and $[S_{21}]_{n'n}$ the corresponding scattering coefficients. Assuming no reflections at the horn aperture (no $S_{22}$ terms), the farfield beam pattern of the horn can be obtained using the superposition principle by summing the product of scattering coefficients and the farfield patterns of the TE and TM waveguide modes instead of the fields at the aperture $\mathbf{e}_n^{sc,ff} = \sum_{n'} [\mathbf{S}_{21}]_{n'n} (\mathbf{e}_{n'})_{ff}$ , where the subscript *ff* implies farfield.

It is useful to now switch to Cartesian co-ordinates for the aperture field, particularly for tracking polarisations. The expressions for the transverse components of the electric and magnetic fields for the TE modes in these co-ordinates are

$$\left(e_{nl}^{TE}\right)_x = \sqrt{\frac{(2-\delta_{n0})\left|Z_{TE_{nl}}\right|}{4\pi a^2 (1-(n/q_{nl})^2) J_n^2(q_{nl})}} \left( J_{n-1}\left(q_{nl}\frac{r}{a}\right) \begin{bmatrix} \cos(n-1)\phi \\ -\sin(n-1)\phi \end{bmatrix} + J_{n+1}\left(q_{nl}\frac{r}{a}\right) \begin{bmatrix} \cos(n+1)\phi \\ -\sin(n+1)\phi \end{bmatrix} \right)$$

$$\left(e_{nl}^{TE}\right)_y = -\sqrt{\frac{(2-\delta_{n0})\left|Z_{TE_{nl}}\right|}{4\pi a^2(1-(n/q_{nl})^2)J_n^2(q_{nl})}}\left(J_{n-1}\left(q_{nl}\frac{r}{a}\right)\begin{bmatrix}\sin(n-1)\phi\\\cos(n-1)\phi\end{bmatrix}-J_{n+1}\left(q_{nl}\frac{r}{a}\right)\begin{bmatrix}\sin(n+1)\phi\\\cos(n+1)\phi\end{bmatrix}\right)$$

$$\left(h_{nl}^{TE}\right)_x = \frac{1}{Z_{TE_{nl}}}\sqrt{\frac{(2-\delta_{n0})\left|Z_{TE_{nl}}\right|}{4Z_{TE_{nl}}^2\pi a^2(1-(n/q_{nl})^2)J_n^2(q_{nl})}}\left(J_{n-1}\left(q_{nl}\frac{r}{a}\right)\begin{bmatrix}\sin(n-1)\phi\\\cos(n-1)\phi\end{bmatrix}-J_{n+1}\left(q_{nl}\frac{r}{a}\right)\begin{bmatrix}\sin(n+1)\phi\\\cos(n+1)\phi\end{bmatrix}\right)$$

$$\left(h_{nl}^{TE}\right)_y = \frac{1}{Z_{TE_{nl}}}\sqrt{\frac{(2-\delta_{n0})\left|Z_{TE_{nl}}\right|}{4Z_{TE_{nl}}^2\pi a^2(1-(n/q_{nl})^2)J_n^2(q_{nl})}}\left(J_{n-1}\left(q_{nl}\frac{r}{a}\right)\begin{bmatrix}\cos(n-1)\phi\\-\sin(n-1)\phi\end{bmatrix}+J_{n+1}\left(q_{nl}\frac{r}{a}\right)\begin{bmatrix}\cos(n+1)\phi\\-\sin(n+1)\phi\end{bmatrix}\right)$$

(2.50)

Note again because of the symmetry there is a pair of modes (a degeneracy of 2) for all azimuthal orders $n > 0$ as expressed by the pairs of trigonometric function terms in $(n+1)\phi$ and $(n-1)\phi$. The components for the transverse components of the electric and magnetic fields for the TM modes are

$$\left(e_{nl}^{TM}\right)_x = \sqrt{\frac{(2-\delta_{n0})\left|Z_{TM_{nl}}\right|}{4\pi a^2 J_{n+1}^2(p_{nl})}}\left(J_{n-1}\left(p_{nl}\frac{r}{a}\right)\begin{bmatrix}\cos(n-1)\phi\\-\sin(n-1)\phi\end{bmatrix}-J_{n+1}\left(p_{nl}\frac{r}{a}\right)\begin{bmatrix}\cos(n+1)\phi\\-\sin(n+1)\phi\end{bmatrix}\right)$$

$$\left(e_{nl}^{TM}\right)_y = -\sqrt{\frac{(2-\delta_{n0})\left|Z_{TM_{nl}}\right|}{4\pi a^2 J_{n+1}^2(p_{nl})}}\left(J_{n-1}\left(p_{nl}\frac{r}{a}\right)\begin{bmatrix}\sin(n-1)\phi\\\cos(n-1)\phi\end{bmatrix}+J_{n+1}\left(p_{nl}\frac{r}{a}\right)\begin{bmatrix}\sin(n+1)\phi\\\cos(n+1)\phi\end{bmatrix}\right)$$

$$\left(h_{nl}^{TM}\right)_x = \frac{1}{Z_{TM_{nl}}}\sqrt{\frac{(2-\delta_{n0})\left|Z_{TM_{nl}}\right|}{4Z_{TM_{nl}}^2\pi a^2 J_{n+1}^2(p_{nl})}}\left(J_{n-1}\left(p_{nl}\frac{r}{a}\right)\begin{bmatrix}\sin(n-1)\phi\\\cos(n-1)\phi\end{bmatrix}+J_{n+1}\left(p_{nl}\frac{r}{a}\right)\begin{bmatrix}\sin(n+1)\phi\\\cos(n+1)\phi\end{bmatrix}\right)$$

$$\left(h_{nl}^{TM}\right)_y = \frac{1}{Z_{TM_{nl}}}\sqrt{\frac{(2-\delta_{n0})\left|Z_{TM_{nl}}\right|}{4Z_{TM_{nl}}^2\pi a^2 J_{n+1}^2(p_{nl})}}\left(J_{n-1}\left(p_{nl}\frac{r}{a}\right)\begin{bmatrix}\cos(n-1)\phi\\-\sin(n-1)\phi\end{bmatrix}-J_{n+1}\left(p_{nl}\frac{r}{a}\right)\begin{bmatrix}\cos(n+1)\phi\\-\sin(n+1)\phi\end{bmatrix}\right).$$

(2.51)

The Cartesian $\hat{\imath}$ and $\hat{\jmath}$ directions can be associated with the co-polar and cross-polar directions for the $n = 1$ case. The interpretation is more complex for the $n \neq 1$ due to the corresponding symmetries. However, the "co-polar" modes are polarised along the x-axis in the $\phi = 0$ direction while the "orthogonal" modes are polarised along the y-axis in the $\phi = 0$ direction. There are two sets of mutually orthogonal modes for each

46

azimuthal order because of the cylindrical symmetry, except for the $n = 0$ order, and these do not scatter into each other.

S21

File  Edit  View  Graphics  Debug  Desktop  Window  Help

Stack: Base

S21 <60x60 double>

| | 1 | 2 | 3 | 4 | 5 | 6 | 7 | 8 | 9 |
|---|---|---|---|---|---|---|---|---|---|
| 1 | -0.5422 + 0.6379i | 0.0000 + ... | 0.0000 + ... | 0.0000 + ... | 0.0000 + ... | 0.0000 + ... | 0.0000 + ... | 0.0000 + ... | 0.0000 + ... |
| 2 | -0.1928 + 0.0857i | 0.0000 + ... | 0.0000 + ... | 0.0000 + ... | 0.0000 + ... | 0.0000 + ... | 0.0000 + ... | 0.0000 + ... | 0.0000 + ... |
| 3 | 0.0008 - 0.0213i | 0.0000 + ... | 0.0000 + ... | 0.0000 + ... | 0.0000 + ... | 0.0000 + ... | 0.0000 + ... | 0.0000 + ... | 0.0000 + ... |
| 4 | -0.0072 + 0.0103i | 0.0000 + ... | 0.0000 + ... | 0.0000 + ... | 0.0000 + ... | 0.0000 + ... | 0.0000 + ... | 0.0000 + ... | 0.0000 + ... |
| 5 | 0.0034 - 0.0079i | 0.0000 + ... | 0.0000 + ... | 0.0000 + ... | 0.0000 + ... | 0.0000 + ... | 0.0000 + ... | 0.0000 + ... | 0.0000 + ... |
| 6 | -0.0023 + 0.0063i | 0.0000 + ... | 0.0000 + ... | 0.0000 + ... | 0.0000 + ... | 0.0000 + ... | 0.0000 + ... | 0.0000 + ... | 0.0000 + ... |
| 7 | 0.0012 - 0.0040i | 0.0000 + ... | 0.0000 + ... | 0.0000 + ... | 0.0000 + ... | 0.0000 + ... | 0.0000 + ... | 0.0000 + ... | 0.0000 + ... |
| 8 | -0.0012 + 0.0039i | 0.0000 + ... | 0.0000 + ... | 0.0000 + ... | 0.0000 + ... | 0.0000 + ... | 0.0000 + ... | 0.0000 + ... | 0.0000 + ... |
| 9 | 0.0011 - 0.0008i | 0.0000 + ... | 0.0000 + ... | 0.0000 + ... | 0.0000 + ... | 0.0000 + ... | 0.0000 + ... | 0.0000 + ... | 0.0000 + ... |
| 10 | -5.2321e-04 + 8.3887e-04i | 0.0000 + ... | 0.0000 + ... | 0.0000 + ... | 0.0000 + ... | 0.0000 + ... | 0.0000 + ... | 0.0000 + ... | 0.0000 + ... |
| 11 | 2.0755e-04 - 7.2962e-04i | 0.0000 + ... | 0.0000 + ... | 0.0000 + ... | 0.0000 + ... | 0.0000 + ... | 0.0000 + ... | 0.0000 + ... | 0.0000 + ... |
| 12 | -1.3220e-05 + 5.7904e-04i | 0.0000 + ... | 0.0000 + ... | 0.0000 + ... | 0.0000 + ... | 0.0000 + ... | 0.0000 + ... | 0.0000 + ... | 0.0000 + ... |
| 13 | -1.0685e-04 - 4.2345e-04i | 0.0000 + ... | 0.0000 + ... | 0.0000 + ... | 0.0000 + ... | 0.0000 + ... | 0.0000 + ... | 0.0000 + ... | 0.0000 + ... |
| 14 | 1.7741e-04 + 2.7756e-04i | 0.0000 + ... | 0.0000 + ... | 0.0000 + ... | 0.0000 + ... | 0.0000 + ... | 0.0000 + ... | 0.0000 + ... | 0.0000 + ... |
| 15 | -2.1374e-04 - 1.4795e-04i | 0.0000 + ... | 0.0000 + ... | 0.0000 + ... | 0.0000 + ... | 0.0000 + ... | 0.0000 + ... | 0.0000 + ... | 0.0000 + ... |
| 16 | 2.2613e-04 + 3.7460e-05i | 0.0000 + ... | 0.0000 + ... | 0.0000 + ... | 0.0000 + ... | 0.0000 + ... | 0.0000 + ... | 0.0000 + ... | 0.0000 + ... |
| 17 | -2.2190e-04 + 5.3120e-05i | 0.0000 + ... | 0.0000 + ... | 0.0000 + ... | 0.0000 + ... | 0.0000 + ... | 0.0000 + ... | 0.0000 + ... | 0.0000 + ... |
| 18 | 2.0647e-04 - 1.2415e-04i | 0.0000 + ... | 0.0000 + ... | 0.0000 + ... | 0.0000 + ... | 0.0000 + ... | 0.0000 + ... | 0.0000 + ... | 0.0000 + ... |
| 19 | -1.8393e-04 + 1.7673e-04i | 0.0000 + ... | 0.0000 + ... | 0.0000 + ... | 0.0000 + ... | 0.0000 + ... | 0.0000 + ... | 0.0000 + ... | 0.0000 + ... |
| 20 | 1.5741e-04 - 2.1243e-04i | 0.0000 + ... | 0.0000 + ... | 0.0000 + ... | 0.0000 + ... | 0.0000 + ... | 0.0000 + ... | 0.0000 + ... | 0.0000 + ... |
| 21 | -1.2930e-04 + 2.3312e-04i | 0.0000 + ... | 0.0000 + ... | 0.0000 + ... | 0.0000 + ... | 0.0000 + ... | 0.0000 + ... | 0.0000 + ... | 0.0000 + ... |
| 22 | 1.0143e-04 - 2.4082e-04i | 0.0000 + ... | 0.0000 + ... | 0.0000 + ... | 0.0000 + ... | 0.0000 + ... | 0.0000 + ... | 0.0000 + ... | 0.0000 + ... |
| 23 | -7.5120e-05 + 2.3763e-04i | 0.0000 + ... | 0.0000 + ... | 0.0000 + ... | 0.0000 + ... | 0.0000 + ... | 0.0000 + ... | 0.0000 + ... | 0.0000 + ... |
| 24 | 5.1340e-05 - 2.2562e-04i | 0.0000 + ... | 0.0000 + ... | 0.0000 + ... | 0.0000 + ... | 0.0000 + ... | 0.0000 + ... | 0.0000 + ... | 0.0000 + ... |
| 25 | -3.0680e-05 + 2.0679e-04i | 0.0000 + ... | 0.0000 + ... | 0.0000 + ... | 0.0000 + ... | 0.0000 + ... | 0.0000 + ... | 0.0000 + ... | 0.0000 + ... |
| 26 | 1.3510e-05 - 1.8301e-04i | 0.0000 + ... | 0.0000 + ... | 0.0000 + ... | 0.0000 + ... | 0.0000 + ... | 0.0000 + ... | 0.0000 + ... | 0.0000 + ... |
| 27 | 5.0000e-08 + 1.5596e-04i | 0.0000 + ... | 0.0000 + ... | 0.0000 + ... | 0.0000 + ... | 0.0000 + ... | 0.0000 + ... | 0.0000 + ... | 0.0000 + ... |
| 28 | -1.0020e-05 - 1.2714e-04i | 0.0000 + ... | 0.0000 + ... | 0.0000 + ... | 0.0000 + ... | 0.0000 + ... | 0.0000 + ... | 0.0000 + ... | 0.0000 + ... |
| 29 | 1.6550e-05 + 9.7790e-05i | 0.0000 + ... | 0.0000 + ... | 0.0000 + ... | 0.0000 + ... | 0.0000 + ... | 0.0000 + ... | 0.0000 + ... | 0.0000 + ... |
| 30 | -1.9710e-05 - 6.8850e-05i | 0.0000 + ... | 0.0000 + ... | 0.0000 + ... | 0.0000 + ... | 0.0000 + ... | 0.0000 + ... | 0.0000 + ... | 0.0000 + ... |

**Figure 2-5 : The $S_{21}$ scattering matrix for the Planck 353 GHz horn antenna (only first 30 rows and first 9 columns are shown here for clarity).**

As an example, let us consider the case of the so called 'single mode' 353 GHz horn on the HFI. The horn is assumed to be fed by a blackbody source so in theory all modes are possibly present at the input and will be generated by the black body source independently of each other. Shown in Figure 2-5 is a screen shot showing the terms of the $S_{21}$ matrix for the front end of the 353 GHz back-to-back horn fed by such a black body cavity. The first thirty rows and first nine columns of the $S_{21}$ scattering matrix are listed. The 353 GHz horn antenna is actually 'single' moded with power only being carried by one hybrid $HE_{11}$ mode. In fact, of course, there is a pair of orthogonal modes because of symmetry as discussed above. This effectively degenerate hybrid mode is described by the non-zero elements of the scattering matrix which, in this case, detail how power from a $TE_{11}$ mode at the input is scattered into

other waveguide modes of azimuthal order 1, i.e. the non-zero elements in the first column which describe power scattered from the $TE_{11}$ mode. The scattered field at the aperture of the horn is the $HE_{11}$ hybrid field and is given by

$$\mathbf{e}_{1,ap}^{sc} = \sum \left[\mathbf{S}_{21}\right]_{n'1} \mathbf{e}_{n'}^{ap} \quad , \tag{2.52}$$

where $\mathbf{e}_{n'}^{ap}$ are the waveguide modes at the horn aperture where 1 represents the $TE_{11}$ mode. Again in reality there are a pair of fields that are possible for the two possible $(TE)_{11}$ degenerate fields at the input of the horn corresponding to the first column of the $S_{21}$ matrix for azimuthal order $n = 1$. A linear plot of the intensity pattern at the aperture, normalised to unity on-axis, that was calculated from this matrix is shown in Figure 2-6. As detailed in Chapter 1 (section 1.8), there are 8 polarised and 4 unpolarised 353 GHz channels on HFI. In the polarised channels there are, in fact, two bolometric detectors which are polarisation sensitive and couple to only one of the possible $HE_{11}$ pair of fields propagating in the waveguide of the back-to-back 353 GHz horn. In reality, the $TM_{11}$ mode at the input to the system also propagates through to the aperture and gets scattered as it does, but in this case it also only scatters into a $HE_{11}$ field so that the beam pattern is the same as for the $TE_{11}$ case. In this sense there is only one true hybrid mode that can propagate through the system and the horn is truly 'single' moded.
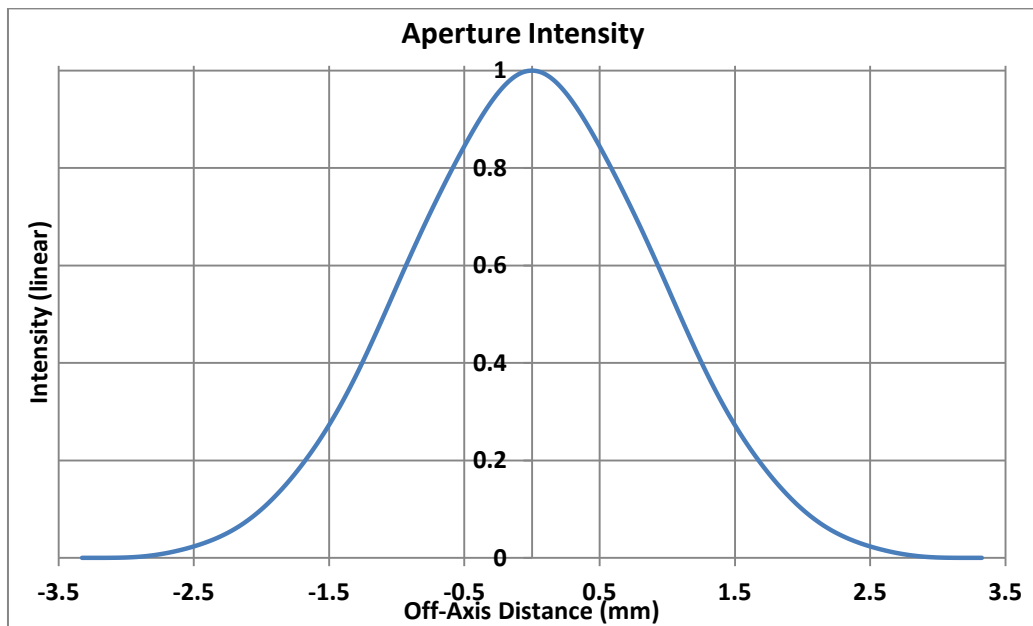


**Figure 2-6 : Plot of the normalised intensity of the aperture field of the Planck 353 GHz horn antenna.**

# 2.5 Computing Farfield Beam Patterns

The farfield patterns of the TE and TM modes can be acquired by Fourier transforming the mode fields at the aperture of the horn (Fraunhofer diffraction). For single mode horns it can be useful for the measurement of polarisation to define co-polar and cross polar fields [Olver 1994]:

$$\mathbf{E_{co}} = \mathbf{E_\theta}\cos\phi_o - \mathbf{E_\phi}\sin\phi_o \ , \tag{2.53}$$

$$\mathbf{E_{xp}} = \mathbf{E_\theta}\sin\phi_o + \mathbf{E_\phi}\cos\phi_o \ , \tag{2.54}$$

where $\phi_o$ is as defined in Figure 2-7 and the spherical polar components are given by the following approximation

$$E_\theta \propto \left(1+\cos\theta_o\right)\left(f_x\cos\phi_o + f_y\sin\phi_o\right) \tag{2.55}$$

$$E_\phi \propto \left(1+\cos\theta_o\right)\left(-f_x\sin\phi_o + f_y\cos\phi_o\right) \ , \tag{2.56}$$

where $f_x$ and $f_y$ are associated with the Fourier transforms of the $x$ and $y$ components of the aperture field (only one of the pair of possible modes is chosen). In this approximation, the fields at the aperture are assumed to be of transverse electromagnetic mode (TEM) type fields so that $E_{ax} = Z_0 H_{ay}$ and $E_{ay} = -Z_0 H_{ax}$, where $\mathbf{E}_a$ and $\mathbf{H}_a$ are the aperture electric and magnetic fields. $\theta_o$ is the elevation angle in the farfield with respect to the z-axis, and $\phi_0$ is the azimuthal angle, in the farfield (as defined in Figure 2-7).
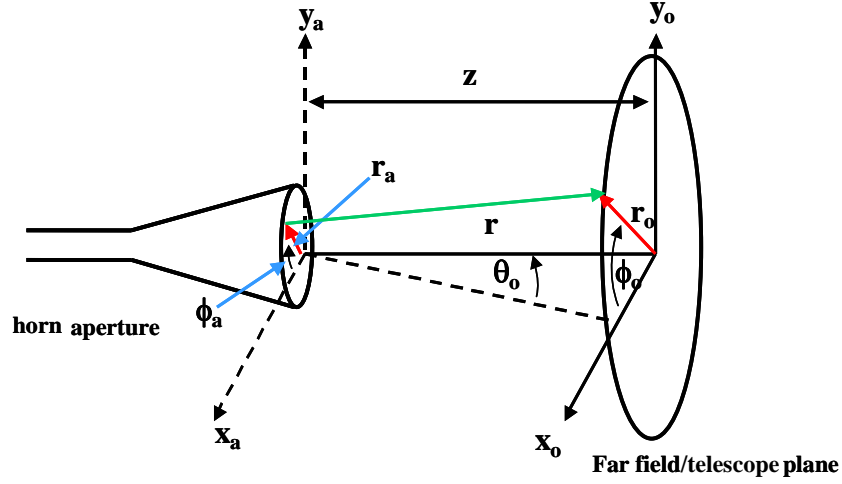
The Cartesian components of the Fourier Transform (Fraunhofer diffraction) are given by [Gleeson, 2004]

$$f_x(\theta_o, \phi_o) = \int\limits_{\phi_a=0}^{\phi_a=2\pi} \int\limits_{r_a=0}^{r_a=a} E_{ax}(r_a, \phi_a) \exp\{ jkr_a \sin\theta_o \cos(\phi_o - \phi_a)\} r_a dr_a d\phi_a \quad , \quad (2.57)$$

$$f_y(\theta_o, \phi_o) = \int\limits_{\phi_a=0}^{\phi_a=2\pi} \int\limits_{r_a=0}^{r_a=a} E_{ay}(r_a, \phi_a) \exp\{ jkr_a \sin\theta_o \cos(\phi_o - \phi_a)\} r_a dr_a d\phi_a \quad , \quad (2.58)$$

where $\phi_a$ corresponds to the $\phi$ angle in the horn aperture (again as defined in Figure 2-7). Combining these with equations (2.53), (2.54), (2.55), and (2.56) the co-polar (*x*-direction) and cross-polar (*y*-direction) farfield expressions are

$$E_{co} = \frac{jke^{-jkr}}{4\pi r}\left(1 + \cos\theta_o\right) f_x(\theta_o, \phi_o) \qquad\qquad (2.59)$$

$$E_{xp} = \frac{jke^{-jkr}}{4\pi r}\left(1 + \cos\theta_o\right) f_y(\theta_o, \phi_o) \quad . \qquad\qquad (2.60)$$

As shown by [Gleeson, 2004], for small angles $\theta_o$ the far field of a mode can be re-expressed by its co-polar (i.e. '*x*' direction) and cross-polar (i.e. '*y*') directions as

$$\left[\mathbf{e}_{nl}^{TE/TM}(\theta_o, \phi_o)\right]^{FF} \propto \left(I_{n-1,l}^{TE/TM}(\theta_o, \phi_o) \pm I_{n+1,l}^{TE/TM}(\theta_o, \phi_o)\right)\hat{\mathbf{i}} \pm \left(I_{n-1,l}^{TE/TM}(\theta_o, \phi_o) \pm I_{n+1,l}^{TE/TM}(\theta_o, \phi_o)\right)\hat{\mathbf{j}}$$

$$(2.61)$$

where

$$I_{n\pm1,l}\left(\theta_o,\phi_o\right)=\int\limits_{r_a=0}^{r_a=a} J_{n\pm1}\left(\chi_{nl}\,r_a\,/\,a\right) J_{n\pm1}\left(k r_a \sin\theta_o\right) 2\pi i^{n\pm1} \begin{bmatrix} \cos(n\pm1)\phi_o \\ \sin(n\pm1)\phi_o \end{bmatrix} r_a dr_a \quad ,$$

and $\chi_{nl}=p_{nl}$ or $q_{nl}$, again for the two possible orientations of a pair of 'degenerate' modes for each $TE_{nl}$ and $TM_{nl}$ in the waveguide at the horn aperture. The integration over $r_a$ can be performed as

$$\Im_{n\pm1}^{FF}\left(\theta_o;\chi_{nl}\right)=\int\limits_{r_a=0}^{r_a=a} J_{n\pm1}\left(\chi_{nl}r_a\,/\,a\right) J_{n\pm1}\left(k r_a \sin\theta_o\right) r_a dr_a$$

$$=\frac{\left\{\chi_{nl}\,J_{n\pm1}\left(ka\sin\theta_o\right) J'_{n\pm1}\left(\chi_{nl}\right)-\left(ka\sin\theta_o\right) J_{n\pm1}\left(\chi_{nl}\right) J'_{n\pm1}\left(ka\sin\theta_o\right)\right\}}{\left(k\sin\theta_o\right)^2-\left(\dfrac{\chi_{nl}}{a}\right)^2} \quad , \qquad (2.62)$$

so that the far field expressions for $x$ and $y$ components of the $TE$ and $TM$ modes as given by [Gleeson, 2004] are

$$\left[e_{nl}^{TMx}\left(\theta_o,\phi_o\right)\right]_x^{FF}\propto\left(1+\cos\theta_o\right)\sqrt{\frac{\left(2-\delta_{n0}\right)}{4\pi a^2 J_{n+1}^2(p_{nl})}}\times$$

$$\left(\Im_{n-1}^{FF}\left(\theta_o;p_{nl}\right)\begin{bmatrix}\cos(n-1)\phi_o\\-\sin(n-1)\phi_o\end{bmatrix}\frac{2\pi}{i^{-(n-1)}}-\Im_{n+1}^{FF}\left(\theta_o;p_{nl}\right)\begin{bmatrix}\cos(n+1)\phi_o\\-\sin(n+1)\phi_o\end{bmatrix}\frac{2\pi}{i^{-(n+1)}}\right) \quad (2.63)$$

$$\left[e_{nl}^{TMy}\left(\theta_o,\phi_o\right)\right]_x^{FF}\propto-\left(1+\cos\theta_o\right)\sqrt{\frac{\left(2-\delta_{n0}\right)}{4\pi a^2 J_{n+1}^2(p_{nl})}}\times$$

$$\left(\Im_{n-1}^{FF}\left(\theta_o;p_{nl}\right)\begin{bmatrix}\sin(n-1)\phi_o\\\cos(n-1)\phi_o\end{bmatrix}\frac{2\pi}{i^{-(n-1)}}+\Im_{n+1}^{FF}\left(\theta_o;p_{nl}\right)\begin{bmatrix}\sin(n+1)\phi_o\\\cos(n+1)\phi_o\end{bmatrix}\frac{2\pi}{i^{-(n+1)}}\right) \quad (2.64)$$

$$\left[e_{nl}^{TEx}\left(\theta_o,\phi_o\right)\right]_y^{FF}\propto\left(1+\cos\theta_o\right)\sqrt{\frac{\left(2-\delta_{n0}\right)}{4\pi a^2 (1-(n/q_{nl})^2)J_n^2(q_{nl})}}\times$$

$$\left(\Im_{n-1}^{FF}\left(\theta_o;q_{nl}\right)\begin{bmatrix}\cos(n-1)\phi_o\\-\sin(n-1)\phi_o\end{bmatrix}\frac{2\pi}{i^{-(n-1)}}+\Im_{n+1}^{FF}\left(\theta_o;q_{nl}\right)\begin{bmatrix}\cos(n+1)\phi_o\\-\sin(n+1)\phi_o\end{bmatrix}\frac{2\pi}{i^{-(n+1)}}\right) \quad (2.65)$$

$$\left[e_{nl}^{TEy}\left(\theta_o,\phi_o\right)\right]_y^{FF}\propto-\left(1+\cos\theta_o\right)\sqrt{\frac{\left(2-\delta_{n0}\right)}{4\pi a^2 (1-(n/q_{nl})^2)J_n^2(q_{nl})}}\times$$

$$\left(\Im_{n-1}^{FF}\left(\theta_o;q_{nl}\right)\begin{bmatrix}\sin(n-1)\phi_o\\\cos(n-1)\phi_o\end{bmatrix}\frac{2\pi}{i^{-(n-1)}}-\Im_{n+1}^{FF}\left(\theta_o;q_{nl}\right)\begin{bmatrix}\sin(n+1)\phi_o\\\cos(n+1)\phi_o\end{bmatrix}\frac{2\pi}{i^{-(n+1)}}\right). \quad (2.66)$$

For a single moded horn feeding a polarisation sensitive bolometer (or fed by a rectangular waveguide) only a single coherent field propagates from the horn aperture

to the sky. This field is effectively produced by a $TE_{11}$ mode in the waveguide feeding the horn (assuming the scattering computation is started in the waveguide). As in the previous case of the 353 GHz horn the first column of the $S_{21}$ scattering matrix can be used to provide the farfield mode coefficients, and the farfield beam pattern can be calculated as

$$\mathbf{e}_1^{sc,ff} = \sum_{n'} \left[ \mathbf{S}_{21} \right]_{n'1} \mathbf{e}_{n'}^{ff} . \qquad (2.67)$$

The farfield pattern for the 353 GHz horn is presented in Figure 2-8 which was calculated using the farfield expressions 2.64-2.66. The aperture field of the same horn is presented earlier in Figure 2-6.
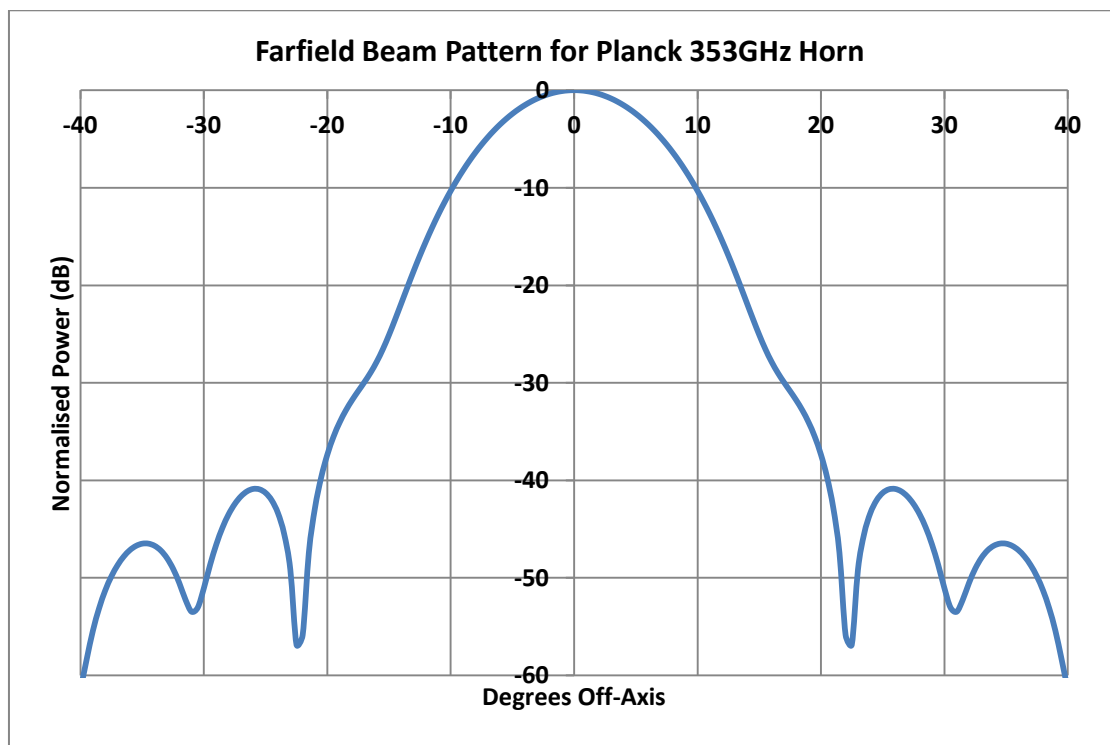


**Figure 2-8 : Plot of the farfield beam pattern of the Planck 353 GHz horn antenna.**

In the case of a multimode horn the situation is more complicated. Assuming the waveguide feeding the horn (or indeed the back horn itself) is multimoded, there will be several columns of $S_{21}$ matrix with non-zero elements. Each column of $[S_{21}]$ corresponds to an aperture mode at the input and how it is scattered as it propagates to the aperture. Since we assume black body illumination of the input port of the waveguide these modes are effectively independent of each other [Murphy, 2001].

We therefore calculate the farfield power pattern for each of these modes and sum the power patterns to get the overall beam on the sky,

$$\mathbf{e}_n^{sc,ff} = \sum_{n'} [\mathbf{S}_{21}]_{n'n} \mathbf{e}_{n'}^{ff} \ , \qquad (2.68)$$

where $\mathbf{e}_{n'}^{ff}$ are the farfields of the modes. Giving the power pattern on the sky as

$$P_{sky} \propto \sum_n \left| \mathbf{e}_n^{sc,ff} \right|^2 \ . \qquad (2.69)$$

Examples of multimode horn beam patterns are shown in the next section.

# 2.6  The SCATTER Software

SCATTER is the in-house software code developed in Maynooth for modelling horn antennas using mode matching. The original SCATTER software to implement the mode matching techniques described in the last section was written by R. Colgan in Mathematica [Colgan, 2001]. The program was adapted for MATLAB by E. Gleeson [Gleeson, 2004]; the conversion to MATLAB was undertaken for several reasons, the most important being to take advantage of MATLAB's better use of computer memory compared to the original versions written in Mathmatica, thus making it possible to include more TE and TM modes in the simulations. This MATLAB version of the SCATTER code (Figure 2-9) was the one primarily used for the modelling of the multimode channels of the Planck satellite, as is detailed in the Chapters 3, 4, and 5 of this thesis. A number of additional improvements were implemented in the SCATTER code during the course of this work; firstly to eliminate some numerical instabilities (see Section 3.3), and also, to obtain the true hybrid mode eigenfields of the antennas using SVD analysis (Section 2.7). Additional code was also added to calculate the roots of the Bessel functions and their derivatives for the required large number of modes and azimuthal orders dictated by the high frequency multimode horn antennas of the HFI instrument on Planck. In fact, prior to these improvements only the roots required for first 10 TE and 10 TM modes, i.e. the 20 lowest orders, were needed. This number of modes were assumed sufficient to

describe the horn antennas [Noviello, 2008]. However, as will be explained later in Chapter 3, a much greater number of modes, at least 60, was required to obtain a more complete and more numerically robust and stable description of the Planck multimode horns, particularly at all of the large number of sample spot frequencies computed across their operational bands.
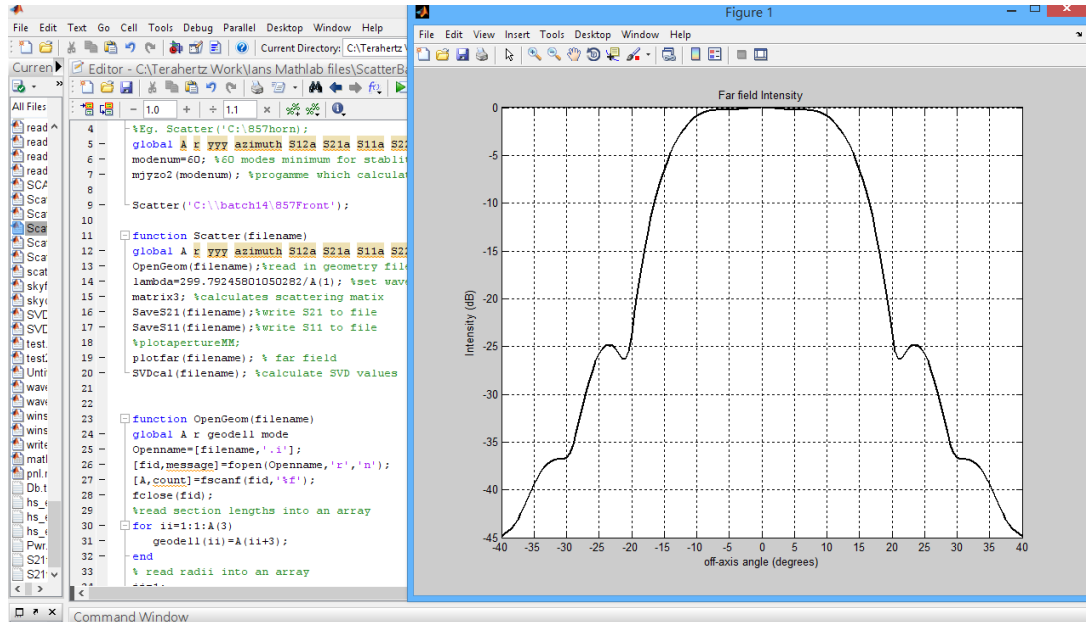


**Figure 2-9 : A screen capture showing the SCATTER code in MATLAB and a plot of a farfield beam pattern.**

To begin with, when running an example, the description of the horn antenna in terms of circular waveguide sections is read into SCATTER from a geometry file. The geometry files are text files, with extensions either ".txt" or ."i", containing the frequency in GHz, highest azimuthal order required (1 for single mode antennas, >1 for multi-moded horns which computes all the orders from $n = 0$ to the maximum order), the number of sections, and the length and radius of each step (section) in millimetres (see Table 2-1). The file also contains an estimated minimum number of modes needed to model each section. This is, in fact, not used by SCATTER but by another single mode horn design program called CORRUG which was used by collaborators in Manchester and Cardiff for modelling single mode horns (CORRUG cannot simulate multi-mode horns which was one of the reasons for originally developing SCATTER). The structure of the geometry file is shown in Figure 2-10. A plot of the geometry file for the front horn of the Planck 857 GHz back-to-back horn pair is shown in Figure 2-11. A magnified view of the waveguide filter and throat

section of the horn is provided in Figure 2-12, and shows the corrugations slots and fins which make up the horn profile.

| Line 1 | Frequency | Highest Azimuthal Order | Number of Sections (N) |
|---|---|---|---|
| Line 2 ⋮ Line N+1 | Length of Each Section | | |
| Line N+2 ⋮ Line 2N+1 | Radius of Each Section | Approx Number of Modes | |

Table 2-1 : Structure of a horn geometry file.
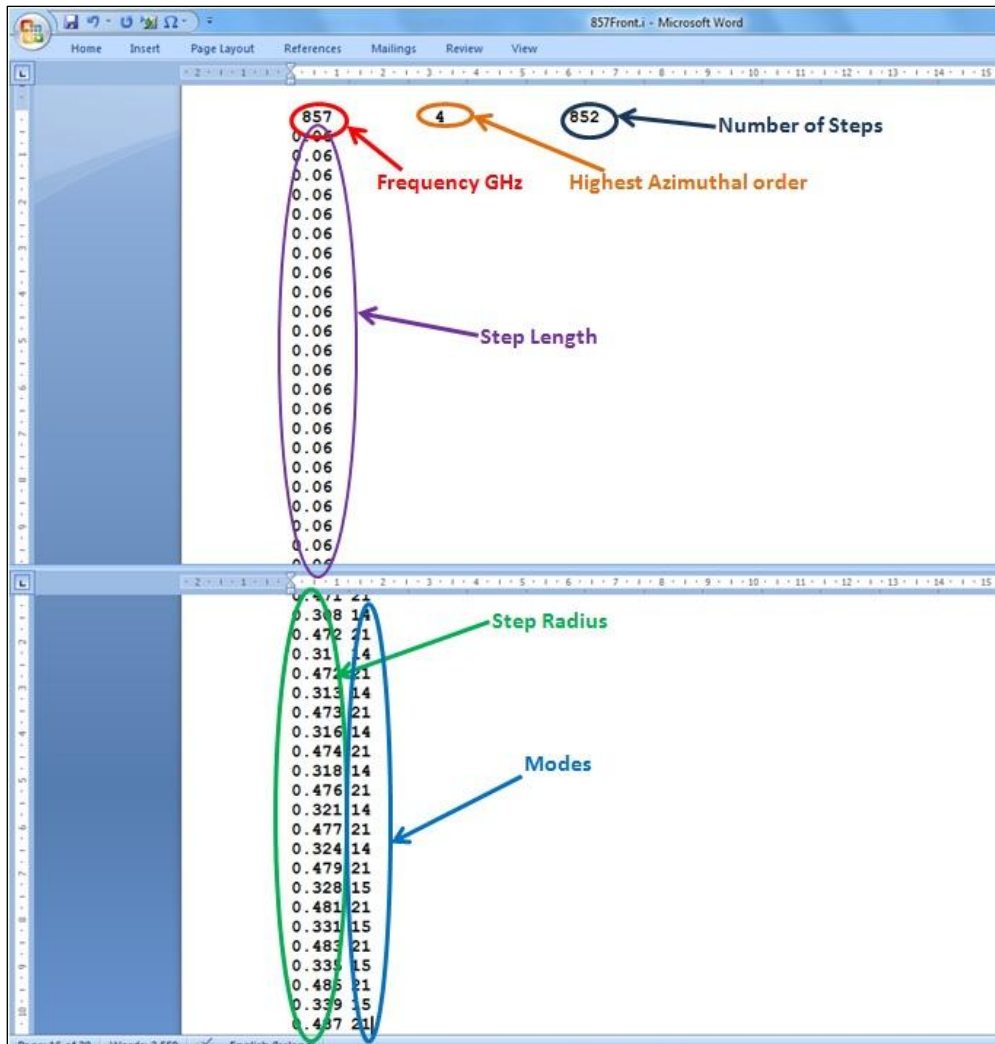


Figure 2-10 : A screen shot of an example of a SCATTER input geometry file.  The upper panel shows how the lengths of the sections are listed while the lower panel shows how the radius of each section is listed.  The file shown is the front section of the Planck 857 GHz back-to-back horn.
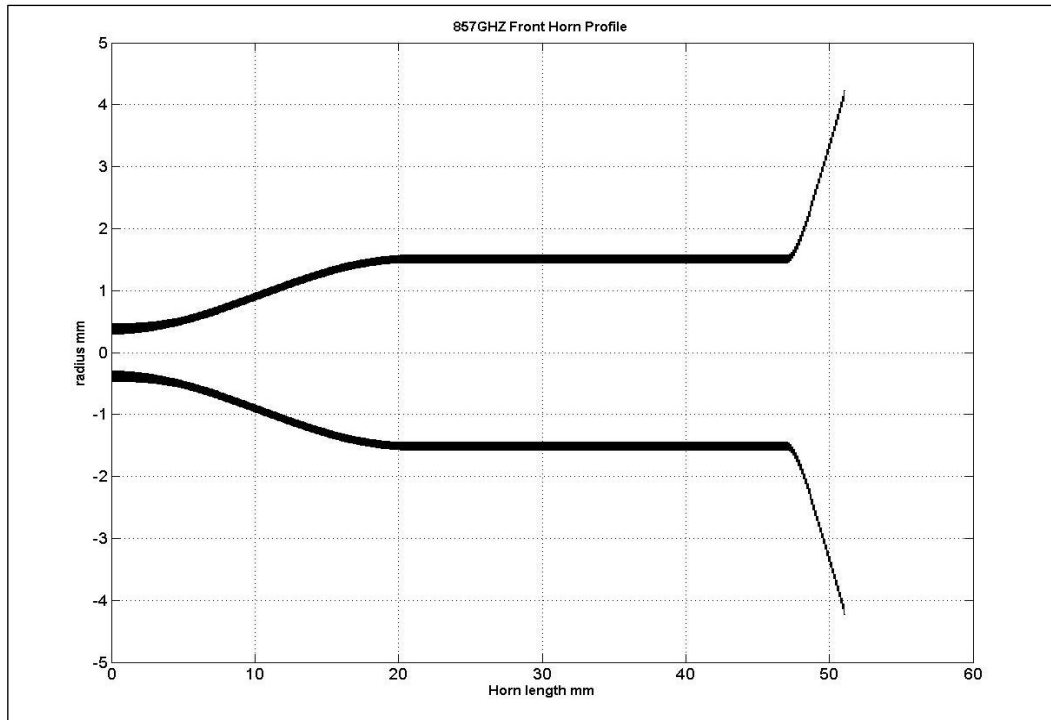
**Figure 2-11 : Plot of the profile of the front section of the Planck 857 GHz back-to-back horn.**
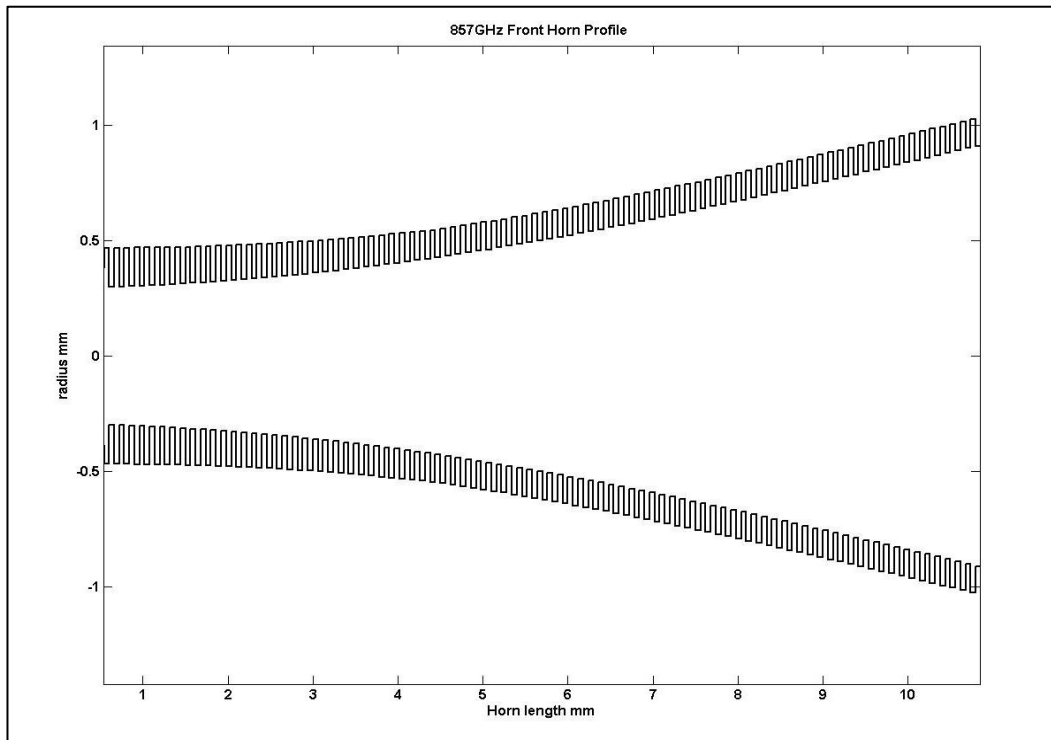


**Figure 2-12 : Close up plot of a section of the Planck 857 GHz back-to-back horn shown in the previous figure above. The individual corrugations are visible in this zoomed-in plot.**

The overall structure of the SCATTER code is shown in Table 2-2. Once the geometry file has been read in, and roots of the required Bessel functions and their derivatives calculated, SCATTER proceeds to calculate the scattering matrices ($[S_{11}]$,

56

$[S_{12}]$, $[S_{21}]$, & $[S_{22}]$) for each section of the horn sequentially as described in section 2.3 . To calculate these (equation 2.26) the power coupling integrals are required. For multi-moded horns the scattering matrices for each azimuthal order are calculated separately as different azimuthal orders do not scatter into each other starting with the lowest azimuthal order. For single mode horns the azimuthal order is fixed at $n = 1$. At each junction, the power coupling $P$ matrix is constructed from four sub-matrices representing all the possible power couplings between the TE and TM modes on both sides of a step, using equations 2.33 ,2.34, and 2.35,

$$[P] = \begin{bmatrix} [P_{TE-TE}] & [P_{TE-TM}] \\ [P_{TM-TE}] & [P_{TM-TM}] \end{bmatrix}, \qquad (2.70)$$

where $[P_{TE\text{-}TE}]$ is as defined in equation 2.46, and similarly $[P_{TM\text{-}TM}]$, $[P_{TE\text{-}TM}]$, and $[P_{TM\text{-}TE}]$ are given by equations 2.45, 2.47, and 2.48 respectively. The self coupling power matrices $[Q]$ and $[R]$ are of a similar format with entries defined by equations 2.41 and 2.42 for the $[Q]$ matrix and by equations 2.43 and 2.44 for the $[R]$ matrix. From these the scattering matrices $[S_{11}]$, $[S_{12}]$, $[S_{21}]$,and $[S_{22}]$ are computed using equations 2.37, and then each is cascaded with a matrix describing the propagation of the beam along length of the circular waveguide section to the next junction (the $[V]$ matrices as in equation 2.26). These matrices are then cascaded with the overall scattering matrices for the horn up to that point using equations 2.25 before adding in the next section in a sequential manner. Once the overall scattering matrices for the entire horn have been calculated for one azimuthal order, the process is repeated for the next azimuthal order in the case of multimode horns until the scattering matrices for all azimuthal orders have be obtained. Of course for single mode horns only $n = 1$ azimuthal order is required. The aperture beam pattern and the farfield beam pattern are then calculated and the data concerning the beam patterns saved to separate output files. Details of the calculation of the aperture and farfield are given in Sections 2.4 and 2.5 respectively.

**Read in geometry file**

**For each azimuthal order**

**Step 1: For each mode evaluate the power coupling coefficients *P*, *R*, *Q*. (Equations 2.27, 2.28, & 2.29)**

**Step 2: Compute the scattering matrix of the junction using power coupling coefficients. (Equations 2.30)**

**Step 3: Cascade the scattering matrix of the junction with the matrix describing beam propagation in uniform circular waveguide. (Equations 2.22)**

**Step 4: Then cascade the matrix for the junction and uniform waveguide section with the overall matrix for the horn up to that point.  (Equations 2.21)**

**Step 5 : Move on to next section and go back to step 1 else if it is the last section save the overall scattering matrices $S_{11}$, $S_{12}$, $S_{21}$, and $S_{22}$ for the azimuthal order.**

**Compute farfield beam patterns**

Table 2-2: Sequence of computational steps in the SCATTER software.

In the SCATTER code, each column of a scattering matrix contains the output amplitude mode coefficients for the input TE or TM mode corresponding to that column.  The modulus squared of the individual coefficients in each column are a measure of the amount of power in that input mode that is scattered to other modes of the same azimuthal order.  In this case (as defined in Section 2.2), the modes are normalized for power, and hence $[Q]$ and $[R]$ matrices have diagonal entries of absolute value of unity so that $\left| [Q] \right| = \left| [R] \right| = I$.

An example $S_{21}$ matrix is shown in Figure 2-13 with the input modes indicated in red above their respective columns and the corresponding output modes shown in blue to the left of their associated row.  Looking at the highlighted column, it contains the coefficients for the output field after scattering associated with a $TM_{11}$ mode field

at the input to the system. The coefficient in the first row of that column, $\left(S_{21}^{1}\right)_{1,\left(\frac{N}{2}+1\right)}$,

represents the amount of the input TM$_{11}$ mode that is scattered to the output TE$_{11}$ mode; the next coefficient represents the amount that is scattered to the output TE$_{12}$ mode and so on down the column. In this case, a total of $N/2$ TE and $N/2$ TM modes were used in the basis set of waveguide modes, making up a total of $N$ waveguide modes in describing the scattering sufficiently accurately.

$$
\begin{array}{c}
\phantom{TE_{11}} \quad \text{TE}_{11} \quad\quad \text{TE}_{12} \quad\quad \cdots \quad\quad \text{TM}_{11} \quad\quad \cdots \quad\quad \text{TM}_{1N} \\
\begin{array}{c} \text{TE}_{11} \\ \text{TE}_{12} \\ \vdots \\ \text{TM}_{11} \\ \vdots \\ \text{TM}_{1N} \end{array}
\begin{bmatrix}
\left(S_{21}^{1}\right)_{11} & \left(S_{21}^{1}\right)_{12} & \cdots & \left(S_{21}^{1}\right)_{1\left(\frac{N}{2}+1\right)} & \cdots & \left(S_{21}^{1}\right)_{1N} \\
\left(S_{21}^{1}\right)_{21} & \left(S_{21}^{1}\right)_{22} & \cdots & \left(S_{21}^{1}\right)_{2\left(\frac{N}{2}+1\right)} & \cdots & \left(S_{21}^{1}\right)_{2N} \\
\vdots & \vdots & \ddots & \cdots & \ddots & \vdots \\
\left(S_{21}^{1}\right)_{\left(\frac{N}{2}+1\right)1} & \left(S_{21}^{1}\right)_{\left(\frac{N}{2}+1\right)2} & \cdots & \left(S_{21}^{1}\right)_{\left(\frac{N}{2}+1\right)\left(\frac{N}{2}+1\right)} & \cdots & \left(S_{21}^{1}\right)_{\left(\frac{N}{2}+1\right)N} \\
\vdots & \vdots & \ddots & \vdots & \ddots & \\
\left(S_{21}^{1}\right)_{N1} & \left(S_{21}^{1}\right)_{N2} & \cdots & \left(S_{21}^{1}\right)_{N\left(\frac{N}{2}+1\right)} & \cdots & \left(S_{21}^{1}\right)_{NN}
\end{bmatrix}
\end{array}
$$

**Figure 2-13 : A N×N S21 matrix of azimuthal order n = 1. In this case for the [$S_{21}$] scattering matrix elements the superscript refers to the azimuthal order.**

Up till now it has been assumed just pure modal fields exist at the input for both single and multi-mode horns. For the analysis of most of the examples considered in this thesis (either a single mode horn or a multimode horn feeding a blackbody cavity) this is sufficient. Generally, however, any coherent input field can be written as a sum of modes represented by a vector (i.e. a one dimensional matrix) of mode coefficients $[A] = [a_1, a_2, a_3 ....]$ such that the input field is given by

$$
\left[a_1^{(0)}, a_2^{(0)}, a_3^{(0)} \ldots a_1^{(1)}, a_2^{(1)}, a_3^{(1)} \ldots\right] \mathbf{E}_{in} = \sum_{n=0}^{n_{\max}} \left( \sum_{i=1}^{N/2} a_i^n \mathbf{e}_{\text{TE}_i}^{(\mathbf{n})} + \sum_{i=N/2+1}^{N} a_i^n \mathbf{e}_{\text{TM}_i}^{(\mathbf{n})} \right), \quad (2.71)
$$

where $\mathbf{e}_{\text{TE}_i}^{(\mathbf{n})}$ and $\mathbf{e}_{\text{TM}_i}^{(\mathbf{n})}$ are the modal fields of azimuthal order $n$. The transmitted field is given by the vector of mode coefficients $[B] = [S_{21}][A]$ where $[B] = \left[b_1^{(0)}, b_2^{(0)}, b_3^{(0)} \ldots b_1^{(1)} \ldots\right]$ and $b_j^{(1)} = \sum_i \left(S_{21}^{n=1}\right)_{ij} a_i^{(1)}$. For a partially coherent field the situation is more complex and is discussed in the next section.

59

Figure 2-14 shows three examples of horn antennas with plots of their aperture and farfield beam patterns as simulated using SCATTER. The first example is a standard 100 GHz corrugated conical horn antenna from Thomas Keating Ltd. This horn antenna is used in the experimental laboratories of Far Infrared Space Optics Group at Maynooth University Department of Experimental Physics as a useful horn antenna and as a feed for detectors and sources. It was, in fact, used for the millimetre-wave holography research work described in Chapter 5. The second example, the Spline-like Piecewise Conical Profile Horn Antenna, is a smooth walled horn specially designed as a technology demonstration for future possible CMB experiments. More details of the horn are also provided in Chapter 6, in which a novel holographic technique is described that was used to determine the phase centre of the horn. A Winston cone provides the third example of a horn antenna, in this case an over-moded structure. This Winston cone is a smooth walled horn although corrugated Winston cone profiles have also been developed at Manchester [Maffei, 2004, & 2014]. The example here is similar to the Winston cone horn used in the experimental setup by Cardiff University to make their pre-flight measurements of the Planck HFI horn antennas described in Chapter 5. The results of these measurements and their comparison to SCATTER simulations are discussed in more detail in Chapter 5. The corrugated conical horn and the piecewise conical profile horn both produce farfield beams which are Gaussian-like but have somewhat different aperture fields. The aperture field of the piecewise conical profile horn is top-hat like, but that of the corrugated conical horn is more Gaussian-like. The multimode Winston cone produces a top-hat like farfield beam pattern while its aperture field has a similar top-hat like structure. The slight ripples seen in the linear plot at the aperture plane are less than 1 dB in size. In these cases the non-Gaussian aspects of the beam give rise to the off-axis side lobe structure in the farfield.

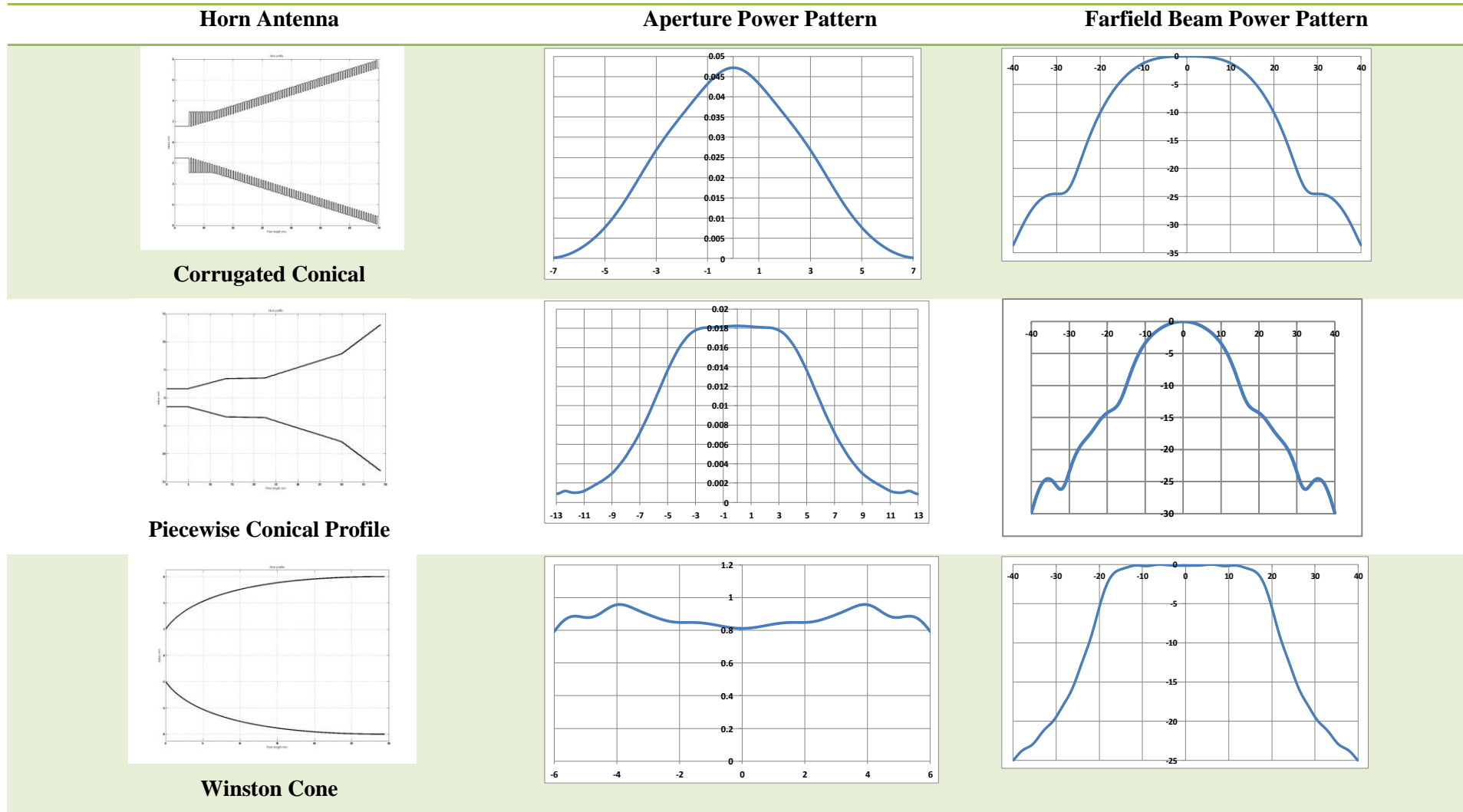| Horn Antenna | Aperture Power Pattern | Farfield Beam Power Pattern |
|---|---|---|
|  **Corrugated Conical** |  |  |
|  **Piecewise Conical Profile** |  |  |
|  **Winston Cone** |  |  |

**Figure 2-14 : Examples of the beam patterns computed using SCATTER for three different horn types. The *x*-axis in aperture field plot are in mm with power (linear) on the *y*-axis. In the farfield plots *x*-axis are in degrees off-axis with power in dB on the *y*-axis.**

# 2.7 Application of Single Value Decomposition in SCATTER to Determine Hybrid Modes

The mode-matching technique described in the previous sections makes use of the natural TE and TM modes of cylindrical waveguides to describe the evolution of the electromagnetic field as it propagates through the horn antenna. The resultant $[S_{21}]$ scattering matrix contains $N \times N$ coefficients which describe the field at the aperture of the horn in terms of how the component TE and TM modes at the input of the horn are scattered (as described at the end of the last section). In a single mode antenna (horn fed by a waveguide through which only a single mode can propagate) these modes are coherent with respect to each other, i.e. they have a definite phase relationship between them, as they are generated by a single coherent input field (usually the TE$_{11}$ mode), and can be combined into a single field (or hybrid mode) which can then be propagated through an optical system such as the primary and secondary mirrors of a telescope.

In a multimode horn antenna the field at the entrance is essentially partially coherent so that effectively more than one field is incident. Therefore, higher order waveguide modes are present at the input to the horn which are not necessarily all coherent with respect to each other. Thus, at the output of the horn, clearly, they cannot be combined into a single field. The field at the aperture of a multimode corrugated antenna can in fact be better described in terms of individual hybrid modes, each of which are made up of a coherent sum of TE and TM waveguide modes and which can pass through the system as a whole without scattering into other modes to which the horn might be coupled. These hybrid mode fields are a more useful basis set which can be used to propagate any arbitrary input field through an optical system. Compared to using the TE and TM modes, fewer hybrid modes are required, and therefore are computationally much more efficient, and the scattering process can be very efficiently described. In fact, the modelling of the propagation of the Planck multimode channels though the Planck optical systems (secondary and primary mirrors) was only possible using such an approach because of its efficiencies. This

was the approach taken by D. Wilson, [Wilson, 2014], who used the hybrid field descriptions produced as part of the work for this thesis, as described in Chapter 4. Single Value Decomposition (SVD) is ideally suited as a practical means for obtaining a basis set of Eigen fields which are effectively these hybrid modes and will be now considered.

First consider again the general case of a waveguide field $\mathbf{E}_w$ which can be written in terms of a linear superposition of basis vectors $\mathbf{e}_m$ (i.e. waveguide modes) as

$$\mathbf{E}_w = \sum_{m=1}^{M} a_m \mathbf{e}_m \ , \tag{2.72}$$

where $[A] = [a_1 \ a_2 \ \cdots\cdots]$ can be regarded as a column vector of mode coefficients ($a_m$), and $\mathbf{e}_m$ are clearly the appropriate waveguide TE and TM modes. In general, the finite sum of $M$ basis fields will only represent an approximation to the field $\mathbf{E}_w$ if its $M$ basis vectors do not span the space in which $\mathbf{E}_w$ is located [Withington, 2004]. Mathematically this implies that the basis set is not complete as there may not be enough modes to describe an arbitrary possible field. However we will assume that $M$ is always large enough so that the approximation is sufficiently accurate. Now consider the effect of the propagation of this field through a waveguide system by the usual scattering matrices so that the output field at the horn aperture

$$\mathbf{E}_{\mathbf{out}} = \sum_{m=1}^{N} b_m \mathbf{e}'_m \ , \tag{2.73}$$

where $\mathbf{e}'_m$ are the basis fields at the output plane of the horn, and $b_m$ are the amplitude coefficients at the output aperture. Clearly, $b_m = \sum_{n=1}^{N} (S_{21})_{ml} a_l$ . In matrix notation we can write $[B] = [S_{21}][A]$ , eqn. (2.73a), where $[B] = [b_1 \ b_2 \ \cdots\cdots]$. The Singular Value Decomposition (SVD) of $S_{21}$ is given by

$$[S_{21}] = [U][\Sigma][V^+] \ , \tag{2.74}$$

where $[U]$ is a $N \times N$ unitary matrix, $[V]$ is a $M \times M$ unitary matrix and $[\Sigma]$ is a $N \times M$ diagonal matrix. Note $N$ does not have to be the same as $M$, of course, as discussed earlier, although in our discussion it will be assumed that they are the same.

The non-zero coefficients, $\sigma_{ii}$, of $[\Sigma]$ are the singular values of $[S_{21}]$.    Substituting equation 2.74 into equation 2.73a

$$[B] = [U][\Sigma][V]^{+}[A] \ . \tag{2.75}$$

If a particular output field is required, for example, this equation can now be solved by applying the complex conjugate of each of the SVD matrices in the reverse order to both sides of the equation yielding

$$[A] = [V][\Sigma]^{-1}[U]^{+}[B] \ . \tag{2.76}$$

This assumes $[\Sigma]^{-1}$ exists which it cannot if any of the singular values are zero, which will be the case if the scattering matrix $[S_{21}]$ is singular and therefore not be invertible.

Applying Single Value Decomposition (SVD), $[S] = [U][\Sigma][V]^{+}$, to the $S_{21}$ transmission scattering matrix for a horn antenna (with TE and TM modes as the basis fields), it is possible to obtain the hybrid modes of the antenna by associating the columns of the $[V]$ matrix with the coefficients of the hybrid modes at the input plane and the columns of the $[U]$ matrix with the coefficients of the corresponding hybrid modes at the output plane.  The $[\Sigma]$ matrix is a diagonal matrix with the singular values along the diagonal which describe by how much a particular hybrid mode field at the input of the system is being transformed into the corresponding hybrid mode at the output plane.  Thus, the number of singular values indicates the number of hybrid modes that are propagating through the waveguide mode filter for a back-to-back horn configuration, for example.  This is expressed by the equation

$$[S_{21}][V] = [\Sigma][U] \ , \tag{2.77}$$

so that a particular column of the matrix $[V]$, which we denote by $[V_i]$ and which describes a hybrid mode at the input plane in terms of its amplitude coefficients, is scattered into the hybrid mode with coefficients given by $[U_i]$ where now

$$[S_{21}][V_i] = \sigma_{ii}[U_i] \ . \tag{2.78}$$

In terms of hybrid modes, what is required are fields that effectively do not scatter into each other, having propagated through a corrugated waveguide horn system.  That is what the $[V_i]$ and $[U_i]$ provide in terms of mode coefficients for the TE

and TM basis set. The $i^{th}$ hybrid mode can thus be described at the input as

$$\mathbf{E}_{h,i}^{in} = \sum_{ji=1}^{N} V_{ji} \, \mathbf{e}_j^{in}$$ and at the output as $$\mathbf{E}_{h,i}^{out} = \sum_{j=1}^{N} U_{ji} \, \mathbf{e}_j^{out}$$ . Each of these waveguide

hybrid modes can be regarded as independently carrying power which is not scattered to other hybrid modes. Also, because the [$V$] and [$U$] matrices are unitary, these hybrid modes form an orthonormal basis set.

It is clear, from the discussion in section 2.5, that the calculation of the farfield would involve $N$ calculations for each azimuthal order where $N$ is the number of TE and TM modes used as the basis set at the aperture. Using the Singular Value Decomposition approach outlined above, the number of calculations can be reduced to the number of hybrid modes propagating, which is generally a much smaller number of fields and corresponds to the case where $\sigma_{ii}$ are not insignificant (the number of non-zero values). Thus for a single mode horn, there is only one such hybrid field pattern at the aperture, for example.

The power carried in a hybrid at the output of a corrugated waveguide system is related to the power in that mode at the input port by

$$
\begin{aligned}
P_{out,i} = [U_i]^+ [U_i] &= \sigma_{ii}^2 [V_i]^+ [V_i] \\
&= \sigma_{ii}^2 P_{in,i}
\end{aligned}
\tag{2.79}
$$

Thus, since these hybrid modes do not scatter into each other on transmission through the horn, they act as independent channels for power that is not leaked into other channels. These fields represented by [$U_i$] and [$V_i$] we will refer to interchangeably as hybrid modes, or by their more mathematically correct name of Schmidt (decomposition) fields.

An example of the two approaches applied to the Planck 857 GHz back-to-back horn antenna is shown in Figure 2-16. The figure shows the farfield beam pattern of the horn antenna obtained using the full TE and TM mode basis set and the [$S_{21}$] scattering matrix. The same field is obtained when the hybrid modes are used as the basis set. The farfields of the hybrid modes of azimuthal orders, $n = 0$ through to $n = 3$, are shown in Figure 2-15(a)-(d). As expected, on-axis power is carried by the modes of order $n = 1$ with the $HE_{11}$ and $HE_{12}$ modes featuring on-axis peaks. Higher order modes, i.e. of order $n \neq 1$, have an on-axis minimum and thus, as expected,

contribute power that is carried off-axis. These 'higher' order modes thus both widen the main beam compared to the beam if only $n = 1$ modes were present. Similarly, these modes of order $n \neq 1$ contribute to higher side lobes, again, compared to a beam containing only modes of order $n = 1$. The farfields of the hybrid modes were added in quadrature, as expected, to determine the overall farfield beam pattern of the back-to-back horn shown in Figure 2-16. The hybrid mode (Schmidt decomposition field) description is very efficient computationally and reduced the time for calculating the farfield beam patterns for the 857 GHz horn from approximately half an hour to approximately 5 – 6 minutes.
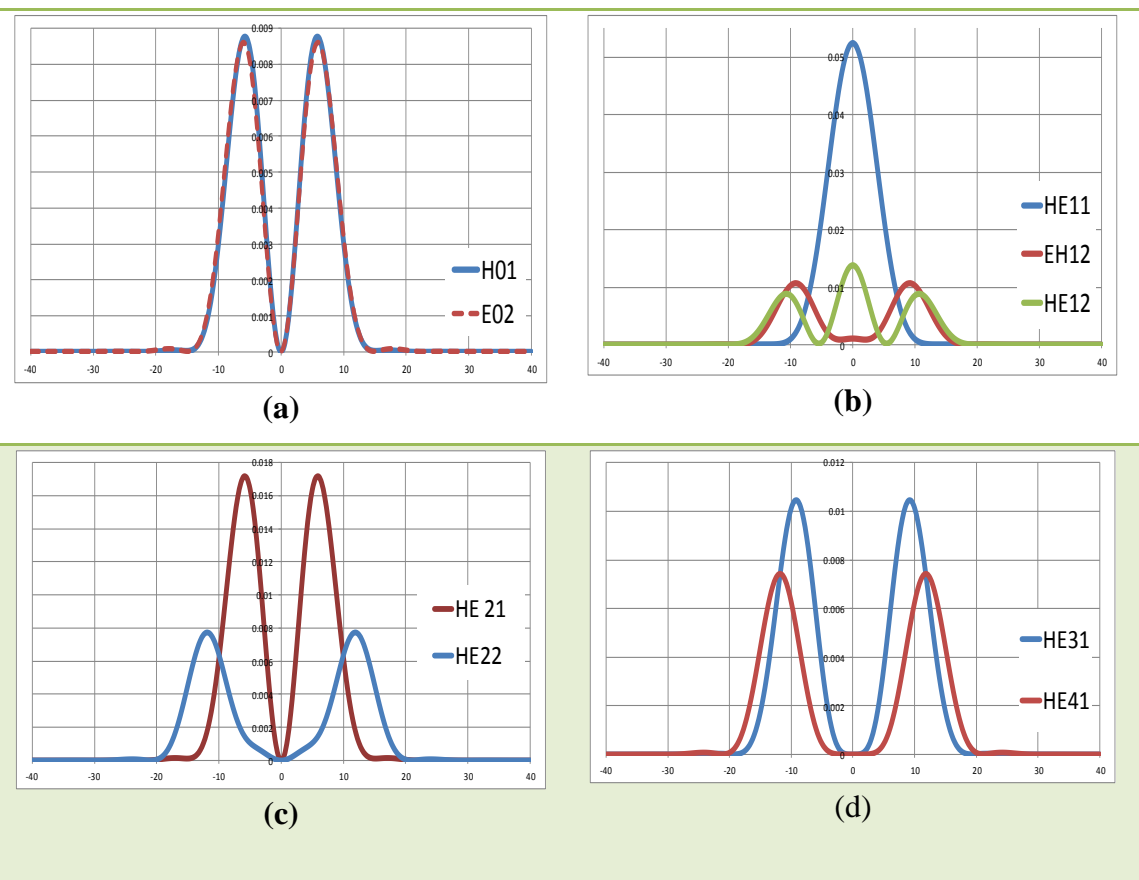


**Figure 2-15 : Plots of the farfields of the hybrid modes of the 857 GHz Planck back-to-back horn. (a) Hybrid modes of azimuthal order n = 0. (b) Hybrid modes of azimuthal order n = 1. (c) Hybrid modes of azimuthal order n = 2. (d) Hybrid modes of azimuthal orders n = 3 and n = 4.**

**Farfield Beam Pattern of the 857 GHz Horn**

857GHz Farfield

857GHz Farfield Eigen modes
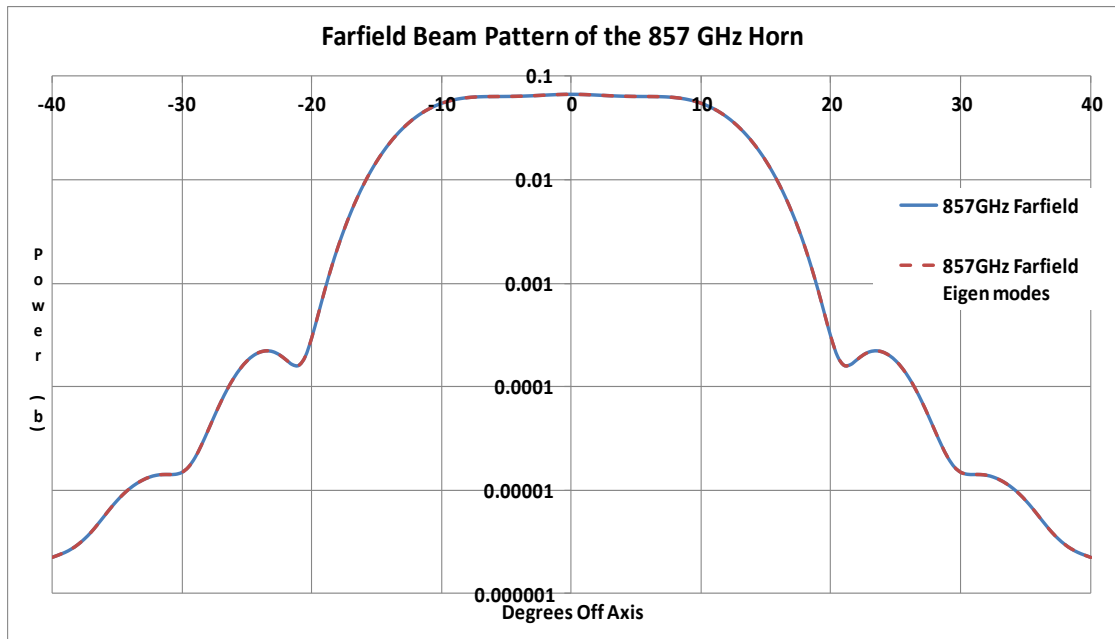
Degrees Off Axis

**Figure 2-16 : Plot showing a comparison of the farfield beam patterns of the 857 GHz Planck back-to-back horn using both the full TE &TM mode basis set and the eigenfield (hybrid) modes using the SVD approach.**

As mentioned earlier, these hybrid modes form a more useful basis set which can be used to propagate the field through an optical system, compared to using the TE and TM modes. This is because far fewer hybrid modes are required than TE and TM waveguide modes to describe the field at the input to the optical system and, therefore, they are computationally much more efficient. The modelling of the propagation Planck multimode channels through the Planck optical systems was only possible using such a hybrid mode approach. This work will be described in more detail in chapter 4, but for the moment we will limit our discussion to a general overview.

Packages, such as GRASP9 [TICRA, 2016], are used to predict the beam patterns of optical systems such as telescopes by propagating a field from a feed source through the optical system and on to a "detection grid" located in either the nearfield or farfield of the telescope where the field can be visualized. This analysis can be performed using an number of techniques such as Physical Optics (PO) and the Physical Theory of Diffraction (PTD), or Geometrical Optics (GO) and the Geometrical Theory of Diffraction (GTD). Regardless of the method chosen for the analysis, each field at the input must be propagated through the optical system and onto the "detection plane". The greater the number of fields, the greater the number of calculations to be performed which grow approximately as the square of the number of fields, and so the proportionately greater the computational power (memory space)

required, and of course the longer the time to complete the analysis. For a multimode system such as the 857 GHz and 545 GHz channels of HFI a large number of TE and TM waveguide modes for each azimuthal order was required to describe the aperture fields (which would be used as the input to GRASP9). There are also a very large number of corrugation steps in these horns, so the determination of the $[S_{21}]$ scattering matrices is also slow. Using the SVD approach, this number was reduced to only the hybrid mode fields for the optical modelling, a much smaller number of coherent fields, thus making it possible to predict the beam on sky for the highest frequency channels of Planck's HFI.

# 2.8 Alternative Approach using the Surface Impedance Model for Corrugated Structures

An alternative approach to the mode matching technique for modelling corrugated waveguides and corrugated horn antennas is the surface impedance model. In this approach, the corrugation surface is replaced with a hypothetical equivalent wall of uniform non-isotropic impedance, that is, it has different impedances in the transverse and axial directions [Clarricoats, 1984]. This approximation relies on the assumption that there are many corrugations (>3) per wavelength and that the fin thickness between corrugations is narrower than the corrugation width. For the high frequency channels of Planck (545 GHz and 857 GHz) this was not the case as there were only two corrugations per wavelength at the top end of the band and also the thickness of the fins was the same size as the slot thickness. Thus the Single Value Decomposition, as outlined in the previous section, was required to determine the hybrid modes, as the surface impedance model is not reliable beyond this limit. As the hybrid modes have different cut-on and cut-off characteristics, which are dependent on the depths of the corrugations and the guide radius, compared to pure TE or TM modes, the surface impedance model is useful to predict these mode cut-on and cut-off effects in waveguide filter sections. Thus, for an intuitive understanding of how the waveguide mode filter operates, this approach is useful [Gleeson, 2005]. It is also useful for a general understanding of what general form the hybrid modes can be

expected to have at the horn aperture. In particular for a wide cylindrical waveguide with corrugation depths of $\lambda/4$, the fundamental mode is the balanced hybrid HE$_{11}$ mode [Murphy, 2001]. In this case, for any currents flowing across the corrugations the effective impedance is infinite, such that $H_\phi$ and $E_\phi$ are zero. Similarly, in a multi-moded horn antenna, higher order balanced hybrid modes are present and these are discussed further in this section below.
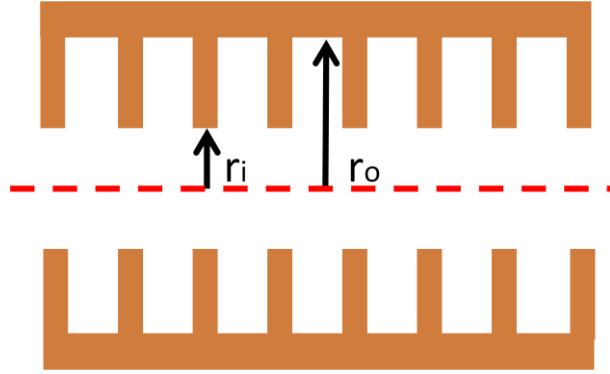


**Figure 2-17 : A corrugated waveguide with inner radius r$_i$ and corrugation of radius r$_o$.**

Since the effective wall of the waveguide is now no longer a perfect conductor, pure TE and TM modes are not possible in general when one applies the boundary conditions. If we consider a corrugated inner waveguide of radius $r_i$ with corrugations grooves of radius $r_o$ (Figure 2-17), then the axial components of the electric and magnetic fields in the open central part of the waveguide ($r < r_i$) must be assumed to exist for a mode, and are given by [Clarricoats, 1984]

$$E_z(r,\phi,z) = A_n J_n(k_c r)\begin{pmatrix}\cos n\phi \\ \sin n\phi\end{pmatrix} e^{j(\omega t - \beta z)} \tag{2.80}$$

$$H_z(r,\phi,z) = A_n \frac{\overline{\Lambda}}{Z_o} J_n(k_c r)\begin{pmatrix}\sin n\phi \\ -\cos n\phi\end{pmatrix} e^{j(\omega t - \beta z)} \tag{2.81}$$

where $Z_o = \sqrt{\mu_o/\varepsilon_o}$ is the surface impedance free space, $\overline{\Lambda}$ is the normalised hybrid factor which measures the relative strengths of the TE and TM components of the hybrid mode, $(k_c)^2 = (\chi_{nl}/a)^2 = k^2 - \beta^2$ is the hybrid mode cut-off wave number of the HE$_{n+1,l}$ and EH $_{n-1,l}$ modes, and $\beta$ is the guide wave-number as given by [Clarricoats, 1985]. We consider the two possible polarisations for a mode (in general,

modes have a degeneracy of 2 for $n \neq 1$, as in the case of cylindrical waveguides).  The transverse field components in the same region are given by [Clarricoats, 1984]

$$E_r(r,\phi,z) = -j\frac{A_n k}{k_c}\left\{ \overline{\beta}J'_n(k_c r) + n\overline{\Lambda}\left( \frac{J_n(k_c r)}{k_c r} \right) \right\}\binom{\cos n\phi}{\sin n\phi}e^{j(\omega t - \beta z)} \qquad (2.82)$$

$$E_\phi(r,\phi,z) = j\frac{A_n k}{k_c}\left\{ n\overline{\beta}\left( \frac{J_n(k_c r)}{k_c r} \right) + \overline{\Lambda}J'_n(k_c r) \right\}\binom{\sin n\phi}{-\cos n\phi}e^{j(\omega t - \beta z)} \qquad (2.83)$$

$$H_r(r,\phi,z) = -j\frac{A_n k}{Z_o k_c}\left\{ \overline{\beta}\overline{\Lambda}J'_n(k_c r) + n\left( \frac{J_n(k_c r)}{k_c r} \right) \right\}\binom{\sin n\phi}{-\cos n\phi}e^{j(\omega t - \beta z)} \qquad (2.84)$$

$$H_\phi(r,\phi,z) = -j\frac{A_n k}{Z_o k_c}\left\{ n\overline{\beta}\overline{\Lambda}\left( \frac{J_n(k_c r)}{k_c r} \right) + J'_n(k_c r) \right\}\binom{\cos n\phi}{\sin n\phi}e^{j(\omega t - \beta z)} \qquad (2.85)$$

where $\overline{\beta} = \dfrac{\beta}{k}$ is the ratio of the waveguide wave number to the free space wave number.

The hybrid mode factor can be written as $\overline{\Lambda} = -n\overline{\beta}\,/\,F_n(k_c r_i)$ where $F_n(k_c r) = k_c r\dfrac{J'_n(k_c r)}{J_n(k_c r)}$ . As $E_\phi$ is zero at $r = r_i$, thus the characteristic equation for $\beta$ is

$$F_n(k_c r_i) - \frac{(n\overline{\beta})^2}{F_n(k_c r_i)} = \left( \frac{k_c}{k} \right)^2 S_n(kr_i, kr_o). \qquad (2.86)$$

where $r_0$ is the radius to the bottom of a corrugation and $S_n(kr, kr_o)$ is a cylindrical function of order $n$ given by [Clarricoats,1984]

$$S_n(kr, kr_o) = kr\frac{J'_n(kr)Y_n(kr_o) - J_n(kr_o)Y'_n(kr)}{J_n(kr)Y_m(kr_o) - J_n(kr_o)Y_n(kr)} = kr\frac{S_n^N(kr, kr_o)}{S_n^D(kr, kr_o)} \qquad (2.87)$$

where $Y_n(y)$ is a Bessel function of the second kind of order $n$, and the assumption is made that only the lowest order TM standing wave can exist in the corrugation slot. By solving equation (2.86) a particular value of $kr_i$ can be found and thus used to predict the low and high frequency cut-off values for the modes which can propagate in the waveguide.

The general forms of the two orthogonal sets of HE and EH modes at the horn aperture are simpler (assuming a slot depth of $\lambda/4$ and that the aperture is wide $\gg \lambda$) and given by [Murphy, 2001]

$$\mathbf{e}_{HEnl} = \frac{J_{n-1}(\chi_{n-1l}r/a)\exp(-jkr^2/2L)}{\sqrt{4\pi a^2[J_n(\chi_{n-1l})]^2 \big/ Z_0}}\left(\begin{array}{l}\cos[(n-1)\phi]\hat{\mathbf{i}} - \sin[(n-1)\phi]\hat{\mathbf{j}} \\ \sin[(n-1)\phi]\hat{\mathbf{i}} + \cos[(n-1)\phi]\hat{\mathbf{j}}\end{array}\right) \quad (2.88)$$

$$\mathbf{e}_{EHnl} = \frac{J_{n+1}(\chi_{n+1l}r/a)\exp(-jkr^2/2L)}{\sqrt{4\pi a^2[J_n(\chi_{n+1l})]^2 \big/ Z_0}}\left(\begin{array}{l}\cos[(n+1)\phi]\hat{\mathbf{i}} + \sin[(n+1)\phi]\hat{\mathbf{j}} \\ \sin[(n+1)\phi]\hat{\mathbf{i}} - \cos[(n+1)\phi]\hat{\mathbf{j}}\end{array}\right) \quad (2.89)$$

where the square root term in the denominator is the normalisation constant for the mode in question, here given by $\int \mathbf{e} \times \mathbf{h}^* \cdot d\mathbf{A} = 1$, again, assuming a wide aperture so that impedance of mode is approximately unity. The field lines of some of the lower order "balanced" hybrid modes (TE and TM are of equal importance) are plotted in Figure 2-18. The $\chi$ coefficients for the hybrid modes used in the results are listed in Table 2-3 [Gleeson, 2004]. These modes have similar forms to those derived in the previous section and thus the hybrid modes derived using SCATTER can be associated with those from an idealised horn, as listed in equations (2.88) and (2.89).

| Mode | $\chi$ |
|:---:|:---:|
| $HE_{11}$ | 2.405 |
| $HE_{21}$ | 3.831 |
| $E_{02}$ | 3.831 |
| $H_{01}$ | 3.831 |
| $HE_{31}$ | 5.134 |
| $EH_{12}$ | 5.137 |
| $HE_{12}$ | 5.520 |

Table 2-3: $\chi$ coefficients for the hybrid modes used in field line plot [Gleeson, 2004]
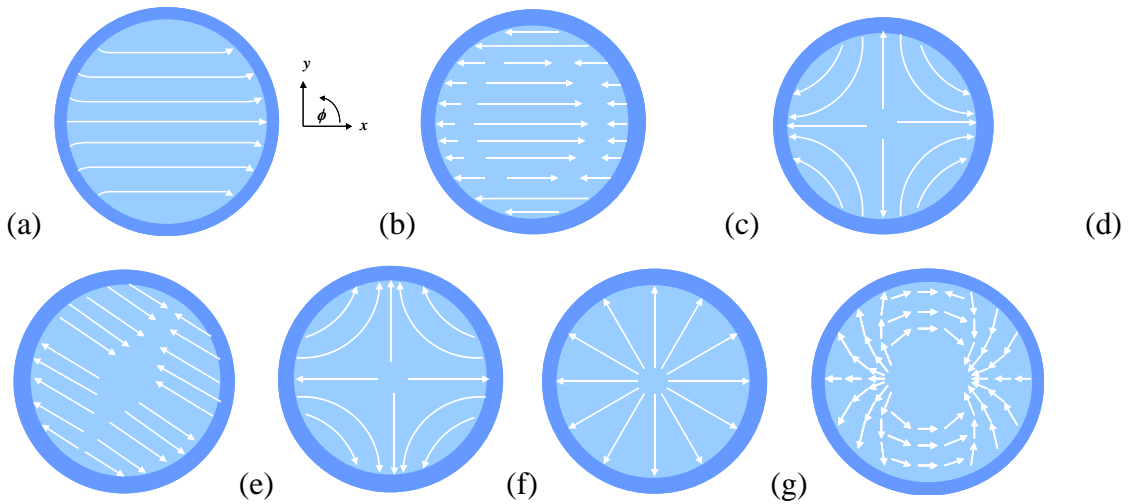
**Figure 2-18 Transverse electric field line configuration of the (a) HE11 (b) HE12 (c) HE21 (d) HE31 (e) H01 (f) E02 (g) EH12 modes in a circular waveguide. [Gleeson, 2004]**

The aperture intensity plots of the same lower order balanced hybrid modes plotted in Figure 2-18 are shown in Figure 2-19. Comparing these to the plots shown in Figure 2-16 in section 2.7, it can be seen that the surface impedance model and SVD yield the hybrid modes of similar structure for the two examples. The hybrid modes of azimuthal order $n = 1$ feature an on-axis peak in the $HE_{11}$ and $HE_{12}$ modes. The $EH_{12}$ mode and $HE$ modes of order $n \neq 1$ have an on-axis minimum.



$HE_{11}$

$HE_{12}$

$EH_{12} / HE_{31}$

$HE_{21} / E_{02} / H_{01}$
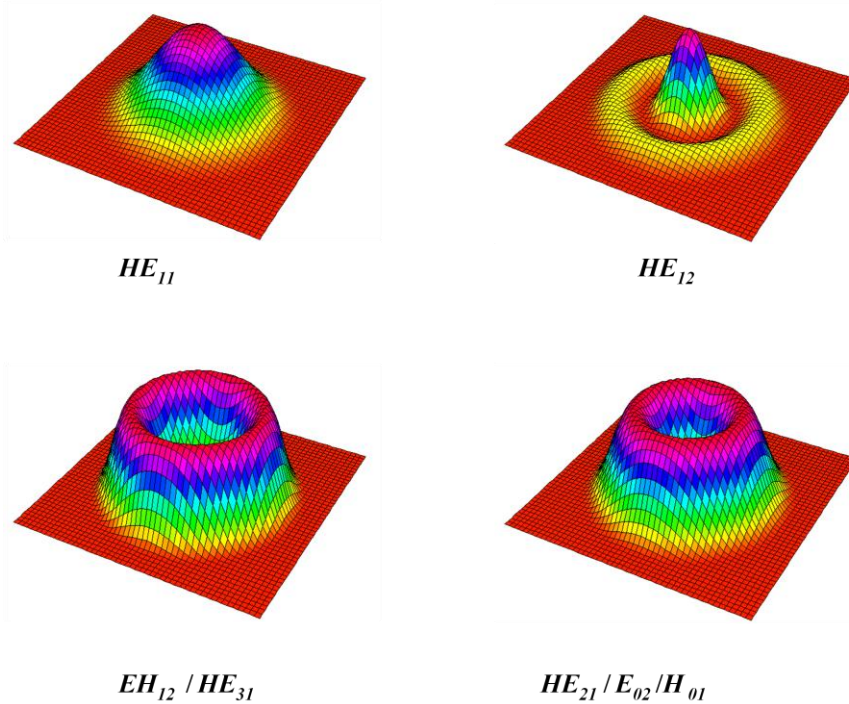
**Figure 2-19 Aperture intensity patterns of some low order balanced hybrid modes. [Gleeson, 2004]**

The surface impedance model was also used to plot the dispersion curves for modes in the waveguide filter section of the Planck 857 GHz horn, shown in Figure 2-20, as it was a quick way to get an indication the number of modes propagating based approximately where the modes cut on etc. [O'Sullivan, 2014]. This model predicts that at the horn's central frequency, 857 GHz, that eight modes propagates through the waveguide filter. The SCATTER simulations, which are discussed in Section 3.2, show that there are nine modes propagating at this frequency. The surface impedance method is only an approximation in this case but it does provide a indication of the number of modes.
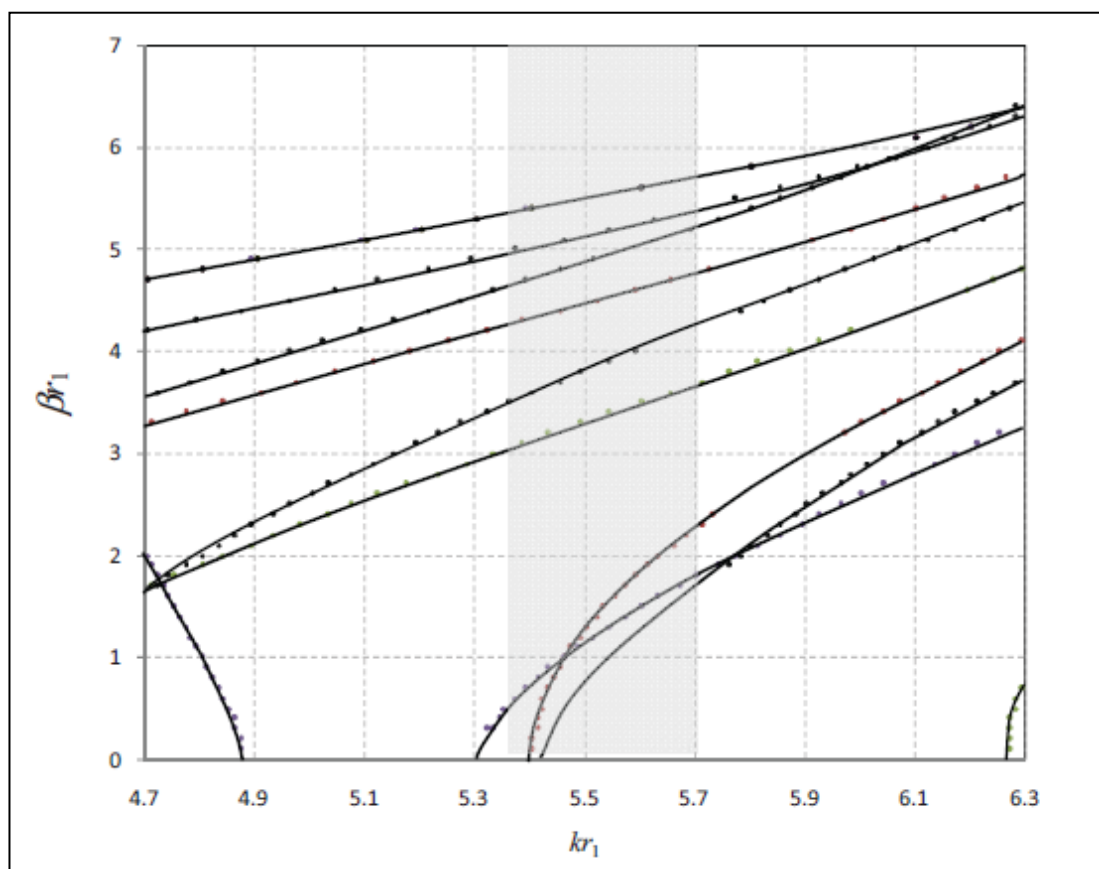


**Figure 2-20 : Dispersion curves for modes in the 857-GHz horn waveguide filter section (inner and outer corrugation radii $r1/r0 = 0.64$) showing modes cutting on in the centre of the band [O'Sullivan, 2014].**

# 2.9 Conclusion

In this chapter the details of the mode matching techniques used to model horn antennas have been presented.  The SCATTER software, developed by Maynooth University (NUI Maynooth) and extended and upgraded by the author of this thesis, to implement these techniques has also been described.  Examples of the aperture and farfield beam patterns of some horn antennas, with relevance to the work described in the subsequent chapters, were given.  The addition of singular value decomposition (SVD) analysis to the software, in order to obtain the Eigen fields (hybrid modes) of horn antennas, has been detailed.  It has been shown how these hybrid modes can be used to obtain the farfield beam pattern of a multi-moded horn antenna, and this method yields the same result as that obtained by using TE and TM waveguide modes as the basis set.  In the following chapters, the SCATTER software detailed in this chapter is used to model and analyse the multi-moded high frequency channels of the Planck satellite, the 545 GHz and 857 GHz channels, and the 353 GHz single moded channel;  the results of this work is presented and discussed.

# Chapter 3  The Planck Multimode Channels

## 3.1 Introduction

As described in Chapter 1 the ESA Planck satellite was a specialised cosmology mission focused on measuring the temperature fluctuations and polarisation characteristics of the CMB.  Planck mapped the sky simultaneously over a wide frequency range to permit the separation of the galactic and extra-galactic foreground sources from the cosmological background radiation.  The LFI covered the frequency range from 27 GHz to 77 GHz and the HFI consisted of an array of 52 bolometric detectors operating at 0.1K covering a frequency range of 83 GHz to 990 GHz in six bands (figure 3-1b).  Each HFI detector was fed by a horn and filter section which was coupled to Planck's off-axis Gregorian dual-mirror telescope by a corrugated back-to-back horn(figure 3-1a) [Tauber, 2010a].
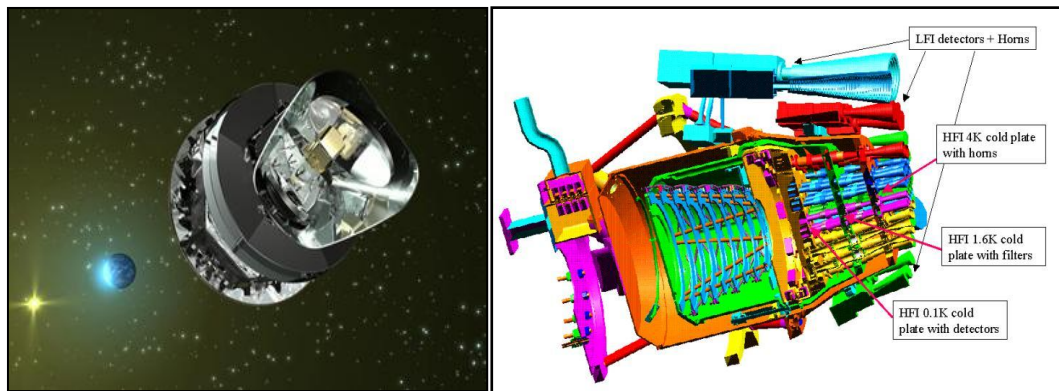


**Figure 3-1 : (a) The Planck satellite. (b) Diagram showing both the Low Frequency Instrument and the High Frequency Instrument.**

As indicated in Chapter 1, the channel centred on 857 GHz was the highest frequency channel of the HFI.  This channel, along with the 545 GHz Channel, used specialized multi-mode feedhorns, and was dedicated to observing foreground sources which were important to remove from the CMB data.  All of the HFI horns were in the same back-to-back configuration in which the signal was transmitted through either high pass filters (single mode channels) or both low band pass and high band pass filters (multimode channels) to a detector horn (Figure 3-2) [Maffei, 2010a].   IR blocking filters were also used to thermally insulate the 0.1K detector horn and

bolometer from the warmer background. In the single mode channels (see Chapter 1) the waveguide section of the back-to-back horn also acted as a high pass filter defining the lower edge of the corresponding band.
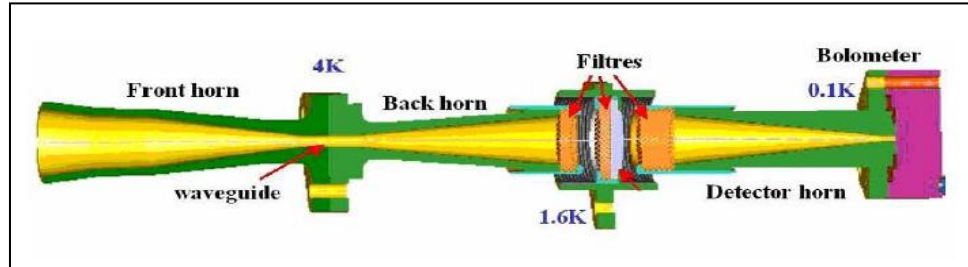


**Figure 3-2 : Reproduction of Figure 1-16 for convenience. A diagram of the back-to-back horn and the detector feed horn which was used in each of the 857 GHz and 545 GHz channels.**

The Far Infrared Space Optics Group at Maynooth University Department of Experimental Physics have been involved in the development of the HFI instrument on the Planck Satellite since 1996. During the early phases of the definition of the instrument a number of researchers in Maynooth contributed significantly to the work of designing of the prototype horn antennas in collaboration with the Institute d'Astrophysique Spatiale, Universitat Paris Sud, France and Cardiff University, Wales. As part of this work the SCATTER software, as described in Chapter 2, was developed by Ruth Colgan and Emily Gleeson ([Colgan, 2001],[Gleeson, 2004]) and Maynooth supported the designs and testing of both the single mode channels and multimode channels. The designs generally were optimised at the centre of the corresponding bands for low edge taper at the telescope (~ -30 dB) and low sidelobe levels so as to minimise spillover onto the sky which could corrupt the weak CMB signals being detected if they intercepted nearby bright galactic sources. Some attention was paid to the extended behaviour across the various bands but only a small number of spot frequencies were simulated before the horn design was frozen. Maynooth continued to support the further qualification and definition of the flight horns for Planck, in particular predicting the behaviour of the CMB channels of Planck in their interaction with the telescope using GRASP physical optics software [Murphy, 2010], [Noviello, 2008].

Generally because of the computational requirements the number of waveguide modes used in the simulations, particularly of the high frequency multimode horn antennas at 545 GHz and 857 GHz, was restricted to the minimum required to give

stable results at the central frequency of the band. This nevertheless did result in there being some instabilities, as detailed by Fabio Noviello [Noviello, 2008], at some other spot frequencies and a prediction of rather narrower beams on the sky than expected for the high frequency horns. Tully Peacocke worked on an efficient method for modelling the propagation through the telescope of the multimode channels across the band further improving the predictions for the beams on the sky when the "real" telescope was included as predicted by the telescope measurements [Peacocke, 2012]. The author of this thesis began supporting the Planck project around the time of launch in 2009. Two areas particularly needed attention and Chapters 3, 4, and 5 describe the author's resulting work on the multimode channels of the HFI at 545 and 857 GHz.

In this chapter we will examine the challenge to derive the broadband beams with fine frequency sampling which would be accurate enough that the effects of imperfections in the horn corrugations on the beam patterns could be simulated with sufficient confidence. The necessary high accuracy of these simulations tested the modelling techniques and revealed numerical issues with the running of SCATTER which had to be addressed in order to have full confidence in the results of the simulations. The results of this work in addition to the producing the broadband beam patterns also reveal the variation in the hybrid mode content of the 857 GHz and 545 GHz multimode channels over their respective frequency ranges and their effects on the beam pattern. In addition to the 857 GHz and 545 GHz multi-mode channels this chapter describes the simulation work carried out on the 353 GHz single mode channel.

In Chapter 4 we investigate an issue that surfaced after Planck had made a number of full sky surveys. In particular in the multimode channels at 857 GHz it was noted that when two single year Planck all-sky maps (one map made when the Planck scanning axis was looking the centre of the galaxy, the other when Planck was pointing away) were subtracted from each other faint banana shaped residuals appeared in some channels but not others. As will be explained in Chapter 4 only a full analysis of the effects of tolerances and possible manufacturing defects on the beams could explain these effects. Although such effects have negligible implications for CMB science, their analysis will allow improved maps to be made of foreground sources important because of the very high sensitivity of the multimode 857 GHz channels.

In Chapter 5 we concentrate on analysing and understanding the results of prelaunch laboratory measurements made of the Planck multimode channels in 2009-2010. Such measurements, as will be discussed in detail, are quite difficult to make in a laboratory environment because of the high frequencies involved and the background loading of thermal radiation on the detectors. Nevertheless a good understanding of the system and the results were achieved through a rigorous electromagnetic and quasi-optical analysis, which verified the multimode behaviour of the horns. In fact previously only scale model measurements (~ 150 GHz) were made of such multimoded behaviour, as discussed in E. Gleeson's thesis [Gleeson, 2004]. Various other issues associated with the approximations made in modelling the system (such as the black body approximation for the detector) were also investigated as part of this work.

## 3.2 Beam Pattern Simulations of the 857 GHz Channel

The 857 GHz pixel consists of a spider-web bolometric detector in a cylindrical cavity fed by a detector horn which in turn is fed by a back-to-back horn arrangement as shown in Figure 3-2. Simulations of the beam patterns of the 857 GHz channel were performed to determine the beam width, sidelobe levels, gain, and throughput across the frequency band of operation. A waveguide mode matching technique was utilized to model the propagation of the signal through this structure with the SCATTER program, as described in the previous chapter, used as the basic software tool for undertaking this analysis. Simulations were run using the geometry of the entire 857 GHz channel which including the detector horn and the back-to-back horn. However, because the centre waveguide section of the back-to-back horn, as indicated in Figure 3-2, acts as a mode filter which allows more than one mode through, the beam pattern at the aperture of the horn system, and hence in the farfield, is predominantly determined by both the number of modes through the filter waveguide section and the geometry of the front section of the back-to-back horn. The geometry of the back part of the horn has little effect provided that its profile is

gradual and essentially the detector horn plus the bolometer in the cavity act as a perfect absorber.

E. Gleeson outlines the uses of corrugated waveguides as high pass filters for CMB experiments [Gleeson, 2005]. The waveguide section connecting the front and back horn sections of the back-to-back horn, illustrated in Figure 3-2, fulfils this mode filter role in each of the HFI channels. The waveguide mode filter in the detector horn is designed to allow a higher number of modes to propagate compared to the filter in the back-to-back horn so that any scattering into higher order modes between these horns should not result in a loss of power allowing us to assume the front horn is connected directly with the detector cavity in terms of power absorbed. This is an approximation but it means that by simulating mode propagation in the front horn and filter waveguide sections of the back-to-back horn only, it is possible to compute the beam patterns for the full pixel to a reasonable accuracy. Figure 3-3 shows the beam pattern, as computed by SCATTER, for the full configuration, full back-to-back horn, and its front section only. As can be seen from the graph the beam patterns for the front section and the complete back-to-back horn agree to high accuracy. The agreement between beam patterns of the front horn and the full pixel is less perfect. However the mode content, and hence the structure, of the two beam patterns are very similar (see Figure 3-3). It therefore can be assumed that by modelling the front section only the beam patterns obtained are a good approximation to the full pixel beam patterns. As the front horn and waveguide filter is shorter than the complete configuration of back-to-back pair and detector horns, and thus contains fewer corrugations, it takes significantly less time to compute the scattering matrix. In fact this reduces the number of steps to be calculated to almost one third of the number of steps in the full pixel, thus cutting the time needed to run each simulations by the same amount. The same approach was taken by both Gleeson and Peacocke in determining beam patterns for similar reasons [Gleeson, 2004],[Peacocke, 2012]. In section 3.7 the absorbing detector has been included in the simulations and some more significant differences are seen although not major and verifies the general approach of just simulating the waveguide filter and front horn.

Another issue is that at the operational temperature of the back-to-back horn of the HFI, 4K, the dimensions of the back-to-back horn are smaller than they are at room temperature due to contraction of the electroformed copper from which the horns

were made. The horn geometries were specified at room temperature for the manufacturing process from which the dimensions of the operational cold horn geometries were then determined, which were then in turn used for simulation purposes. Figure 3-4 shows the simulations of the beam patterns for both the warm, room temperature, and the cold, operational temperature, horn geometries. There is only a very small difference between the beam patterns, mostly visible in the peak height level of the first side lobe, but in any case for all further simulations the cold operational geometry was used.



**Farfield Beam Patterns of the 857GHz Channel**

Legend:
- Front Horn Only
- Back to Back Horns
- BTB & Detector feed Horns + Cavity

Axis labels: Power (dB) (vertical), Degrees Off Axis (horizontal)
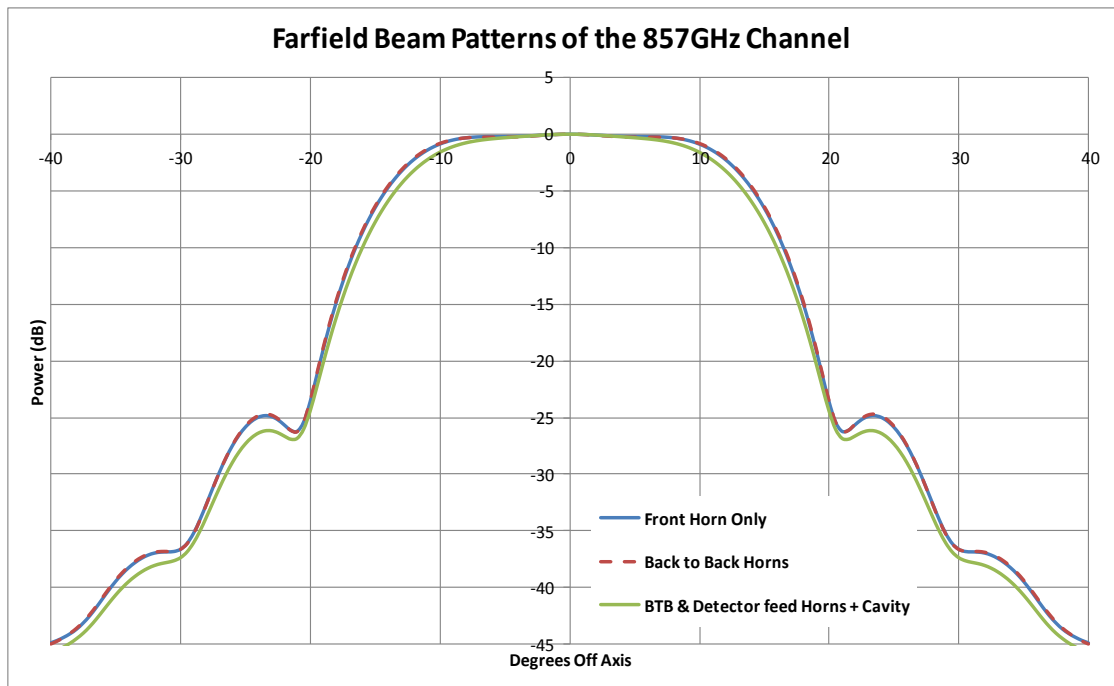
**Figure 3-3: SCATTER simulations of the farfield beam patterns for the 857 GHz channel. The back-to-back horn case agrees with the front horn case to very high accuracy.**
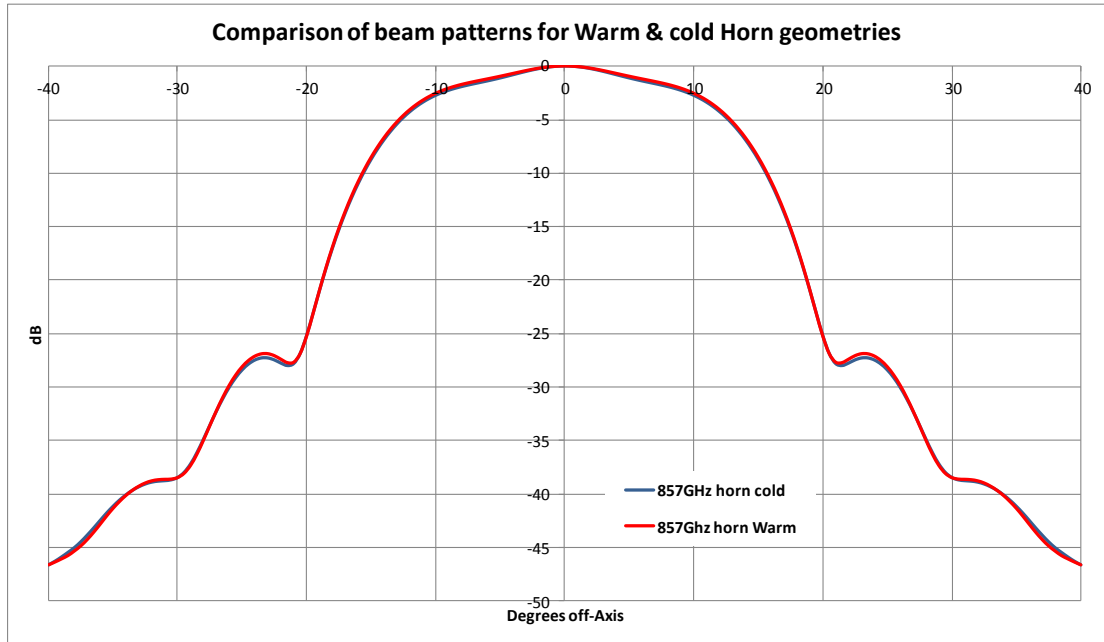
**Figure 3-4 : SCATTER simulations for the warm and cold horn geometries.**

The 857 GHz horns has a 30% bandwidth approximately, 730 GHz to 990 GHz, therefore to cover this frequency band simulations were run at a large number of spot frequencies over this band at intervals of 10 GHz. The farfield beam intensity patterns at these spot frequencies (Figure 3-22) were combined in quadrature before the total intensity pattern was then normalised to zero dB on-axis thus providing the estimated broadband farfield beam pattern (Figure 3-8). The exact beam pattern that would be measured using a given source would, of course, depend on its spectrum. The Rayleigh–Jeans law was also used to weight the intensity pattern at each of the spot frequencies across the band used, in forming the estimated broadband farfield beam pattern. Formally the spectral radiance (energy emitted per unit area per unit solid angle per spectral unit) for a blackbody with a Rayleigh-Jeans spectrum is given by $B_\upsilon(T) = 2\upsilon^2 k_B T \big/ c^2$ so that the power emitted per unit area per solid angle is $dP = B_\upsilon d\upsilon$. We thus apply a weighting of $\upsilon^2$ to the spot frequencies uniformly spaced.
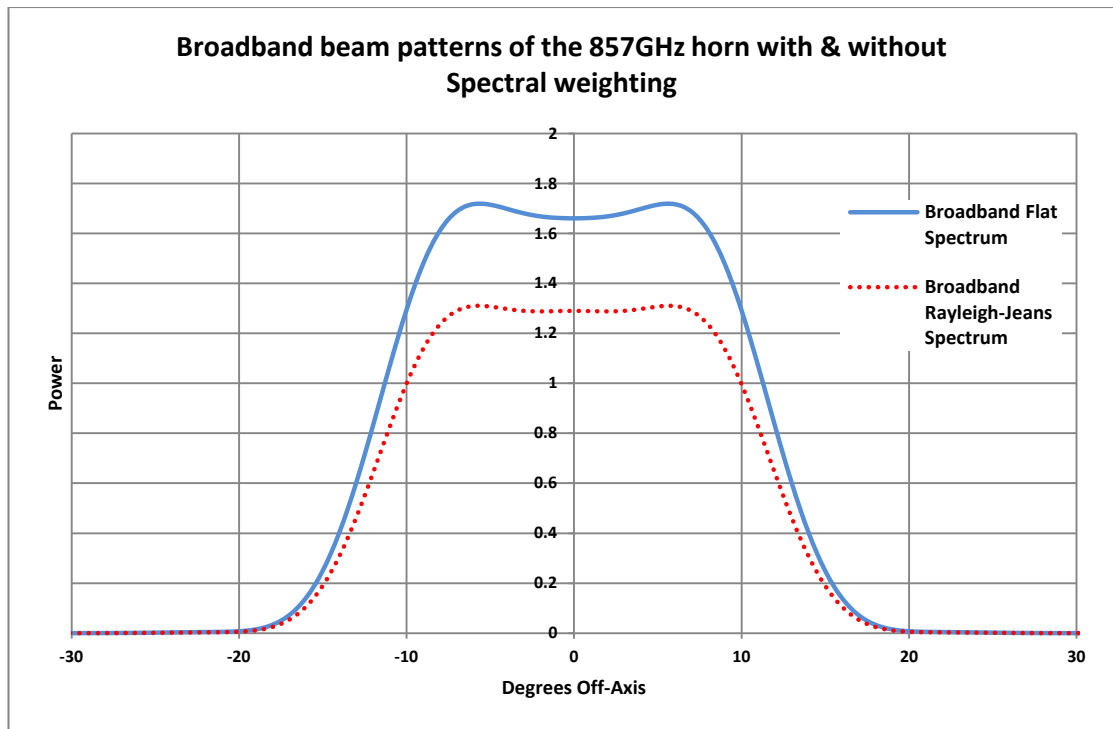
**Figure 3-5 : Linear plot comparing the beam patterns of the 857 GHz Horn with and without spectral weighting.**

In Figure 3-5 a comparison of the broadband beam patterns with a Rayleigh-Jeans spectrum and without this spectral weighting (i.e. a flat spectrum) is shown. The spectral weighting results in the attenuation of the broadband beam compared to the un-weighted beam. The effect of the weighting on the overall shape of the beam is minimal as can be seen in the log scale plot (Figure 3-6 & Figure 3-7). The position and levels of the sidelobes are unaffected and the beam widths for both are similar. This is due to the stability of the beam width and sidelobe levels over the entire operational band as is described below in section 3.4. As the overall beam profile varies little with spectral weighting for the moment we will use a flat spectrum (i.e. weighting all spot frequencies equally), and proceed to carry out our analysis on this basis.

82
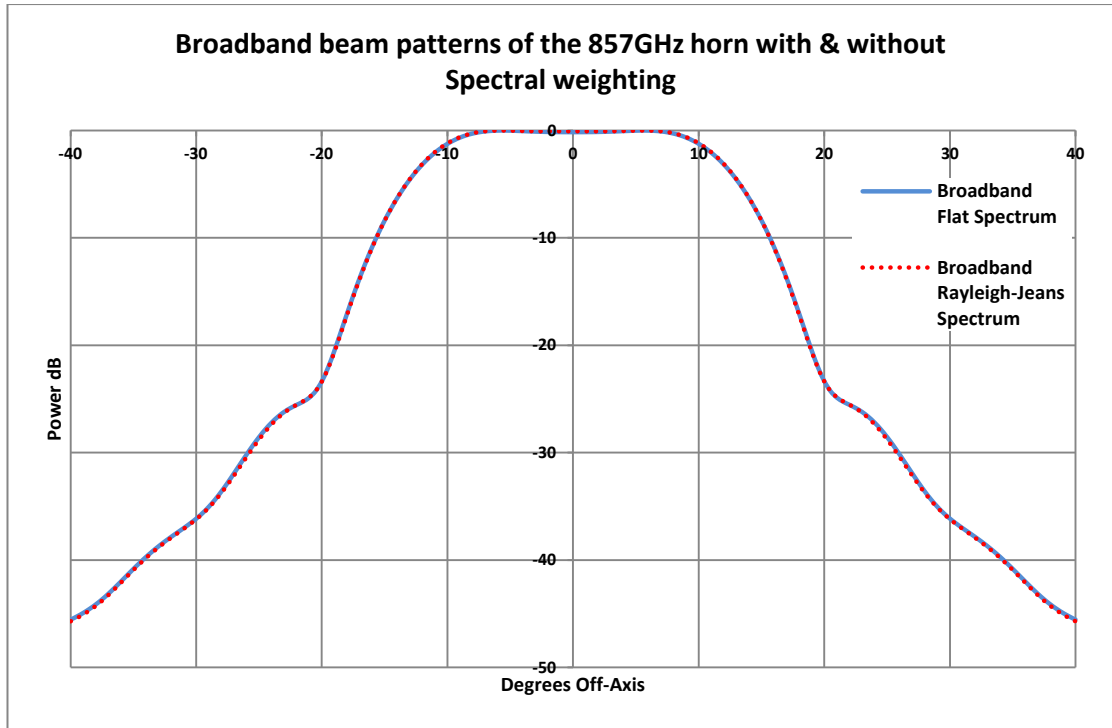
**Figure 3-6 : Log plot comparing the beam patterns of the 857 GHz Horn with and without spectral weighting. Note there is a slight difference around the region close to the centre of the beam which is shown in Figure 3-7.**
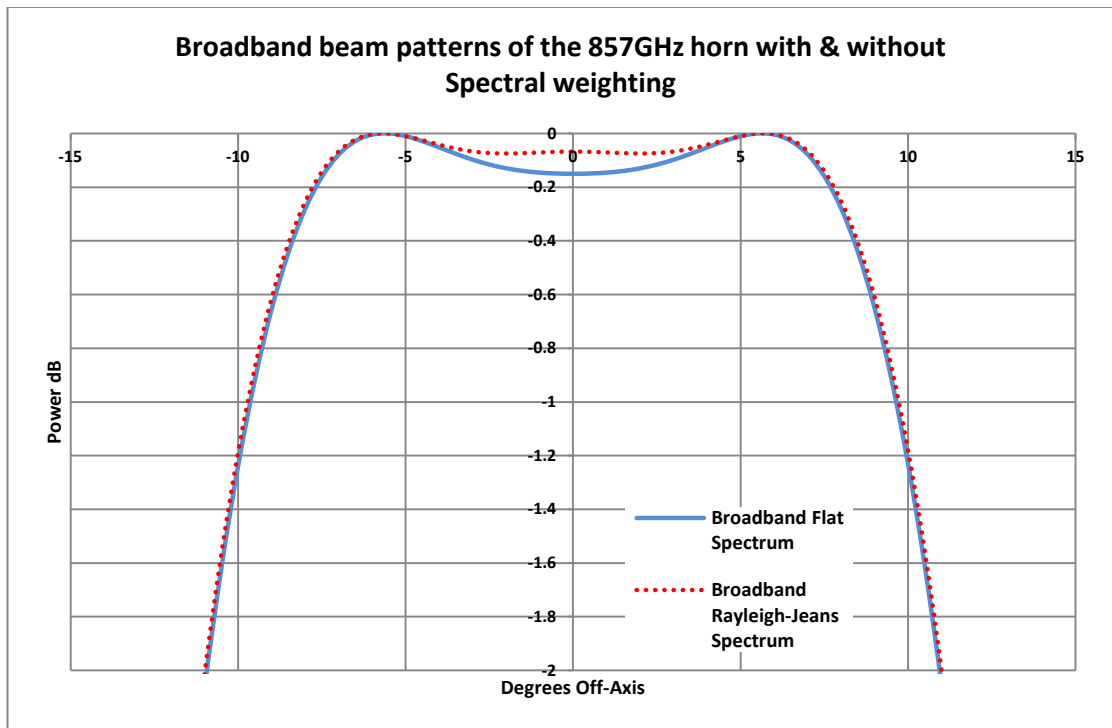


**Figure 3-7 : Log plot comparing the beam patterns for the centre of the main beam of the 857 GHz Horn with and without spectral weighting.**

In Figure 3-8 the flat spectrum broadband beam is shown alongside the beam pattern for the 875 GHz central frequency. Both beams have similar widths and

sidelobe positions. As the frequency is increased the width of the beam narrows as expected. However because this is a multimode channel, as the frequency increase additional modes are excited in the horn, and more modes can pass through the waveguide filter of the back-to-back horn. These additional modes widen the beam overcoming the narrowing effect of the increasing frequency due to diffraction of individual modes. Thus the full width half maximum (FWHM) of the beam as a whole only varies by approximately 1 degree over the whole frequency range (see section 3.4 for details). This is one reason why the central frequency can be used as an approximation of the broadband beam across the frequency band. Being able to make this approximation greatly reduces the computational time required for simulations of the propagation of the beam through various models of the Planck satellite optics while still obtaining results indicative of the broadband behaviour of the system. It was also very useful during the design and definition phases of Planck when the horn configuration needed to be computed quickly. However obtaining stable beam patterns at a large number of spot frequencies across the band using the pre-existing SCATTER code did highlight some issues with numerical instabilities which had to be investigated to produce a high level of confidence in the simulations and indeed to allow the actual determination of the broadband beam.
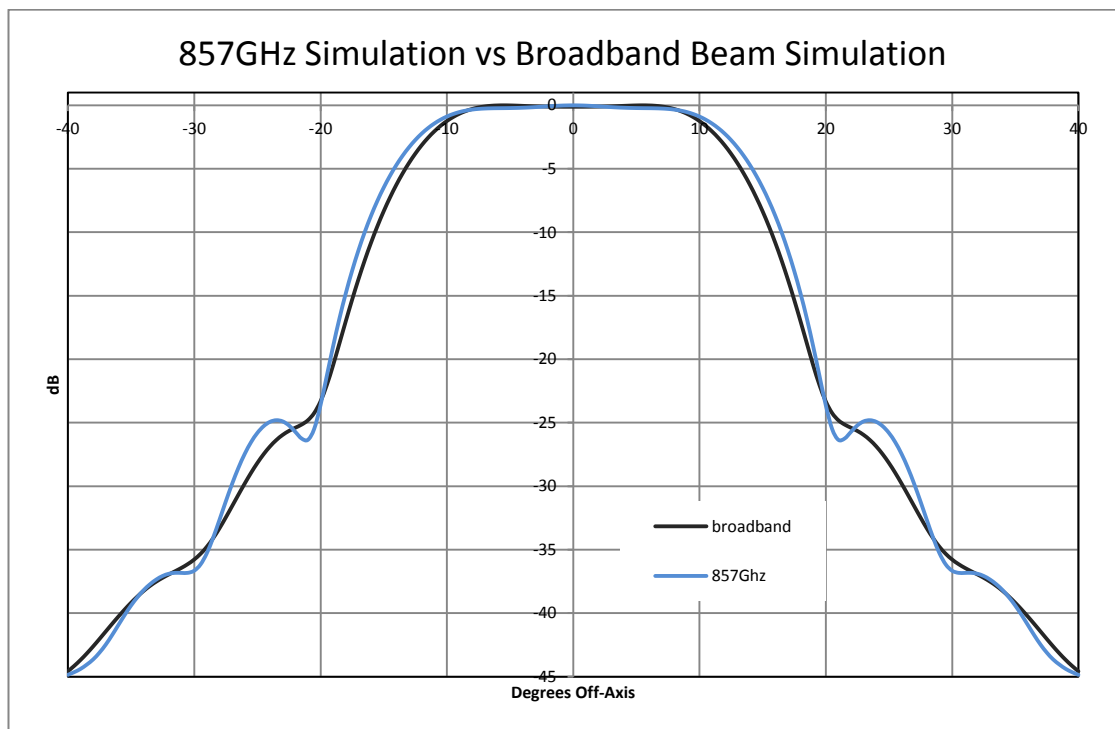


**Figure 3-8 : Simulations of the farfield patterns of the 857 GHz Horn at 857 GHz and broadband beam.**

# 3.3 Numerical Issues with Running SCATTER for the Broadband Beam Predictions

## 3.3.1 Numerical Instabilities

The modelling of the Planck multimode horns as reported in previous theses, [Gleeson, 2004] and [Noviello, 2008], suffered from some numerical instabilities. In fact these instabilities were partly associated with not using an appropriately large number of modes, mainly for reasons of computational efficiency when simulations were run on previous generations of PCs. When the simulations of the multimode horns were extended across the band these instabilities became apparent at certain spot frequencies. Although at these spot frequencies the beam pattern appeared unphysical and could be ignored it does reduce confidence in the modelling approach and so it was decided to study such effects and seek to eliminate them. For this study the 857 GHz channel was concentrated on.

Examining the true hybrid mode content of the waveguide filter and front horn proved invaluable for this study. As described in the previous chapter (Section 2.7) by applying Single Value Decomposition (SVD), $[S] = [U][\Sigma][V^+]$, to the $[S_{21}]$ transmission scattering matrix for a back-to-back corrugated horn configuration with TE and TM modes as the basis fields, it is possible to obtain the hybrid modes of the waveguide/horn combination by associating the $[V]$ matrices with the true hybrid modes at the input plane and the $[U]$ matrices with the hybrid modes at the output plane. The $[\Sigma]$ matrix is a diagonal matrix with the singular values along the diagonal, with the number of singular values indicating the number of hybrid modes that are propagating through the waveguide mode filter for the back-to-back horn configuration. By computing the singular values at a large number of frequencies across the band the variation of the number of modes propagating in the horn antennas with frequency can be plotted. The number of modes propagating for the 857 GHz horn as simulated by the pre-existing SCATTER code is shown in Figure 3-9. The number of modes should increase monotonically with frequency as the threshold cut-on frequencies for the higher order modes are passed. It turns out that in calculating

85

the singular values for the $[S_{21}]$ scattering matrix a number of issues with respect to the numerical stability of the $[S_{21}]$ matrix became apparent. In the plot of the number of modes propagating as a function of frequency, Figure 3-9, a number of these features, which are due to numerical instabilities, are visible. At frequencies between 800 GHz and 950 GHz several features are visible that seem to indicate a loss of modes. At 860 GHz this effect is most pronounced with a sharp dip in number of modes propagating which mimics a resonance feature but such a feature is unexpected and was presumed to be numerical rather than physical thus requiring further study and to be solved for running SCATTER reliably.
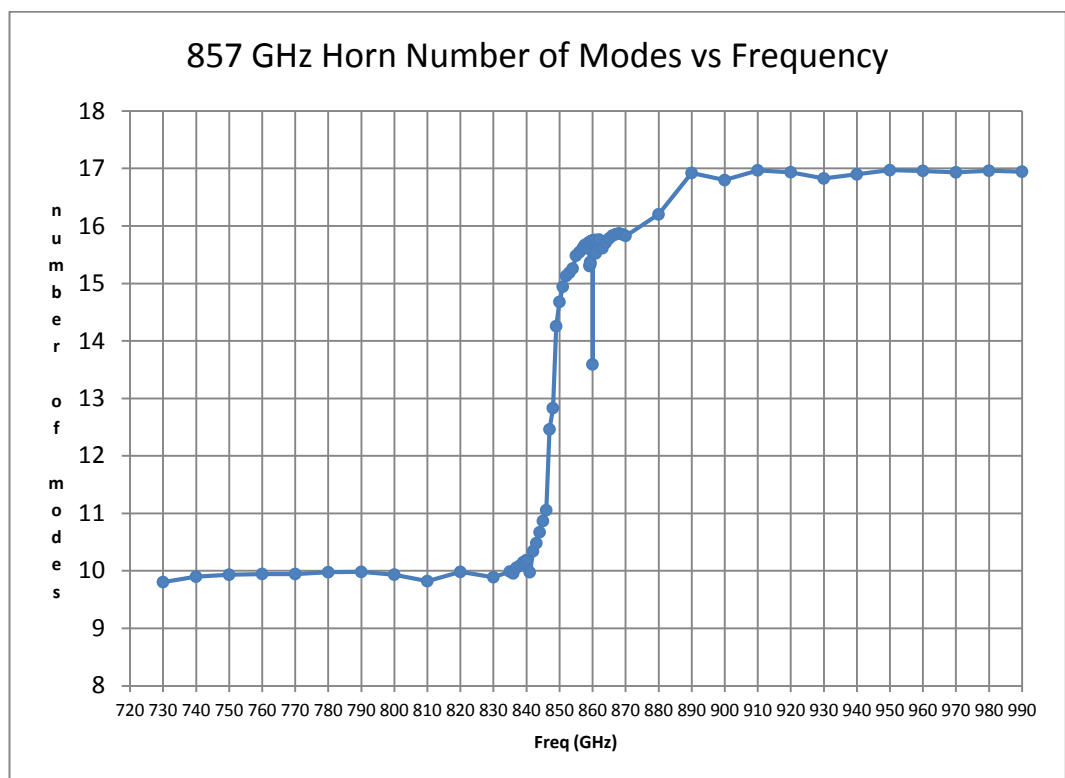


**Figure 3-9 : Plot of the number of propagating modes as a function of frequency.**

First in order to probe the nature of the instability at 860 GHz, as seen in Figure 3-9, additional simulations were run with finer and finer steps in frequency around 860 GHz. The step size was reduced to a 1 GHz step size between 840 GHz and 880 GHz, which showed the drop in throughput (the effective number of modes) at the "resonance" at 860 GHz to be less than 1 GHz wide. Further reducing the step size to 0.1 GHz again showed that the apparent sudden loss of modes was at 860.0 GHz and was less than one frequency step, i.e. 0.1 GHz, wide (Figure 3-10). This seems to imply an apparent loss in mode throughput that must be too sharp a resonant-

like feature to be of a physical origin and points to a numerical instability that arises in running SCATTER. Other less pronounced features, such as the drop in the number of modes (effectively a drop in power) propagating, which are noticeable in Figure 3-10 at 858 GHz, 589 GHz, 861 GHz, would not be expected if the modes were to cut on smoothly and then remain as a propagating mode. These features it was concluded therefore are also due to numerical instabilities occurring at certain frequencies that predict unlikely physical behaviour in the simulations.
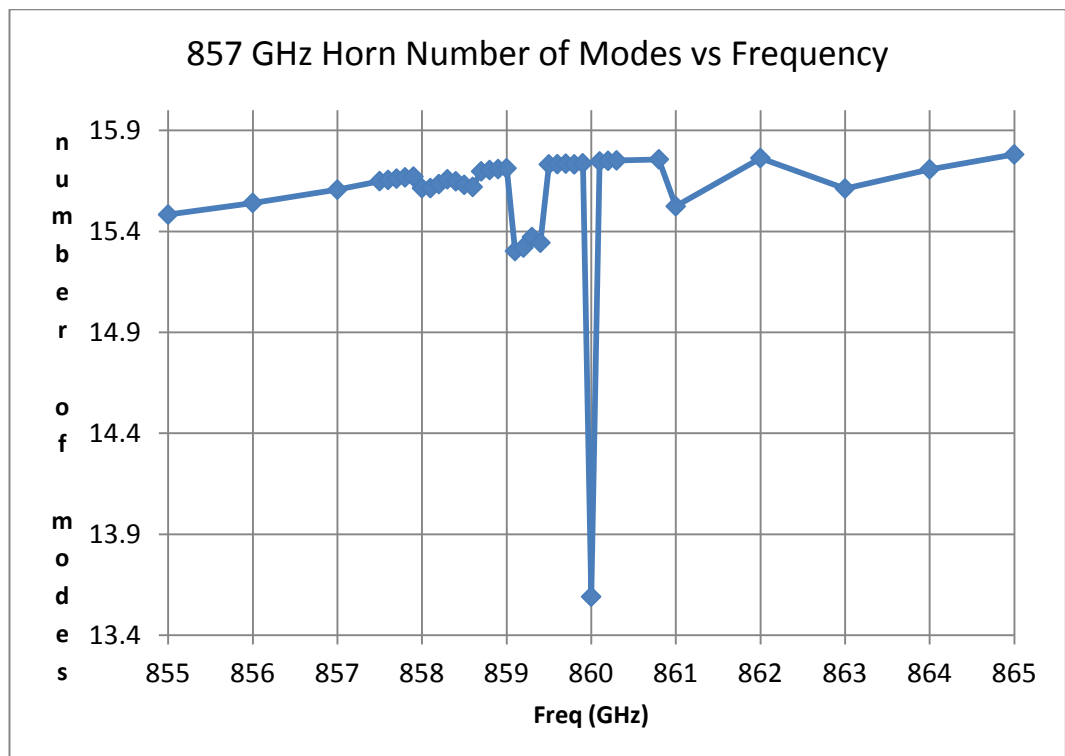


**Figure 3-10 : Plot of the number of propagating modes as a function of frequency in 0.1 GHz steps. When pre-existing SCATTER code was run resonant-like features shown appear to be unphysical in nature and point to numerical issues.**

Not surprisingly apparent non-physical behaviour was also seen when the beam patterns at various frequencies across the band were computed, such as at frequencies below 760 GHz for example when the numerical instabilities occurring in running the original SCATTER code resulted in simulated farfield beam patterns wider than should be assuming the beam pattern remains approximately of the same width across the band, which is expected from throughput considerations. Figure 3-16 shows an example of this, with the farfield beam pattern at 730 GHz plotted before (red line) and after (black line) the source of these stability issues had been solved as will be discussed below. At 10 and 20dB the 'before' beam pattern computed with the

original SCATTER code is approximately 4 degrees wider. The first sidelobe is also 3 dB lower in addition to being displaced by about 4 degrees.

It turned out that after some significant investigation there were three issues when running the original SCATTER code, which all contributed in varying degrees to the apparent non-physical anomalies discussed above seen at certain spot frequencies in particular. By monitoring the evolution of the scatting matrix in the waveguide filter section of the back-to-back horn as each corrugation was cascaded with the overall scattering matrices up to that point it was possible to discover if the SCATTER program was suffering from numerical instabilities particularly at frequencies close to where the number of modes able to propagate suddenly changes such as when a mode is at cut-off giving rise to the number of true hybrid modes able to propagate changing suddenly from one corrugation to the next. This was achieved by keeping track of the singular values of the $[S_{21}]$ and $[S_{12}]$ scattering matrices as these indicate the true number of independent hybrid modes present. These singular values are also expected to be close to unity representing a hybrid mode propagates without attenuation.

The first issue which became obvious in taking this approach to monitoring the $[S_{21}]$ scattering matrix had to do with evanescent modes excited at the input plane, in this case in the waveguide filter section of the back-to-back horn pair. After the first couple of steps the problem began to manifest with some of the singular values in the $\Sigma$ matrix rising above 1. This was due to the fact that all modes are assumed to be excited at the entrance port to the horn including the evanescent modes. These modes cause problems as for a very short piece of waveguide the $[S_{11}]$ and $[S_{22}]$ will be zero (for no step) while the $[S_{12}]$ and $[S_{21}]$ will show mode attenuation. Therefore, the complex power is not conserved leading to unphysical results when the scattering matrices are cascaded. Including a step in the section combining sections 1 and 2 effectively in Figure 3-11 results in non-zero $S_{11}$ and $S_{22}$ terms but still does not result in power being conserved.
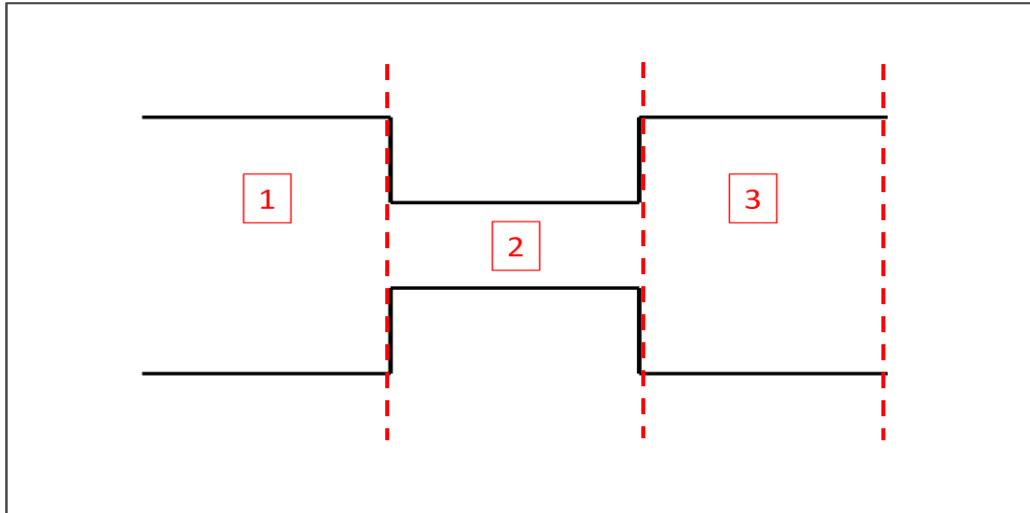
**Figure 3-11 : Diagram of three waveguide sections which form two junctions, one between section 1 and 2, and a second junction between sections 2 and 3. Adding a long uniform section before the first step eliminated any evanescent modes being present at the first step between sections 1 and 2.**
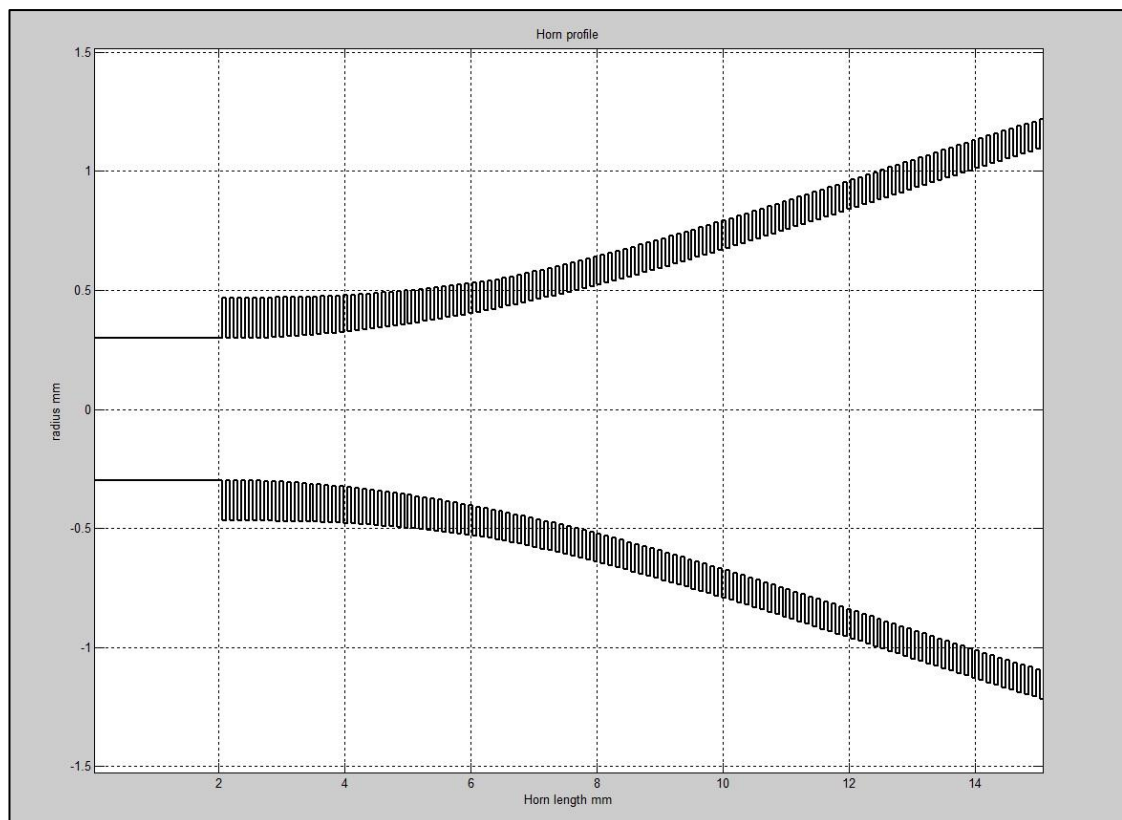


**Figure 3-12: Plot showing the geometry waveguide filter and throat area of the front section of the 857 GHz back-to-back with the addition of the finite length of waveguide at the enterance of the horn to supress the evanescent modes.**

In practice evanescent modes should not be excited at the entrance port as such modes could not have existed there unless there was a waveguide before the input port. The solution therefore was to add a waveguide of finite length at the start of the

horn geometry file which was long enough to eliminate all evanescent modes (Figure 3-12). Since the corresponding $[S_{12}]$ and $[S_{21}]$ diagonal matrices for this guide are zero for evanescent modes (i.e. $(S_{21})_{ii} = \exp(-\gamma_i l)$, where $l$ is the section length, and $\gamma_i$ the positive attenuation coefficient for the mode in question) the effect on the output fields of the evanescent modes is removed. However, there could be issue with the extra phase introduced in the $S_{12}$ and $S_{21}$ terms for propagating modes. This can be eliminated in turn by setting these terms $(S_{12})_{ii}$ and $(S_{21})_{ii} = \left| \left( e^{-j\beta l} \right) \right| = 1$ so that effectively the sections does not exist for propagating modes. Figure 3-13 shows the SVD singular values of the $[S_{21}]$ scattering matrix for azimuthal order $n = 1$ as it is scattered through some of the first sections of the 857 GHz front end horn. As can be seen without the addition of the long guide section there are three modes propagating but with one singular value above unity in each case. This is nonphysical as the singular value represents the amount of power in the mode and a value greater than 1 means that power has been added to the system. After the guide section has been added there are only two modes propagating, both with singular values of 1.0 to within the numerical accuracy expected.
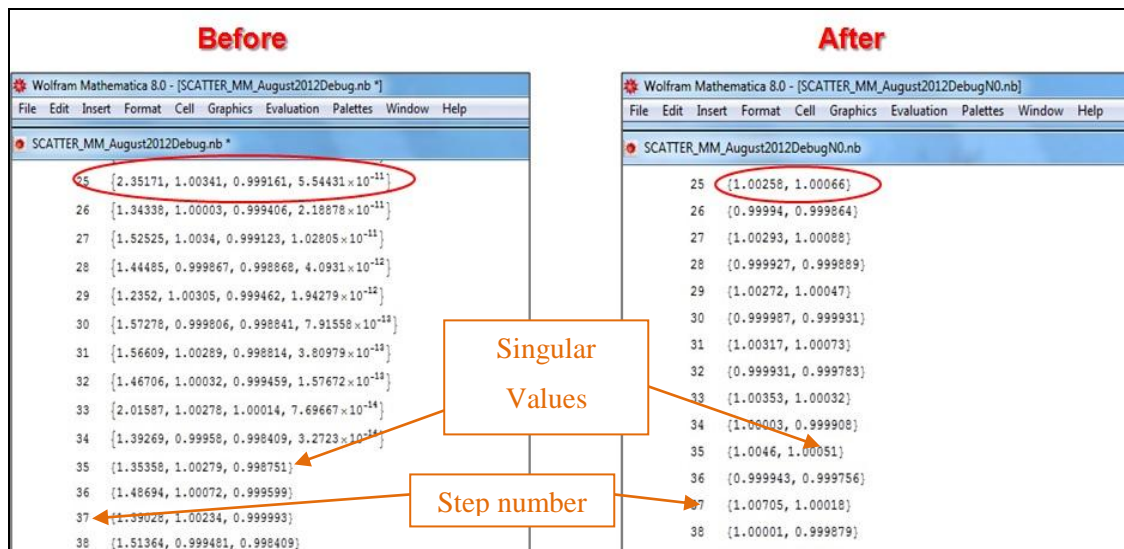


**Figure 3-13 : SVD values of the $[S_{21}]$ matrix as the steps in the corrugated waveguide are added for early sections of the 857 GHz front end horn before and after the addition of the finite section of waveguide at the beginning of the horn geometry in the SCATTER code. A step occurs when the waveguide radius changes as one goes from a slot to a fin or vice-versa. Clearly we could ignore the very tiny singular values with a high negative power of 10.**

The next (second) issue had to do with unphysical singular values of the $[S_{21}]$ matrix for the horn as a whole at certain spot frequencies as discussed previously. By

continuing the painstakingly detailed step by step examination of the scattering matrix calculations at the frequencies where the singular value remained above 1.0 for the $[S_{21}]$ of the horn as a whole it was possible to discover where in the horn/waveguide the $[S_{21}]$ matrix became numerically unstable during the cascading process (Figure 3-14). This is what was occurring at 860 GHz, for example, where the $[S_{21}]$ matrix became approximately singular due to the inverse of an approximately singular matrix being taken at a particular step (step 41, Figure 3-14) in the waveguide section for this exact value of the frequency.

$$\left[S_{21}^c\right] = \left[S_{21}^b\right]\left[[I]-\left[S_{22}^a\right]\left[S_{11}^b\right]\right]^{-1}\left[S_{21}^a\right]$$  (3.1)

where $[I]$ is the identity matrix, $[S^a]$ are the overall scattering matrices for the horn up to this step, $[S^b]$ are the scattering matrices for the current step, and $[S^c]$ are the overall scattering matrices for the horn including the current step obtained by cascading $[S^a]$ with $[S^b]$. In order to prevent this the SCATTER code (both in MATLAB and Mathematica) was rewritten using pseudoinverses in place of the inverse matrixes in the equation 3.1 used to cascade together of the matrixes.

The case of the $[S_{21}]$ matrix becoming singular corresponds to trapped power when reflection from the step just added followed by reflection at the output port looking into the waveguide section are in phase so that the power round trip becomes numerically unstable to calculate as the matrix to be inverted becomes singular. For example considering a single mode system with a reflection coefficient $r$ from some step and reflection $re^{2i\delta}$ from a second step (where $\delta$ is the phase difference for a return trip by the wave) then the transmission can be written as a Fabry Perot like transmission coefficient (due to the multiple reflections)

$$t = \frac{(1-r)^2}{\left[1-r^2 e^{2i\delta}\right]}$$  (3.2)

where $t$ is the transmission coefficient and $r$ is the reflection coefficient (for amplitudes). If $re^{2i\delta} \approx 1$ then the calculation of the inverse of $\left[[I]-[S_{22}^a][S_{11}^b]\right]$ becomes numerically unstable (infinite Q factor, which is the unphysical case of r = 1.0 in a Fabry Perot cavity).

As is highlighted on the left-hand side of Figure 3-14, before the introduction of pseudoinverses into the code a singular value for the total S21 up to that point of 3.075 occurred on the $41^{st}$ step in the waveguide filter, for the 860 GHz calculation. Which is, of course, nonphysical as the singular value represents the amount of power in the mode and values greater than 1.0 mean that power appears to have been introduced into the system via the numerical instability. After the matrix inverse was replaced with the pseudoinverse a singular value of 1.00 (unity) occurs at the same step, as indicated on the right of Figure 3-14.
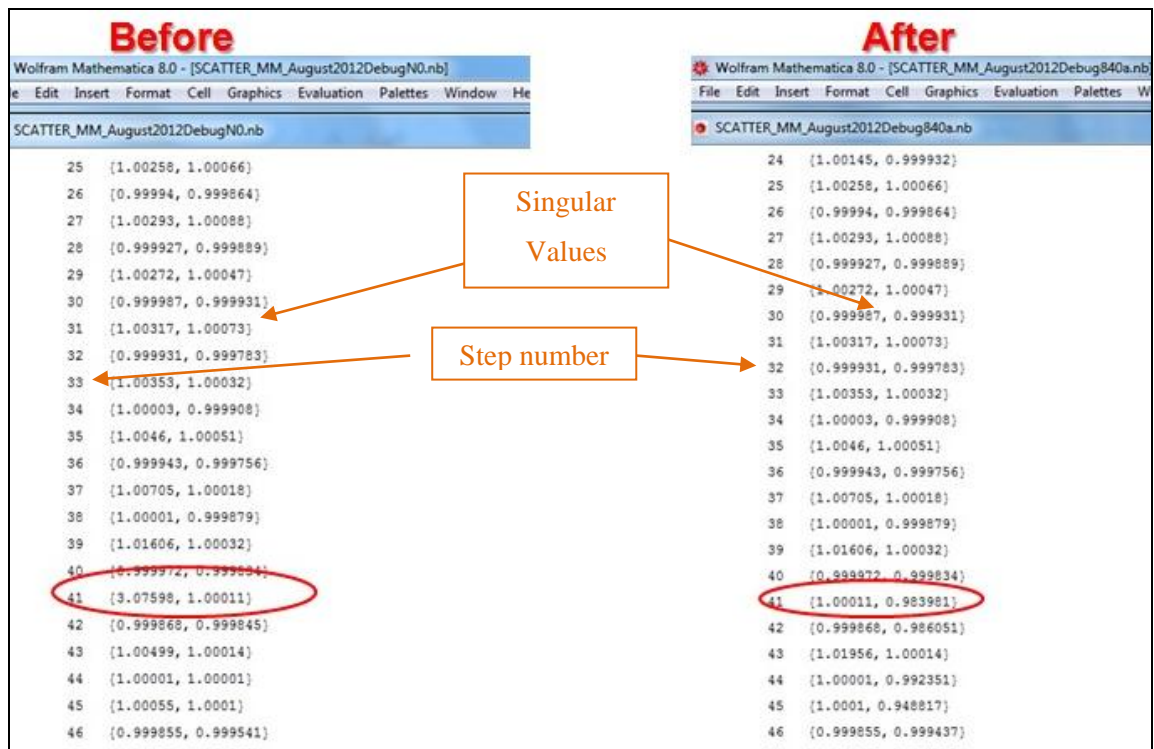


**Figure 3-14 :SVD values of the [S$_{21}$] for some of the early sections of the 857 GHz front end horn for the 860 GHz spot frequency before and after replacing the matrix inverse with pseudo-inverse in the SCATTER code.**

It must be noted that while this solved one problem it subtly introduced another. In Matlab the pseudoinverse used is a Moore-Penrose pseudoinverse which is calculated using singular value decomposition. When the singular values are calculated those values below a preset tolerance are set to zero. If the value of this tolerance is set to too high a level, it can result in a propagating mode being set to zero. A poor choice of tolerance can thus result in the sudden loss modes which is the very problem it was introduced to fix! It was found that when the tolerance level was set to $10^{-4}$ for the pseudoinverses introduced into the SCATTER code, it gave reliable

results in modelling across the band for the 857 GHz horn for all spot frequencies evaluated.

The third issue had to do with was the number of TE and TM waveguide modes used to describe the hybrid fields accurately. The number of TE and TM modes used in the original SCATTER code was 24 modes, 12 TE and 12 TM modes, during the previous phase of modelling of the 857 GHz channel. This number was due in part to memory limitations of older versions of Mathematica and the then available computers. Although adequate during the design and definition phase of the Planck multimode channels, nevertheless in order to fully describe the hybrid mode fields of multimode horns (such as in the Planck 857 GHz channels) more modes are needed. In fact it was found that at least 60 modes, consisting 30 TE and 30 TM, are required for a complete representation of the propagating fields. Careful comparisons of beam patterns and singular values showed that using fewer modes results in wider than expected beam patterns at certain frequencies and corresponding singular values greater than unity for the $[S_{21}]$ scattering matrix in some of these cases. In particular, using too few modes prevents power being scattered into higher order modes, which clearly leads to the information on the sidelobes being lost as compared to the lower order modes, the higher order modes contribute more off-axis than lower order modes in general (for azimuthal orders greater than $n = 1$, especially). This is illustrated in the example shown in Figure 3-15. The farfield beam patterns for the front horn at 840 GHz are shown. Beyond 30 degrees off-axis there is a clear difference in the sidelobe levels for the original version of SCATTER run with 20 mode, 10 TE and 10 TM modes, and run with 60 modes, 30 TE and 30 TM modes. Although the main beam is unaffected, the sidelobes are not well described and this is crucial to the work described in Chapter 4 of the tolerancing effects on the spillover beam patterns of the telescope, as this work required an understanding of the far-out sidelobe structure of the beams.
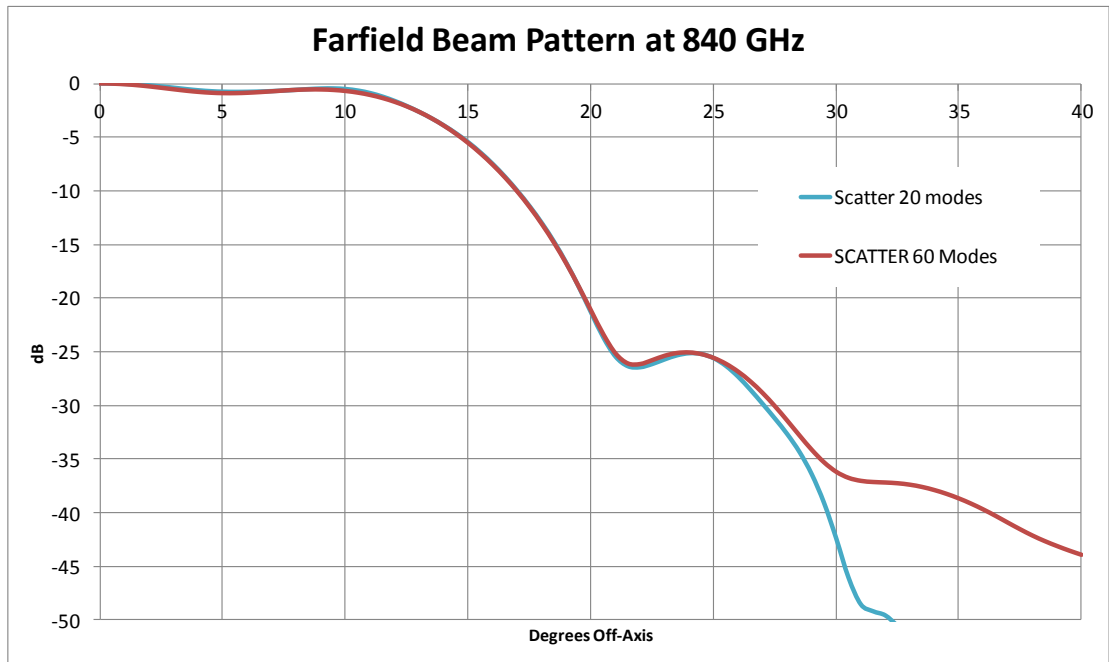
**Figure 3-15 : The farfield beam patterns as computed by SCATTER using 20 mode and 60 modes.**
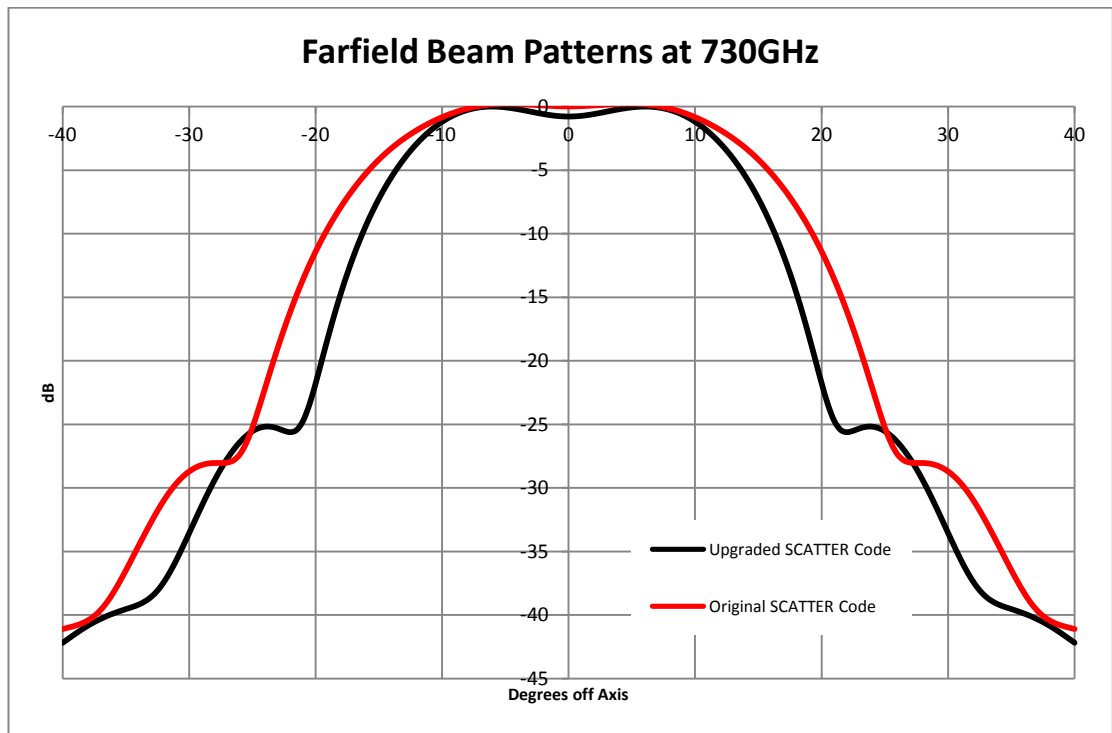


**Figure 3-16 : Plot of the Farfield beam pattern of the 857 GHz horn at 730 GHz before and after the stability issues in the SCATTER code had been dealt with.**

Figure 3-16 shows the farfield beam at a spot frequency of 730 GHz before and after the various changes to the code, i.e. the increased number of TE and TM modes, the introduction of pseudoinverses, and dealing with the evanescent modes at the input, had been implemented. At the -10 dB and -20 dB levels the 'before' beam

94

pattern is approximately 4 degrees wider. This is therefore critical when considering edge tapers. The first sidelobe is also 3 dB lower in addition to being displaced by 4 degrees, again indicating very different spillover levels. This example shows rather strikingly why the various issues associated with the SCATTER code needed to be addressed particularly before dealing with subtle tolerancing effects.

## 3.3.2 SCATTER Geometry File Anomalies

As described in Chapter 2 the definition of the corrugated horn antennas in terms of circular waveguide sections is fed into SCATTER using "geometry" files. These are text files, with extensions of either .txt or .i, containing information about the frequency in GHz, the number of steps (sections), and the length and radius of each step (section) in millimetres (Figure 2-10 in Chapter 2). The file also contains an estimated minimum number of modes needed to use in the modelling of each section, although this is not used by SCATTER but are instead needed by another program CORRUG [SMT, 2016].

For the Planck 857 GHz back-to-back horn the geometry file was created in the same fashion as the real (physical) antennas by combining the geometry files of the front and back end horns together. This however created an unexpected issue that exposed a bug in the SCATTER software. When the two geometry files were merged together the radii of the sections where the horns met were the same. This resulted in two sections of length 0.03mm each instead of one section 0.06mm in length where the two horns were joined (see Figure 3-17). SCATTER was designed for step in radius at each section junction and no provision had been made in the code for two successive sections of the same radius and a computational step was jumped over. This resulted in an error in the scattering matrixes and beam patterns calculated by SCATTER for the 857 GHz back-to-back horn pair.
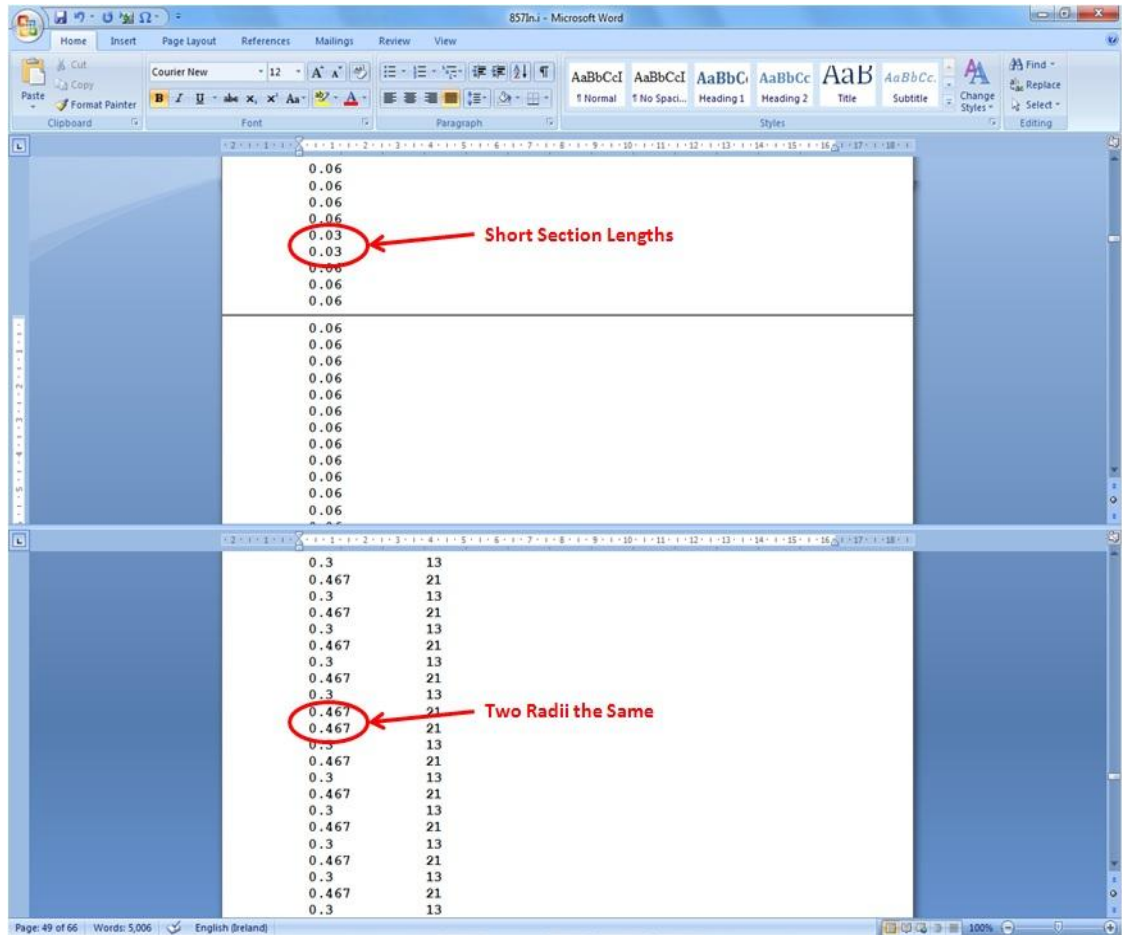
**Figure 3-17: The original input geometry file for the back-to-back horn pair. Note the two short length sections highlighted and of their corresponding waveguide radii of same radius.**

This problem first came to light during simulations of the broadband farfield beam pattern. When the beam at 840 GHz was simulated it was observed to be anomalous with a three peak structure that can be seen in Figure 3-18. At first it was difficult to identify the source of the problem. The problem appeared similar to the stability issues described in the previous section in this chapter as it was only at particular frequencies that its effects were noticeable. However, when the front horn section of the back-to-back horn pair was used in order to reduce the number of calculations needed there was a clear difference at all frequencies between beam patterns for the two geometries. At 857 GHz the beam pattern for the original geometry file has a sharper main beam and lower side lobes than the front horn section only (Figure 3-19).
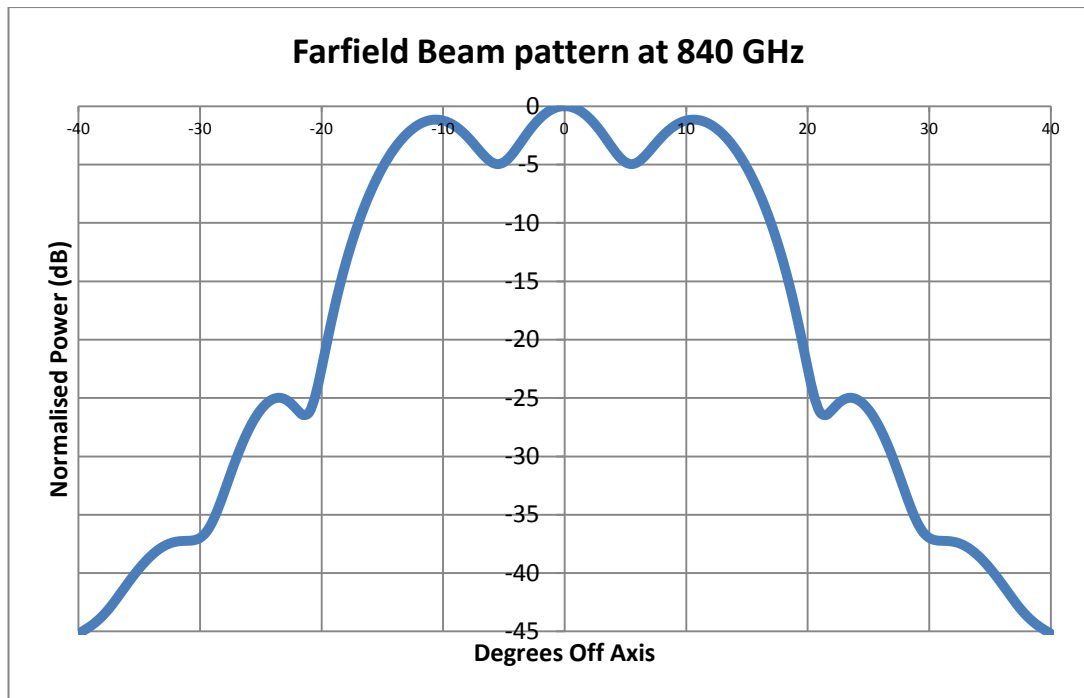
**Figure 3-18 : Farfield beam pattern at 840 GHz simulated using the original geometry file.**

The difference in these beam patterns can be understood in terms of what happened in the SCATTER code when two successive sections have the same radius. SCATTER used two variables to store the radii of the current sections, for two sections of different radii variable one was set equal to the larger radius and the second variable set equal to the smaller radius. The scattering matrixes for this step was then calculated and cascaded with the overall scattering matrixes. When the radii of the two sections were the same, neither variable was overwritten, the same scattering matrixes were calculated, and again scattered into the overall scattering matrixes resulting in an error in the calculation.

The code was edited to deal with this case and the geometry file was also amended to replace the two sections with one longer section. The result of this was excellent agreement between the beam patterns of the back-to-back horn pair and the front section horn fed by the filter waveguide on its own as shown in Figure 3-19. This now allowed for the front section with the waveguide filter to be used in place of the full back-to-back horn pair in order to reduce the time required for simulations by reducing the number of steps to be calculated. This is discussed in more detail below.

97
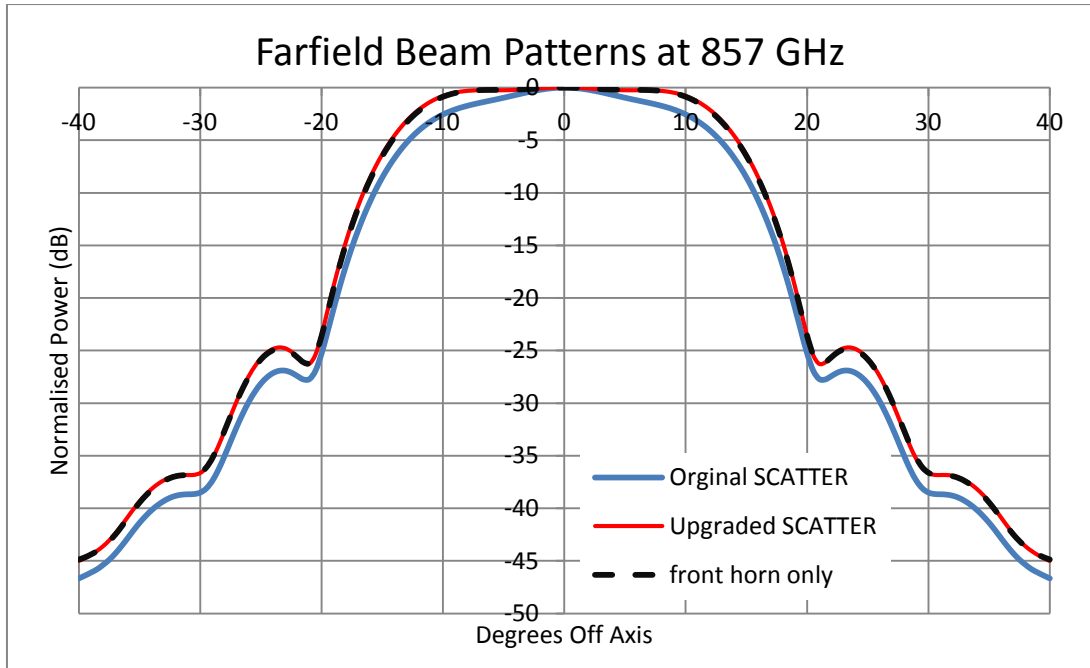
**Figure 3-19 : Farfield beam pattern at 857 GHz for the back-to-back horn pair run in original SCATTER, the front horn only, and the back-to-back horn pair run in the upgraded SCATTER.**

# 3.4  Simulation Results Across the Band

Once these changes had been made to the SCATTER program the simulations of the beam patterns were re-run across the band.  The number of hybrid modes per frequency (derived from the singular values of the total $[S_{21}]$ matrix) now showed the expected smooth growth in numbers with frequency as can be seen in Figure 3-20 with the expected "jumps" in the total number of modes when extra modes "cut-on".  The total number of modes is obtained by summing the $\sigma_i^2$, singular values for the hybrid modes, including the degeneracies except for $n = 0$ modes.  Comparing the plot in Figure 3-20 to that in Figure 3-9 it is clear just how much of an effect the numerical stability issues were having on the results of the simulations.  While the same overall trends are similar in both plots, with increasing number of propagating modes as cut-on frequencies are passed, the fine details shown in the two plots are clearly quite different.  The original version of SCATTER actually appeared to predict modes switching off suddenly above the normal cut-on frequency which is unphysical.  The upgraded version of SCATTER shows that once a mode is switched on it remains on

within the frequency range of the band as expected for the hybrid modes (see Section 2.8 on the surface impedance model). Hybrid modes should behave in a similar way to smooth walled waveguide modes in this sense.

Listed in Table 3-1 are the singular values of the hybrid modes of each azimuthal order propagating at various spot frequencies across the band. At 730 GHz at the lower end of the band we can identify, two hybrid mode fieldss of azimuthal order $n = 0$ ($H_{01}$ and $E_{02}$), four hybrid modes fields of azimuthal order $n = 1$ when one includes the degeneracy (the pairs of $HE_{11}$ and $EH_{12}$ modes), two hybrid mode fields of azimuthal order $n = 2$ (the $HE_{21}$ pair), and two hybrid mode fields of azimuthal order $n = 3$ (the $HE_{31}$ pair) all of which are propagating. Moving up the frequency band additional higher order modes switch on until at the top end of the band; three modes of azimuthal order $n = 0$ ($H_{01}$, $E_{02}$, and $H_{02}$), three mode pairs of azimuthal order $n = 1$ ($HE_{11}$, $EH_{12}$, and $HE_{12}$), two mode pairs of azimuthal order $n = 2$ ($HE_{21}$ and $EH_{22}$), one mode pair of azimuthal order $n = 3$ ($HE_{31}$), and one mode pair of azimuthal order $n = 4$ ($HE_{41}$) are present. For azimuthal orders $n \geq 1$ each mode is degenerate in general with two orthogonal pair of fields. For the lowest azimuthal order $n = 0$, whose modes are cylindrically symmetric, the modes are not degenerate, i.e. each mode field does not have an orthogonal pair. Thus, at 730 GHz there is a total of ten independent hybrid modes, including all degenerate modes, propagating while at 990 GHz there are seventeen modes present. The square of the singular values, $\sigma_i^2$, for each azimuthal order listed in Table 3-1 describe the power propagating in each hybrid mode for unit power incident at the waveguide port. In reality the mode is either propagating or not, the singular values provide information about the power in each mode output at the aperture relative to the power excited in that mode in the waveguide at the back of the front horn. Any differences from unity indicate reflected power which in most cases is negligible. This reflected power is expected because the waveguide impedance for a mode close to cut-off becomes zero for the TM modes and infinity for TE modes leading to a large mismatch at any junctions.

| Frequency GHz | Azimuthal Order & Hybrid Mode | | | | | | | | | | Total |
|---|---|---|---|---|---|---|---|---|---|---|---|
| | 0 | | | 1 | | | 2 | | 3 | 4 | |
| | $H_{01}$ | $E_{02}$ | $H_{02}$ | $HE_{11}$ | $EH_{12}$ | $HE_{12}$ | $HE_{21}$ | $EH_{22}$ | $HE_{31}$ | $HE_{41}$ | |
| 730 | 1.00 | 1.00 | | 1.00 | 0.97 | | 1.00 | | 0.98 | 0.00 | 9.90 |
| 740 | 1.00 | 1.00 | | 1.00 | 0.97 | | 1.00 | | 0.99 | 0.00 | 9.91 |
| 750 | 1.00 | 1.00 | | 1.00 | 0.99 | | 1.00 | | 0.99 | 0.00 | 9.95 |
| 760 | 1.00 | 1.00 | | 1.00 | 0.99 | | 1.00 | | 0.99 | 0.00 | 9.96 |
| 770 | 1.00 | 1.00 | | 1.00 | 0.99 | | 1.00 | | 0.99 | 0.00 | 9.97 |
| 780 | 1.00 | 1.00 | | 1.00 | 0.99 | | 1.00 | | 1.00 | 0.00 | 9.98 |
| 790 | 1.00 | 1.00 | | 1.00 | 1.00 | | 0.99 | | 1.00 | 0.00 | 9.97 |
| 800 | 1.00 | 1.00 | | 1.00 | 1.00 | | 1.00 | | 1.00 | 0.00 | 9.98 |
| 810 | 1.00 | 1.00 | | 1.00 | 1.00 | | 1.00 | | 1.00 | 0.00 | 9.99 |
| 820 | 1.00 | 1.00 | | 1.00 | 1.00 | | 1.00 | | 1.00 | 0.00 | 9.99 |
| 830 | 1.00 | 1.00 | | 1.00 | 1.00 | | 1.00 | 0.00 | 1.00 | 0.00 | 10.00 |
| 835 | 1.00 | 1.00 | | 1.00 | 1.00 | | 1.00 | 0.01 | 1.00 | 0.00 | 10.02 |
| 840 | 1.00 | 1.00 | | 1.00 | 1.00 | | 1.00 | 0.10 | 1.00 | 0.00 | 10.20 |
| 845 | 1.00 | 1.00 | | 1.00 | 1.00 | | 1.00 | 0.44 | 1.00 | 0.00 | 10.88 |
| 850 | 1.00 | 1.00 | | 1.00 | 1.00 | 0.71 | 1.00 | 0.83 | 1.00 | 0.81 | 14.69 |
| 855 | 1.00 | 1.00 | | 1.00 | 1.00 | 0.90 | 1.00 | 0.95 | 1.00 | 0.90 | 15.49 |
| 859 | 1.00 | 1.00 | | 1.00 | 1.00 | 0.95 | 1.00 | 0.99 | 1.00 | 0.93 | 15.72 |
| 860 | 1.00 | 1.00 | | 1.00 | 1.00 | 0.96 | 1.00 | 0.99 | 1.00 | 0.93 | 15.74 |
| 861 | 1.00 | 1.00 | | 1.00 | 1.00 | 0.96 | 1.00 | 0.98 | 1.00 | 0.94 | 15.76 |
| 865 | 1.00 | 1.00 | | 1.00 | 1.00 | 0.98 | 1.00 | 0.98 | 1.00 | 0.96 | 15.83 |
| 870 | 1.00 | 1.00 | | 1.00 | 1.00 | 0.99 | 1.00 | 0.99 | 1.00 | 0.97 | 15.90 |
| 875 | 1.00 | 1.00 | | 1.00 | 1.00 | 0.99 | 1.00 | 0.99 | 1.00 | 0.98 | 15.92 |
| 880 | 1.00 | 1.00 | 0.30 | 1.00 | 1.00 | 0.99 | 1.00 | 0.99 | 1.00 | 0.98 | 16.23 |
| 885 | 1.00 | 1.00 | 0.89 | 1.00 | 1.00 | 0.99 | 1.00 | 1.00 | 1.00 | 0.99 | 16.83 |
| 890 | 1.00 | 1.00 | 0.98 | 1.00 | 1.00 | 0.99 | 1.00 | 1.00 | 1.00 | 0.99 | 16.93 |
| 900 | 1.00 | 1.00 | 1.00 | 1.00 | 1.00 | 1.00 | 1.00 | 1.00 | 1.00 | 0.99 | 16.96 |
| 910 | 1.00 | 1.00 | 1.00 | 1.00 | 1.00 | 1.00 | 1.00 | 1.00 | 1.00 | 0.99 | 16.98 |
| 920 | 1.00 | 1.00 | 1.00 | 1.00 | 1.00 | 1.00 | 1.00 | 1.00 | 1.00 | 1.00 | 16.98 |
| 930 | 1.00 | 1.00 | 0.99 | 1.00 | 1.00 | 1.00 | 1.00 | 1.00 | 1.00 | 1.00 | 16.97 |
| 940 | 1.00 | 1.00 | 0.99 | 1.00 | 1.00 | 1.00 | 1.00 | 1.00 | 1.00 | 1.00 | 16.98 |
| 950 | 1.00 | 1.00 | 0.99 | 1.00 | 1.00 | 1.00 | 1.00 | 1.00 | 1.00 | 1.00 | 16.97 |
| 960 | 1.00 | 1.00 | 0.98 | 1.00 | 1.00 | 1.00 | 1.00 | 1.00 | 1.00 | 1.00 | 16.96 |
| 970 | 1.00 | 1.00 | 0.98 | 1.00 | 1.00 | 1.00 | 1.00 | 1.00 | 1.00 | 1.00 | 16.96 |
| 980 | 1.00 | 1.00 | 0.98 | 1.00 | 1.00 | 0.99 | 1.00 | 1.00 | 1.00 | 1.00 | 16.96 |
| 990 | 1.00 | 1.00 | 0.98 | 1.00 | 1.00 | 0.99 | 1.00 | 0.99 | 1.00 | 1.00 | 16.95 |

**Table 3-1 The singular values of modes propagating of each azimuthal order propagating at frequencies across the band. Near cut-on the singular values are less than unity indicating a reflection of the mode (as expected because of impedance mismatch)**

These changes were also implemented in the original Mathematica version of SCATTER as well as the MATLAB version. The results of the simulations from both the MATLAB and Mathematica version of SCATTER were cross checked against each other providing a useful verifacation test of the code. The beam patterns produced by these simulations are shown in Figure 3-21. Both upgraded versions of SCATTER, in the MATLAB & Mathematica enviroments, agree with each other.

**857 GHz Horn number of modes SCATTER fixed**
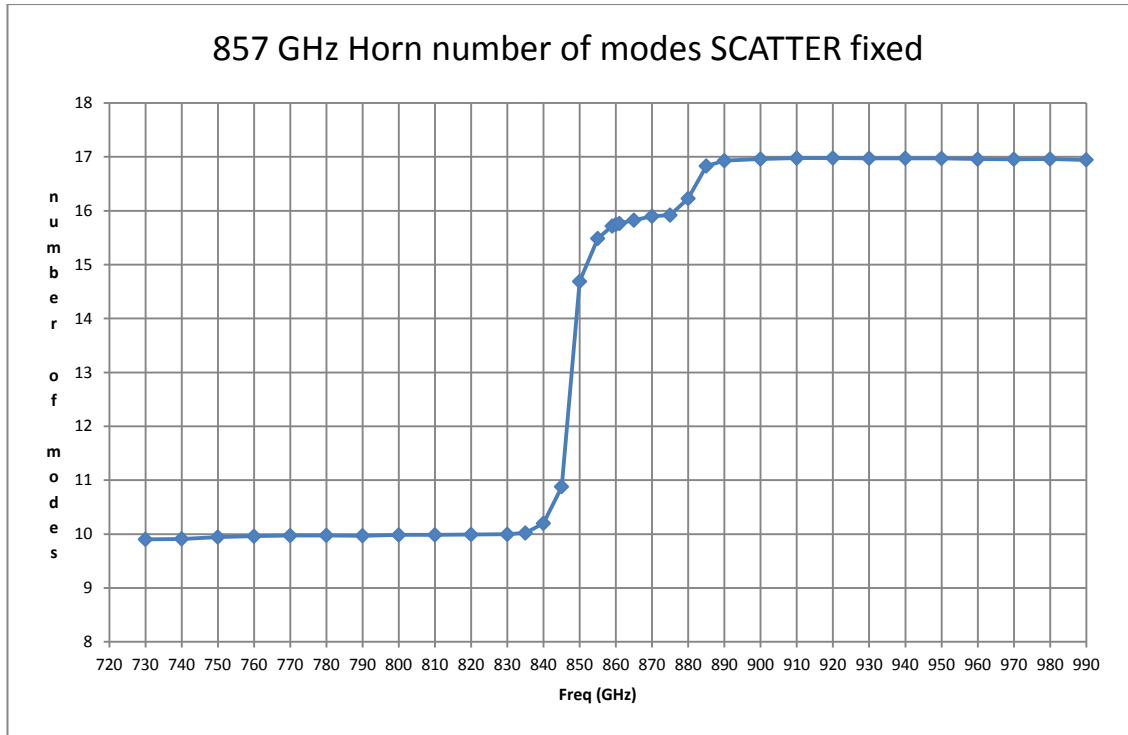
**Figure 3-20 : Plot of the number of propagating modes as a function of frequency using the corrected version of SCATTER.**



**Farfield Beam Pattern at 840 GHz**
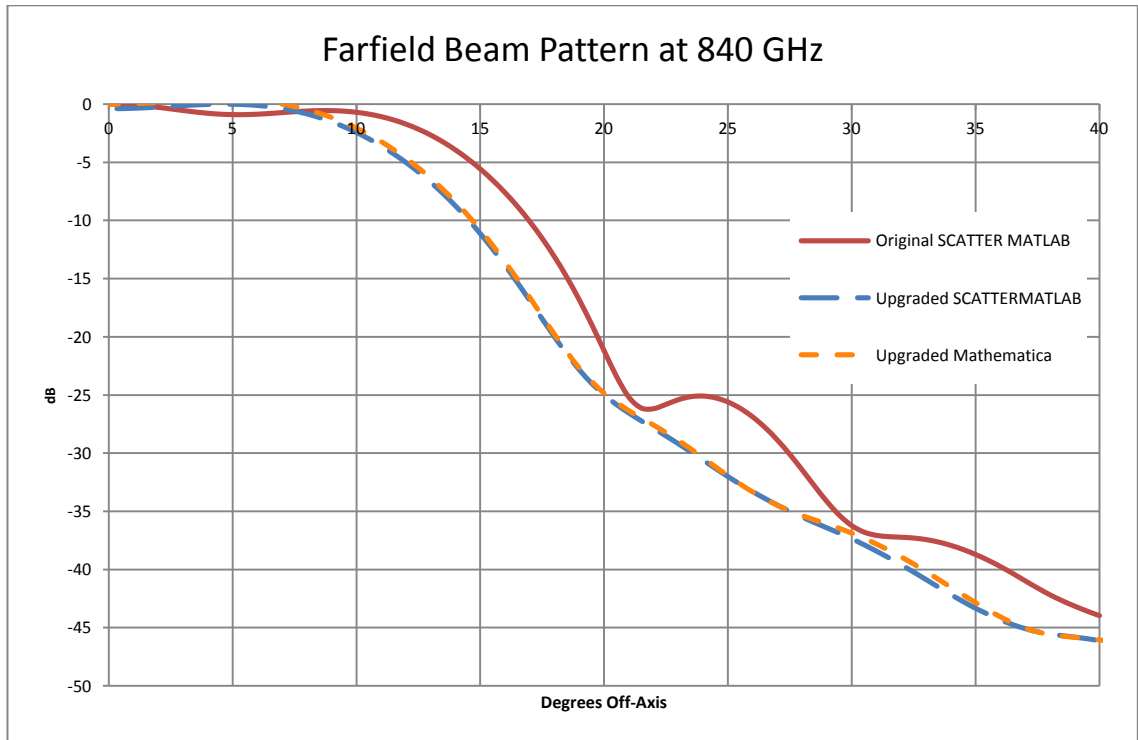
**Figure 3-21 : Farfield beam patterns of the 857 GHz horn at 840 GHz as simulated by SCATTER, using MATLAB and Mathematica. Clearly the original version of SCATTER suffered from numerical issues which have been removed in the upgraded versions.**

Now looking at the evolution of the farfield beam pattern as a function of frequency, it can be seen that the beam pattern is well behaved over the full range of

101

the operational frequency bandwidth. Plots of the SCATTER simulations of the farfield beam patterns for the 857 GHz horn antenna across the lower end, lower mid-range, higher mid-range and upper end of the operational band are shown in Figure 3-22, Figure 3-23, Figure 3-24, and Figure 3-25 respectively. All the farfield patterns are normalised to 0dB on-axis. These plots illustrate how relatively uniform the beam pattern remains in terms of shape and width across the whole frequency range. All the beam patterns reach the -10 dB level at approximately 15 degrees off-axis. The first side lobe is located between 23 and 24 degrees off-axis in each plot and in fact the edge taper at 25 off-axis (nominal edge of the primary as seen by the horn) lies between -26 and -33 dB. the required edge taper for the 857 GHz channel was around -30 dB which is on average achieved across the band. Also it can been seen that the beam pattern at the central frequency, 857 GHz, is a good approximation to the broadband beam in terms of beam width and location of first sidelobe and edge taper. The simulated beam pattern at 860 GHz is plotted in all the figures for ease of comparison.



**Figure 3-22 : Plots of the simulated farfield beam patterns of the 857 GHz horn antenna across the lower half of the operational band, 730-790 GHz.**

**Figure 3-23 : Plots of the simulated farfield beam patterns of the 857 GHz horn antenna across the lower half of the operational band, 800-860 GHz.**
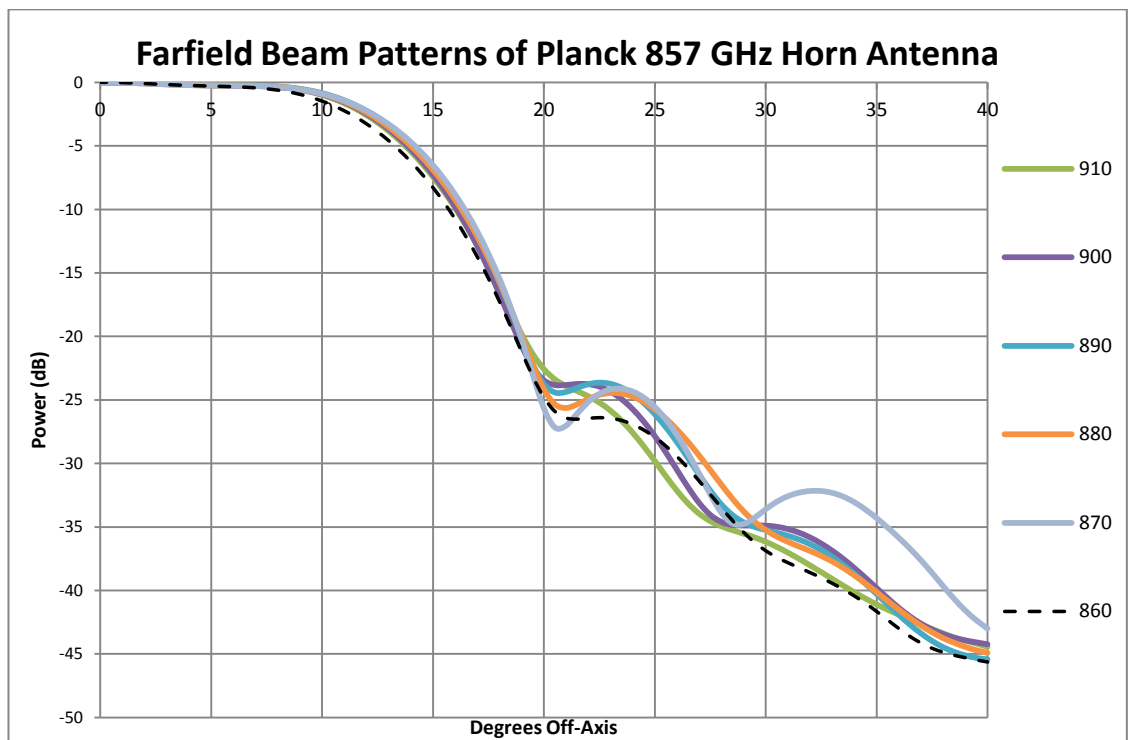


**Figure 3-24 : Plots of the simulated farfield beam patterns of the 857 GHz horn antenna across the upper half of the operational band, 860-910 GHz.**
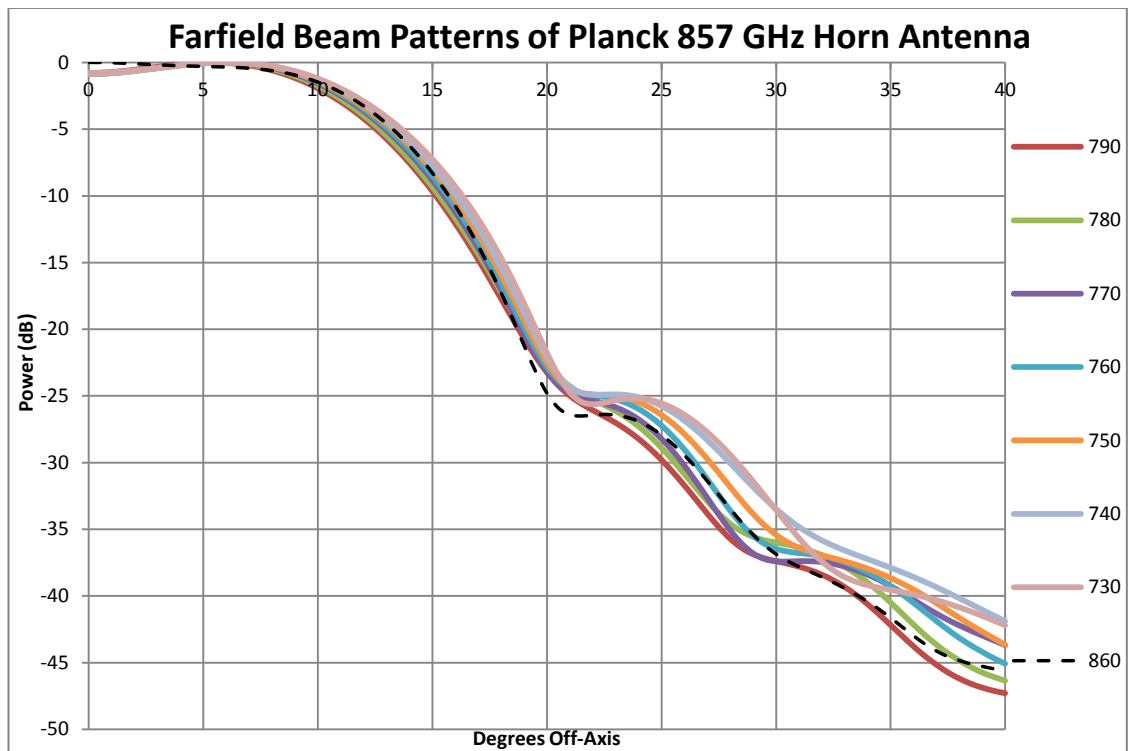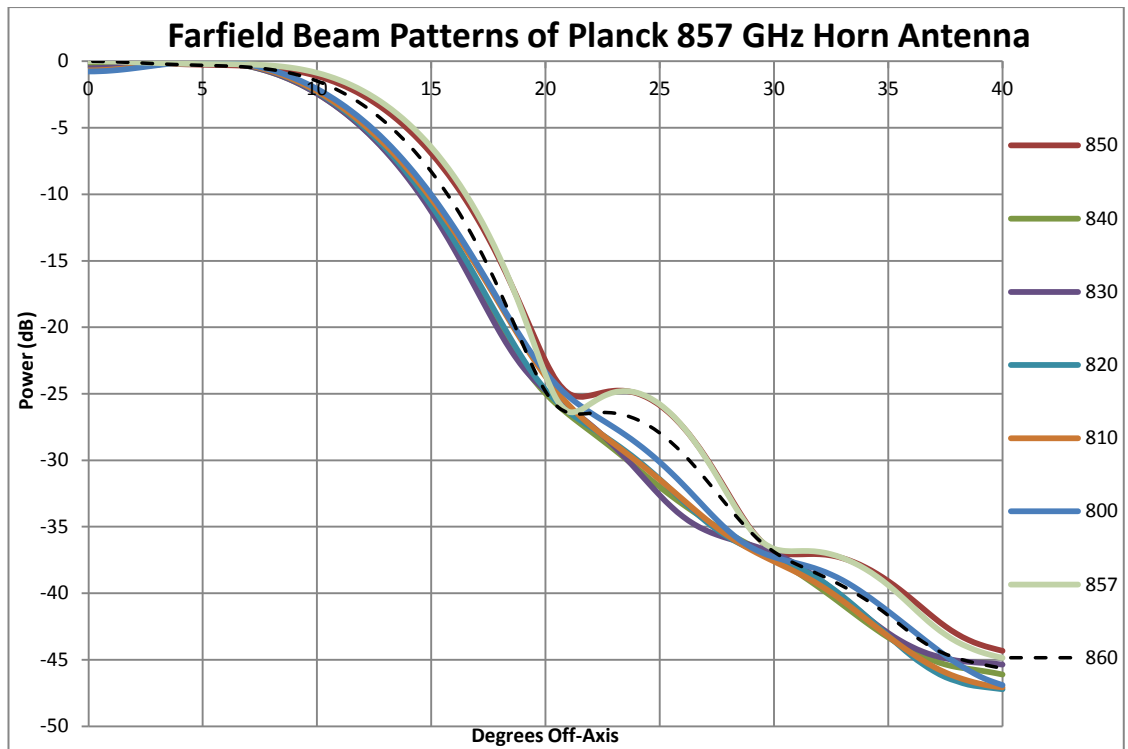
103
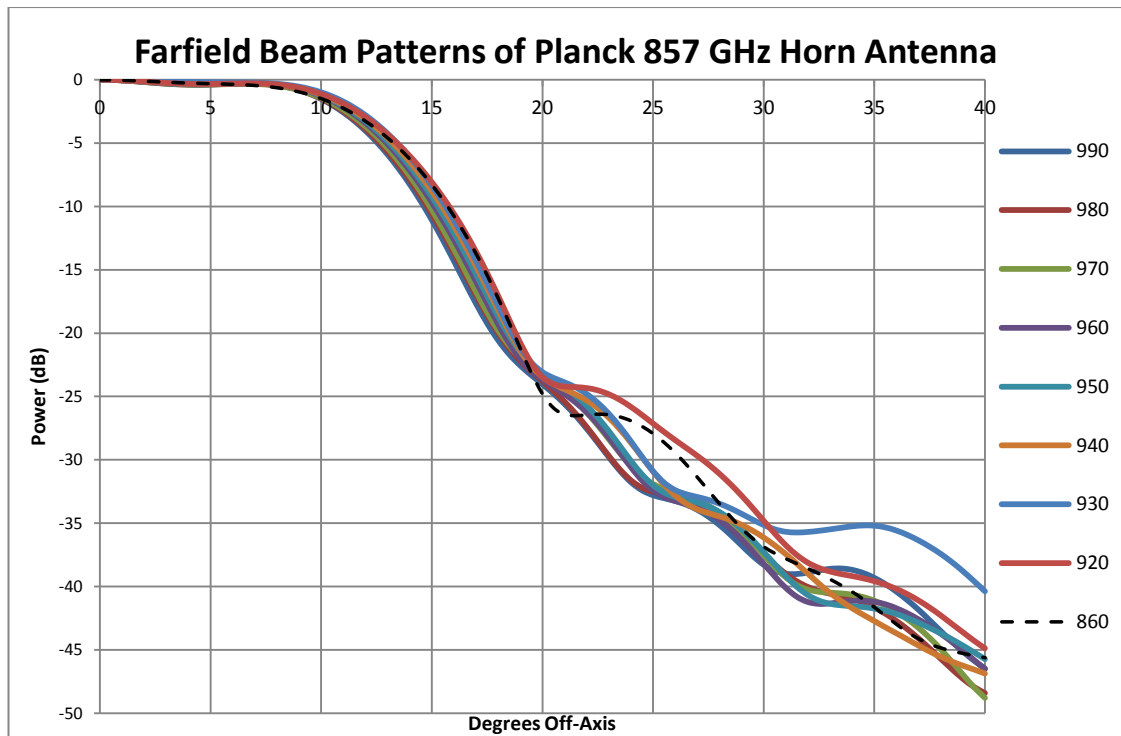
**Figure 3-25 : Plots of the simulated farfield beam patterns of the 857 GHz horn antenna across the upper half of the operational band, 920-990 GHz.**

By focusing on just some of the frequencies plotted in the lower half of the band the evolution of the beam pattern can be more clearly seen. Figure 3-26 shows the beam patterns in the range from 730 GHz to 830 GHz. Starting at 730 GHz, as the frequency is increased, the beam pattern decreases in width as expected from diffraction considerations. At 730 GHz the -15 dB level occurs at 18 degrees, at 790 GHz it occurs at 17 degrees off-axis, and by 830 GHz the -15 dB level occurs at just over 16 degrees off-axis. Between 840 GHz and 850 GHz the number of modes propagating increases (Figure 3-20 & Table 3-1). As a result of these higher order modes the beam pattern widens (Figure 3-27). The -15 dB level at 857 GHz occurs at approximately 18 degrees off-axis back the same as at 730 GHz. Between 857 GHz and 870 GHz the number of mode cutting-on continues to rise and the beam width remains constant with the -15 dB level still at approximately 18 degrees off-axis. This pattern of the beam narrowing then being reset by the additional higher order modes propagating repeats as the frequency increases and the threshold frequencies for these modes are passed.

**Figure 3-26 : Plots of the simulated farfield beam patterns of the 857 GHz horn antenna at three spot frequencies in the lower end of the frequency band.**



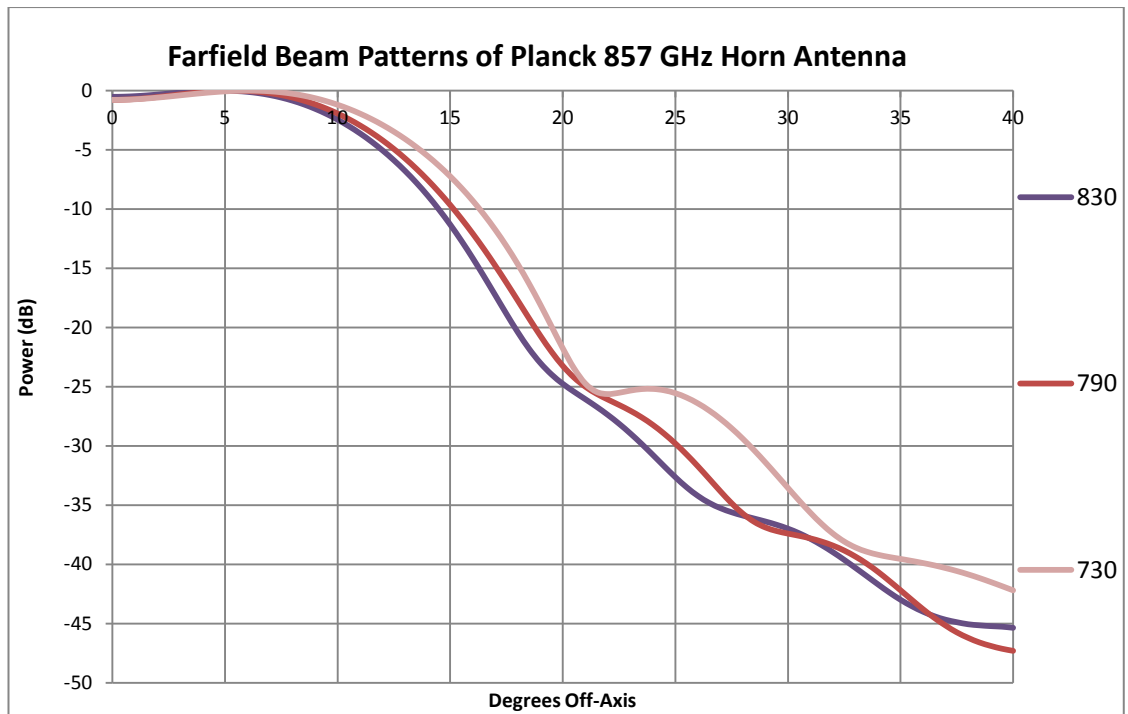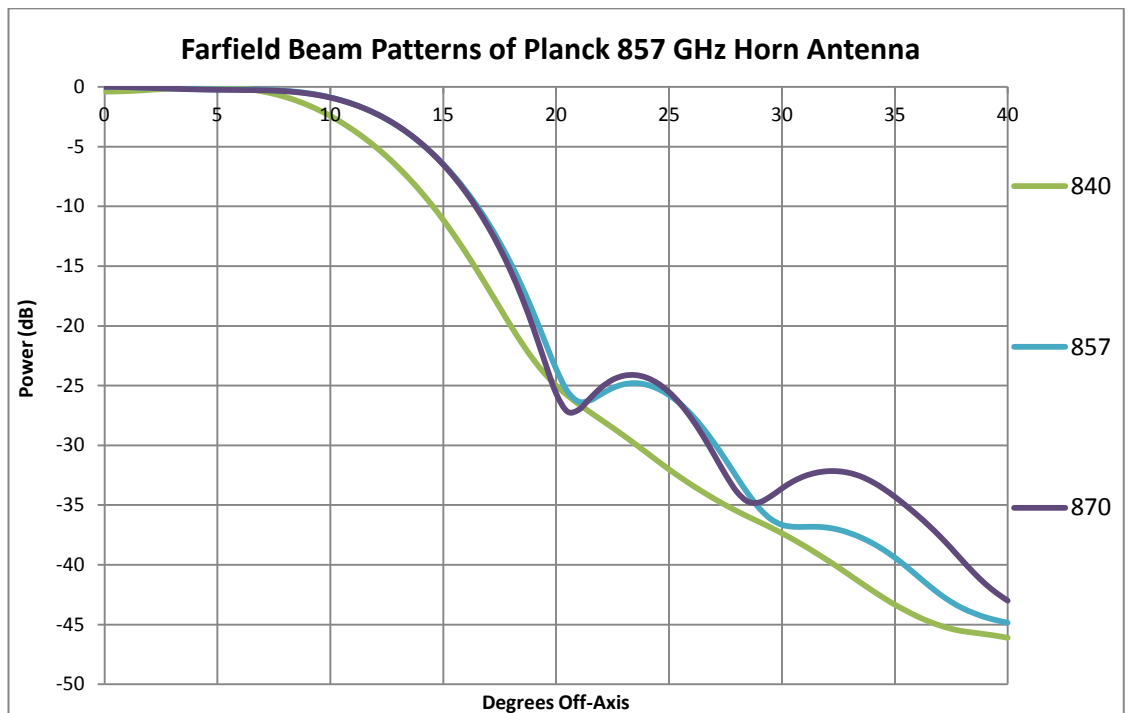**Figure 3-27 : Plots of the simulated farfield beam patterns of the 857 GHz horn antenna at three spot frequencies in the middle of the frequency band.**

The 857 GHz and 545 GHz channels of Planck were designed to be multi-moded as they were required to produce a beam width of 5 arcmin on the sky (the same as the 353 GHz channels, see discussion in Chapter 1). Additionally this multi-

moded design had the benefit of increasing the effective throughput of the horn antennas as each extra mode contributed to the power detected, which increased the sensitivity of the detector assembly and maximised its response to point sources [Murphy, 2010]. The broadband beam is plotted in Figure 3-28 for comparison with some selected spot frequencies. To create the broadband beam, the power at each of the spot frequencies from 730 GHz to 990 GHz were combined in quadrature before being normalised to 0 dB on-axis. At each of the spot frequencies, the power in each mode at the input is normalised so that this corresponds to the response to a flat spectrum source for the broadband beam of the horn plus detector as shown in Figure 3-28. As discussed earlier in this chapter (Section 3.2) for a beam which is observing typical astronomical sources the power arriving at the horn would be different at different frequencies depending on the spectrum of the source (which is assumed to be broadband). However because of the essentially non-varying beam width of the 857 GHz horn over its operational range, the broadband beam pattern effectively maintains the same general shape whatever the source (Figure 3-5) which is another advantage of multimode horns.
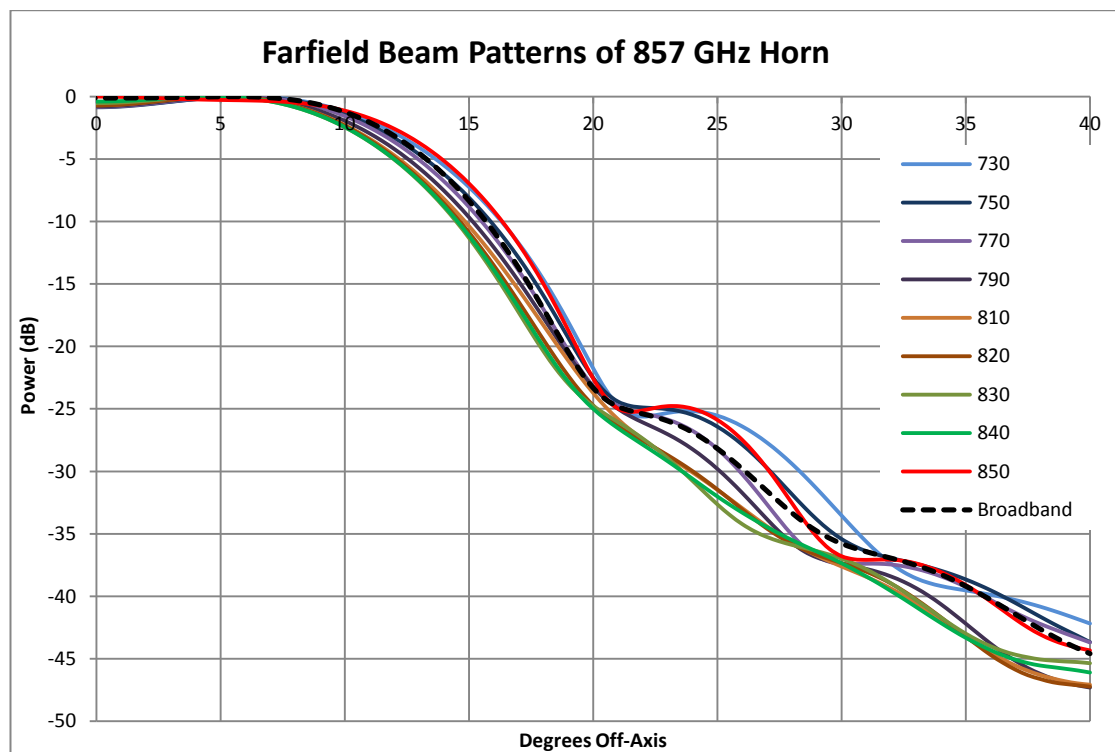


**Figure 3-28 : Plots of the simulated farfield beam patterns of the 857 GHz horn antenna at selected frequencies along with the broadband beam for comparison.**

106

# 3.5 Planck 545 GHz Channel

Up to now in this chapter the main focus of the multi-mode antenna simulation work reported on in this thesis has been on the 857 GHz channel. In this section we concentrate on the other multi-mode channel of the HFI at 545 GHz. The four 545 GHz channels were the second highest frequency channels on the HFI and were again primarily used for detection of foreground sources. Like the 857 GHz channels, the 545 GHz channels consisted of a back-to-back horn pair arrangement feeding a detector horn and an unpolarised spider web bolometer.

The campaign of simulation work on the 545 GHz channels followed along the same lines as those outlined previously in this chapter for the 857 GHz channels. A series of simulations at spot frequencies across the full width of the operational frequency band were carried out using the upgraded version of SCATTER. These simulations were used to construct a broadband farfield beam pattern (Figure 3-29) and to determine the evolution of the propagating modes (Figure 3-30) in the same manner as that had been done for the 857 GHz channel.
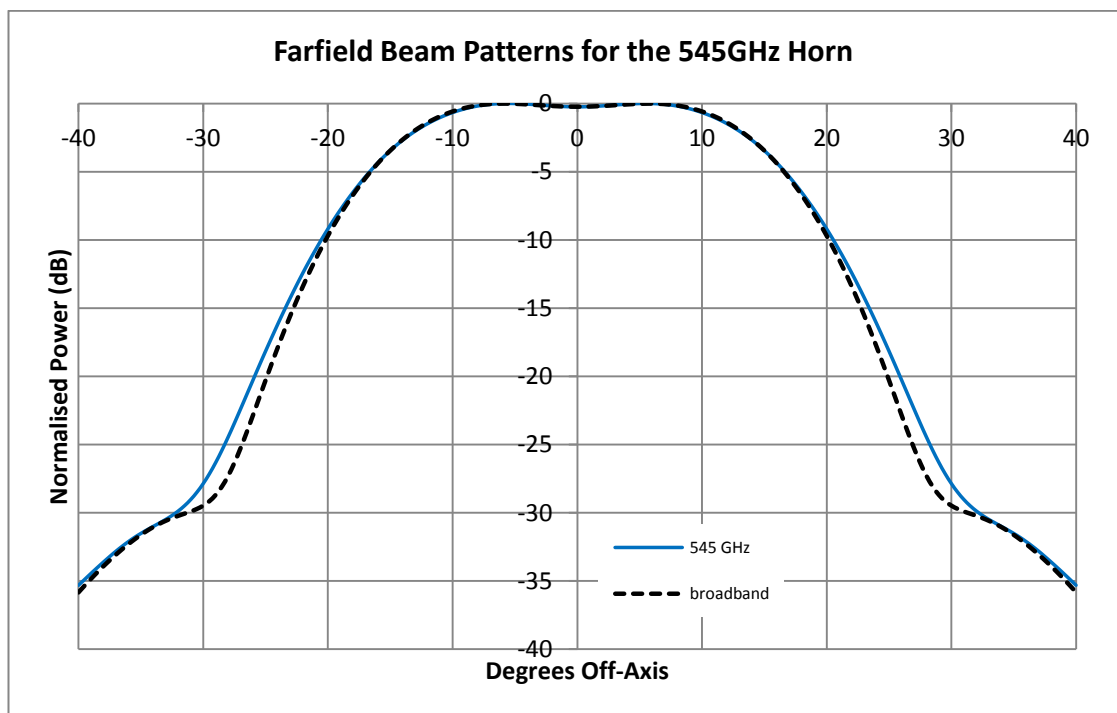


**Figure 3-29 : Simulated broadband and central frequency farfield beam patterns for the 545 GHz horn.**

As was the case for the 857 GHz, the central frequency of the 545 GHz channel proved to be a good representation of the broadband beam as can be seen in Figure 3-29. The number of modes propagating as a function of frequency in the 545 GHz also followed a similar pattern to that seen in the other multimode channel (857 GHz). The number of modes increases with frequency as expected (Table 3-2). As the frequency increases it passes the threshold cut-on frequency for successive higher order modes. At the lower end of the band, 465 GHz, two modes of azimuthal order $n = 0$ ($H_{01}$ and $E_{02}$), two mode fields of azimuthal order $n = 1$ (the $HE_{11}$ pair of modes), and two mode fields of azimuthal order $n = 2$ (the $HE_{21}$ pair of modes) are propagating. Moving up the frequency band additional higher order modes switch on until at the top end of the band; two modes of azimuthal order $n = 0$ ($H_{01}$ and $E_{02}$), two pairs of mode fields of azimuthal order $n = 1$ ($HE_{11}$ and $EH_{12}$), one pair of mode fields of azimuthal order $n = 2$ ($HE_{21}$), one pair of azimuthal order $n = 3$ ($HE_{31}$), and one pair of mode fields of azimuthal order $n = 4$ ($HE_{41}$) are present.
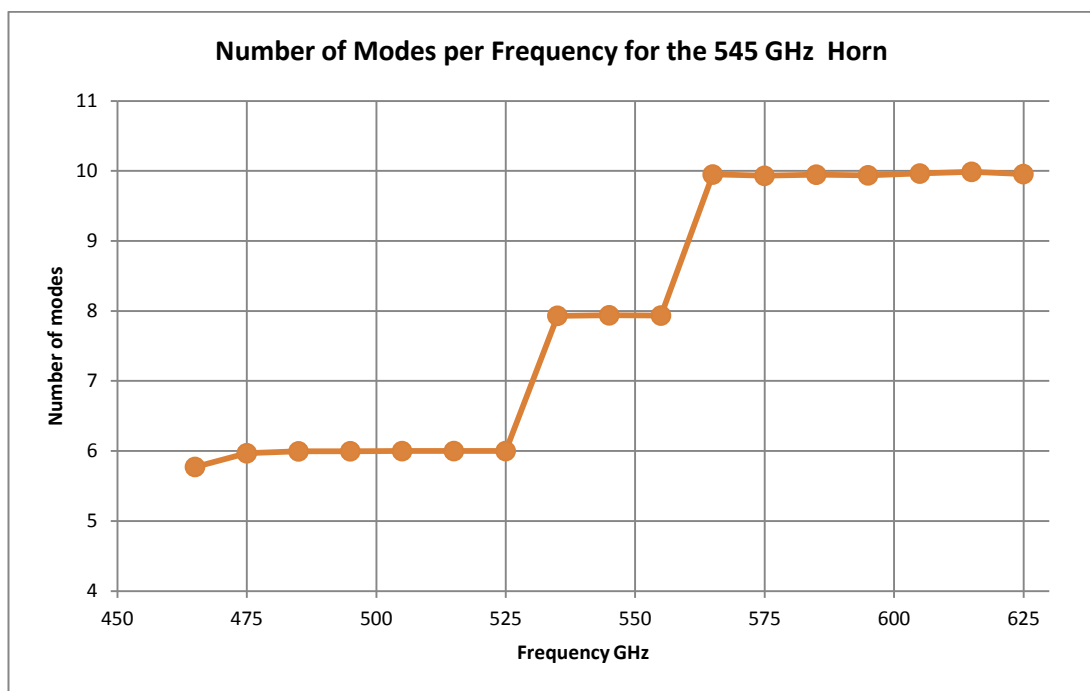


**Figure 3-30 : Number of modes propagating as a function of frequency in the 545 GHz back-to-back horn.**

As the frequency increases and additional modes cut-on the same effects on the width of the beam pattern are observed for the 545 GHz horn as were seen for the 857 GHz horn. In Figure 3-32, Figure 3-33, Figure 3-34, and Figure 3-35 the farfield beam patterns for spot frequencies across the upper and lower parts of the operational frequency band of the 545 GHz are presented. At 475 GHz the -15 dB level occurs at

23.5 degrees off-axis and at 525 GHz the beam pattern reaches this level at just over 21 degrees off-axis (Figure 3-32). Between 525 GHz and 545 GHz additional hybrid modes cut-on and the beam widens such that the -15 dB level occurs again at 23.5 degrees off-axis (Figure 3-31). Moving further up the frequency band until by 575 GHz more modes have cut-on and the -15 dB level occurs at approximately 23 degrees off-axis (Figure 3-34) as the additional hybrid modes counter the narrowing of the beam pattern with increased frequency.

| Frequency GHZ | Azimuthal Order & Hybrid Mode | | | | | | | Total |
|---|---|---|---|---|---|---|---|---|
| | 0 | | 1 | | 2 | 3 | 4 | |
| | $H_{01}$ | $E_{02}$ | $HE_{11}$ | $EH_{12}$ | $HE_{21}$ | $HE_{31}$ | $HE_{41}$ | |
| 465 | 0.9985 | 0.7885 | 0.9999 | | 0.9928 | | | 5.7724 |
| 475 | 0.9997 | 0.9926 | 0.9999 | | 0.9879 | | | 5.9679 |
| 485 | 0.9991 | 0.9974 | 0.9998 | | 0.9995 | | | 5.9951 |
| 495 | 0.9996 | 0.9995 | 1.0000 | | 0.9987 | | | 5.9965 |
| 505 | 1.0000 | 0.9998 | 0.9994 | | 1.0000 | 0.0000 | | 5.9986 |
| 515 | 0.9998 | 0.9997 | 0.9999 | | 1.0000 | 0.0000 | | 5.9993 |
| 525 | 0.9998 | 0.9997 | 1.0000 | | 1.0000 | 0.0001 | | 5.9997 |
| 535 | 1.0000 | 0.9720 | 1.0000 | | 0.9999 | 0.9798 | | 7.9314 |
| 545 | 0.9998 | 0.9435 | 0.9984 | | 1.0000 | 0.9991 | | 7.9383 |
| 555 | 1.0000 | 0.9416 | 0.9992 | 0.0002 | 0.9998 | 0.9975 | | 7.935 |
| 565 | 0.9998 | 0.9986 | 1.0000 | 0.9995 | 0.9985 | 0.9773 | | 9.949 |
| 575 | 0.9999 | 0.9843 | 1.0000 | 0.9989 | 0.9985 | 0.9758 | | 9.9306 |
| 585 | 1.0000 | 1.0000 | 1.0000 | 0.9975 | 0.9975 | 0.9786 | | 9.9472 |
| 595 | 1.0000 | 1.0000 | 1.0000 | 0.9994 | 0.9959 | 0.9736 | | 9.9378 |
| 605 | 1.0000 | 1.0000 | 1.0000 | 0.9929 | 1.0000 | 0.9750 | 0.0136 | 9.963 |
| 615 | 0.9999 | 0.9998 | 0.9998 | 0.9955 | 0.9989 | 0.9990 | 0.0007 | 9.9875 |
| 625 | 1.0000 | 0.9999 | 1.0000 | 0.9992 | 0.9916 | 0.9795 | 0.0075 | 9.9555 |

**Table 3-2:The number of modes of each azimuthal order propagating at frequencies across the band.**
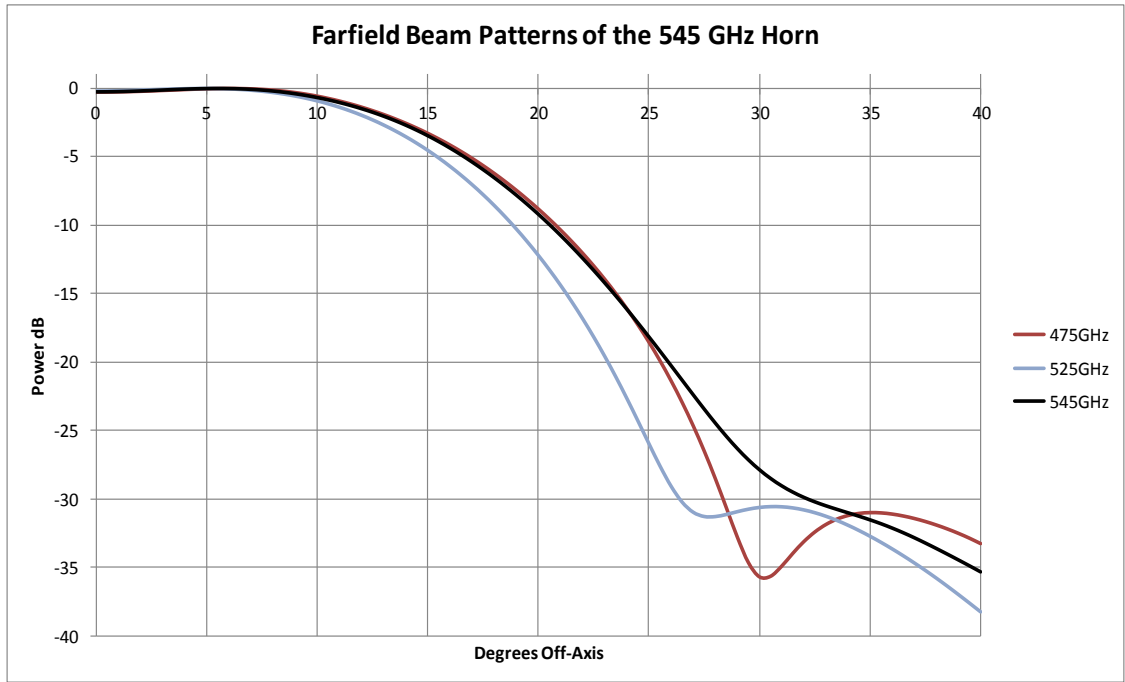
**Figure 3-31 : Plots of the simulated farfield beam patterns of the 545 GHz horn antenna at 475 GHz 525GHz and 545 GHz**



**Figure 3-32 : Plots of the simulated farfield beam patterns of the 545 GHz horn antenna in the lower part of the operational band, 465-495 GHz.**

**Figure 3-33 : Plots of the simulated farfield beam patterns of the 545 GHz horn antenna in the lower to middle part of the operational band, 505-545 GHz.**
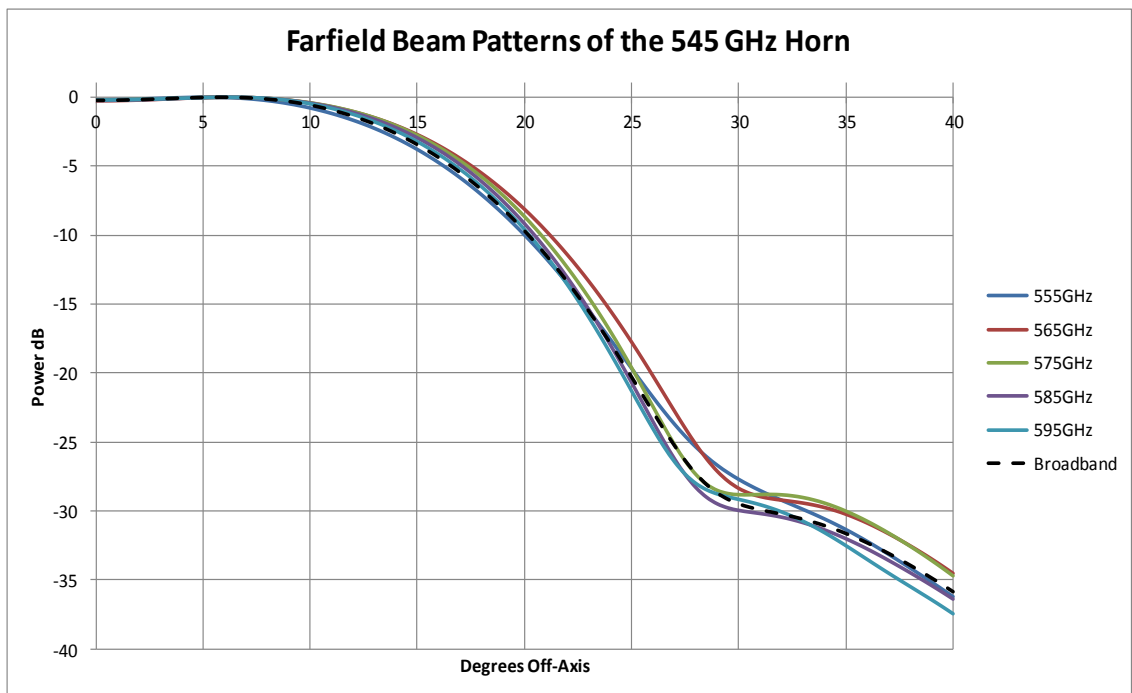


**Figure 3-34 :Plots of the simulated farfield beam patterns of the 545 GHz horn antenna in the middle to upper part of the operational band, 555-595 GHz.**

During the pre-flight testing phase test measurements of the beam pattern of the 545 GHz back-to-back qualification horn were made at 435 GHz by Cardiff University. 435 GHz is below the operational band of the 545 GHz channel and the horn is single moded at this frequency (i.e. only the $HE_{11}$ hybrid mode is propagating). The beam pattern measured in these tests is presented in Figure 3-36 along with the farfield beam pattern predicted by SCATTER. As can be seen there is good agreement between the test measurement and the SCATTER simulation over the main beam profile. The difference in the depth of the first null at 25 degrees off-axis can be explained by the sensitivity limits of the experimental setup and the minor differences in the first sidelobe fall within the experimental error.
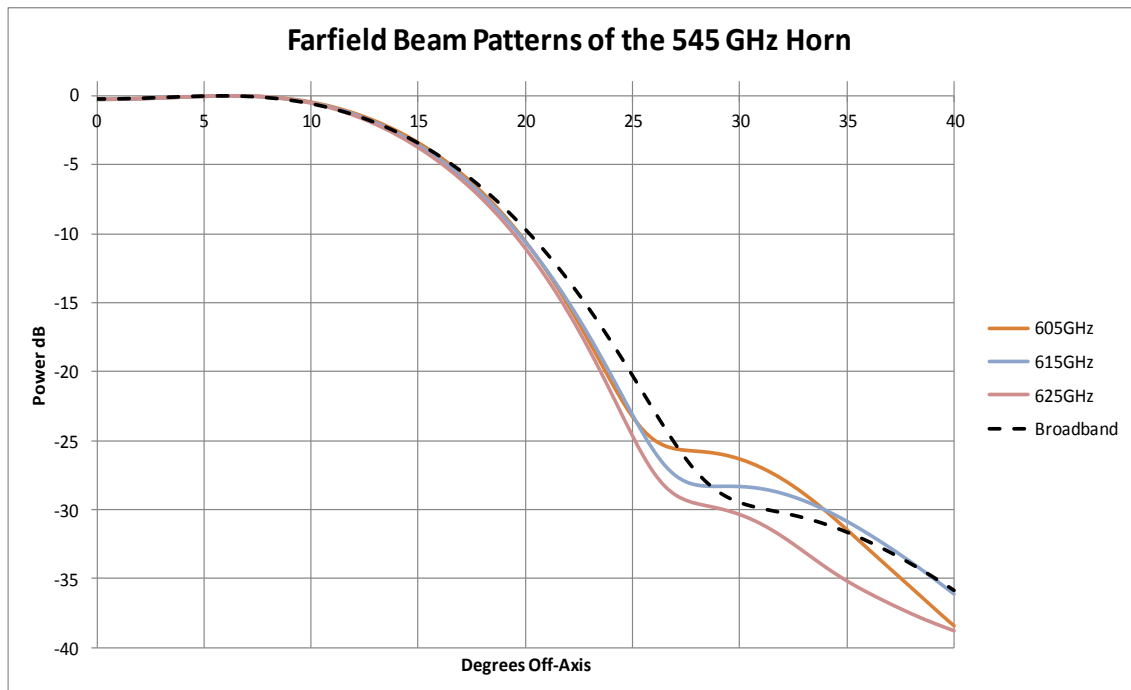


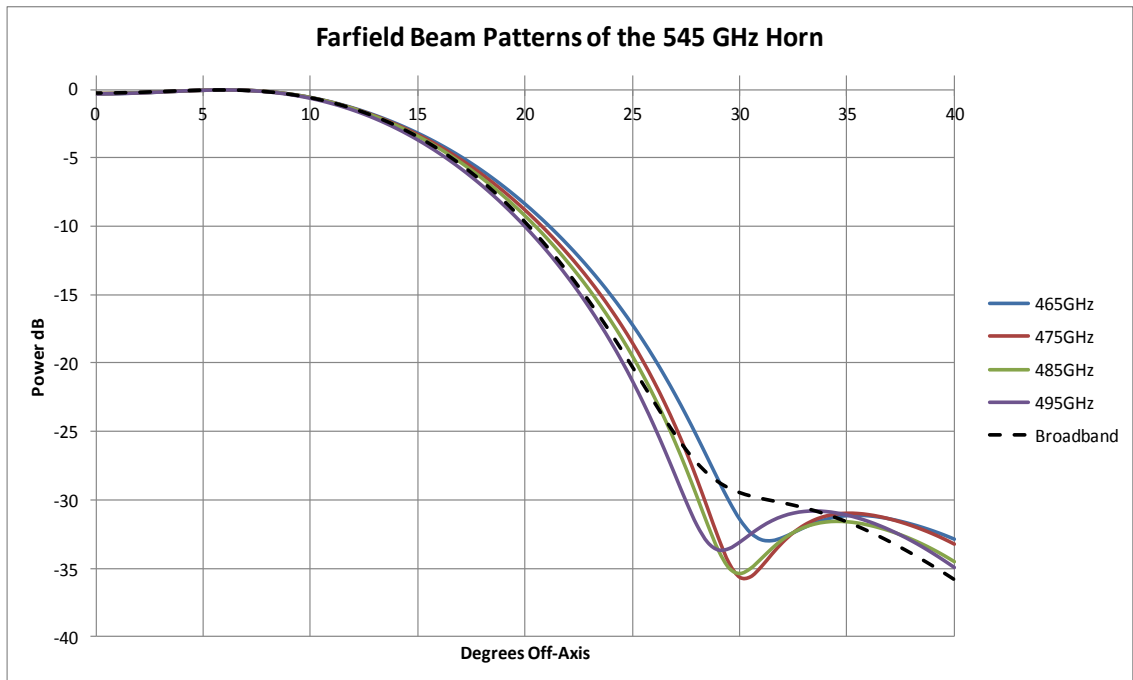**Figure 3-35 : Plots of the simulated farfield beam patterns of the 545 GHz horn antenna in the upper part of the operational band, 605-625 GHz.**
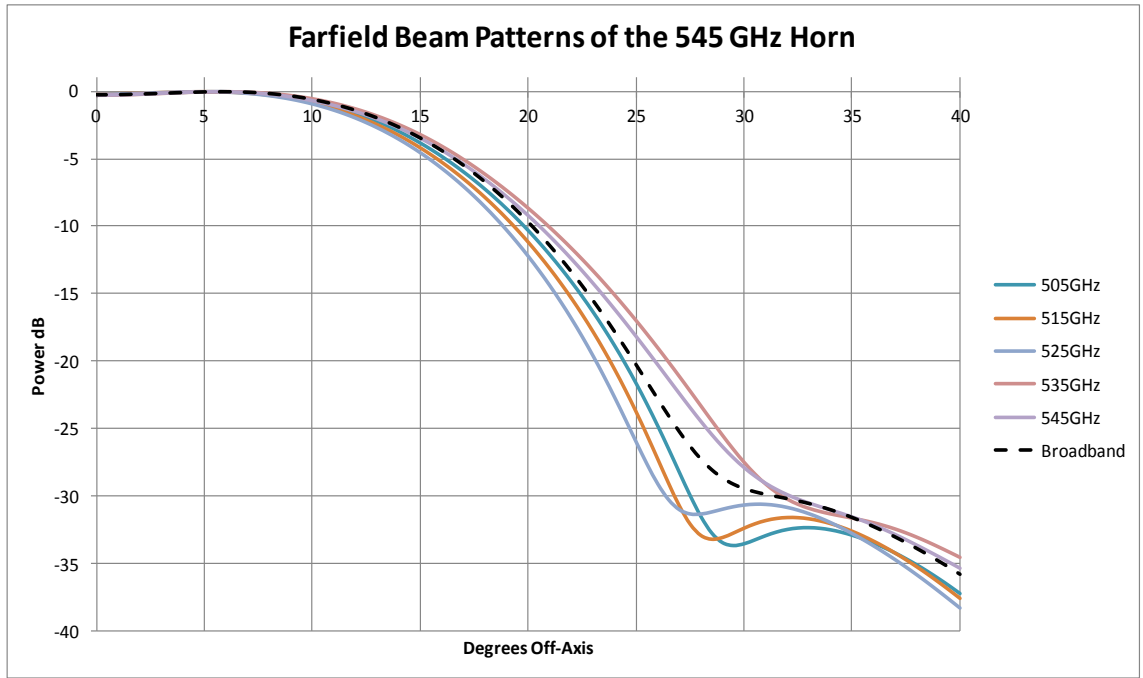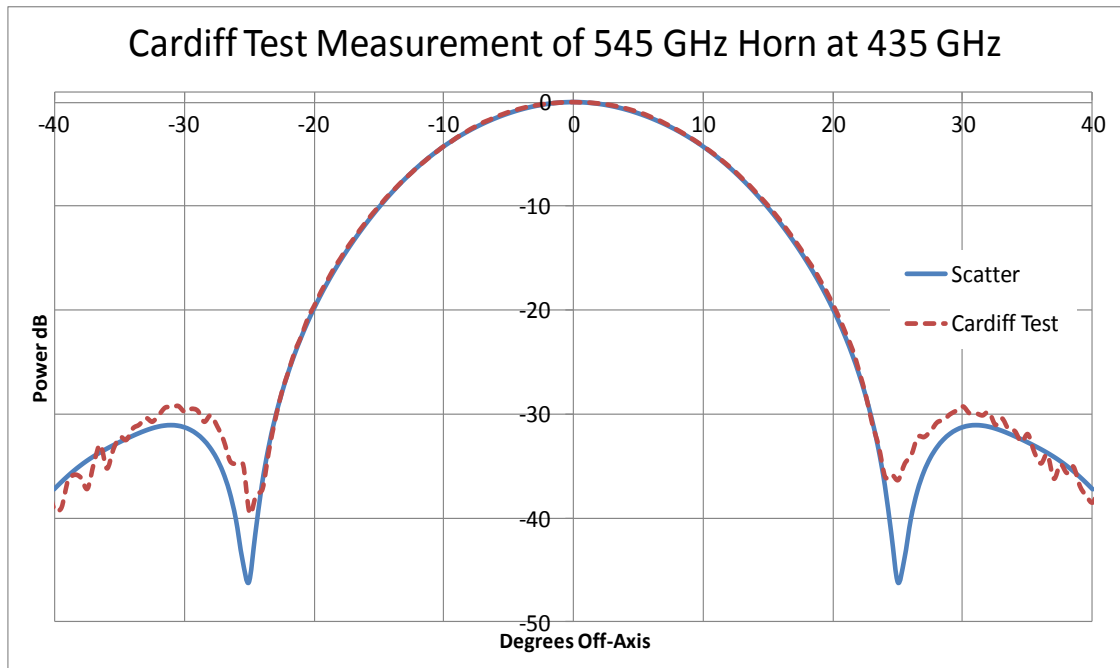
**Figure 3-36 : Plot of the beam pattern of the 545 GHz qualification horn measured at 435 GHz by Cardiff University along with the SCATTER simulation at the same frequency.**

# 3.6 Planck 353 GHz Channel

The twelve 353 GHz channels were the highest frequency single moded channels of the HFI. Like the other channels of the HFI, the 353 GHz channels consisted of a back-to-back horn pair and detector feed horn arrangement as described in Chapter 1. Eight of the 353 GHz channels fed polarised detectors, while the remaining 4 channels were unpolarised [Tauber, 2010a]. A series of simulations of the 353 GHz back-to-back horn were performed for use as inputs to a GRASP model of the Planck satellite optics. Shown in Figure 3-37 are the farfield beam patterns at a number of spot frequencies across the operational band of the 353 GHz channel. As the frequency is increased the width of the beam narrows as expected. However, unlike the multimode channels described in the previous sections, as the frequency increases there are no additional modes excited in the horn. Thus the beam width is not reset by additional modes as it narrows and is ever changing across the band.
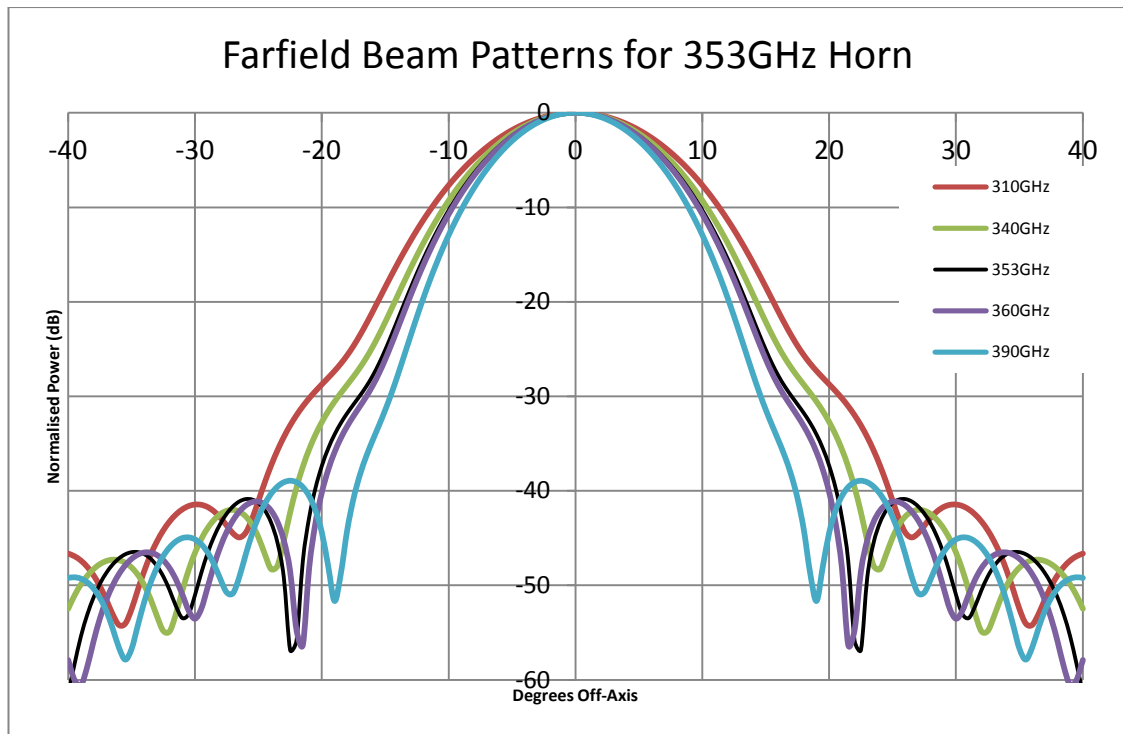
**Figure 3-37 : Farfield beam patterns of the 353 GHz back-to-back horn for several frequencies across the band. These beam patterns are simulations of the unpolarised 353 GHz channels as they include both the *x* and *y* polarisation and orthogonal components.**

# 3.7 Modelling the Detector in the Cavity

The mode matching techniques for modelling corrugated horn antennas presented so far in this chapter have assumed reciprocity, thus regarding the reception pattern of the antenna as identical to the transmission pattern. It was assumed that all modes are excited equally, as though by a black body in the cavity at the back of the horn antenna. However, the detector in the cavity might not absorb all hybrid modes equally so the assumption of black body cavity for the detector might not yield a complete prediction of the reception pattern. In the case of single-mode horns this assumption does not affect the beam pattern on the sky although it does affect efficiency calculations. However, for multi-mode horns the beam is sensitive to how accurately the cavity behaviour is captured by the simulations. The different hybrid modes may couple to the detector with different efficiencies for realistic absorbers.
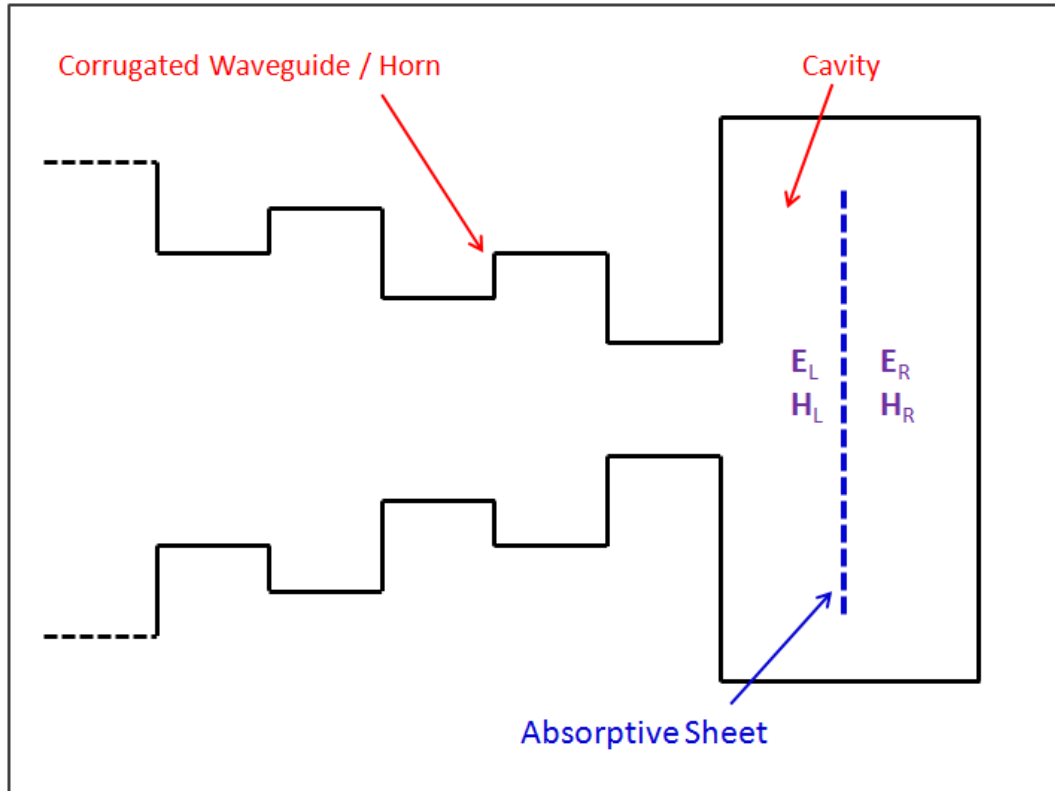
**Figure 3-38 :Diagram showing a cavity with an absorptive sheet attached to a corrugated waveguide / horn.**

The approach taken to model what the effects of the detector are on the beam pattern is to treat the whole pixel as an actual receiver so that the information about its behaviour can be recovered from the $[S_{11}]$ reflection matrix for the horn-cavity system when an absorbing device is included in the detector cavity. This is because any power not reflected back out from the horn must have been absorbed by the detector since it can be assumed that ideally there are no other losses in the system. The absorber (bolometric detector) can be modelled as a lossy current sheet (Figure 3-38) to provide a realistic approximation to a detector which can either fill or partially fill the waveguide/cavity diameter with a resistance that gives rise to ohmic losses causing the absorber temperature to change [Doherty, 2012][Bracken, 2015].

We can derive the usual relevant scattering matrices $[S_{11}]$, $[S_{12}]$, $[S_{21}]$, and $[S_{22}]$ for the absorber following the derivation in [Doherty, 2012] and [Bracken, 2015]. As before, see Section 2.3, the electric and magnetic fields on the left-hand side of the absorber (see Figure 3-38) are

$$\mathbf{E_L} = \sum_{n=1}^{N} \left\{ A_n \exp(-\gamma_n z) + B_n \exp(\gamma_n z) \right\} \mathbf{e_{nL}}$$

$$\mathbf{H_L} = \sum_{n=1}^{N} \left\{ A_n \exp(-\gamma_n z) - B_n \exp(\gamma_n z) \right\} \mathbf{h_{nL}} \qquad (3.3)$$

where $A_n$ and $B_n$ are the forward and reflected amplitudes coefficients of the $n^{th}$ mode on the left-hand side of the absorber. On the right-hand side of the absorber the electric and magnetic fields are

$$\mathbf{E_R} = \sum_{n=1}^{N} \left\{ C_n \exp(-\gamma_n z) + D_n \exp(\gamma_n z) \right\} \mathbf{e_{nR}}$$

$$\mathbf{H_R} = \sum_{n=1}^{N} \left\{ - C_n \exp(-\gamma_n z) + D_n \exp(\gamma_n z) \right\} \mathbf{h_{nR}} \qquad (3.4)$$

where $C_n$ and $D_n$ are the forward and reflected amplitudes coefficients of the $n^{th}$ mode on the right-hand side of the junction. For a lossy current sheet of radius $a$ representing the absorber, the boundary conditions from Maxwells equations applied to the right-hand side of the absorbing sheet (as indicated in Figure 3-38) for the electric and magnetic fields are determined by the sheet resistance $R_S$ (in ohms per square).

$$\mathbf{E}_L = \mathbf{E}_R \qquad for\ r < r_0$$

$$\mathbf{H}_L = \mathbf{H}_R - \mathbf{K} \times \hat{\mathbf{k}} \qquad for\ r \leq a$$

$$\mathbf{H}_L = \mathbf{H}_R \qquad for\ r > a$$

$$\mathbf{K} = \mathbf{E}_L / R_s = \mathbf{E}_R / R_s \qquad (3.5)$$

where $\mathbf{E}_L, \mathbf{E}_R, \mathbf{H}_L, \mathbf{H}_R$ refer to the corresponding fields on the input and output side of the detector, $\mathbf{K}$ is the current density, and $\hat{\mathbf{k}}$ is a unit vector in the forward $z$ direction. Thus, if an absorbing sheet partially fills the guide (and assuming $z = 0$ at the detector) then we can rewrite these equations as:

$$\sum_{n=1}^{N} \left\{ A_n + B_n \right\} \mathbf{e}_n = \sum_{n=1}^{N'} \left\{ D_n + C_n \right\} \mathbf{e}_n$$

$$\sum_{n=1}^{N} \left\{ A_n - B_n \right\} \mathbf{h}_n = \sum_{n=1}^{N'} \left\{ D_n - C_n \right\} \mathbf{h}_n - \left[ R_s(r) \right]^{-1} \sum_{n=1}^{N} \left\{ A_n + B_n \right\} \mathbf{e}_n \times \hat{\mathbf{k}} \qquad (3.6)$$

where $R_s(r) = 0$ outside absorber and $R_s(r) = R_s$ at the absorber and allowing different numbers of modes $N$ and $N'$ in the basic waveguide mode set on either side of the absorber. This implies

$$\sum_{n=1}^{N}\left\{A_n+B_n\right\}\mathbf{e}_n\times\mathbf{h}_m^* = \sum_{n=1}^{N'}\left\{D_n+C_n\right\}\mathbf{e}_n\times\mathbf{h}_m^*$$

$$\sum_{n=1}^{N}\left\{A_n-B_n\right\}\mathbf{e}_m^*\times\mathbf{h}_n = \sum_{n=1}^{N'}\left\{D_n-C_n\right\}\mathbf{e}_m^*\times\mathbf{h}_n - \left[R_s(r)\right]^{-1}\sum_{n=1}^{N}\left\{A_n+B_n\right\}\mathbf{e}_m^*\times(\mathbf{e}_n\times\hat{\mathbf{k}})$$

$$(3.7)$$

Now letting $N' = N$ for simplicity and matrix $[Q]$ be the usual diagonal matrix with elements $Q_{ii} = \int_S (\mathbf{e_i}\times\mathbf{h_i^*}).\hat{\mathbf{k}}\, dS$ then integrating over the area of the guide gives:

$$\left\{A_m+B_m\right\}Q_{mm} = \left\{D_m+C_m\right\}Q_{mm}$$

$$\left\{A_m-B_m\right\}Q_{mm}^* = \left\{D_m-C_m\right\}Q_{mm}^* - R_s^{-1}(r)\sum_{n=1}^{N}\Gamma_{mn}\left\{A_n+B_n\right\} \qquad (3.8)$$

where the matrix $\Gamma_{mn} = -\int_{S_{abr}}\mathbf{e_m^*}\times(\mathbf{e_n}\times\hat{\mathbf{k}}).\hat{\mathbf{k}}\, dS = \int_{S_{abr}}\left[\mathbf{e_m^*}.\mathbf{e_n}\right]dS$, and

$Q_{mm} = \int_{S_{abr}}\mathbf{e_m}\times\mathbf{h_m^*}.dS = 1/Z_m^*$ where $S_{abr}$ refers to the surface area of the absorber.

Thus in matrix form:

$$[A]+[B]=[D]+[C]$$

$$Q^*.([A]-[B]) = Q^*.([D]-[C]) + R^{-1}\,\Gamma([A]+[B]) \qquad (3.9)$$

We can solving for $[B]$ and $[D]$ in terms of $[A]$ and $[C]$ so that the $[S_{11}]$, $[S_{12}]$, $[S_{21}]$, and $[S_{22}]$ scattering matrices for the absorber are

$$[S_{11}] = [I+[P]]^{-1}.[P]$$

$$[S_{12}] = [I+[P]]^{-1}$$

$$[S_{21}] = 2[2-[P]]^{-1}[1-[P]] \qquad (3.10)$$

$$[S_{22}] = -[2-[P]]^{-1}[P]$$

where $[P] = [Q^*]^{-1}[\Gamma]/2R$ [Bracken, 2015] .

If we then calculate the scattering matrix for the cavity as a whole including the waveguide feeding the cavity, the overall $[S_{11}]$ matrix will contain information about the loss in the cavity. These expressions for the $[S_{11}]$ matrix describe the power lost, or reflected back out, due to different coupling of each hybrid mode to the detector. These coupling differences can be found by computing the singular values of $[S_{11}]^+[S_{11}]$ as these singular values show which modes are partially absorbed by the absorber/detector. Hybrid modes with singular values of unity were fully reflected

and were therefore not absorbed by the absorptive sheet (detector). Hybrid modes associated with non-zero singular values less than one were partially absorbed and therefore they contribute to the reception pattern of the horn. The reception pattern is synthesized by adding in quadrature the far field patterns of these hybrid modes which are absorbed or partially absorbed. By applying SVD analysis to the $[S_{11}]$ so that $[S_{11}] = [U][\Sigma][V^+]$ then

$$
\begin{aligned}
[S_{11}]^+[S_{11}] &= [V][\Sigma^+][\Sigma][V^+] \\
&= \sum_n \sigma_n^2 [V_n]^+[V_n]
\end{aligned}
\quad ,
\tag{3.11}
$$

where $[V_n]$ is the $n^{\text{th}}$ Schmidt field vector (i.e. hybrid mode). This corresponds to power reflected, and therefore the power absorbed by each $[V_n]$ is $\left(1 - \sigma_n^2\right)$ which implies the beam on the sky is given by

$$
P_{sky}(\theta,\phi) = \sum_{ni} \left(1 - \sigma_n^2\right)[v_{in}][e_i^{ff}(\theta,\phi)] \quad ,
\tag{3.12}
$$

where $e_i^{ff}$ is the farfield pattern of the waveguide mode $n$, and $[v_i]$ is the $i^{\text{th}}$ coefficient of the vector $[V_n]$; in other words $v_{in}$ are the row and column elements of the right singular matrix $[V]$ of the SVD expression [Wilson, 2014].

For a cylindrically symmetric system the $[\Gamma]$ matrix is given by terms very similar to the P matrices as discussed in Chapter 2 (Section 2.3). For TM modes coupling to TM modes when $l \neq l'$,

$$
\Gamma_{nl',l} = \sqrt{\frac{|Z_{TM_{nl'}}^a|}{J_{n+1}^2(p_{nl'})}} \sqrt{\frac{|Z_{TM_{nl}}^a|}{J_{n+1}^2(p_{nl})}} \frac{2R}{a} \frac{\left[ p_{nl'}J_n'\left(p_{nl}\frac{R}{a}\right)J_n\left(p_{nl'}\frac{R}{a}\right) - p_{nl}J_n'\left(p_{nl'}\frac{R}{a}\right)J_n\left(p_{nl}\frac{R}{b}\right)\right]}{\left[p_{nl'}^2 - p_{nl}^2\right]}
$$
.
$$
\tag{3.13}
$$

For TE modes coupling to TE modes when $l \neq l'$,

$$
\Gamma_{nl',l} = \sqrt{\frac{|Z_{TE_{nl'}}^a|}{\left(1 - \left(\frac{n}{q_{nl'}}\right)^2\right)J_n^2(q_{nl'})}} \sqrt{\frac{|Z_{TE_{nl}}^a|}{\left(1 - \left(\frac{n}{q_{nl}}\right)^2\right)J_n^2(q_{nl})}} \frac{2R}{a} \frac{\left[q_{nl'}J_n'\left(q_{nl}\frac{R}{a}\right)J_n\left(q_{nl'}\frac{b}{a}\right) - q_{nl}J_n'\left(q_{nl'}\frac{b}{a}\right)J_n\left(q_{nl}\frac{b}{b}\right)\right]}{[q_{nl'}^2 - q_{nl}^2]}
$$
,
$$
\tag{3.14}
$$

For TE modes coupling to TM modes when $l \neq l'$,

$$\Gamma_{nl',l} = \frac{2R}{a} \sqrt{\frac{|Z^a_{TM_{nl'}}|}{J^2_{n+1}(p_{nl'})}} \sqrt{\frac{|Z^a_{TE_{nl}}|}{\left(1 - \left(\frac{n}{q_{nl}}\right)^2\right) J^2_n(q_{nl})}} \frac{nJ_n\left(\frac{q_{nl}R}{a}\right) J_n\left(\frac{p_{nl'}R}{a}\right)}{q_{nl} p_{nl'}} \,, \qquad (3.15)$$

and for TM modes coupling to TE modes when $l \neq l'$,

$$\Gamma_{nl',l} = \frac{2R}{a} \sqrt{\frac{|Z^a_{TM_{nl}}|}{J^2_{n+1}(p_{nl})}} \sqrt{\frac{|Z^a_{TE_{nl'}}|}{\left(1 - \left(\frac{n}{q_{nl'}}\right)^2\right) J^2_n(q_{nl'})}} \frac{nJ_n\left(\frac{q_{nl'}R}{a}\right) J_n\left(\frac{p_{nl}R}{a}\right)}{q_{nl'} p_{nl}} \,. \qquad (3.16)$$

When $l = l'$ the elements of $[\Gamma]$ for TM modes coupling to TM modes are given by

$$\Gamma_{nl,l} = \frac{R^2}{2\,a^2} \frac{|Z^a_{TM_{nl}}|}{J^2_{n+1}(p_{nl})} \left( J^2_{n-1}\left(p_{nl}\frac{R}{a}\right) + J^2_{n+1}\left(p_{nl}\frac{R}{a}\right) - J_n\left(p_{nl}\frac{R}{a}\right) \left\{ J_{n-2}\left(p_{nl}\frac{R}{a}\right) + J_{n+2}\left(p_{nl}\frac{R}{a}\right) \right\} \right)$$
$$(3.17)$$

and for TE modes coupling to TE modes when $l = l'$,

$$\Gamma_{nl,l} = \frac{R^2}{2\,a^2} \frac{|Z^a_{TE_{nl'}}|}{\left(1 - \left(\frac{n}{q_{nl}}\right)^2\right) J^2_n(q_{nl})}$$
$$\left( J^2_{n-1}\left(q_{nl}\frac{R}{a}\right) + J^2_{n+1}\left(q_{nl}\frac{R}{a}\right) - J_n\left(q_{nl}\frac{R}{a}\right) \left\{ J_{n-2}\left(q_{nl}\frac{R}{a}\right) + J_{n+2}\left(q_{nl}\frac{R}{a}\right) \right\} \right).$$
$$(3.18)$$

These were implemented in the Mathematica version of SCATTER [Doherty, 2012][Bracken, 2015] and have been included here for completeness.

Returning to simulating the 857 GHz channel, up to this point the front horn of the back-to-back horn has been taken as representative of the full 857 GHz channel or pixel. In Section 3.2 the beam pattern at 857 GHz for the front horn plus the waveguide filter was compared to the full back-to-back horn pair and also to the full 857 GHz channel relay (back-to-back horn, detector feed horn, and integrating cavity, see Figure 3-39), but always assuming blackbody illumination of the input to the

system and treating each configuration as a radiator. A section of waveguide wider than the detector horn and the back horn was also included to represent where the band pass filters were housed although filters themselves were not modelled (as in Figure 3-39). The mode content, and hence the structure, of the three beam patterns were to a good approximation the same (see Figure 3-3). It was therefore assumed that by modelling the front section only the beam patterns obtained were a reasonable approximation to the full pixel beam patterns. This comparison of the front horn verses the full pixel will now be revisited, but this time including an absorber in the cavity and treating the full pixel as a true receiver rather than a radiator.



**Figure 3-39: Plot of the geometry file for the 857 GHz channel consisting of the back-to-back horn pair, detector feed horn, and integrating cavity (Note vertical axis not to scale with horizontal axis).**

In order to model the absorber in the cavity using the technique described above additional code had been added to the Mathematica version of the SCATTER software which when prompted by the geometry file about the presence of an absorber SCATTER would call a new function that would determine the scattering matrices for the absorber located at that plane. Additionally the rear wall of cavity was "sealed" by adding a short extremely narrow waveguide length (radius $\ll \lambda$) so that all modes are reflected at this point. Finally the whole geometry is reversed relative to previously so the aperture of the front horn is now the input plane of the geometry file, since by

120

examining how much of the incident power is not reflected and instead absorbed, it can be determine which hybrid modes have been absorbed by the absorber (detector) in the cavity (Figure 3-40). The short extremely narrow waveguide length used to "seal" the cavity can be seen in the close-up view of the cavity in Figure 3-41.



**Figure 3-40 : Plot of the geometry file for the 857 GHz channel consisting of the back-to-back horn pair, detector feed horn, and integrating cavity used to model the full pixel including a detector (absorber) in the cavity.**



**Figure 3-41: Zoomed in view of the narrow waveguide length, highlighted by the red circle, used to "seal" the back of the cavity.**
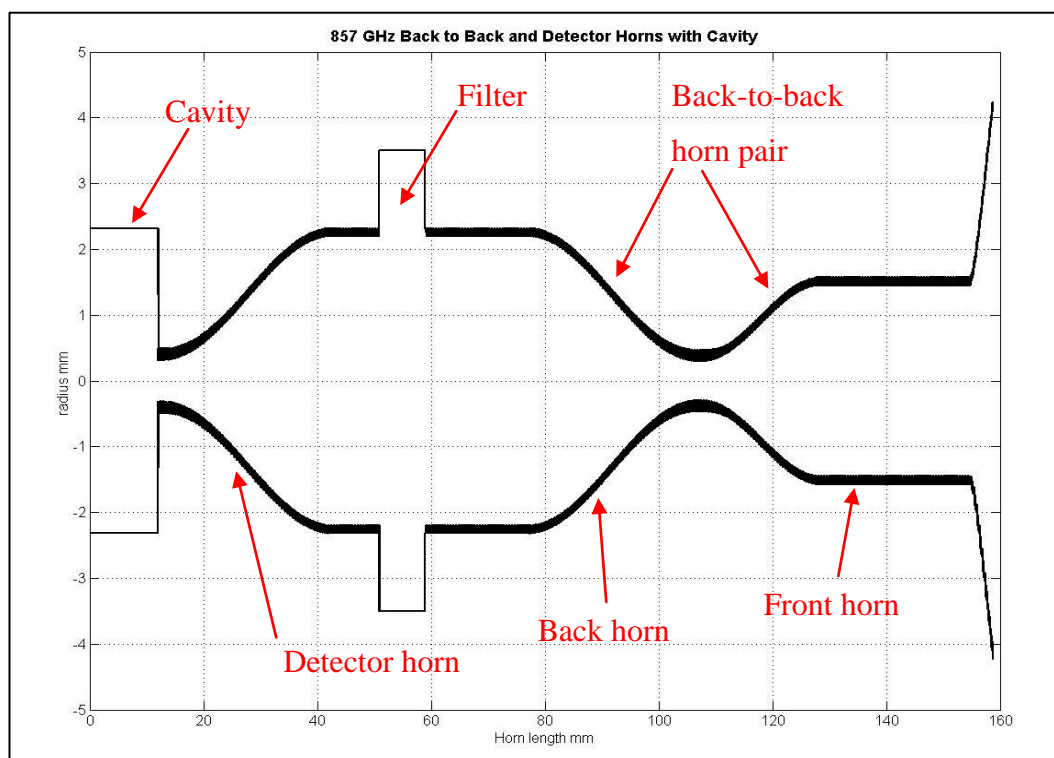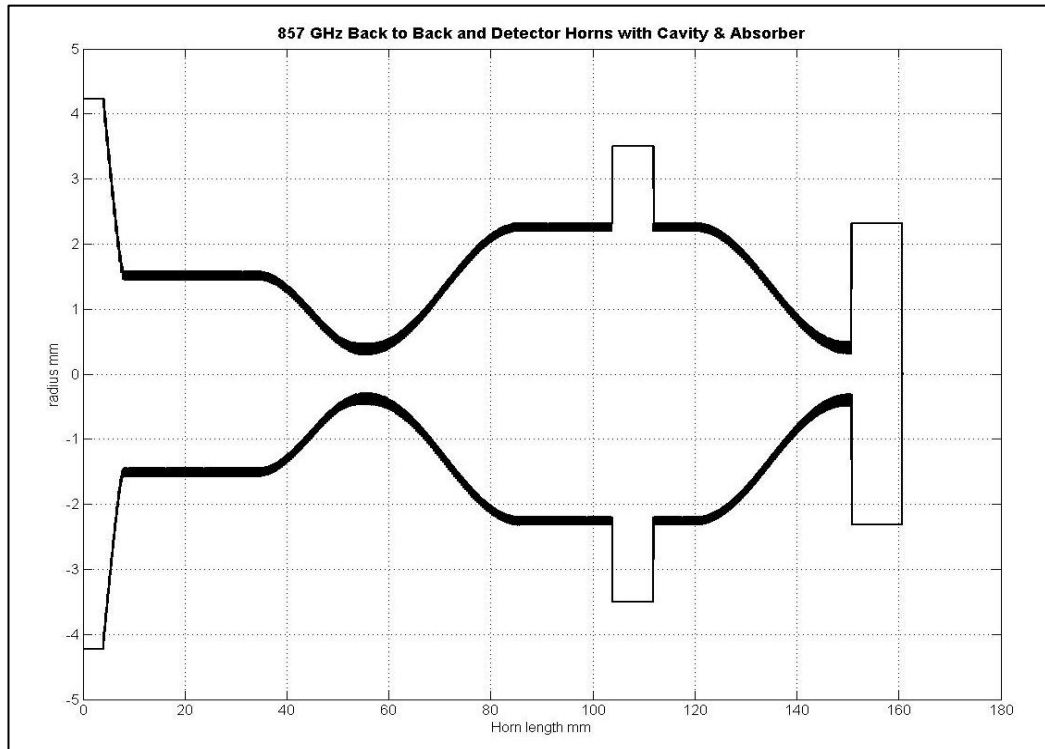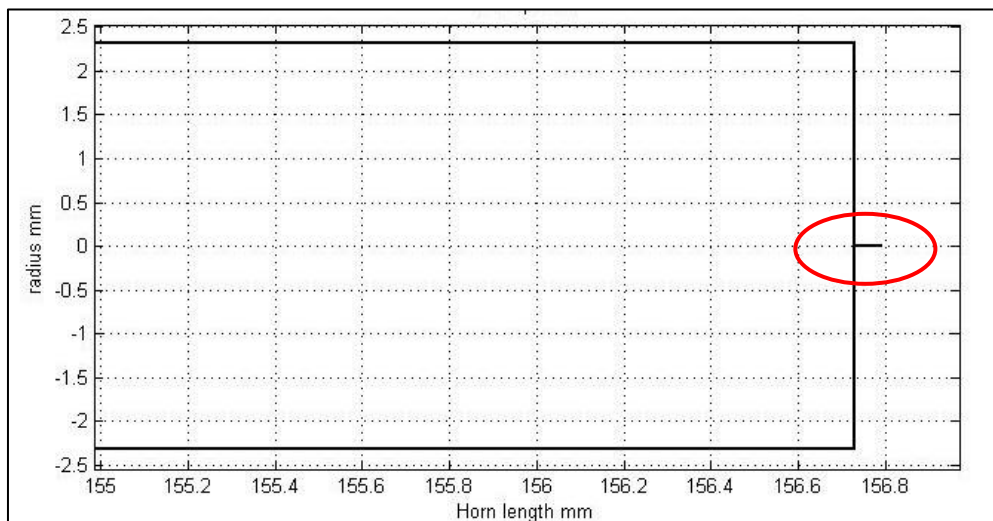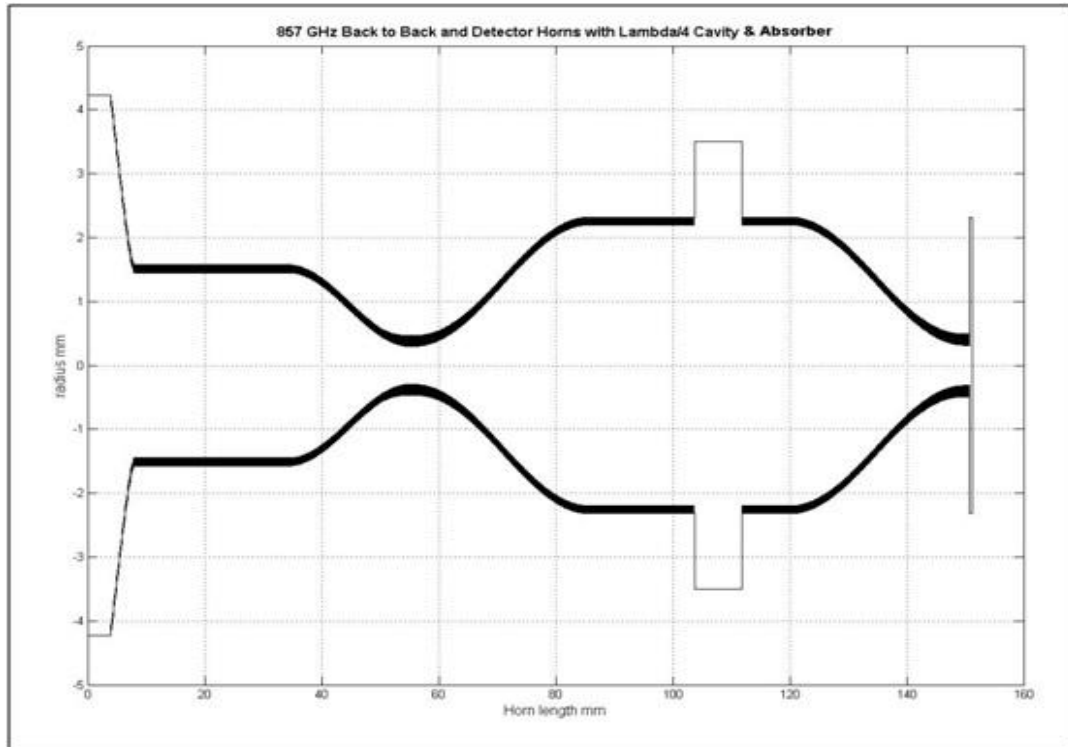
**Figure 3-42 : Plot of the geometry file for the 857 GHz channel consisting of the back-to-back horn pair, detector feed horn, and integrating cavity with a detector (absorber) in the cavity positioned λ/4 from the back wall of the cavity.**

Two cases for the size of the cavity were simulated: the first case assumes a large integrating cavity as shown in Figure 3-40, the second was for a resonant cavity with the absorber positioned a $\frac{\lambda}{4}$ in front of the back wall effectively forming a back short (see Figure 3-42). This second case is more representative of the real 857 GHz detector cavity which had a similar back short however, as the precise actual dimensions of the cavity are not known by the author and actual absorbing properties of the detector are only approximated by SCATTER, analysing both cases is interesting in terms of overall absorption of the incident radiation. The farfield beam patterns (normalised to 0 dB on-axis) resulting from these simulations are presented in Figure 3-43. In both cases with the absorber present the beam patterns although broadly similar do show some differences when compared to the simulation based on the front horn only. The beam patterns for the cases with the absorbing cavity are less top-hat like than that of the front horn alone although all three beam patterns have similar widths between -10 dB and -25 dB (approximately $16^o$ to $20^o$ off-axis) which are the important levels for edge taper definition (relative to 0 dB on-axis of course in both cases). Also while the levels of the first sidelobe in the cases with the absorbing

122

cavity are slightly lower than that for the front horn simulation only, the position of the sidelobes off-axis are the same for all three plots.
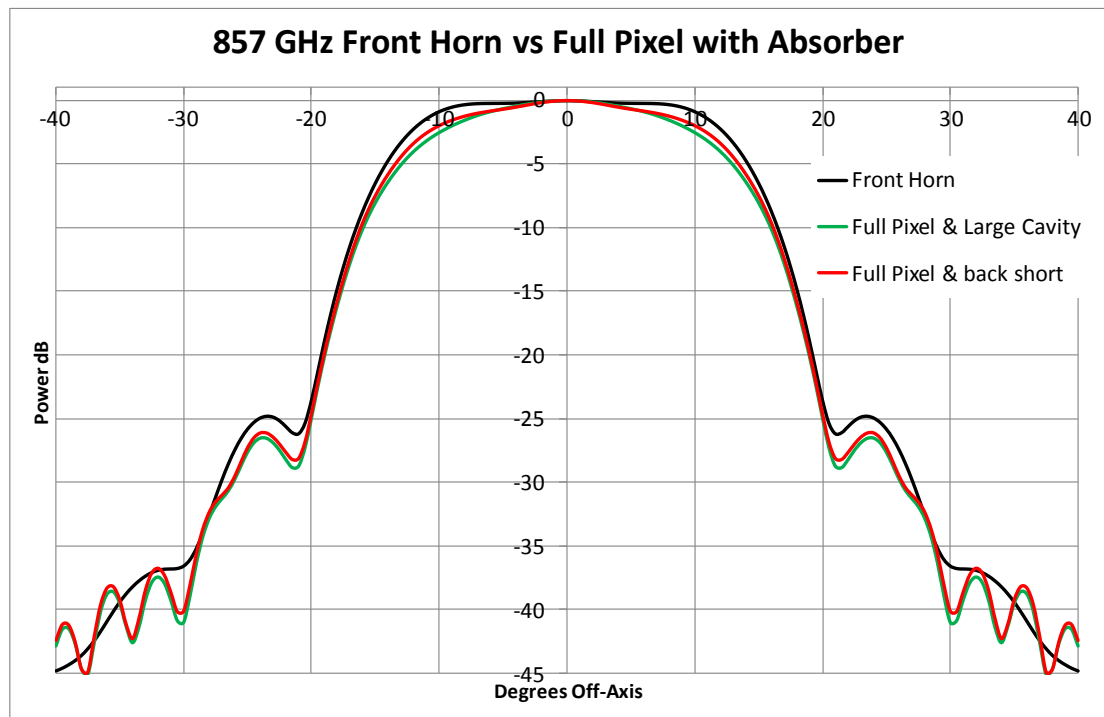


**Figure 3-43 : Plot of the SCATTER simulations of the farfield beam pattern normalised to 0 dB on-axis for the 857 GHz front horn and the full pixel with absorber.**

The plots in Figure 3-43 were normalised to 0 dB on-axis which is the usual approach taken when comparing beam widths. However, it is also interesting to plot the beams for the cases where the power in the individual modes is normalised to the same normal value (including degeneracy effects). As can be seen in Figure 3-44 the relative power levels of the three plots remain unchanged. Again this suggests that the mode content, and hence the structure, of the three beam patterns were broadly the same. Therefore the assumption that by modelling the front section only the beam patterns obtained are a reasonable approximation to the full pixel beam patterns is valid, particularly useful for the study of edge taper and spillover effects. Additionally we can also compare the case of the larger integrating absorbing cavity (non-resonant) with the earlier simulation of the same configuration without the absorber (as presented in section 3.2, Figure 3-3). In Figure 3-45 the two farfield beam patterns are presented and once again some minor differences can be seen (as expected) but the mode content and overall the structure of both beam patterns are broadly the same. Therefore the assumption that we obtain a reasonable model of the full system using just the front section only remains valid.

123
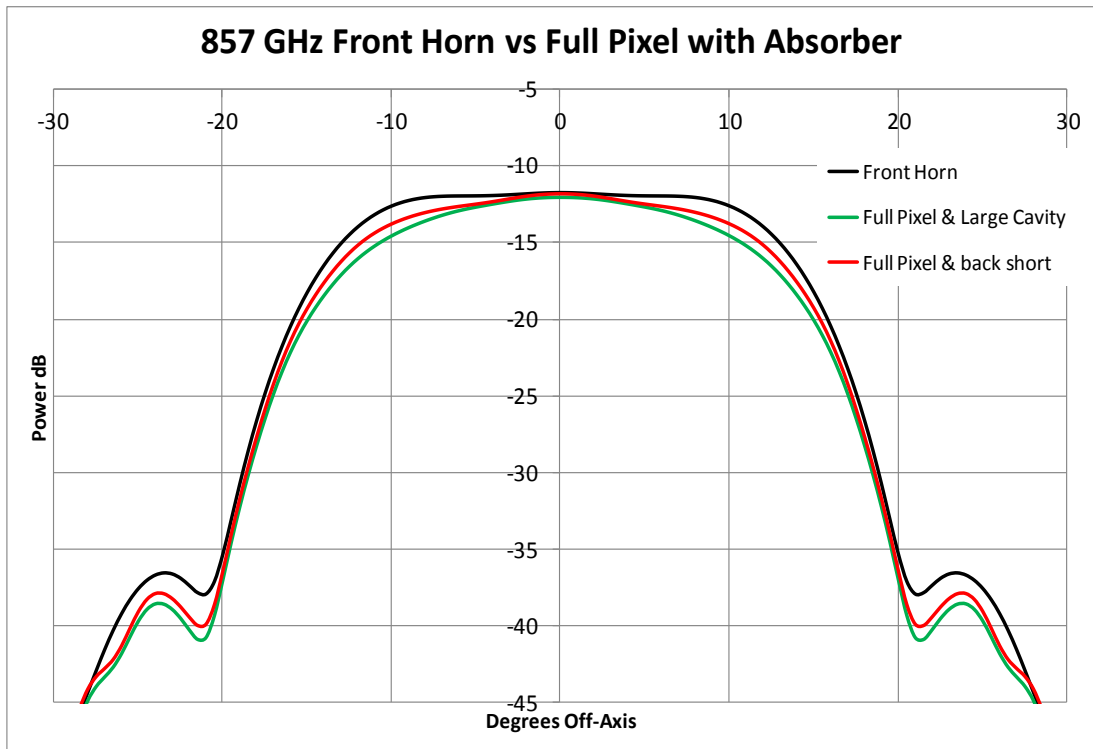
**Figure 3-44 : Plot of the SCATTER simulations of the farfield beam pattern (non-normalised) for the 857 GHz front horn and the full pixel with absorber.**
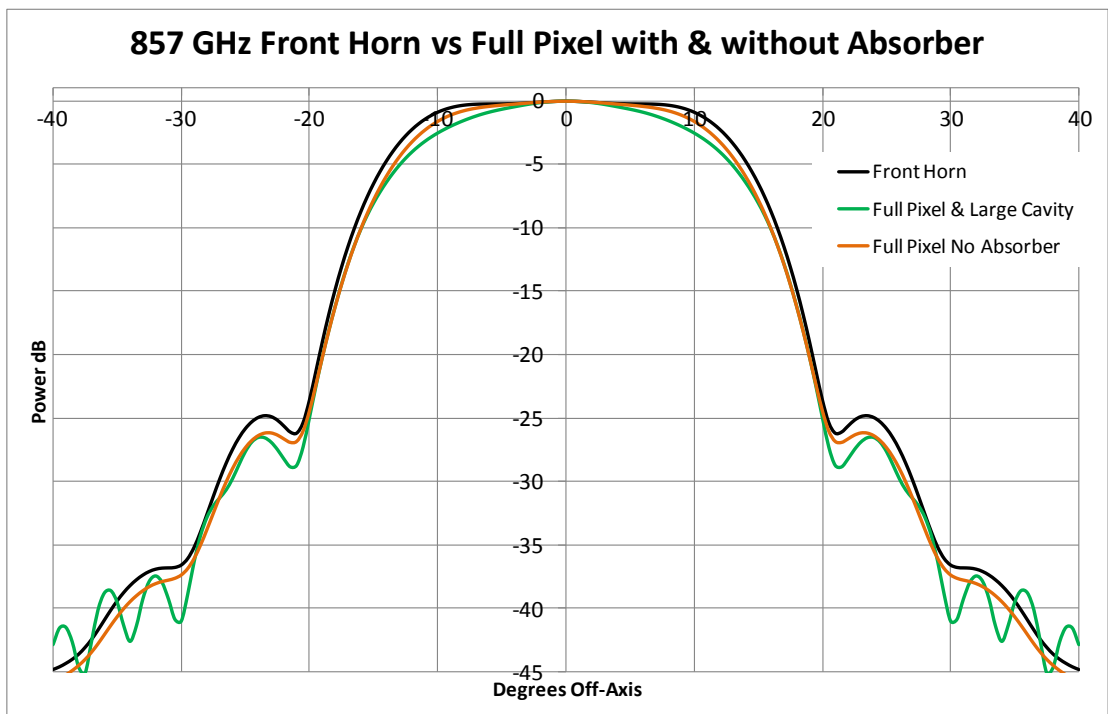


**Figure 3-45 : Plot of the SCATTER simulations of the farfield beam pattern normalised to 0 dB on-axis for the 857 GHz front horn, the full pixel with large (non-resonant) absorbing cavity and the full pixel without an absorber modelled as a radiator with a large (non-resonant) blackbody cavity.**

# 3.8 Conclusion

In this chapter, the challenge of deriving the broadband beams with fine frequency sampling accurate enough for the further analysis of the horns, such as the effects of small imperfections in the horn corrugations on the sidelobes of the beam patterns, was discussed in detail. The high accuracy of these simulations stretched the pre-existing modelling code and revealed numerical issues with the running of SCATTER which had to be addressed. Applying single value decomposition (SVD) to the scattering matrices at each junction and analysing the singular values provided an invaluable tool to probe these numerical issues.

The numerical issues encountered included the presence of evanescent modes at the waveguide filter input of the front horn which would not be present in reality at that part of the system but which in the simulations could scatter power into propagating modes causing errors in the overall scattering matrices of the waveguide / horn system. This issue was resolved by adding an extra phasing section at the start of the geometry to allow the evanescent modes to die off before being scattered at the input aperture of the horn. The next issue had to do with unphysical singular values of the $S_{21}$ matrix for the horn as a whole at certain spot frequencies when running simulations over the frequency range of the 857 GHz horn from 730 GHz to 990 GHz. This issue was traced to a numerical instability which occurred when the inversion of matrices within SCATTER became singular as modes cut-on. To prevent this occurring the SCATTER code was rewritten using pseudo-inverse of the matrices in place of the actual inverse matrix. The final issue with the running of SCATTER concerned the number of TE and TM modes required to obtain a complete description of the fields at the aperture. In previous versions of SCATTER only 12 TE and 12 TM waveguide modes were considered sufficient to describe this field. However for the multimoded horns of Planck it was found that a minimum of 30 TE and 30 TM were required for sufficiently stable computation across the band.

Once the numerical issues encountered while running SCATTER were resolved the modelling of the broadband beam patterns of the 857 GHz and 545 GHz multimode channels was undertaken. For both horns these were obtained by simulating the beam patterns of the horn antennas at numerous spot frequencies across

the operational bands of the horns. The beam patterns of both horns are remarkably stable over their operational frequency bands with the width of beam varying by only a degree or two over their respective band (effectively due to conservation of throughput as modes cut on as the frequency increases). In this regard the variation in the hybrid mode content of the 857 GHz and 545 GHz multimode channels over their respective frequency ranges was investigated in detail. For both horns the number of modes propagating increases as the cut-on frequencies of higher order modes are passed. These additional modes counteract the narrowing of the beam patterns with increasing frequency due to diffraction resulting in the beam width widening once more to its original width at the start of the frequency band. It is this property of mutimoded horn antennas that leads to the observed approximately constant of beam widths in both the 857 GHz and 545 GHz channels of Planck across the band. This also implies, of course, the broadband beam pattern will not be affected by the spectrum of the source, as would be the case for a single mode horn. In fact the results of the simulations of beam patterns of the 353 GHz single moded horn show how the beam pattern narrows as expected with increasing frequency. Furthermore we have shown that the beam patterns predicted by SCATTER for the 545 GHz back-to-back horn are in good agreement with the test measurements made by Cardiff University at 435 GHz where the horn is single moded.

Lastly in this chapter it was described how the SCATTER code was modified to include an absorber in the detector integrating cavity to represent the bolometric detector of the real 857 GHz horn antenna chain. As expected some minor differences were seen in the farfield beam patterns of the full Planck pixel with the absorber compared to the result for just the front horn of the back-to-back horn pair. Nevertheless the mode content and overall the structure of both beam patterns are broadly the same so that it is valid to model the front section only including the waveguide filter and the beam patterns obtained are a reasonable approximation to those of the full pixel beam patterns.

Having upgraded SCATTER next attention was turned to the effects of manufacturing tolerances on the operations of the horn antennas and these will described in Chapter 4.

# Chapter 4 The Effects of Manufacturing Tolerances on the Planck Multi-Mode Horn Antennas

## 4.1 Introduction

In the all-sky surveys by the Planck telescope a far sidelobe (FSL) signature was detected at 857 GHz at a very low, although higher than expected, level in some (but not all) of the channels [Planck Collaboration, 2014b]. The difference map between sequential all-sky surveys, shown in Figure 4-1, reveals the effects of these far sidelobe levels in the 857 GHz Channels [Planck Collaboration, 2014d]. In addition to the Zodiacal emission and residual Galactic emission a streaking effect caused by the higher far-out spillover sidelobe levels can be seen, which actually corresponds to this sidelobe detecting sources along the galactic plane when the main beam is pointed in a different direction. This sidelobe corresponds to spillover past the primary mirror of the horn beam reflected by the secondary. The difference maps between sequential surveys show such features because in one of these of surveys the galactic centre region is detected by the sidelobe whereas the other survey the less intense outer galaxy is coupled to the sidelobe, resulting in the so called "banana" feature appearing in the difference maps. The higher frequency channels show this effect more strongly because of their high sensitivity. The effect can clearly be seen in 857 GHz channels 1 and 3, Figure 4-1 top and bottom, while channel 2 any effects of the sidelobe level is less prominent, Figure 4-1 middle. It should be noted that due to the bolometer in 857 GHz channel 4 suffering from "random telegraphic noise", [Planck Collaboration, 2014a], difference maps were only available for only channels 1, 2 and 3.
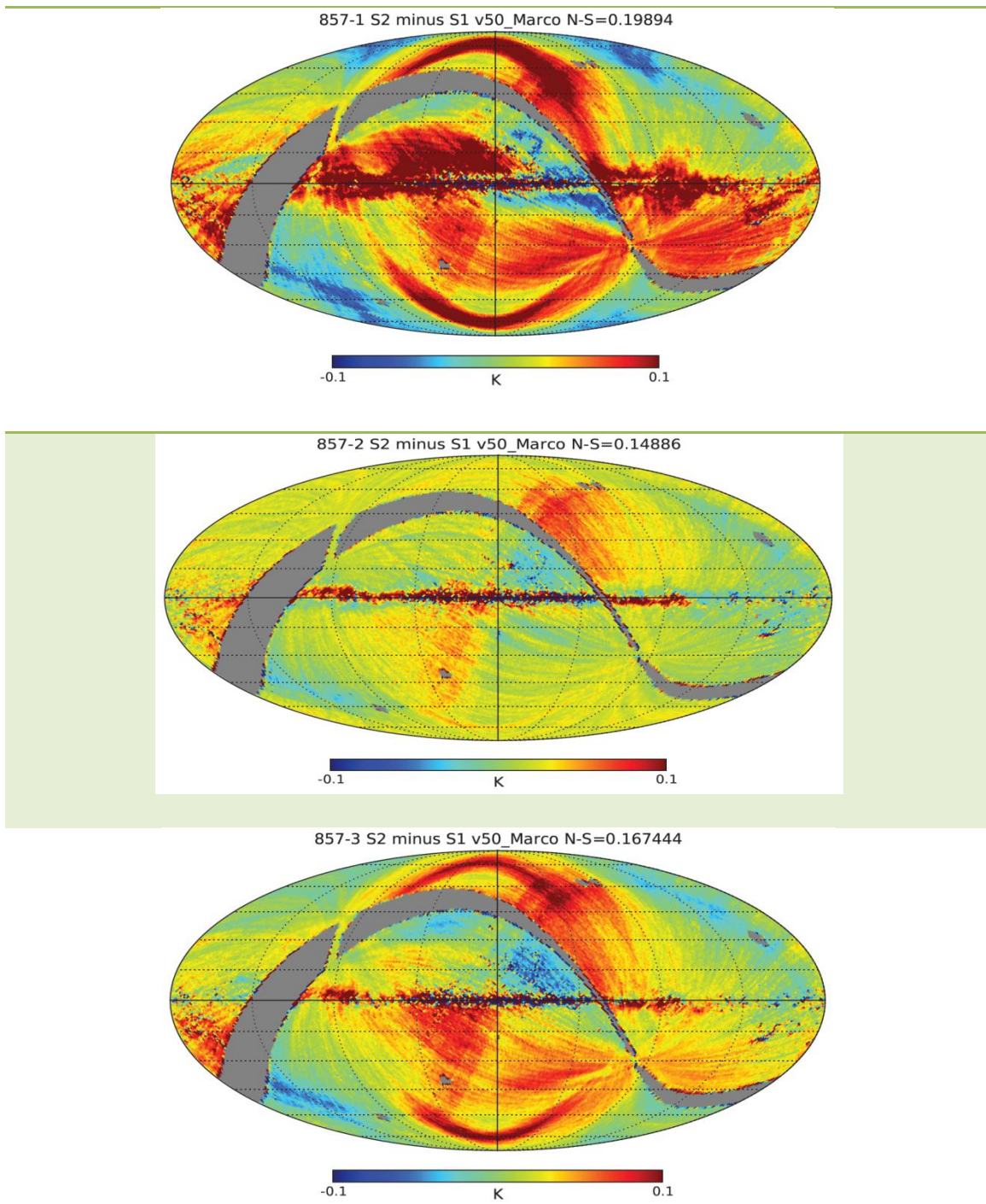
**Figure 4-1 :  Difference map for three of the 857 GHz channels obtained by subtracting all-sky Survey 1 from Survey 2. Top: 857-1 channel. Middle 857-2 channel. Bottom 857-3 channel [e.g. Planck Collaboration, 2014d]. The equator marks the galactic plane.**

In terms of the corrugations for the higher frequency channels the specifications for the horn fabrication were quite demanding. Small variations in corrugation quality, while still within the mechanical tolerances, might give rise to significant variations in the level of sidelobe spillover although without affecting the main beam [Planck Collaboration, 2014b].  However not all the 857 GHz channels

show the effect and one possibility is this effect is enhanced by imperfections introduced during the manufacturing process particularly in terms of the corrugations. In order to investigate these manufacturing imperfections and particularly their effects on the beam pattern and the far-out sidelobe levels a study was undertaken to quantify the possible effects of various types of imperfections that were noted in the horns delivered to the project after manufacture. Indeed certain imperfections were noted in the final flight horn antennas in visual inspections of the horns carried out by Cardiff University during pre-flight testing which had to do with the non-ideal condition of the corrugations in certain parts of the horn profile. To home in on what these imperfections might be and their effects on the beam patterns of the flight horn antennas on HFI it is useful to first consider the fabrication process itself.
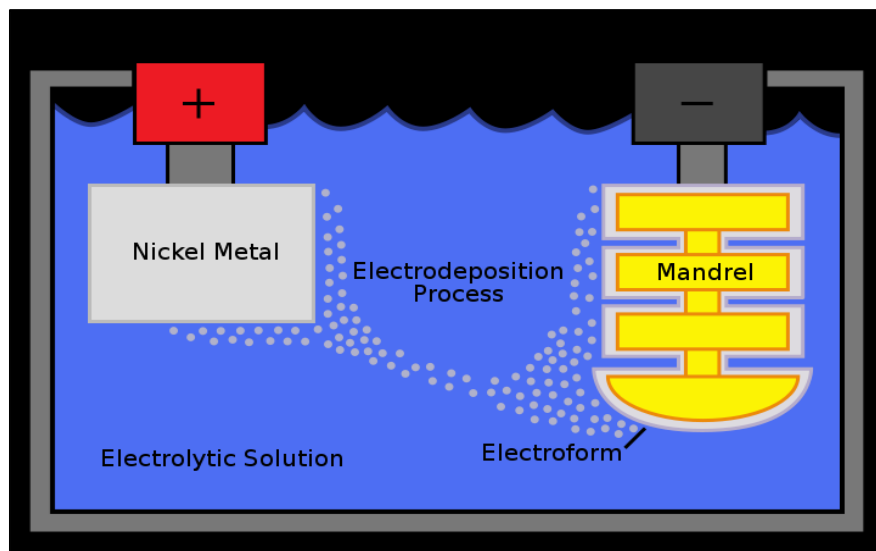


**Figure 4-2 : Schematic diagram showing how a corrugated structure, such as a horn, can be formed using electroplating.**

The manufacturing of horn antennas is a multistage process which begins with the production of a mandrel which is the negative of the horn design geometry milled into an aluminium form. Electroforming is then used to grow the actual horn by electrochemically depositing copper or nickel onto the mandrel surface in an electroplating bath until the desired wall thickness is achieved (Figure 4-2). The aluminium mandrel is then chemically etched away to leave only the actual copper horn antenna structure. This block of copper is then further machined to give the horn an external profile (shape) as required. A mandrel and a cross-section of a finished horn are shown in Figure 4-3, the horn cross-section is a negative of the mandrel and the corrugations are clearly visible in this image.

129

The mechanical milling process of the mandrel can be controlled to a desired precision on a high quality lathe. However, the electroplating and chemical etching processes could gives rise to minor deviations from the desired design. These variations could arise from a failure of the electroplating to deposit the metal forming the horn corrugations evenly and completely onto the mandrel. This could lead to missing or badly formed fins (possibly fragile fins that later break off) between the corrugations. The etching process could also fail to completely remove all the metal of the mandrel from the horn leaving corrugations that could be left partly or fully filled with aluminium.
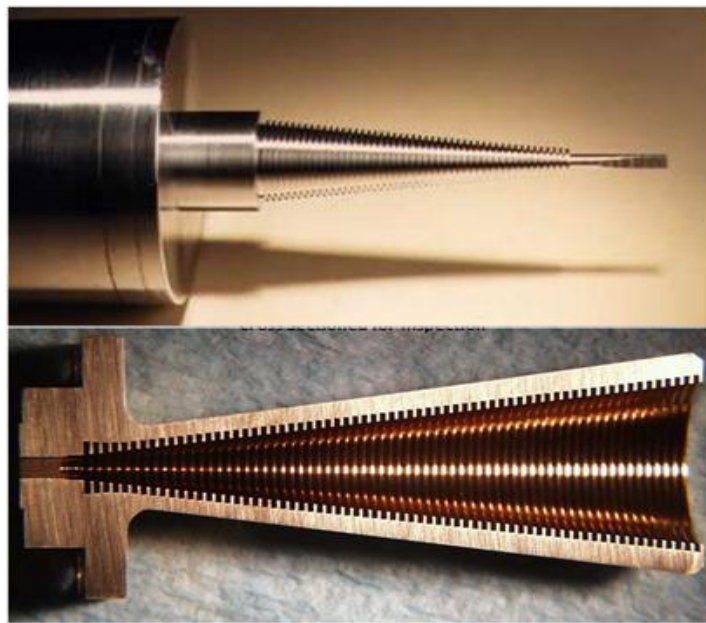


**Figure 4-3: Top image, a mandrel ready for electrochemical depositing. Bottom image, a cross-section of a horn antenna showing the internal structure.**
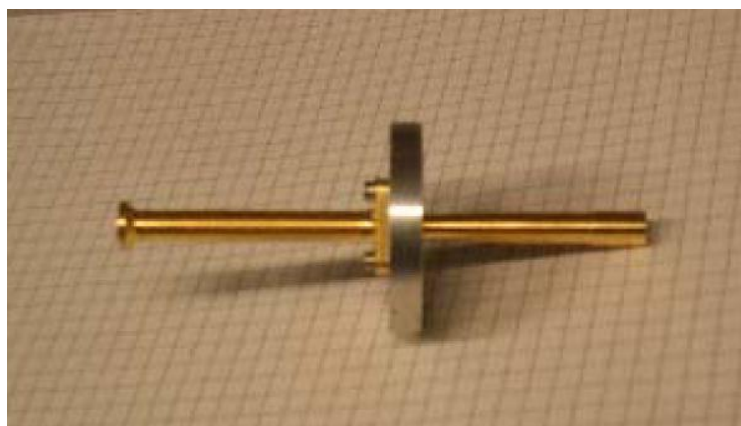


**Figure 4-4: Planck 857 GHz back-to-back horn during pre-flight testing. [credit: Cardiff University]**

It is well known that mode scattering to higher order modes occurs preferentially in the horn throat and any imperfections in this region in particular may affect the beam shape. However, due to their long and narrow shape and relatively small size compared to the other channels, as can be seen in Figure 4-4, visual inspection of the corrugations within the finished 857 GHz horns was difficult. The visual inspections carried out by Cardiff University when the flight horns were delivered, none-the-less revealed a number of imperfections. The visual inspection reports are presented in Appendix B for reference. The results of the visual inspections of the front horn of each of the back-to-back horn pairs are summarised in Table 4-1. Both damage to corrugations, and pieces of swarf and residual aluminium from the mandrel, were noted within the horns. Where possible, remedial action to remove these and improve the horn was carried out at the time (such as the removal of swarf and extra cleaning etc.). It is plausible however, that as noted earlier, the higher than predicted far-out sidelobe levels variations that became apparent in the all sky survey difference maps could be due to these imperfections remaining even after remedial action was carried out.

| Horn antenna | Non-dissolved Aluminium | State of corrugations |
|---|---|---|
| **PF857F-1A** | Yes | Last half corrugation irregular |
| **PF857F-1B** | Yes | Last corrugation asymmetric |
| **PF857F-1C** | Yes | Ok |
| **PF857F-1D** | Yes | Ok |
| **PF857F-1E** | Yes | Last half corrugation pushed in |
| **PF857F-1F** | Yes | Ring of swarf in last corrugation |

Table 4-1 : Some notes from the visual inspections of the front horn antennas of the 857GHz back-to-back horn pairs.

Although these issues clearly only became obvious sometime after launch, the qualification horn antenna (which was used for pre-flight qualification testing but was not flown in the mission) was available for testing. When it was manufactured its beam pattern was measured at 460 GHz where it is single moded and a coherent source was available. In fact the horn had to be etched further until the profile of the main beam matched the expected single mode beam pattern from simulations. The flight horn antennas were tested in a similar way but at 511 GHz. The limitation of these tests, of course, is that the 857 GHz horn antennas are single moded at both

460 GHz and 511 GHz. This means that only a single hybrid mode propagates through the waveguide filter, which is of course the fundamental $HE_{11}$ hybrid mode at these frequencies. Any variation in the horn that does not affect the beam pattern of this mode would not be detected by this test. Also the frequency being lower means that the radiation is less sensitive to imperfections. Furthermore if a cylindrically symmetric imperfection only affected the beam pattern of a mode, of any azimuthal order other than that of the $HE_{11}$ mode, it could only be detected by making measurements at a frequency at which that mode propagates.
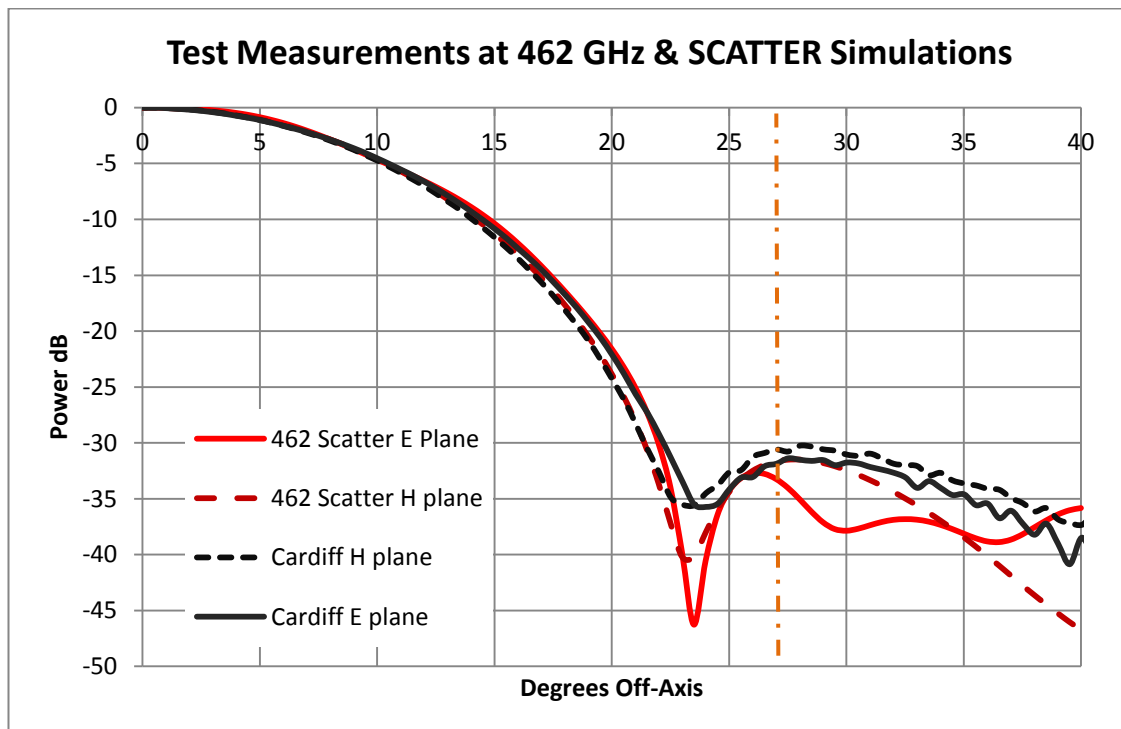


**Figure 4-5 : Test measurements of the prototype 857 GHz Horn at 462 GHz shows agreement with SCATTER simulations for both the E and H planes. The dashed orange line indicates the approximate position (27° off-axis [Maffei, 2010b]) of the edge taper of the primary mirror as viewed by the 857 GHz horns.**

Tests at frequencies at the high end of the band, where the maximum number of modes propagate, could not be carried out as the ready availability of sources and test facilities at such high frequencies were not available to the project in Cardiff where the measurements of the flight horns were made pre-launch. In fact these measurements of the beam patterns at 460 GHz of the prototype qualification 857 GHz horn are in agreement with the SCATTER simulations of the perfect horn profile at the same frequency (Figure 4-5). Also the set of measurements for the flight horns at 511 GHz is shown in Figure 4-8. All horns have acceptable single mode beam patterns which agree well with the SCATTER predictions down to -35 dB approximately and

to off-axis angles up to 40$^{\text{o}}$. These tests form the baseline against which to compare the simulations at higher frequencies of the horns with possible imperfections arising from manufacturing tolerances and weaknesses in the integrity of the corrugations. In other words, any such imperfections should not affect the single mode beam pattern at either 460 GHz or 511 GHz. We will return to discuss the pre-flight measurements of the flight horns further in section 4.5.

It is important to note that as well as considering the types of imperfections such as if the corrugations are filled with aluminium (not etched out), or partly filled (partially etched), or missing fins, it is also important to consider where these defects are located inside the horn as the consequences for the beam pattern of the horns varies markedly over the length of the horn. Examples of these possible types of defects are shown in Figure 4-6 and the different locations examined are discussed in the following sections of this chapter.
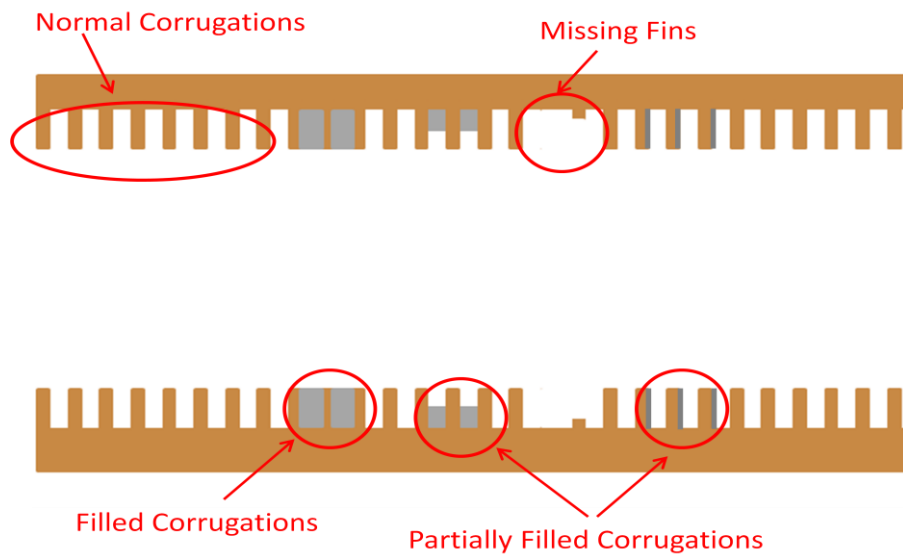


**Figure 4-6 : Shown here is a section of corrugated waveguide with examples of the types of imperfections which may occur during manufacturing such as corrugations filled or partially filled with aluminium and missing or poorly formed fins.**

The various locations in the front horn of the back-to-back horn pair in which possible imperfections were investigated are described in detail in the next section but first let us consider waveguide filter and back horn. Defects in the back section of the back-to-back horn were found to have no significant influence on the overall beam pattern, presumably because the narrow waveguide section in the middle of the back-to-back horn acts as a very effective mode filter. It would appear higher order modes, into which power is scattered by missing fins or filled corrugations, cannot propagate

133

(are evanescent) into this narrower waveguide and are thus reflected back and effectively filtered by this section. Examples of simulations shown in Figure 4-7 indeed have verified that this is the case. Thus it is only necessary to consider in greater detail the front horn in order to obtain the beam pattern of the overall horn and particularly the part of this beam pattern that spilled past the primary mirror and which ultimately can be expected to give rise to the sidelobe features seen in some of the difference maps, as marked in Figure 4-10.

For each possible type of defect in each of the areas of the horn shown in Figure 4-9 simulations were performed at the centre of the operational band (857 GHz) and at the single mode test frequencies (460 GHz and 511 GHz) at which the horns were tested for satisfactory operation. The test measurements qualification horn were made at 460 GHz by Cardiff University. Six flight horns sets (detector horn and back-to-back horn pair) were later manufactured and the best four were chosen for the HFI. The beam patterns of all six sets of flight horns were measured by Cardiff University to determine whether they were functioning as they were designed or not. The measurements for the four flight horns made at 511 GHz that were chosen to fly on Planck are shown in Figure 4-8 alongside the beam pattern predicted by SCATTER. As mentioned above at 511 GHz the 857 GHz Planck horns are single mode i.e. only the $HE_{11}$ mode can propagate in the horn. Thus by comparing simulations with possible imperfections at both single mode frequencies (460 GHz or 511 GHz) and multimode frequencies (857 GHz) allows for the possible effects of these imperfections at operational frequencies to be estimated while at the same time checking if these effects would have been seen in the single mode tests. It should be noted that initially only the measurement data for the tests on qualification horn were available to the author and thus the simulations of possible imperfect horns were made at 460 GHz. When the data of the measurements of the flight horns became available, some of these simulations were repeated at the flight horn test frequency of 511 GHz. It was decided not to repeat the simulations for all the possible imperfect horn cases at 511 GHz. If the beam pattern for the imperfect horn scenario was effected in such a way that it visibly diverged from the beam pattern of the ideal horn at 460 GHz the simulation was, in general, not repeated at 511 GHz.

For the horns at operational frequencies in particular we are interested in the variation in the beam pattern sidelobe structure beyond $27^{\circ}$ which misses the primary

mirror, [Maffei, 2010b], and acts as a far-out sidelobe for the telescope beams. Note that the secondary mirror is oversized relative to the primary as viewed from the 857 GHz horns. However part of the beam on one side between $27^o$ and $40^o$ off-axis is refected towards the primary but misses the primary and ends up on the sky at a large off-bore site angle. We will return to this later in the chapter. Effectively however we can regard the spillover region as starting at $27^o$ for the "average" 857 GHz horn (the precise angle depends on the location on the focal plane).
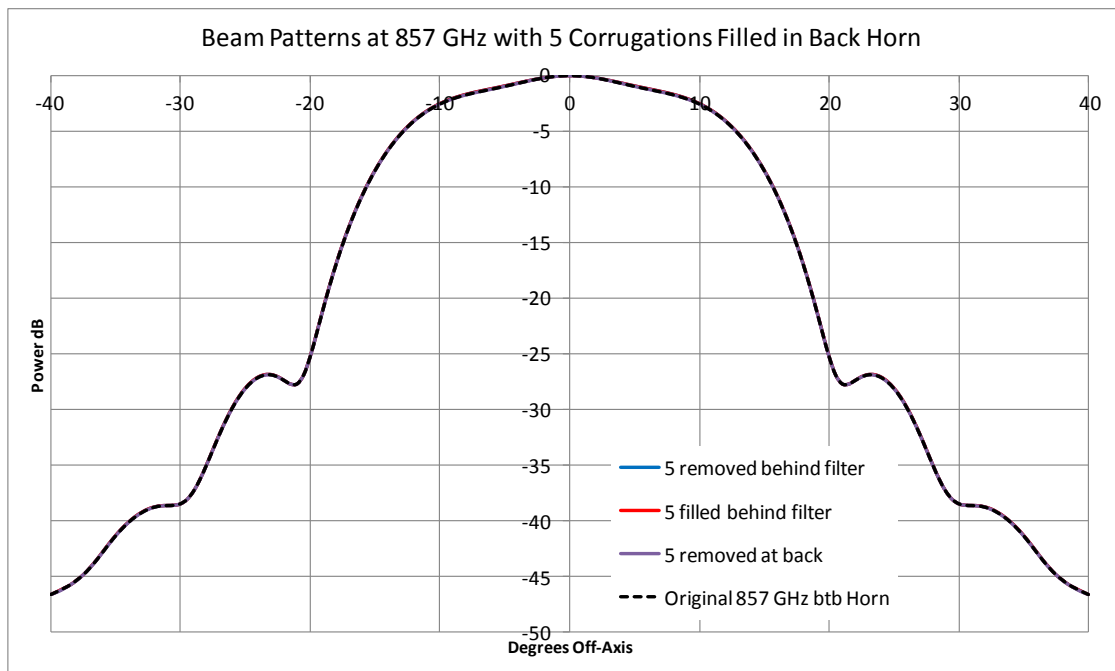


**Figure 4-7: Beam patterns for the back-to-back (btb) horn pair with corrugations altered in the back horn, i.e. behind the waveguide filter (note this is the original btb horn see section 3.3.2 ).**
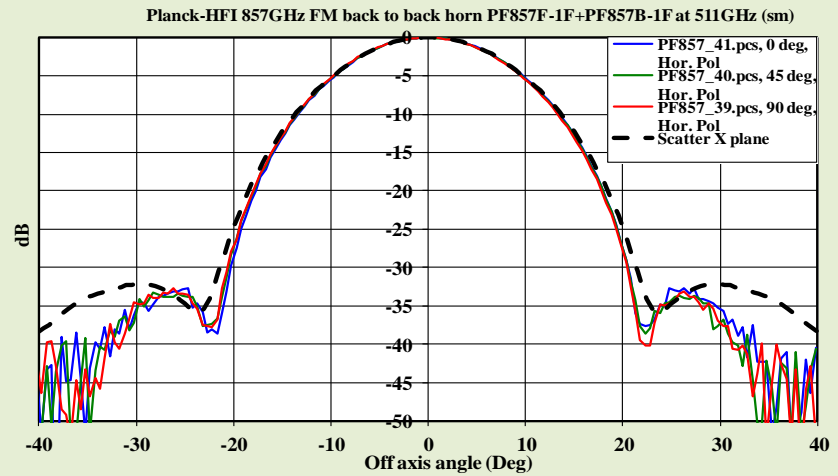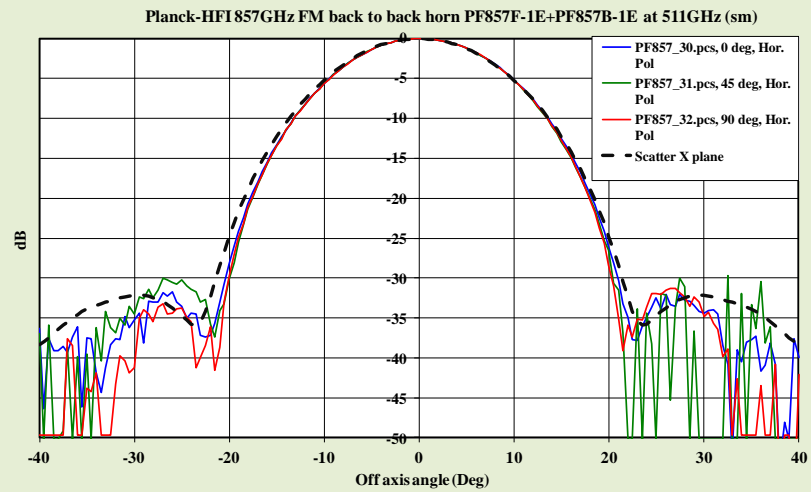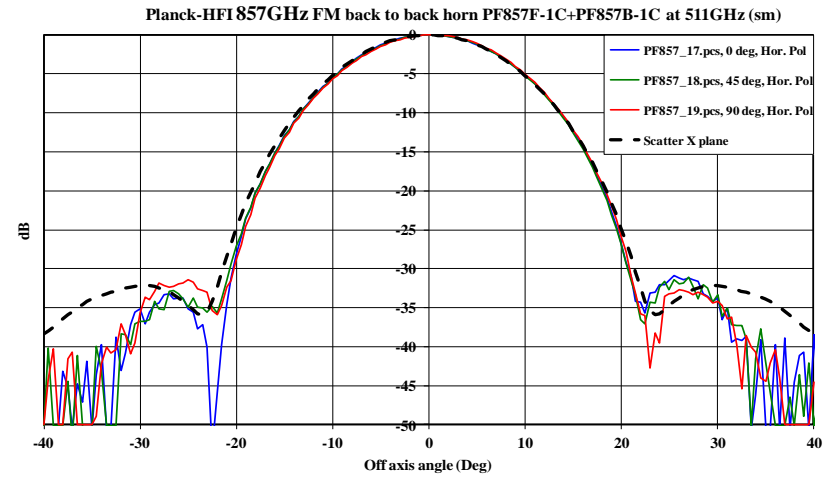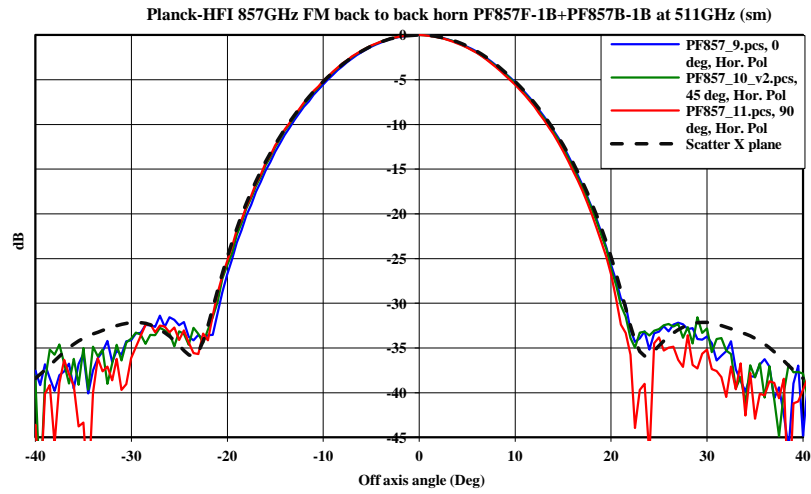
**Figure 4-8 : Pre-flight beam pattern measurements of each of the four flight horns at 511 GHz. The beam pattern predicted by SCATTER is shown by the dashed black line.**

# 4.2 The Effects of Filled Corrugations on the Planck horn

The first type of imperfection investigated was that of residual aluminium remaining inside the corrugations after the etching process. Two possible cases were considered, one where none of the aluminium of the mandrel was removed leaving the corrugation slot fully filled, and the second case where some of the aluminium was etched away leaving the corrugation partially filled with residual aluminium.
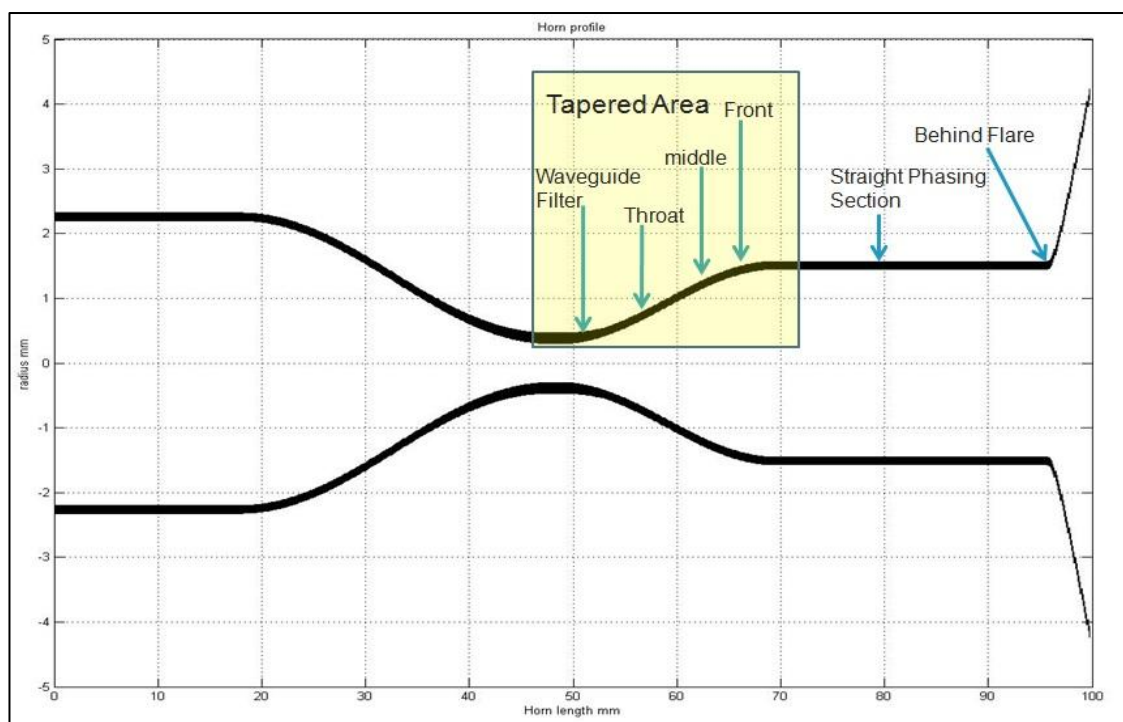


**Figure 4-9 : A diagram showing the 857 GHz back-to-back horn with the various sections of the horn labelled. (Note vertical axis not to scale with horizontal axis).**

As a first step the case where a section with a sequence of neighbouring corrugations was fully filled was simulated by altering the horn geometry file so as to remove the corrugation slots leaving just the inner waveguide. A section with a sequence of five fully filled corrugations was altered in each of the areas of interest chosen, shown in Figure 4-9, to form the test cases. It was assumed that any difficulty in the etching process would likely effect a section of several corrugations. Five corrugations represent a variation in approximately 0.5% of the total number of corrugations in the horn. The six areas of the horn where corrugations were altered, as

indicated in Figure 4-9, are as follows: just behind the flare at the aperture of the horn, in the straight phasing section, at the front of the tapered section, the middle of the tapered section, the throat area at back of the tapered section, and at the beginning of the waveguide filter connecting the front and back horn. Figure 4-10 and Figure 4-11 each show the simulated farfield beam patterns of three of these defect scenarios along with the pattern for the ideal horn for comparison at 857 GHz. In all cases a general increase in sidelobe levels at angles greater than $30^{o}$ off-axis is predicted (see Table 4-2). The sidelobe level rises from about -36 dB to above -30 dB. The only exception is for the case of filled corrugations within the waveguide filter section (Figure 4-11). Here as expected there is almost no variation from the perfect horn as the narrow radius of this section prevents power scattering into higher order modes.



**Beam patterns at 857GHz with 5 Corrugations Filled**

Legend:
- 857 GHz Ideal Horn
- 857 Behind Flare
- 857 Phasing Straight
- 857 Tapered Front

Y-axis: Power dB
X-axis: Degrees Off Axis
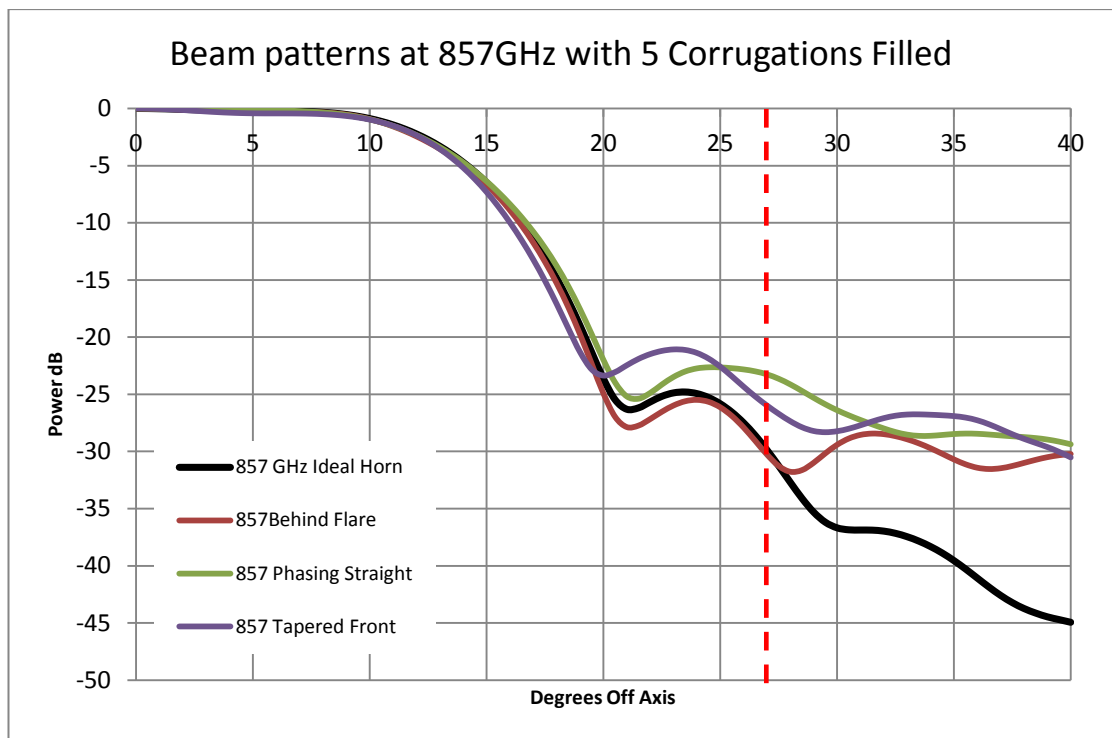
**Figure 4-10 : The simulated beam patterns of the 857 GHz Planck horn at 857 GHz with 5 corrugations filled for the three positions within the horn as indicated. The part of this beam pattern that spilled past the primary mirror and which was ultimately expected to give rise to the large sidelobe features seen in the difference maps is marked by the red dashed line ($27^{o}$ off-axis) .**

It should be noted that just one or two corrugations filled had less effect on the beam than five corrugations which again is not surprising as the corrugations have a pitch of only a fraction of the free space wavelength. Five corrugations on the other hand is of the order of the wavelength and so might be expected indeed to have some

consequences for the beams. We will return to look at the case of just a few corrugations affected later in this section.



**Figure 4-11 : The simulated beam patterns of the 857 GHz Planck horn at 857 GHz with 5 corrugations filled at the three locations within the horn indicated. Again the part of this beam pattern that spilled past the primary mirror is marked by the red dashed line (27° off-axis).**

Several of the test cases of possible non-perfect corrugation profiles show increased edge taper levels at 27° off-axis. Here the power level rises from -30 dB to values ranging from -21 dB to -26 dB. The simulations indicate that filled corrugations on the back of the Throat/Tapered area, near the waveguide filter, would actually affect the main beam beyond 17 degrees as well the sidelobe levels and give rise to a larger edge taper than the ideal for horn definition and operation. Table 4-2 summarises the results of the simulations of the sidelobes for the test case of five corrugations filled in various sections of the front horn. Imperfections in the tapered/ throat section of the horn have a marked effect on the edge taper raising it to -20 dB approximately. Imperfections in other sections (straight parallel phasing section, back of the flare, and front of the tapered section), while not dramatically raising the edge taper, do raise the general sidelobe level with the level of the highest sidelobe in the 30° to 40° region raised by 10 - 15 dB.

139

| Tolerance Test Case (all five filled corrugations) | Level at $\theta = 27°$ (Edge Taper) | Max Level of Sidelobe ($\theta \geq 30°$) | Angle of Max Level |
|---|---|---|---|
| **Ideal horn (No filled corrugations)** | -30 dB | -36.7 dB | 30° |
| **Corrugations filled behind the flare** | -30 dB | -28.4 dB | 32° |
| **Corrugations filled in the phasing section** | -23 dB | -26.4 dB | 30° |
| **Corrugations filled in the front of the tapered section** | -26 dB | -26.7 dB | 33.5° |
| **Corrugations filled in the middle of the tapered section** | -21.5 dB | -26.7 dB | 33° |
| **Corrugations filled in the back of the tapered section (throat section)** | -24 dB | -26.9 dB | 30° |
| **Corrugations filled at the front of the waveguide filter section** | -30 dB | -36.4 dB | 30° |

Table 4-2 : Summary of the results of the simulations of the tolerance test cases at 857 GHz.

Since the qualification horn and flight horns were tested at low frequencies (460 GHz and 511 GHz) outside of their operational band where they are single moded, we now check these beam patterns for the same possible imperfections. The same test cases as outlined above were therefore simulated at 460 GHz as this is the frequency at which the qualification horn antenna was tested. We will examine the test cases at 511 GHz later in this Chapter in section 4.5 when we look at the pre-launch measurements of the flight horn in more detail. Any major effects on the main beam pattern would have been noticed in these tests clearly. However, a rise in sidelobe levels particularly at large off-axis angles and at relatively low levels would not have resulted necessarily in the horn being rejected since the data were noisy in some cases and particularly if the main beam as predicted at this frequency was unaffected in terms of beam width and the discrepancy in the main sidelobe was of the order of a few dB. Figure 4-12 and Figure 4-13 each show the beam patterns for three of the test cases at 460 GHz as simulated in SCATTER. It is clear that the three test cases with imperfections in the horn shown in Figure 4-13 ( that is at the middle of the tapered area, at the throat (the back of the tapered area), or at front of the waveguide

filter section) would have a major effect on the single mode propagating at this frequency (460 GHz). In all three of these cases an increase of between 12 dB to 20 dB can been seen in the sidelobe levels either at 25 degrees or 30 degrees off-axis (see Table 4-3). The main beam pattern is also altered which clearly contradicts the measurements.
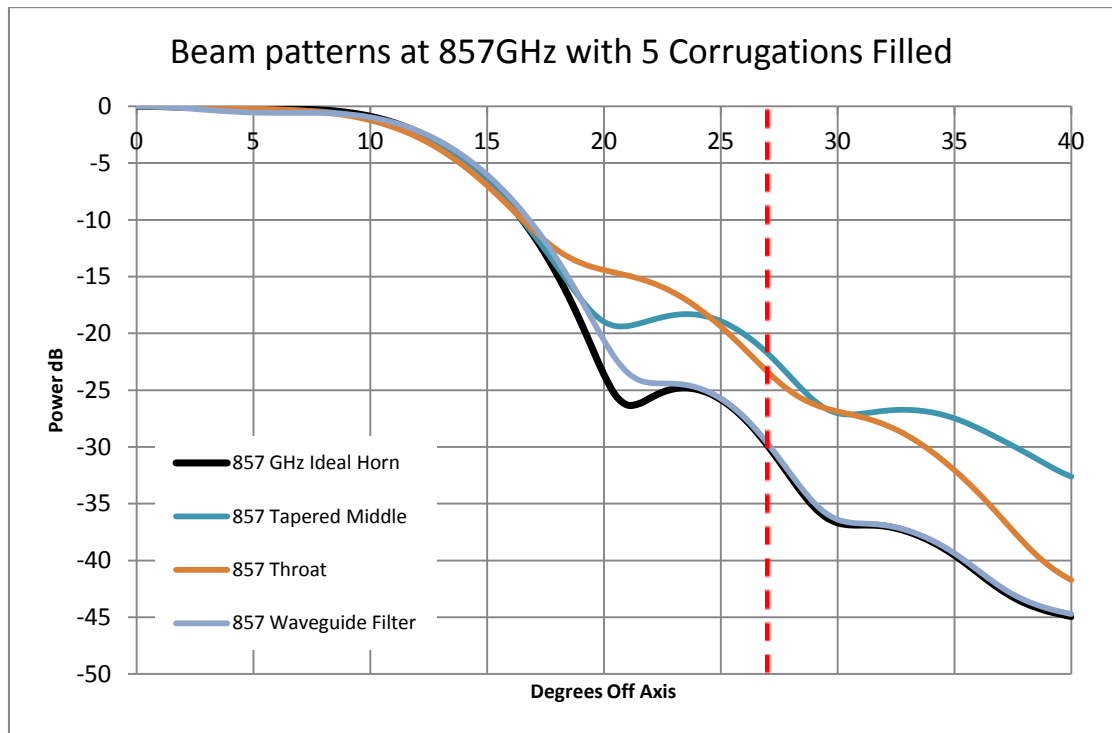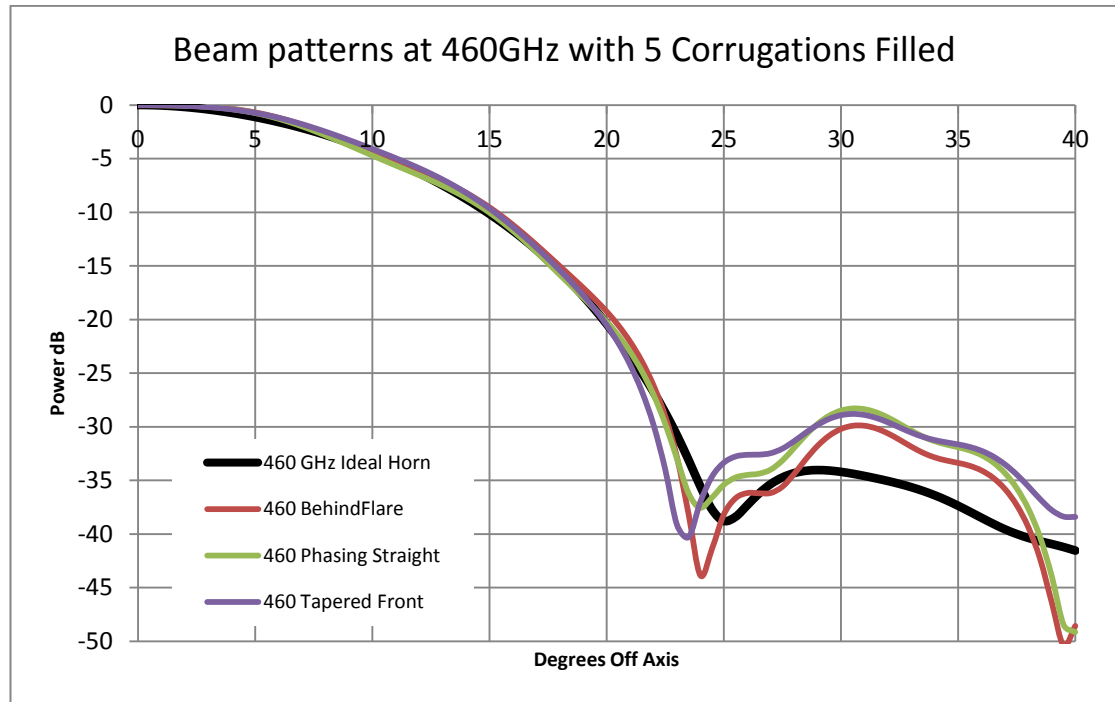


**Figure 4-12 : The simulated beam patterns of the 857GHz Planck horn at 460 GHz with 5 corrugations filled at the three locations within the horn indicated.**

For each of the remaining three cases, 5 corrugations filled in behind the flare, in the parallel straight phasing section, or at the front of the throat/tapered area, the main beam pattern is unaffected as seen in Figure 4-12. There is a rise in sidelobe levels but only of 5 dB from the -34 dB level of the ideal horn rather than the average change of 15 dB as in the other case for filled corrugations in the throat area. The position and level of the first null is also consistent with the perfect horn to such a degree that it is plausible that it could fall within the experimental error of a pre-flight measurement on a real Planck horn. Table 4-3 summarises the results for the single mode simulations as shown in Figure 4-12 and Figure 4-13. Clearly any imperfections in the throat area of the kind being investigated (a number of filled corrugations) is unlikely. However such imperfections in other parts of the front horn would not affect the main beam and the max level of the sidelobes beyond $30^{o}$ is not inconsistent with the measurements.
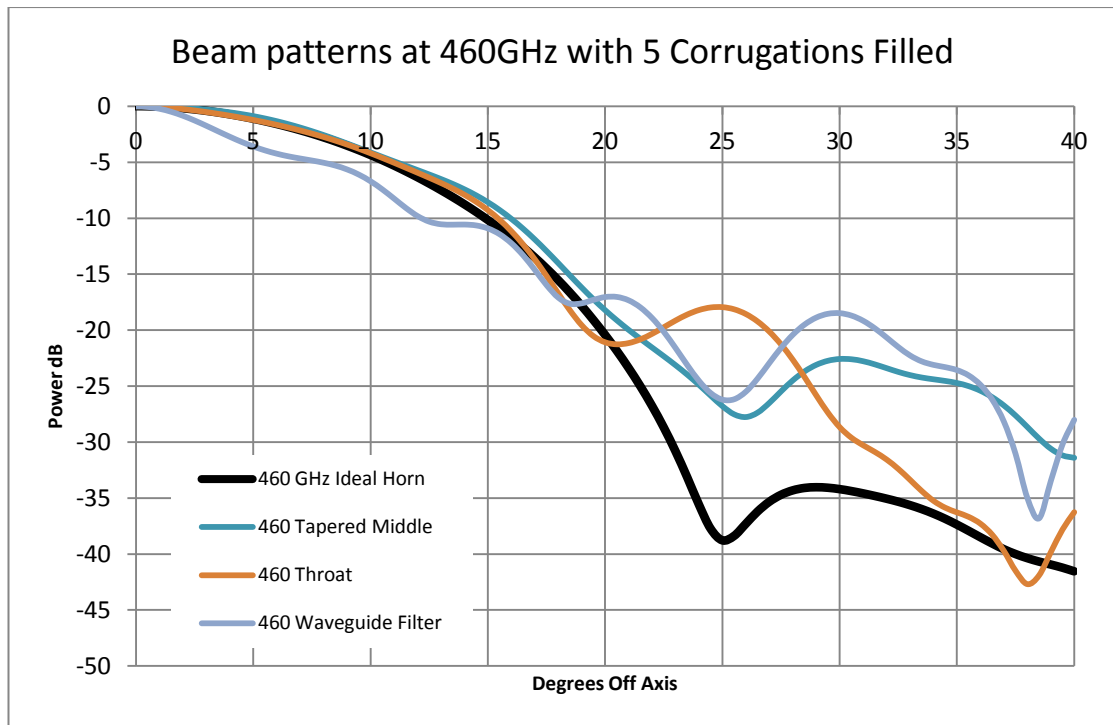
**Figure 4-13 : The simulated beam patterns of the 857GHz Planck horn at 460 GHz with 5 corrugations filled at the three locations within the horn indicated.**

| Tolerance Test Case (all five filled corrugations) | Level at θ = 25º Off-Axis | Max Level of Sidelobes (θ≥30º) | Angle of Max Level |
|---|---|---|---|
| **Ideal horn (No filled corrugations)** | -38.7 dB | -34.2 dB | 30º |
| **Corrugations filled behind the flare** | -38.1 dB | -29.9 dB | 31º |
| **Corrugations filled in the phasing section** | -35.4 dB | -28.7 dB | 31.5º |
| **Corrugations filled in the front of the tapered section** | -33.3 dB | -28.8 dB | 30.5º |
| **Corrugations filled in the middle of the tapered section** | -26.8 dB | -22.6 dB | 30º |
| **Corrugations filled in the back of the tapered section** | -17.9 dB | -28.7 dB | 30º |
| **Corrugations filled at the front of the waveguide filter section** | -26.2 dB | -18.5 dB | 30º |

**Table 4-3 : Summary of the results of the simulations of the tolerance test cases at 460 GHz.**

Since from the visual inspections of the horns there were issues with etching the aluminium mandrel (see Appendix B), the cases of corrugations filled with aluminium at the front and at the back of the throat area were taken as a best and worst case scenario respectively. These best and worst cases were then simulated across the

full operational frequency band. This required the computation of the multimode beam at a large number of spot frequencies across the operational band (730 GHz - 990 GHz). These simulations were then used to form a broadband beam pattern for the two test case horns. The farfield beam patterns resulting from the simulations for the case of five corrugations filled at the front of the tapered section are shown in Figure 4-14. There is clearly a general rise in the sidelobe level beyond $20^o$. The broadband beam patterns for both test cases are shown in Figure 4-15 along with the broadband beam pattern of the ideal horn for comparison. The same rise in sidelobe levels seen at 857 GHz are present in the broadband beams for both test cases. As in the case of the ideal horn, the simulated beam patterns at 857 GHz agree with the broadband beam pattern to such an extent as to be a useful indicator as to the behaviour of the horn across the band as can be seen in Figure 4-16.
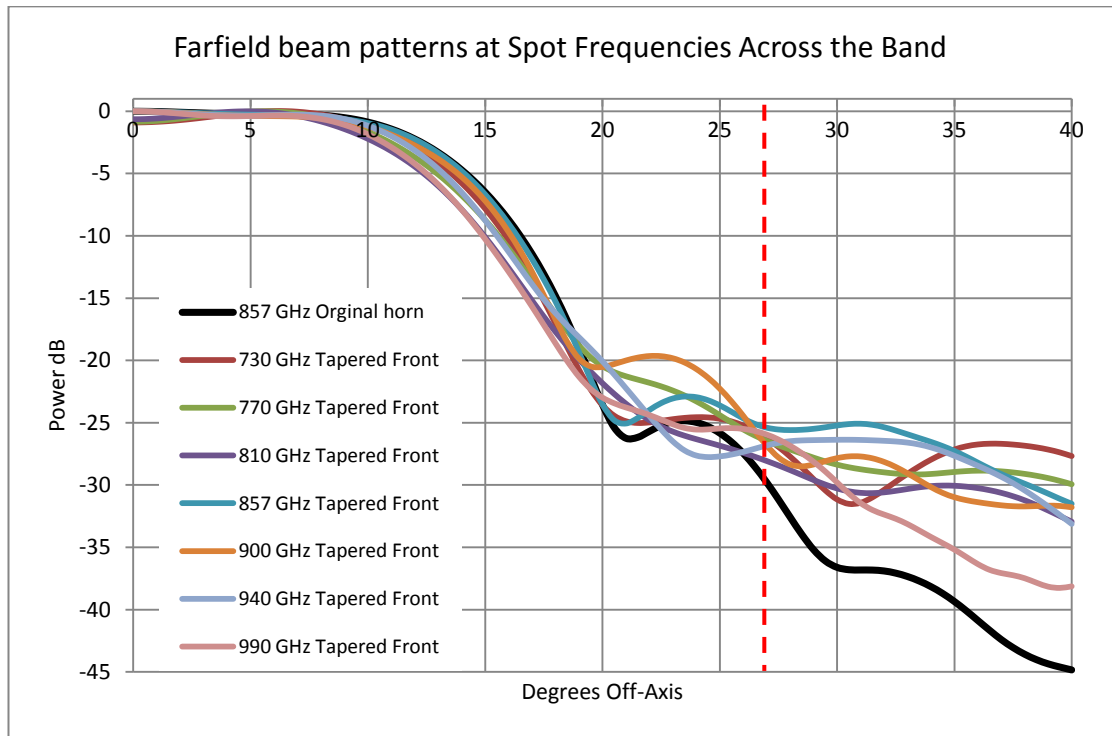


**Figure 4-14 : Farfield beam patterns at spot frequencies across the band for the case of five corrugations filled at the front of the tapered area. The part of this beam pattern that spilled past the primary mirror is marked by the red dashed line ($27^o$ off-axis).**
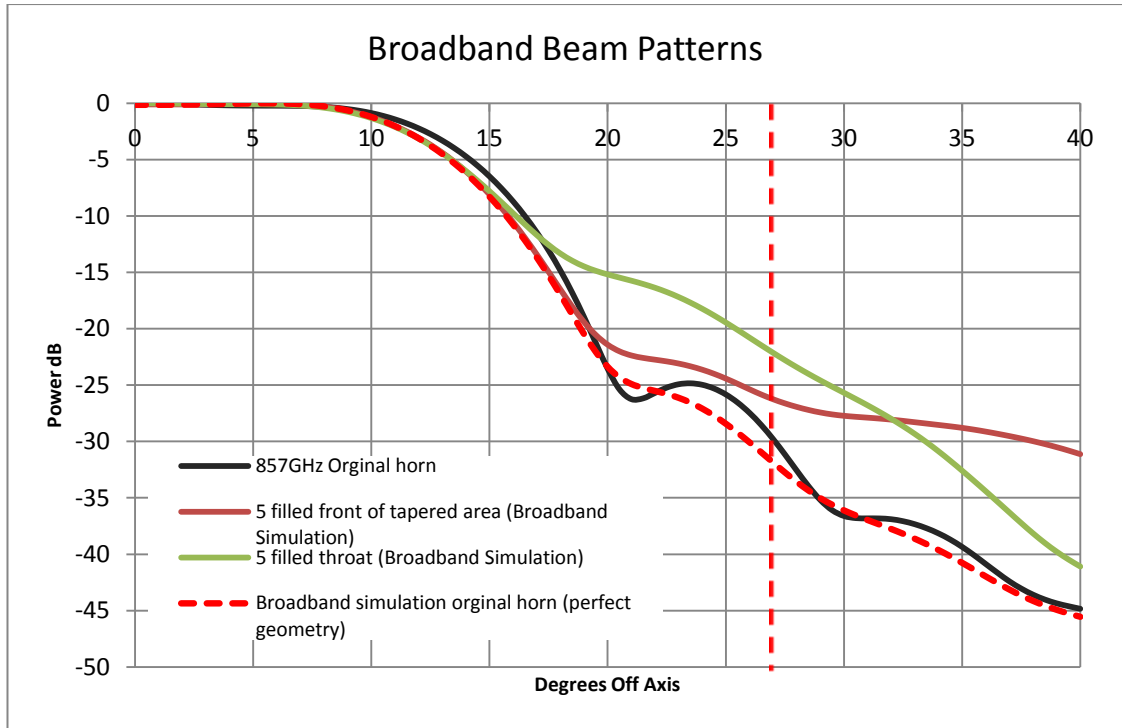
**Figure 4-15 :The simulated broadband beam patterns for the original Planck Horn and for 5 corrugations filled at the front of the tapered area, and at the throat area. The part of this beam pattern that spilled past the primary mirror is marked by the red dashed line (27° off-axis).**
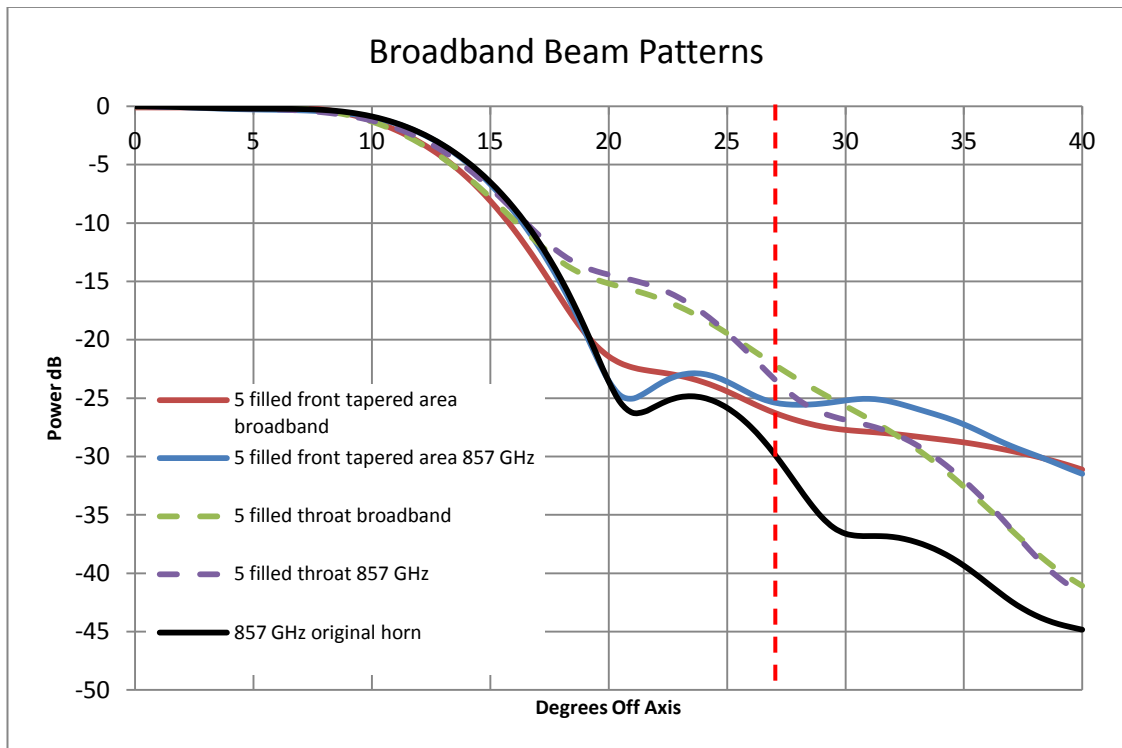


**Figure 4-16 : The simulated broadband beam patterns for 5 corrugations filled at the front of the tapered area, and at the throat area plotted with the beam patterns at 857 GHz for the same test cases. The dashed red line at 27° off-axis marks the part of this beam pattern that spilled past the primary mirror.**

144

The effects of a smaller and a larger number of filled corrugations were also investigated. It was found that as few as 2 fully filled corrugations could have some effect on the sidelobe levels. In general the greater the number of corrugations filled the greater the distortion of the beam pattern and the higher the resulting sidelobes (Table 4-4). There were exceptions found for some cases where 20 or more corrugations were filled. In these the sidelobe levels were still increased relative to the perfect horn but to levels lower than for fewer (e.g. 10) filled corrugations. However, the distortion of the main beam was greater for these cases which, of course, is much more significant and rules such cases out. Figure 4-17 shows an example of this where various number of corrugations were filled with aluminium at the same point at the front of the tapered area of the horn. The front of the tapered area was chosen rather than the throat at the back of the tapered area as this area is the 'plausible case scenario' for imperfections due to corrugations not being etched, i.e. the case where the main beam is unaffected and the rise in the sidelobe levels is not as pronounced as in the 'worst case'. The effect of filling a varying number of corrugations at the front of the tapered area on the sidelode levels beyond 27° off-axis were easier to track as they are not dominated by their effects on the beam at angles of less than 27° off-axis as was the case for the 'worst case scenario'. A steady increase in sidelobe levels can be seen as more corrugations are filled until at 20 corrugations the shape of the main beam is affected (becomes less top hat like) and the beam width increases.

| Number of corrugations fully filled front of the tapered section | Level at $\theta = 27°$ Off-Axis | Max Level of Sidelobes ($\theta \geq 30°$) | Angle of Max Level |
|---|---|---|---|
| **Ideal horn (No filled corrugations)** | -30 dB | -36.7 dB | 30° |
| **2** | -28 dB | -32.7 dB | 30° |
| **5** | -26 dB | -26.7 dB | 33.5° |
| **10** | -23 dB | -22.1 dB | 30.5° |
| **20** | -21.5 dB | -25.8 dB | 30° |

**Table 4-4 : Summary of the results of the simulations at 857 GHz of varying numbers of corrugations fully filled at the front of the tapered area.**
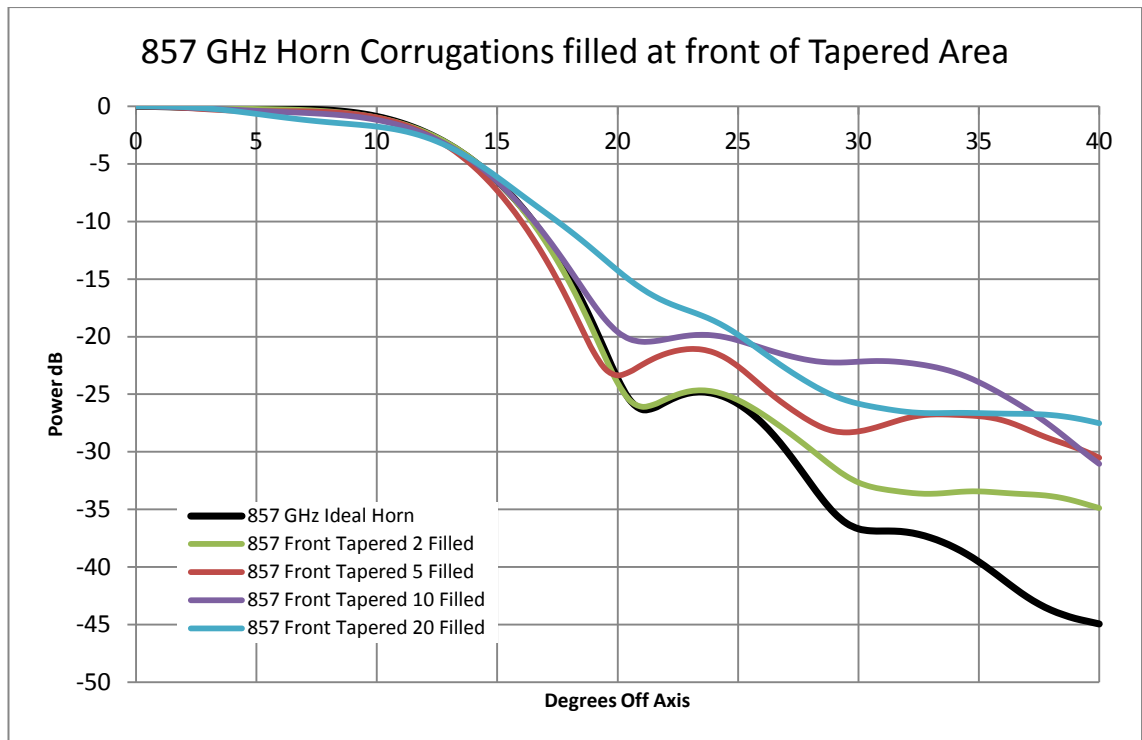
**Figure 4-17 : Beam patterns for test cases of different number of corrugations filled at the same place in the 857GHz horn.**

At 460 GHz, the frequency used to test the qualification horn, the same behaviour for the same number of filled corrugations is observed as for the high frequency band simulations, see Figure 4-18. The same steady increase in sidelobe levels can be seen as more corrugations are filled until at 20 corrugations the shape of the main beam is affected significantly and once more the beam width increases which is clearly inconsistent with measurements. Furthermore the position and level of the first null for the cases of 2 and 5 corrugations filled are also consistent with the perfect horn to such a degree that it is plausible that it could fall within the experimental error of a pre-flight measurement on a real Planck horn. In the case of 10 corrugations filled, the sidelode level is consistent with the perfect horn however the position of the first null has shifted such that it may have been possible to detect it during pre-flight measurements.
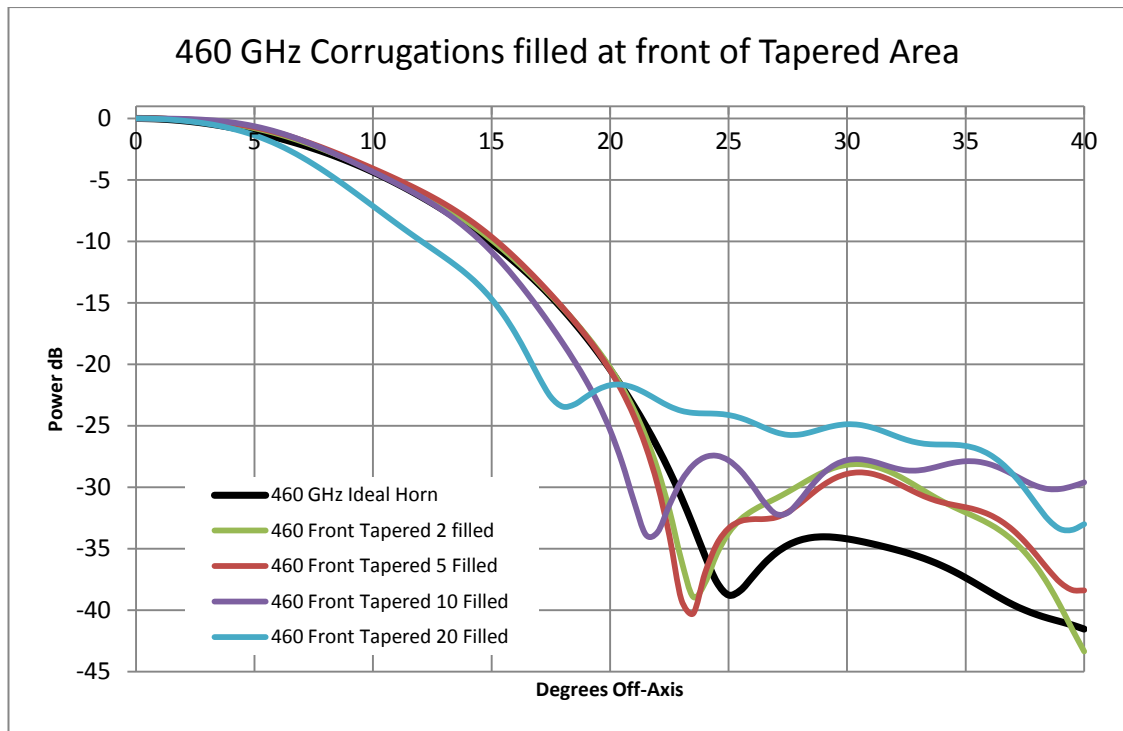
**Figure 4-18 : Beam patterns at 460 GHz for test cases of different number of corrugations filled at the same place in the horn.**

# 4.3 The Effects of Partially Filled Corrugations on the Planck horn

So far only the effects of fully filled corrugations have been described.  It is also possible for the corrugations to be partially filled with un-etched aluminium mandrel residue.  That is to say that the etching process removed some but not all of the mandrel aluminium from the corrugations.  The etching process could leave material at the bottom of the corrugation decreasing the depth of the corrugation or it could leave material along the side of the corrugation narrowing it.  While a combination of these two situations is likely it was decided to simulated the effects of each possibility separately in order to obtain a clearer understanding of the resultant degradation of the beam patterns.

To represent the case of a partially filled corrugation, one filled to half its depth was chosen (Figure 4-6).  In Figure 4-19 the beam patterns are shown for a series of test cases with different numbers of corrugations altered in this way at the

front of the tapered section of the horn. As in the case of fully filled corrugations the simulations show an increase in sidelobe levels in the region around 30 degrees off-axis corresponding to spillover onto the sky past the Planck primary mirror. For the case of just 5 corrugations altered the sidelobe level is actually higher than if the corrugations had been fully filled (Table 4-5). However, for this test scenario of half etched corrugations, more corrugations being affected in this way does not lead to a higher increase in sidelobe levels compared to altering just a few. At 460 GHz the beam patterns for both 5 and 10 corrugations half filled would have effects possible visible in the test measurements.

| Number of corrugations filled to half depth at the front of the tapered section | Level at $\theta = 27°$ Off-Axis | Max Level of Sidelobes ($\theta \geq 30°$) | Angle of Max Level |
|---|---|---|---|
| Ideal horn (No filled corrugations) | -30 dB | -36.7 dB | 30° |
| 5 | -23 dB | -23.6 dB | 30° |
| 10 | -22 dB | -23.8dB | 30° |

Table 4-5: Summary of the results of simulations at 857 GHz of the effects of partially filling corrugations to a half of the corrugation depth at the front of the throat/tapered area.
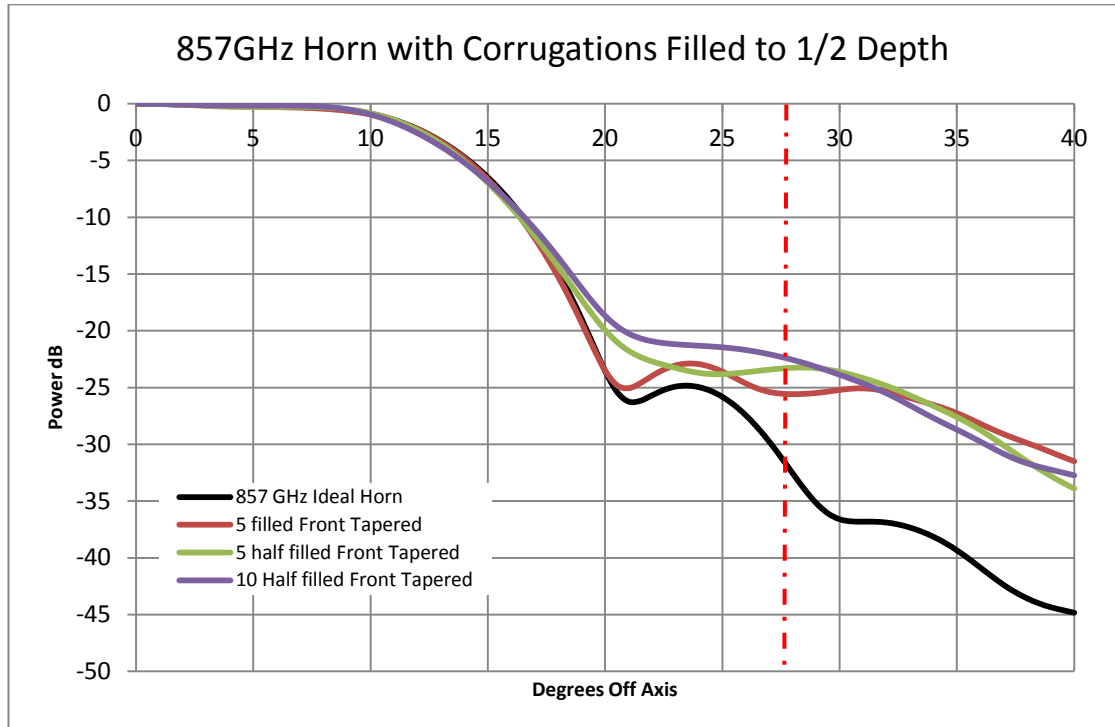


Figure 4-19 : Beam patterns of the 857 GHz horn with corrugations filled to 1/2 depth at the front of the tapered section of the horn. The red dashed line at 27° marks the part of the beam that spills over past the primary.

A similar approach was taken to the narrowing of the corrugations for the case of aluminium adhering to the fins (Figure 4-6). Once more a corrugation was modelled as being half filled with material such that its width was reduced by a half. The sidelobe levels rose from approximately 35 to 30 dB at 30 degrees off-axis while the main beam remained unchanged (Figure 4-20) in a similar way to previous cases. However the increase in the sidelobe level is less than for the test cases were the corrugations were fully filled and half filled by depth.

The effects of widening the corrugations, i.e. narrowing the fins, was also investigated. Unlike the previous test case which could have resulted from the etching process leaving un-etched mandrel material deposited in the corrugations, narrower fins would be caused by manufacturing (milling) tolerances in the production of the mandrel or not enough copper or nickel being deposited during the electroforming process. In the same manner used to model the narrower corrugations for this case the corrugations were widened by half their width. As can be seen from the beam patterns shown in Figure 4-21 widening the corrugations has a minimal effect on the beam pattern of the horn. This is not unexpected as the theory of corrugated waveguide design shows that the details of the field structures of the modes depends on the depths of the corrugation and actually assumes a relatively thin fin between the corrugations without specifying when the width for the fins affects the modes.

| Number of corrugations filled to half depth at the front of the tapered section | Level at $\theta = 27°$ Off-Axis | Max Level of Sidelobe ($\theta \geq 30°$) | Angle of Max Level |
|---|---|---|---|
| **Ideal horn (No filled corrugations)** | -30 dB | -36.7 dB | 30° |
| **5** | -29 dB | -30.1 dB | 31° |
| **10** | -27 dB | -29.9dB | 30° |

Table 4-6 : Summary of the results of simulations at 857 GHz of the effects of partially filling corrugations to a half the corrugation width at the front of the throat/tapered area.
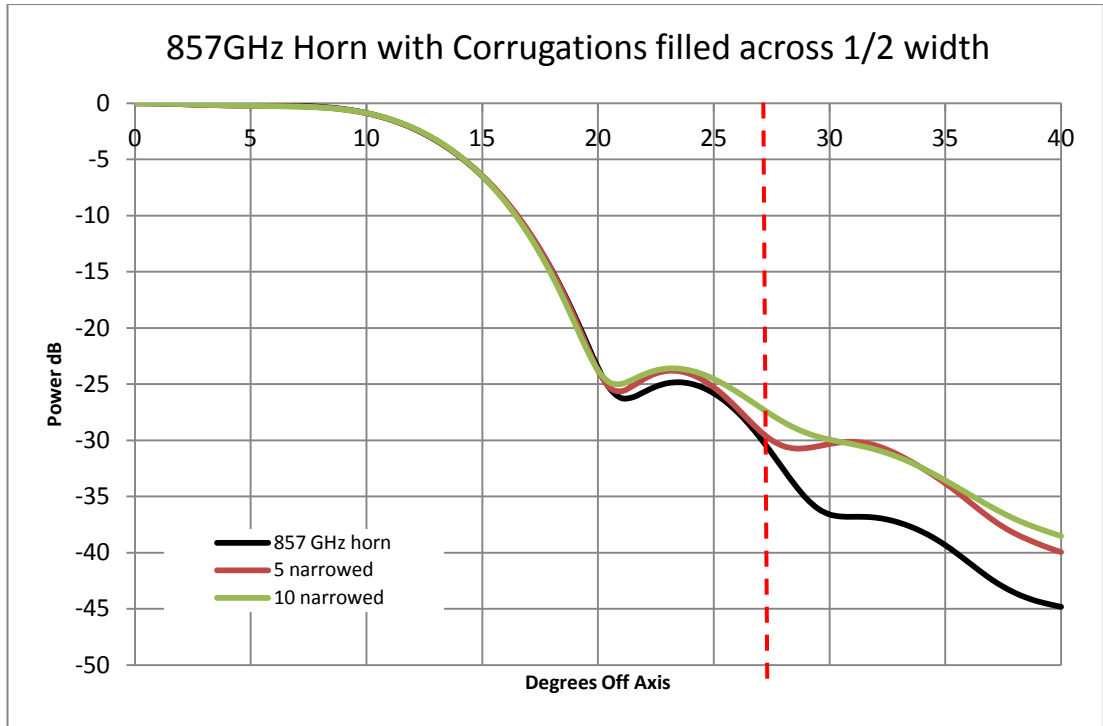
**Figure 4-20 : Beam patterns for simulations of corrugations narrowed at the front of the tapered section. The part of this beam pattern that spilled past the primary mirror is marked by the red dashed line (27° off-axis).**
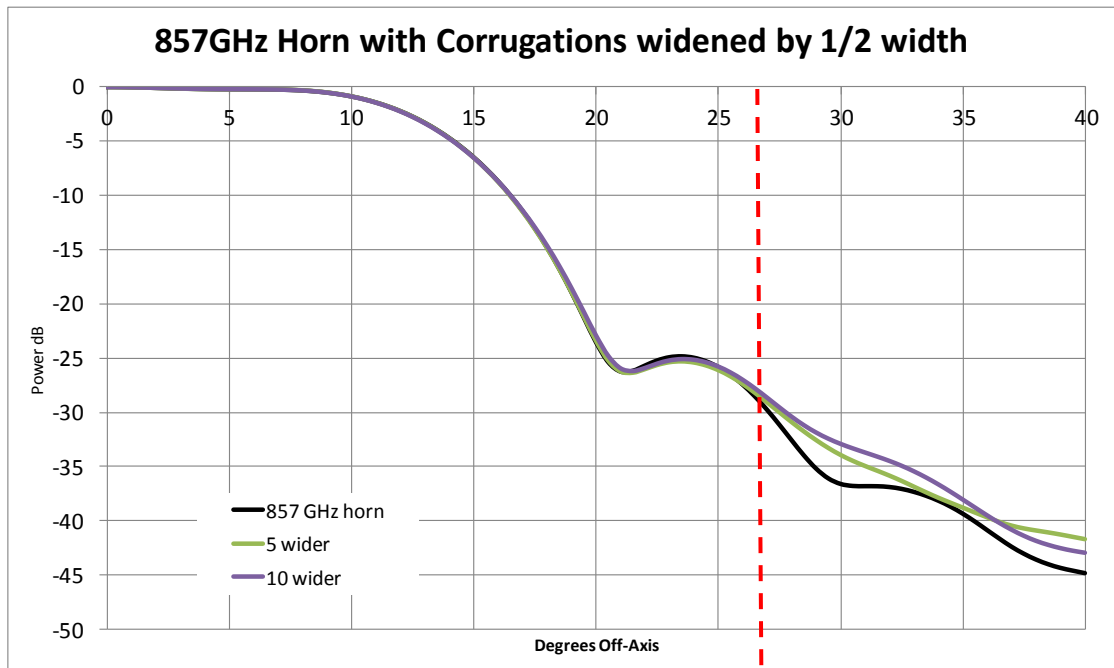


**Figure 4-21 : Beam patterns for simulations of corrugations widened at the front of the tapered section. The red dashed line (27° off-axis) marks the part of this beam pattern that spilled past the primary mirror.**

150

# 4.4 The Effects of Missing Fins on the Planck horn

The electroplating process used to form the horn on the mandrel is a more controllable process than the etching process. Thus in general it is less likely that defects, such as missing fins, would have occurred during this part of the fabrication of a horn. However in the case of a high frequency horn, such as the 857 GHz Planck horns, this may not be entirely true, indeed the visual inspection reports mention some defects such as flattened sections of copper (see Appendix B), so it is still important to investigate the possible effects of missing fins on the beam pattern of the horn.

As for the simulations of filled corrugations, a series of scenarios for different numbers of missing fins in each of the different sections of the horn were simulated. The results of these simulations were broadly comparable to those for the equivalent filled corrugation scenario, i.e. removing fins and filling corrugations in the same area had an effect of similar magnitude on the beam pattern with the throat region having the most dramatic effect. In fact Figure 4-22 shows the beam patterns for the cases of removing fins in the front of the tapered section of the horn. These beam patterns show similar dramatic features to those for filled corrugations in the same region (Figure 4-17). That is a rise in sidelobe levels is observed while the main beam is unaffected although the edge tapers at $27^o$ are rather high. The results are summarised in Table 4-7.

| Number of fins removes in the front region of the tapered section | Level at $\theta = 25^o$ | Max Level of Sidelobe ($\theta \geq 30^o$) | Angle of Max Level |
|---|---|---|---|
| **Ideal horn (No fins removed)** | -25.8 dB | -36.7 dB | 30° |
| **5** | -22.7 dB | -26.3 dB | 30° |
| **10** | -19.6 dB | -21.9 dB | 30° |
| **15** | -15.5 dB | -19.7 dB | 30° |

**Table 4-7 : Summary of the results of simulations at 857 GHz of the effects of missing fins in the front area of the throat/tapered area.**
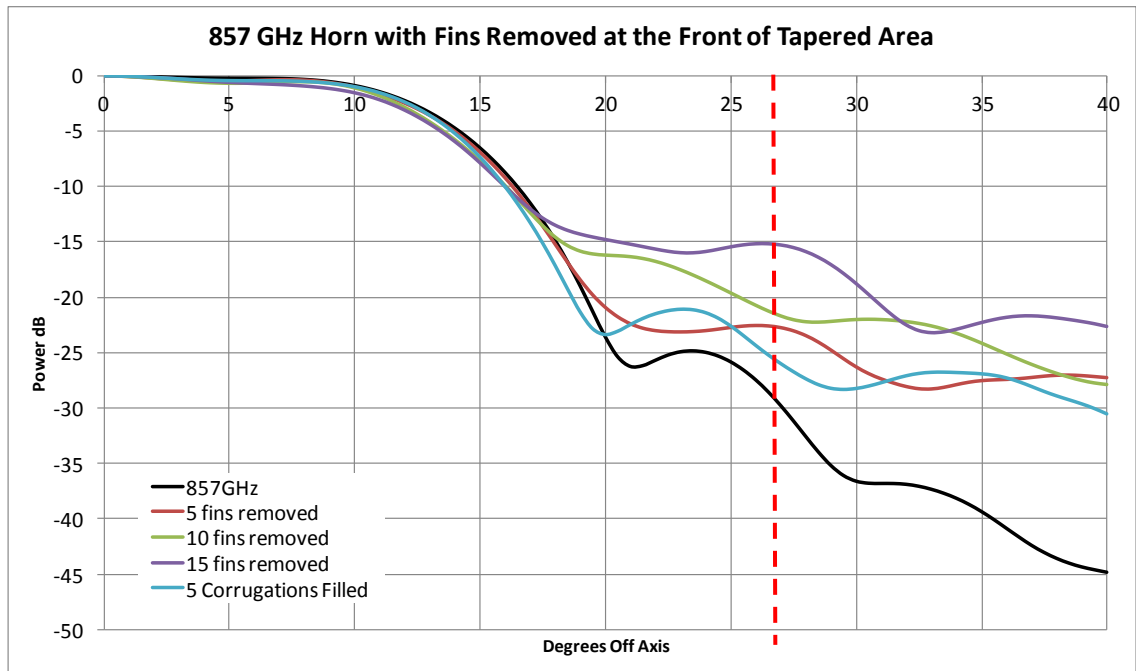
**Figure 4-22 : Beam patterns for the cases of missing fins in the front of the tapered area of the horn. The pattern for five corrugations filled in the same area of the tapered section is shown for comparison. Again the red line marks the spillover past the primary.**

# 4.5 Flight Horns

As already mentioned six flight horns were manufactured for use in the HFI on the Planck satellite, and four of these horns were chosen to fly on the satellite based on laboratory tests carried out by Cardiff University. Also as previously stated these horns were first visually inspected for defects (see Table 4-1 & Appendix B). Remedial action, where possible, was taken to fix any imperfections found. None the less it is possible that there may still have been some imperfections present in the horns which were either too small to be seen on inspection or impossible to remove with remedial action. After this visual inspection the beam patterns of the flight horns were measured at 511 GHz at which frequency the horns are single moded. Figure 4-23 shows beam patterns measured by Cardiff University for one of the chosen flight horn pairings. The dashed line is the SCATTER simulation of the farfield pattern at the same frequency (511 GHz). It is clear that the main beam, up to 20 degrees off-axis, as simulated agrees well the measurements. The minor differences in the sidelobe levels may be due to practical limitations in the test measurement setup that

cannot be included in the simulations. In any case the measurement data is rather noisy. Apart from this difference of about 2 - 3 dB in the intensity levels, the position and structure of the side lobes in both agree reasonably well.
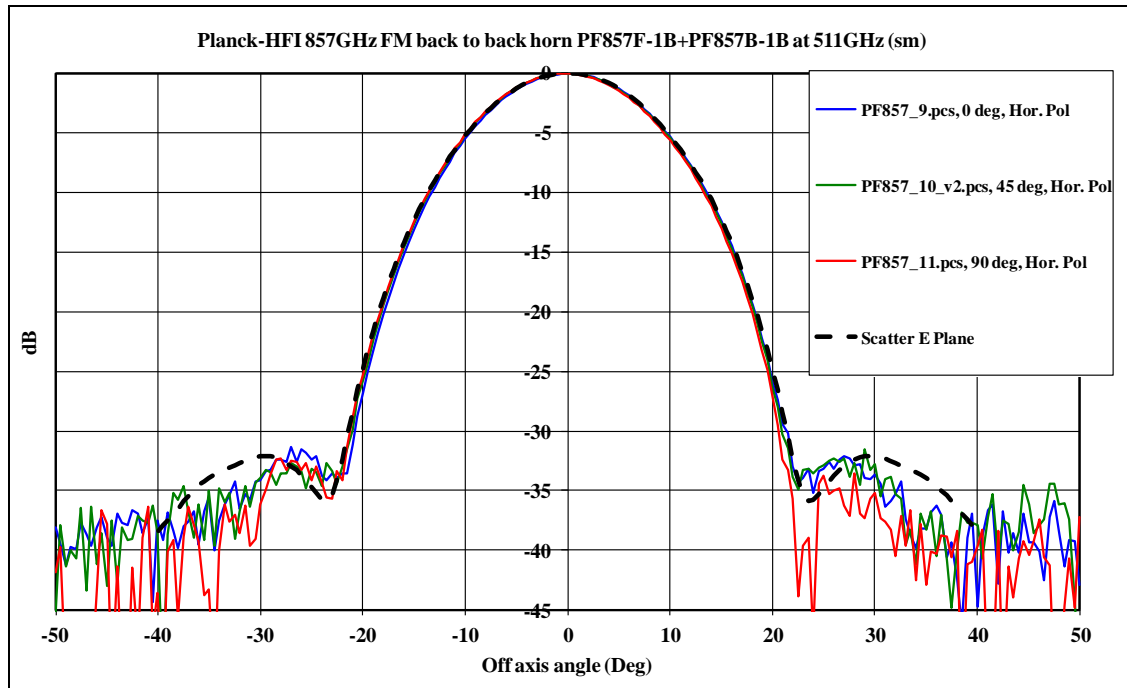


**Figure 4-23: Test measurements of the beam pattern of one of the 857 GHz back-to-back horn and detector horn assemblies (E Plane). The scatter simulation of the horns is shown in the black dashed line. This set of horns was chosen for flight.**

Based on the results of the simulations described in the previous sections, it was decided that the Cardiff test data would be compared with simulations with the possible imperfections present in the corrugations in the throat and tapered sections of the front horn. Simulations of fully and partially filled corrugations in these sections were made at 511 GHz. Examples of these simulations are shown overlaid on the Cardiff measurements in Figure 4-24 and Figure 4-25. A single filled or half-filled corrugation does not change the beam pattern from that of a perfect horn at this frequency. When multiple corrugations are filled or half-filled the main beam pattern is however changed. This is clear from the simulation shown in Figure 4-24 of the case with five wholly filled corrugations in the front of the tapered section of the front horn alongside the test measurements of one of the back-to-back flight horns. Figure 4-25 shows the simulation for partly filled corrugations in the same location in the horn along with the test data . In these cases the main beam pattern changes at about 17 degrees off-axis and is clearly also not consistent with the experimental test measurements.

153
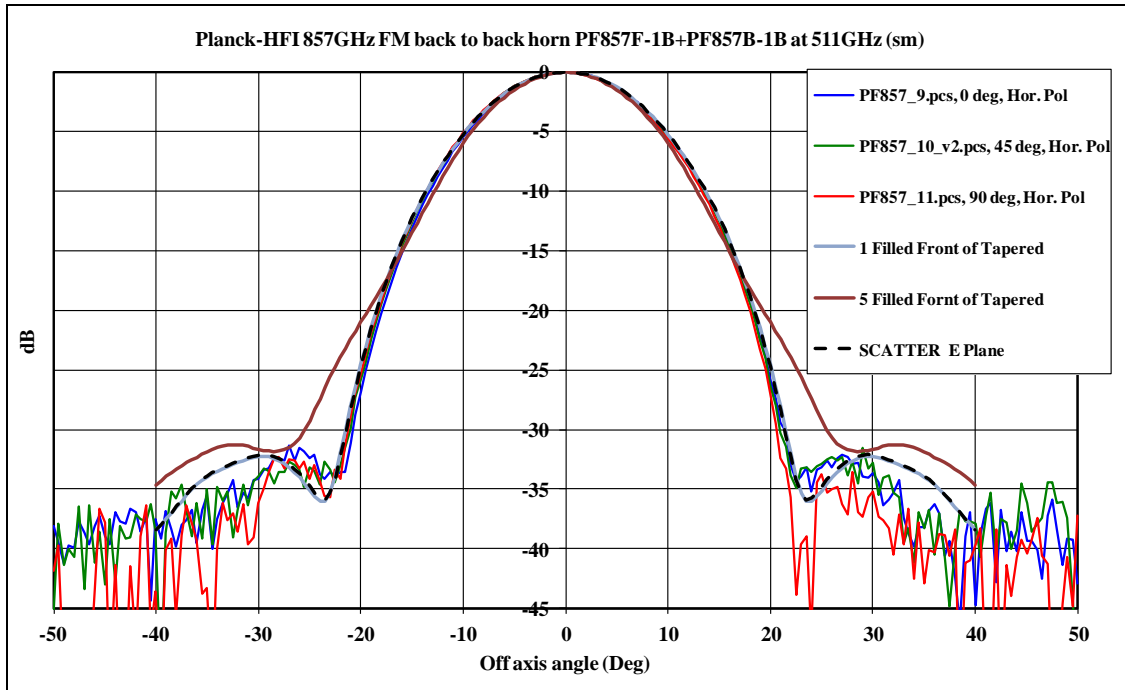
**Figure 4-24 : Shown here are the Cardiff measurements of a flight back-to-back horn pair and simulations of possible imperfections in the front of the tapered section of the 857 GHz back-to-back horn.**
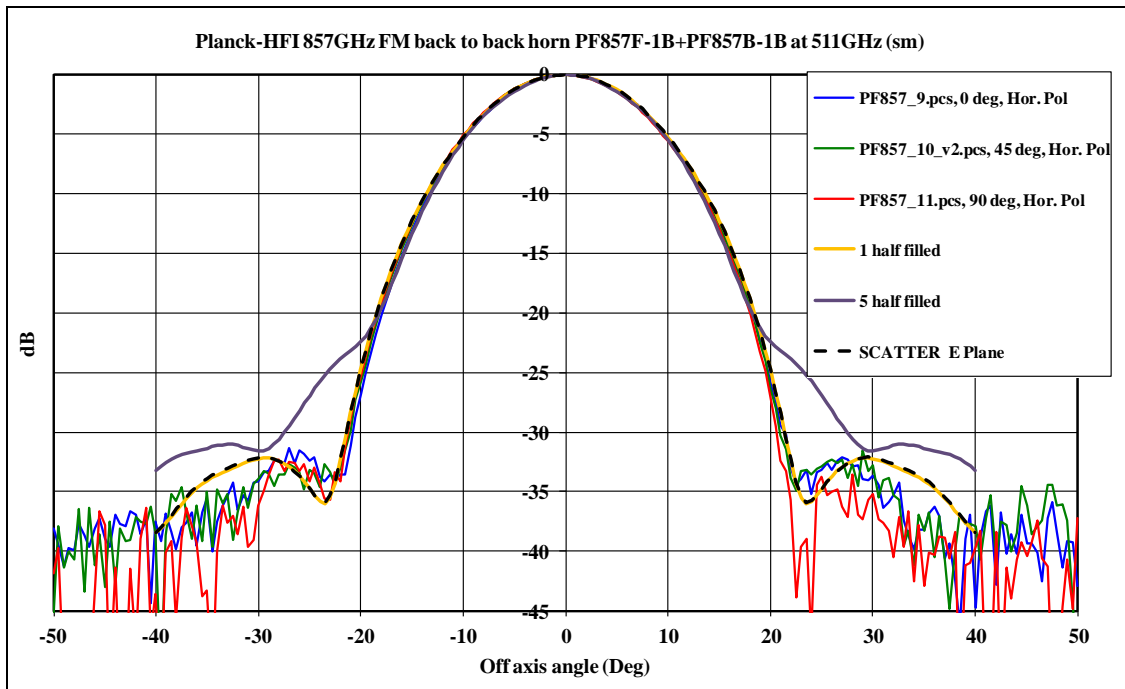


**Figure 4-25 : Shown here are the Cardiff measurements of a flight back-to-back horn pair and simulations of possible imperfections in the front of the tapered section of the 857 GHz back-to-back horn.**
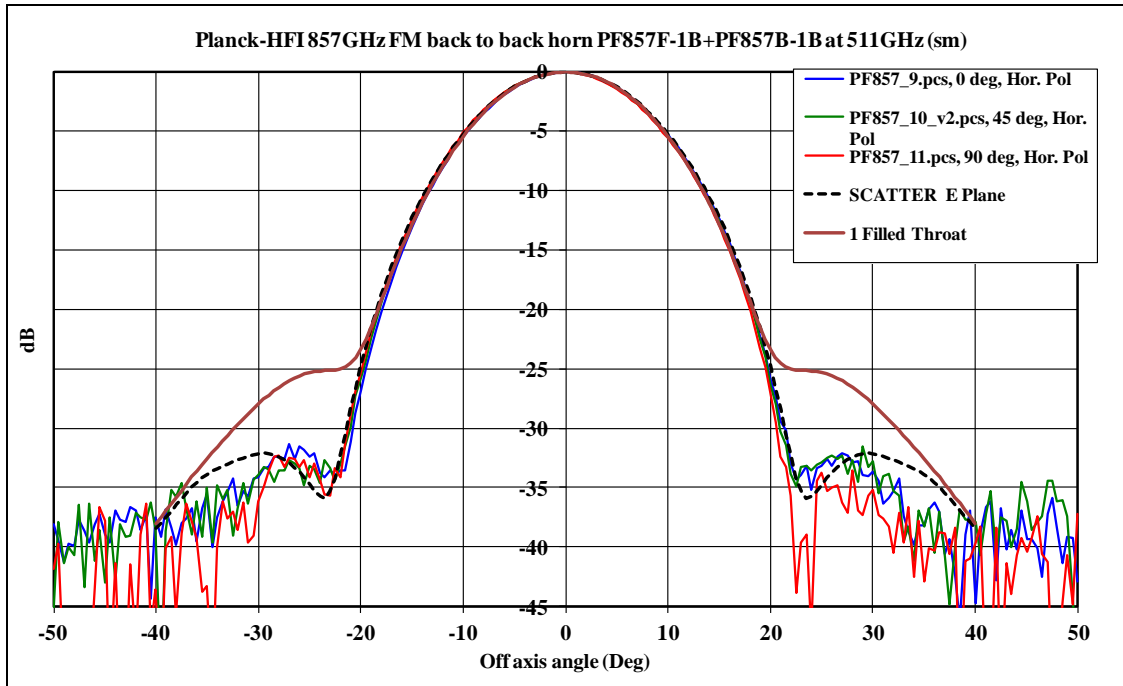
**Figure 4-26 : Shown here are the Cardiff measurements of a flight back-to-back horn pair and simulations of possible imperfections in the throat section of the 857 GHz back-to-back horn.**

The case of one corrugation fully filled in the throat section was also investigated. A simulation of the beam pattern at 511 GHz showed that the sidelobe levels would be significantly raised by a non-ideal in the throat of the horn. The sidelobe at $30^o$ off-axis rises from -32 dB for the ideal horn to -27 dB. While at $25^o$ the level rises from -34 dB to -25dB. Levels such as these fall outside of the experimental error of the test measurements and would have been measurable in the pre-flight tests. In fact the throat section of the horn is one of the parts of the horn that could be visually inspected and any imperfections found in this area during inspection (see Appendix B) would have been subject to remedial actions.

As it is not possible to detect single fully filled corrugation imperfection in the tapered section by measuring the beam pattern of a flight horn at 511 GHz it was decided to re-simulate the beam patterns at the central operational frequency, 857 GHz, to check for possible changes in the beam pattern in multimode operation. Once more SCATTER was used to calculate the farfield beam patterns for the front horn with just one corrugation filled in the tapered area, and also with one half-filled at the same location within the horn as shown in Figure 4-27 and compared with the beam patterns simulated at 857 GHz. The main beam out to 20 degrees off-axis is the same for both horns. The first sidelobe at 23 degrees differs marginally between the

two but at 30 degrees off-axis the difference in the sidelobes has risen 5dB. Looking at the case of a half-filled corrugation, Figure 4-28, a similar result is seen. The main beam is unaffected but the sidelode levels at 30 degrees off-axis are again higher for the horn with the partially filled corrugation. The same variations can be seen in the broadband beams shown in Figure 4-29 which were again created using individual simulations at spot frequencies across the band. No variation is seen in the broadband beams until 20 degrees off-axis is reached. At 30 degrees the sidelobe levels are 6 dB higher for the horn with the half-filled corrugation. Interestingly the sidelobe level for the horn with a single corrugation filled is only 2 dB higher than the broadband beam of the ideal horn which illustrated that such effects are generally much larger when around five sequential corrugations are involved.
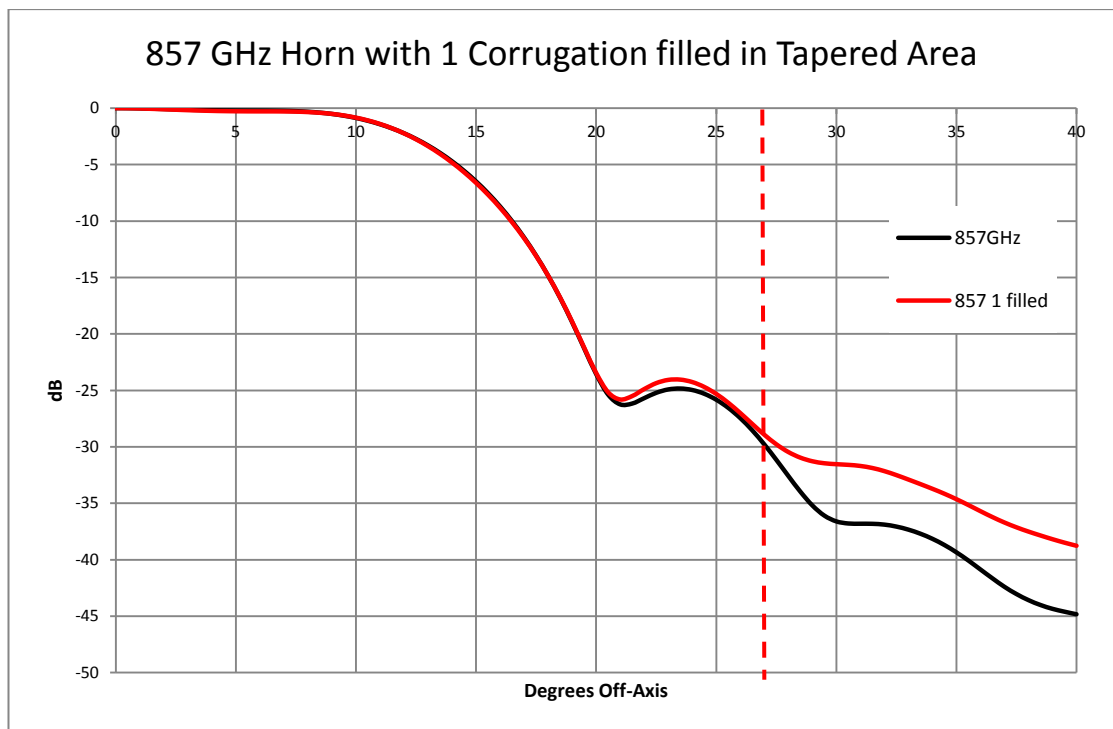


**Figure 4-27 : SCATTER simulations of the beam patterns for an ideal 857 GHz horn and a horn with 1 corrugation filled at 857 GHz. The red dashed line (27° off-axis) marks the part of this beam pattern that spilled past the primary mirror.**
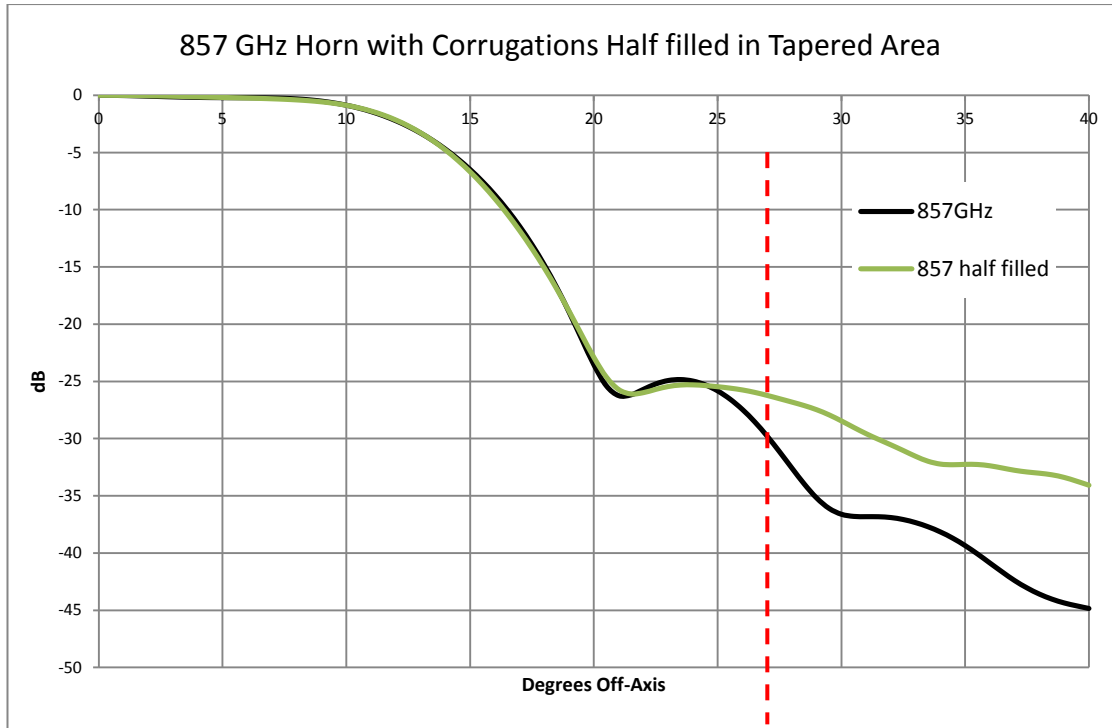
**Figure 4-28 :SCATTER simulations of the beam patterns for an ideal 857 GHz horn and a horn with 1 corrugation half-filled at 857 GHz. As in previous plots the red dashed line (27° off-axis) marks the part of this beam pattern that spilled past the primary mirror.**
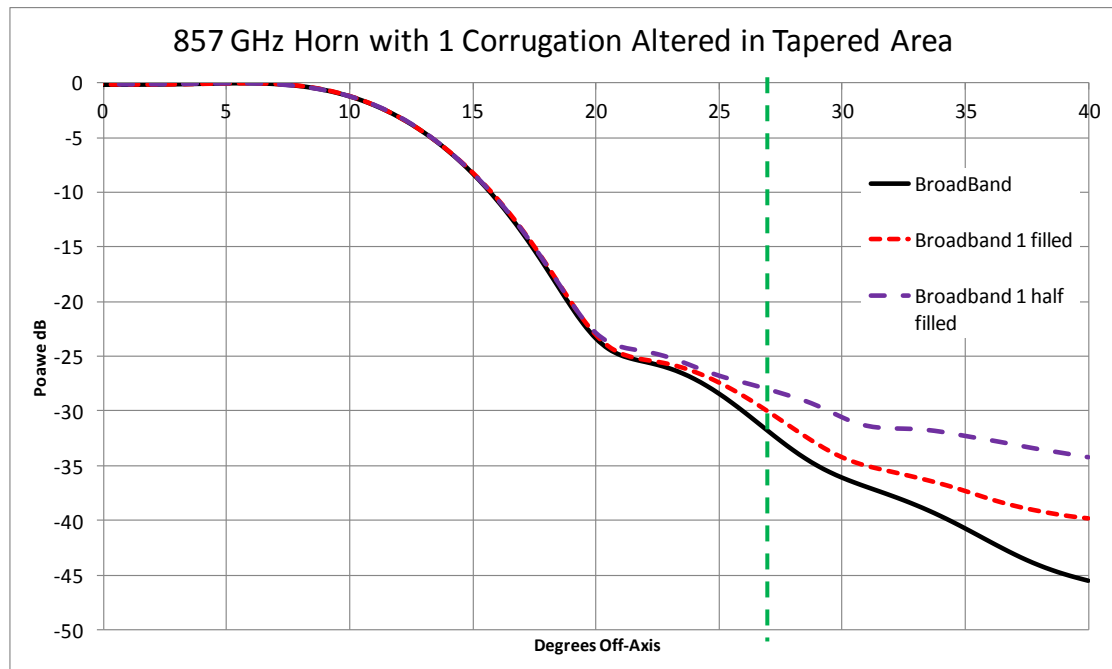


**Figure 4-29 : SCATTER simulations of the broadband beam patterns for an ideal 857 GHz horn and a horn with 1 corrugation filed and half-filled. The green dashed line at 27° off-axis marks the part of this beam pattern that spilled past the primary mirror.**

In summary the simulations described in sections 4.3 - 4.5 clearly illustrate how imperfections in the real horns due to the fabrication processes can produce higher than expected sidelobe levels and in more extreme cases also alter the main

157

beam pattern. Defects in as few as 5 sequential corrugations out of the more than 800 corrugations that make up the horn can result in a higher sidelobe level which is significant for spill over levels. It is also clear that the position at which these imperfections are located within the horn is also a strong factor in determining the level of the resultant change in the beam pattern. A defect in a single corrugation in certain areas, such as the throat or tapered section of the front horn, can cause a significant rise in the sidelobe levels at frequencies in the operational band.

In the case of the flight horns, the most likely position at which any defects may have gone unnoticed in pre-flight tests is at the front of the tapered section of the horn. Deviations in this area produce increases of about 6 to 10 dB in the sidelobe levels at 30 degrees off-axis at the central frequency of 857 GHz. At the frequency at which the pre-flight measurements were made, 511 GHz, it may not be possible to distinguish any change in the beam pattern for the case of damage to a small number of corrugations as the level of variation in the beam may fall within the systematic fluctuations of the measurement setup.

# 4.6 Modelling Sidelobe Spillover

Although the farfield patterns of the horns could be used directly to predict the far-out sidelobes (after reflection from the secondary mirror) nevertheless in order to obtain the relative levels of the far-out sidelobes a full sky model is required using appropriate antenna modelling tools. As mentioned in chapter 2, packages such as GRASP9 are used to predict the beam patterns of optical systems such as telescopes by propagating a field from a feed source through the optical system and on to a "detection" grid located in either the near field or farfield of the telescope. This analysis can be performed using a number of techniques such as Physical Optics (PO) combined with the Physical Theory of Diffraction (PTD) or Geometrical Optics (GO) combined with the Geometrical Theory of Diffraction (GTD). Daniel Wilson, [Wilson, 2014], developed a full model of the Planck telescope in GRASP9 and used the hybrid field descriptions of the 857 GHz channel produced by the author of this thesis as described in this chapter and the previous chapter as inputs to this model.

The results of this modelling that are relevant to our investigation of the effects of small manufacturing imperfections on the beam pattern, in particularly the Far-out Sidelobe Levels (FSL) will be described here.
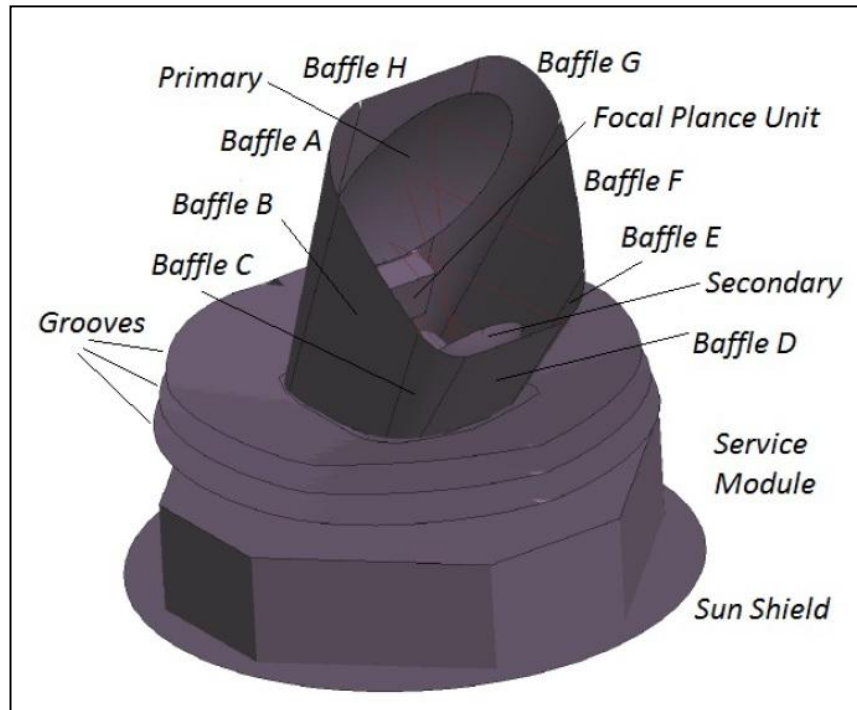


**Figure 4-30 : The complete mode of the Planck telescope in GRASP9. [Credit Dan Wilson, Maynooth University]**

The complete model of the Planck telescope (shown in Figure 4-30) included not only the primary and secondary mirrors but also the various baffles and other components which contribute to the overall far-out sidelobe structure of the beam on the sky. While all the baffles (labelled A - H in Figure 4-30 ) contribute some scattered power to the beam on the sky, of greatest concern for the modelling are baffles A, G and H which intercept spillover past the primary mirror and thus have the greatest impact on the far-out sidelobe region beyond a few degrees off the telescope optical axis. PO was used to model the primary and secondary reflectors and these baffles, while reflections from the remaining baffles, which have much lower level contributions to the beam on the sky and therefore did not justify the large computation time required to model them using PO, were modelled using GTD. Thus a combination of PO and GTD was used to minimise computation time while still providing a model of the beam on the sky to the required accuracy to investigate the far-out sidelobes.

For similar computational reasons it was decided to model the beam on the sky at 730 GHz at the lower end of the 857 GHz channel frequency band. Since each hybrid mode field must be independently propagated through the optical system computational time can thus be minimised by modelling the beam on the sky at the lower end of the frequency band where the number of the higher order modes propagating are fewer than at higher frequencies. A full calculation of the field on the sky for each hybrid mode inputted to the GRASP9 model took roughly 50 hours on a cluster of 66 CPUs to complete. Thus, for the five hybrid modes and their orthogonal fields at 730 GHz (in the 857 GHz channel horn) the full beam on the sky calculation took roughly three weeks to complete. The importance of using SVD in SCATTER to determine the hybrid modes is clear, as without a hybrid mode description the individual TE and TM waveguide modes originally used as basis set in SCATTER would have to be propagated through the system. For the 857 GHz horn this would have required the computation of a minimum of 300 fields (30 TE and 30 TM modes for each of the 5 azimuthal orders), a number which would have made the calculation impossible on the available CPU cluster!

Therefore, given the length of time required to calculate the full GRASP9 beam on the sky it was also decided to simulate only one "plausible" case and one "worst" case for possible imperfections in the corrugations (in addition to the beam for the ideal horn case). The "plausible" (or "bad") case would correspond to manufacturing imperfections that might not have been detected during pre-flight testing. The "worst" case was one which probably would have been seen in pre-fight tests, but was still thought to be possible if any damage had occurred due to vibration of the delicate corrugation structure during the Ariane 5 launch. For the "plausible" case the scenario of five corrugations fully filled at the front of the tapered area of the front 857 GHz horn, as described earlier in section 4.2, was chosen. The scenario of five corrugations fully filled at the actual throat section was selected as the "worst" case. While the test cases chosen to model were of filled corrugations, as has been shown earlier, the effect on the beam pattern of missing fins in the same section of the horn are broadly similar (see section 4.4). As can be seen in the farfield beam patterns shown in Figure 4-15 both cases result in significantly higher sidelobe levels at 857 GHz compared to the ideal horn in the region between $27^o$ and $42^o$ off-axis (the spill over region for the primary as viewed by the horn). However, at the pre-flight single

mode test frequency (511 GHz) the "plausible" case shows a rise in sidelobe levels that would have fallen within the experimental error of the measurement set (see Figure 4-12), while at the same frequency (511 GHz) the "worst" case would have been detectable as it causes a rise in sidelobe levels well outside the experimental error and also affects the main beam (see Figure 4-13). Ultimately we wish to see if the chosen "plausible" and "worst" cases as described above are possible causes of the banana features seen in the survey difference maps discussed in section 4.2.
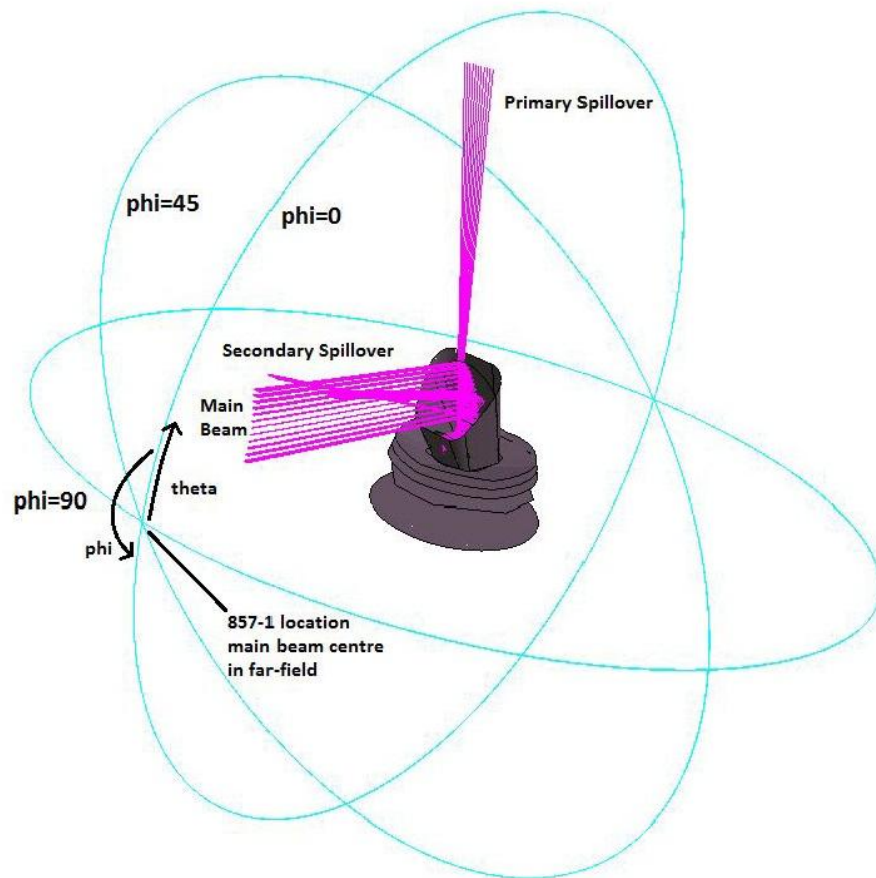


**Figure 4-31 : GRASP9 model of Planck with the prominent rays and cuts around the sphere taken for the beam on the sky plots.**
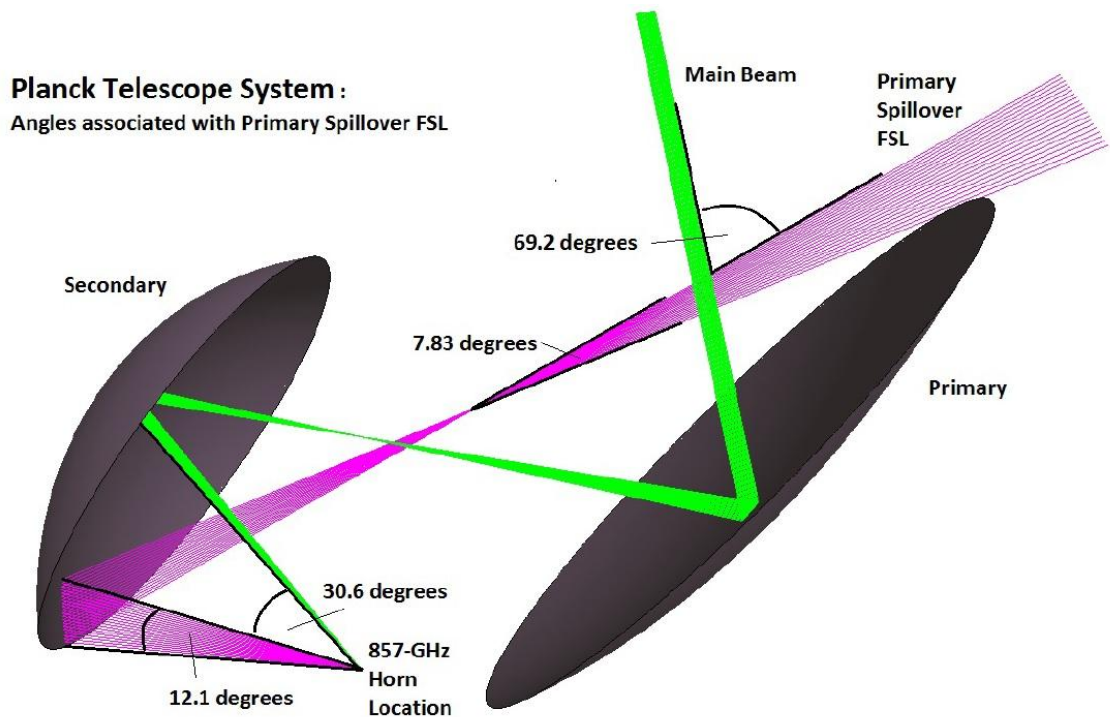
**Figure 4-32: Ray diagram showing the angles associated with the spillover of the beam fromm the 857 GHz horn past the primary mirror which produces the far-out sidelobes under investigation.**

Therefore for the 3 cases of ideal horn, horn with "plausible" imperfections, and "worst" case scenario (damaged horn) the corresponding hybrid modes were generated by the author of this thesis for input into the GRASP9 model of Planck run by Daniel Wilson [Wilson, 2014]. Three cuts through the beam on the sky (at $\phi = 0^{o}$, $45^{o}$, and $90^{o}$ see Figure 4-31) were generated and the beam on the sky for the ideal horn along each of the three cuts are shown in Figure 4-33. The prominent peak in the $\phi = 0^{o}$ cut at around $80^{o}$ off-axis is a far-out sidelobe of interest produced by spillover of the main beam beyond the edge the primary mirror (as indicated in Figure 4-32). The sharp edge of this peak at $80^{o}$ is the point where the beam is truncated by the edge of the primary. The shape of this peak down towards $65^{o}$ is a result of the spillover of the first sidelobe past the primary mirror which is responsible for the smaller peak at $72^{o}$ off-axis. At $60^{o}$ there is another edge which corresponds to the truncating edge of the secondary mirror (see Figure 4-32). The smaller peak at approximately $10^{o}$ visible in the $\phi = 0^{o}$ and $\phi = 45^{o}$ corresponds to spillover of the beam directly past the secondary mirror [Planck Collaboration, 2014b], as illustrated in Figure 4-31.
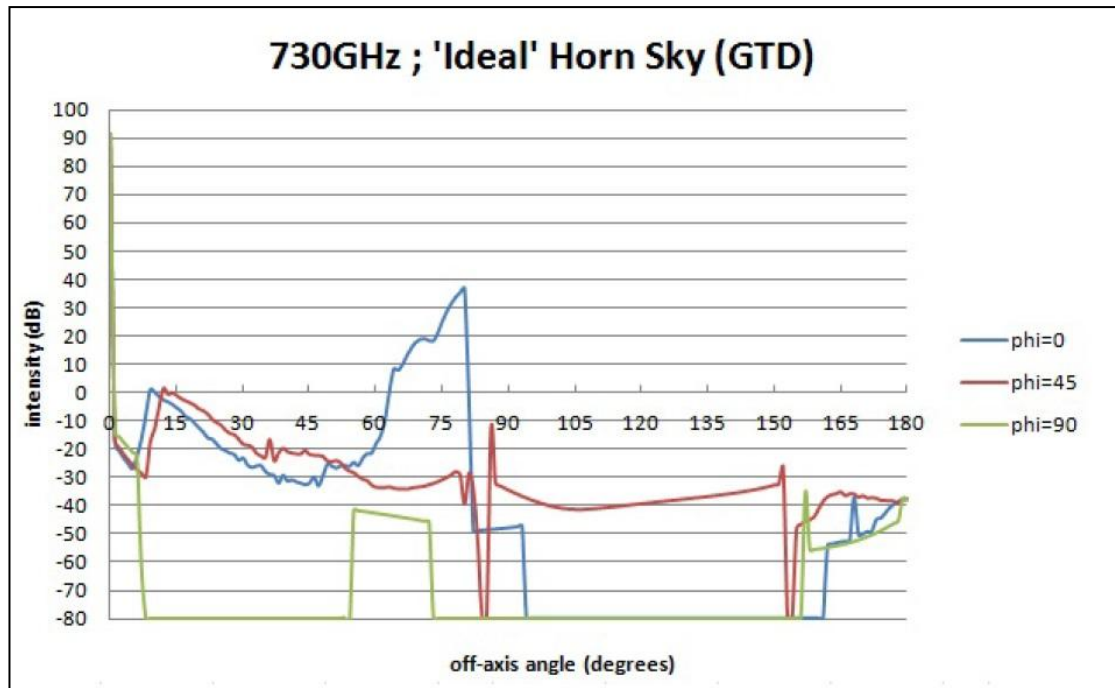
**Figure 4-33 : Beam on the sky for an ideal 857 GHz back-to-back horn simulated at 730 GHz using GRASP9. [credit Dan Wilson, Maynooth University]**

For the non-ideal cases significant variations are visible in the sidelobe at $72^{o}$ off-axis as expected due to the effects of the imperfections on the sidelode levels of the horn farfield beam patterns (which are of course essentially mapped onto this part of the sky by reflection from the secondary mirror). In the "plausible" case of 5 corrugations filled at the front of the tapered section, the edge of the sidelobe rises from the ideal level of less than 10 dB to approximately 20 dB. In the worst case of filled corrugations at the throat of the horn in addition to the peak edge rising to 20 dB the sidelobe peak at $72^{o}$ increases by 10 dB from 20 dB to 30 dB. Thus the main beam is unaffected by the filled corrugations (as shown earlier in section 4.2) and thus the peak at $80^{o}$ off-axis due to main beam spillover is unaffected in both cases. The overall effect of these changes on the shape of the FSL is there exists the possibility to couple more power to the telescope for the cases with imperfections in the horn corrugations when compared to a perfect horn profile.

163
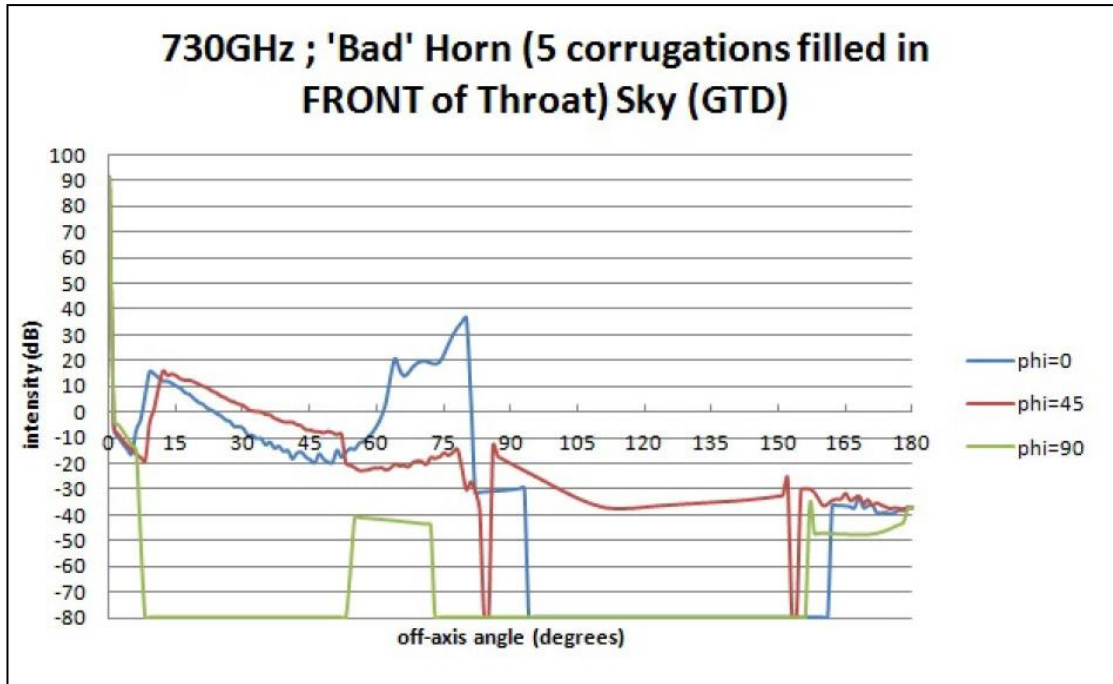
**Figure 4-34 : Beam on the sky for an plausible (or bad) case where 5 corrugations are fully filled at the front of the tapered section of the 857 GHz front horn simulated at 730 GHz. [credit Dan Wilson, Maynooth University]**
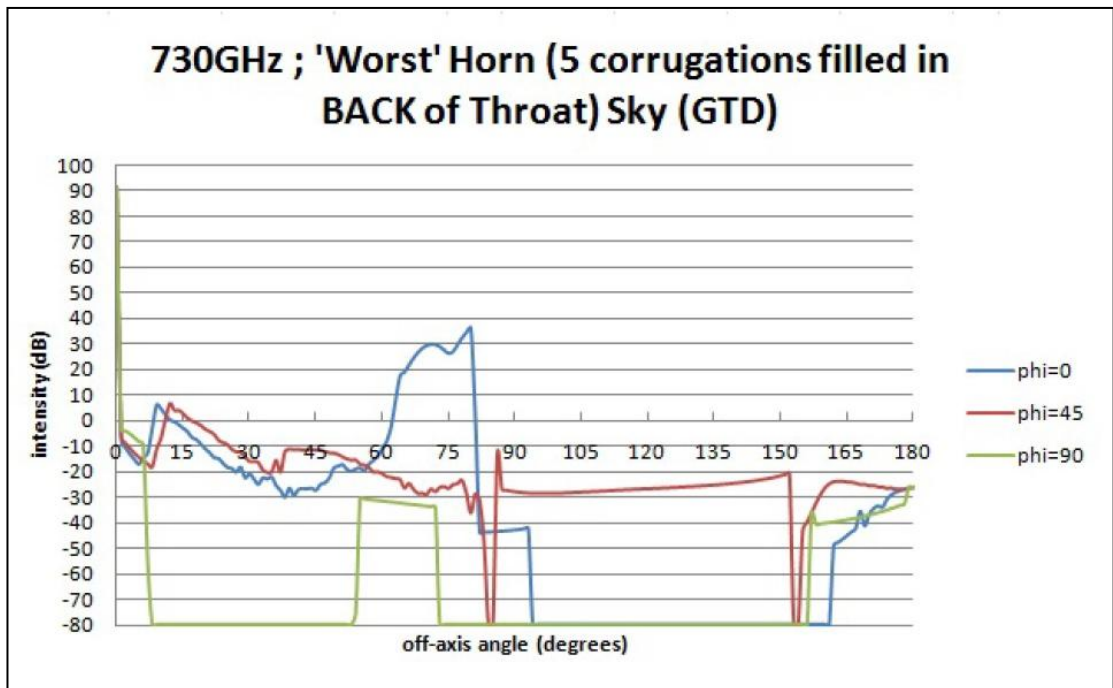


**Figure 4-35 : Beam on the sky for an plausible (or bad) case where 5 corrugations are fully filled in the throat area of the 857 GHz front horn simulated at 730 GHz. [credit Dan Wilson, Maynooth University]**

Clearly from the simulations of the telescope using GRASP9 by Daniel Wilson [Wilson, 2014] the far-out sidelobe feature between about $61^o$ and $77^o$ is due to spillover of the horn beam past the primary mirror at effective angles greater than $27^o$

as viewed by the horn. This primary mirror spillover is nearly aligned with the spin axis of the spacecraft, and therefore scans very little of the sky on 1 minute time-scales [ Planck Collaboration, 20141b]. When this sidelobe overlaps with the galactic plane, the telescope main beam will be pointing somewhere between $61^o$ and $77^o$ away from this direction. This sidelobe will remain aligned with the galactic plane for a time as the telescope rotates about its spin axis and the main beam sweeps over an area of the sky. This is consistent with the "banana" features in two of the difference maps shown in Figure 4-1 as this sidelobe level could vary by up to 10 dB as is clear from Figure 4-33- Figure 4-35, and clearly in the perfect "ideal horn" scenario (Figure 4-33) we might expect little residual signal which is most likely the case for the 857-2 channel (i.e. this horn might well not have damaged or filled corrugations). It had been planned that these all sky realistic telescope beams would have been used in simulations by the Planck data analysis team but to date this has not yet taken place (although it is still possible in the future).

# 4.7 Conclusions

In this chapter motivated by a higher than expected far sidelobe signature detected at 857 GHz the author of this thesis has examined the effects of possible manufacturing tolerances and the limitations of the electroforming process on the beam patterns of the multi-moded 857 GHz channel. The difference map between two sequential all-sky Planck surveys, shown in Figure 4-1, revealed the significant variations in the far sidelobe levels of the 857 GHz Channels between the flight horns. In fact some mechanical imperfections were found during the pre-flight visual inspections of the horns and where possible corrective actions were taken. However, due to the size and geometry of the horns this does not preclude the possibility of remaining defects in certain sections of the horn going undetected.

To begin this investigation into the effects of possible imperfect corrugations upon the sidelobes of the beam patterns of the horn, a number of plausible scenarios were investigated. To mimic the fact that some residual aluminium from the mandrel might remain unetched, five corrugations were "filled" in the geometry file in the

different sections of the perfect horn profile and the beam patterns at 857 GHz were simulated using SCATTER. It was found that, depending on where the corrugations were made non-ideal, there was quite a variation in the effect on the beam patterns for example no deterioration was seen for defects within the waveguide filter or there could be a rise in the sidelobe levels as power is scattered into higher order modes as particularly when corrugations were altered in the throat or tapered section of the front horn. The effects of filling different numbers of corrugations were also investigated and it was found that as few as one or two fully filled corrugations could have increased the sidelobe levels if they occurred in the throat area. In general the greater the number of corrugations filled the greater the distortion of the beam pattern and the higher the sidelobe levels.

The test cases for five sequentially filled corrugations were then simulated at 460 GHz (a frequency where the 857 GHz Horn is single moded and at which laboratory tests were made) and compared to the perfect horn to determine which sections produced effects that would have been noticed in the pre-flight test measurements. It was found that filled corrugations at the front of the tapered section and into the adjoining parts of the parallel phasing section produced an increase in the sidelobe levels that might not have been noticeable within the experimental errors of the single mode pre-flight measurements at 511 GHz. Meanwhile filled corrugations behind this point in the throat area of the horn produce an increase in sidelobe levels which would have been larger than the experimental error and in some cases would have resulted in distortion of the main beam itself, especially for non-ideal corrugations in the throat area.

Broadband beams for these mechanical tolerance test cases were also created by simulating the beam patterns at a number of spot frequencies across the band and then summing the fields in quadrature. As for the perfect horn (shown in the previous chapter) the central frequency 857 GHz proved to be a good representation of the broadband beam pattern. This was not entirely expected as the variation of the beam pattern sidelobes with frequency was not expected to be as predictable as those for the perfect horn. However, the variations in the sidelobe levels proved to be remarkably stable in terms of the level across the band and thus the central frequency in fact still provided a useful representation of the broadband beam pattern.

Next the effects of other types of mechanical imperfections were tested such as partially filled (i.e. partially etched), narrow, and wider corrugation slots (corresponding to poor copper growth) on the beam pattern. For the corrugations filled to half their depth the resulting beam patterns showed similar increases in (and in some cases higher) sidelobe levels to the corresponding horn with fully filled examples. This can be understood by considering that the depth of the corrugations is critical to the horn design in achieving the desired beam pattern (see Chapter 2 Section 2.8 on hybrid modes). Narrowing the corrugations (i.e. widening the fins between the corrugations) results in an increase in sidelobe levels compared to the ideal horn but to a lower level than when the corrugations are fully or partially filled. Finally widening the corrugations had little effect in the beam pattern of the horn. This is not unexpected as the hybrid mode theory of corrugated waveguide design assumes a thin fin between the corrugations without specifying its width.

The final possible type of mechanical defect investigated was that of completely missing fins between the corrugations. As for the simulations of filled corrugation slots a series of scenarios with different numbers of missing fins in each section of the horn were simulated. The results of these simulations for each scenario were broadly comparable to those for the equivalent filled corrugations, in other words removing fins and filling corrugations slots in the same area had an effect of similar magnitude on the sidelobes of the beam pattern.

The simulations of beam patterns for the non-ideal horn antennas were compared to pre-flight measurements of the flight horns. It was shown that it was possible to fit beam patterns for the ideal horn and for horns with mechanical defects to the test data within the experimental error of the measurements. Thus, it was shown to be possible that variations in the profile of the corrugations associated with manufacturing tolerances could produce increased sidelobe levels while not affecting the main beam and that these effects may not have been detectable in pre-flight tests. It should be emphasised here that in terms of the main beam and the edge taper the horn still behaves essentially as specified by the Planck requirements and only the spillover sidelobe structure is affected.

The results of the modelling of the Planck telescope by Daniel Wilson in his thesis [Wilson, 2014] using the author's beam pattern simulations as input were

presented. This work showed how the non-ideal horn corrugations could indeed lead to variations in the far-out sidelobes of the beams on the sky. These differences in the sidelobes compared to those of a "perfect" horn profile will couple more power to the telescope and explain the banana feature seen in some of the survey difference maps of the 857 GHz channels due to manufacturing tolerances or damage on launch.

# Chapter 5 Analysis of Pre-Launch Test Campaign Data for Planck HFI Multimode Channels

## 5.1  The Cardiff Pre-Launch Test Campaign

It turned out  not to be possible to fully test a full 857 GHz pixel (back-to-back horn, detector horn, and bolometric detector) in the laboratory during the pre-launch testing phase of Planck-HFI.  One of the critical issues for the 857 GHz channel from the point of view of both resolution and sensitivity was to what extent it was truly multi-moded, which is important because the more modes that propagate through the filter in the front back-to-back horn, the more power that is transmitted to the detector. More modes also means a wider beam illuminates the telescope as long as the edge taper requirement is still met.  The 857 GHz back-to-back and detector flight horns were actually tested at lower frequencies (460 GHz and 511 GHz) where their operation was single moded.  As explained in the last chapter these pre-launch verification tests were aimed at checking the integrity of the corrugations of the horns and were not ultimately a test of their multi-mode characteristics.  However, Cardiff University did perform a laboratory campaign (in 2008) on the prototype qualification horn to determine if the 857 GHz back-to-back horn section of the pixel was truly multi-moded at its operational frequencies.

Two different types of tests were actually performed at Cardiff to probe the multimode nature of the back-to-back horns.  Antenna response tests were made where the Planck multimode horns were rotated about their phase centre to map out their beam patterns.  For this test a black body source was placed in the farfield, as viewed by the horn, and the receiver was rotated.  Single frequency measurements using a coherent source were also made at spot frequencies within the 857 GHz band.  Beam profile measurements were furthermore made where the Planck back-to-back horn was fed radiation from a telescope simulator, in which a black body source was moved in

the object plane of the telescope simulator to scan the image of the source across the horn aperture and thus map out the telescope beam profile. A He3 detector system within a cryostat with a large window and sufficient room to incorporate the Planck back-to-back horn pair with its entrance aperture close to the window was used for an integrated pixel test (see Figure 5-1) although initially the back-to-back pair was placed outside the cryostat. However the actual Planck 0.35K detector itself was unavailable so instead a standard parabolic (Winston cone) triple horn relay was setup internally in the cryostat with the Planck back-to-back horn located externally as shown in Figure 5-1 (in the initial set-up).
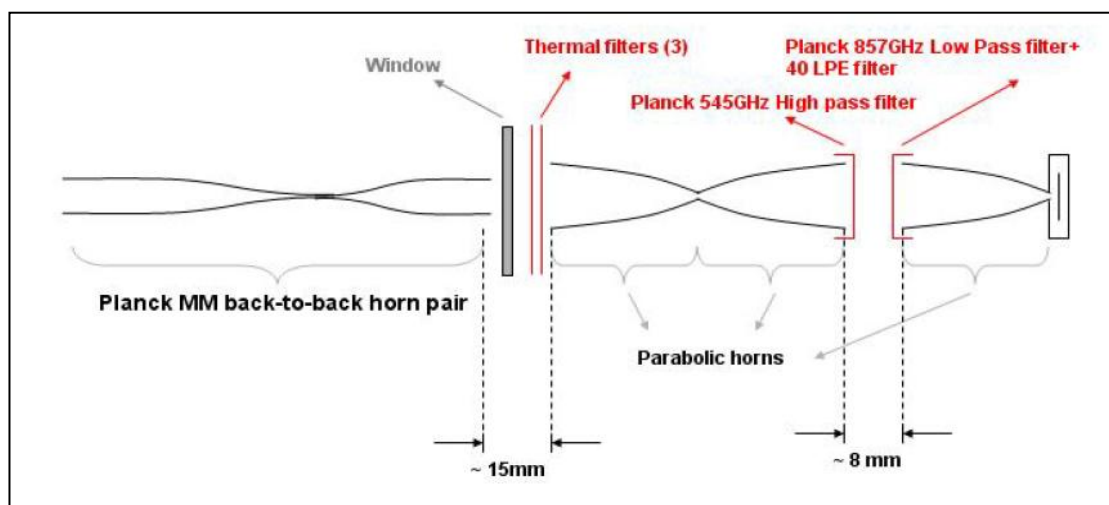


**Figure 5-1 : Test set up used by Cardiff University for multi-mode spot frequency tests. [credit: Cardiff University]**
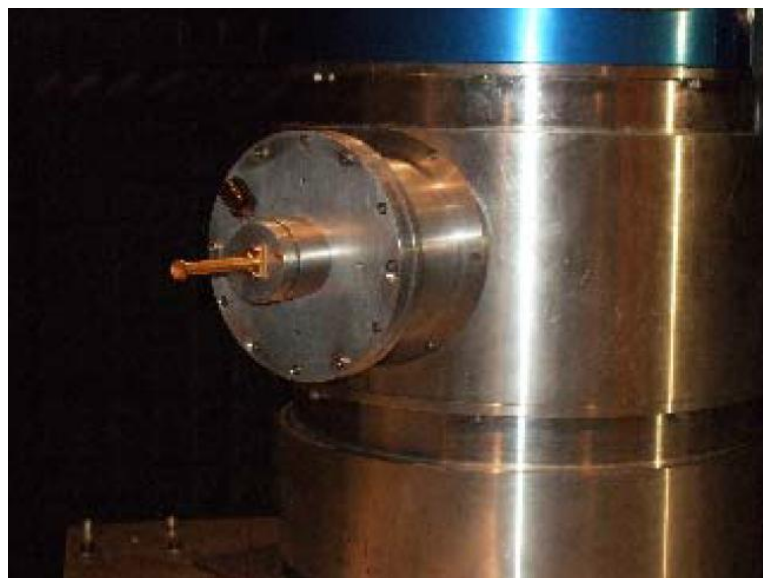


**Figure 5-2 : An 857 GHz back-to-back horn under test at Cardiff University. [credit: Cardiff University]**

Thermal filters were used between the window and the back-to-back horn pair to reflect out near-infrared power. Band selection was made using a combination of the Planck-HFI 857 GHz low pass filter and 545 GHz high pass filter positioned in front of the detector horn. The initial approach of only using the back-to-back horn pair externally was validated by measuring the change in the antenna pattern with coupling between the internal and external horns (Figure 5-4). The gap through the cryostat window was investigated by measuring the beam pattern of the back-to-back horn for varying distances between it and the parabolic horn pair without changing the position of the Planck horns relative to the source. The plot of these beam patterns shown in Figure 5-3 reveals little change in the coupling with varying distance. The spectral response of the system was further verified using an FTS (Fourier Transform Spectrometer) to verify the correct Planck pass band. The spectral responses of the 857 GHz low pass filter and 545 GHz high pass filter are shown in Figure 5-5.
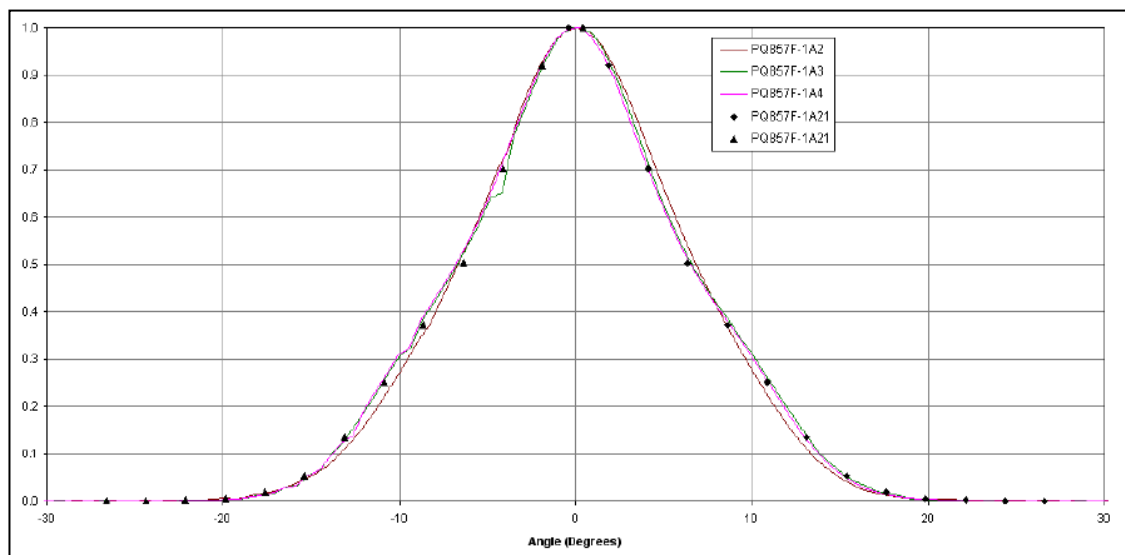


**Figure 5-3 : Linear plot of the beam patterns for varying distances between the parabolic horn pair and the Planck back-to-back horn. [credit: Cardiff University] (note: the exact distances are not known to the author)**

The results of the broadband measurements of the beam pattern of the 857 GHz back-to-back horn using the mercury arc lamp (MAL) as a blackbody source are shown in Figure 5-6. The SCATTER simulations of the horn broadband beam pattern and spot frequency beam pattern at 857 GHz are also plotted in the same figure for comparison. It is clear that there is significant discrepancy between the measured beam patterns and the SCATTER simulations. The beams measured in the tests are

171

narrower than the SCATTER simulations which are also more top hat like than the measured beams.
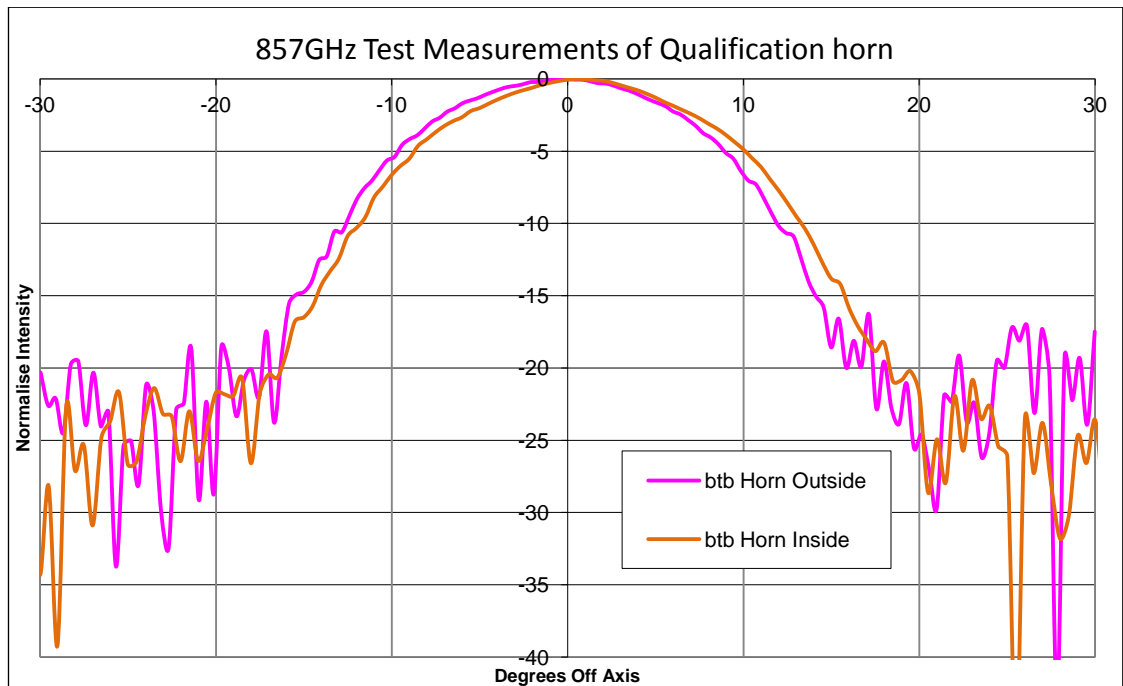


**Figure 5-4 : Plot of Cardiff 857 GHz back-to-back horn broadband test measurements inside and outside the Dewar window [credit:  Cardiff University].**
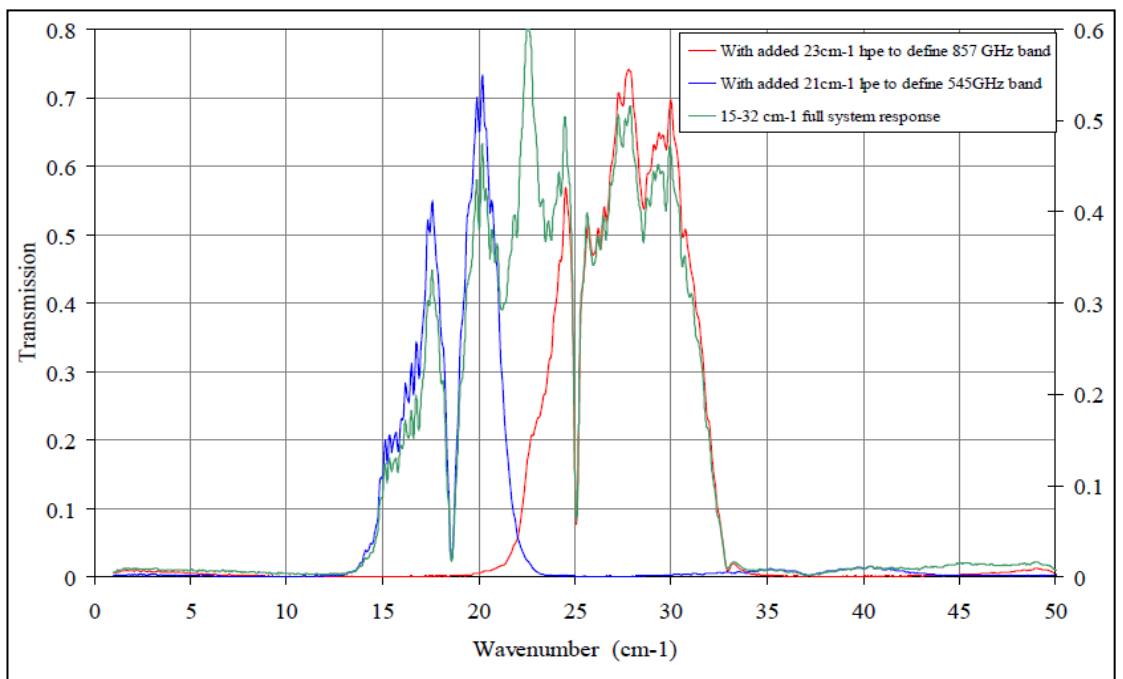


**Figure 5-5 : Plot of the spectral responses of the high and low pass filters used by Cardiff University.  [credit: Cardiff University]**
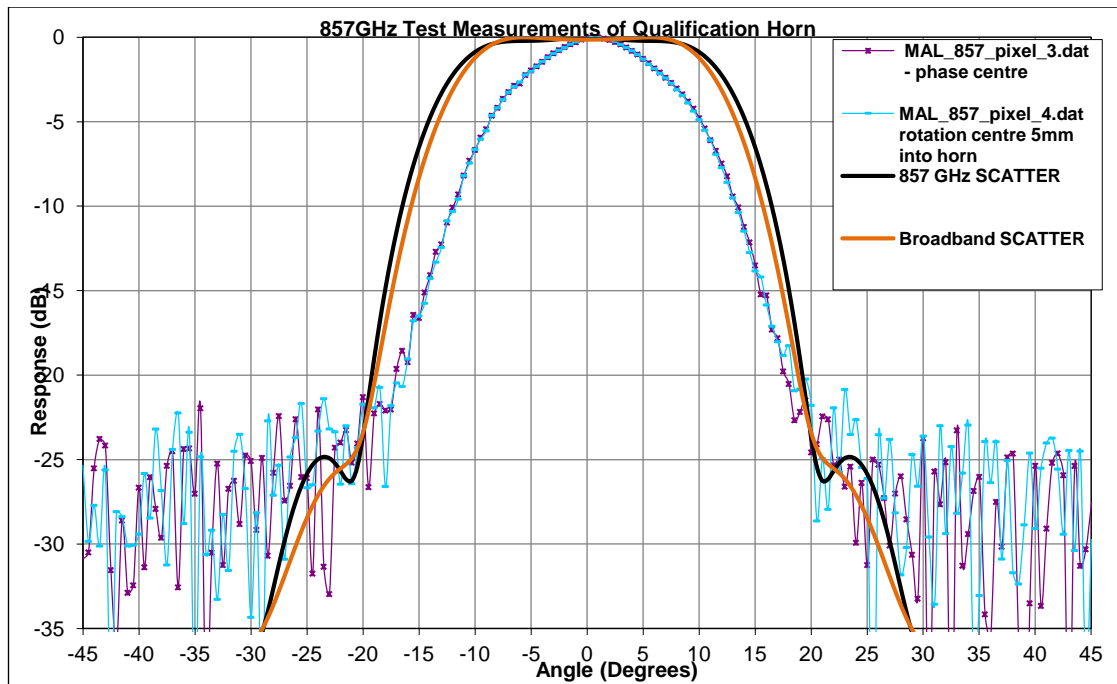
**Figure 5-6 : Plot of the test measurements varying the position of the centre of rotation to check the effect on the beam pattern of the 857 GHz Back-to-back horn using the broadband MAL source [credit: Cardiff University]. SCATTER simulations of the broadband beam pattern and at 857 GHz are shown for comparison.**

Two variations of the setup as outlined above were used for these measurements: one with the Planck 857 GHz back-to-back horn assembly outside the Dewar window and the other with the horn inside the Dewar window (the position of the back-to-back horn in both cases is shown in Figure 5-7) to determine if having the back-to-back horn external was the reason the beams were narrower than those predicted by SCATTER. Measurements of the broadband beam pattern were made for both configurations and the data are similar as can be seen in the 857 GHz test plots in Figure 5-4. In both configurations the noise floor of the measurements is about -20 dB and encountered at approximately $17^{o}$ to $21^{o}$ off-axis. The measurement test data for each of the configurations are also asymmetric about the on-axis direction. This was clearly caused by a practical asymmetry in the experimental setup. However, the exact cause is not known as precise knowledge of the experimental setup was unavailable from Cardiff but is most likely due to a reflection from a plane surface on one side. In Figure 5-8 the data for the negative and positive angles have been averaged to reduce the effect of the asymmetry. The beams measured in the tests are again narrower than the SCATTER simulations at each frequency, the Cardiff measurement reaches the -10dB level at approximately 12 degrees whereas the SCATTER beam pattern reaches -10dB at approximately 16 degrees off-axis. To

173

determine whether these differences between the measured beam patterns and the SCATTER simulations were due to effects present across the band or just at particular frequencies further testing was undertaken at Cardiff.
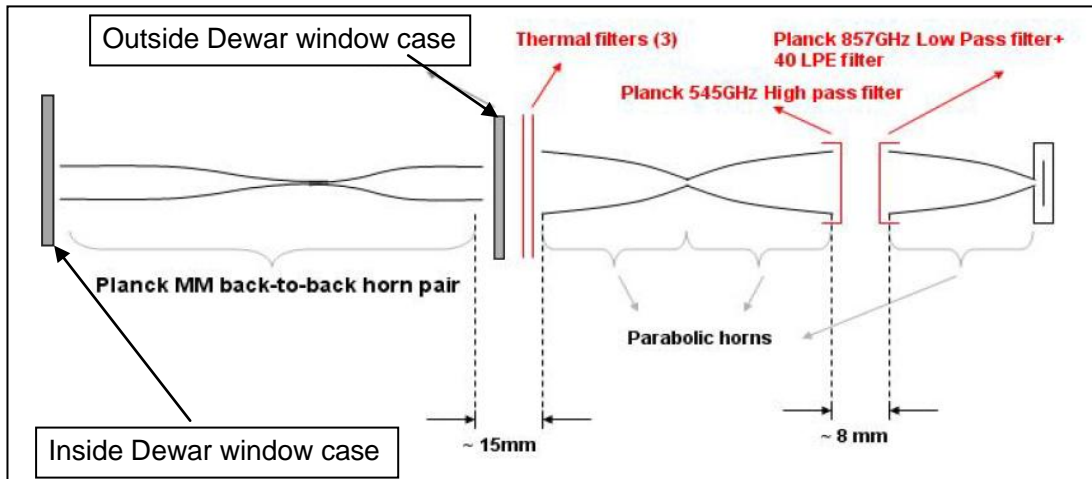


**Figure 5-7 : Diagram showing the position of the horns relative to the Dewar window for the cases of the back-to-back horn pair located either inside or outside the cyrostat.**
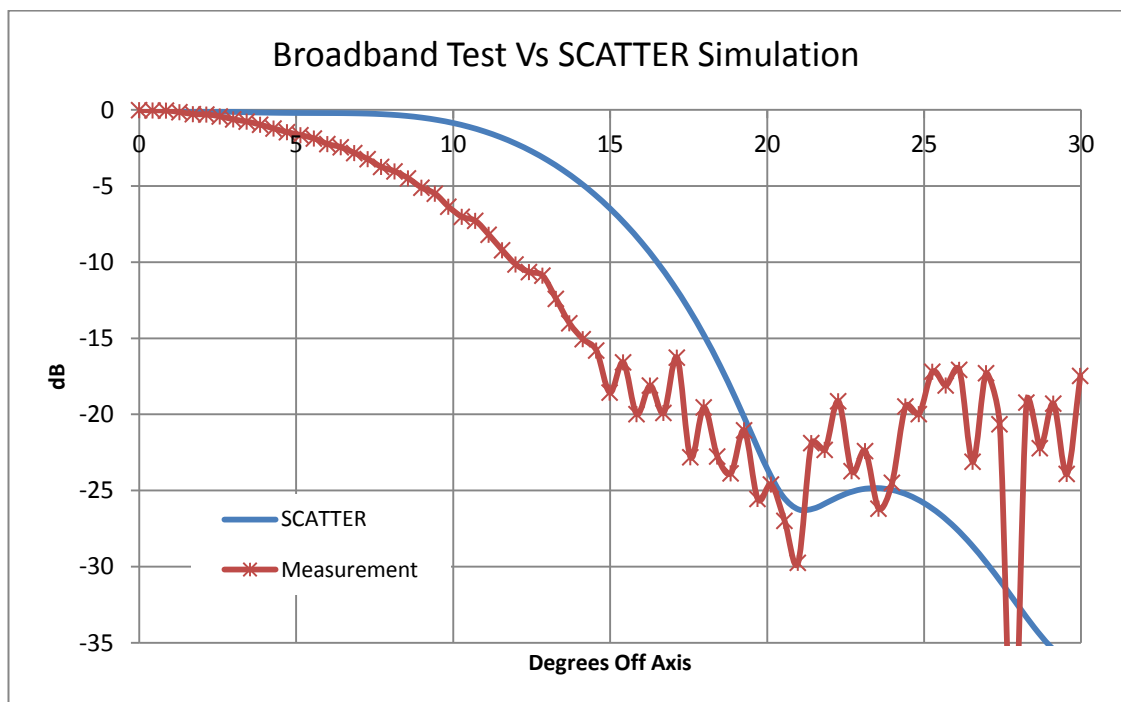


**Figure 5-8 : Cardiff test measurement versus SCATTER simulation at 857 GHz. The data for the negative and positive angles has been averaged to reduce the effect of the asymmetry.**

These test measurements were made at four spot frequencies in the lower end of the band, 730 GHz, 780 GHz, 819 GHz, and 844 GHz where it was possible to make such measurements. The polarisation of the coherent source was not specified in these tests although it was expected the beam should be symmetric in any case. The

174

test measurements were compared with SCATTER simulations at the corresponding frequencies and also the SCATTER broadband beam simulations already presented (Figure 5-9 and Figure 5-10). At least two measurements were made at each frequency as can be in Figure 5-9 with three beam measurements made at 842 GHz (test numbers 18, 21, and 22). Figure 5-10 shows one measurement from each of the spot frequencies (740 GHz, 780 GHz, 820 GHz, and 840 GHz) and once again the data for the negative and positive angles have been averaged to reduce the effect of the asymmetry in the measurements. In these figures the discrepancies between the measured beam patterns and the simulated beam patterns predicted by SCATTER at each of the spot frequencies can be clearly seen. The beams measured in the tests are still narrower than the SCATTER simulations at each frequency, for example at 740 GHz the Cardiff measurement reaches the -10dB level at approximately 12 degrees whereas the SCATTER beam pattern reaches -10dB at approximately 16 degrees off-axis. The SCATTER simulated beam patterns are again as expected also more top-hat like in shape than the measurement beam patterns.
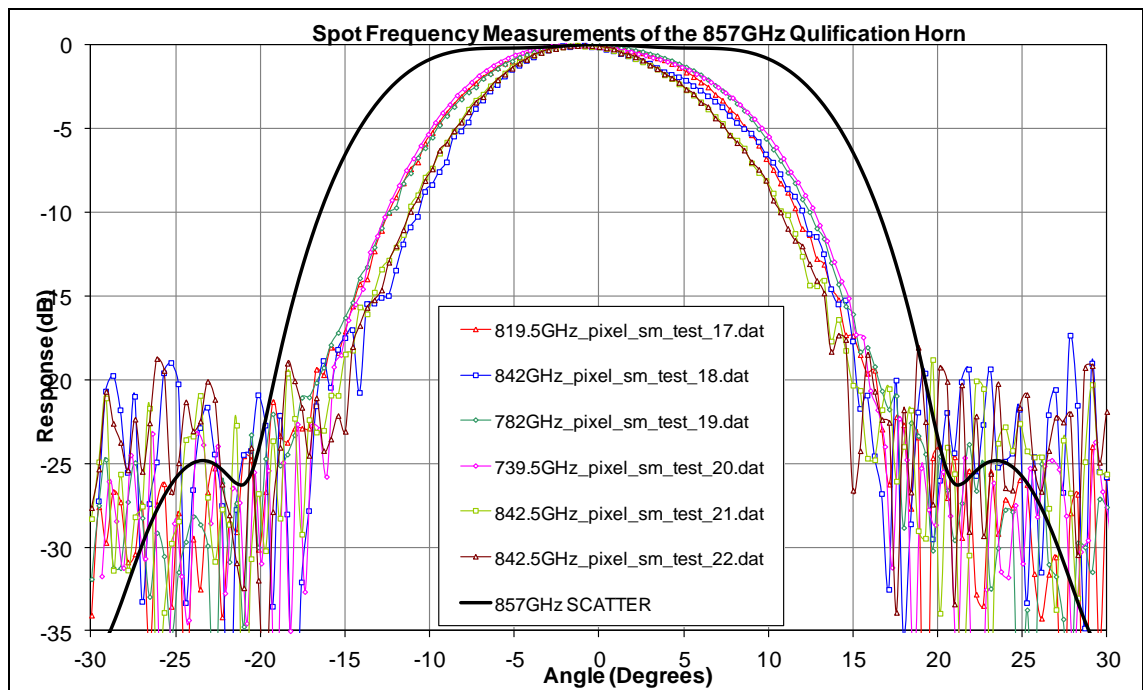


**Figure 5-9 : Plot of the Cardiff test measurements at each of the spot frequencies of the beam pattern of the 857 GHz back-to-back horn [credit: Cardiff University]. The SCATTER simulation of the beam pattern at 857 GHz are shown for comparison.**
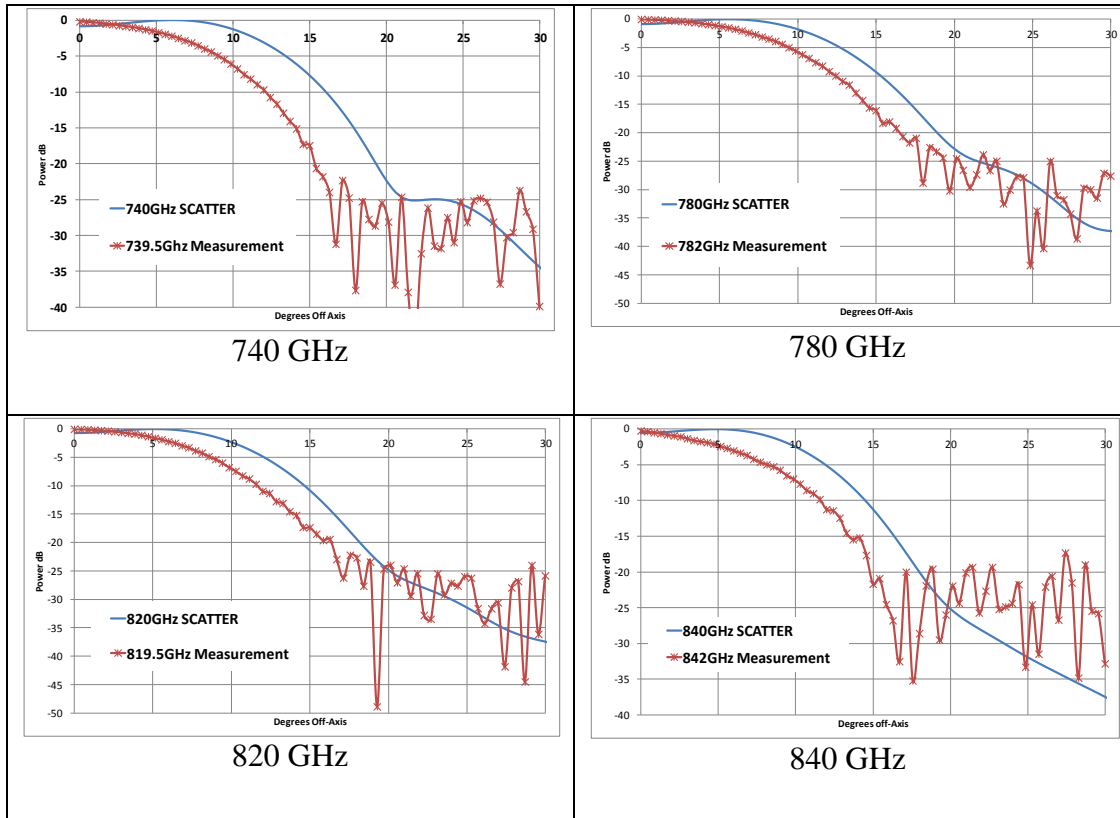
**Figure 5-10 : Cardiff spot frequency test measurement versus SCATTER simulation at 740 GHz, 780 GHz, 820 GHz and 840 GHz. In each case the SCATTER simulation is shown in blue and the Cardiff measurement in red. The data for the negative and positive angles has been averaged to reduce the effect of the asymmetry.**

There are a number of possible reasons for the discrepancy between the measured beams and the predicted beams and these clearly needed to be investigated. Some of the higher order modes would appear to be missing or at least reduced in amplitude or intensity resulting in the narrower test beams. This could be due to losses in the corrugations due to resistive losses in the metal walls. There may also be some effects due to manufacturing imperfections (see Chapter 4) that may cause higher order modes to be reflected and not transmitted efficiently through the waveguide filter. Another alternative is the relay system horn apertures are not matched to those of the back-to-back horn and there may be reflection of the higher order modes within the system.

In order to make progress in this analysis first the extent to which particular higher order modes contribute to the beam width given their particular off-axis nature was investigated by the author of this thesis. A best fit to the measured beams of the possible modes that could in theory propagate using a simple curve fit 'by inspection' was undertaken. Following on from this an alternative a MATLAB routine for fitting positive real functions (i.e. intensity patterns of the hybrid mode farfields) was applied

176

to the measured beam patterns where only positive coefficients for the sum are clearly allowed. Finally the issues associated with the relay system of the Winston cones (parabolic profiles) with possible mismatches occurring between the beams was examined, through a scattering matrix multimode analysis, and the conclusions drawn from this analysis work is summarised at the end of this chapter.

Before beginning this study it is important to address the question of how to measure the "beam-width" in a consistent way (since there is clearly a discrepancy between the size of the measured and the predicted beams). The beam shapes are not Gaussian or cosine-like so that normalizing the intensity to 0 dB on-axis and using the full width at half max (FWHM) is not necessarily best way to compare beams, especially as the beams in theory should be multimoded and more top-hat like. Therefore, the parameter used to investigate the comparisons was the included power in the beam inside a given radius $\theta_{1/2}$. The width of the beam is then taken as being the angle at which the included power is at the 50% level.

As can be seen in the plots above (Figure 5-8, to Figure 5-10) at approximately -25 dB the measured data reaches a noise floor. The noise levels are high enough that it is necessary to neglect data from the measurements beyond about 18 degrees off-axis so that we have to truncate the analysis at 18 degrees. When the included power as a function of angle was calculated using

$$P(\theta) = \frac{\int_0^\theta I(\theta')\theta'\,d\theta'}{\int_0^{\theta_m} I(\theta')\theta'\,d\theta'} \tag{5.1}$$

where $\theta_m$ was the angle at which the data became too noisy. The averaged data for the positive and negative angles were used and plots, similar to those for 857 GHz as shown in Figure 5-11, were obtained for each of the test frequencies. These plots thus show the power contained inside the area within the angle off-axis $\theta$ increasing from zero on-axis to the normalised maximum of unity at 18 degrees (as this is the entire beam width for this truncated plot). From these the useful included power beam widths were found by locating the angle at which the normalised power reached the 0.5 level. The resulting included power beam widths at 857 GHz for the

simulated beam pattern and measured beams, both in the case of the back-to-back horn inside and outside the cryostat, are listed in Table 5-1.

| Beam Pattern | $\theta_{1/2}$ (degrees) |
|---|---|
| Simulated | 8.5 |
| Measurement Inside Dewar | 6.65 |
| Measurement outside Dewar | 6.85 |

**Table 5-1 : Widths of the simulated and measured broadband beams of the 857 GHz back-to-back horn using 50% power included level.**
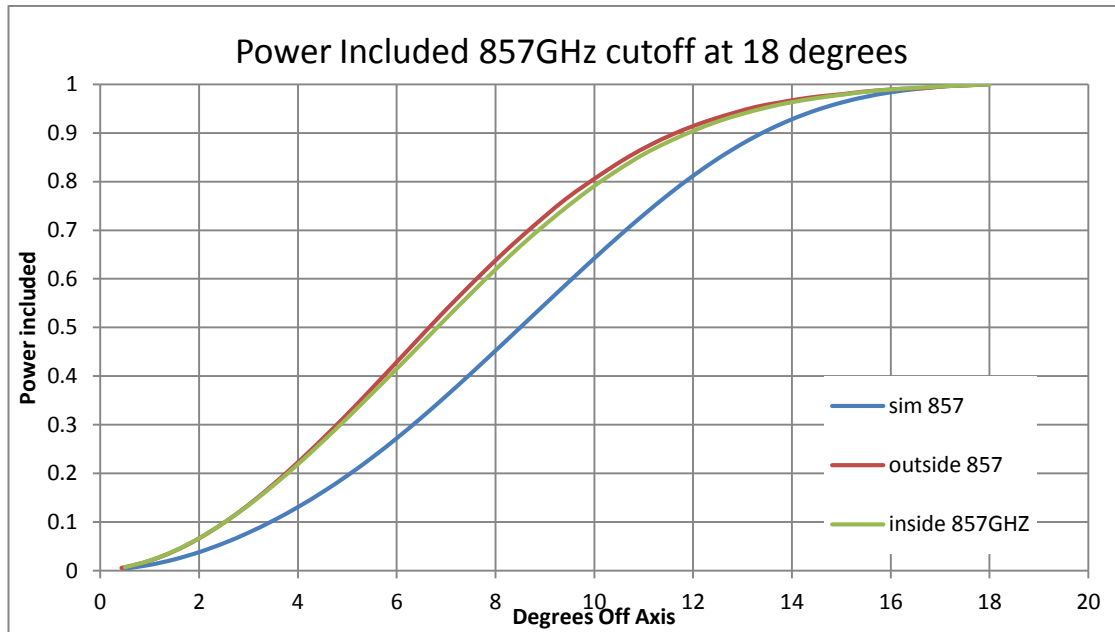


**Figure 5-11 : Plot of the normalised power included for test measurements made for the cases of the 857 GHz horn inside and outside the cryostat and simulated beam at 857 GHz.**

Both of the measured beams have similar widths which are narrower than the simulated beam pattern. At the other spot frequencies at which measurement were made, the results of the analysis are similar to the measured beam widths being narrower than those of the SCATTER simulations (see Table 5-2). This clearly suggests, of course as stated earlier, that the higher order mode content of the measured beams is reduced somewhat. The question now was how to determine which modes seem to be missing from the beams. Clearly some of the higher order modes are missing, as if they were present, they would give power further off-axis. This is now investigated in the next section.

| Frequency (GHz) | Measured beam width (degrees) | Simulated beam pattern width (degrees) |
|---|---|---|
| 739 | 6.4 | 8.1 |
| 780 | 7 | 8.5 |
| 819 | 6.4 | 7.5 |
| 844 | 6.5 | 7.8 |
| 857 | 6.7 | 8.5 |

**Table 5-2 : Beam widths for the simulated and measured beam patterns for the spot frequencies measured by Cardiff.**

## 5.2 Investigation of the Modes Content of the Beam

A scattering matrix analysis of a multimode horn (such as used in SCATTER) expresses the fields at the horn aperture in terms of the waveguide mode basis set. These waveguide modes are then propagated to the far-field in SCATTER to enable the beam pattern to be computed. In modelling the back-to-back horn we assume that when acting in reception any power that is transmitted through the waveguide filter is absorbed by the detector. We have shown in Chapter 3 that this is a reasonably good approximation and that therefore when invoking reciprocity the waveguide is effectively fed by a blackbody at the entrance port. This means all waveguide modes can exist at the entrance port but evanescent modes are quickly attenuated leaving only those modes that propagate. These waveguide modes are the usual TE and TM modes of smooth walled cylindrical waveguides so as they propagate they are scattered into coherent combinations of modes that we recognise as the hybrid modes, of which there are only a finite number as discussed in Chapter 3. Thus the large number of TE and TM modes at the entrance port get scattered into a much smaller number of hybrid HE and EH modes arriving at the output port and propagating to the farfield of the horn.

TE and TM Modes for *n* = 1

TE and TM Modes for **n=0**

*n* = 0

TE and TM Modes for n = 2

*n* = 2

TE and TM Modes for **n=3**

*n* = 3

TE and TM Modes for **n= 4**

*n* = 4
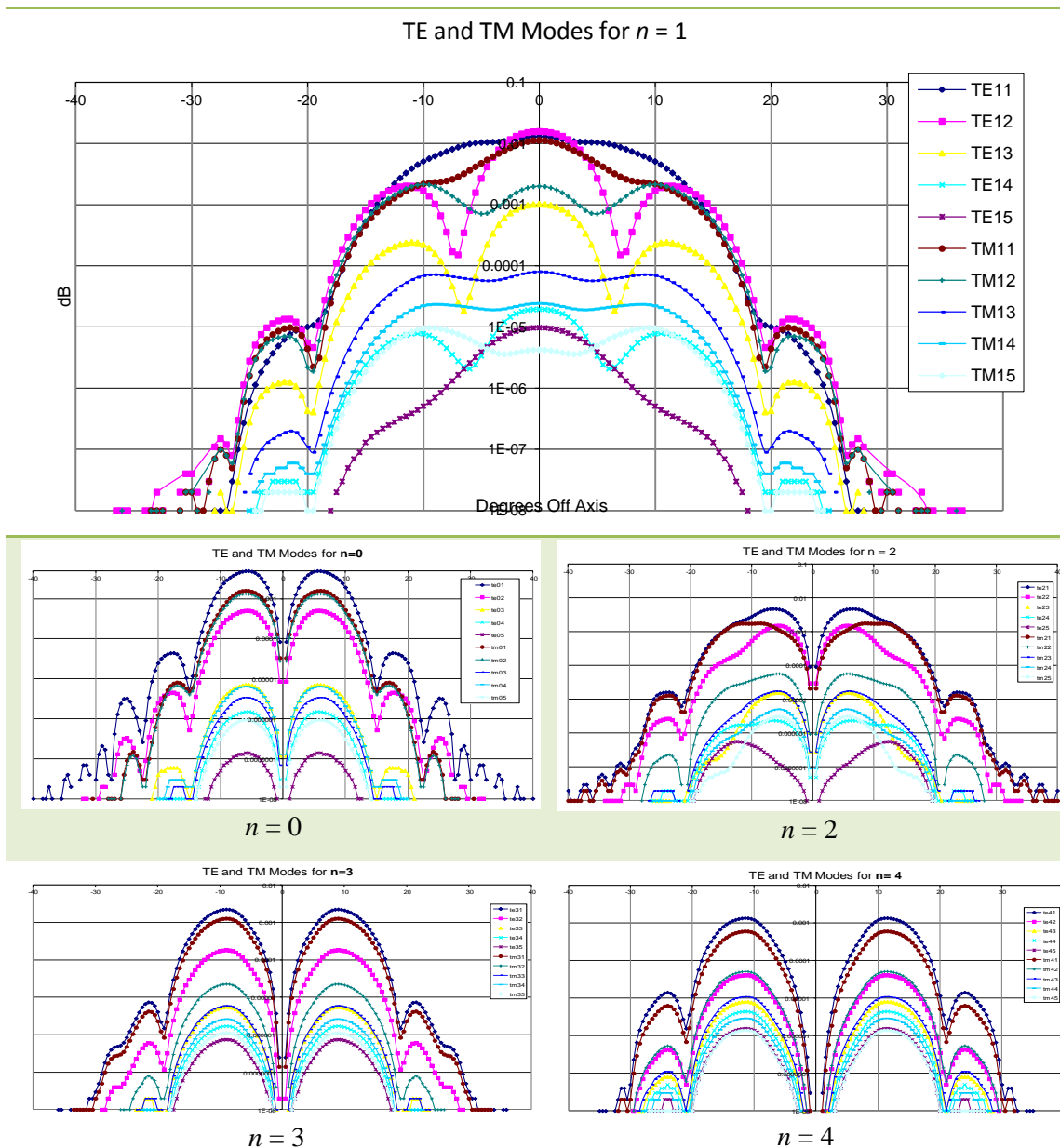
**Figure 5-12 : The farfield beam patterns of the first 5 TE and TM waveguide modes of order *n* = 1 (top plot) and *n* = 0, 2, 3, & 4 for the 857 GHz Horn.**

Therefore in order investigate the mode content of the test measurements it was necessary to first gain an understanding of which cylindrical TE and TM modes were used in SCATTER (to describe the beam) and how the modes of each azimuthal order in particular contribute to the overall farfield beam width. The farfield patterns of the first five input TE and TM modes of azimuthal orders *n* = 0 to 4 for the 857 GHz horn are shown in Figure 5-12. The output farfields are listed for the different input modes at the input plane (the input to the waveguide filter of the back-to-back horn) of the scattering matrix analysis assuming this will give us a good description of the horn (as explained in Chapter 3). Only modes of order *n* = 1 carry any power on-axis, whereas

all modes of azimuthal order other than $n = 1$ have a zero on-axis. Thus as the measured beams do not have a central (on-axis) null there must be some modes of order $n = 1$ present. Also given that the measured beams are narrower than predicted suggests that modes which contribute power further off-axis, such as those of azimuthal order other than $n = 1$, may be attenuated or missing. Clearly many of these plots have very similar shapes for the farfield patterns. These plots in fact all correspond to different TE and TM modes at the input plane in the analysis of the horn. Such modes scatter into essentially a few hybrid mode fields at the aperture as stated above and so we can especially see this where there is only one hybrid mode of order $n = 2$ and all the $TE_{2n}$ and $TM_{2n}$ scatter into this hybrid mode only so the farfield patterns are identical in shape (and just vary in amplitude).
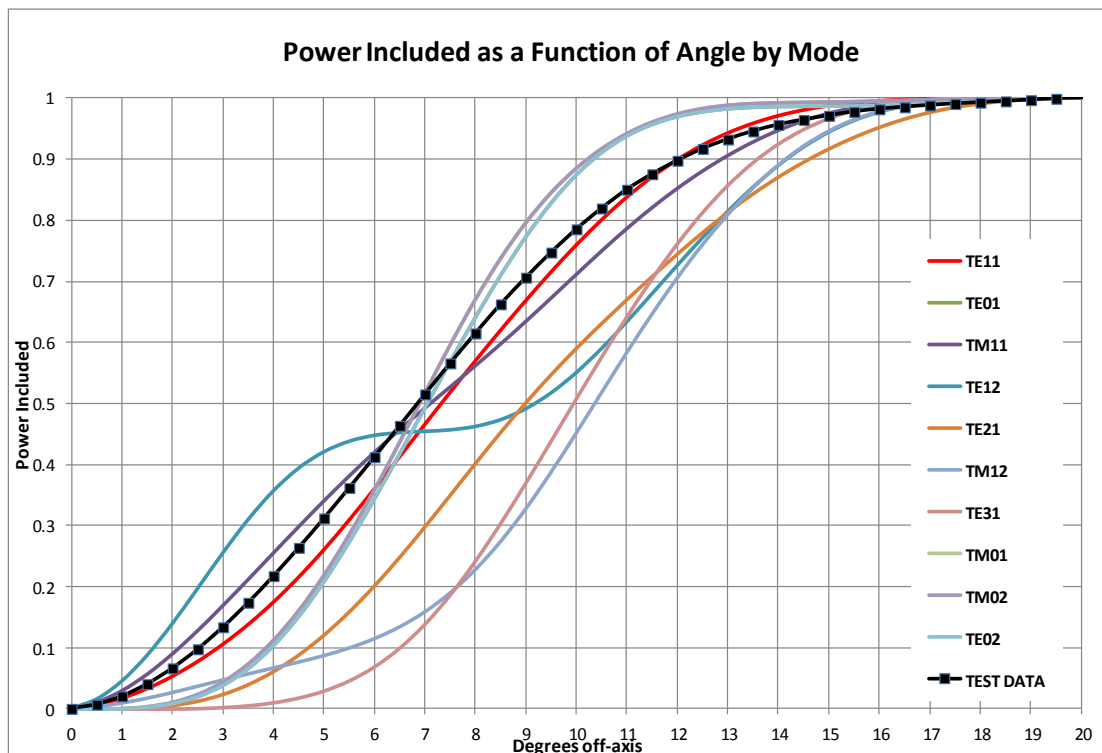


**Figure 5-13 : Plot of the power included in each TE and TM mode at 857 GHz.**

Let us return to the included power as a function of angle in this case calculating it for each individual input waveguide mode at a single frequency of 857 GHz (see Figure 5-13) in order to determine which modes have a beam width compatible with the measured data and which are too wide and so must be missing or greatly attenuated. As a first approximation the $TE_{11}$ mode was compared to the test data but this mode on its own is too wide which is rather surprising, but this input mode obviously scatters to higher order $n = 1$ modes that are too wide to be consistent

with the measured beam. Other modes such as the $TM_{11}$ actually have beam widths closer to that of the test data. Next various combinations of the farfield of the input TE and TM modes of different azimuthal orders were summed together in quadrature. The power included per angle was calculated for each of these combinations and plotted against the test measurements in order to get a fit to the data at 857 GHz (see Figure 5-14 and Figure 5-15) in a trial and error fashion. Some combinations of lower order input waveguide modes of azimuthal order 0 and 1 (e.g. $TE_{11}+TM_{11}+TE_{01}+TE_{12}$) have widths similar to the test data (Figure 5-15). However, the addition of input modes of azimuthal order 2 or 3, for example $TE_{21}$, increase the beam width to angles beyond that of the test data (Figure 5-14). This seems to indicate that the test measurements at 857 GHz are multi-moded but that modes of order higher than $n = 0$ or 1 do not appear to be present as predicted from theory of a perfect Planck pixel. For example, again for $n = 2$ there is clearly only one hybrid mode present at the horn aperture and many of the $TE_{2l}$ and $TM_{2l}$ modes can scatter into this hybrid mode (the $HE_{21}$ mode) to a greater or lesser extent as we can see in Figure 5-12. The higher order $n = 2$ hybrid modes are attenuated completely. This is consistent with the discussion on hybrid modes in Chapter 2. For the $n = 1$ case it is a little more complicated. In fact there are 3 hybrid modes present and all of the input $TE_{1n}$ and $TM_{1n}$ modes couple to coherent combinations of these to a greater or lesser extent. The plots for all of these farfields however show clearly where off-axis the power tends to be concentrated for the different orders. We can now derive the included power for all these fields as a single parameter useful for expressing where the power is concentrated and what the effective beam widths are for these modes. The results are presented in Figure 5-15 where the included power plot for the test data matches quite well a combination of $TE_{11}$, $TM_{11}$, $TE_{01}$ and $TM_{01}$ (with equal contributions from each mode-clearly an approximation- but the fit is actually very good).
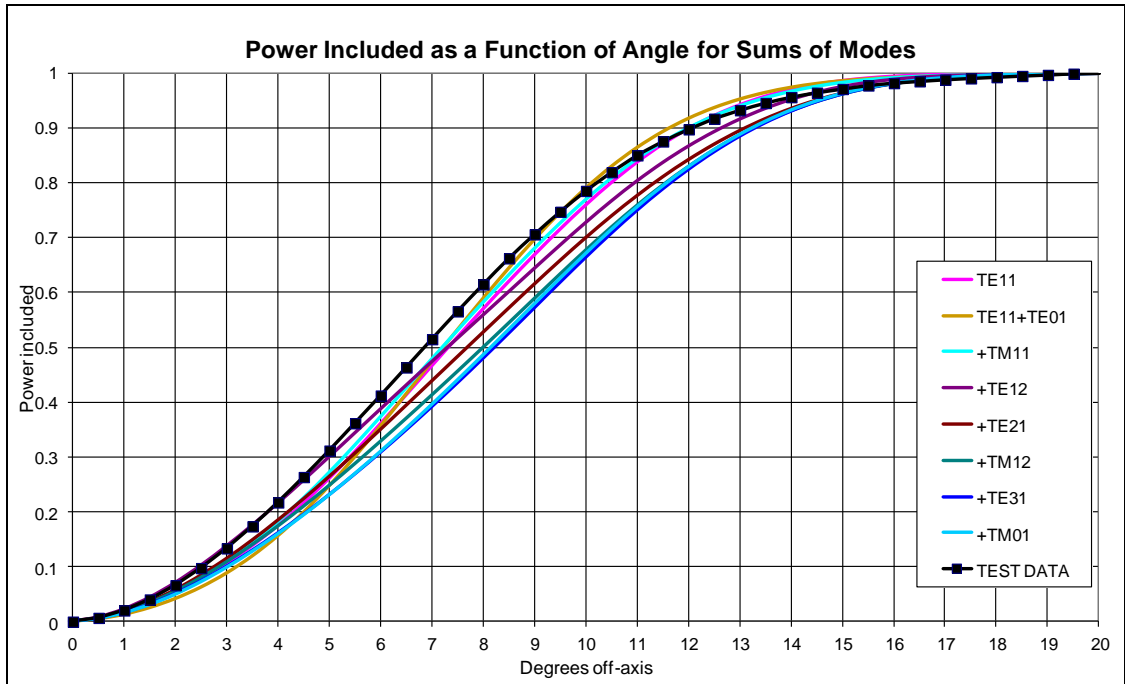
**Figure 5-14 : Plot of the power included as modes are seqentually added to the fundamental TE11 mode at 857 GHz.**
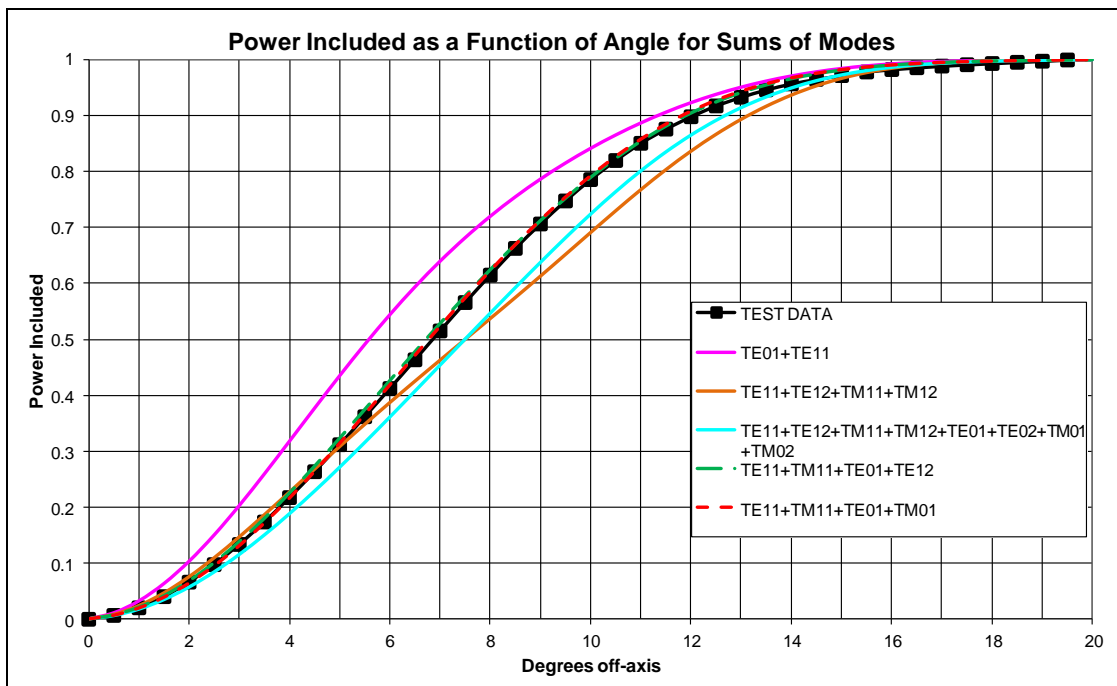


**Figure 5-15 : Plot of the power included for various sums of TE and TM modes at 857 GHz.**

Repeating this analysis for the test measurements at the other spot frequencies yielded similar results. At 819 GHz, for example, the test measurement is wider than the field at the output due to the $TE_{11}$ mode at the input but a combination of all $n = 0$ and $n = 1$ order input modes that should be propagating is wider than the measured

beam (see Figure 5-16) at the output farfield. Again this suggests that some of the higher order modes must be attenuated in the test measurement.

It is also possible to make a rough estimate of the relative number of modes present in the test data compared to the predicted beam pattern by comparing the beam areas of both and using diffraction theory, in particular the throughput equation. This is given in the usual form $A_{eff}\Omega = n\lambda^2$ which relates the beam solid angle ($\Omega$) at the horn subtended by the beam due to the effective area $A_{eff}$ of the aperture (where $A_{eff} = \eta_A A_{phy}$, where $\eta_A$ is the aperture efficiency and $A_{phy}$ is the physical area) and the number of propagating modes present ($n$) i.e.

$$\frac{A'_{eff}\Omega_{measured}}{A_{eff}\Omega_{predicted}} = \frac{n_{measured}}{n_{predicted}} \tag{5.2}$$

where $A_{eff}$ and $A'_{eff}$ are the effective areas for the predicted and measured beams respectively. These, of course, are approximately the same (related to the physical area of the aperture by the efficiency term, $\eta_A$, typically 0.4 to 0.8). Since we can approximate the beam solid angle with $\Omega = \left(\pi\dfrac{\theta^2}{4}\right)$ where $\theta$ is the angular beam width then

$$n_{measured} = \left(\frac{\theta_{measured}}{\theta_{predicted}}\right)^2 n_{predicted} \cdot \tag{5.3}$$

Thus the ratio of the two widths for test measurements and the theoretical prediction gives:

| Frequency (GHz) | Measured beam width (degrees) | Simulated beam pattern width (degrees) | Ratio |
|---|---|---|---|
| 739 | 6.4 | 8.1 | 0.38 |
| 780 | 7 | 8.5 | 0.45 |
| 819 | 6.4 | 7.5 | 0.52 |
| 844 | 6.5 | 7.8 | 0.47 |
| 857 | 6.85 | 8.5 | 0.43 |

Table 5-3: Ratio of beam widths for each of the test spot frequencies.

At each of the test spot frequencies the ratio of measured beam width to predicted beam width is less than one which suggests that the mode content of the measured beams is less than that predicted by the SCATTER simulations. This basic analysis suggests that the measured beam may only contain on average only 45% of the modes in theoretically beams predicted by SCATTER.
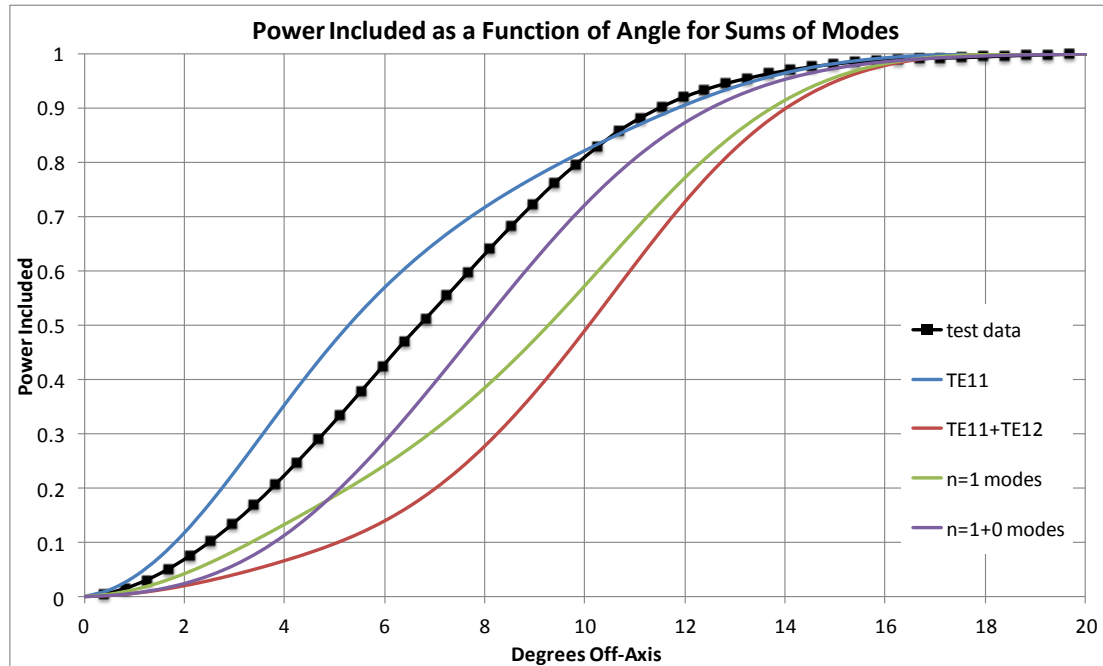


**Figure 5-16 : Plot of the power included for various sums of TE and TM modes at 819 GHz.**

In conclusion fitting by inspection yields some interesting results. It is clear that the beam widths of modes of azimuthal orders $n = 2$ and higher are not consistent with the measured beams and thus are either absent or at least highly attenuated in the test measurements. For modes of orders $n = 0$ and $n = 1$, the analysis suggests the that a combination of some, but not all, of the modes of both orders provides the best fit to the measured beams (Figure 5-15). The throughput equation and the relative beam widths of the predicted and measured beams provide an estimation of the ratio of number of modes present in the predicted beams to those present in the measured beams. This suggests that up to 65% of the predicted modes are missing or attenuated in the measured beams. The analysis is further complicated by the fact that different input waveguide modes scatter into the same output hybrid mode thus making it difficult to estimate which output modes are present in the measured data. To investigate the attenuation of the output hybrid modes themselves in more detail a

more mathematical approach based on single value decomposition is taken in the next section.

# 5.3 The Use of SVD to Investigate Mode attenuation in the Test Measurements

With the addition of SVD analysis of the system scattering matrices to the SCATTER code, it became possible to describe the true hybrid modes, recovering the eigenfields, the *U* and *V*, left and right singular vector of the SVD, of the $S_{21}^{+}S_{21}$ and $S_{21}S_{21}^{+}$ matrix products (Figure 5-17). There are far fewer of these modes, and it becomes feasible to do a least squares fit to the measured beam in terms of such modes. Thus for example, comparing the fundamental *HE₁₁* mode to the test measurement (Figure 5-18) it is clear that the measured beam is wider than the *HE₁₁* mode, therefore the measured beam pattern must be multimode to some degree as additional hybrid modes must be present along with the fundamental mode. The question now is what modes are present and to with what amplitude.

The best way to examine these questions is to use an appropriate fitting routine to perform a best fit of the hybrid modes to the measured beams. As mentioned before the test data are not symmetrical about the 0 degrees optical axis due to some inherent asymmetry in the manufactured horns or in the test setup. In order to fit the simulated hybrid mode sum to the measurements it was therefore necessary to shift the simulated data to an off-axis position matching the displaced optical axis of the measurements. These shifted hybrid mode fields were then fitted to the test measurement using non-negative Least Squares Fitting (LSF) in MATLAB. Non-negative fitting routines differs from normal fitting in that they only allow positive components of the fit to be added together, i.e. $y = a_1 x_1 + a_2 x_2 + \cdots a_n x_n$ where the coefficients *a₁, a₂,..,aₙ* must all be positive and *x₁, x₂,..,xₙ* are the column vector of samples of the fields at a set of points being fitted to the data *y*. This is important for our application here as hybrid modes are combined by summation in quadrature (i.e. the intensities are added) to form the overall intensity pattern therefore any fitting algorithm which allowed

negative coefficients to obtain a fit to the test data would be unphysical. MATLAB has an inbuilt non-negative LSF function called "*lsqnonneg()*" which was used to perform the desired fitting of the hybrid mode fields to the test data.
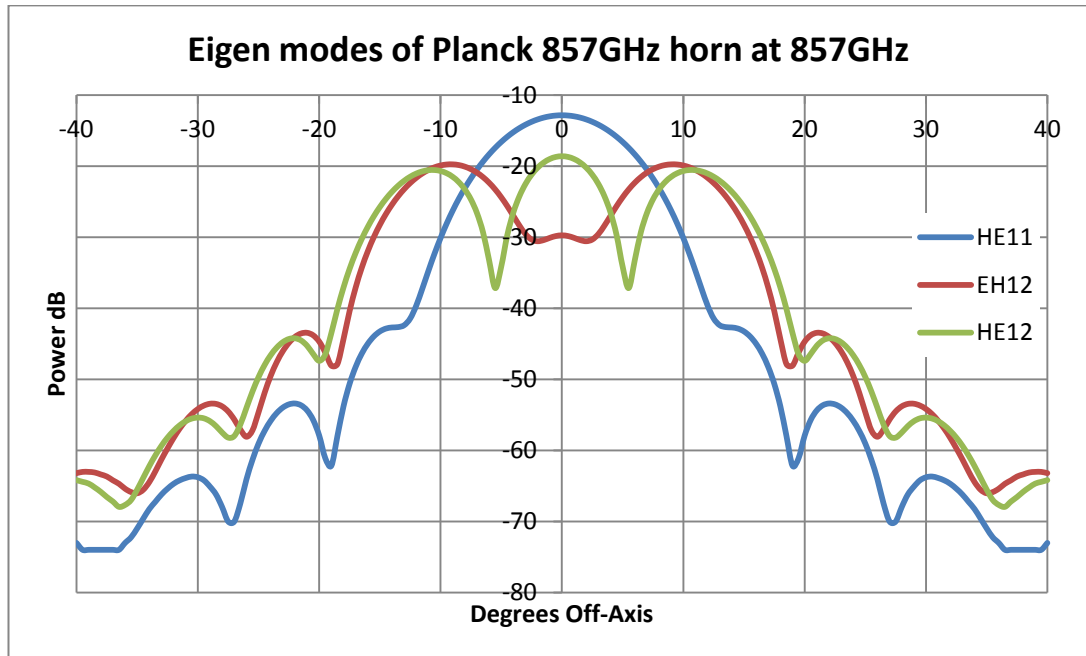


**Figure 5-17 : Farfield plots of the hybrid mode fields of the 857 GHz back-to-back horn of azimuthal order n = 1 at a spot frequency of 857 GHz (higher orders are ploted in Chapter2 section 2.7).**
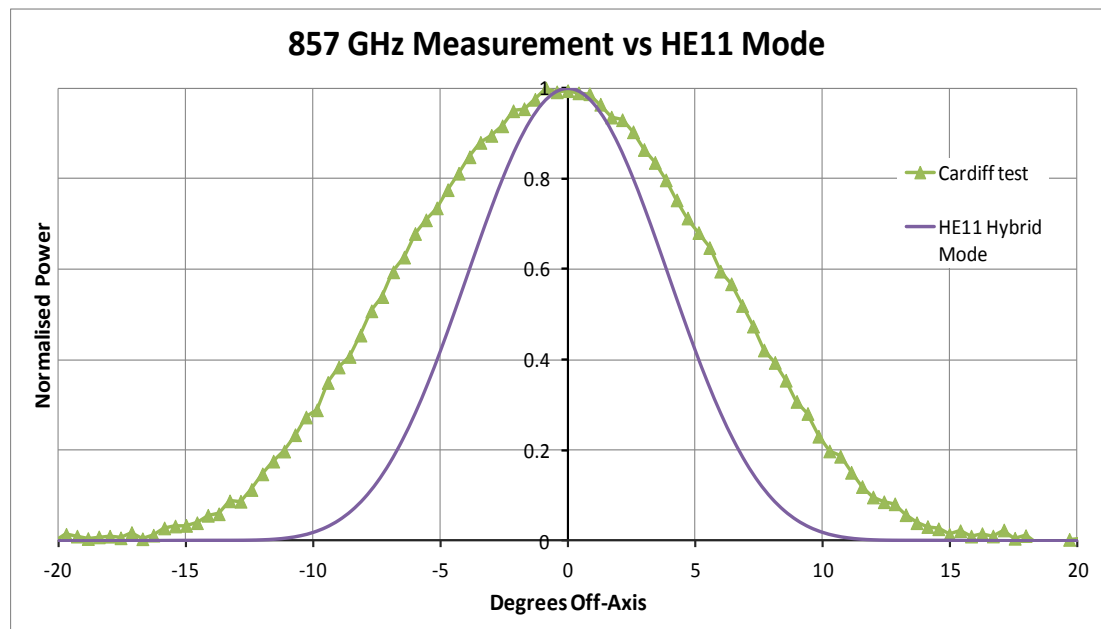


**Figure 5-18: Plot of the test measurement at 857 GHz and the HE11 mode.**

The LSF matched the simulated farfield hybrid mode intensity patterns to the test measurement by determining a best fit coefficient for each mode which estimated how much relative power each mode carried to produce a fit to the measurement

where the mode was allowed to be attenuated. In Figure 5-19 the test data for the broadband measurement made using the MAL source are plotted (green curve) along with the simulated farfield beam pattern of the horn at 857 GHz when all hybrid mode fields are present (the blue curve). This pattern was then displaced off-axis to match the asymmetry of the test measurement is shown in red. Finally the fitted beam was obtained using the non-negative LSF and is plotted in orange for comparison.

This analysis was repeated at each of the test spot frequencies and the resulting fitting coefficients for each of the Schmidt fields at each frequency are listed in Table 5-4. These coefficients give an estimate of how much the hybrid mode field was attenuated in the test measurement to be consistent with the non-negative LSF. After fitting the coefficients are re-normalised to a maximum value of 1 which corresponds to that the mode being present with the least attenuation. As can be seen from Table 5-4 the LSF estimates that there are between two and three modes present in the measured beam pattern at each of the test frequencies. In particular modes of azimuthal order 2 and higher have coefficients of zero or near zero values and appear to be fully attenuated. The hybrid modes of azimuthal order $n = 1$ are present but appear to be somewhat attenuated. This is broadly, at least, in agreement with the findings of analysis using the input TE and TM waveguide modes described earlier in the last section which found by trial and error that the best match to the test data was a particular combination of input TE and TM smooth walled waveguide modes of order $n = 0$ and $n = 1$ mode fields only. The LSF analysis, however, should provide a more mathematically rigorous picture of the combination of hybrid modes of these orders present in the test data. Hybrid modes which carry power closest to on-axis are present while those with power off-axis are attenuated. This suggest clearly again that off-axis power is being lost in the test measurements. As previously then the attenuation of these higher order modes possibly indicates higher resistive losses in the corrugations for these modes. Comparing the average number of modes present in the fitted patterns, 2.64, to those of the predicted full beam patterns, 11.24 modes (see Table 3-1), gives a ratio of 0.23 which is less than that estimated earlier, 0.45, using the TE and TM waveguide modes approach. On the other hand, if we compare the FWHM beam widths of the $HE_{11}$ mode and the test data shown in Figure 5-18 we get a factor of about 1.6 again clearly indicating test data is significantly still multi-moded.
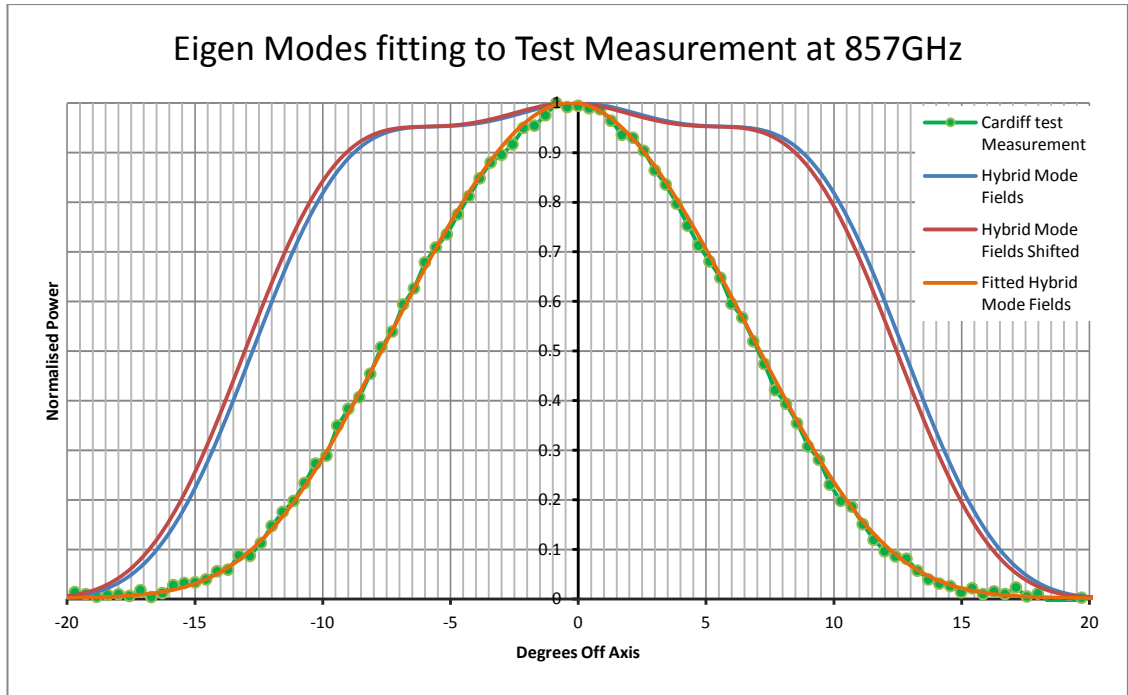
**Figure 5-19 : Plot showing the farfield beam pattern of the SCATTER simulation using hybrid mode farfields, the same pattern shifted to match asymmetry of data, and the hybrid mode farfield simulation fitted to the test measurement.**
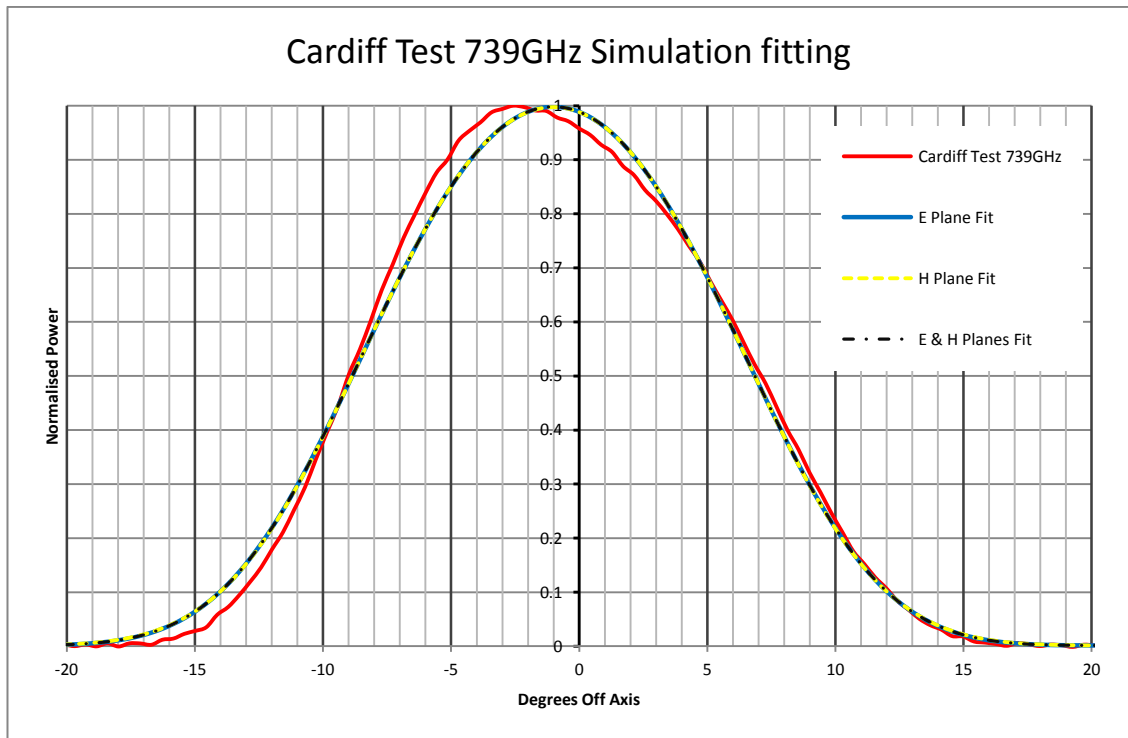


**Figure 5-20 : E and H plane hybrid mode farfields fitted to the Cardiff test data at 739 GHz.**

189

| Frequency (GHz) | Hybrid Modes | | | | | | | | | | Total |
|---|---|---|---|---|---|---|---|---|---|---|---|
| | $H_{01}$ | $E_{02}$ | $H_{02}$ | $HE_{11}$ | $EH_{12}$ | $HE_{12}$ | $HE_{21}$ | $EH_{22}$ | $HE_{31}$ | $HE_{41}$ | |
| 739 | 1.00 | 0.00 | 0.00 | 0.67 | 0.05 | 0.00 | 0.00 | 0.00 | 0.09 | 0.00 | 2.62 |
| 780 | 1.00 | 0.02 | 0.00 | 0.43 | 0.00 | 0.00 | 0.00 | 0.00 | 0.11 | 0.00 | 2.10 |
| 819 | 1.00 | 0.00 | 0.00 | 0.72 | 0.38 | 0.00 | 0.00 | 0.00 | 0.00 | 0.00 | 3.19 |
| 844 | 0.00 | 1.00 | 0.00 | 0.61 | 0.43 | 0.00 | 0.00 | 0.00 | 0.00 | 0.00 | 3.07 |
| 857 | 0.00 | 1.00 | 0.00 | 0.44 | 0.02 | 0.15 | 0.00 | 0.00 | 0.00 | 0.00 | 2.20 |
| | | | | | | | | Average | | | 2.64 |

Table 5-4 : The normalised fitting coefficients for each hybrid mode by azimuthal order for each test spot frequency and 857GHz which was fitted to the broadband test.

However, there are more variables to be considered when fitting simulated hybrid modes to the test data. For the spot frequency measurements a coherent source was used. Such a source would be linearly polarised although the direction of polarisation was not specified. This meant that for the $n = 1$ modes it could have been either an E-cut or H-cut that was measured depending on whether the source was polarised in the scan plane or perpendicular to it. For the $n = 0$ and $n = 2$ modes the beam is symmetric with respect to the scan planes but not necessarily for the $n = 1$ modes. In general although the horns are corrugated and it should not matter as for pure HE or EH modes as those are symmetric, however, combinations of HE and EH modes are not necessarily symmetric, so therefore it is possible for the eigenfields to be asymmetric as generated from the $S_{21}$ SCATTER matrix output. The SCATTER simulations initially consisted of a quadratic average of the E and H planes and, of course, both were not necessarily measured during horn testing. It was therefore necessary to perform simulations for both possible planes separately at each of the four spot frequencies and to fit these to the test data using the same procedure as outlined above for the broadband beam. Thus we can see if there was any effect upon the estimated number of modes due to the polarisation and possibly even obtain a better fit to the test data.

An example of this analysis for the test measurement at 739 GHz is shown in Figure 5-20. The fitted beam patterns produced by the LSF for the E plane modes alone (blue curve), H plane modes alone (yellow curve), and modes of both planes (black curve) overlap such that they are almost identical. The predicted number of modes for the best fit varies for each plot (see Table 5-5 for the E plane and Table 5-6 for the H plane fitting coefficients). The full broadband model (average of E and H

planes) suggests 2.62 modes are present, while the number of modes in the E plane fit is 3.05 and for the H plane 3.25 modes are used in the fit although, of course, the broadband beam included higher frequency components than those of the spot frequencies. In all three cases modes of order $n = 2$ and $n = 4$ are not present. For the E plane fit and H plane fit there is an attenuated mode present of order $n = 3$ in each. Note that for the $n = 0$ modes those with radial field lines can only couple to the E plane measurements while those with azimuthal field lines couple to the H plane. It maybe that the $n = 3$ modes are associated with the fit to the beams that was not necessary in the case of the broadband beams because the symmetry is not broken in that case. This is difficult to disentangle.

| Frequency (GHz) | Hybrid Modes | | | | | | | | | | Total |
|---|---|---|---|---|---|---|---|---|---|---|---|
| | $H_{01}$ | $E_{02}$ | $H_{02}$ | $HE_{11}$ | $EH_{12}$ | $HE_{12}$ | $HE_{21}$ | $EH_{22}$ | $HE_{31}$ | $HE_{41}$ | |
| 739 | 0.00 | 0.34 | 0.00 | 1.00 | 0.00 | 0.00 | 0.14 | 0.00 | 0.35 | 0.00 | 3.32 |
| 780 | 0.00 | 0.34 | 0.00 | 1.00 | 0.00 | 0.00 | 0.14 | 0.00 | 0.35 | 0.00 | 3.32 |
| 819 | 0.00 | 0.34 | 0.00 | 1.00 | 0.00 | 0.00 | 0.14 | 0.00 | 0.35 | 0.00 | 3.32 |
| 844 | 0.00 | 0.34 | 0.00 | 1.00 | 0.00 | 0.00 | 0.14 | 0.00 | 0.35 | 0.00 | 3.32 |
| 857 | 0.00 | 0.34 | 0.00 | 1.00 | 0.00 | 0.00 | 0.14 | 0.00 | 0.35 | 0.00 | 3.32 |
| | | | | | | | | | Average: | | 3.32 |

Table 5-5 : Fitting coefficients for each mode by azimuthal order at each test frequency when only the E plane is considered.

| Frequency (GHz) | Hybrid Modes | | | | | | | | | | Total |
|---|---|---|---|---|---|---|---|---|---|---|---|
| | $H_{01}$ | $E_{02}$ | $H_{02}$ | $HE_{11}$ | $EH_{12}$ | $HE_{12}$ | $HE_{21}$ | $EH_{22}$ | $HE_{31}$ | $HE_{41}$ | |
| 739 | 0.94 | 0.00 | 0.00 | 1.00 | 0.00 | 0.00 | 0.00 | 0.00 | 0.30 | 0.00 | 3.54 |
| 780 | 1.00 | 0.00 | 0.00 | 0.72 | 0.00 | 0.00 | 0.00 | 0.00 | 0.15 | 0.00 | 2.73 |
| 819 | 0.58 | 0.00 | 0.00 | 1.00 | 0.89 | 0.00 | 0.00 | 0.00 | 0.00 | 0.00 | 4.37 |
| 844 | 0.00 | 0.72 | 0.00 | 0.95 | 1.00 | 0.00 | 0.00 | 0.00 | 0.00 | 0.00 | 4.63 |
| 857 | 0.00 | 0.87 | 0.00 | 1.00 | 0.00 | 0.00 | 0.00 | 0.00 | 0.63 | 0.00 | 4.14 |
| | | | | | | | | | Average: | | 3.88 |

Table 5-6 : Fitting coefficients for each mode by azimuthal order at each test frequency when only the H plane is considered.

The same pattern is seen in the fitting at the other three spot frequencies. Again when only one plane is considered at a time, either E or H, some modes of higher order are indeed present in the fitted beam pattern. For all of the cases the overall number of modes present in the test measurements are significantly less than the number of modes present in the simulations at the same frequency as set out in

Table 3-1. The average number of modes required for an E plane only fitting is 3.32 while 3.88 modes are needed for a H plane fitting. Once more this is significantly less than the average of 11.24 modes for the predicted full beam patterns at these same spot frequencies. To summarise these results, the ratio of the number of modes in the fits to the test data compared to the number of modes in the predicted beams are 0.30 for the E plane fit and 0.35 for the H plane fitting. The conclusion therefore is that the horns are multi-moded and that there is always a high fundamental mode $HE_{11}$ content with some higher order $n = 0$, $n = 1$ mode content but no content of azimuthal order $n = 2$ or higher.

In the earlier analysis using the input TE and TM waveguide modes the estimate of the modes present in the test data was made by weighting the test data by the power inside an area of the beam itself and then using the 50% power included level as a measure of beam width rather than fitting to the beam pattern. This weighted the analysis away from matching any 'on-axis' peak in power, in favour of power spread over the beam width. We therefore also investigated a fit to the included power profiles for the test beams using a similar least squares fit approach but using the farfield intensity patterns of the hybrid mode fields as the basis set. This effectively means all of the intensity patterns are weighted by the off-axis angle and fitted to the test data which would also need to be weighted in the same fashion for the fitting purposes. The power included as a function of angle is given by equation 5.1 as discussed in section 5.1. This process was repeated at each frequency for each of the scenarios already considered, that is separately for the E plane only and for the H plane only.

| Frequency (GHz) | Hybrid Modes | | | | | | | | | | Total |
| --- | --- | --- | --- | --- | --- | --- | --- | --- | --- | --- | --- |
| | $H_{01}$ | $E_{02}$ | $H_{02}$ | $HE_{11}$ | $EH_{12}$ | $HE_{12}$ | $HE_{21}$ | $EH_{22}$ | $HE_{31}$ | $HE_{41}$ | |
| 739 | 1.00 | 0.00 | 0.00 | 0.67 | 0.05 | 0.00 | 0.00 | 0.00 | 0.09 | 0.00 | 2.62 |
| 780 | 0.00 | 1.00 | 0.00 | 0.39 | 0.16 | 0.00 | 0.00 | 0.00 | 0.00 | 0.00 | 2.10 |
| 819 | 1.00 | 0.00 | 0.00 | 0.52 | 0.21 | 0.00 | 0.00 | 0.00 | 0.00 | 0.00 | 2.47 |
| 844 | 0.00 | 1.00 | 0.00 | 0.50 | 0.31 | 0.00 | 0.00 | 0.02 | 0.00 | 0.00 | 2.65 |
| 857 | 0.00 | 1.00 | 0.00 | 0.38 | 0.06 | 0.19 | 0.00 | 0.00 | 0.00 | 0.00 | 2.27 |
| | | | | | | | | | Average: | | 2.42 |

**Table 5-7 : Fitting coefficients for each mode by azimuthal order at each test frequency using included power.**
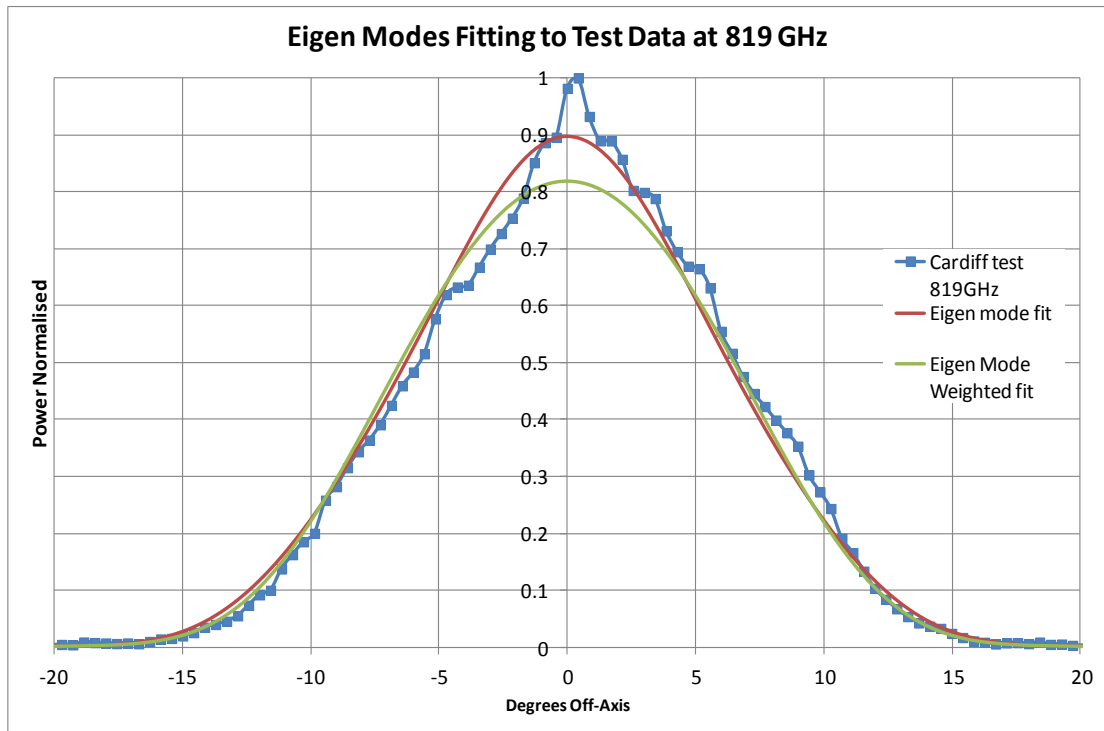
**Figure 5-21 :Fitting to test measurement at 819 GHz both with and without using the off-axis angle to weight the fitting.**

| Frequency (GHz) | Hybrid Modes | | | | | | | | | | Total |
|---|---|---|---|---|---|---|---|---|---|---|---|
| | $H_{01}$ | $E_{02}$ | $H_{02}$ | $HE_{11}$ | $EH_{12}$ | $HE_{12}$ | $HE_{21}$ | $EH_{22}$ | $HE_{31}$ | $HE_{41}$ | |
| 739 | 0.00 | 0.34 | 0.00 | 1.00 | 0.00 | 0.00 | 0.01 | 0.00 | 0.35 | 0.00 | 3.06 |
| 780 | 0.00 | 1.00 | 0.88 | 0.28 | 0.00 | 0.00 | 0.00 | 0.00 | 0.00 | 0.00 | 2.44 |
| 819 | 0.00 | 0.00 | 0.00 | 0.80 | 0.28 | 0.00 | 1.00 | 0.00 | 0.00 | 0.00 | 4.15 |
| 844 | 1.00 | 0.00 | 0.00 | 0.96 | 0.48 | 0.00 | 0.00 | 0.02 | 0.00 | 0.00 | 3.92 |
| 857 | 0.96 | 0.00 | 0.00 | 1.00 | 0.47 | 0.00 | 0.00 | 0.07 | 0.00 | 0.00 | 4.05 |
| | | | | | | | | | Average: | | 3.52 |

**Table 5-8 : Fitting coefficients for each mode by azimuthal order at each test frequency using on the E plane using included power.**

| Frequency (GHz) | Hybrid Modes | | | | | | | | | | Total |
|---|---|---|---|---|---|---|---|---|---|---|---|
| | $H_{01}$ | $E_{02}$ | $H_{02}$ | $HE_{11}$ | $EH_{12}$ | $HE_{12}$ | $HE_{21}$ | $EH_{22}$ | $HE_{31}$ | $HE_{41}$ | |
| 739 | 0.94 | 0.00 | 0.00 | 1.00 | 0.00 | 0.00 | 0.00 | 0.00 | 0.16 | 0 | 3.26 |
| 780 | 0.00 | 0.00 | 0.00 | 0.74 | 0.00 | 0.00 | 1.00 | 0.00 | 0.18 | 0 | 3.84 |
| 819 | 0.83 | 0.00 | 0.00 | 1.00 | 0.70 | 0.00 | 0.00 | 0.00 | 0.00 | 0 | 4.22 |
| 844 | 0.00 | 0.99 | 0.00 | 1.00 | 0.93 | 0.00 | 0.00 | 0.00 | 0.00 | 0 | 4.85 |
| 857 | 0.00 | 0.93 | 0.00 | 1.00 | 0.00 | 0.00 | 0.00 | 0.05 | 0.60 | 0 | 4.23 |
| | | | | | | | | | Average: | | 4.08 |

**Table 5-9 : Fitting coefficients for each mode by azimuthal order at each test frequency using on the H plane using included power.**

The weighted (i.e. included power) and un-weighted (i.e. beam pattern) fitting at 819 GHz is shown in Figure 5-21. The effect of the weighting on the fit to the data can be clearly in the lower on-axis peak of the weighted fit. This is as expected because the weighting is designed to fit the data to the off-axis area in which most of the power would be carried as outlined earlier in section 5.2. The fitted beam patterns for the E plane only and H plane only are shown in Figure 5-22. The number of modes present in the fitted beam patterns is broadly in line with the earlier fitting results. In all cases hybrid modes of azimuthal order $n = 0$ and $n = 1$ are present and the higher order modes are largely attenuated. Comparing the weighted fitting to the un-weighted fitting the number of modes for the E plane is 3.5 for the weighted fitting (see Table 5-8) compared to 3.88 from before. Meanwhile for the H plane there are 4.08 modes for the weighted fitting (Table 5-9) and 3.88 modes for the beam pattern fitting. When both the E and H planes are considered together the weighted fitting has 2.24 modes (Table 5-7) and the un-weighted fitting has 2.64 modes. Clearly while the weighting has an effect on the exact number of modes in each of the three scenarios the overall results are broadly consistent.
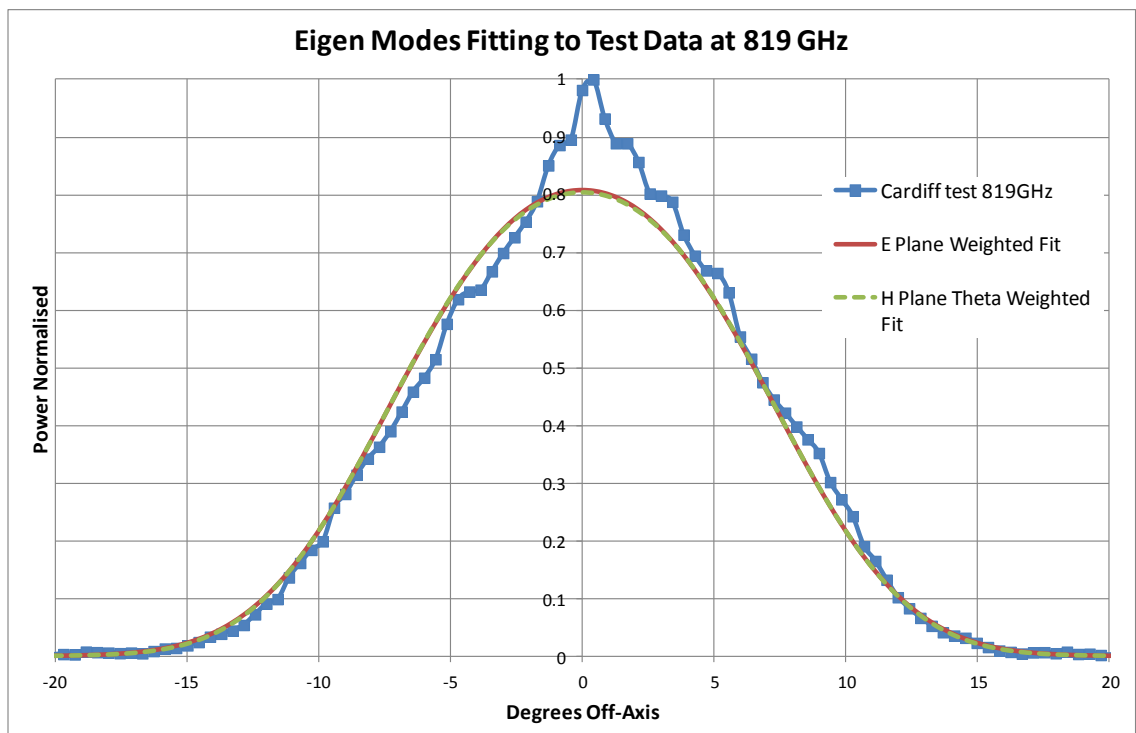


**Figure 5-22 : E and H Plane fitting to test measurement at 819 GHz both with and without using the off-axis angle to weight the fitting.**

A final consideration is the degeneracy of the hybrid modes of order $n = 0$. The $H_{01}$ and $E_{02}$ each lack an orthogonal component but they are orthogonal to each other and have the same overall beam pattern. For the fitting process this last fact is an important consideration as we just use the intensity patterns (and not the polarisation direction). The LSF routine only used one of the two $n = 0$ modes when fitting to the test measurements as it was fitting the beam patterns of the modes to the measured beam pattern. Thus two modes with the same beam pattern would be degenerate for the purposes of the fitting process. However this may not physically accurate. It is possible that both modes could have been present in the test measurement if the source could couple to both (was not pure linearly polarised in one direction) therefore it was necessary to force the fitting routine to use either both (splitting power evenly between them) or neither of the $n = 0$ modes to check the effect of this degeneracy had on the fit to the test data. The resulting fitting coefficients at 857 GHz for all hybrid modes (including both E and H planes) are shown in Table 5-10 and it can be seen that the result is an increase in the number modes propagating compared to when only one zero azimuthal order hybrid mode was used in the fitting.

However, the overall result is still consistent with the findings that the overall number of modes is greatly reduced. For this case the ratio of hybrid modes in the fitted beam pattern compared to the predicted beam is 0.40. Again this shows that the mode content of the measured beam pattern is reduced compared to the predicted beam pattern and that the higher order modes are attenuated. Nevertheless the measured beams are multi-moded and at least this was clearly established, an important pre-flight result. However, it was clear that the experimental set up was not exactly that of the full Planck pixel particularly in the use of Winston cones (parabolic horns), so in the next section we consider the possibility that in fact this may have contributed to the unexpected lower level of higher order mode content of the beam.

| Frequency (GHZ) | Hybrid Modes | | | | | | | | | | Total |
|---|---|---|---|---|---|---|---|---|---|---|---|
| | $H_{01}$ | $E_{02}$ | $H_{02}$ | $HE_{11}$ | $EH_{12}$ | $HE_{12}$ | $HE_{21}$ | $EH_{22}$ | $HE_{31}$ | $HE_{41}$ | |
| 857 | 1.0 | 1.0 | 0.0 | 0.76 | 0.12 | 0.38 | 0.0 | 0.0 | 0.0 | 0.0 | 4.53 |

**Table 5-10 : Fitting coefficients for each mode by azimuthal order at 857 GHz when the fitting routine is forced to use both modes of order $n = 0$.**

# 5.4 Simulating the Test measurement Set up

As mentioned earlier a relay system of standard parabolic (Winston cone type) horns were used to couple the 857 GHz back-to-back qualification horn to the detector inside the cryostat (Figure 5-23). This relay system consisted of a back-to-back pair of such horns which coupled to a third Winston cone feeding the detector.
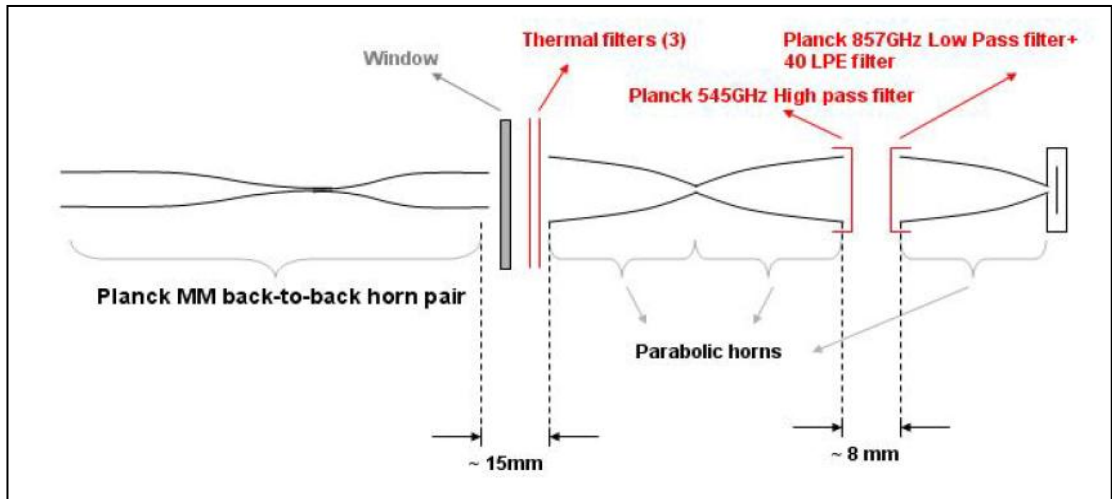


**Figure 5-23 : Test set up used by Cardiff University for multi-mode spot frequency tests. The parabolic horns used to couple the Planck horn to the detector were standard Winston cones.**

Winston cones have traditionally been used as detector feeds in far-infrared cosmological experiments. They are usually designed using ray tracing, which becomes a very poor approximation when the number of spatial modes propagated by the horn is small in number, often the case at the longest wavelengths, a more accurate approach involves electromagnetic modelling of Winston cones using a rigorous electromagnetic mode matching technique in which case they often referred to as Winston horns or Winston profiled horns [Maffei, 2004]. A Winston cone as originally designed [Welford & Winston, 1978] is an off-axis parabolic profiled light pipe designed to maximise the collection of incoming rays within a field of view determined by its dimensions (see Figure 5-24). Equation 5.4 describes the Winston cone geometry where $x$ is the distance from the horn throat, $y$ is the horn radius, and $l$ is the semi-latus rectum [Gleeson, 2002].

$$y^2 \cos^2(\alpha) + y[2x\cos(\alpha)\sin(\alpha) + 2l\sin(\alpha)] + [x^2 \sin^2(\alpha) - l^2 - 2lx\cos(\alpha)] = 0 \ . \quad (5.4)$$

The maximum angle α defines the geometrical limit at which the incoming rays reach the exit aperture of the cone.

$$\sin(\alpha) = \frac{d}{D} \quad , \tag{5.5}$$

where $D$ is the diameter of the horn aperture and $d$ is the diameter of the horn throat.
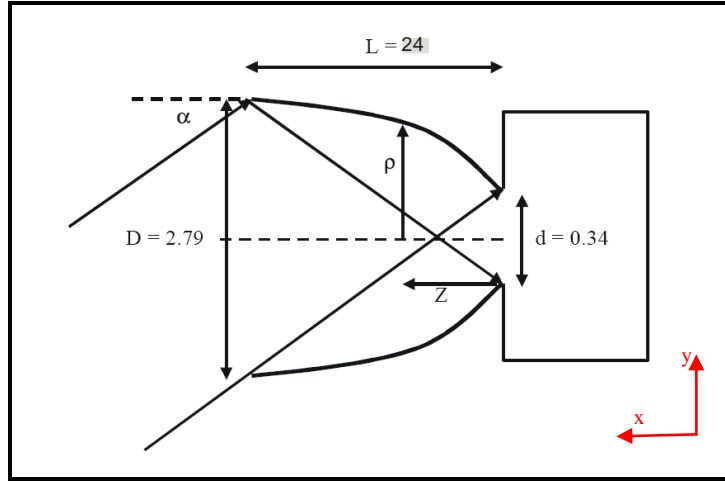


**Figure 5-24 : Schematic diagram of a Winston cone with a cavity**

In the analysis of the test measurements in the previous sections of the chapter it has been assumed that the coupling between the Planck horn and the Winston cones was such that it did not affect the measurement of the beam pattern of the Planck horn. However, this assumption may not be accurate in fact because the loss of higher order modes in the measured beams compared to the predicted beams leads to suspicion that the coupling may not be ideal. To investigate the possible effects of a mismatch in the coupling between the horns SCATTER was modified to allow modes to be lost to free space upon reflection at the aperture of the Winston cone.

At this step we match the fields over the aperture of the smaller horn. Assuming that we are going from the Winston cone (left hand side of the step) to the Planck back horn (right hand side of the step) gives no reflections for the step itself (i.e. $[S_{11}] = [S_{22}] = 0$) and that the radius of the Winston cone is $b$ and the radius of the back-to-back horn is $a$ then,

$$\sum_n A_n \mathbf{h}_{nL}^{(b)} = \sum_n D_n \mathbf{h}_{nR}^{(a)} \tag{5.6}$$

$$\sum_n A_n \mathbf{e}_{mL}^{(b)*} \times \mathbf{h}_{nL}^{(b)} = \sum_n D_n \mathbf{e}_{mR}^{(a)*} \times \mathbf{h}_{nR}^{(a)} \quad . \tag{5.7}$$

197

$$[P]^+[A] = [R^*][D] \ . \tag{5.8}$$

Thus the $S_{21}$ scattering matrix is given by

$$[S_{21}] = [R^*][P^*]^+ \ , \tag{5.9}$$

where $P_{mn} = \int_0 \mathbf{e}_{nR}^{(a)} \times \mathbf{h}_{mL}^{(b)*} .d\mathbf{A}$ and $R_{mn} = \int_0 \mathbf{e}_{nR}^{(a)} \times \mathbf{h}_{mL}^{(a)*} .d\mathbf{A}$ as in section 2.3 with the left

and right had sides interchanged as here the first guide (on the left of the junction) has the larger radius. Similarly,

$$[S_{12}] = [Q]^{-1}[P^*]^+ \ . \tag{5.10}$$

Code was added to the MATLAB version of SCATTER to trigger the calculation of these scattering matrices at the appropriate step during the computation of the scattering matrices for the overall Winston cone / back-to-back horn combination. A geometry file for a Winston cone of a similar type to that used by Cardiff University was initially used to simulate a configuration of the Planck back-to-back horn feeding a Winston cone. The radius of the aperture of the Winston cone was taken to be 5 mm and the radius of the throat was set to 1mm. The farfield beam pattern calculated from this simulation of the Winston cone and back-to-back horn combination is shown in Figure 5-25 along with the beam pattern of the back-to-back horn on its own for comparison. As can be seen there is no significant difference between the two beam patterns. However, the Winston cone used in this model was likely not exactly the actual one used in the test measurements, furthermore, it was not possible to run the simulations of the gap between the horns, and this also could have an effect on the coupling of the horns.

In order to investigate this further, the radius of the throat of the Winston cone was varied to determine whether there was an effect on the coupling to the back-to-back horns. The radius of the throat was first reduced to 0.3 mm, the same size as the waveguide filter section of the back-to-back horn. It might have been expected that as the higher order hybrid modes could propagate through both waveguide filters, there should be no effect on the coupling for this radius. However, this is not the case as power is scattered into higher order modes at the step between the two horns and these cannot propagate in the narrower radius at the throat of the

Winston cone parabolic horn. As can be seen in Figure 5-25 the beam pattern for this Winston cone and back-to-back horn arrangement is narrower than the broadband beam measured by Cardiff. An even narrower Winston cone with a throat radius of 0.25 mm yields a correspondingly narrower beam pattern for the whole configuration as would be expected.
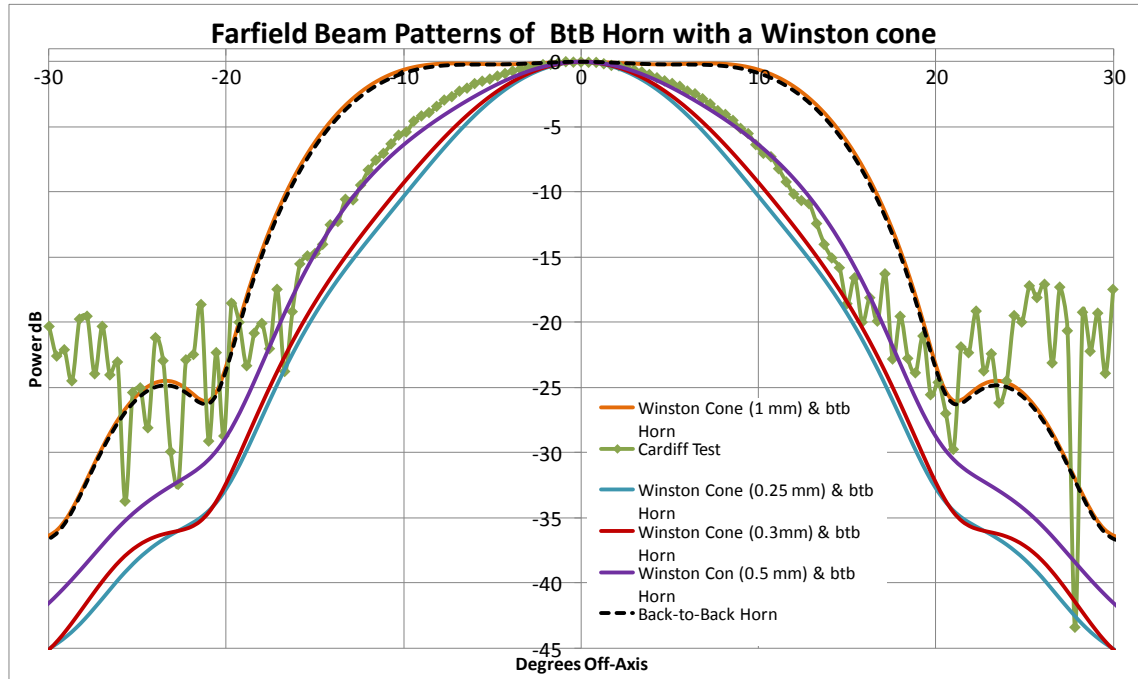


**Figure 5-25: Plot of the far field beam patterns of the SCATTER simulations of the back-to-back horn coupled to a Winston cone. The Cardiff broadband test measurement is shown for comparison, as is the beam pattern for the front horn only.**

| Hybrid Modes | | | | | | | | | | Total |
|---|---|---|---|---|---|---|---|---|---|---|
| $H_{01}$ | $E_{02}$ | $H_{02}$ | $HE_{11}$ | $EH_{12}$ | $HE_{12}$ | $HE_{21}$ | $EH_{22}$ | $HE_{31}$ | $HE_{41}$ | Total |
| 0.956 | 0.38 | 0.09 | 0.49 | 0.07 | 0.0 | 0.15 | 0.0 | 0.05 | 0.0 | 3.756 |

**Table 5-11: Power in the hybrid modes propagating in the combination of a Winston cone with throat radius of 5 mm and the Planck back-to-back horn.**

A Winston cone with a throat radius of 0.5 mm results in a farfield beam pattern that is a good match to the test measurement (again shown in Figure 5-25). Furthermore the singular values of the $S_{21}$ scattering matrix of this configuration of back-to-back horn and Winston cone indicate that there are two modes of order $n = 0$ ($H_{01}$ and $E_{02}$) propagating, and one mode ($HE_{11}$) of order $n = 1$ propagating (see Table 5-11). The simulation indicates that there are some more additional modes present but the power in these modes is negligible. The overall number of modes is in good

agreement with the number found using the least squares fitting approach in the previous section.

In conclusion it is clear that the coupling between a parabolic horn (Winston cone) and the Planck back-to-back horn more than likely is reduced due to the geometry of the parabolic horn (in particular the radius of the throat section). It is quite likely actually a Winston cone with a throat radius of less than 1 mm, but still greater than the radius of the waveguide filter of the back-to-back horn, was used in the measurement experiments to couple the back-to-back horn to a detector, and that some filtering of the higher order modes most probably took place. The analysis described in this section does not take the gap between the parabolic horn and the back-to-back horn into account. As this gap would also result in further reduction of the coupling between the two horns, it is possible that a combination parabolic horn with a radius greater than 5 mm with a gap between it and the back-to-back horn could also result in a similar loss of higher order modes. The most likely scenario that explains  the reduction in the number of modes contributing to the farfield pattern of the 857 GHz horn was poor coupling to the detector through the parabolic horn relay.

# 5.5 Conclusions

The pre-flight test measurements made by Cardiff University of the Planck 857 GHz back-to-back qualification horn were designed to test whether or not the horn was multi-moded as designed. In undertaking these tests Cardiff University faced a number of limitations in their experimental setup including not having access to a Planck 857 GHz detector feed horn and detector. They overcame this by using a parabolic feed horn relay as described earlier. The measured beam patterns were narrower than the predicted beam patterns at each of the spot frequencies tested. An extensive analysis campaign was then undertaken by the author to examine the mode content of the measured beams in order to determine if they were multi-moded and to explain the discrepancy between them and the predicted beam.

Using the TE and TM waveguide modes as a basis set it was possible to show that the measured beams must contain modes of higher azimuthal orders in addition to

those of order $n = 1$.  This was done by using the power included inside a given angle as a measure of beam width and using this to fit combinations of TE and TM waveguide modes to the measured beams by trial and error.  Using the through put equation and the relative beam widths of the predicted and measured beams it was estimated that only about 45% of the mode predicted were present in the measured beams.

Following on from this a more extensive analysis was performed using the hybrid modes of the predicted beams.  It is clear that the measured beams were wider than the fundamental $HE_{11}$ mode and therefore that the beams must be multimoded.  To determine to what extent the beams were multimoded the hybrid modes were fitted to the measured beams at each of the spot frequencies using non-negative least squares fitting.  This approach again showed that the mode content of the measured beams patterns were reduced compared to the predicted beams and that in particular modes of azimuthal orders other than of orders $n = 0$ and 1 were greatly attenuated or missing entirely.  While it is known that a mercury arc lamp was used as a source in combination with a spider web bolometer for some of the measurements at 857GHz, it is not known what sources or detectors were used for the majority of the measurements.  It is possible that the source or detector used in any of these measurements may only have been sensitive to one polarisation.  By fitting either the E or H planes of the predicted beams it was possible to examine a number of possible scenarios for the setup of the source and detector used in experiment.  The results of this analysis supported the conclusion that the measured beams were multimoded but that the higher order mode content was reduced, possibly being between 30% to 40% of the predicted beams.

It should also be noted that the test data beyond 20 degrees off-axis at all frequencies reaches a noise floor and is not suitable for fitting.  Given that the first side lobe is predicted just beyond this point at between 20 degrees and 25 degrees, this noise floor in the measured data leaves us without any information on the sidelodes levels of the measured beams.  As the higher order modes, due to their off-axis peaks in power, contribute most to the sidelobes the lack of useable data in this region may contribute to a slight biasing of the fitting towards lower order modes which contribute more power 'on-axis' within 20 degrees off-axis.  However, the fact that the measured beams are narrower than the predicted beams shows that there is a loss of higher order

mode content, and thus the truncation of the analysis beyond 20 degrees off-axis due to the lack of data does not affect the overall conclusion that the measured beams are multimoded but with a somewhat reduced mode content.

An analysis was also made of the coupling between the back-to-back horn pair and the Winston cone. It was suspected this might be where the higher order modes were lost. It has been shown that the coupling between the two horns is dependent on the exact geometry of the Winston cone. A Winston cone with a throat radius of less than 1 mm but still greater than 0.3 mm (the radius of the back-to-back horn waveguide filter), could result in an attenuation of the higher order mode of a similar scale as that observed in the test measurements. It is also possible that modes were also lost due to the gap between the horns but it has not been possible to run the simulations and future work in this area could certainly be undertaken to check this effect although it would involve rather complicated optical analysis. However probably the most logical approach would be to repeat the measurements with a better matched system and with all optical components as precisely defined as possible.

The fact that the measured beams were multimoded was an important pre-flight result. In flight measurements of the beam widths of the 857 GHz channels were made using Uranus and Neptune [Planck Collaboration, 2014a]. The beam width measured in flight, 4.63 arcmin [Planck Collaboration, 2014b], agrees with the predicted beam widths of 4.95 arcmin [Maffei, 2010a]. This supports the conclusion that the 857 GHz channel is multimoded and that the actual predicted number of modes seem to propagate as predicted in the horns. It is therefore reasonable to conclude that factors in the experimental setup used to make the preflight measurements resulted in the filtering (loss) of the higher order modes.

Finally for completeness it should be noted that the measurements made with the telescope simulator at Cardiff referred to earlier were inconclusive. The system was, however, analysed by Daniel Wilson in his thesis [Wilson, 2014]. The modelled beams were in good agreement with test measurements. Crucially, however, any differences in beam pattern from horn to horn based on imperfections (as discussed in Chapter 4) would be in no way obvious on analysis of the telescope simulator beam patterns.

# Chapter 6 Determination of the Phase Centres of Horn Antennas using MM-Wave Holography

## 6.1 Introduction

In this chapter we describe the use of millimetre-wave holography for the determination of the phase centres of non-standard horn antennas in the millimetre and sub-millimetre wave bands. In particular we present an example of the technique applied to a smooth-walled horn antenna specially designed for CMB polarisation experiments. Such smooth-walled horn antennas are required as large arrays of 1000's of horns are being proposed for such projects and corrugated horns (as have been discussed up to now) are both prohibitively expensive and too massive for cryogenic reasons. An example profiled horn was designed at Maynooth University (NUI Maynooth) and the beam pattern measured using a Vector Network Analyser (VNA) for the W-band (75-100 GHz). In this chapter we describe a holographic technique for experimentally locating the phase centres of such horns which does not require the use of a VNA and can therefore be applied in any frequency band in the millimetre and submillimentre part of the spectrum.

The phase centre of a feed horn is usually defined in engineering practice as the centre of curvature of the radiating beam defined by the on-axis curvature of the equiphase fronts [Goldsmith, 1998]. The location of the phase centre is important to ensure correct focusing in an optical system or a telescope. As indicated above, a VNA clearly could be used to determine the phase centre [Villa, 2002][Maffei, 2000] however such systems are very expensive in the millimetre/sub-millimetre band. What is proposed here is a holographic phase retrieval method that is simple and inexpensive to implement.

This chapter goes on to describe in detail the author's work on the application of holographic techniques in the millimetre-wave and terahertz range for phase

retrieval. An experimental arrangement, adapted from off-axis near-field holography at visible wavelengths, was employed that utilizes a raster scanning detector to record the holograms digitally [Mahon, 2006][Mahon,2011]. Then using phase retrieval methods, the recorded holographic interference pattern can be used to determine the required effective phase centres of radiating feed antennas, including non standard radiators such as planar lens antennas as well as shaped horns proposed for future CMB experiments.

# 6.2 Holography

Holography is a powerful technique that encodes, in the form of an interference pattern, the amplitude and phase of a scattered beam, recording the whole wavefront. At visible wavelengths this pattern is usually formed by light scattered from an object being interfered with a coherent reference beam such as a laser. Both amplitude and phase information in the recorded hologram can be recovered from the fringe pattern produced. At visible wavelengths the hologram has traditionally been recorded using wet photographic techniques and through silver halide emulsions. When the hologram is re-illuminated with the reference laser beam a virtual image of the original object is produced. This "re-illumination" can also be performed using a computational approach where the hologram has been recorded digitally by a CCD or other means as described in detail in the forthcoming sections of this chapter. Computational simulations of holographic reconstruction in fact can be used at any wavelength allowing holography to be used at any wavelength where a visible image could not be reproduced such as at millimetre wavelengths.

In the 1960s E.N.Leith and Y.Upatniks devised the near field off-axis holographic technique using an obliquely incident reference beam [Kreis, 2005] which is the basis for the approach taken here also. The long coherence length of the newly invented laser made this arrangement practical. By using an off-axis arrangement the reconstructed image, its conjugate, and the reference beam were separated thus improving the quality of the reconstructed image whereas previously (before lasers became available) these where all in line making the image difficult to see. The

general off-axis arrangement for recording a hologram is shown in Figure 6-1. A single beam of coherent light is split in two using a beamsplitter. One beam is reflected onto the photographic plate by a mirror, which is referred to as the reference beam. The second beam illuminates the object and the light scattered by the object onto photographic plate forms the object beam.
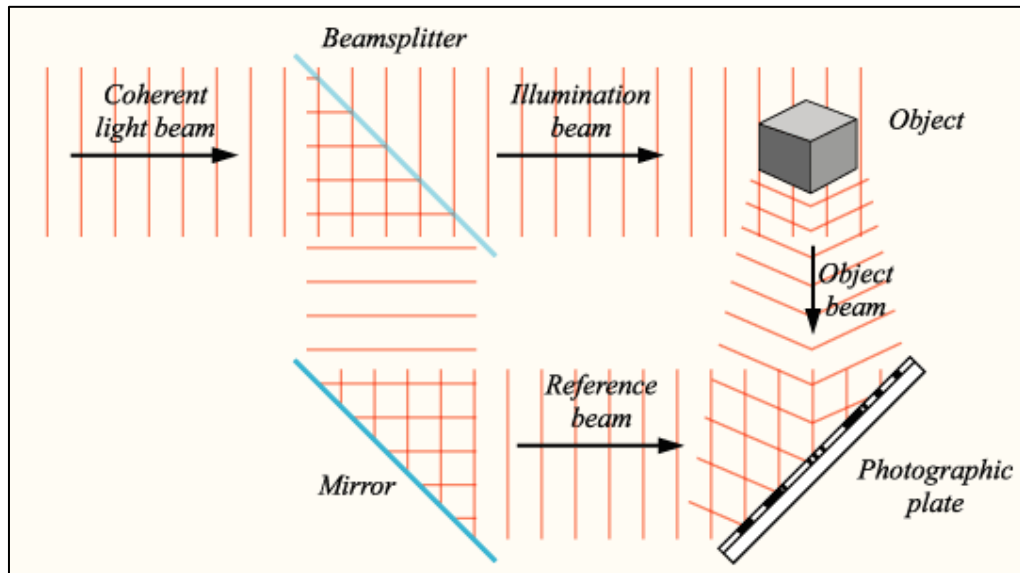


**Figure 6-1: Diagram showing the general arrangement used to record an off-axis hologram.[credit: Wikipedia]**

For visible light holography, where the image is viewed by eye, the image of the object is reconstructed by re-illuminating the recorded hologram with the reference beam. The hologram acts like a grating whose lines are those of the recorded interference pattern. Thus re-illuminating this grating with the reference beam results in a diffraction pattern which mimics the original object beam with the zero order of the grating corresponding to the transmission of the reference beam. The result of the re-illumination of the setup shown in Figure 6-2 is a virtual image of the object behind the photographic plate on which the hologram is recorded. This form of holography is known as transmission holography, referring to the fact that the reference beam is transmitted through the hologram in order to reconstruct the image of the object. This is in contrast to reflection holography where when recording the hologram the reference beam and object beam are incident on the holographic plate from opposite sides. In this latter case it is a real image that is reconstructed and it is viewed from the same side as the incident reference beam.
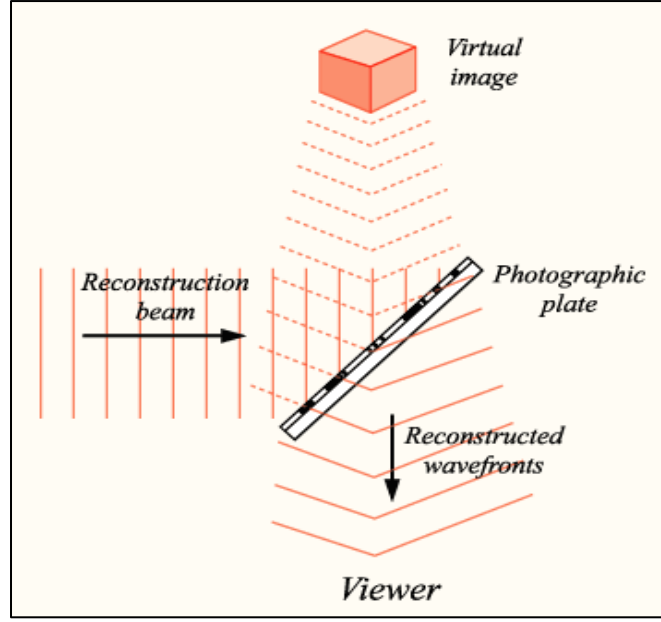
**Figure 6-2: Reconstruction of the object image by re-illuminating the hologram with the reference beam. [credit: Wikipedia]**

From a theoretical viewpoint the formation and holographic reconstruction can be understood as follows (which will also be relevant to the development of the millimetre wave holographic approach described later); defining the object beam, $E_o$, and the reference beam, $E_r$, as

$$E_o = O(x, y)e^{i\phi_o(x,y)} \quad , \tag{6.1}$$

$$E_r = R(x, y)e^{i\phi_r(x,y)} \quad , \tag{6.2}$$

where $\phi_o$ and $\phi_r$ are the phase of the object beam and reference beam at the plane of the hologram respectively. The interference pattern recorded as a result of the interference of these two beams can be written as

$$h(x, y) = |E_o + E_r|^2 = |Oe^{i\phi_o} + Re^{i\varphi_r}|^2$$
$$= |O|^2 + |R|^2 + ORe^{i\phi_o - i\phi_r} + ROe^{i\phi_r - i\phi_o} \quad , \tag{6.3}$$

where the dependence on $x$ and $y$ is understood in the various terms. When the holographic image is reconstructed by illuminating the hologram with the reference beam, it can be written as

$$E_1 = E_r(x, y)T(x, y)$$
$$= E_r(|O|^2 + |R|^2) + |R|^2 Oe^{i\phi_o} + |R|^2 Oe^{2i\phi_r - i\phi_o} \quad , \tag{6.4}$$

where $T(x,y)$ is the transmission of the photographic plate. In this case $|O|^2$, effectively the intensity of the scattered light, varies slowly with $x$ and $y$, while $|R|^2$

clearly must also vary slowly for a well behaved reference beam. On the other hand $\phi_o$ and $\phi_r$ vary rapidly with position on the order of a wavelength. Assuming a linear recording process, i.e. all parts of the photographic plate have the same response to uniform illumination, the transmission can be written as $T(x,y) = T_0 h(x,y)$ where $T_0$ is the transmissivity of the plate and $h(x,y)$ is the interference pattern recorded in the hologram (clearly an approximation). The three terms in this equation represent three independent optical fields at the plane of the hologram.

$$E_1^1 = E_r \left( |O|^2 + |R|^2 \right) \qquad\qquad (6.5)$$

$$E_1^2 = |R|^2 O e^{i\phi_o} = E_o |R|^2 \qquad\qquad (6.6)$$

$$E_1^3 = |R|^2 O e^{2i\phi_r - i\phi_o} = E_o^* |R|^2 e^{2i\phi_r} \quad . \qquad\qquad (6.7)$$

The $E_1^1$ term represents the propagation of the reference beam through the hologram. The second term $E_1^2$ contains the information about the object beam when the hologram is viewed from the opposite side to the original object. This is the term associated with the formation of a virtual image of the object. The third term $E_1^3$ forms a conjugate real image which appears like a distorted image of the object. Figure 6-3 illustrates this general case for a hologram re-illuminated by the reference beam used to create the hologram in which the virtual and real (conjugate) images are shown. Clearly if $E_1^1$, $E_1^2$, and $E_1^3$ are independent diffraction order beams that happen to overlap in the plane of the hologram, the actual original object beam would appear identical to a viewer, when viewed by eye, as the diffracted beam from the reference illuminated plate ($E_1^2$). Thus to a viewer the field $E_1^2$ appears to come from an object (the original scatter) at the relevant plane. The real image and reference beam would also be visible but separated spatially from the virtual (true undistorted) image.
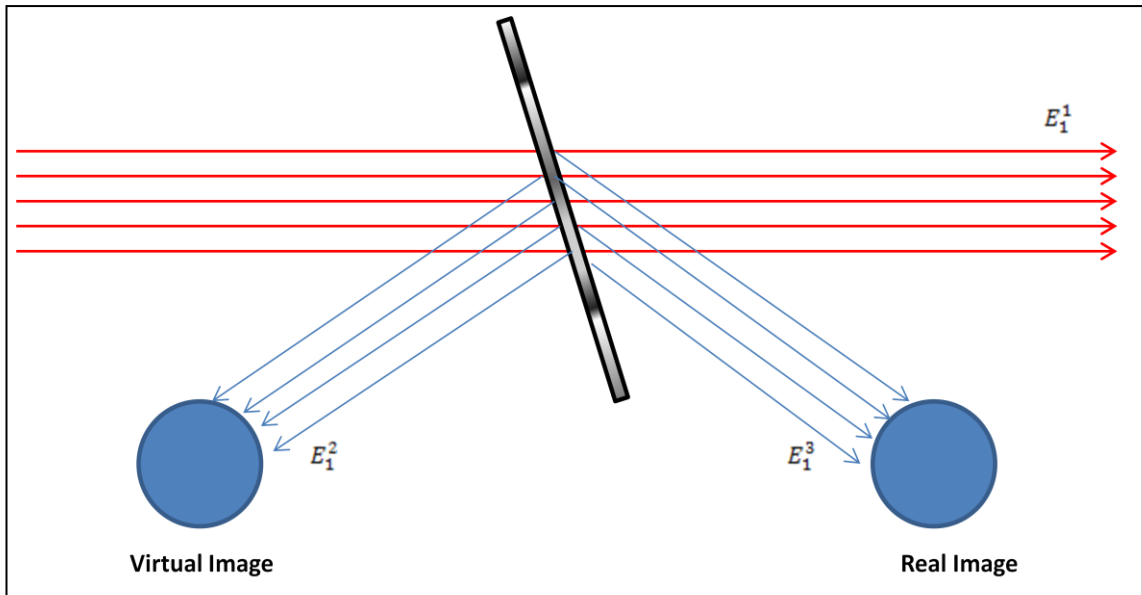
**Figure 6-3: Reconstruction of images from an off-axis hologram.**

# 6.3 Digital Holography

In the previous section the basic concepts of holography have been outlined. That description was based on the traditional methods of using photographic plates to record a physical hologram and viewing the reconstructed image by eye. The advent of digital recording devices, such as CCD arrays, now allows for the hologram to be easily captured digitally at visible wavelengths. As the hologram is no longer a physical entity the reference beam cannot be used to re-illuminate the hologram. However, clearly an appropriate transmission diffractive element based on the recorded holographic interference pattern can be produced [Lukin, 2007]. Clearly it is also possible to simulate the reconstruction of the image computationally.

In order to simulate the propagation of the beam away from the plane of the hologram it is necessary to expand the formulas developed in the last section. Let us begin by treating the object and reference beams as 3-dimentional with each having an axis of propagation defined by $z$ and $z'$ respectively and where the $(x,y)$ and $(x',y')$ planes are transverse to the direction of propagation (Figure 6-4).

208
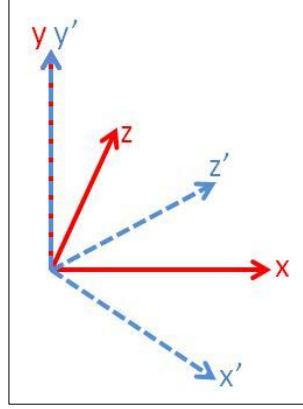
**Figure 6-4 : Diagram of the geometry used to describe the direction of propagation of the object and reference beams.**

Let the object beam be given by $E_O(x, y, z)$ and the reference field be given by $E_R(x', y', z')$, where the optical axis for the two beams are $z$ and $z'$ respectively. We can record the hologram at the plane $z = 0$ for example. We assume the axes of the beams are aligned so that the $(x, 0, z)$ plane and the $(x', 0, z')$ plane coincide (so that $y' = y$) and also so that the two beam axes intersect at $z = z' = 0$. If we orient the plane at which we measure the intensity of the interference pattern resulting from the overlap of the two beams so that it lies parallel to the $x$-$y$ plane at $z = 0$ then this is given by:

$$I(x, y, 0) \propto \left| E_O(x, y, 0) + E_R(x', y, z') \right|^2 = \left| E_O(x, y, 0) \right|^2 + \left| E_R(x', y, z') \right|^2 + 2\,\mathrm{Re}\left[ \{ E_O(x, y, 0) \}^* E_R(x', y, z') \right]$$

(6.8)

and is equivalent to the previous equation (6.3). Clearly $\left| E_O(x, y, 0) \right|^2$ and $\left| E_R(x', y, z') \right|^2$ vary only slowly with $x$ and $y$, whereas the interference term $\mathrm{Re}\left[ \{ E_o(x, y, 0) \}^* E_R(x', y, z') \right]$ varies rapidly with $x$ and $y$ as the two beam axes ($z$ and $z'$) are not aligned. Here all terms are real which is useful for visualizing the interference pattern whereas previously in equation 6.3 the phase terms were preserved to emphasise the different diffraction orders viewed during reconstruction. If we express $E_O(x, y, z)$ and $E_R(x', y', z')$ in polar form as $O(x, y, 0)\exp(-j\phi_O(x, y, 0))$ and $R(x', y, z')\exp(-j\phi_R(x', y, z'))$ the intensity pattern can be rewritten as

$$I(x,y,0) \propto (O(x,y,0))^2 + (R(x',y,z'))^2 + 2O(x,y,0)R(x',y,z')\cos[\phi_O(x,y,0) - \phi_R(x',y,z')]$$

$$= (O(x,y,0) - R(x',y,z'))^2 + 4O(x,y,0)R(x',y,z')\cos^2\left[\frac{\Delta\phi_{OR}(x,y,0)}{2}\right]$$

(6.9)

where again $O(x,y,0)$ and $R(x',y,z')$ are slowly varying real functions (amplitudes) of position whereas the interference term $\cos^2[\Delta\phi_{OR}(x,y,0)/2]$ varies rapidly. Generally $R(x',y,z')$ should be adjusted so that over the centre of the pattern the visibility of fringes is as high as possible, so that $O(x',y,z') - R(x',y,z') = 0$ (i.e. slowly varying background intensity). This is important for recovering information about the scattered field to high accuracy.

If the angle between the optical axis of the object and reference beam is taken to be α then the relationship between the coordinate representations of the beams is $x' = x\cos\alpha, y' = y, z' = x\cos\alpha$. Thus for a reference beam with a planar wavefront the interference phase term is given by: $\Delta\phi_{OR} = \phi_O(x,y,0) - kx\cos\alpha$. Therefore, if the object beam has a simple spherical wavefront of radius $R_O$ (such as scattering from a small point like object) then assuming the paraxial approximation the interference term is given by: $\Delta\phi_{OR} = k(x^2 + y^2)/2R_O - kx\sin\alpha$. Thus, it should be possible to recover $R_O$ for the object beam. In general however, the object beam will be more complicated and various characteristics of this beam should be recoverable from investigation of the hologram interference pattern.

In visible light holography the object beam is viewed by eye by re-illuminating the hologram intensity pattern with the reference beam. This reconstruction can be modelled by computer simulation and therefore applied to other wavelengths using a plane wave representing the reference beam to illuminate the hologram. The object beam propagation can then be followed forward or backward along its path using near field diffraction theory. The Fresnel-Kirchoff integral [Goodman, 1996] results in the complex amplitude $E(x,y,z)$ at a plane, $z = d$, of:

$$E(x_d, y_d, d) = \frac{i}{\lambda d} e^{-i\frac{\pi}{\lambda d}(x_d^2 + y_d^2)} \iint\limits_{(x,y)} R(x,y)t(x,y)e^{-i\frac{\pi}{\lambda d}(x^2 + y^2)} \times e^{i\frac{2\pi}{\lambda d}(xx_d + yy_d)} dxdy \quad , \quad (6.10)$$

where $x_d$ and $y_d$ represent the point's off-axis location in the plane $z = d$. $E(x_d, y_d)$, can be recovered by performing a Fast Fourier Transform (FFT) of the function $R(x, y)t(x, y)e^{-i\frac{\pi}{\lambda d}(x^2+y^2)}$ , where $t(x,y)$ represents the "transmission" of the digital hologram in the simulations and which is proportional to the recorded interference pattern $I(x,y,0)$. At the position of the original object we should therefore recover a virtual image while the reference beam and the beam associated with the real image should also be present at this plane but extended and diffuse.

Although it is assumed that the reference beam is a uniform plane wave here the intensity pattern of the reference beam used in the experiments described later is in fact Gaussian. However over the small region which the hologram is recorded the reference beam varies only slowly and these large scale intensity changes are dominated by the fringes of the interference pattern produced by the interaction of the beam with the object beam. Therefore we assume for the moment that the reference beam can be approximated through its phase front only, which is considered to be planar i.e.

$$R(x, y, 0) = \exp(i(k_x x + k_y y)) = \exp(ikx\cos\alpha), \qquad (6.11)$$

where $(k_x, k_y)$ are the directional cosines for the reference beam wave vector (general case).

With this mathematical framework in place for 3-D analysis of beam diffraction it is now possible to move forward to describe in detail the application of holographic techniques for phase retrieval and the determination of the phase centres of horn antennas. As alluded to above, the location of the phase centre is extremely important to ensure correct focussing in an optical system or a telescope. The experimental arrangement employed in this work is detailed in the following section of this chapter. Additionally the software developed by the author to perform the simulations of the reconstruction process is described. Subsequent sections report on the results of these experiments for phase centre determination and on the results of additional experiments in the area holographic imaging.

# 6.4 Experimental Set-up for Digital Holography at MM-Wavelengths

An experimental arrangement based on off-axis near-field holography configurations traditionally employed at visible wavelengths as described in the last section was adapted using a raster scanning detector to record the holograms at millimetre wavelengths (Figure 6-5). In this case the object is the radiating horn of interest. The object and reference beams were produced using the two radiating horn antennas fed by a single coherent source via a cross-guide coupler (Figure 6-5). The majority of the measurements were made in the W-band (75-110 GHz) at a spot frequency of 100 GHz ($\lambda = 3$ mm). The parabolic mirror was positioned such the quasi-Gaussian beam produced by the corrugated conical horn that produces the reference beam had a waist at the recording plane of the scanner. This allowed for the use of the assumption of a planar phase front for the reference beam as in the reconstruction method described previously.

An Osctek 10A-002 Gunn oscillator was used as the coherent 100 GHz source for the majority of the experiments described in this chapter. The bias power supply of the oscillator was modulated at 13 Hz using a function generator so that a lock-in amplifier could be used to filter noise from the signal from the detector. A Flann Microwave 3 dB directional coupler was used to split the output of the oscillator between the two horn antennas. One of the horn antennas was positioned such that it pointed directly at the scanner plane (Figure 6-5). This provided either the object beam or the illumination beam for scattering off an object. The output of the second horn, the reference beam, was reflected off the parabolic mirror to provide the collimated beam that interferes with the object beam at the plane where the holographic recording was made. The mirror was orientated ensuring that the reference beam crossed the object beam at the scanner plane at an angle of about 45° (see Figure 6-5).

Two attenuators, one between the coupler and each of the horn antennas, allowed for the intensity of both the reference and object beams to be controlled. The quantity of fringe visibility is given by

$$Q = \frac{\left(I_{max} - I_{min}\right)}{\left(I_{max} + I_{min}\right)} \qquad , \qquad (6.12)$$

which defines the contrast of an interference pattern $I$, where $I_{max}$ and $I_{min}$ are the maximum and minimum intensities recorded. Clearly it is important that this contrast is maximised in order to obtain good fringe visibility. This quantity can be expressed in terms of the intensity of the object beam, $I_o$, and reference beam, $I_r$, as

$$Q = \frac{2I_r I_o}{I_r^2 + I_o^2} \qquad . \qquad (6.13)$$

Thus by using the attenuators to balance the amplitudes of the object and reference beams the fringe visibility of the hologram can be maximised (i.e. $I_o = I_r$).
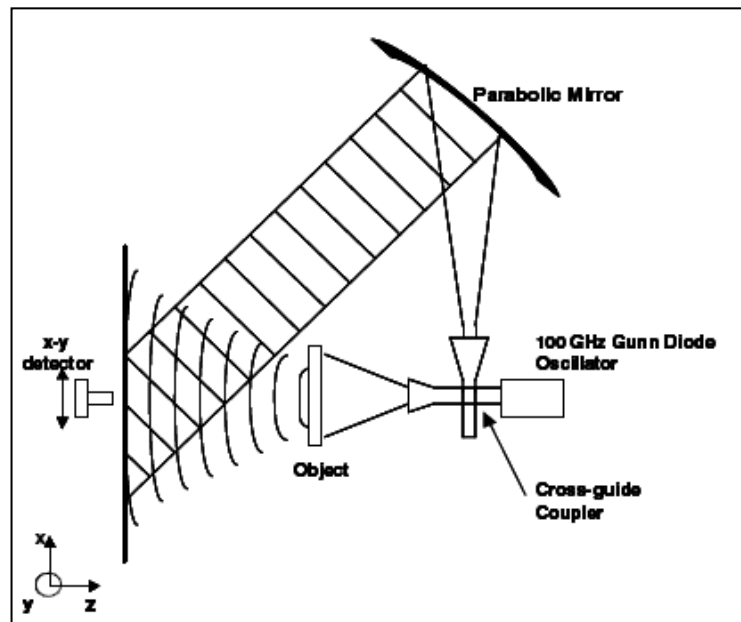


**Figure 6-5 : Diagram outlining the basics of the experimental setup used [Mahon,2011].**

A Dorado CD10 Schottky barrier diode detector was used to measure the intensity of the interference pattern of the two beams (i.e. the hologram). The signal from the detector was fed through a preamp stage to the EG&G model 5104 lock-in amplifier to filter the detector signal before being recorded by the computer controlling the experiment.

The detector was mounted on a raster scanner so that it could be translated across the plane of the hologram. This *x-y* scanner used when the experimental technique was being developed is visible in Figure 6-6. Two stepper motors were

used to control a set of belts which moved the detector around the scan plan. The motion of the detector was controlled via custom Labview software running on a PC. The software also collected the data from the detector and wrote it to a file.
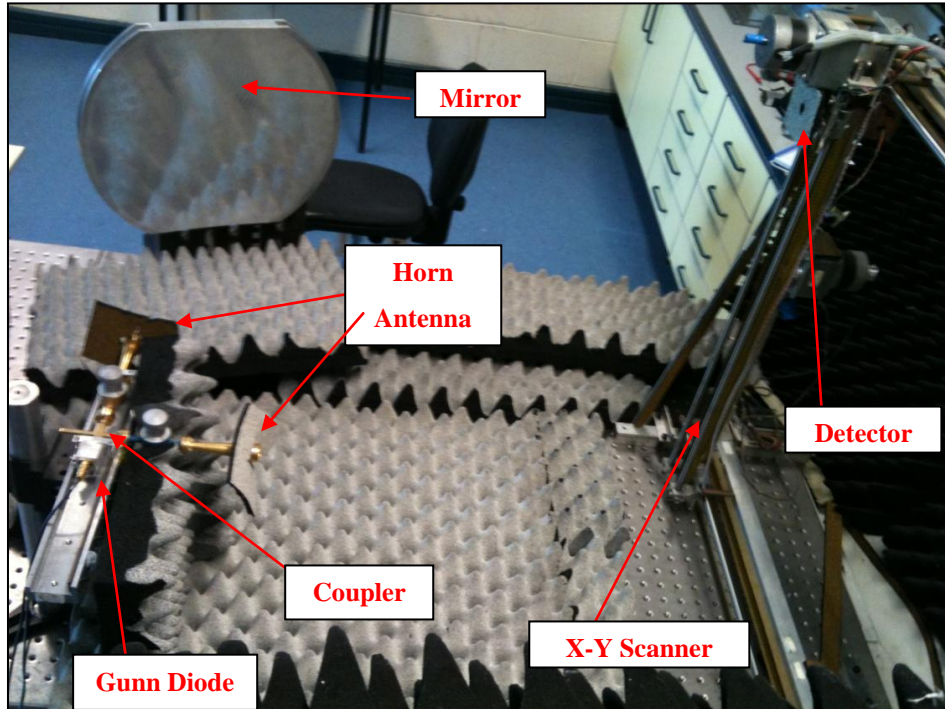


**Figure 6-6 : Photograph of the original experimental setup featuring the x-y scanner.**
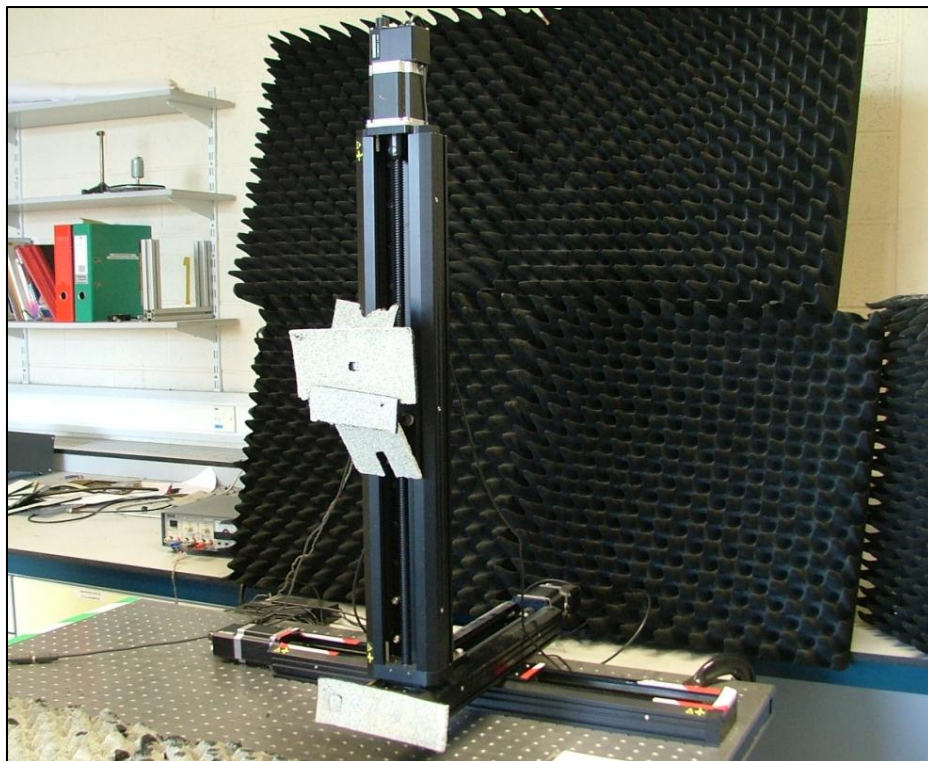


**Figure 6-7 : The new scanner made up of three Zaber linear stages.**

214

The lightweight frame of the scanner on which the motors and belts were mounted proved to be prone to vibrations during operation. The decision was made to replace the scanner with a new system after it was damaged due to a malfunction when a positional opto sensor failed. The frame was replaced by a three axis system so that in addition to the $x$ and $y$ axis it would also be capable of movement in the $z$ direction allowing for the fine tuning of the position of the plane where the hologram is recorded. Three Zaber T-LST series computer controlled motorized linear stages were purchased as the basis for the new system, in which two 500 mm stages were used for the $x$ and $y$ axis while a 250 mm stage was used for the $z$ axis (Figure 6-7). The stages move on precision leadscrew driven by a stepper motor. Each stage was set to a micro-step size of 0.5 µm which provided a high degree of positional precision. Additionally each stage has an integrated controller to control the motion of the stage and uses an encoder to monitor the position of the stage relative to its home (zero) position at all times. This position can be stored in one of 16 memory blocks for later recall. The stages are also designed to be mounted directly on optical benches using the standard 6 mm bolts, which is extremely useful in aligning the scanner on the optical bench. When these features are combined it makes it possible to repeat any number measurements accurately over exactly the same scan plane.
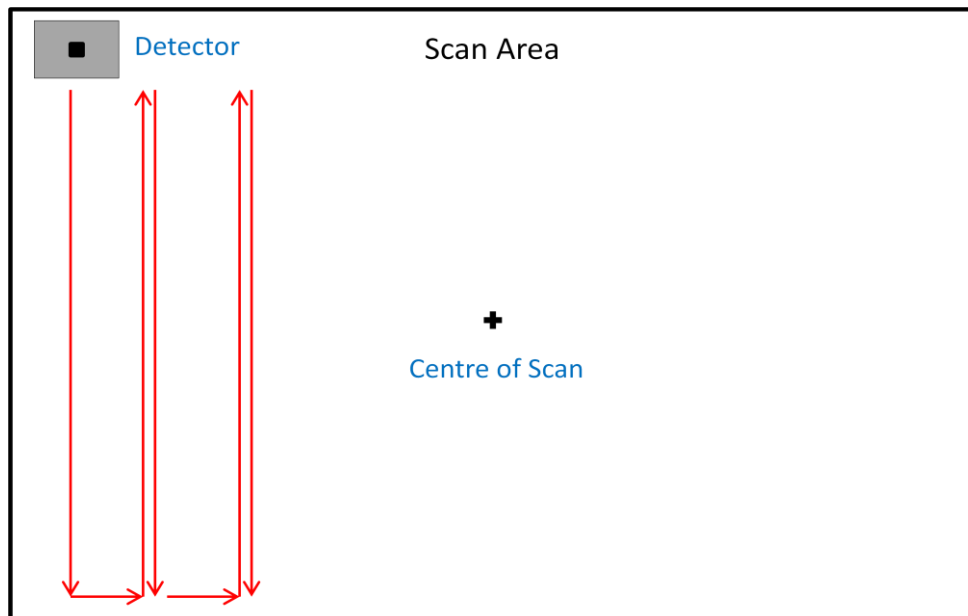


**Figure 6-8 : Diagram illustrating the scanning strategy used to cover the scan area of the hologram. A measurement is taken at each step during the downward movement phases**
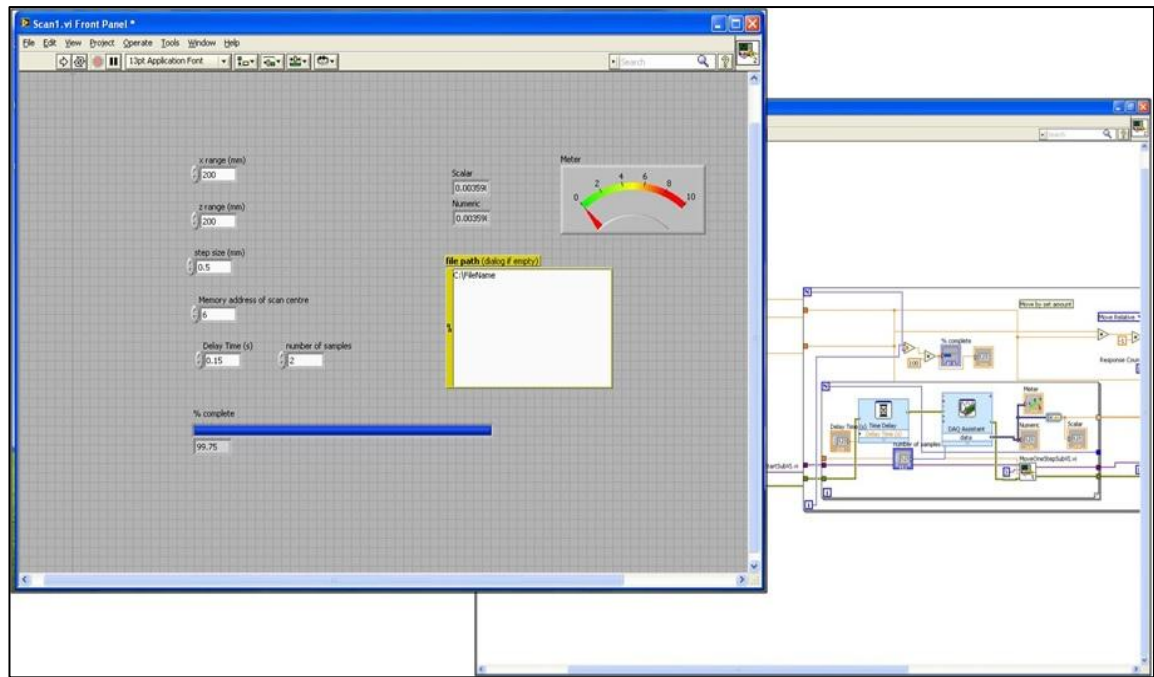
**Figure 6-9 : Front panel and block diagram of the scanner control program written in Labview.**

The same scanning strategy that had been used for the original scanner is used in the new system. At the beginning of an experiment run the detector is positioned in the centre of the area to be scanned. The detector is then moved to the upper left corner of the scan area. From there it is moved vertically down in predefined steps recording the intensity of the interference pattern. When the detector reaches the lower end of the scan area it is moved one step to the right and returned to the top of the scan area. This is repeated until the detector reaches the bottom right corner of the scan area and the intensity of the interference pattern is recorded over the entire area of interest. This scanning strategy is illustrated in Figure 6-8 where a measurement is taken at each step during the downward movement phases. A custom Labview program was written to control the system (Figure 6-9). The three stages were supplied with Labview sub-VIs which read data (e.g. position, axis speed) from and send movement / control commands to integrated controllers built into the stages. These sub-VIs formed the basic building blocks of the code. Combining these with an appropriate algorithm it was possible to create a full control program to implement the desired scanning strategy. In addition to this custom written software the manufacturer's "Zaber Console" control software can be used also to setup and optimise the stages (Figure 6-10). Each stage can also be moved either by computer control or by a manual control on the stage itself to any desired position, e.g. the centre point of the scan area and the Zaber console software can be used to store this

position in memory built into the stages. This can then be accessed by the labview program as needed.
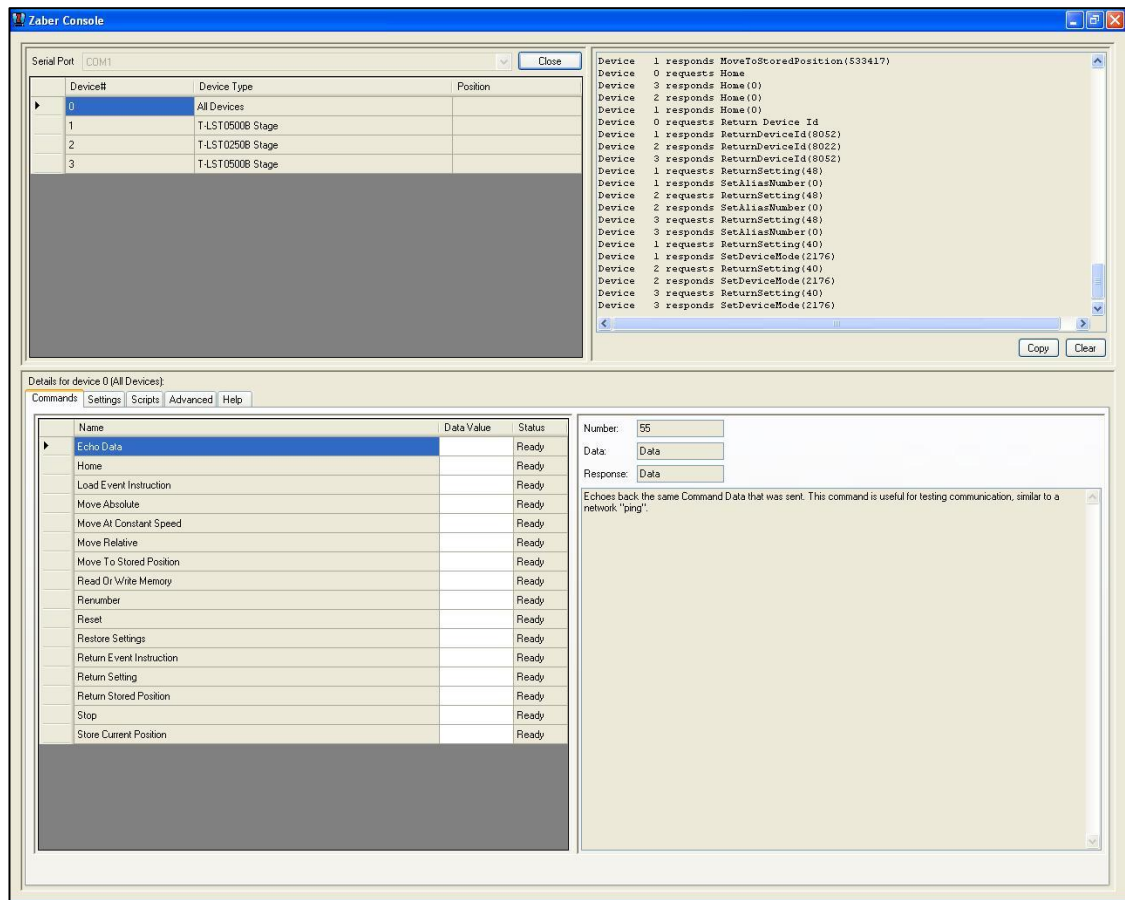


**Figure 6-10 : The Zaber Console software supplied with the linear stages by the manufacturer.**

Using the Zaber console software the speed, acceleration, and micro-step size of the stepper motors of each axis were adjusted to minimise vibrations during scanning. It was decided that these settings should not be adjustable in the Labview program in order to avoid inadvertent changes being made to them. The maximum travel speed that the stages are capable of being driven at by the stepper motors is of the order of 3 cm s$^{-1}$. An acceleration of up to 2 cm s$^{-2}$ is possible however over the short distance of each movement in a typical scan these maximum values are not ideal. The rapid movements and sudden stops that these accelerations entail produce vibrations in the system that result in noise being introduced into the recorded data. Therefore significantly lower values were chosen for both the acceleration (0.320 mm s$^{-2}$) and maximum travel speed (2.5 mm s$^{-1}$) so that the movement from scan point to scan point was a smooth as possible while still maintaining a reasonable

scan time (i.e. not too long).  Over the millimetre step size distances in a typical scan these values were found to produce little vibration and negligible noise in the system.

It was found that compared to the original belt and frame system (Figure 6-6) the Zaber stages (Figure 6-7) provided more stability and greater precision in positioning allowing for greater accuracy and repeatability in the experimental results using the newer system.

# 6.5  Test Results  for mm-wave Holographic Imaging

In order to verify the holographic technique proposed here for millimetre wavelengths a known object field was used to form an interference pattern with a well defined reference beam using an off-axis configuration and the holographic virtual image recovered.   It should be possible to recover the object beam from the holographic interference pattern recorded using Equation 6.9.  Alternatively Equation 6.10 can be used to simulate the back propagation of the object beam towards the position of the source object beam or the forward propagation to the farfield.

To test the experimental setup and the holographic reconstruction technique a number of holograms were made of known scattering objects.  The test objects were chosen for their recognisable shapes and contours which were desirable for verifying that a millimetre wave image could be reconstructed.  A mask was made from some Eccosorb (an absorbing material) with a clear opening in the shape of the letter M removed (Figure 6-11).  This mask was mounted on aeroboard, which is essentially transparent at millimetre wavelengths, and illuminated by a conical horn antenna thus providing the 'object' beam to scatter the radiation on passing through the M-shaped aperture in the Eccosorb.  Figure 6-11 actually shows the setup used to record the hologram of the M shape.  As can be seen the object is positioned a distance from the non-reference beam horn antenna (fed by a 50:50 waveguide beam splitter) which illuminates it allowing the beam to diverge sufficiently to cover the aperture in the

mask. However care had to be taken to ensure that the object was not so far from the horn that its positioning vignetted the reference beam (Figure 6-5).
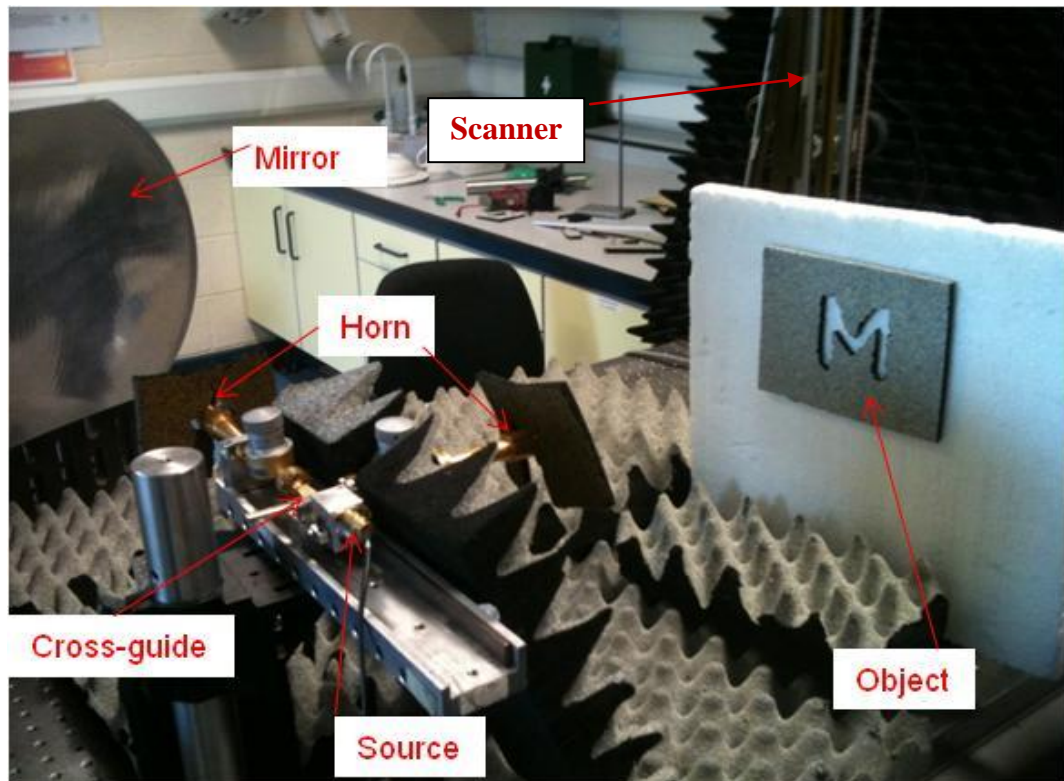


**Figure 6-11 : Experimental setup used to record a hologram of the M-shaped object.**

The hologram recorded of the interference pattern produced by the object beam from the M shaped aperture in the Eccosorb and the reference beam is shown in Figure 6-12(a). The image reconstructed using the back propagation software code (based on using FFT to perform the Fresnel Diffraction described in equation 6.10) is shown in Figure 6-12(b). The reconstruction was scaled to focus in on the virtual image, Figure 6-12(c) shows the complete reconstruction at the distance of the original object from the hologram plane. In addition to the virtual image of the object, the zero order reference beam and the first order real image beam can also be seen next to it. The technique can clearly be used to reconstruct the object beam, reference beam, and real image beam at any distance from the plane of the hologram. By performing the FFT Fresnel diffraction calculation at successively increasing distances from the hologram plane to the point of the location of the original object, where a clear M-shape image can be seen, the evolution of the beam can be seen as it propagates from the object to the hologram. In Figure 6-13 the virtual object beam, reference beam, and real image beam are reconstructed at four different distances from the hologram plane. At 50 mm

the reference beam and object beams are still overlapping thus an interference pattern is recovered. By 120 mm from the hologram the three beams have separated and an M-like pattern can be seen in the object beam. At 220 mm the three beams have fully diverged and the M shape can be clearly seen. At 290 mm, a significant distance behind the original object position, the image of the M seems to have moved out of focus again as expected of course.



(a)



(b)



(c)
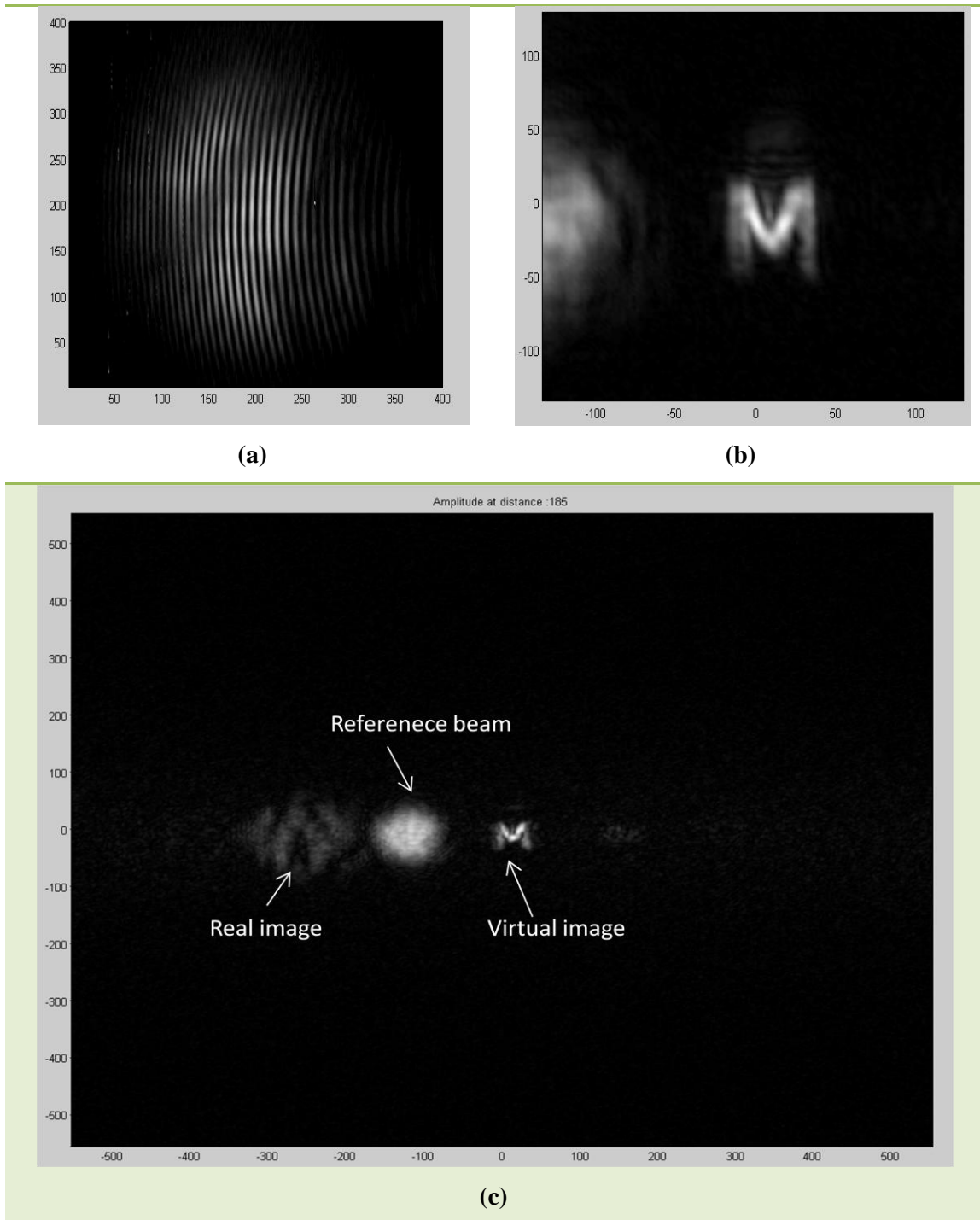
**Figure 6-12 : (a) The recorded hologram. (b) The reconstructed image of the M shape. (c) the complete reconstruction with the virtual image, reference beam, and real image beam visible. All axis are in mm.**
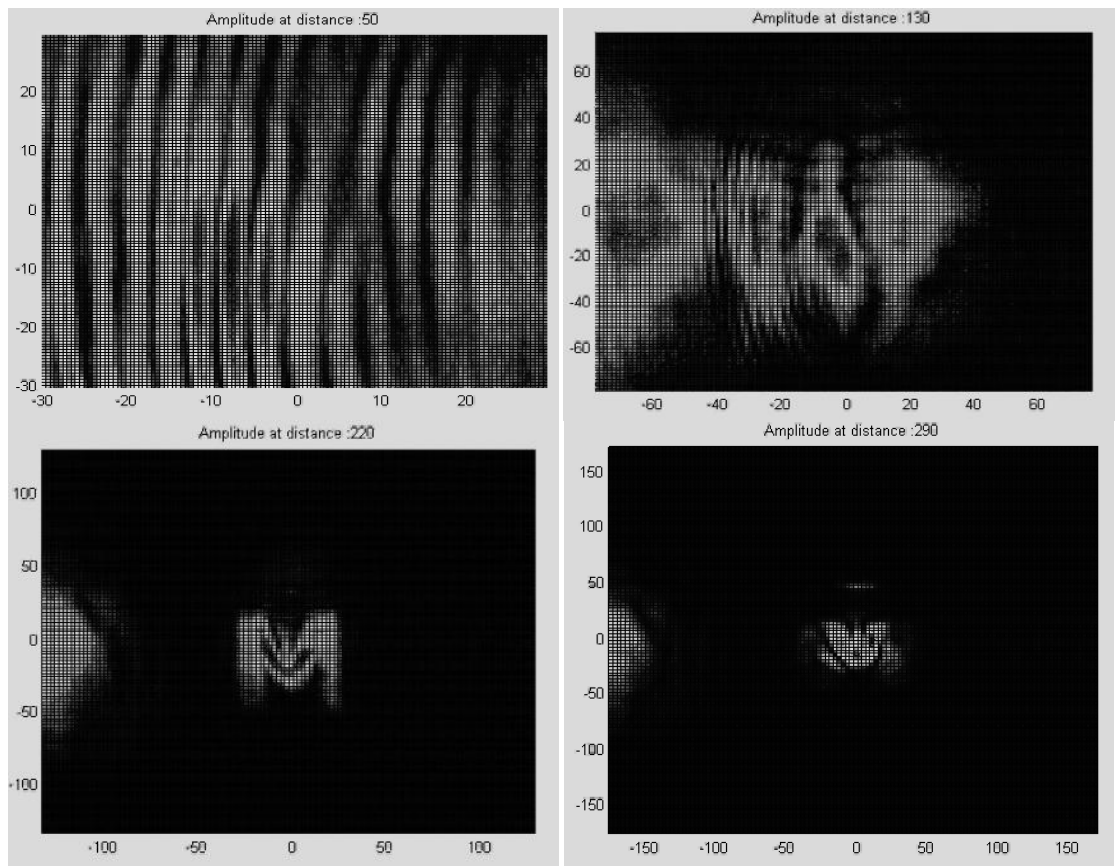
**Figure 6-13 : Each frame shows the reconstruction of the object beam at a distance of 50 mm, 130 mm, 220 mm, and 290 mm respectively from the hologram plane. All axes are in mm.**

By computing such beam reconstructions at a large number of transverse planes it is possible to recreate a 3-D data cube of the object beam as it is back propagated away from the hologram along the $z$-axis so that the 3-D evolution of the beam can be investigated. A plan view, such as the $x$-$z$ plane at y = 0, provides insight into the evolution of the object beam as it propagates. The plan view for the M shape hologram reconstruction is shown in Figure 6-14. The real image beam is visible at the top of the plot, while the reference beam is along the centre and the object beam at the bottom.
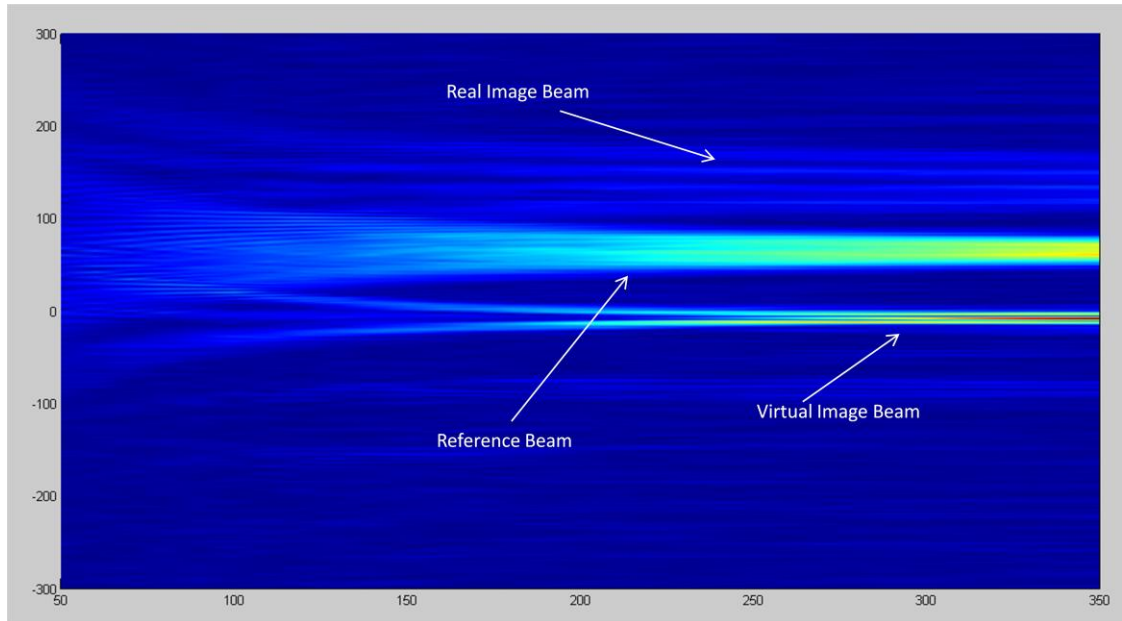
**Figure 6-14 : Plan view of the virtual image beam, reference beam, and real image beam as they are back propagated from the hologram along the z-axis. The horizontal z axis is in mm. While the vertical x axis is marked in step from the centre.**
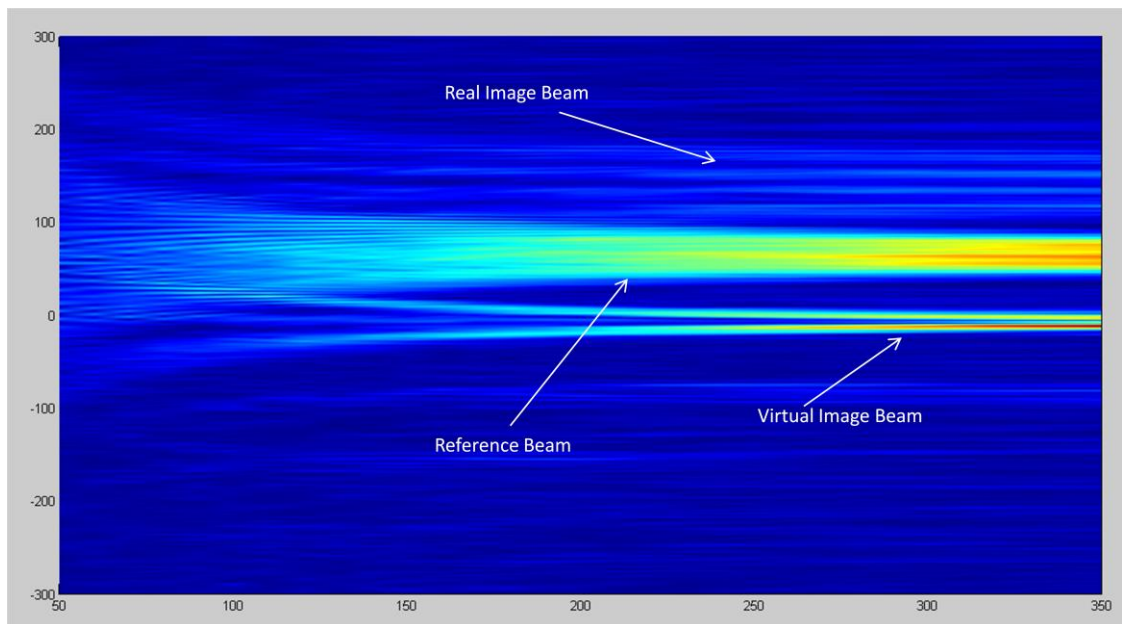


**Figure 6-15 Plan view of the virtual image beam, reference beam, and real image beam as they are back propagated from the hologram along the z-axis. In this plot the correction has been applied and a difference in the virtual image beam and reference beam can been seen in comparison to the uncorrected beams shown in Figure 6-14. The horizontal z axis is in mm. While the vertical x axis is marked in step from the centre.**

Clearly the reconstruction method recovers the correct intensity pattern (i.e. a clear M illuminated aperture) at the apparent location of the object. However, if the reference beam is not truly collimated but has some curvature then the image will be reconstructed at the wrong place in terms of the placement of the original object when making the hologram. Particularly this is possible in long wavelength systems as the

222

beam remains collimated over a relatively finite distance $\sim \left( \dfrac{\pi W_0}{\lambda} \right)$ where $W_0$ is the

Gaussian beam width of the reference beam at its waist. This is a critical issue if the technique is to be extended so as to locate the phase centre of a horn antenna which is the goal of this chapter. A correction is clearly necessary to the technique. In order to investigate this, a very simple object beam was used (i.e. a point like object -actually produced by a bare waveguide source by replacing the horn from the object illumination source in Figure 6-4). Clearly this needs to be corrected in the reconstruction method by including a curvature term for the reference beam. The *x-z* plane plot of the back propagation of the beams show in Figure 6-14 was made before any such correction was applied. In Figure 6-15 the same *x-z* plane plot is shown but with a correction for the reference beam curvature in place. Differences in the virtual image beam and reference beams can be seen between the two plots. In particular it can be seen that in Figure 6-14 the beams converge more rapidly as one moves away from the hologram than in Figure 6-15 and thus the virtual image of the original of the M shape object was reconstructed closer to the plane of the hologram than the original object.

A final consideration is that using the FFT to perform the integral transforms the linear *x-y* coordinates of the recorded hologram into an angular separations. The position on the *x*-axis at a distance *d* from the hologram plane for an element in the $n^{th}$ row of the matrix describing the reconstructed beam is given by

$$ x = \frac{\lambda dn}{xrange} \qquad , \qquad (6.14) $$

where the *xrange* is the range of the *x*-axis of the hologram in millimetres. A similar equation describes the *y*-axis at a distance *d* from the hologram. The dependence on the distance *d* in these equations means that as the reconstruction moves away from the hologram plane the separation between each point (pixel) in the *x-y* plane of the reconstructed beams increase. The images of the object beam shown in Figure 6-13 show the change in scale on each axis at the position of each reconstruction. This change in scale has not been applied to the plan views shown in Figure 6-14 or Figure 6-15. In Figure 6-16 the same *x-z* plane plot is shown again but with the correct *x*-axis scale at each distance along the *z*-axis. The angular effects of the FFT can be seen

in this plot. This view clearly shows the separation of the virtual image beam, the reference beam, and the real image beam as they move away from the hologram.
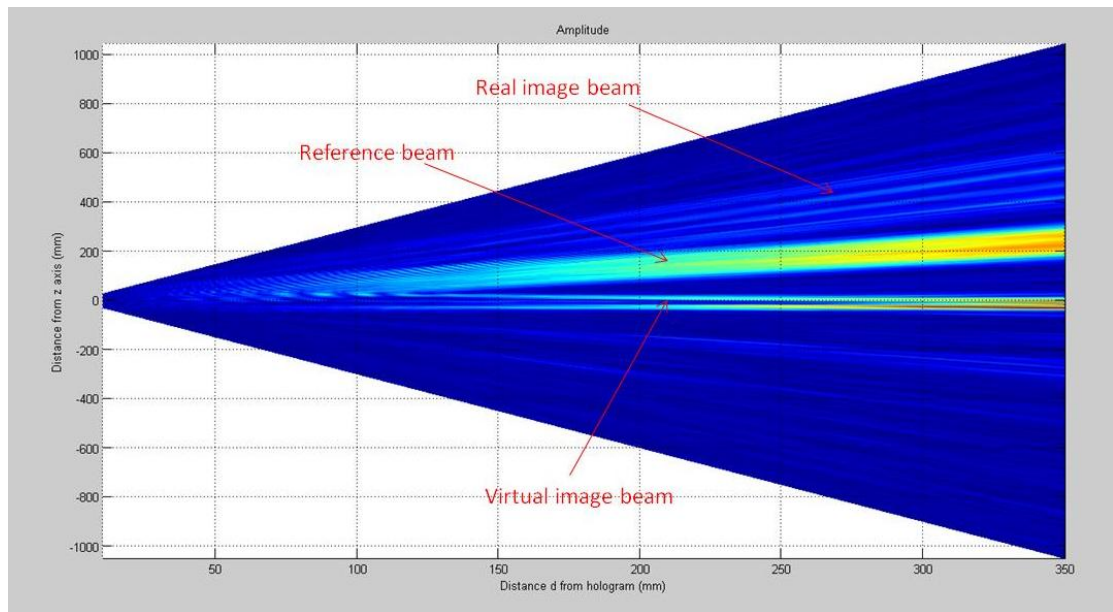


**Figure 6-16 : Plan view of the virtual image beam, reference beam, and real image beam as they are back propagated from the hologram along the *z*-axis. The correct scale for *x*-axis has been applied at each distance along the *z*-axis from the hologram plane. All axis are in mm.**

# 6.6 Recovering the Phase Curvature of the Reference Beam

Clearly, as we have seen in the last section, one significant source of error in recovering the object is in the assumption that the reference beam has a pure plane wavefront and its possible curvature can be neglected. Since in the practical experimental set up the reference beam was produced by a scalar horn with a quasi-Gaussian beam pattern and a recollimating mirror, as shown in Figure 6-5, it was not possible to guarantee that the Gaussian beam actually had a waist precisely at the scan plane where the interference intensity pattern was recorded. Thus the true phase front of the reference beam should have a curvature term so that:

$$E_{ref} = E_R \exp\left(\frac{-r'^2}{w_0^2}\right)\exp\left(-j\frac{kr'^2}{2R_{ref}}\right)\exp\left(-jkz'\right)\exp\left(j\phi(z')\right) \, , \qquad (6.15)$$

where $r'^2 = (x'^2 + y'^2)$ as defined in the previous section. If we assume the object beam has the form

$$E_0 = E_0(x, y)\exp(-j\phi_0(x, y))\exp\left(-j\left[kz + \frac{k(x^2 + y^2)}{2R_0}\right]\right) \quad , \quad (6.16)$$

where the phase variation $\phi_0(x, y)$ is only slowly varying and $E_0(x, y)$ is the amplitude (also slowly varying) then the interference pattern (hologram) will be dominated by the fringes produced by the fast varying phase terms. So that the intensity pattern at $z = 0$ (the plane of the hologram) can written approximately as

$$I(x, y) \propto \left| A\exp\left(-jk\frac{k(x^2 + y^2)}{2R_0}\right) + B\exp\left(-jk\left[z' + \frac{k(x'^2 + y'^2)}{2R_{ref}}\right]\right) \right|^2 . \quad (6.17)$$

Transforming the $(x', y', z')$ coordinates gives

$$x' = x\cos(\alpha) - z\sin(\alpha), \quad y' = y, \quad z' = z\cos(\alpha) - x\sin(\alpha),$$

which implies (again with $z = 0$) that:

$$I(x, y) \propto \left| 1 + Re\left(-jk\left[x\sin(\alpha) - \left(\frac{x^2\cos^2(\alpha) + y^2}{2R_{ref}}\right) - \frac{x^2 + y^2}{2R_{ref}}\right]\right) \right|^2 , \quad (6.18)$$

where $r = B/A$ and $Re(z)$ is the real part of $z$. Thus,

$$I(x, y) \propto \left| 1 + Re\left(-jk\left[x\sin(\alpha) - \left(\frac{x^2}{2R'_x}\right) - \frac{y^2}{2R'_y}\right]\right) \right|^2 = \left| 1 + Re(-j\Delta\phi_{or}) \right|^2, \quad (6.19)$$

where $\dfrac{1}{R'_x} = \dfrac{1}{R_0} - \dfrac{\cos^2(\alpha)}{R_{ref}}$ and $\dfrac{1}{R'_y} = \dfrac{1}{R_0} - \dfrac{1}{R_{ref}}$ and in this case the interference term is clearly

$$\Delta\phi_{OR} = \frac{kx^2}{2R'_x} - \frac{ky^2}{2R_y} - kx\sin\alpha . \quad (6.20)$$

Clearly if $R_{ref} = \infty$ (collimated beam) the correct centre of curvature for the wavefront and the correct image position for the object can recovered. On the other hand if

$R_{ref} \neq \infty$ the recovered apparent positions for the object ($z = -R'_x$ & $R'_y$) will be astigmatic and at the wrong plane. It is clearly important therefore in any reconstruction that $R_{ref}$ be known. This can be measured and recovered from a calibration hologram if the position of a calibration object, such as a point source, is known.

Although the phase radius of curvature of the reference beam may be very large (very low curvature) nevertheless it can introduce significant errors for a system where one is locating the phase centre of a radiating antenna to wavelength accuracy. It can easily be shown that for a tolerance on the phase centre position of $\delta$, we require the reference beam radius of curvature $R_R > R_o^2/\delta$, which could be quite challenging unless extreme care was taken in setting up the test experiment.



**(a)**



**(b)**　　　　　　　　　　　　　**(c)**
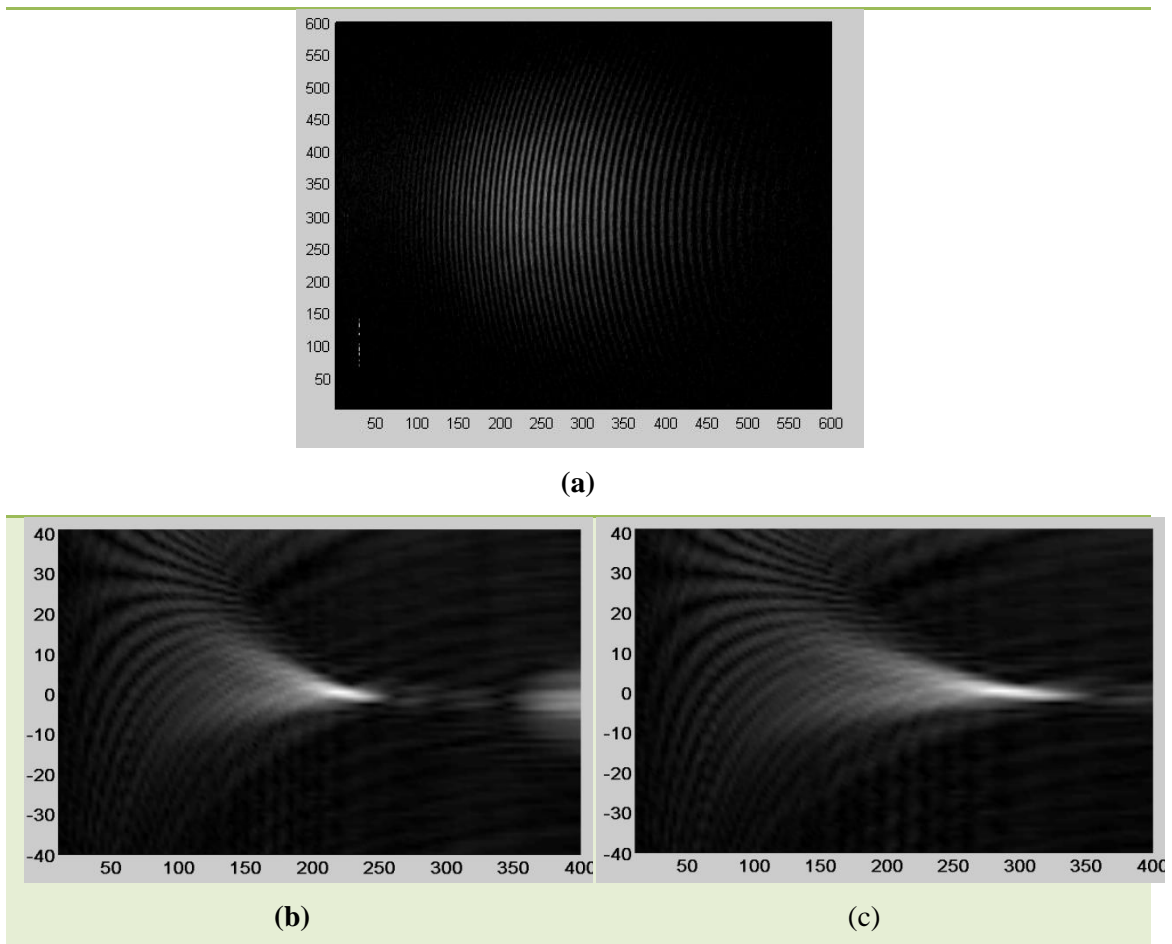
**Figure 6-17 : a) Hologram of a point source (bare waveguide aperture) at a wavelength of 3 mm measured on test set-up shown in Figure 1. The axis are in number of steps. b) Reconstruction of the beam along the z-axis back towards waveguide without error correction which locates phase centre at incorrect location. c) Reconstruction of the beam propagated along the z-axis back towards waveguide with error correction which locates phase centre correctly at aperture of waveguide. For plots (b) and (c) the horizontal z axis is in mm. While the vertical x axis is marked in step from the centre.**

We can thus recover $R_R$ by using a bare radiating waveguide which acts as a point source object with a phase centre position precisely known. In effect this can be thought of in terms of the bare waveguide becoming the reference beam (i.e. well known and understood) and the quasi-collimated beam from the scalar horn becoming the object beam! However keeping to the same symbols as previously $R_x$ and $R_y$ can be recovered from the intensity measurements (the hologram) and $R_R$ for the collimated scalar horn beam then estimated at the measurement plane. An example of this is shown in Figure 6-17 in which account was taken of the curvature of the reference beam derived from the hologram of a point source in the form of a bare waveguide aperture. In the experimental setup the bare waveguide was placed at a distance from scan plane (hologram plane) that was measured as accurately as possible. This known distance was compared to the distance obtained by back propagating the object beam reconstructed from the hologram before the reference beam curvature was included. The difference between the two was used to calculate the correction to be applied to the radius of curvature of the simulated reference beam used in reconstruction program. As can be seen in Figure 6-17 (b) before a correction for the phase error in the reference beam was applied the reconstruction of the waveguide beam locates the phase centre, i.e. the aperture of the waveguide at an incorrect distance from the hologram. By applying the phase correction the phase centre is located at the correct position, Figure 6-17 (c).

# 6.7  Holography Applied to Millimetre-wave Antenna Measurements

The primary aim of this research into millimetre-wave holography was to investigate applications for studying the radiation characteristics of millimetre-wave antennas. In this case the object beam is actually the beam radiated by the horn antenna of interest fed directly by the beam splitter / cross guide coupler (see Figure 6-5). In particular it would be extremely useful also to determine the effective phase centres of non-standard antennas, including planar lens antennas as well as shaped horn antennas (particularly those specially designed for CMB experiments). Once the

phase error of the reference beam had been determined as described in the last section it is then possible to use back propagation of the object beam as a means of precisely locating the phase centre of a millimetre-wave antenna. Using the recorded holographic interference pattern one can numerically propagate the recovered object beam back towards the source plane in order to recover the object beam in the vicinity of the waist (the effective phase centre) to determine the effective phase centre. Assuming that the position of the antenna relative to the scanner / hologram plane (phase centre of the detector) is known to a sufficient accuracy the location of the phase centre relative to the antenna can then be determined. The amplitude and phase of the fields there can also, of course, be recovered as well as location. A number experimental test campaigns were undertaken, and measurements were taken, for a lens antenna and two different horn designs (a corrugated conical horn and a piecewise conical profile horn). Experimental results for two of these millimetre-wave antennas, the corrugated conical horn and the lens antenna, are presented here (we will return to the piecewise conical profile horn later).



**Figure 6-18: Conical horn used in testing of the experimental holographic techniques for determining antenna phase centres.**

The conical corrugated horn with a known phase centre chosen for the initial experiments, shown in Figure 6-18, has an aperture radius of 7.15 mm and an axial length of 80 mm. The hologram of the horn antenna was recorded as previously described above and is shown in Figure 6-19. The object beam was then reconstructed, Figure 6-20, and the phase centre deduced. The slight asymmetry in the reconstructed beam is due to a slight misalignment in the system. A VNA was used to provide an independent measurement of the phase centre of the horn for comparison

with holographic method. The VNA determined that the phase centre was located 4.9 mm behind the aperture of the horn. By back propagation the phase centre was found to be located precisely at the horn aperture with an error of ±20 mm. Both results are consistent given the associated experimental errors although the error associated with the holographic method is large (~ ±6 λ).
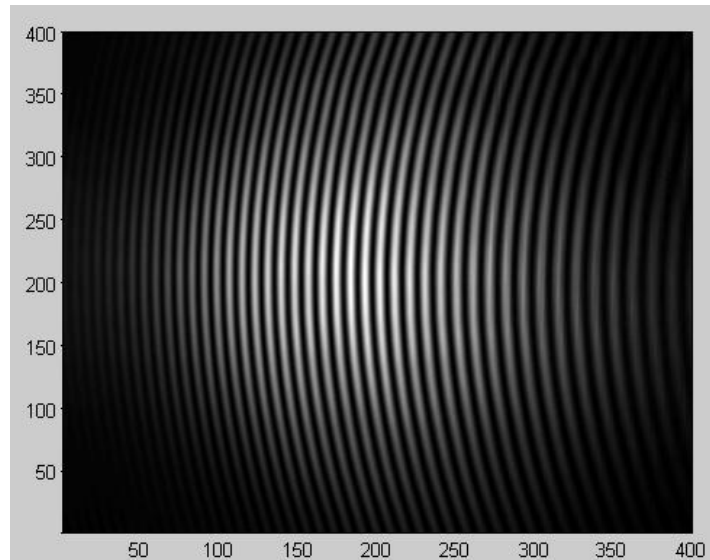


**Figure 6-19 : Hologram of beam from the conical horn. The axis are marked in number of steps.**
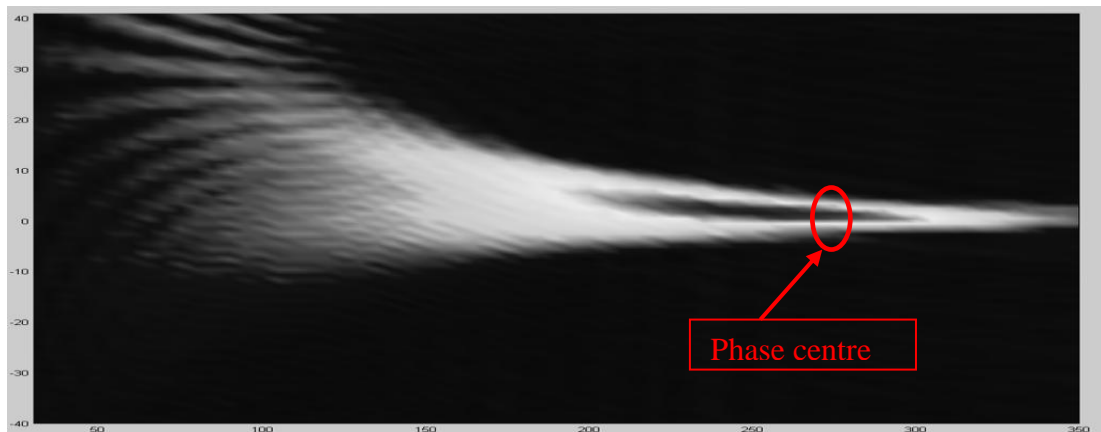


**Figure 6-20 : back propagation of the beam of the conical horn used to determine its phase centre. The horizontal z axis is in mm. While the vertical x axis is marked in step from the centre. The red circle indicates the approximate location of the phase centre.**

Another type of feed antennas investigated was a lens antenna. The term lens antenna is in general used to describe a range of antenna designs which feature a combination of a planar antenna and a collimating lens which is often placed in contact with the antenna. Lens antennas have been used in terahertz and millimetre-wave projects such as the high frequency channels of the HIFI instrument of the Herschel space telescope [Jellema, 2008] above 1.0 THz. Lens antennas, such as a

lens combined with sinuous antennas, have been proposed for CMB polarization missions [Lee, 2009][Suzuki, 2012]. Unlike waveguides and most single moded horn antennas the phase centres of lens antennas are often ill-defined as they are difficult to model and thus it is important to able to measure them by experimental methods.

An example of a lens antenna was manufactured and tested. In this case the high density polyethylene (HDPE) lens used for the antenna was designed to mechanically fit on the flange of a standard WR10 rectangular waveguide rather than being fed by a planar antenna. The waveguide aperture feeding the signal to the lens was located at the focus of the lens (Figure 6-21) mimicking the phase centre of an equivalent planar antenna. This method of feeding the lens was used as a planar antenna was not available at 100 GHz in the experimental test laboratory at Maynooth University.



**Figure 6-21 : (Left) A schematic diagram of the dielectric lens milled from HDPE. (Right) Photograph of the lens attached to the waveguide.**
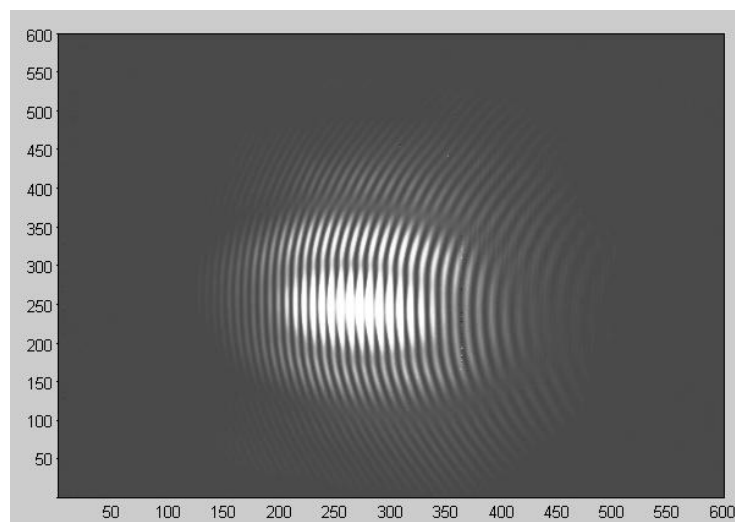


**Figure 6-22 : Hologram of beam from the lens antenna. The axis are marked in number of steps.**

230
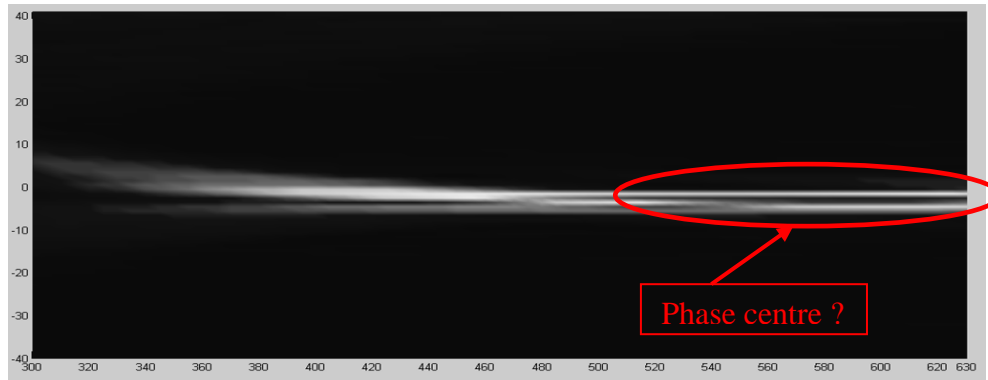
**Figure 6-23: Profile of the beam from a conical horn constructed from the hologram of a lens antenna using back propagation. The horizontal z axis is in mm. While the vertical x axis is marked in step from the centre. The red circle indicates the area in which the phase centre may be located.**

Again back propagation was used to find the phase centre (Figure 6-23). However, it is difficult to discern the position of beam waist (which is approximately at the same location as the phase centre) due to the high degree of collimation of the beam which introduces a large error in to the method. From this method is was determined that the phase centre of the lens antenna was 25 mm ± 30 mm behind the apex of the lens towards the waveguide.

Clearly an alternative method is needed to locate the phase centre with greater accuracy to be useful and in fact this is also true for the case of the corrugated conical horn. In order to see how such a method might be devised we next return to reconsider the hologram fringe pattern and what limits its usefulness for high accuracy determination of the phase centre location (which ideally an error of the order of a wavelength or less i.e. ±3 mm in this case).

# 6.8 Recovering the Phase Centre Through Fringe Pattern Analysis

Let us first consider the sources of inaccuracy in analysing a hologram. Up to this point the analysis has assumed that the alignment of the system was optimised such that the reference beam and object beam intersect at the plane of the hologram. However, in an experimental setup at millimetre wavelengths, where the radiation is invisible and the depth of field relatively long, it is not possible to align the system

with the precision required to ensure that the two beams intersect at exactly at this point. Therefore let us now examine the more general case, which is indicative of the real experimental setup, where the reference beam and object beam are slightly misaligned. As before let us describe the object and reference beams as 3-dimentional each having an axis of propagation defined by $z$ and $z'$ respectively and where the $(x,y)$ and $(x',y')$ planes are transverse to the direction of propagation (see Figure 6-24). Again let the object beam be given by $E_O(x, y, z)$ and the reference field be given by $E_R(x', y', z')$, where the optical axis for the two beams are $z$ and $z'$ respectively. We can record the hologram at the plane $z = 0$ as before. This time however we will allow for the reference beam to be displaced relative to the object beam. This means that at the hologram plane while both $z = 0$ and $z' = 0$ are equal to zero the $y$ axes no longer coincide i.e. $y' \neq y$ (see Figure 6-24).
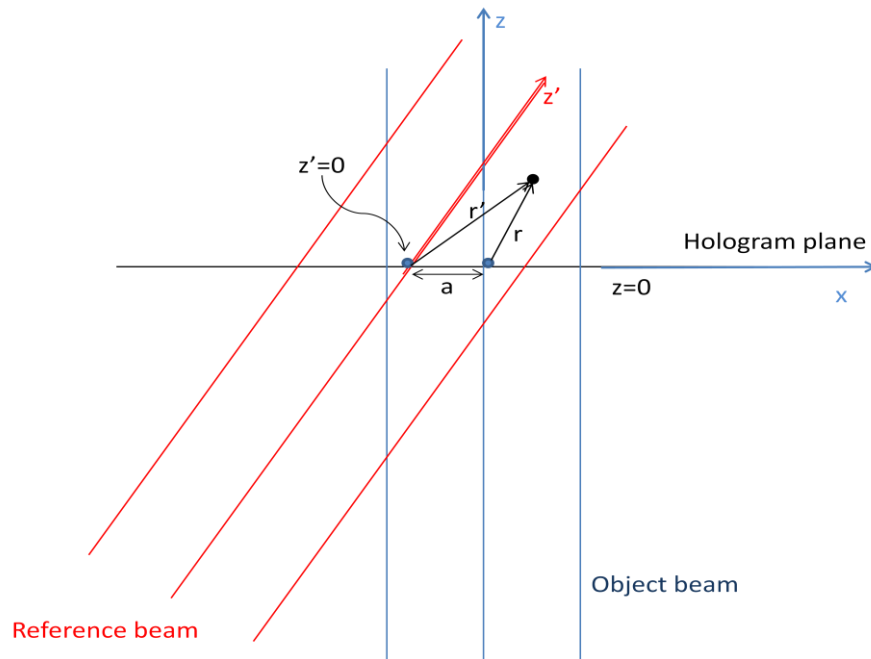


**Figure 6-24 : Plan view of the more general case where the reference beam and the object beam don't intersect exactly at the plane of the hologram.**

If we now consider the point defined by the vector $\mathbf{r}$ in the coordinates of the object beam then it is defined in the coordinates of the reference beam as

$$\mathbf{r}' = \mathbf{a} + \mathbf{r}$$
$$\mathbf{r}' = x'\hat{\mathbf{i}}' + y'\hat{\mathbf{j}}' + z'\hat{\mathbf{k}}' \qquad , \qquad (6.21)$$
$$= (a + x)\hat{\mathbf{i}} + (b + y)\hat{\mathbf{j}} + z\hat{\mathbf{k}}$$

where $a$ and $b$ are displacements in the $x$ and $y$ directions as shown in Figure 6-25.

232
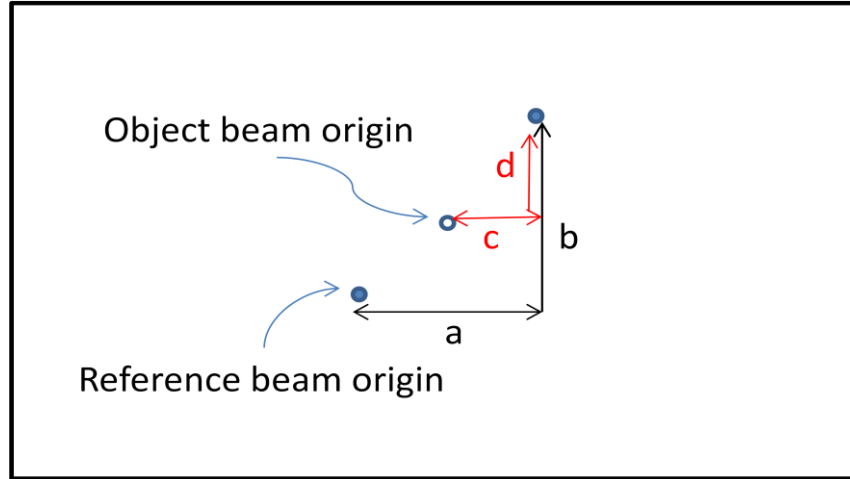
## Hologram Plane



**Figure 6-25 : View of the hologram plane (*x-y* plane at *z* = 0) showing a point displaced from the origin of both the object and reference beam coordinates**

Taking the dot product $\mathbf{r}'$ of with $\hat{\mathbf{i}}'$ and $\hat{\mathbf{k}}'$ gives

$$x' = (a+x)\cos(\alpha)$$
$$z' = (a+x)\sin(\alpha) \qquad (6.22)$$

where $\alpha$ is the angle between the object and reference beams and clearly since the origin is defined as lying on the hologram plane, $z = 0$. Similarly for the object beam if its axis is displaced from the nominal origin it can be shown that at the plane $z = 0$ that $x'' = (x+c)$ and $y'' = (y+d)$ while still assuming $z'' = 0$.

Returning to the equation for the intensity of the interference pattern derived earlier (equation 6.17) and rewriting in terms of the coordinates of this general case with beams misaligned gives

$$I(x,y,0) \propto \exp\left(-jk\left[(a+x)\sin\alpha + \left(\frac{(a+x)^2\cos^2\alpha + (b+y)^2}{2R_{ref}}\right) - \frac{(c+x)^2 + (d+y)^2}{2R_o}\right]\right)$$

$$(6.23)$$

For a constant value of $x$ the variation of the phase term with respect to $y$ in the exponent has the form

$$\Delta\phi(y) = -jk\left[\eta(x) + \frac{y^2}{2}\left[\frac{1}{R_{ref}} - \frac{1}{R_o}\right] + y\left[\frac{b}{R_{ref}} - \frac{d}{R_o}\right]\right], \qquad (6.24)$$

$$= -jk\left[\eta x + \beta y^2 + \gamma y\right]$$

233

where $\beta = \dfrac{1}{2}\left[\dfrac{1}{R_{ref}} - \dfrac{1}{R_o}\right]$ and $\gamma = \left[\dfrac{b}{R_{ref}} - \dfrac{d}{R_o}\right]$.  Thus if we take a cut across the hologram in the $y$-direction, keeping $x$ constant, we will obtain a minimum for the intensity pattern when

$$\eta(x) + \beta y_m^2 + \gamma y_m = (2m-1)\lambda \ , \tag{6.25}$$

where $m$ is an integer.  An example of such an intensity pattern in the $y$-direction (keeping $x$ constant) is shown in Figure 6-26.  This is symmetric about some value of $y = \delta$.  Then clearly the minima on either side of the centre at $y = \delta$ must satisfy

$$\eta'(x) + \beta(y_n - \delta)^2 = n\lambda, \tag{6.26}$$

where $\delta = -\gamma/2\beta$, $\eta'(x) = \alpha(x) - \gamma/4\beta$ which is symmetric around $y = +\delta$.  We can therefore after some algebraic manipulation write for the $N^{th}$ minimum on either side of this axis at $y = \delta$ that

$$\eta'(x) + \beta\frac{(\Delta y_N)^2}{4} = N\lambda, \tag{6.27}$$

where $\Delta y_N = y_{+N} - y_{-N}$.  $\Delta y_N$ is the distance in the $y$-direction between the two $N^{th}$ minima on either side of the symmetry axis at $y = \delta$.  Clearly by taking the $1^{st}$ minimum $N = 1$ and the $N^{th}$ minimum we can recover $\beta$ from

$$\beta = \frac{4(n-1)\lambda}{(\Delta y_N)^2 - (\Delta y_1)^2}, \tag{6.28}$$

and we actually do not need to estimate $\delta$ only the distances between $y_{+N}$ and $y_{-N}$, and between $y_{+1}$ and $y_{-1}$ are required.  Thus by examining a cut through the recorded hologram for a fixed value $x$ the value of $\beta$ can be determined for that hologram.  Figure 6-26(b) shows an example of a cut in the $y$ direction through a hologram of a prototype horn with examples of minima chosen for $y_1$, $y_{+N}$, and $y_{-N}$ marked.  If the distance from the object to the hologram plane, $R_o$, is known then the value of the $R_{ref}$ can be calculated from

$$\beta = \frac{1}{2}\left[\frac{1}{R_{ref}} - \frac{1}{R_o}\right] . \tag{6.29}$$

234
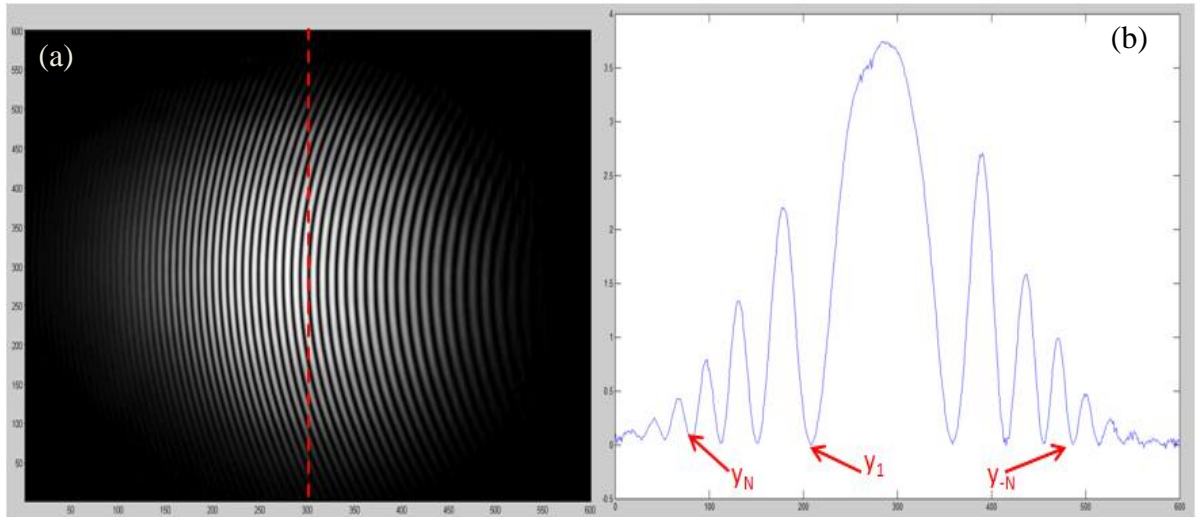
**Figure 6-26 : (a) a hologram recorded using a prototype CMB horn as the object. (b) A cut through the hologram along the y direction (as shown by dashed line in (a)), example postions of minima $y_1$, $y_N$, and $y_{-N}$ are shown.**

Alternately since there is a linear relationship between $(\Delta y_n)^2$ and $N$ we can recover $\beta$ by under taking a least squares fitting approach by minimising the fit to all of the minima:

$$K(\beta, \alpha(x)) = \sum_{n=1}^{N} \left[ (\Delta y_n)^2 - 4n\frac{\lambda}{\beta} - \eta(x) \right]^2, \qquad (6.30)$$

for a given cut. This can be solved using a standard approach to recover the slope $4\frac{\lambda}{\beta}$ from which $\beta$ can be extracted. Thus in this case

$$4\frac{\lambda}{\beta} = \frac{\overline{(\Delta y_n)^2 n} - \bar{n}\overline{(\Delta y_n)^2}}{\overline{n^2} - (\bar{n})^2}, \qquad (6.31)$$

where the average is taken in the usual fashion e.g. $\overline{(\Delta y_n)^2 n} = \frac{1}{N}\sum_{n=1}^{N} (\Delta y_n)^2 n$.

235

# 6.9  Phase Centre Determination with Increased Accuracy
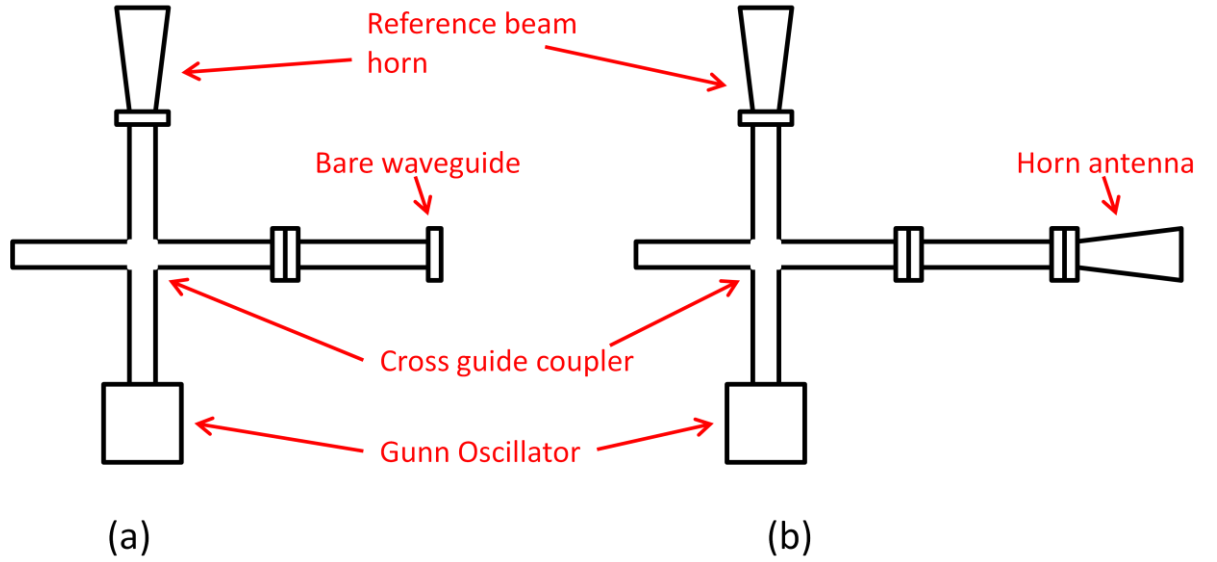


**Figure 6-27: Setup for determining movement of the phase centre when a horn fitted is to the end of a bare waveguide. (a) Setup with bare waveguide as object beam source. (b) Setup with horn antenna fitted to the waveguide.**

If we now consider two holograms made using the two experimental setups shown in Figure 6-27. The reference beam is the same for both setups but in case (a) the object beam is provided by a bare waveguide and in case (b) it is provided by a horn antenna fitted to the same waveguide. If it is possible to determine the shift in the position of the apparent phase centre of the object beam, $\Delta R$, between the two cases this would give the position of the phase centre relative to the phase centre of the bare waveguide, which is known to be at its aperture. Thus the position of the phase centre of the horn antenna could be determined without needing to determine $R_{ref}$. For each case the respective $\beta$ is

$$\beta_a = \frac{1}{2}\left[\frac{1}{R_{ref}} - \frac{1}{R_{oa}}\right] \quad \text{and} \quad \beta_b = \frac{1}{2}\left[\frac{1}{R_{ref}} - \frac{1}{R_{ob}}\right]. \qquad (6.32)$$

Subtracting these two $\beta$ gives

$$\Delta\beta = \beta_a - \beta_b = \frac{\Delta R}{2R_{oa}R_{ob}} , \qquad (6.33)$$

where $\Delta R = R_{oa} - R_{ob}$. Rearranging the expression gives

$$\Delta R = \frac{2 \Delta \beta R_{oa}^2}{1 + 2 \Delta \beta R_{oa}} \quad . \tag{6.34}$$

As the error in determining each $\beta$ and hence $\Delta\beta$ is dominant over the relative error in determining $R_{oa}$ it is possible to use this expression to estimate $\Delta R$ with high degree of accuracy. The phase centre of the bare waveguide is at its aperture and provided that the location of the aperture of the horn is known to high accuracy relative to the bare waveguide the location of the horn phase centre can be found. Using this approach the phase centres of a number of example feeds were determined: a corrugated conical horn, a lens antenna fed by a waveguide, and a specially designed smooth walled piecewise conical profile horn antenna for future CBM projects.

The piecewise conical profile horn antenna features a variable profile design as shown in Figure 6-28 [McCarthy, 2014]. It was designed by McCarthy et al. as a technology demonstration for future possible CMB polarisation experiments. Such experiments require sensitivity to extremely low level signals to make the polarisation measurements that will allow inflationary theories in cosmology to be further constrained, thus improving our understanding of the formation and evolution of the Universe. In order to achieve high levels of sensitivity, it is likely that a densely packed focal plane array will be used (for example the proposed CorE+ mission to the European Space Agency, ESA, [Delabrouille, 2015]). While corrugated horns can provide the required performance in terms cross-polar power, main beam symmetry, and sidelobe levels for such missions, they do carry thermal and mechanical penalties, which when many thousands are required, become overwhelming.

Thus, possible alternatives to corrugated horns have been investigated, and the optimization of shaped smooth-walled horns to meet the performance requirements of such missions across the band were considered in *McCarthy, 2014*. Such optimized smooth-walled horns can provide the required levels of performance in the areas of interest (e.g. cross polarisation levels), but with lower penalties than those associated with corrugated horns. The design described by [McCarthy, 2014] was kept as simple as possible using a piecewise conical profile design consisting of six sections (Figure 6-28). The horn was manufactured by Rutherford Appleton Laboratories (RAL) and

measurements of the far field beam patterns were found to agree very well with predictions, verifying the horn performs extremely well across the band. At the design frequency of 100 GHz, sidelobe levels of -50 dB are realized, with a highly symmetric main beam [McCarthy, 2014].

For each source, (horn antennas, waveguides, lens antenna), a hologram was recorded. In each hologram in order to determine the value for $\beta$ multiple cuts along the $y$-direction were made for constant values of $x$ and a value for $\beta$ was calculated from each cut. From these values a mean value for $\beta$ for each hologram was obtained. Table 6-1 below lists the $\beta$ values for each hologram and the standard deviations for each value.



(a)                                                                (b)
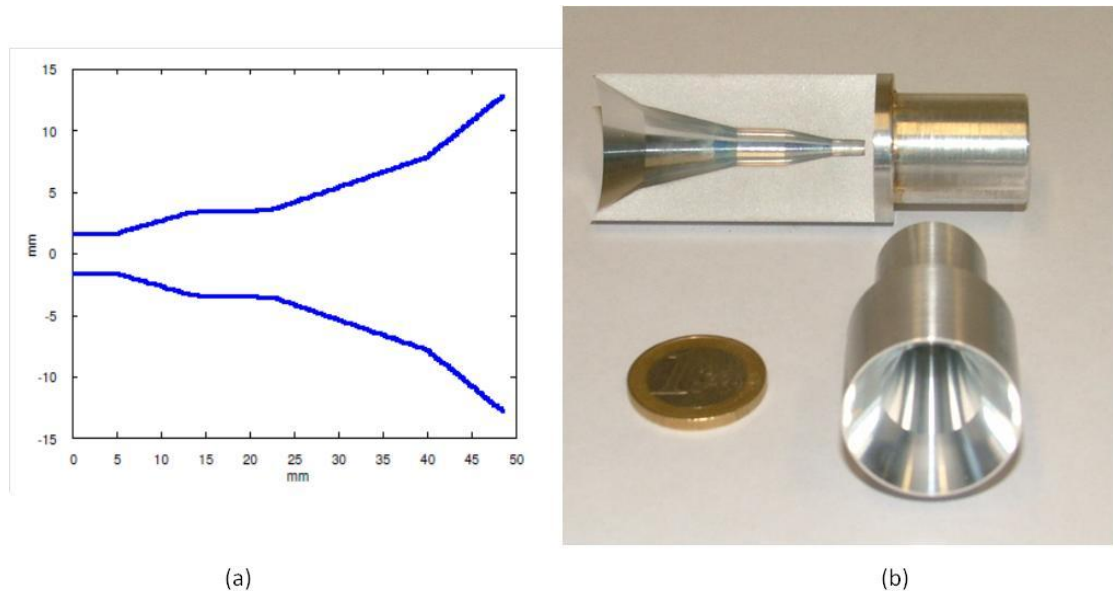
**Figure 6-28 : (a) Profile of the prototype smooth walled piecewise conical profile horn antenna designed for possible future CMB missions. (b) Photograph of the prototype horn and a cross-section cut showing the shape of the horn profile. [McCarthy, 2014]**

| | $\beta$ (m$^{-1}$) | $\sigma$ (m$^{-1}$) | Position of phase centre behind aperture |
|---|---|---|---|
| **Waveguide 1** | 0.00139 | 2.7E-05 | - |
| **Corrugated Conical Horn** | 0.00095 | 2.4E-05 | 13 mm ± 12 mm |
| **Waveguide 2** | 0.00139 | 1.1E-05 | - |
| **Lens Antenna** | 0.00132 | 9.4E-07 | 13 mm ± 16 mm |
| **Piecewise Conical Profile Horn Antenna** | 0.00150 | 2.2E-08 | 25 mm ± 15 mm |

**Table 6-1 : Table of $\beta$ values and there standard deviations for the various holograms used to determine the phase centres of the antenna under test.**

Using these values the phase centre of the corrugated conical horn was determined to be 13 mm ± 12 mm behind the aperture of the horn. This compares to the VNA measurement which placed the phase centre at 4.9 mm behind the aperture. A theoretical value for the location of the beam waist, which is approximately at the same position as the phase centre, can be calculated from

$$\Delta z = \frac{L}{\left[1 + \dfrac{\pi w_a}{\lambda L}\right]^2} \quad , \quad\quad\quad (6.35)$$

where $L$ is the slant length of the horn, $w_a = 0.6435a$, and $a$ is the aperture radius of the horn [Goldsmith, 1998]. The corrugated conical horn is 65 mm long and has an aperture radius of 7 mm. At 100 GHz it yields a theoretical position for the phase centre at 6.7 mm behind the aperture of the horn. The depth of field of this horn at 100 GHz is approximately 6 mm which may explain the discrepancy between these values results.

For the lens antenna this holographic method puts its phase centre at 13 mm ± 16 mm behind the front of the lens. The VNA gave a result of 18.6 mm ± 2.5 mm behind the front of the lens. However, the depth of field of the lens antenna beam is very long and may again explain the discrepancy between the two results.

The phase centre of the piecewise conical profile horn antenna was found to be located at a point 25 mm ± 15 mm behind the horn aperture. This agrees with the VNA measurement of the horn which placed the phase centre at 24.7 mm ± 1mm behind the aperture. One limitation on the accuracy of this approach turned out to be the quality of the hologram of the bare waveguide. The intensity of the hologram was considerably lower because of the non-directional nature of the radiation from this point-like source. This resulted in a lower signal to noise ratio than for the horn antennas.

While the above approach yielded acceptable results, improving upon the accuracy of the approach was investigated by comparing just the phase centre displacement between the piecewise conical horn and the corrugated conical horn and using the knowledge of the corrugated conical horn phase centre from literature. A

large number of cuts were also taken by varying $x$ over a significant part of the hologram. As can be seen in Figure 6-29 the value of $\beta$ varies with $x$ across the cuts which indicates that the curvature of the reference beam varies due to the non-normal angle of incidence with the scan plane. The value for $\varDelta\beta$ ($\Delta\beta = \beta_a - \beta_b$) however is constant for any particular $x$ as shown in Figure 6-30. Now taking this average $\varDelta\beta$ for the two horns for the range of $x$ values probed, the relative positions of the two phase centres can be estimated.
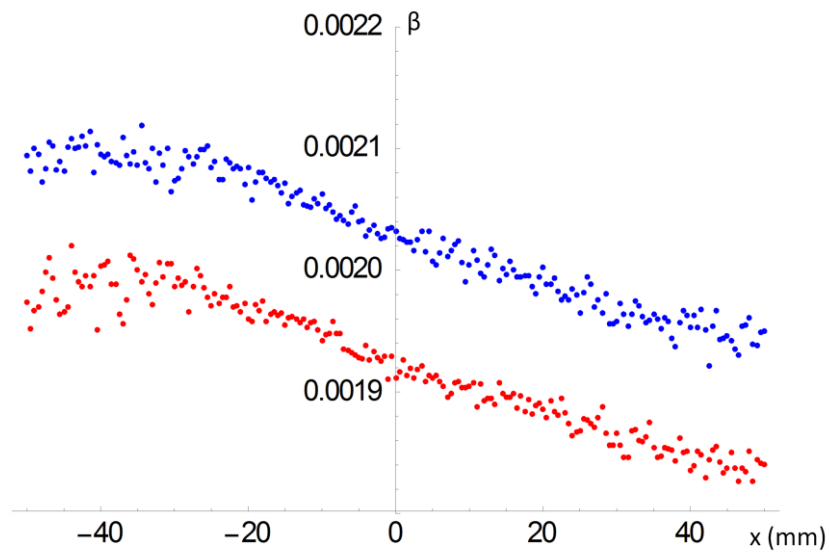


**Figure 6-29 : Plot of $\beta$ as a function of $x$. The red plot is the data for the piecewise conical profile horn antenna . While the blue plot shows the data for the corrugated conical horn.**
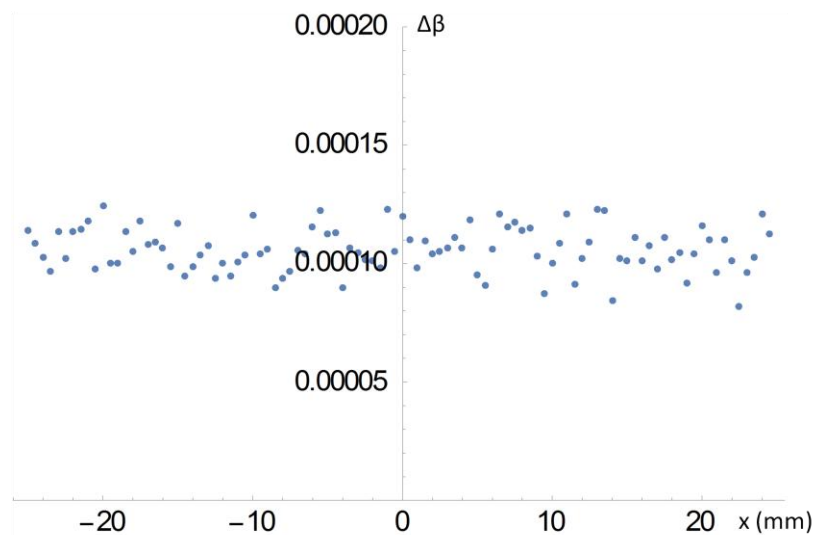


**Figure 6-30 : Plot of the differences of the $\beta$ values ($\varDelta\beta$) between the piecewise conical profile horn and corrugated conical horn as a function of $x$.**

In the experimental set-up both horns were mounted on the same waveguide flange. The distance from the flange interface with the waveguide to the aperture of the piecewise conical profile horn is 50.7 mm while for the corrugated horn block including the waveguide transition has its effective aperture at the longer value of 75.0 mm from the flange, giving a relative distance of 24.3 mm between their apertures. The aperture of the corrugated conical horn was 541 mm from the scan plane. The phase centre location of the corrugated horn is 6.7 mm behind its aperture, assuming the theoretical value derived earlier in this section (equation 6.35), so that it is 18.0 mm in front of the location of the piecewise conical profile horn aperture. From the plot in Figure 6-30 the average value of $\Delta\beta$ is $(1.06 \pm 0.1) \times 10^{-4}$ mm$^{-1}$ which yields a value of 33 mm $\pm$ 3 mm for $\Delta R$. Therefore the phase center of the piecewise conical profile horn must be $[(33 \pm 3) -18]$ mm = 15 mm $\pm$ 3 mm behind its own aperture. When the depth of field is also included for the corrugated horn (about $\pm$ 2.1 $\lambda$ = 6.3 mm) this implies that the beam waist region for the piecewise conical profile horn lies in the range 9 mm to 21 mm behind its aperture.

| Horn type | Measurement (mm) | Theory (mm) | Depth of Focus (mm) |
|---|---|---|---|
| Piecewise conical profile horn | $15.0 \pm 3.0$ | 18.0 | $\pm 6.3$ |

**Table 6-2: Comparison of the phase centre with respect to the horn aperture for the piecewise conical profile horn.**

In this case it was also possible to compare this result with the theoretically predicted phase centre (the horn was designed using mode matching software). The analysis of the phase error of the theoretically predicted beam pattern gives a phase centre approximately 18.5 mm behind the aperture when the phase error is fitted with a spherical wave over the main beam. Since once more the depth of focus of the horn effectively implies an uncertainty in the phase centre (again of the order of 2 $\lambda$ = 6 mm), we see that the theoretical and measured positions for the phase centres agree quite well, particularly given the large depth of field for these horns, clearly demonstrating the usefulness of the holographic fringe analysis approach. The results are summarized in Table 6-2.

The conclusion therefore is that in order to make the most accurate measurements of the phase centre location of a horn the best approach is to compare it with the phase centre location of a well known calibration horn, such as a conical

corrugated horn, which gives a more intense hologram thus improving the signal to noise ratio.

# 6.10  Double Exposure Method

An alternative approach to locating these phase centres is to employ a technique based on ideas used in holographic interferometry. In the so called double exposure method in visible light holography the photographic plate is exposed twice, the second time after the object under investigation has been stressed in some way. Any movements of the order of a wavelength or more shows up as a fringe pattern superimposed on the hologram. In the current millimetre wave setup by combining two holograms though the addition or multiplication of their intensity pattern, one of an antenna with a known phase centre and one with an unknown phase centre, it is possible to similarly recover the distance between the two phase centres. By insuring the positions of the two antennas within the experimental setup are measured accurately, recovering the distance between the phase centres determines the position of the unknown phase centre relative to position of the known phase centre. Hence the unknown phase centre's position within its antenna can be found [McAuley, 2011]. This does rely on both holograms being similar in structure which is a reasonable assumption given that both fields are approximately spherical wave like over the part of the beams with significant intensity. The interference patterns of each of the two holograms are due to the rapidly varying phase terms (again ignoring any misalignments):

$$\Delta\phi_{O1-R} = \phi_{O1} - \phi_R = \left[ \frac{k(x^2 + y^2)}{2R_{O1}} - kx\sin\alpha - \frac{k(x\cos^2\alpha + y^2)}{2R_R} \right] + \varepsilon_1 \qquad (6.36)$$

$$\Delta\phi_{O2-R} = \phi_{O2} - \phi_R = \left[ \frac{k(x^2 + y^2)}{2R_{O2}} - kx\sin\alpha - \frac{k(x\cos^2\alpha + y^2)}{2R_R} \right] + \varepsilon_2 \qquad (6.37)$$

Here it is assumed that the axis of both the object and reference beams lie in the *x-z* plane (i.e. no offsets) and cross at $z = 0$ where the holograms are recorded. From these equations which we can recover the interference between the two reference patterns if

we can arrange that the phases of the two hologram intensity patterns are subtracted (effectively compared with each other in some way)

$$\left[\Delta\phi_{O1R} - \Delta\phi_{O2R}\right] = \frac{k(x^2 + y^2)}{2}\left[\frac{1}{R_{O1}} - \frac{1}{R_{O2}}\right] = \frac{k(x^2 + y^2)\Delta z}{2R_{O1}(R_{O1} + \Delta z)} + \varepsilon_2 - \varepsilon_1 \quad , \qquad (6.38)$$

where $\Delta z = R_{O2} - R_{O1}$ is the separation of the phase centres. The advantage of this approach, similar to the approach in the last section, is that the reference beam phase is common to both interference terms and so disappears when the difference is taken. By adding the two interference patterns together (equivalent to double exposure holography at optical wavelengths) and observing the beating between the two patterns we obtain that $\Delta\phi_{O1R}$ and $\Delta\phi_{O2R}$ must be out of phase giving a minimum when

$$\Delta\phi_{O1R} - \Delta\phi_{O2R} = (2N+1)\pi = \frac{k(x^2 + y^{2)}}{2R_{01}(R_{01} + z)} \quad , \qquad (6.39)$$

where $R_O = R_{O1}R_{O2}/(R_{O1} + R_{O2})$. The regular fringe pattern will have a beat pattern superimposed on it given by the first term so that by fitting $k(x^2 + y^2)\Delta z/4R_{av}^2$ to the radius of minimum visibility of the pattern $\Delta z$ can be extracted where $R_{av} = (R_{01} + R_{02})/2 \approx R_{01}$.

Example simulations of such interference patterns are shown in Figure 6-31. One difficulty that arose was that any phase offset between the two patterns resulted in an uncertainty in the phase at the centre of the disk of the pattern when $x = y = 0$. This was simulated by adding an arbitrary phase factor to equation 6.38, which resulted in an offset of the fringes with possible destructive interference in the centre of the ring structure for example. In order to recover $\Delta z$, this had to be included the fitting which implied that to extract useful information from a double exposure approach more than one ring should in theory be examined. In this case the relevant equation is

$$(2N+1)\pi + \Delta\varepsilon = \frac{k(x^2 + y^2)}{2R_{01}(R_{01} + \Delta z)} \quad . \qquad (6.40)$$

The intensity of the fringe pattern at any point is the sum of the intensity of the holograms, $I_1$ and $I_2$ respectively, at that point. The minimum contrast in the fringes

occurs when the maximum intensity of one hologram fringe pattern coincides with the minimum intensity of the second hologram fringe pattern.

$$\left(\Delta\phi_1 - \Delta\phi_2\right) = \left(2N+1\right)\pi = \frac{k\left(x^2 + y^2\right)}{2R_{o1}\left(R_{o1} + \Delta z\right)} + \Delta\varepsilon \ . \tag{6.41}$$

Choosing two dark rings, for the $1^{st}$ ring

$$\pi = \frac{k\left(x_1^2 + y_1^2\right)}{2R_{o1}\left(R_{o1} + \Delta z\right)} + \Delta\varepsilon \ , \tag{6.42}$$

while for the second dark ring

$$3\pi = \frac{k\left(x_2^2 + y_2^2\right)}{2R_{o1}\left(R_{o1} + \Delta z\right)} + \Delta\varepsilon \ , \tag{6.43}$$

subtracting equation (6.42) from (6.43) yields

$$2\pi = \frac{k}{2R_{o1}\left(R_{o1} + \Delta z\right)}\left[r_2^2 - r_1^2\right] \ , \tag{6.44}$$

where $r_1$ and $r_2$ are the radii of the $1^{st}$ and $2^{nd}$ dark rings respectively. From this equation we can find $\Delta z$, the distance between the phase centres of the two antennas.
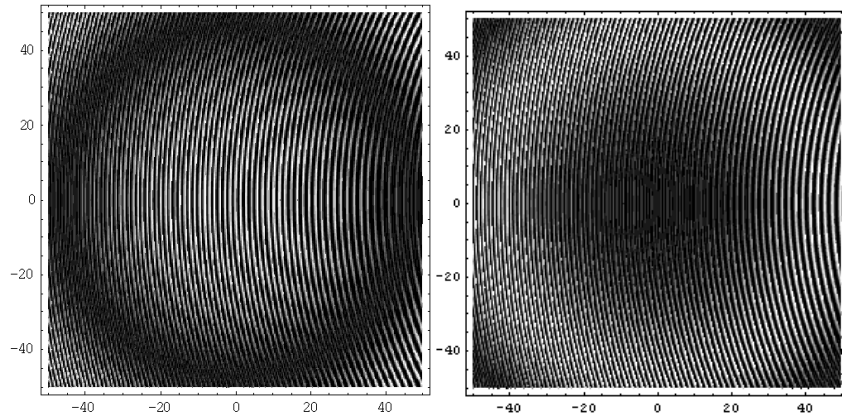


**Figure 6-31 :Simulation of an example case where both object beams are produced by point sources with $R_{O1}$ = 200 mm, RO2 = 220 mm, the scan goes from -50 mm to 50 mm in both $x$ and $y$ directions, with $\lambda = 1$ mm**

(a)



(b)



(c)
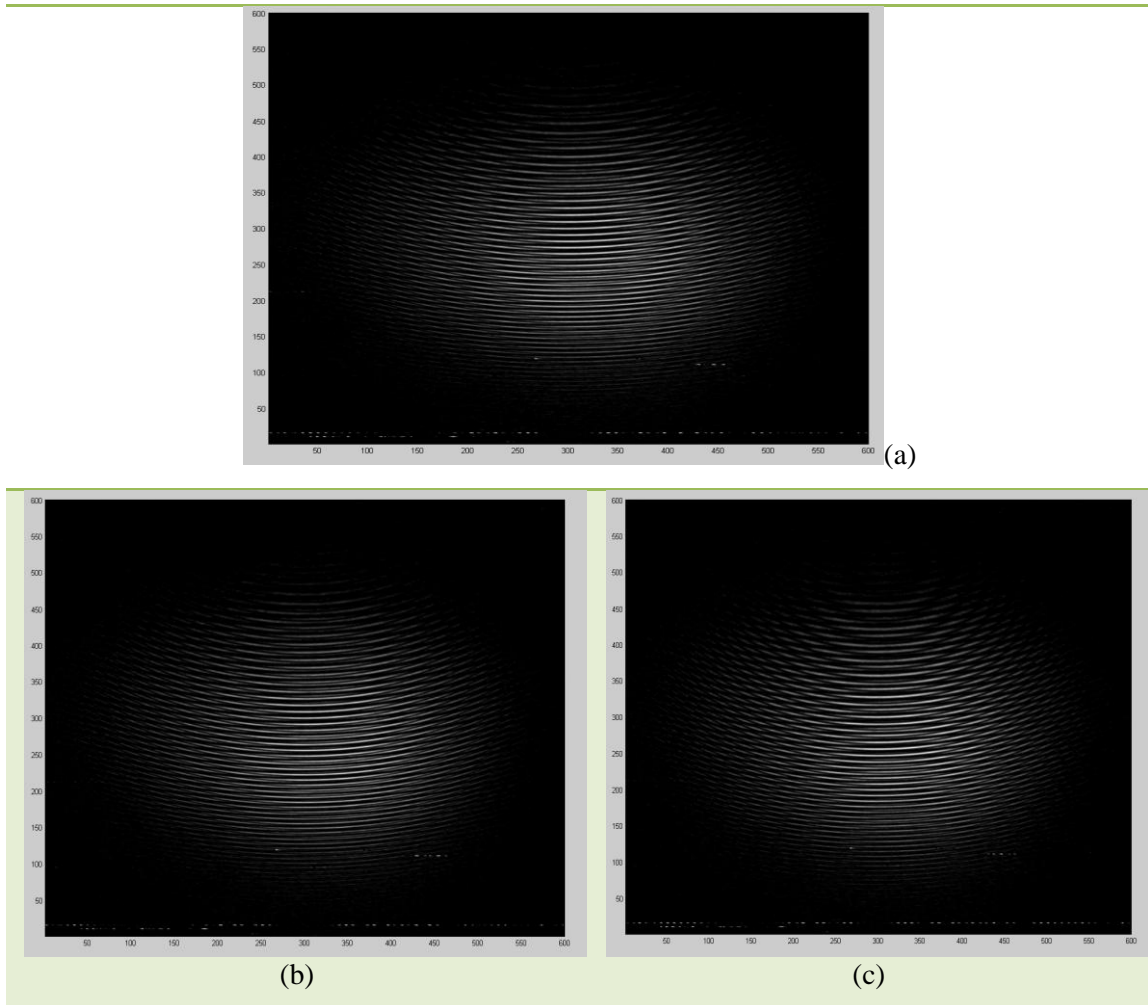
**Figure 6-32 : The results of combining the hologram of the conical horn with simulated holograms of a point source with reference beam angles of a) 41 degrees, b) 45 degrees, c) 35 degrees. All axis are in number of steps.**

The double exposure method can also be used to check various alignments of the beams including the angle of incidence between the reference beam propagation-axis and the normal to the recording plane of the hologram (i.e. the angle $\alpha$ in equation 6.36). For example if a simulated hologram of a bare waveguide is combined with the recorded hologram of the conical horn, Figure 6-19, a ringed beating pattern is observed in the resulting image. If in the simulation of the waveguide hologram the angle of incidence $\alpha$ assumed for the reference beam and the normal to the recording plane of the hologram is not the same as the real angle in the actual experimental setup the beating between the two patterns will be offset from the centre of the combined holograms. Shown in Figure 6-32 (a,b,c) are the results of combining the conical horn hologram with simulated holograms each of which has a different angle "$\alpha$" for the reference beam. In the experimental setup used to record the hologram the angle between the reference beam and the object beam was 41 degrees. As can been seen in

Figure 6-32(a), when this correct angle α for the reference beam is used the circular beat pattern is centred on the area of hologram interference fringes. When the angle in the simulation is not equal the actual one for the experimental set up the beating pattern is offset as can be seen in Figure 6-32(b),(c) (where the simulation angle is 45 and 35 degrees respectively). The use of simulated holograms in this manner provides a way to check the angle of incidence for the reference beam as well as the alignment of the axis.
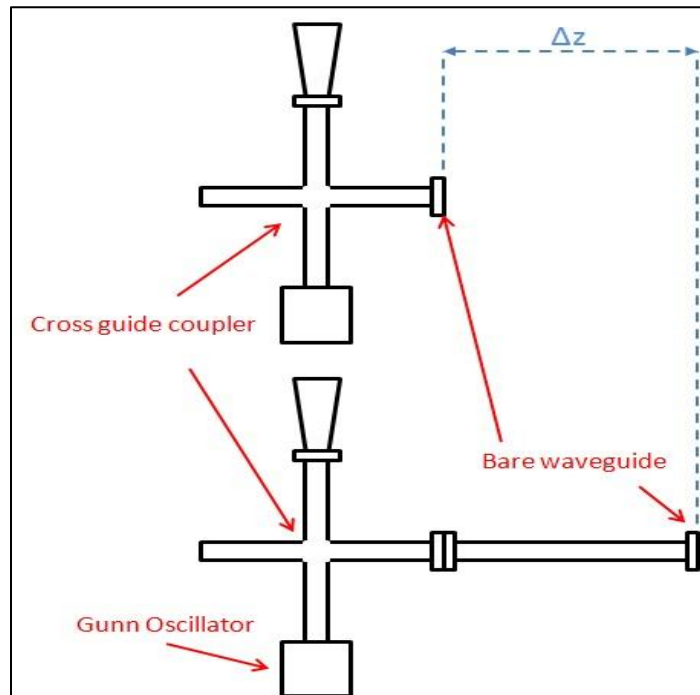


**Figure 6-33 : Schematic diagram showing how a long waveguide section was used to maximise the separation of the antenna phase centres.**

The double exposure method was verified experimentally by measurements using the experimental apparatus described in section 6.4. The first step in this endeavour was to calibrate the system using a well defined displacement of a phase centre. This removed the need to individually determine a number of parameters of the experimental setup, e.g. phase centre of the reference beam. Instead a single calibration source was utilized thus minimising the experimental error, this being a bare waveguide flange which provided the known phase centre location. In order to maximise the number of rings visible in the beating pattern of the combined holograms it was desirable to increase somewhat the distance between the phase centres of the antennas used to create each hologram. This was achieved by increasing the length of the waveguide sections after the cross-guide coupler feeding the bare

waveguide when recording one of the holograms (Figure 6-33). To maximise the power from the bare waveguide (the known phase centre for calibration purposes) it was decided to increase the waveguide feed section to position it as close to the scanner as possible without impinging on the reference beam (Figure 6-34). The holograms recorded for both positions of the waveguide were combined to produce a double exposure interference pattern. The known displacement, approximately 25 cm, through which the waveguide, and hence its phase centre, had been moved and the radii of rings the beating pattern were used to determine the experimental parameters represented by $k$ and $R_{o1}$ in equation (6.44). These parameters could then be used to find the displacement of the phase centre of an antenna under test relative to phase centre of the waveguide using the same experimental setup.

The bare waveguide hologram for the second position (close to the recording plane) was then combined with a hologram of the corrugated conical horn using the double exposure approach. The corrugated conical horn was directly mounted on the end of the bare waveguide flange at the end of the attenuator without the extra waveguide sections. For these configurations the distance between the phase centre of the horn and bare waveguide was 230 mm. The resultant pattern from the combination of the two holograms is shown in Figure 6-35. The ring pattern resulting from the beating of the two interference patterns can clearly be seen. This pattern was used to check the calibration of the system. The radii of rings in the beating pattern were used with equation (6.44) and the previous obtained values for the experimental parameters to determine $\Delta z$. The $\Delta z$ found using this method agreed with the known shift of $230 \pm 10$ mm. Having now confirmed that using this approach with these calibrated experimental parameters that the phase centre of a horn antenna could be recovered the experiment progressed to determine the phase centre of an antenna for which it is not well defined. The lens antenna was chosen as the example antenna.
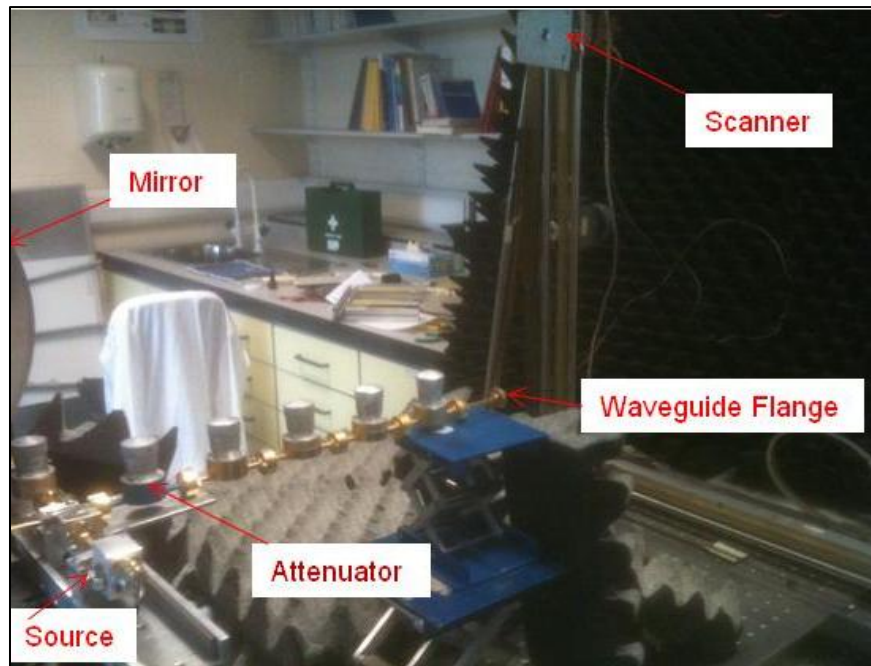
**Figure 6-34 : Experimental setup with extra waveguide (attenuator) sections between the cross-guide coupler and the bare waveguide.**
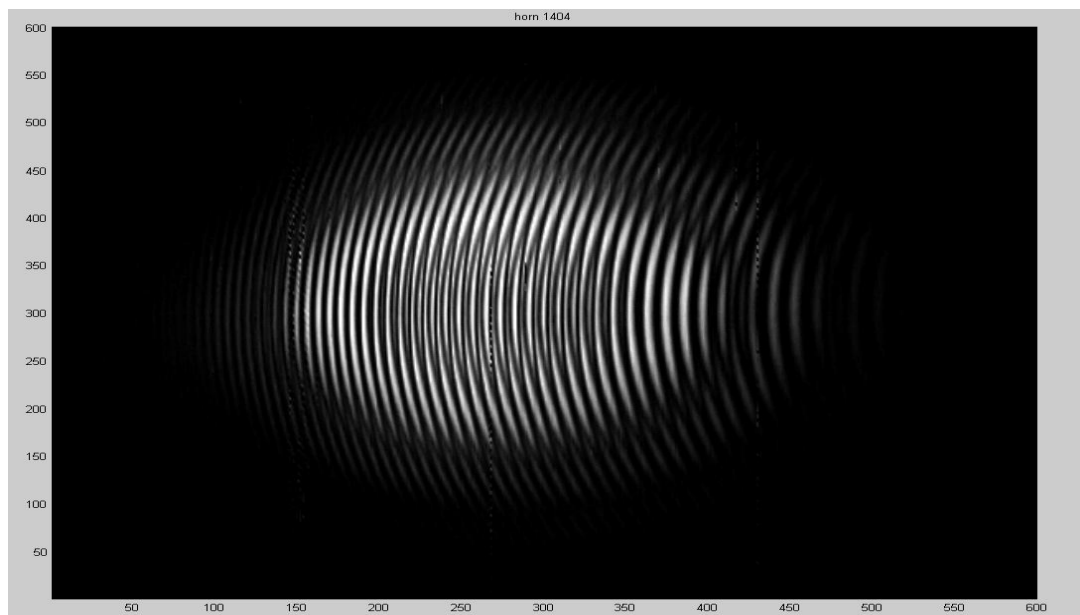


**Figure 6-35 : Combination of the waveguide and conical horn holograms.**

A hologram of the lens antenna detailed in section 6.7 was made (using the setup shown in Figure 6-36) and combined with the waveguide hologram using the double exposure method once more.  The result of this combination is shown in Figure 6-37.  From this the distance between the position of the waveguide phase centre and that of the lens antenna was calculated to be 200 mm.  As the lens antenna was positioned 170 mm behind the waveguide aperture this places the phase centre 30 mm

± 10 mm behind the front of the lens. A measurement of the location of the phase centre of this lens antenna using a VNA gave it a result of 18.6 mm ± 2.5 mm behind the front of the lens. These two measurements are just about consistent given the associated experimental errors. We note that the error using this method is larger than for the single exposure with fringe analysis as in the last section (section 6.8) because of the need to have a large enough distance between the phase centres so that at least two interference rings are seen in the combined hologram as in Figure 6-35. This to some extent limits its usefulness for high accuracy phase centre determination.

One major advantage of the holographic method as presented in this chapter is cost. The cost of a VNA in the W-band range (75-100 GHz) is of the order of one hundred and twenty five thousand euro which is far more than the scanning system required for holographic measurements. The cost increases with frequency, for example at 300 GHz (J-band) the cost of a VNA system rises to the order of three hundred thousand euro. The reason for this increase in cost is the heterodyne mixer used convert from the lower frequency at which the VNA is designed to operate to the higher millimetre-wave frequencies.
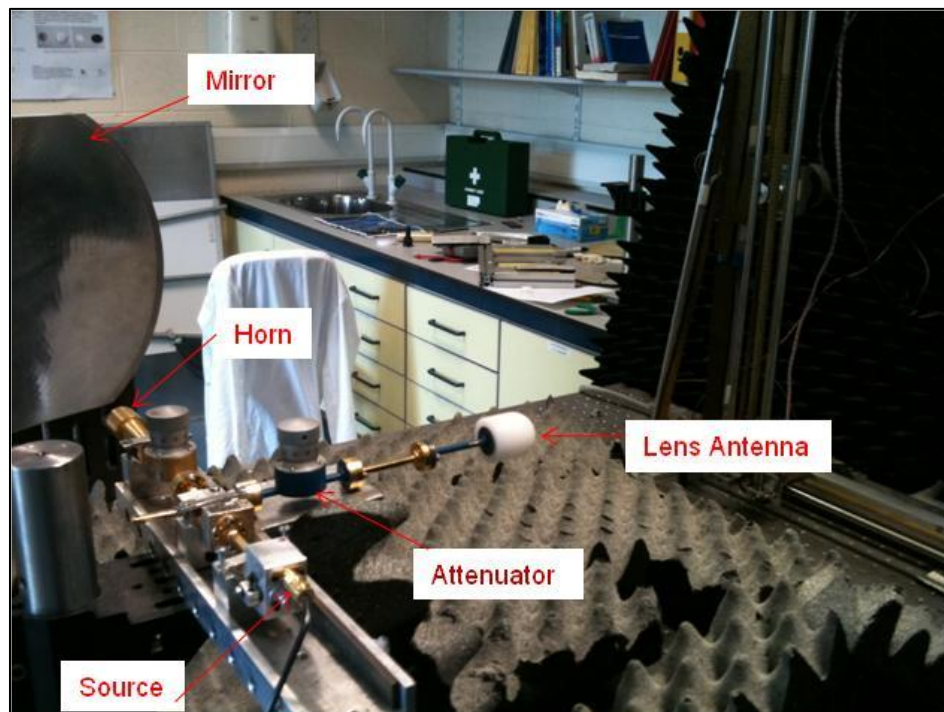


**Figure 6-36 : Photo showing the lens antenna in position for the double exposure method measurement.**
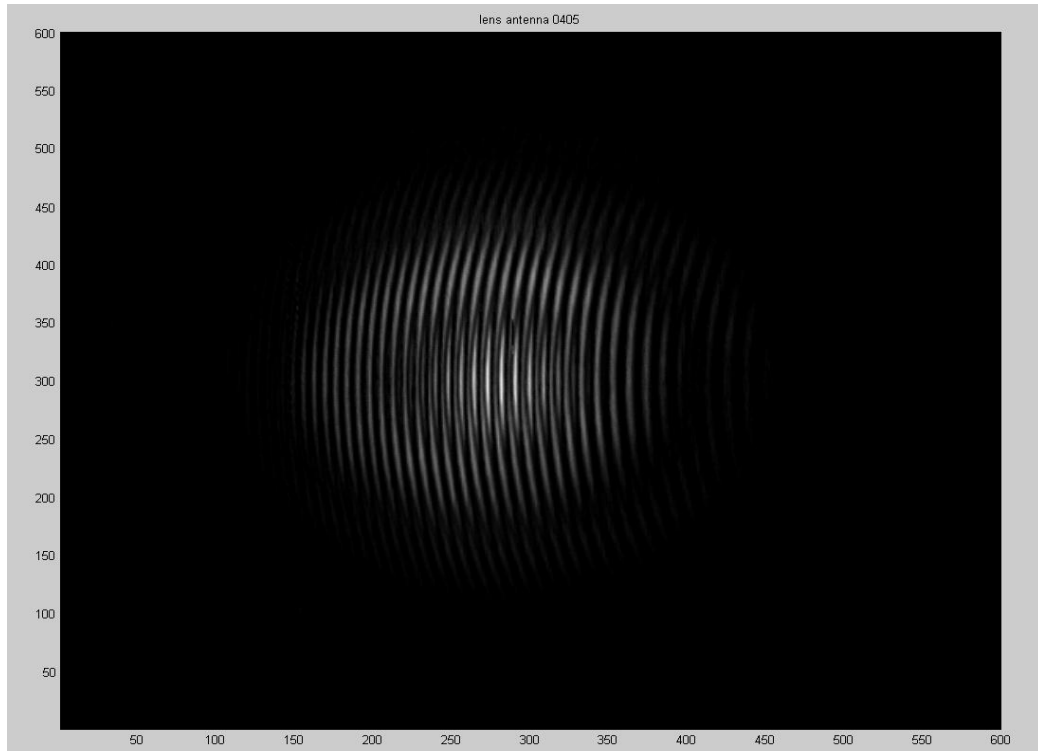
**Figure 6-37 : Combination of the waveguide and lens antenna holograms.**

# 6.11 Imaging and Other Applications of Millimetre Wave Holography

We conclude this chapter with a short overview of other millimetre wave holographic applications investigated by the author as part of the work for this thesis. Just as at visible wavelengths, millimetre-wave holography has numerous applications in addition to phase retrieval as presented so far in this chapter. Some of these applications will be discussed in this section both in terms of the current state of that art developments. The area of mm-wave imaging has seen advances in recent years. The offer of good resolution and good transmission characteristics through most dielectrics has spurred on research into these imaging techniques. This research has developed applications for non-destructive inspection and quality control in diverse industries such as aerospace and food production [Kemp,2010] [Feger, 2013]. The non-ionizing nature of mm-wave radiation has in addition lead to its use in security and proposed use in biomedical applications [Luukenen, 2012] [McAuley, 2006].

These imaging methods in general rely on focusing elements such as lenses and mirrors which can be large and bulky at mm-wavelengths. Holography offers an alternative approach [Tamminen, 2010] [Fernandez-Cull, 2010]. Holography does not need optical components to focus the object beam. Instead the image is recorded in the form of interference pattern through its combination with a reference beam. This lack of focusing optics opens up the possibility of lighter and less bulky imaging systems at mm-wavelengths.

As previously described a holographic recording of a test object was made to test the reconstruction method (as presented earlier in section 6.5). In the configuration of the experimental apparatus as described, the object beam arriving at the recording plane has been transmitted through or scattered by the object under test. Compared to a configuration where the object beam is scattered (reflected) off the object onto the recording plane, the transmission arrangement allows for more power to arrive at the detector. This is advantageous as it provides for a greater signal to noise ratio for certain applications. As many materials are transparent, to varying degrees, at mm-wavelengths this arrangement makes it possible to gather information about the interior of certain test objects, e.g. examine an object concealed in an envelope. In general this form of imaging is well suited to security applications.

Using this setup, holograms of various other test objects were made and millimetre wave images reconstructed. These included objects containing a mix of metals and dielectrics, objects concealed inside envelopes, and containers part filled with liquid. A floppy disc was used for a test object as it is a well known object consisting of plastic (dielectric) and metallic parts. The plastic case of the disc is transparent at 100 GHz and the beam propagates through it will minimal absorption. The metal workings of the disc scatter the beam producing distortion in the fringes of the hologram. The reconstructed image of the floppy disc, Figure 6-38 (c), shows the metal sections clearly. In particular the centre hub and shutter are visible as is the overall outline of the disc.
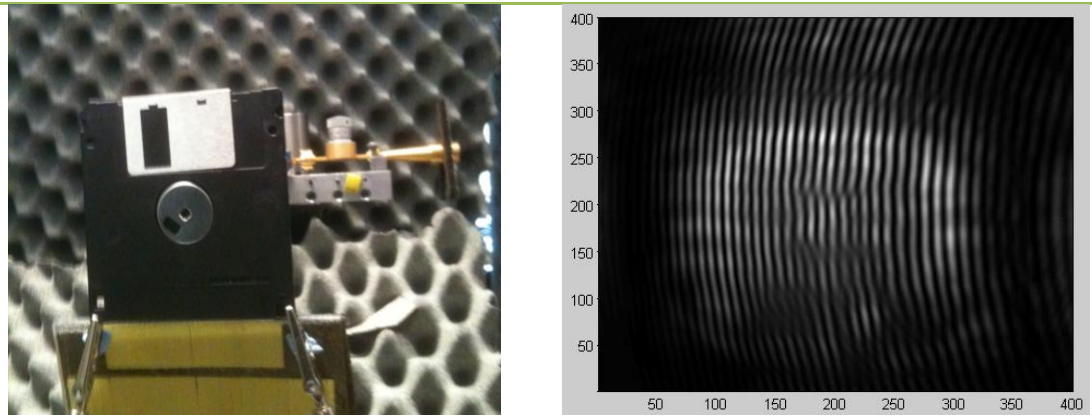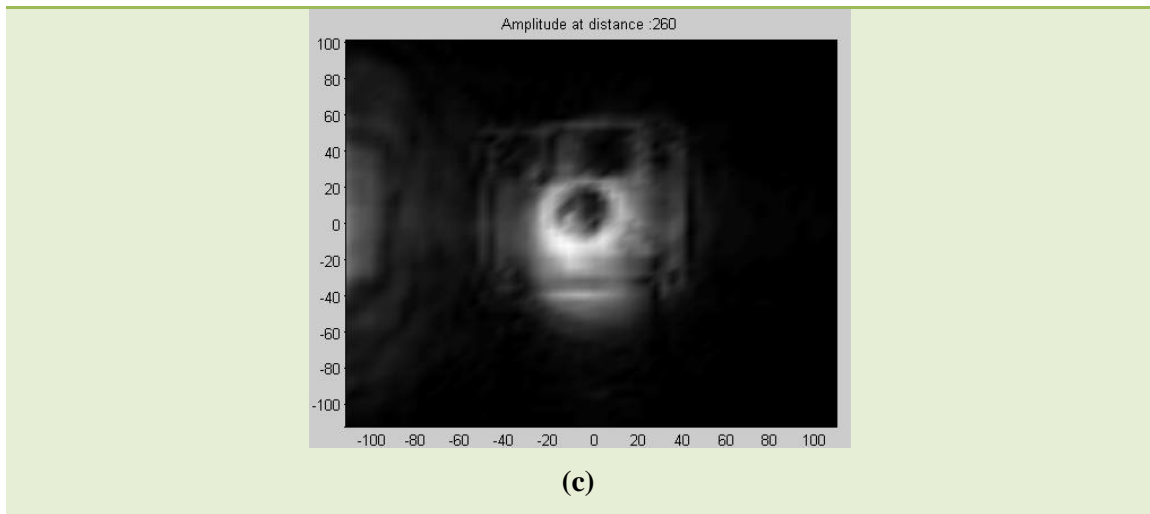
**Figure 6-38 : (a) Floppy disc positioned in the path of the object beam. (b) Hologram recorded using the floppy disc as an object. The axis are in number of steps. (c) Reconstructed image of the floppy disc with axis in mm. The parts of the disc are visible in the image.**

To further explore the possible uses of holography for security purposes an envelope was affixed to a polystyrene board and position in object beam path (Figure 6-39). At 100 GHz the polystyrene board is transparent making it a good choice for use as a mounting prop in this experimental setup. Various objects were placed in turn inside this envelope and holograms recorded for each one. The first object chosen was a one-sided blade. The blade was visible in reconstructed image, Figure 6-40, while the envelope is not seen as it is completely permeable at this frequency. The next test object was a film canister half filled with water. The plastic canister is made is transparent but the water is highly absorbent at 100 GHz. Figure 6-41 shows the reconstructed image of the canister. Its outline can be clearly made out in the image. The beam passed through the empty top half of the canister and is seen as the bright area inside this outline. The water filled half of the container absorbed the beam and is the dark area in the image. The promising results of these three test cases illustrate

the possible advantages that mm-wave holography could bring to potential security applications.
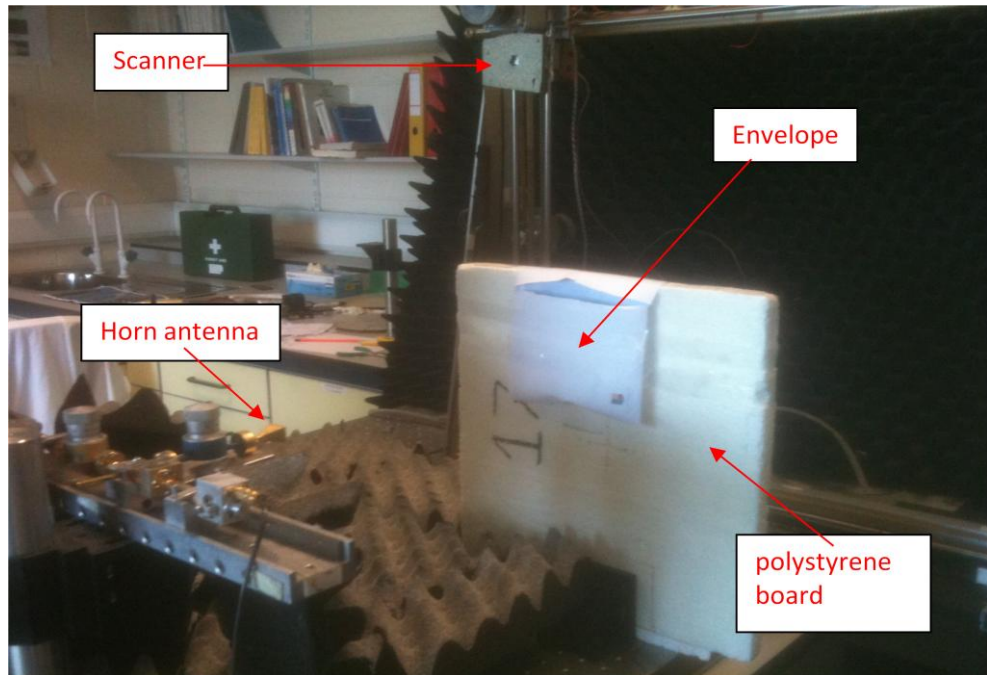


**Figure 6-39 : Photograph showing the arrangement used to test the system's ability to scan objects concealed in a envelope.**
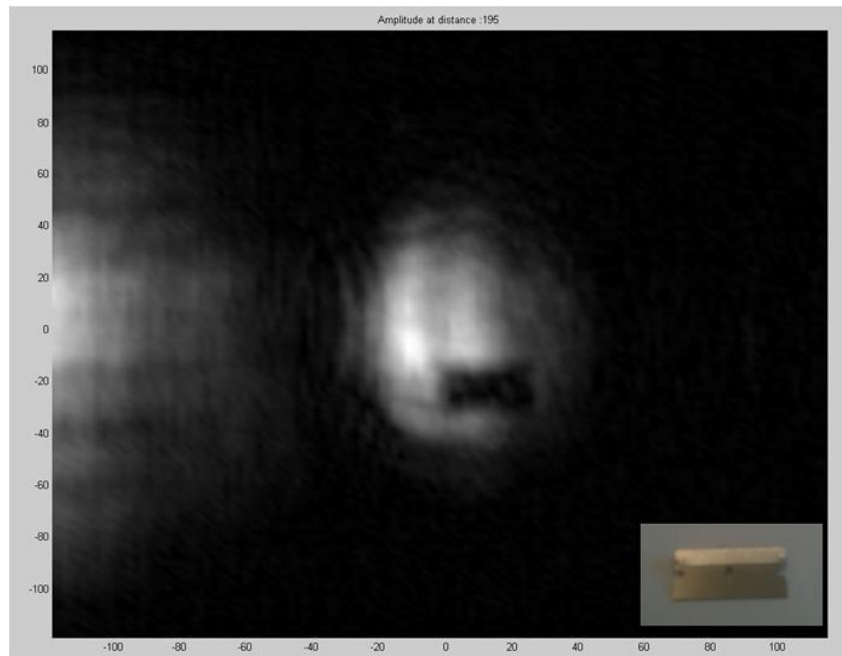


**Figure 6-40 : Reconstructed image of the one-sided blade inside the envelope with axis in mm. Insert shows a photograph of the blade for comparison.**
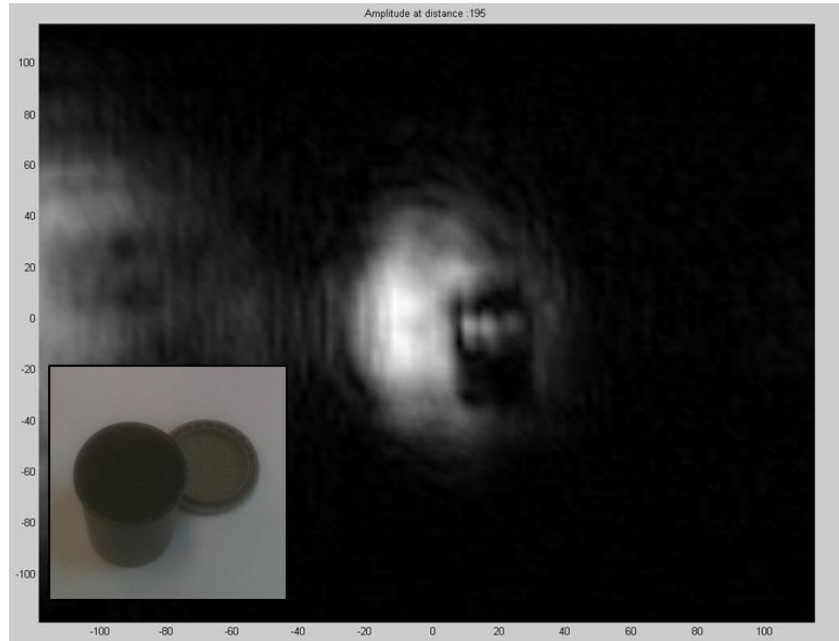
**Figure 6-41: Reconstructed image of film canister half filled with water with axis in mm. Insert shows a photograph of the canister.**

In the previous experiments only the reconstruction of the amplitude of the object beam was investigated. Holograms, of course, also record phase information as was illustrated earlier in this chapter. An object made of a dielectric, high density polyethylene (HDPE), was used to introduce a phase shift into the object beam (Figure 6-42). An M shape of the same dimensions as M shaped mask, section 6.5, was milled into the dielectric to a depth of one wavelength (3mm at 100 GHz). This causes a phase shift between the sections beam passing through the cut and uncut areas of the HDPE which has a refractive index of 1.5.
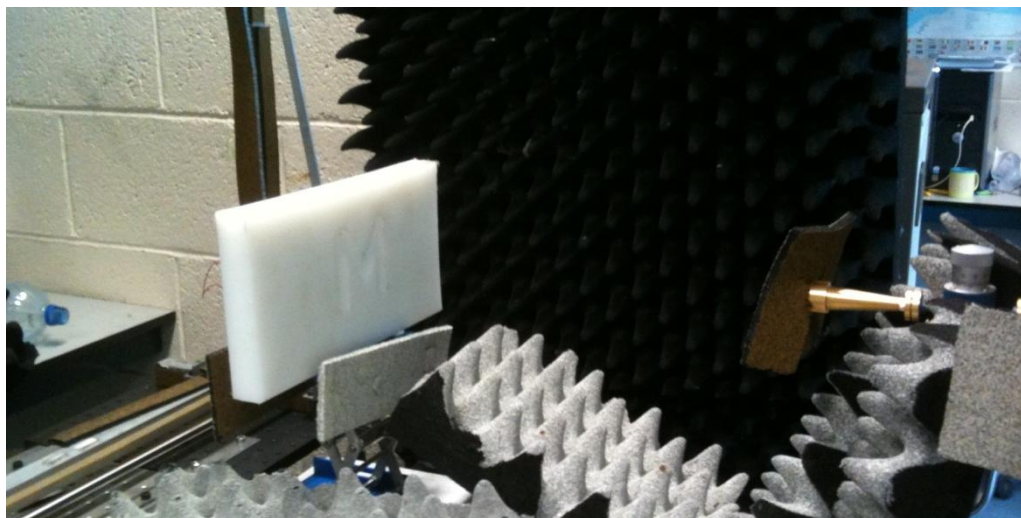


**Figure 6-42: HDPE block, with M shape cut into it, positioned in the object beam.**

In the reconstructed amplitude image the M shape can be seen due to scattering from the step at the edge of the shape, Figure 6-43. A reconstruction using the phase of the object beam is shown in the left image of Figure 6-44. The shift in phase introduced by the M shape cut into the HDPE can be seen as a alteration in the circular pattern of the beam phase contours. The plot on the right of Figure 6-44 shows a horizontal cut (dashed line in Figure 6-43) through the centre of the beam phase. The changes in phase produced by the step in the thickness of the HDPE are clear.
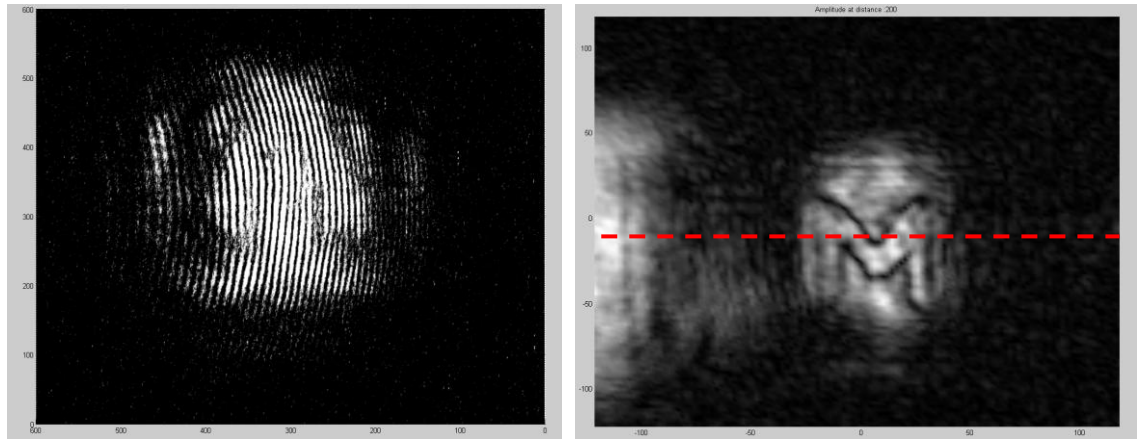


**Figure 6-43 : Left, Hologram of M shape cut into HDPE. Right, Reconstructed image of object beam with M shape visible.**
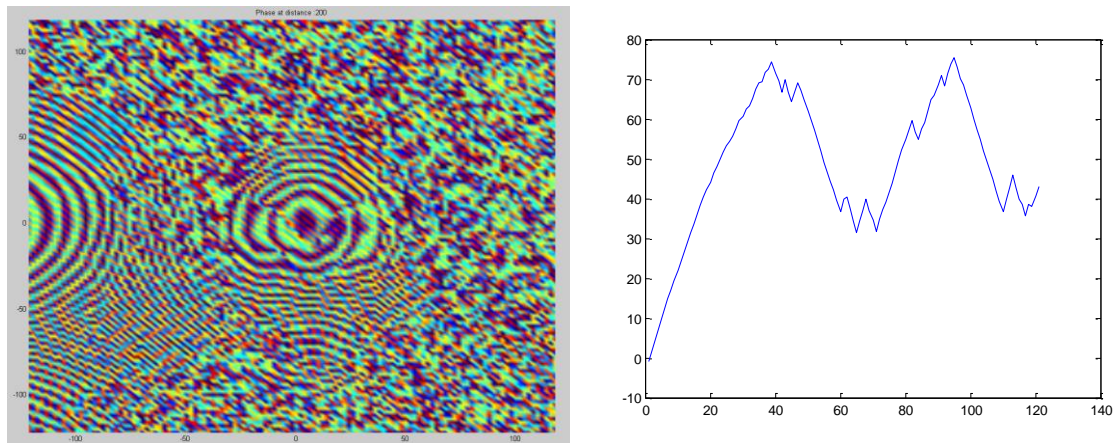


**Figure 6-44 : Left, Reconstruction of the phase of the object beam. Right, A horizontal cut through the phase reconstuction.**

Another area in which holography has been applied is in the development of optical components [Lukin, 2007]. Holographic optical elements (HOE) are used to transform a wavefront in a similar fashion to conventional optical components such as lenses, mirrors, or spectral filters. HOEs can either be recorded as a conventional hologram or be designed and synthesised from computer generated hologram. Illuminating the HOE with a reference beam results in an object beam with

255

characteristics of a beam from the desired optical component. In general HOEs are wavelength dependent so operate best at the frequency for which they were recorded or designed. As they rely on wavelength dependent diffraction effects rather than reflection or refraction for their operation. In spite of their narrow band of operation HOEs do have some advantages however. As they can be made from a thin layer of material and are in general much more compact and lightweight compared to the equivalent conventional component. A number of HOEs can be combined into a single layer of material with each set of interference fringes occupying the same space [Toal, 2012]. This is useful as it means a single HOE can be used to correct anomalies or distortions within an existing optical system. This again offers a space and weight saving over the multiple conventional components that would otherwise be needed.

At millimetre-wavelengths the attributes of HOEs offer several interesting prospective applications. Millimetre-wave systems are often designed to operate over a narrow bandwidth around a single central frequency. Within systems whose operation covers multiple frequencies over an extended range separate channels are generally used for each frequency. This aspect of mm-wave work means that the frequency dependence of HOEs is not a disadvantage. A HOE can be manufactured using suitable materials such as copper on a Mylar base. The copper is etched away to form the fringe pattern on the Mylar base [Häkli, 2005]. An example use of a HOE at millimetre-wavelengths is described by J. Häkli et al. in their 2005 paper [Häkli,2005]. In that paper the authors report on the design, manufacture, and use of a HOE in a compact antenna test range. Their results demonstrate that HOEs have practical benefits at millimetre-wavelengths.

As part of future research work HOEs may be developed and integrated into the experimental test facilities in the Experimental Physics Department at Maynooth University (National University of Ireland, Maynooth). These facilities are used for verification of the results of computational design and modelling of mm-wave optical systems and components [Yurchenko, 2014] [Hargrave, 2013]. This could allow the development of a more advanced compact test range and or new optical components for mm-wave experiments. Such HOEs could be manufactured either from a computer design or from a hologram recorded using the experimental system described in section 6.4.

# 6.12 Conclusion

In this chapter the application of holographic techniques at millimetre wavelengths has been described. The use of numerical holographic image reconstruction at millimetre wavelengths using a straightforward and compact experimental system has been demonstrated. We have considered how the accuracy of the object beam reconstruction can be improved by recovering phase errors in the reference beam. The ability to calculate phase and amplitude information from a single experiment was used in the analysis of millimetre wave receiver horns, particularly the determination of phase centres of horn antennas and lens antennas. A number of holographic techniques for determining the phase centre of a millimetre-wave antenna were described. These methods included back propagation of the object beam, fringe pattern analysis, and a double exposure method. A comparison of the results obtained using each of the techniques shows that while all the techniques were successful in recovering the position of the phase centre, the use of fringe pattern analysis of the hologram yields the most accurate results. In particular it was possible to locate the phase centre of a specially designed horn for CMB polarisation experiment at 100 GHz to within one wavelength ($\pm 3$ mm).

The back propagation method involved reconstructing the image of the object beam at multiple positions between the hologram scan plane and the object horn using on Fresnel Diffraction performed with FFT. This method was successful in locating the phase centre of the corrugated conical horn to within $\pm 8$ mm of its known location. However, for the lens antenna it is difficult to discern the position of the phase centre due to the high degree of collimation of the beam which introduces a large error in to the method.

The fringe pattern analysis method used the analysis of two holograms to recover the phase centre of the antenna of interest. One of the holograms was recorded using an antenna with a phase centre at a known location (e.g. a bare waveguide or the corrugated conical horn). A second hologram was recorded using the antenna under investigation whose phase centre we wished to locate. By analysing cuts along the $y$-direction in both holograms it was possible to recover the distance between the positions of the two phase centres and hence the location of the phase

centre of the antenna under investigation. Using this method the phase centre of the piecewise conical profile horn was found to be $15 \pm 3$ mm behind its own aperture which is consistent with its theoretical position from computer modelling which places the phase centre 18 mm behind the aperture.

The third method investigated was the double exposure method. As in the case of the fringe pattern analysis, two holograms were recorded (one with the antenna of interest, the other with a antenna with a known phase centre location) however for this technique the holograms were combined into a single interferogram. The difference in positions between the two phase centres results in a ring structure superimposed on the combined interference pattern. Thus from this ring pattern the location of the phase centre of the antenna under test can be found relative to that of the known phase centre of the other antenna. It should be noted that the error using this method is larger than for the fringe analysis approach because of the need to have a large enough distance between the phase centres so that at least two interference rings are seen in the combined (double exposure) hologram. Using this method the phase centre of the lens antenna was determined to be 30 mm $\pm$ 10 mm behind the front of the lens.

The evaluation of optical components at millimetre wave and terahertz frequencies can be very time consuming and often requires the measurement of diffracted or reflected fields at several planes. Here, we have shown how from one experimental measurement, numerical techniques can be used to reconstruct the entire output field from a linear optical arrangement.

Holography in the visible band has provided hundreds of applications, either obvious imaging modalities, or more abstract information and signal processing techniques. The application of some of these at millimetre wavelengths was discussed and in the case of imaging applications the results of experiments carried out using the apparatus described in section 6.4 were reported. With the rapid expansion of technology applicable to terahertz and millimetre wave photonics, it is difficult to see how holography cannot provide several further techniques to these fields.

# Chapter 7 Conclusions

In the preceding chapters of thesis research concerned with the modelling and laboratory test measurement of novel horn antennas for Cosmic Microwave Background experiments has been presented. The computational modelling work involved improvements and upgrading of pre-existing in-house mode-matching software (SCATTER) for more realistic simulations of the sub-millimetre multimode horn antennas of the High Frequency Instrument of the European Space Agency Planck satellite. This software was used in the analysis of pre-launch laboratory test measurements of the flight horns to understand the actual in-flight spillover beams on the sky. An application of millimetre-wave holography was applied in the laboratory verification of specially designed profiled smooth walled horns for future CMB polarisation experiments using an experimental setup developed in the Experimental Physics Laboratories to test W-band (75-110 GHz) antennas for such applications using digital holographic techniques to recover the amplitude and phase of the beams from the antennas.

We have discussed in detail the challenge of deriving the broadband beams with fine frequency sampling necessary for the Planck high frequency multimode channels (545 GHz and 857 GHz) which revealed numerical issues with the running of the pre-existing SCATTER code which had to be addressed. The beam patterns of both the 545 GHz and 857 GHz horns are remarkably stable over their operational frequency bands with the width of beam varying by only a degree or two over their respective band. In this regard the variation in the hybrid mode content of the 857 GHz and 545 GHz multimode channels over their respective frequencies ranges was investigated in detail. Additional modes cutting on counteract the narrowing of the beam patterns with increasing frequency due to diffraction. This also implies of course the broadband beam pattern will not be affected by the spectrum of the source, as would be the case for a single mode horn.

The SCATTER code was also modified to include an absorber in the detector integrating cavity to represent the bolometric detector of the real 857 GHz horn antenna chain. Some minor differences, as expected, were seen in the farfield beam

patterns of the full Planck pixel with the absorber compared to the result for just the front horn of the back-to-back horn pair. Nevertheless the mode content and overall the structure of both beam patterns are broadly the same so that it is valid to model the front section only including the waveguide filter as a reasonable approximation to those of the full pixel beam patterns.

A higher than expected far sidelobe signature was detected at 857 GHz and prompted an investigation of the effects of possible manufacturing tolerances and the limitations of the electroforming process on the beam patterns of the multi-moded 857 GHz channel. In fact some mechanical imperfections had been found during the pre-flight visual inspections of the horns and where possible corrective actions were taken. The author investigated the effects of a number of plausible scenarios of possible imperfect corrugations on the sidelobes of the beam patterns of the 857 GHz horn. It was found that as few as one or two corrugations full filled with un-etched aluminium could have increased the sidelobe levels if they occurred in the throat area of the front horn of the back-to-back pair.

The defective horn cases were simulated at 460 GHz and 511 GHz and compared to the perfect horn to determine which sections produced effects that would have been noticed in the pre-flight test measurements. It was found that filled corrugations at the front of the tapered section and into the adjoining parts of the parallel phasing section produced an increase in the sidelobe levels that might not have been noticeable within the experimental errors of the single mode pre-flight measurements. A number of other defects such as missing fins, and partially filled corrugations were investigated both at the central frequency of 857 GHz and for the broadband beams. It was found that the throat and tapered sections of the horn were the most sensitive areas to non-perfect corrugation profiles.

The results of the modelling of the Planck telescope by Daniel Wilson in his thesis [Wilson, 2014] using the author's beam pattern simulations as input showed how the non-ideal horn corrugations could indeed lead to variations in the far-out sidelobes of the beams on the sky. These differences in the sidelobes compared to those of a "perfect" horn profile will couple more power to the telescope and explain the residual "banana" features seen in some of the survey difference maps of the 857 GHz channels due to manufacturing tolerances or damage on launch.

The pre-flight test measurements made by Cardiff University of the Planck 857 GHz back-to-back qualification horn were designed to test whether or not the horn was multi-moded as designed. The measured beam patterns were narrower than the predicted beam patterns at each of the spot frequencies tested. An extensive analysis campaign was then undertaken by the author to examine if the horns were multi-moded and to explain the discrepancy between them and the predicted beam.

Using the TE and TM waveguide modes as a basis set it was possible to show that the measured beams must contain modes of azimuthal orders other than those of order $n = 1$. Following on from this a more extensive analysis was performed using the hybrid modes (or Eigenfields). It is clear that the measured beams were wider than the fundamental $HE_{11}$ mode and therefore that the beams must be multimoded. A non-negative least squares fit of the hybrid modes to the measured beams at a number of the spot frequencies again showed that the mode content of the measured beams patterns were reduced compared to the predicted beams and that in particular modes of azimuthal orders other than of orders $n = 0$ and 1 were greatly attenuated or missing entirely.

As the Cardiff test set-up used a parabolic horn (Winston cone) relay to couple the Planck horn to the detector, an analysis was made of the coupling between the back-to-back horn pair and the parabolic horn. It was suspected this might be where the higher order modes were lost and indeed a scenario was investigated which demonstrated poor coupling to the parabolic horns would explain the discrepancies between the measured beam and the SCATTER predictions.

Nevertheless, the fact that the measured beams were multimoded was an important pre-flight result. In flight measurements of the beam widths of the 857 GHz channels were made using Uranus and Neptune [Planck Collaboration, 2014a]. The beam width measured in flight, 4.51 arcmin, agrees with the predicted beam widths of 4.3 arcmin [Tauber, 2010b]. This supports the conclusion that the 857 GHz channel is multimoded and that the actual predicted number of modes seem to propagate as predicted in the horns. It is therefore reasonable to conclude that factors in the experimental setup used to make the preflight measurements resulted in the filtering (loss) of the higher order modes as shown in the analysis.

Following on from the release of the full Planck data archive and CMB analysis in 2015 attention is once more returning to the foregrounds sources measured by Planck and to the highest frequency channels in particular. The higher than expected sidelobes seen in the 857 GHz channel are once more of interest as complete models of the scanning beam on the sky will be required to deconvolve the beams from data. The work present in this thesis and by Daniel Wilson [Wilson, 2014] provide an analysis of the sidelobe level of the 857 GHz channel which will be of use in this endeavour.

The application of holographic techniques at millimetre wavelengths was described and a number of holographic techniques for determining the phase centre of a millimetre-wave antenna discussed. These methods included back propagation of object beam, fringe pattern analysis, and a double exposure method. A comparison of the results obtained using each of the techniques shows that while all the techniques were successful in recovering the position of the phase centre sufficiently accurately, the use of fringe pattern analysis of the hologram yields the most accurate results. In particular it was possible to locate the phase centre of a specially designed horn for CMB polarisation experiment at 100 GHz to within one wavelength (±3 mm).

With the rapid expansion of technology applicable to terahertz and millimetre wave photonics, it is difficult to see how holography cannot provide several further techniques to these fields. Holographic optical elements may be developed as part of future research work and integrated into the experimental test facilities in the Experimental Physics Department at Maynooth University, which are used for verification of the results of computational design and modelling of mm-wave optical systems and components. This could allow the development of a more advanced compact test range and or new optical components for mm-wave experiments. This would be useful for the development of specialised horn designs for future CMB space missions to detect and map characteristics of the B-mode polarisation.

# References

Alpher, R. A., Bethe, H., & Gamow, G., "The Origin of Chemical Elements", Phys. Rev. 73, 803, 1 April 1948

Alpher, R., Herman, R., "Evolution of the Universe," Nature, vol. 162, pp. 774-775, 1948.

Alpher, R., Herman, R., "Remarks on the Evolution of the Expanding Universe," Physical Review, vol. 75, no. 7, p. 1089, 1949.

Baker J. C., Grainge, K., Hobson M.P., Jones, M. E., Kneissl, R. , Lasenby, A.N., O'Sullivan, C.M.M., Pooley, G., Rocha, G., Saunders, R. , Scott, P.F., Waldram, E.M., "Detection of Cosmic Microwave Background Structure in a Second Field with the Cosmic Anisotropy Telescope", Mon. Not. R. Astron. Soc. 308, 1173-1178, April 1999.

Battistelli, E., et al., 'QUBIC: The QU Bolometric Interferometer for Cosmology'. Astroparticle Physics, 34:705 − 716, 2011

Bersanelli B., Mandolesi N., et al., "Planck pre-launch status: Design and description of the Low Frequency Instrument", Astronomy & Astrophysics Volume: 520 Article Number: A4 DOI: 10.1051/0004-6361/200912853 Published: SEP-OCT 2010.

BICEP2/Keck and Planck Collaborations, "A Joint Analysis of BICEP2/Keck Array and Planck Data", Phys. Rev. Lett. 114, 101301, 2015

Bracken C., Electromagnetic Techniques for Analysis and Design of Ultra Sensitive Receivers for Far-Infrared Astronomy. PhD thesis, National University of Ireland Maynooth, 2015.

Carlstrom, J. E., Kovac, J., Leitch, E. M., Pryke, C., " Status of CMB polarization measurements from DASI and other experiments", New Astronomy Reviews, Volume 47, Issue 11-12, p. 953-966, 2003.

Clarricoats P.J.B., Olver A.D., "Corrugated Horns for Microwave Antennsa", Peter Peregrins (for IEE), 1984.

Carroll B.W., Ostile D.A., "Introduction to Modern Astrophysics", Second Edition, Pearson for Addison-Wesley, pg. 1247-1262 ,2006

Colgan R., Electromagnetic and quasi-optical modelling of horn antennas for far-IR space applications. PhD thesis, Ph. D. Thesis, NUI Maynooth, 2001.

Delabrouille J., "COrE+ The Cosmic Origins Explorer a proposal for ESA's M4 space mission", http://conservancy.umn.edu/handle/11299/169642, 2015.

Dicke R., Peebles P., Roll P., and Wilkinson D., "Cosmic Black-Body Radiation.", The Astrophysical Journal, vol. 142, pp. 414-419, 1965

Doherty S., "Optical and Quasi-Optical Design and Analysis of Astronomical Instrumentation including a Prototype SAFARI Pixel.", PhD thesis, National University of Ireland Maynooth, 2012.

Enayati A., et al., "THz Holographic Imaging: A Spatial-domain Technique for Phase Retrieval and Image Reconstruction", Microwave Symposium Digest, IEEE, June 2012.

ESA website, "Planck Mission Overview", http://www.esa.int, (European Space Agency, 2009)

ESA website, " Planck history of Universe zoom",
http://www.esa.int/spaceinimages/Images/2013/03/Planck_history_of_Universe_zoom
(European Space Agency, 2015)

Feger R., Fischer A., Stelzer A., "Low Cost Implementation of a Millimetre Wave Imaging System Operating in W-Band", Microwave Symposium Digest, IEEE, June 2013.

Fernandez-Cull C., Wikner D.A., et al., "Sparse sampling and enhanced axial resolution in millimeter-wave holographic imaging", Proc. of SPIE Vol. 7670,76700B, 2010.

Fixsen, D. J., "The Temperature of the Cosmic Microwave Background". The Astrophysical Journal 707 (2): 916–920, 2009.

Friedman, A., "On the Curvature of Space," General Relativity and Gravitation, vol. 31, no. 12, pp. 1991-2000, 1999.

Frieman, J. A., Turner, M. S., Huterer, D., "Dark Energy and the Accelerating Universe". Annual Review of Astronomy and Astrophysics 46 (1): 385–432. arXiv:0803.0982 (September 2008).

Gleeson E., et al., " Electromagnetic modelling of few-moded Winston cones in the far-infrared ", AIP Conf. Proc. 616, 295 , 2002; http://dx.doi.org/10.1063/1.1475647

Gleeson E., "Single and Multi-moded Corrugated horn Design for Cosmic Microwave Background Experiments", Ph.D. thesis, NUI Maynooth, 2004.

Gleeson E. et al., "Corrugated waveguide band edge filters for CMB experiments in the far infrared", Infrared Phys. Technol. 46, 493, 2005.

Goldsmith P.F., "Quasioptical Systems", IEEE Press, 1998.

Goodman J.W. , "Introduction to Fourier Optics", second ed., McGraw Hill, 1996.

Guth A., "Inflationary universe: A possible solution to the horizon and flatness problems", Physical Review D, vol. 23, no. 2, p. 347, 1981.

Häkli J., et al., "Testing of a 1.5m reflector antenna at 322GHz in a CATR based on a hologram", IEEE, Transactions on Antenna and Propagation, Volume 53, No. 10, pp 3142-3150, October 2005.

Hargrave P.C., et al., "Coated dielectric lens design, modelling and measurements for future CMB polarimetry missions," Proc. 7th European Conference on Antennas and Propagation, April 2013.

Hoyle, F., "The Synthesis of the Elements from Hydrogen," Mon. Not. R. Astron. Soc, vol. 106, 1946.

Hubble, E., " A Relation Between Distance And Radial Velocity Among Extra-Galactic Nebulae.", Proc Natl. Acad. Sci. U S A. ;15(3):168-73, Mar. 15th 1929.

Jellema W., et al., "The HIFI Focal Plane Beam Characterization and Alignment Status", Proc. 19th International Symposium on Space Terahertz Technology, pp 448-455, April 2008.

Kemp I., et al., "Sub-mm wave imaging techniques for non-destructive aerospace materials evaluation", Aerospace and Electronic Systems, IEEE, volume 25, issue 8, August 2010.

Kovac J., Leitch E., Pryke C., Carlstrom J., Halverson N., and Holzapfel W., "Detection of Polarization in the Cosmic Microwave Background using DASI", Nature 420, 772-787, 2002.

Kreis T., "Handbook of Holographic Interferometry", Wiley-VCH, 2005.

Lamarre J.-M., Puget J.-L. et al., "Planck pre-launch status: The HFI from specification to actual performance", ASTRONOMY & ASTROPHYSICS Volume: 520 Article Number: A9 DOI: 10.1051/0004-6361/200912975 Published: SEP-OCT 2010.

Lee A.T., "Multi-band Dual-Polarization Lens-coupled Planar Antennas for Bolometric CMB Polarimetry ", Journal of Physics: Conference Series 155, 2009, doi:10.1088/1742-6596/155/1/012005

Liddle, A., "An Introduction to modern Cosmology", Second edition, Wiley, 2003

Lukin A.V., "Holographic optical elements", Journal of Optical Technology, Volume 74, Issue 1, pp65-70, 2007.

Luukenen A., et al., "Developments  towards real-time active and passive submillimetre-wave imaging for security applications", Microwave Symposium Digest, IEEE, June 2012

McAuley I., Young L., et al, "Millimetre-wave and Terahertz Imaging Systems with Medical Applications" Proc. IRMMW-THz 2006, Shanghai.

McAuley I., Murphy J. A., et al,  "Applications of holography in the millimeter-wave and terahertz region", Proc. SPIE 7938, 79380H, 2011.

McCarthy D., et al., " Efficient algorithms for optimising the optical performance of profiled smooth walled horns for future CMB and Far-IR missions", Proceedings for Spie Astronomical Telescopes and Instrumentation, Montreal, 2014.

Maffei B., Ade P., Tucker C., Wakui E., Wylde R., Murphy J.A., Colgan R. "Shaped corrugated horns for cosmic microwave background anisotropy measurements." International Journal of Infrared and Millimeter Waves, 21(12): 2023-2033, 2000.

Maffei B., Gleeson E., Murphy J.A., Písano G., "Study of corrugated Winston horns", Proc. SPIE 5498, Millimeter and Submillimeter Detectors for Astronomy II, 812, 2004.

Maffei B., Písano G., et al, "Effects of quasi-optical components on feed-horn co- and cross-polarisation radiation patterns", *Proc. SPIE* 7020, Millimeter and Submillimeter Detectors and Instrumentation for Astronomy IV, 70202H August 28, 2008.

Maffei B. et al, "Planck-HFI beam expectations from the optical optimisations of the focal plane", Astronomy & Astrophysics, 520, A12 ,2010a.

Maffei B., Noviello F., et al, "Planck-HFI optical design and pre-flight performances", Proc. of the Fourth European Conference on Antennas and Propagation (EuCAP), 2010b.

Maffei B., von Bieren A, de Rijk E., Ansermet J-P., Pisano G., Legg S., Macor A., " High performance WR-1.5 corrugated horn based on stacked rings", Proc. SPIE Astronomical Telescopes + Instrumentation 2014 Conference, Vol 9153, Millimeter, Submillimeter, and Far-Infrared Detectors and Instrumentation for Astronomy VII, 91532W, July 2014.

Mahon R.J. et al, "Digital holography at millimeter wavelengths", Optics Communications 260 (2006) 469-473, 2006.

Mahon R.J., "Modal Analysis of Millimetre-wave and Terahertz Imaging Systems.", PhD thesis, National University of Ireland Maynooth, 2011.

Murphy J.A. et al., "Radiation patterns of multi-moded corrugated horns for far-IR space applications", Infrared Phys. Technol. 42 515, 2001.

Murphy, J. A., Peacocke T., Maffei B., McAuley I., et al., "Multi-mode horn design and beam characteristics for the Planck satellite", Journal of Instrumentation, 2010 (5). Art. No. T04001. ISSN 1748-0221, 2010.

Netterfield C., Ade P., Bock J., Bond J., Borrill J., Boscaleri A., Coble K., Contaldi C., Crill B., De Bernardis P., et al., "A Measurement by BOOMERANG of Multiple Peaks in the Angular Power Spectrum of the Cosmic Microwave Background," The Astrophysical Journal, vol. 571, no. 2, p. 604, 2008.

Noviello, F., "Optical Performace of the ESA Planck Surveyor and Techniques for the Study of the Cosmic Microwave Background", Ph.D. thesis, NUI Maynooth, 2008.

Olver A.D. et al., "Microwave Horns and Feeds", IEEE Press, New York, 1994.

O'Sullivan C., Murphy J.A., Mc Auley I., Wilson D., Gradziel M., Trappe N., Cahill F., Peacocke T., Savini G., Ganga K., "Optical modelling of far-infrared astronomical instrumentation exploiting multimode horn antennas", Proc. SPIE 9153, Millimeter, Submillimeter, and Far-Infrared Detectors and Instrumentation for Astronomy VII, 91532V, July 2014

Peacocke, T., "The Modelling of Scattering in Corrugated Waveguides", Ph.D. thesis, NUI Maynooth, 2012.

Penzias, A., Wilson, R., "Measurement of Excess Antenna Temperature at 4080 Mc/s.", The Astrophysical Journal, vol. 142, pp. 419 - 421, 1965.

Planck Collaboration, "The Scientific Programme of Planck (Bluebook)", ESA, 2005 http://www.cosmos.esa.int/web/planck/publications

Planck Collaboration, "Planck 2013 results. I. Overview of Products and Scientific Results", Astronomy & Astrophysics, Volume: 571 Article Number A1, 2014a. http://www.cosmos.esa.int/web/planck/publications

Planck Collaboration, "Planck 2013 results. VII. HFI time response and beams", Astronomy & Astrophysics Astronomy & Astrophysics, Volume: 571 Article Number A7, 2014b. http://www.cosmos.esa.int/web/planck/publications

Planck Collaboration, "Planck 2013 results. XI. All-sky model of thermal dust emission", Astronomy & Astrophysics Astronomy & Astrophysics, Volume: 571 Article Number A11, 2014c http://www.cosmos.esa.int/web/planck/publications

Planck Collaboration, "Planck 2013 results. XIV. Zodiacal Emission", Astronomy & Astrophysics Astronomy & Astrophysics, Volume: 571 Article Number A14, 2014d. http://www.cosmos.esa.int/web/planck/publications

Planck Collaboration, "Planck 2013 results. XX. Cosmology from Sunyaev–Zeldovich cluster counts", Astronomy & Astrophysics Volume: 571 Article Number A20, 2014e. http://www.cosmos.esa.int/web/planck/publications

Planck Collaboration, "Planck 2013 results. XXX. Cosmic infrared background measurements and implications for star formation", Astronomy Astronomy & Astrophysics Astronomy & Astrophysics, Volume: 571 Article Number A30, 2014f. http://www.cosmos.esa.int/web/planck/publications

Planck Collaboration, "Planck 2015 results. I. Overview of products and scientific results", eprint arXiv:1502.01582, 2015a.

Planck Collaboration, "Planck intermediate results XIX, An overview of the polarized thermal emissions from Galactic dust.", Astronomy & Astrophysics, Volume: 576, A104, 2015b

Planck Collaboration, "Planck intermediate results. XXXII, The relative orientation between the magnetic field and structures traced by interstellar dust", Astronomy & Astrophysics manuscript no. PIPXXXII, 2015c

Planck Collaboration, "Planck 2015 results XXVIII, The Planck Catalogue of Galactic Cold Clumps", eprint arXiv:1502.01599, 2015d

Puget J., "Planck Intro - Ecole Doctoral", 2013.

QUaD collaboration, "Second and third season QUaD CMB temperature and polarization power spectra", Astrophys. J. 692:1247-1270, 2009.

Smoot G., Gorenstein M., and Muller R., "Detection of Anisotropy in the Cosmic Blackbody Radiation," Physical Review Letters, vol. 39, no. 14, p. 898-901, 1977.

Smoot G., Bennett C., Kogut A., Wright E., Aymon J., Boggess N., Cheng E., De Amici G., Gulkis S., Hauser M., et al., "Structure in the COBE Differential Microwave Radiometer First-Year Maps," The Astrophysical Journal, vol. 396, p. L1-L5, 1992.

Smoot G., "Microwave Foregrounds", ASP Conference Series #181, ed. A. de Oliveira-Costa and M. Tegmark ISBN 1-58381-006-4, p.61, 1999

Spergel D.N., Verde L., et al., "First Year Wilkinson Microwave Anisotropy Probe (WMAP ) Observations: Determination of Cosmological Parameters", Astrophys. J.Suppl. 148:175-194, 2003.

SMT, http://www.smtconsultancies.co.uk/products/corrug/corrug.php, Accessed: 12-02-2016

Tamminen, A., Ala-Laurinaho, J., Räisänen,A.V., "Indirect holographic imaging at 310 GHz", Proc 5th European Radar Conference, 168-171, 2008.

Tauber J.A., "The Planck Mission' Advances in Space Research", 2003

Tauber, J. A., Norgaard-Nielsen, H. U., Ade, P. A. R., et al., "Planck pre-launch status: The Planck Mission", Astronomy & Astrophysics Volume: 520 Article Number: A1 DOI: 10.1051/0004-6361/200912983 Published: SEP-OCT 2010a.

Tauber, J. A., Norgaard-Nielsen, H. U., Ade, P. A. R., et al., "Planck pre-launch status: The optical system", ASTRONOMY & ASTROPHYSICS Volume: 520 Article Number: A2 DOI: 10.1051/0004-6361/200912911 Published: SEP-OCT 2010b.

TICRA, http://www.ticra.com/ , Accessed: 10-02-2016

Toal V., "Introduction to holography", CRC Press, 2012

Villa, F., et al. "High Performances Corrugated Feed Horns for Space Applications at Millimetre Wavelengths", Experimental Astronomy, no. 14, p. 1-15, 2002

Wayne H., White M., "A CMB polarization primer", New Astronomy 2, 323–344, 1997.

Welford W. T., Winston R., " The optics of nonimaging concentrators : light and solar energy", New York : Academic Press, 1978.

Wilson, D., "Quasi-Optical Modelling of Telescope System for Planck and STERMR", Ph.D. thesis, NUI Maynooth, 2014

Withington,S., Hobson,M.P., Berry, R.H., "Representing the behavior of partially coherent optical systems by using overcomplete basis sets" Journal of the Optical Society of America, Vol. 21, No. 2, February 2004.

Yurchenko V.B. et al. "Double-sided split-step MM-wave Fresnel lenses: design, fabrication and focal field measurements", Journal of the European Optical Society - Rapid Publications, Europe, V.9, February 2014.

# Publications

McAuley I., Young L., et al, 'Millimetre-wave and Terahertz Imaging Systems with Medical Applications' Proc. IRMMW-THz 2006, Shanghai.

Mc Auley I., Murphy J. A., et al, 'Applications of holography in the millimeter-wave and terahertz region', *Proc. SPIE 7938, 79380H* (2011)

Mc Auley I., Murphy J.A., Wilson D., O'Sullivan C., "Optical Modelling of the Planck Multimode Channels", submitted Proceedings of the International School of Physics "Enrico Fermi", Course 186 " New Horizons for Observational Cosmology", SIF, 2013

Mc Auley I., Murphy J.A., et al, "Determination of the Phase Centers of Millimeter-Wave Horn Antennas Using a Holographic Interference Technique", Journal of Infrared, Millimeter, and Terahertz Waves, January 2016.

Maffei B., Noviello F., et al, "Planck-HFI optical design and pre-flight performances", Proc. of the Fourth European Conference on Antennas and Propagation (EuCAP), 2010.

Maffei B. et al, "Planck-HFI beam expectations from the optical optimisations of the focal plane", Astronomy & Astrophysics, 520, A12 ,2010.

Murphy J. A., Peacocke T., Maffei B., Mc Auley I., et al., "Multi-mode horn design and beam characteristics for the Planck satellite", Journal of Instrumentation, 2010 (5). Art. No. T04001. ISSN 1748-0221, 2010.

Murphy J. A, McAuley I., McCarthy D., et al "Quasi-Optical Phase Retrieval of Radiation Patterns of Non-Standard Horn Antennas At Millimetreand Submillimetre Wavelengths," EUCAP-2015, 9th European Conference on Antennas and Propagation, Lisbon, (2015)

O'Sullivan C., Murphy J.A., Mc Auley I., Wilson D., Gradziel M., Trappe N., Cahill F., Peacocke T., Savini G., Ganga K., "Optical modelling of far-infrared astronomical instrumentation exploiting multimode horn antennas", Proc. SPIE 9153, Millimeter, Submillimeter, and Far-Infrared Detectors and Instrumentation for Astronomy VII, 91532V, July 2014

Planck HFI Core Team, " Planck early results. VI. The High Frequency Instrument data processing", A&A, Volume 536, December 2011.

# Appendix A

This appendix contains an extensive list of past, current, and future CMB experiments. The list is arranged chronologically and cover the time frame from 1982 to the present day. The start and end date of the each experiment is given along with whether it was a ground based, airbourne, or space mission and the its location. The detector technology is also provided, as is the main aims or results of the experiment.

| Name | Start | End | Basis | Location | Frequency (GHz) | Detector Technology | Targets |
|---|---|---|---|---|---|---|---|
| Cobra | 1982 | 1990 | Sounding Rocket | University of British Columbia | 27-900 | Bolometers/ FTS | Frequency spectrum of CMB |
| RELIKT-1 | 1983 | 1984 | Space | Earth orbit | 37 | | Temperature anisotropies |
| Tenerife Experiment | 1984 | 2000 | Ground | Tenerife | 10, 15, 33 | HEMT | Temperature anisotropies from degree to arcminute angular scales |
| ARGO | 1988, 1990, 1993 | 1993 | Balloon | | 150-600 | Bolometer | |
| Berkeley-Illinois-Maryland Association (BIMA) | 1986 | 2004 | Ground | | 70-116; 210-270 | SIS | |
| Advanced Cosmic Microwave Explorer (ACME) | 1988 | 1996 | Ground | | 26–35; 38–45 | HEMT | Temperature anisotropies |
| Also HACME: HEMT+ACME | 1988 | 1996 | Ground | | 26–35; 38–46 | HEMT | |

| | | | | | | | |
|---|---|---|---|---|---|---|---|
| Cosmic Background Explorer (COBE) | 1989 | 1993 | Space | Earth orbit | 31.5, 53, 90 (DMR) | | Temperature anisotropies; frequency power spectrum; solar system and galactic dust foregrounds |
| Far Infra-Red Survey (FIRS) | 1989 | 1989 | Balloon | National Scientific Balloon Facility, Fort Sumner, New Mexico | 170-680 | Bolometer | Temperature anisotropy on large angular scales. |
| Australia Telescope Compact Array (ATCA) | 1991 | 1997 | Ground | | 8.7 | HEMT | |
| Medium Scale Anisotropy Measurement (MSAM) | 1992 | 1997 | Balloon | | 150-650 | Bolometer | |
| Python | 1992 | 1997 | Ground | South Pole | 30-90 | HEMT / Bolometer | Temperature anisotropy on intermediate angular scales |
| Saskatoon experiment | 1993 | 1995 | Ground | Saskatchewan | 26-46 | HEMT | |
| Cosmic Anisotropy Telescope (CAT) | 1994 | 1997 | Ground | Mullard Radio Astronomy Observatory | 13-17 | Interferometer / HEMT | Very small scale fluctuations in small regions of the sky. |
| Antarctic Plateau Anisotropy Chasing Experiment (APACHE) | 1995 | 1996 | Ground | Antarctic | 100, 150, 250 | Bolometer | Temperature anisotropies |

| | Start | End | Type | Location | Frequency (GHz) | Detector | Notes |
|---|---|---|---|---|---|---|---|
| Balloon-borne Anisotropy Measurement (BAM) | 1995 | 1998 | Balloon | University of British Columbia and Brown University balloon experiment | 110-250 | Spectrometer | Used differential Fourier Transform Spectrometer to measure degree scale anisotropy |
| Millimeter Anisotropy eXperiment IMaging Array (MAXIMA) | 1995, 1998, 1999 | 1999 | Balloon | Near Palestine, Texas | 150-420 | Bolometer | Intermediate scale temperature fluctuations. |
| QMAP | 1996 | 1996 | Ground | | 30-140 | HEMT / SIS | |
| Sunyaev-Zeldovich Infrared Experiment (SuZIE) | 1996 | — | Ground | Caltech Submillimeter Observatory, Mauna Kea, Hawaii | 150, 220, 350 | Bolometer | SZ effect |
| Mobile Anisotropy Telescope (MAT) | 1997, 1998 | 1998 | Ground | Cerro Toco, Chile | 30-140 | HEMT / SIS | |
| BOOMERanG experiment | 1997 | 2003 | Balloon | Long-duration balloon above Antarctica | 90-420 | Bolometer | Intermediate scale fluctuations |
| COSMOSOMAS | 1998 | 2007 | Ground | Teide Observatory, Tenerife, Spain | Oct-18 | HEMT | Circular scanning experiments for CMB and foregrounds |
| Archeops | 1999 | 2002 | Balloon | | 143, 217, 353, 545 | Bolometer | Measured large and intermediate scale with improved precision at the larger scales. |

| | | | | | | | |
|---|---|---|---|---|---|---|---|
| Cosmological Gene | 1999 | 2009 | Ground | RATAN-600 telescope, Caucasus, Russia | 0.6 to 32 | HEMT | |
| Degree Angular Scale Interferometer (DASI) | 1999 | 2003 | Ground | South Pole | 26-36 | HEMT | Temperature and polarization anisotropy on degree angular scales |
| Background Emission Anisotropy Scanning Telescope (BEAST) | 2000 | — | Balloon, Ground | | 25-35; 38-45 | HEMT | A ground single dish CMB observatory at the University of California's White Mountain Peak Research station. |
| Cosmic Background Imager (CBI) | 2000 | 2008 | Ground | Llano de Chajnantor Observatory, Chile | 26-36 | HEMT | Very small scale temperature and polarization anisotropies in a small patch of sky. |
| Polarization Observations of Large Angular Regions (POLAR) | 2000 | 2000 | Ground | Pine Bluff, Wisconsin, USA | 26-46 | HEMT | Polarization at large angular scales |
| Absolute Radiometer for Cosmology, Astrophysics, and Diffuse Emission (ARCADE) | 2001 | 2006 | Balloon | | 3, 5, 7, 10, 30, 90 | HEMT | CMB Spectrum |
| Arcminute Cosmology Bolometer Array Receiver (ACBAR) | 2001 | 2008 | Ground | South Pole | 150, 219, 274 | Bolometer | Temperature anisotropies |
| Millimeter Interferometer (MINT) | 2001 | 2002 | Ground | Cerro Toco, Chile | 145 | SIS | Temperature anisotropies around multipole 1500 |

| | | | | | | | |
|---|---|---|---|---|---|---|---|
| TopHat | 2001 | 2001 | Balloon | Antarctica | 150-720 | Bolometer | |
| Wilkinson Microwave Anisotropy Probe (WMAP) | 2001 | 2010 | Space | Lagrange 2 | 23-94 | HEMT | Temperature anisotropies & Polarization |
| Cosmic Anisotropy Polarization Mapper (CAPMAP) | 2002 | 2008 | Ground | | 40, 90 | MMIC/HEMT | |
| Princeton I, Q, and U Experiment (PIQUE) | 2002 | 2002 | Ground | Princeton University | 90 | Bolometer | |
| Very Small Array | 2002 | 2008 | Ground | Tenerife | 26-36 | Interferometer / HEMT | Intermediate and small scale fluctuations in small regions of the sky. |
| KU-band Polarization IDentifier (KUPID) | 2003 | — | Ground | Crawford Hill Telescope, New Jersey | Dec-18 | HEMT | |
| Sunyaev-Zeldovich Array (SZA) | 2004 | 2008 | Ground | Owens Valley Radio Observatory | 26-36; 85-115 | Interferometer | Produced sensitive CMB anisotropy constraints at l ~ 4000, measured the SZ effect in 100s of galaxy clusters. Now part of CARMA |
| Arcminute Microkelvin Imager (AMI) | 2005 | — | Ground | UK: Mullard Radio Astronomy Observatory | Dec-18 | Interferometer | SZ effect, Temperature anisotropies |

| | Start | End | Type | Location | Frequency (GHz) | Detector | Purpose |
|---|---|---|---|---|---|---|---|
| QUaD | 2005 | 2007 | Ground | South Pole | 100, 150 | Bolometer | Polarization at intermediate angular scale |
| Background Imaging of Cosmic Extragalactic Polarization (BICEP1) | 2006 | 2008 | Ground | South Pole | 100, 150, 220 | Bolometer | Measured degree-scale polarization with improved precision. |
| South Pole Telescope | 2006 | | Ground | South Pole | | | Small scale temperature and polarization. |
| Array for Microwave Background Anisotropy (AMiBA) | 2007 | — | Ground | Hawaii: Mauna Loa | 86-102 | Interferometer/MMIC | SZ effect; Polarization |
| Atacama Pathfinder Experiment (APEX) | 2007 | — | Ground | | 150, 217 | Bolometer | Temperature anisotropies; SZ effect |
| Atacama Cosmology Telescope (ACT) | 2008 | — | Ground | Chile: Atacama Desert | 148, 218, 277 | Bolometer | Temperature anisotropies |
| Q/U Imaging ExperimenT (QUIET) | 2008 | 2010 | Ground | Llano de Chajnantor Observatory, Chile | 40, 90 | HEMT | |
| BICEP2 | 2009 | 2012 | Ground | South Pole | 150 | Bolometer | Degree-scale B-mode polarization. |
| Planck | 2009 | 2013 | Space | Lagrange 2 | 30-857 | HEMT / Bolometer | Temperature and polarization anisotropies; foregrounds |

| Atacama B-Mode Search (ABS) | 2012 | — | Ground | Chile: Atacama Desert | 145 | Bolometer | Polarization |
|---|---|---|---|---|---|---|---|
| The E and B Experiment (EBEX) | 2012 | 2013 | Balloon | Antarctica | 150-450 | Bolometer | Inflationary gravitational-wave background (IGB) signal in B-mode polarization |
| POLARBEAR | 2012 | — | Ground | Chajnantor plateau (Chile) | 150 | Antenna-coupled TES | CMB Polarization. Primordial and lensed B-modes. |
| Cosmology Large Angular Scale Surveyor (CLASS) | 2015 | - | Ground | Llano de Chajnantor Observatory, Chile | 40, 90, 150, 220 | TES Bolometer | B-mode polarization signal at multipoles from 2 to 100 |
| SPIDER | 2015 | | Balloon | Antarctica | 90, 150, 220 | Bolometer | Large scale polarization. |
| Qubic | Future | — | Ground | | 97, 150, 230 | Bolometer | B-mode polarization |

# Appendix B

Presented in this appendix are the visual inspection records from Cardiff University of the six Planck 857GHz horn antennas sets which were manufactured. Each set consists of a back to back horn pair, front PF857F-1* and back PF857B-1*, and a detector horn, PF857D-1*. Sets B,C,E, and F were chosen as the flight horns for the Planck satellite.

**Horn verification spreadsheet**
Horn name:                          Date: 09/05/05

PF857F - 1A

## I    PART 1 – VISUAL INSPECTION

Inspection under microscope to check for defaults in horn.

| From aperture side: Internal status | | |
|---|---|---|
| Job description | Comment | Status |
| State of corrugations | ✓ | OK |
| Check for non-dissolved Aluminium | Small swarfs and residues | |
| General state (Au coating, irregularities) | ✓ | OK |

| From waveguide section side: Internal status | | |
|---|---|---|
| Job description | Comment | Status |
| State of corrugations | Last half corrugation irregular + pressed down swarf of Cu | |
| Check for non-dissolved Aluminium | ✓ | OK |
| General state (Au coating, irregularities) | ✓ | OK |

| External status | | |
|---|---|---|
| Job description | Comment | Status |
| Check for dents | ✓ | OK |
| Check Au coating | N/A | |
| General state | ✓ | OK |
| Name engraved | PF857F - 1A | OK |

| Part 1 status: | |
|---|---|
| Action: | Ring swarf removed from WG section by PARA |

Verified by: GS          Signature: G. S.
Date: 09/05/05

282

Horn name:　　　　　　　　Date: 09/05/05

PF857F-1B

# I　　PART 1 – VISUAL INSPECTION

Inspection under microscope to check for defaults in horn.

| From aperture side: Internal status | | |
|---|---|---|
| Job description | Comment | Status |
| State of corrugations | Some small dents & or residues on flare corrugations | |
| Check for non-dissolved Aluminium | Many small swarfs and residues | |
| General state (Au coating, irregularities) | ✓ | OK |

| From waveguide section side: Internal status | | |
|---|---|---|
| Job description | Comment | Status |
| State of corrugations | Last corrugation very asymmetric | |
| Check for non-dissolved Aluminium | ✓ | OK |
| General state (Au coating, irregularities) | ✓ | OK |

| External status | | |
|---|---|---|
| Job description | Comment | Status |
| Check for dents | ✓ | OK |
| Check Au coating | N/A | |
| General state | ✓ | OK |
| Name engraved | PF857F-1B | OK |

| Part 1 status: | |
|---|---|
| Action: | Ring of Cu may removed @ WG section by PARA |

Verified by: GS　　　　　Signature:

Date: 09/05/05

1

283

**Horn verification spreadsheet**
Horn name:

Date: 09/05/05

PF857F-1C

CARDIFF
UNIVERSITY
PRIFYSGOL
CAERDY⑬

## I    PART 1 – VISUAL INSPECTION

Inspection under microscope to check for defaults in horn.

| From aperture side: Internal status | | |
|---|---|---|
| Job description | Comment | Status |
| State of corrugations | ✓ | OK |
| Check for non-dissolved Aluminium | Various curves and traces of residues at throat of horn | |
| General state (Au coating, irregularities) | ✓ | OK |

| From waveguide section side: Internal status | | |
|---|---|---|
| Job description | Comment | Status |
| State of corrugations | ✓ | OK |
| Check for non-dissolved Aluminium | ✓ | OK |
| General state (Au coating, irregularities) | ✓ | OK |

| External status | | |
|---|---|---|
| Job description | Comment | Status |
| Check for dents | ✓ | OK |
| Check Au coating | N/A | |
| General state | ✓ | OK |
| Name engraved | PF857F-1C | OK |

| Part 1 status: | |
|---|---|
| Action: | |

Verified by: GS          Signature: G.S.
Date: 09/05/05

1

284

**Horn verification spreadsheet**
Horn name: PF857F-ID                     Date: 09/05/05

## I    PART 1 – VISUAL INSPECTION

Inspection under microscope to check for defaults in horn.

| From aperture side: Internal status | | |
|---|---|---|
| **Job description** | **Comment** | **Status** |
| State of corrugations | ✓ | OK |
| Check for non-dissolved Aluminium | Residules of Al and traces of dirt at throat of horn | |
| General state (Au coating, irregularities) | ✓ | OK |

| From waveguide section side: Internal status | | |
|---|---|---|
| **Job description** | **Comment** | **Status** |
| State of corrugations | ✓ | OK |
| Check for non-dissolved Aluminium | ✓ | OK |
| General state (Au coating, irregularities) | ✓ | OK |

| External status | | |
|---|---|---|
| **Job description** | **Comment** | **Status** |
| Check for dents | ✓ | OK |
| Check Au coating | N/A | |
| General state | ✓ | OK |
| Name engraved | PF857F-ID | OK |

| | |
|---|---|
| **Part 1 status:** | |
| **Action:** | |

Verified by: GS          Signature: GS
Date: 09/05/05

1

**Horn verification spreadsheet**

Horn name: *PF857F-1E*          Date: *09/05/05*

CARDIFF
UNIVERSITY
PRIFYSGOL
CAERDYⱠ

## I    PART 1 – VISUAL INSPECTION

Inspection under microscope to check for defaults in horn.

| From aperture side: Internal status | | |
|---|---|---|
| Job description | Comment | Status |
| State of corrugations | ✓ | OK |
| Check for non-dissolved Aluminium | Residues and dirt in throat of horn | |
| General state (Au coating, irregularities) | ✓ | OK |

| From waveguide section side: Internal status | | |
|---|---|---|
| Job description | Comment | Status |
| State of corrugations | Last half corrugation @ waveguide not turned properly (pushed in) | |
| Check for non-dissolved Aluminium | ✓ | ok |
| General state (Au coating, irregularities) | ✓ | OK |

| External status | | |
|---|---|---|
| Job description | Comment | Status |
| Check for dents | ✓ | OK |
| Check Au coating | N/A | |
| General state | ✓ | OK |
| Name engraved | PF857F-1E | OK |

| Part 1 status: | |
|---|---|
| Action: | Ring of Cu swarf removed @ WS by PARA |

Verified by: *GS*          Signature: *G.S.*
Date: *09/05/05*

1

286

**Horn verification spreadsheet**
Horn name:          Date: 09/05/05

PF857F-1F

CARDIFF
UNIVERSITY
PRIFYSGOL
CAERDY  

## I     PART 1 – VISUAL INSPECTION

Inspection under microscope to check for defaults in horn.

| From aperture side: Internal status | | |
|---|---|---|
| **Job description** | **Comment** | **Status** |
| State of corrugations | ✓ | OK |
| Check for non-dissolved Aluminium | Some residules of Al in throat of horn | |
| General state (Au coating, irregularities) | ✓ | oK |

| From waveguide section side: Internal status | | |
|---|---|---|
| **Job description** | **Comment** | **Status** |
| State of corrugations | Ring swarf on last half corrugation | |
| Check for non-dissolved Aluminium | ✓ | OK |
| General state (Au coating, irregularities) | ✓ | OK |

| External status | | |
|---|---|---|
| **Job description** | **Comment** | **Status** |
| Check for dents | ✓ | OK |
| Check Au coating | N/A | |
| General state | ✓ | OK |
| Name engraved | PF857F-1F | OK |

| Part 1 status: | |
|---|---|
| Action: | Ring swarf removed by PARA |

Verified by: GS          Signature: G.S
Date: 09/05/05

1

287

**Horn verification spreadsheet**
Horn name:

PF857B-1A

Date: 10/5/5

## I    PART 1 – VISUAL INSPECTION

Inspection under microscope to check for defaults in horn.

| From aperture side: Internal status | | |
|---|---|---|
| Job description | Comment | Status |
| State of corrugations | ✓ | OK |
| Check for non-dissolved Aluminium | Some scratches and dirt by front of horn | |
| General state (Au coating, irregularities) | ✓ | OK |

| From waveguide section side: Internal status | | |
|---|---|---|
| Job description | Comment | Status |
| State of corrugations | 2 small cuts on last corrugation | |
| Check for non-dissolved Aluminium | ✓ | OK |
| General state (Au coating, irregularities) | ✓ | OK |

| External status | | |
|---|---|---|
| Job description | Comment | Status |
| Check for dents | ✓ | OK |
| Check Au coating | N/A | |
| General state | ✓ | OK |
| Name engraved | PF857B-1A | OK |

| | |
|---|---|
| Part 1 status: | |
| Action: | |

Verified by: GS

Signature: G.S.

Date: 10/5/5

1

288

**Horn verification spreadsheet**
**Horn name:**                        Date: 10/5/5

PF857B-1B

## I    PART 1 – VISUAL INSPECTION

Inspection under microscope to check for defaults in horn.

| From aperture side: Internal status | | |
|---|---|---|
| **Job description** | **Comment** | **Status** |
| State of corrugations | ✓ | OK |
| Check for non-dissolved Aluminium | Traces of Al residues | |
| General state (Au coating, irregularities) | ✓ | OK |

| From waveguide section side: Internal status | | |
|---|---|---|
| **Job description** | **Comment** | **Status** |
| State of corrugations | ✓ | OK |
| Check for non-dissolved Aluminium | ✓ | OK |
| General state (Au coating, irregularities) | ✓ | OK |

| External status | | |
|---|---|---|
| **Job description** | **Comment** | **Status** |
| Check for dents | ✓ | OK |
| Check Au coating | N/A | |
| General state | ✓ | OK |
| Name engraved | PF857B-1B | OK |

| | |
|---|---|
| **Part 1 status:** | |
| **Action:** | |

Verified by: GS          Signature: G.S.
Date: 10/5/5                                               1

289

**Horn verification spreadsheet**
Horn name:                                    Date:        10/5/5

PF857B·1C

## I    PART 1 – VISUAL INSPECTION

Inspection under microscope to check for defaults in horn.

| From aperture side: Internal status | | |
|---|---|---|
| Job description | Comment | Status |
| State of corrugations | ✓ | OK |
| Check for non-dissolved Aluminium | traces of Al | |
| General state (Au coating, irregularities) | ✓ | OK |

| From waveguide section side: Internal status | | |
|---|---|---|
| Job description | Comment | Status |
| State of corrugations | ✓ | OK |
| Check for non-dissolved Aluminium | ✓ | OK |
| General state (Au coating, irregularities) | ✓ | OK |

| External status | | |
|---|---|---|
| Job description | Comment | Status |
| Check for dents | ✓ | OK |
| Check Au coating | N/A | |
| General state | ✓ | OK |
| Name engraved | PF857B - 1C | OK |

| Part 1 status: | |
|---|---|
| Action: | |

Verified by: GS          Signature: S.S
Date:    10/5/5                                              1

**Horn verification spreadsheet**
Horn name:

PF857B-1D

Date: 12/5/5

## I   PART 1 – VISUAL INSPECTION

Inspection under microscope to check for defaults in horn.

| From aperture side: Internal status | | |
|---|---|---|
| Job description | Comment | Status |
| State of corrugations | ✓ | OK |
| Check for non-dissolved Aluminium | Traces of Al residules | |
| General state (Au coating, irregularities) | ✓ | OK |

| From waveguide section side: Internal status | | |
|---|---|---|
| Job description | Comment | Status |
| State of corrugations | ✓ | OK |
| Check for non-dissolved Aluminium | ✓ | OK |
| General state (Au coating, irregularities) | ✓ | OK |

| External status | | |
|---|---|---|
| Job description | Comment | Status |
| Check for dents | ✓ | OK |
| Check Au coating | N/A | |
| General state | ✓ | OK |
| Name engraved | PF857B-1D | OK |

| Part 1 status: | |
|---|---|
| Action: | |

Verified by: GS        Signature: G.S.

Date: 12/5/5

291

**Horn verification spreadsheet**
Horn name:

Date: 10/5/5

PF857B-1E

## I  PART 1 – VISUAL INSPECTION

Inspection under microscope to check for defaults in horn.

| From aperture side: Internal status | | |
|---|---|---|
| Job description | Comment | Status |
| State of corrugations | / | OK |
| Check for non-dissolved Aluminium | ✓ | OK |
| General state (Au coating, irregularities) | ✓ | OK |

| From waveguide section side: Internal status | | |
|---|---|---|
| Job description | Comment | Status |
| State of corrugations | ✓ | OK |
| Check for non-dissolved Aluminium | ✓ | OK |
| General state (Au coating, irregularities) | ✓ | OK |

| External status | | |
|---|---|---|
| Job description | Comment | Status |
| Check for dents | ✓ | OK |
| Check Au coating | N/A | |
| General state | ι | OK |
| Name engraved | PF257B - 1E | OK |

| Part 1 status: | |
|---|---|
| Action: | |

Verified by: GS          Signature: SS
Date: 10/5/5

1

292

Horn verification spreadsheet
Horn name:

PF857B-1F

Date: 10/5/5

**CARDIFF**
UNIVERSITY
PRIFYSGOL
CAERDYⒷ

# I    PART 1 – VISUAL INSPECTION

Inspection under microscope to check for defaults in horn.

| From aperture side: Internal status | | |
|---|---|---|
| **Job description** | **Comment** | **Status** |
| State of corrugations | | OK |
| Check for non-dissolved Aluminium | Small swarfs of Al stuck in wing | |
| General state (Au coating, irregularities) | ✓ | OK |

| From waveguide section side: Internal status | | |
|---|---|---|
| **Job description** | **Comment** | **Status** |
| State of corrugations | 2 small dents on last corrugation | |
| Check for non-dissolved Aluminium | Traces of dirt or Al residues. | |
| General state (Au coating, irregularities) | ✓ | OK |

| External status | | |
|---|---|---|
| **Job description** | **Comment** | **Status** |
| Check for dents | ✓ | OK |
| Check Au coating | N/A | |
| General state | ✓ | OK |
| Name engraved | PF857B-1F | OK |

| Part 1 status: | |
|---|---|
| Action: | |

Verified by: GS          Signature: G. S.
Date: 10/5/5

I

293

**Horn verification spreadsheet**
Horn name:                                           Date: 19/04/05

PF857D-1A

## I     PART 1 – VISUAL INSPECTION

Inspection under microscope to check for defaults in horn.

| From aperture side: Internal status | | |
|---|---|---|
| Job description | Comment | Status |
| State of corrugations | √ | OK |
| Check for non-dissolved Aluminium | √ | OK |
| General state (Au coating, irregularities) | √ | OK |

| From waveguide section side: Internal status | | |
|---|---|---|
| Job description | Comment | Status |
| State of corrugations | Irregular last half-corrugation Possible swarf of Cu | |
| Check for non-dissolved Aluminium | √ | OK |
| General state (Au coating, irregularities) | √ | OK |

| External status | | |
|---|---|---|
| Job description | Comment | Status |
| Check for dents | Scratch / Mark at exit aperture | |
| Check Au coating | N/A | |
| General state | √ | OK |
| Name engraved | PF857D-1A | OK |

| Part 1 status: | |
|---|---|
| Action: | |

Verified by: GS                  Signature: J.d.
Date: 19/04/05

1

**Horn verification spreadsheet**
Horn name:

Date: 19/04/05

PF857D-1B

## I    PART 1 – VISUAL INSPECTION

Inspection under microscope to check for defaults in horn.

| From aperture side: Internal status | | |
|---|---|---|
| Job description | Comment | Status |
| State of corrugations | ✓ | OK |
| Check for non-dissolved Aluminium | ✓ | OK |
| General state (Au coating, irregularities) | ✓ | OK |

| From waveguide section side: Internal status | | |
|---|---|---|
| Job description | Comment | Status |
| State of corrugations | Very irregular 1st corrugation and 1/2. Possible Cu smurf present | |
| Check for non-dissolved Aluminium | ✓ | OK |
| General state (Au coating, irregularities) | ✓ | OK |

| External status | | |
|---|---|---|
| Job description | Comment | Status |
| Check for dents | Scratch a mark at exit aperture | |
| Check Au coating | N/A | |
| General state | ✓ | OK |
| Name engraved | PF857D-1B | OK |

| Part 1 status: | |
|---|---|
| Action: | |

Verified by: GS          Signature: GS.

Date: 19/04/05

295

1

**Horn verification spreadsheet**
Horn name:

PF857D-1D

Date:

19/04/05

## I    PART 1 – VISUAL INSPECTION

Inspection under microscope to check for defaults in horn.

| From aperture side: Internal status | | |
|---|---|---|
| Job description | Comment | Status |
| State of corrugations | ✓ | OK |
| Check for non-dissolved Aluminium | ✓ | OK |
| General state (Au coating, irregularities) | Streaks of Au plating missing | ~~~~ |

| From waveguide section side: Internal status | | |
|---|---|---|
| Job description | Comment | Status |
| State of corrugations | Irregular first ½ corrugation | |
| Check for non-dissolved Aluminium | ✓ | OK |
| General state (Au coating, irregularities) | ✓ | OK |

| External status | | |
|---|---|---|
| Job description | Comment | Status |
| Check for dents | Various scratches at aperture of horn | |
| Check Au coating | N/A | |
| General state | ✓ | OK |
| Name engraved | PF857D-1D | OK |

| Part 1 status: | |
|---|---|
| Action: | |

Verified by:   GS
Date:   19/04/05

Signature: GS

1

**Horn verification spreadsheet**
Horn name:

PF857D-1E

Date: 19/04/05

## I   PART 1 – VISUAL INSPECTION

Inspection under microscope to check for defaults in horn.

| From aperture side: Internal status | | |
|---|---|---|
| Job description | Comment | Status |
| State of corrugations | √ | OK |
| Check for non-dissolved Aluminium | √ | OK |
| General state (Au coating, irregularities) | √ | OK |

| From waveguide section side: Internal status | | |
|---|---|---|
| Job description | Comment | Status |
| State of corrugations | √ | OK |
| Check for non-dissolved Aluminium | √ | OK |
| General state (Au coating, irregularities) | √ | OK |

| External status | | |
|---|---|---|
| Job description | Comment | Status |
| Check for dents | √ | OK |
| Check Au coating | N/A | |
| General state | √ | OK |
| Name engraved | PF857D-1E | OK |

| Part 1 status: | |
|---|---|
| Action: | |

Verified by: GS          Signature: _GS._

Date: 19/04/05

1

297

**Horn verification spreadsheet**

Horn name:

PF857D-1F

Date: 27/06/05

## I    PART 1 – VISUAL INSPECTION

Inspection under microscope to check for defaults in horn.

| From aperture side: Internal status | | |
|---|---|---|
| Job description | Comment | Status |
| State of corrugations | A few Bent or non well-formed corrug. at aperture + A Patch of stripped corrugations protruding In the horn | !!! |
| Check for non-dissolved Aluminium | | |
| General state (Au coating, irregularities) | See above | |

| From waveguide section side: Internal status | | |
|---|---|---|
| Job description | Comment | Status |
| State of corrugations | Last corrugation presents multiple dents | ! |
| Check for non-dissolved Aluminium | ✓ | o/K |
| General state (Au coating, irregularities) | ✓ | oK |

| External status | | |
|---|---|---|
| Job description | Comment | Status |
| Check for dents | ✓ | oK |
| Check Au coating | N/A | |
| General state | | |
| Name engraved | PF857D-1F | OK |

| Part 1 status: | |
|---|---|
| Action: | Check Special Data for conformance |

Verified by: GS          Signature: G. S.

Date: 27/06/05

1

298